

ERZİNCAN UNIVERSITY JOURNAL OF SCIENCE AND TECHNOLOGY

ISSN: 1307-9085, e-ISSN: 2149-4584

EDITOR IN CHIEF

Assoc. Prof. Dr. Kemal Volkan ÖZDOKUR
Erzincan Binali Yıldırım University

ASSOCIATE EDITORS

Assoc. Prof. Dr. Özlem BARAN ACIMERT
Erzincan Binali Yıldırım University

Ass. Prof. Dr. Fidan ERDEN KARAOĞLAN
Erzincan Binali Yıldırım University

EDITORIAL BOARD

Prof. Dr. Ali Ercan EKİNCİ

Erzincan Binali Yıldırım University

Prof. Dr. Bülent ÇAĞLAR

Erzincan Binali Yıldırım University

Prof. Dr. Suat ÇOLAK

Erzincan Binali Yıldırım University

Prof. Dr. Yeşim KARASULU

Ege University

Assoc. Prof. Dr. Fulya ASLAY

Erzincan Binali Yıldırım University

Ass. Prof. Dr. Agah Oktay ERTAY

Erzincan Binali Yıldırım University

Assoc. Prof. Dr. Neşe ERTUGAY

Erzincan Binali Yıldırım University

Prof. Dr. Salih DOĞAN

Erzincan Binali Yıldırım University

Ass. Prof. Dr. Emre YAVUZ

Erzincan Binali Yıldırım University

Doç. Dr. Tuba AKKUŞ

Erzincan Binali Yıldırım University

Doç. Burcu BOZKURT ÇIRAK

Erzincan Binali Yıldırım University

Ass. Prof. Dr. Vael HAJAHMAD

Erzincan Binali Yıldırım University

Prof. Dr. Süleyman KOÇAK

Manisa Celal Bayar University

Assoc. Prof. Dr. Özgür ARAR

Ege University

**Ass. Prof. Dr. Burçin
TÜRKMENOĞLU**

Erzincan Binali Yıldırım University

Ass. Prof. Dr. Mehmet KUZUCU

Erzincan Binali Yıldırım University

Assoc. Prof. Dr. Tülay ERİŞİR

Erzincan Binali Yıldırım University

Prof. Dr. Öztekin ALGÜL

Mersin University

Ass. Prof. Dr. İrem BOZBEY MERDE

Erzincan Binali Yıldırım University

Ass. Prof. Dr. Arif Onur EDEN

Erzincan Binali Yıldırım University

Ass. Prof. Dr. Mert KARAOĞLAN

Erzincan Binali Yıldırım University

Ass. Prof. Dr. Ali CELEN

Erzincan Binali Yıldırım University

Ass. Prof. Dr. Mehmet Kürşat ÖKSÜZ

Erzincan Binali Yıldırım University

Ass. Prof. Dr. Deniz ELMACI

Dokuz Eylül University

Assoc. Prof. Dr. İsmail TONTUL

Necmettin Erbakan University

Ass. Prof. Dr. Ülgen İlknur KONAK

Avrasya University

Ass. Prof. Dr. Fundagül EREM

Zonguldak Bülent Ecevit University

Ass. Prof. Dr. Takaichi WATANABE

Okayama University

**Ass. Prof. Dr. Ayşenur KELEŞ
DAYAUÇ**

Hitit University

Assoc. Prof. Dr. Aykut ÖZGÜR

Tokat Gaziosmanpaşa University

Ass. Prof. Dr. M. Mustafa ÇETİN

Kadir Has University

Res. Ass. Zehra ÖKSÜZ

Mersin University

**Assoc. Prof. Dr. Kemal
BUHARALIOĞLU**

İzmir Katip Çelebi University

**Assoc. Prof. Dr. Hayrettin Ozan
GÜLCAN**

Eastern Mediterranean University

Prof. Dr. Seyhan ŞAHAN FIRAT

Mersin University

Marin MARİN

Transylvania University of Braşov

Sorin VLASE

Transylvania University of Braşov

Prof. Dr. Alper SEZER

Ege University

AIMS AND SCOPE

The aim of the **Erzincan University Journal of Science and Technology** is to publish original research articles and reviews made in the fields of Science, Engineering in order to create a quality academic contribution in these fields.

Research areas covered in the journal:

- Physics, Chemistry, Biology, Mathematics and related areas
- Mechanical, Electrics-Electronics, Civil and related engineering areas
- Health sciences and related areas

Open Access Policy

Erzincan University Journal of Science and Technology is an open access journal which means that all content is freely available without charge to the user or his/her institution. Users are allowed to read, download, copy, distribute, print, search, or link to the full texts of the articles, or use them for any other lawful purpose, without asking prior permission from the publisher or the author. Erzincan University Journal of Science and Technology signed the Budapest Open Access Declaration (<https://budapestopenaccessinitiative.org/>).

Editor in chief: Doç. Dr. Kemal Volkan ÖZDOKUR

Address: Department of Chemistry, Erzincan Binali Yıldırım University, Erzincan, Türkiye.

E-mail: fbedergierzincan@gmail.com

Publisher: Erzincan Binali Yıldırım University

Address: Erzincan Binali Yıldırım University, Erzincan, Türkiye.

RESEARCH ARTICLES:

Page	Manuscript Title Authors
308-326	Use of Activated and Modified Pumice Stone for Removal of Mercury (II) and Arsenic (III) Ions From Aqueous Solution Vedia Nüket Tirtom
327-337	Exploring the Impact of <i>Gypsophila perfoliata</i> L. Root Extract on Germination and Seedling Growth Parameters of Sweet Sorghum and Hungarian Vetch Muhammet İslam Işık <i>et al.</i>
338-352	A Generalization of Curve Mates: Normal Mate of a Curve Oğuzhan Çelik
353-363	Determination of Some Antioxidant Activity Values in Wines of <i>Vitis vinifera</i> L. Karalahna, Karasakız and Çavuş Grape Varieties Produced in Bozcaada Tuğba Güngör Ertuğral and Gülen Türker
364-376	Synthesis, Characterization and Investigation of Biological Activities of Schiff Base and Its Ni(II) Complex Obtained from 2-Benzoylpyridine and 3-Hydroxy-2-naphthoic hydrazide Murat Çınarlı
377-384	<i>MEFV</i> Gene Mutations in Familial Mediterranean Fever Patients: Erzincan Experience Abdussamed Yasin DEMİR and Özlem ADMIŞ
385-399	Biosynthesis of Naringenin@Cu (II), Zn (II) Hybrid Nanoflower: Anticancer Activity Assay Process Burcu Somtürk Yılmaz
400-409	Investigation of the Effect of Temperature on the Biofuel Performance of Hydrochar Obtained from Kidney Bean Shell Zeynep Yıldız Uzun
410-425	Evaluation of Pro-Drug Properties in a Novel Schiff Base-Incorporated Pt(II) Complex Salih Günnaz <i>et al.</i>
426-444	Energy Production from Flue Gas of Sinter Plant Circular Coolers Tuba Nur Akçalı <i>et al.</i>
445-459	Performance Analysis of NLP-Based Machine Learning Algorithms in Cyberbullying Detection Funda Akar

- 460-473 **All-Solid-State PVC-Membrane Cu(II)-Selective Potentiometric Microsensor Based on a Novel Calix[4]arene Derivative**
Cigdem CAY *et al.*
- 474-487 **Synthesis and Antitubercular Activities of Acetamide-substituted Benzazole Derivatives**
Sule GURSOY *et al.*
- 488-504 **Effect of Deposition Parameters on Structural and Mechanical Properties of Novel h-BN doped TiCrNbN Coatings**
Yaşar Sert and Tefvik Küçükömeroğlu
- 505-522 **Enhanced Production and Therapeutic Evaluation of TP4 Peptide in *Pichia pastoris* Against Hepatocellular Carcinoma HUH-7 Cells**
Seda Kilinc *et al.*
- 523-542 **Comparison of the Performance of Type-1 and Interval Type-2 Fuzzy PI Controllers for Liquid Level Control in a Coupled Tank System**
Hatice Nursoy and Abdullah Başçı
- 543-550 **Magnetic Properties of Borided Co-Cr-Mo Alloy**
Osman İyi *et al.*
- 551-562 **Lepton Flavor Violation of Tau Decays into Lepton-Gamma in the Minimal Supersymmetric Type-I Seesaw Model**
Vael Hajahmad and Rawad Alawadi
- 563-572 **Synthesis of Tungsten Disulfide on B-N-Doped Carbon Nanotubes to Enhance the Electrochemical Performance of Supercapacitors**
Yasar Ozkan Yesilbag *et al.*
- 573-584 **Assessment of Alternative International Organizations for Turkey Using Machine Learning Algorithms**
Ömer Çağrı Yavuz

Use of Activated and Modified Pumice Stone for Removal of Mercury (II) and Arsenic (III) Ions from Aqueous Solution

Vedia Nüket TİRTOM^{id}*

Manisa Celal Bayar University, Faculty of Science and Arts, Department of Chemistry, Muradiye 45140,
Manisa-TURKIYE

Received: 01/11/2023, Revised: 23/05/2024, Accepted: 28/05/2024, Published: 31/08/2024

Abstract

The removal of Hg (II) and As (III) ions from aqueous solutions using activated and modified pumice stone was investigated. The pH, temperature, and initial metal ion concentration, which are very important for removal studies, were investigated by batch method. The experiments showed that the equilibrium adsorption data fit well with the Freundlich isotherm model well for Hg (II) and As (III) ions. The negative values of $\Delta H^\circ = -199.92 \text{ kJ mol}^{-1}$ and $-78.15 \text{ kJ mol}^{-1}$ for mercury (II) and arsenic (III) ions indicate that the adsorption process is exothermic. ΔS° was calculated as $-267.85 \text{ J K}^{-1} \text{ mol}^{-1}$ for As (III) ions and the positive value of $\Delta S^\circ = 0.69 \text{ kJ K}^{-1} \text{ mol}^{-1}$ for Hg (II) ions. The negative value of $\Delta G^\circ = -405.14 \text{ kJ mol}^{-1}$ for Hg (II) ions and $-1.67 \text{ kJ mol}^{-1}$ for As (III) ions indicates that the adsorption is spontaneous. EDTA was found to be a good desorbent in desorption studies for the recovery of arsenic and Hg ions. The experiments show that pumice stone can be used for the removal of Hg (II) and As (III) in aqueous solution.

Keywords Adsorption, Arsenic, Mercury, Pumice stone, Wastewater

Sulu Çözeltiden Cıva (II) ve Arsenik (III) İyonlarının Uzaklaştırılması için Aktifleştirilmiş ve Modifiye Edilmiş Pomza Taşının Kullanımı

Öz

Aktifleştirilmiş ve modifiye edilmiş pomza taşı kullanılarak sulu çözeltilerden Hg (II) ve As (III) iyonlarının giderimi araştırılmıştır. Giderim çalışmaları için çok önemli olan pH, sıcaklık, başlangıç metal iyonu konsantrasyonu kesikli yöntemle araştırılmıştır. Deneysel, denge adsorpsiyon verilerinin Hg (II) ve As (III) iyonları için Freundlich izoterm modeline iyi uyduğunu göstermiştir. Cıva (II) ve arsenik (III) iyonları için $\Delta H^\circ = -199,92 \text{ kJ mol}^{-1}$ ve $-78,15 \text{ kJ mol}^{-1}$ değerlerinin negatif olması adsorpsiyon sürecinin ekzotermik olduğunu göstermektedir. ΔS° , As (III) iyonları için $-267,85 \text{ J K}^{-1} \text{ mol}^{-1}$ ve Hg (II) iyonları için $0,69 \text{ kJ K}^{-1} \text{ mol}^{-1}$ pozitif değeri olarak hesaplanmıştır. Hg (II) iyonları için $\Delta G^\circ = -405,14 \text{ kJ mol}^{-1}$ ve As (III) iyonları için $-1,67 \text{ kJ mol}^{-1}$ negatif değeri adsorpsiyonun istemli olduğunu göstermektedir. Arsenik ve Hg iyonlarının geri kazanımı için yapılan desorpsiyon çalışmalarında EDTA'nın iyi bir desorbent olduğu bulunmuştur. Deneysel, pomza taşının sulu çözeltide Hg (II) ve As (III) giderimi için kullanılabileceğini göstermektedir.

Anahtar Kelimeler: adsorpsiyon, arsenik, cıva, pomza taşı, atık sular

1. Introduction

Hg, a liquid metal, and organic mercury compounds (i.e. methylmercury chloride [MeHg(I)], C_2H_5ClHg , Me_2Hg and C_6H_5ClHg) have toxic effects on both the environment and humans [1]. Even at very low concentrations, mercury is hazardous to living organisms due to its accumulation in the food chain. Accumulation in animals and humans poses serious risks. The distribution of Hg in the environment is due to industrial activities such as mining, use of fossil fuels, use of mercury-containing raw materials containing mercury [2]. According to the European Union, the maximum permissible limit for mercury in drinking water is $1\mu gL^{-1}$ and the limit for wastewater discharge is $5\mu gL^{-1}$, as Hg (II) is considered a priority and hazardous pollutant [3]. Hg has adverse health effects such as direct effects on the central nervous system and kidney system, developmental movement and brain function disorders, muscle weakness, chest pain, shortness of breath, diarrhoea, vomiting [4,5]. Because of its high toxicity, mercury (As (III)) is receiving increasing attention worldwide. As (III) causes very serious problems in the body such as aspigmentation disorder, skin thickening, stomach pain, skin, lung, bladder and kidney cancer, and neurological disorders [6,7,8,9].

In the last century, the provision of clean water to people has become the most serious environmental problem due to the contamination of surface and wastewater with toxic metals [10]. Therefore, it is of great importance to carry out various studies to remove toxic metals such as Hg (II) and As (III) from water. It has also been reported that Hg (II) and As (III) have been removed from surface waters by various methods [3-11]. In recent years, several low-cost natural or modified mineral sorbents, such as activated alumina, red mud, quartz and fly ash, etc., have been investigated for the removal of toxic metals from water by adsorption [12]. One such inexpensive material is pumice. Pumice stone (PS) is a lightweight volcanic rock with a pore volume of up to 85% formed during explosive eruptions [13]. As pumice is an inexpensive, naturally abundant and porous material with a large surface area, it is thought to be very suitable as an adsorbent [14,15]. PS was activated with H_2SO_4 (APS). For the removal of As (III), PS was modified with $FeCl_3 +$ pumice, $FeCl_3 + NaOH$ (MPS). In this study, activated pumice stone (APS) and modified pumice stone MPS were investigated for the removal of Hg (II) and As(III). Several studies were carried out on the effect of agitating time, pH, temperature, initial concentration, isotherms, and kinetics on adsorption. Freundlich and Langmuir isotherm models were applied to elucidate the adsorption. Desorption studies were carried out for the to evaluate the possible metal recovery from APS and MPS by EDTA, HCl and HNO_3 . Surface morphology characterization was carried out by FTIR and SEM analysis. These results indicate the possibility of using APS and MPS for the removal of Hg (II) and As (III) ions in aqueous solution.

2. Materials and Methods

2.1.Reagent

All reagents were of analytical grade. Hg was purchased from Merck, HNO_3 (Merck), $K_2Cr_2O_7$ (Carlo Erba), DW (Milipore), $SnCl_2$ (Merck), As_2O_3 (Merck), NaOH (Sigma-Aldrich), $NaBH_4$ (Merck), Na_2HPO_4 (Merck), NaH_2PO_4 (Merck), NH_3 (Merck), NH_4Cl (Merck). $FeCl_3$ (Merck).1g

of Hg was dissolved in 10 mL of concentrated HNO₃, 0.3 mL of 5% K₂Cr₂O₇ solution was added to prevent adsorption of glass and diluted to 1 L with DW to give 1000 mgL⁻¹ of Hg (II) solution. Dilutions of 1000 mg L⁻¹ solution were made to obtain standard solutions for Hg (II) measurements. 3% w/v solution of SnCl₂ solution was freshly prepared to reduce Hg (II) ions. To prepare a 1000 mg/L As (III) stock solution, 0.3301 ± 0.0002 g As₂O₃ was weighed. After adding 10% NaOH until As₂O₃ dissolved, it was acidified with concentrated HCl solution. 1 g of NaBH₄ was dissolved in 0.5% NaOH solution, and the volume was made up to 100 mL with the same solution. This solution was freshly prepared for each analysis. The following buffer solutions were used at a concentration of 0.1 mol L⁻¹ were used to adjust the pH: acetic acid/sodium acetate (pH 4.0–6.0), Na₂HPO₄-NaH₂PO₄ (pH 6.0–7.0) and NH₃-NH₄Cl (pH 8.0–9.0). The water used to prepare of the solutions and as carrier solution was DW. All glass containers were soaked in 10% nitric acid for 24 hours and rinsed with DW to remove Hg (II) and As (III) and to prevent cross-contamination.

2.2. Instruments

Hg (II) and As (III) concentrations were measured using a Varian 220 FS atomic absorption spectrophotometer (AAS). The AAS equipped with a Hg and As Hallow cathode lamp at the 253.7 nm, 217.6 nm wavelength was used for the determination of Hg (II) and As (III) in sample solutions. VGA-77 model hydride system with quartz cell was used for cold generation of Hg vapour and hybrid generation of arsine vapor. Hanna P211 microprocessor pH meter was used to measure the pH of the solutions.

2.3. Preparation of APS and MPS

PS samples were obtained from the Isparta region of Turkey. Prior to use in the experiments, the PS samples were crushed and sieved through a 200 mesh sieve. It was observed that some colouring substances in the structure of the adsorbents dissolved and leached into the water, and to remove this, they were washed and dried with DW until no longer gave off colour. PS was refluxed with 1 M 250 mL of H₂SO₄ at 80 °C for 8 hours, filtered, washed with DW, and dried to complete the activation process. 10 grams of the washed PS was taken and treated with 0.5 M 50 mL FeCl₃ solution for 12 hours for arsenic (III) adsorption. FeCl₃ is a dark brown-yellow acidic crystalline substance (pH<3). FeCl₃ has good solubility in water and undergoes hydrolysis to hydrochloric acid and iron hydroxide when in solution. The other modification process for arsenic adsorption was carried out by taking 10 grams of adsorbent and using 0.5 M 25 mL FeCl₃ and 0.2 M 25 mL NaOH solutions together. All modified adsorbents were decanted from the solution, washed with DW and dried.

2.4. Batch Adsorption Experiments

Adsorption experiments were performed using the batch technique. For Hg (II) adsorption, 0.10±0.02 g APS was added to a beaker containing 25 mL of 100 mg L⁻¹ Hg (II) solution and the suspension was mixed. For As (III) adsorption studies, 0.10±0.02 g MPS was added to another beaker containing 25 mL of 50 mg L⁻¹ As (III) and the suspension was mixed. After decantation, the concentration of Hg (II) and As (III) ions was analyzed by AAS using the vapour generation method. The effect of agitating time was studied at 5-150 min. for Hg (II) and 5-120 min for As

(III) ions. The effect of pH was studied in the pH range of 3.0-8.0 for Hg (II) ions and As (III) ions. Isotherm studies were performed with a constant APS and MPS weight of 0.10 ± 0.02 g and varying initial concentrations in the range of 25–1000 mg L⁻¹ for Hg (II) ions, 20-1500 mg L⁻¹ for As (III) ions. All the experiments were performed in duplicate.

The percentage adsorption of Hg(II) and As(III) ions on APS and MPS from aqueous solution was calculated according to equation (1):

$$\% A = \frac{C_{int} - C_{fin}}{C_{int}} \times 100 \dots \dots \dots (1)$$

C_{int} is the initial concentration of Hg(II) and As(III) (mg L⁻¹), C_{fin} is the final concentration of Hg(II) and As(III) (mg L⁻¹).

2.5. Desorption and Regeneration Studies

When equilibrium was reached, the Hg (II) saturated APS and As (III) saturated MPS were decanted from the solution and placed in 50 mL beakers containing 25 mL (0.05-0.15 M) HCl, HNO₃ and EDTA solution and shaken at 150 rpm for 30 min at 35 °C. The APS and MPS were then decanted by centrifugation. The concentrations of Hg (II) and As (III) in aqueous solution were determined by CVAAS.

3. Results and Discussion

3.1 Characterizations Studies

3.1.1. FTIR spectroscopy

The FTIR spectra of the APS and MPS adsorbents are shown in Figure 1. The peak at 3545 cm⁻¹ in Figure 1(a) is related to the O-H stretching vibration [16]. The peaks at 1118 cm⁻¹ belong to the stretching vibrations of C-O [17]. The peaks at 2239 cm⁻¹ are characteristic bands belonging to the C-N bending vibration in Figure 1(b), a peak at 800-400 cm⁻¹ can be associated with Si-O stretching [18], bending and Al-O stretching, bending and bending, respectively.

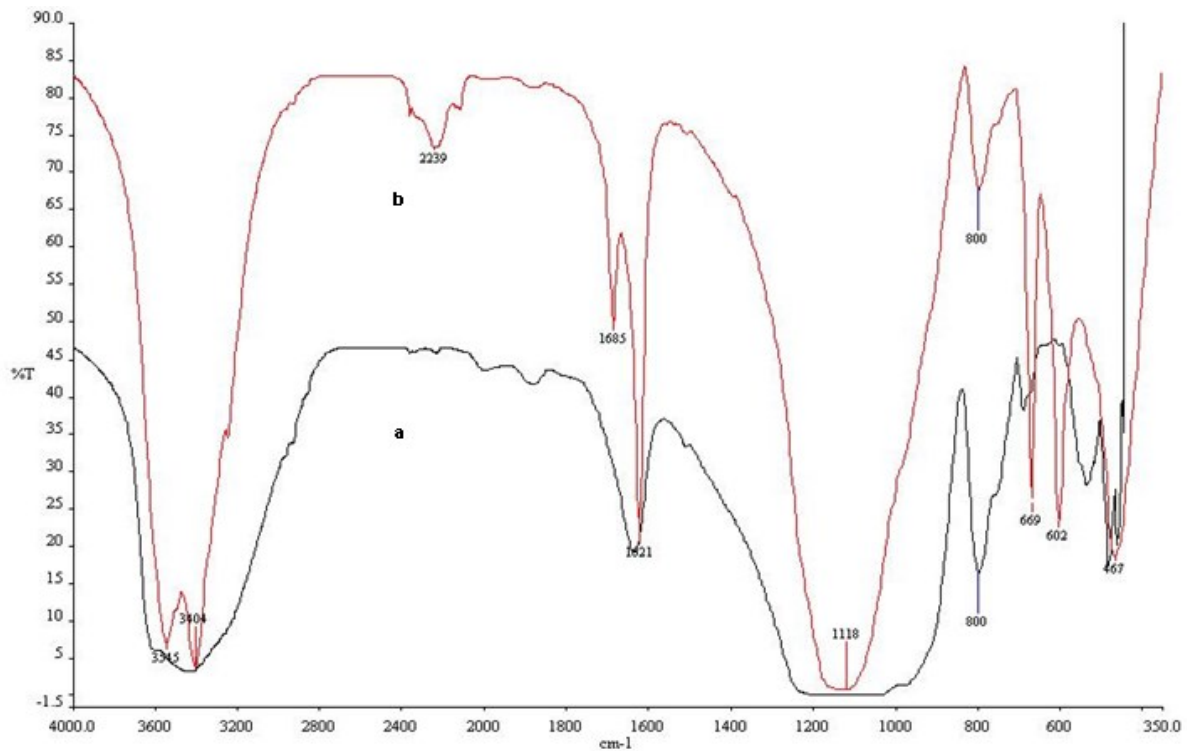


Figure 1. The FTIR spectra of APS and MPS

a) APS b) MPS

3.1.2. Surface morphology

The differences in the scanning electron microscope images of Hg (II) and As (III) adsorbed and desorbed APS and MPS are shown in Figure 2. The surface variation in the SEM micrographs showed the structural changes in the adsorbent before and after the Hg (II) and As (III) adsorption process. The general morphology of the PS before adsorption and after desorption could be characterized as much asperity. It was found that the surfaces of the Hg (II) loaded APS and As (III) loaded MPS were found to be rough layered.

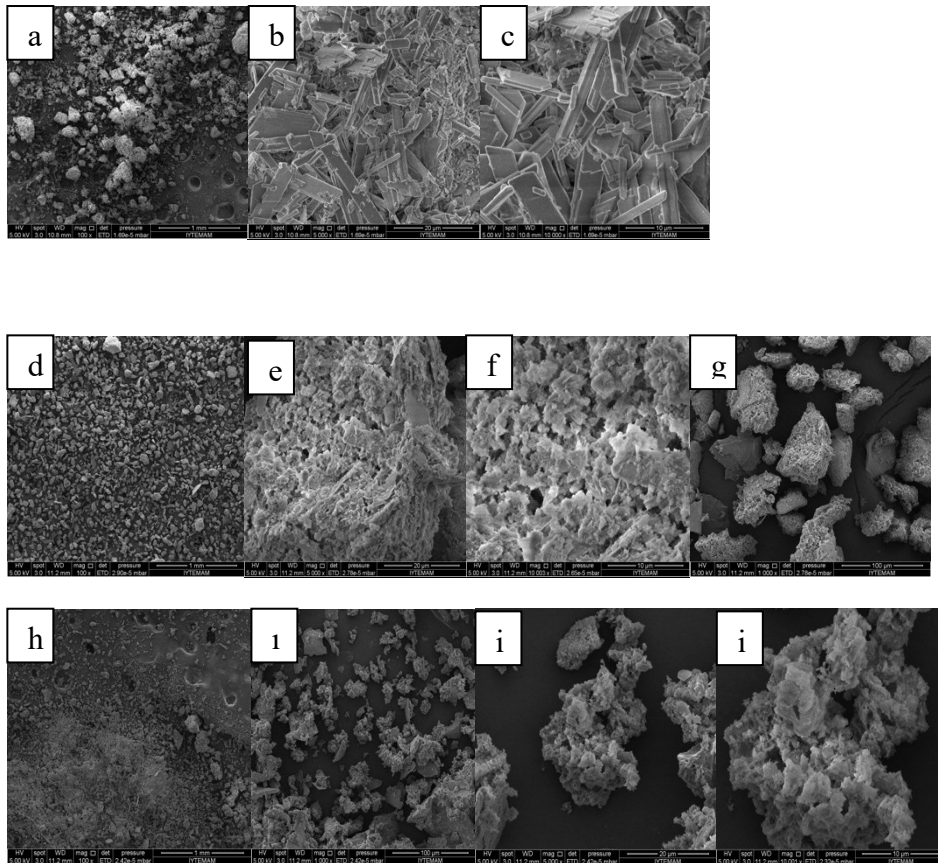


Figure 2. Scanning electron microscope images of PS, APS, MPS, Hg (II) and As (III) adsorbed and desorbed PS, APS and MPS a) Activated pumice stone b) FeCl_3 modified pumice stone (c) $\text{FeCl}_3 + \text{NaOH}$ modified pumice stone (d) Hg (II) loaded activated pumice stone (e) As (III) loaded pumice stone (f) As (III) loaded FeCl_3 pumice stone (g) As (III) loaded $\text{FeCl}_3 + \text{NaOH}$ pumice stone (h) Hg (II) desorbed activated pumice stone (i) As (III) desorbed pumice stone (i) As (III) desorbed FeCl_3 pumice stone, (j) $\text{FeCl}_3 + \text{NaOH}$ desorbed pumice stone

3.2. Effect of agitating time on sorption of Hg (II) and As (III) ions

Stirring time is one of the most critical parameters for the successful utilization of adsorbents [19,20]. Figure 3 shows the effect of agitating time on the adsorption of Hg (II) ions on APS. It can be seen that the percentage removal increases rapidly with increasing agitation time up to 120 minutes and measurements at 150 minutes show that equilibrium is reached after 120 minutes. Therefore, an optimum agitating time of 120 minutes was chosen for further studies. For the arsenic ion agitation time studies, 5, 10, 20, 30, 40, 60 and 120 minutes were determined (Figure 3). 50 mL of 50 mg L^{-1} As (III) solution was added on 0.5 g of MPS (PS, $\text{FeCl}_3 + \text{PS}$, $\text{FeCl}_3 + \text{NaOH} + \text{PS}$) and stirred for the indicated times, and the solutions were filtered and analysed. The optimum was found to be 60 minutes for PS, $\text{FeCl}_3 + \text{PS}$, and $\text{NaOH} + \text{FeCl}_3 + \text{PS}$.

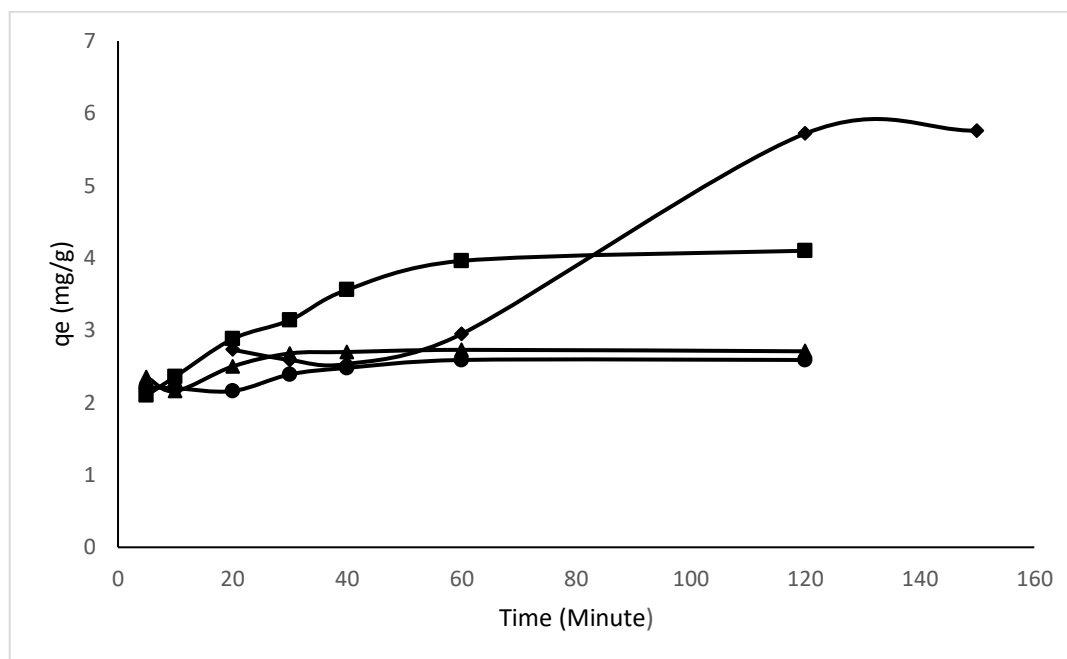


Figure 3. Effect of agitating time on sorption of Hg (II) and As (III) (0.10±0.02 g of APS, 25 mL of 100 mg L⁻¹ Hg (II) solution; 0.5 g of MPS, 50 mL of 50 mg L⁻¹ As (III) solution) (●: PS, ▲: FeCl₃ + PS, ■: FeCl₃ + NaOH + PS, ◆: APS)

The adsorption capacities of PS and FeCl₃ +PS are close to each other. When the adsorption capacities of PS, FeCl₃ + PS, FeCl₃ + NaOH + PS were examined, it was found that the adsorption capacity of FeCl₃ + NaOH + PS was higher. When NaOH is used, there is probably an adsorption mechanism in the form of (Fe-O-As) as the coordination of hydroxyl groups of ferrous hydro(oxides) with OH⁻ ligands in the arsenite molecule [21]. Therefore, higher adsorption capacity was obtained when FeCl₃ + NaOH + PS was used as adsorbent.

3.3. Effect of pH on sorption of Hg (II) and As (III) ions

In order to study the influence of pH on the adsorption capacity of APS for Hg (II), experiments were carried out with an initial concentration of 100 mg L⁻¹ over the pH range 3.0–8.0 and the results are shown in Figure 4. During the pH experiments, analyses were carried out with and without adsorbent (blank). The maximum adsorption percentage of Hg (II) was observed at the pH 5.0. It is reported that, in the presence of Cl⁻, the species such as HgCl₂, (HgCl₂)₂, Hg(OH)⁺ and HgOHCl are also present in small amounts between pH 4.0 and 6.0 [22]. The lower adsorption of Hg (II) at acidic pH is due to the presence of excess H⁺ ions competing with metal ions for the sorption sites. At high pH values (7.0-9.0), the decrease in adsorption is due to the formation of soluble hydroxylated compound (Hg(OH)₂). Similar pH values have been observed for adsorption of Hg (II) from aqueous solution in other studies [23-25]. In this study, the change in adsorption as a function of pH change was investigated for As (III) adsorption (Figure 4). The maximum adsorption percentage of As (III) was observed at the pH 6.0. The adsorption of the adsorbed

substance depends on the pH of the medium. Since the structure of the adsorbed substance can change with pH.

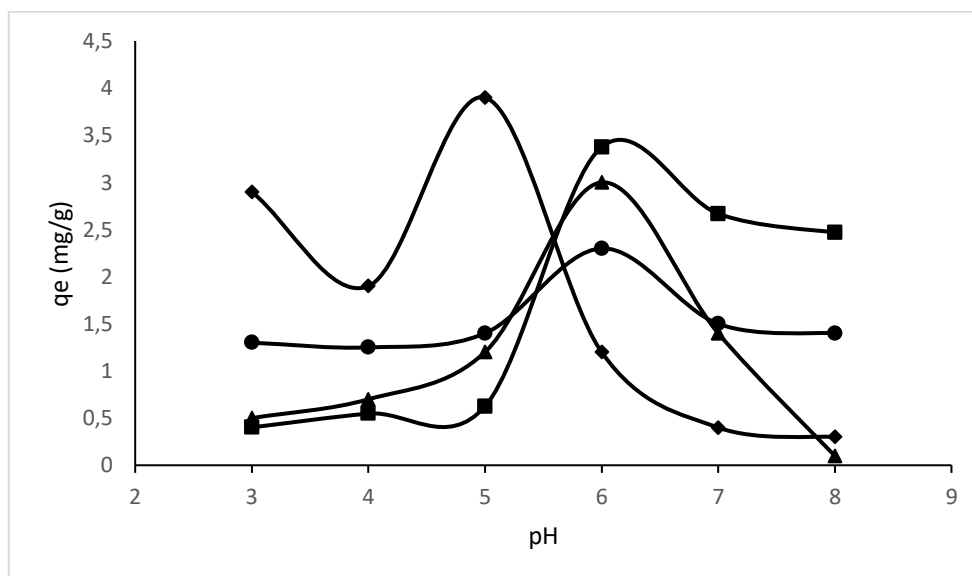


Figure 4. Effect of pH on sorption of Hg (II) and As (III) (0.10±0.02 g of APS, 25 mL of 100 mg L⁻¹ Hg (II) solution; 0.5 g of MPS, 50 mL of 50 mg L⁻¹ As (III) solution) (●: PS, ▲: FeCl₃ + PS, ■: FeCl₃ + NaOH + PS, ◆: APS)

If OH⁻ or H₃O⁺ ions are formed in the pH-dependent solution, these ions compete with the adsorbed material and therefore greatly affect the adsorption efficiency. Anions of acids and cations of bases used to adjust pH can compete with metal ions. The pH-dependent adsorption of substances on the surface of solids is a complex reaction. For these reasons, pH has a major effect on adsorption performance. When the effect of pH on the As (III) adsorption of the adsorbents used was investigated, no adsorption was observed at pH=7.0. This may be due to the more selective adsorption of H₂PO₄⁻ / HPO₄²⁻ anions used as buffers in this study than As (III) species found in uncharged H₃AsO₃ and anionic H₂AsO₃⁻ structures at this pH. The increase in As (III) adsorption observed at low pH can be explained by the increase in positively charged centres on the adsorbent surface, and the increase observed at high pH can be explained by the formation of negatively charged anionic structures of adsorbed As (III).

3.4. Effect of temperature on sorption of Hg (II) and As (III) ions

Temperature is an important parameter in explaining the energy dependent mechanism of adsorption. Temperature changes the equilibrium capacity of the adsorption process. It is generally known that the change in temperature is directly proportional to the reaction rate. It is therefore expected that the reaction rate will increase as the temperature increases. The adsorption reaction is classified as either endothermic or exothermic. Temperature affects the rate and amount of

adsorption. Adsorption experiments were carried out at 20-35 °C for Hg (II) adsorption and the results are shown in Figure 5. Subsequent studies were carried out at 30 °C.

For As (III) adsorption, the effect of temperature was tested at 20, 25, 30, 35 °C (Figure 5). 50 ml of 50 mgL⁻¹ As (III) solution was added to 0.5 grams of adsorbent (PS, FeCl₃ + PS and NaOH + FeCl₃ + PS) and mixed at the indicated temperatures for the indicated time and filtered. The optimum was found to be 30 °C for PS, FeCl₃ + PS and NaOH + FeCl₃ + PS.

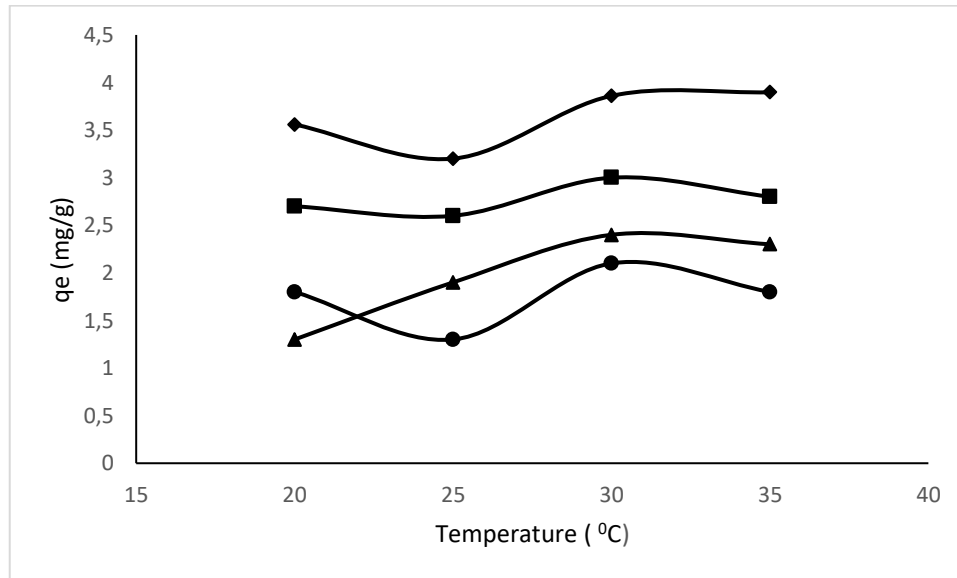


Figure 5. Effect of temperature on sorption of Hg (II) and As (III) (0.10±0.02 g of APS, 25 mL of 100 mg L⁻¹ Hg (II) solution; 0.5 g of MPS, 50 mL of 50 mg L⁻¹ As (III) solution) (●: PS, ▲: FeCl₃ + PS, ■: FeCl₃ + NaOH + PS, ◆: APS)

3.5. Thermodynamics of adsorption

The temperature dependent coefficient of dispersion was calculated using the following formula (Eq .2)

$$K_d = \frac{C_{Ad}}{C_e} \dots\dots\dots(2)$$

K_d is the equilibrium constant, C_{Ad} and C_e are the equilibrium concentrations (mg L⁻¹) of Hg (II) and As (III) ions on the APS and MPS in the solution (Equation 2). As shown in Figure 5, the adsorption process was evaluated between 20-35 °C for Hg (II) and As (III) and it was observed that adsorption increased with temperature. Thus, the adsorption Hg (II) and As (III) adsorption are endothermic in nature. Thermodynamic parameters such as the change in the values of ΔG° , ΔH° and ΔS° were calculated (Table 1, Eq. 4). The values of ΔG° for the adsorption process obtained from Eq. 3 are listed in Table 1. The negative value of ΔH° (-199.919 kJ mol⁻¹ the positive value of $\Delta S^\circ = 688.032 \text{ J K}^{-1} \text{ mol}^{-1}$ for Hg (II)) indicates that the adsorption processes are

exothermic and spontaneous at high temperatures. The negative value of ΔG° ($-405.137 \text{ kJ mol}^{-1}$) indicates that the adsorption process is spontaneous. In arsenic studies, when pumice was used as an adsorbent, the ΔH° value was $37.739 \text{ kJ mol}^{-1}$, $\Delta S = 127.944 \text{ J K}^{-1} \text{ mol}^{-1}$, ΔG° value = $-1.668 \text{ kJ mol}^{-1}$. For the FeCl_3 modified pumice the ΔH° value was $13.35 \text{ kJ mol}^{-1}$, $\Delta S^\circ = 37.268 \text{ J K}^{-1} \text{ mol}^{-1}$, and the ΔG° value was $1.871 \text{ kJ mol}^{-1}$. The ΔH° value for As (III) adsorption on pumice modified with NaOH and FeCl_3 was found to be $-78.148 \text{ kJ mol}^{-1}$, $\Delta S^\circ = -267.85 \text{ J K}^{-1} \text{ mol}^{-1}$, $\Delta G^\circ = 3010.28 \text{ J mol}^{-1}$.

3.5 Adsorption isotherms

The relationship between the equilibrium concentrations and the amount of adsorbed material per unit adsorbent has been shown by isothermal models. The binding between adsorbent and adsorbate can be explained by adsorption models [26]. The best known isotherm models, Langmuir and Freundlich, were applied (Eq 3,5). In this study, Langmuir and Freundlich isotherms were used to determine the adsorption mechanism of APS for Hg (II) ions. 25 mL of Hg (II) ions at different concentrations (25, 50, 75, 100, 125, 125, 150, 175, 175, 200, 400, 600, 800, 1000, 1500 mg L^{-1}) were treated with APS for 60 min (Figure 6).

Table 1. Thermodynamic and Isotherm constant

Freundlich Isotherm Constant				
$\log q_e = \log K_f + \frac{1}{n} \log C_e \dots (3)$				
		R^2	KF (mg g^{-1})	n
Hg (II)	APS	1.000	0.218	1.003
As (III)	PS	0.974	0.827	1.501
	FeCl ₃ + PS	0.896	0.164	1.167
	NaOH + FeCl ₃ +PS	0.939	0.590	1.563
Thermodynamic Parameters				
Equations		$\Delta G^\circ = \Delta H^\circ - T\Delta S^\circ \dots (4)$		
		$\ln K_d = \frac{\Delta S}{R} - \frac{\Delta H}{RT} \dots (5)$		
Ions	Adsorbent	ΔG° (kJ mol^{-1})	ΔH° (kJ mol^{-1})	ΔS° ($\text{J mol}^{-1} \text{K}$)
As(III)	PS	-1.668	37.739	127.944
	FeCl ₃ +PS	1.871	13.350	37.268
	FeCl ₃ +NaOH+PS	3.010	-78.148	-267.850
Hg(II)	APS	-405.137	-199.919	688.032

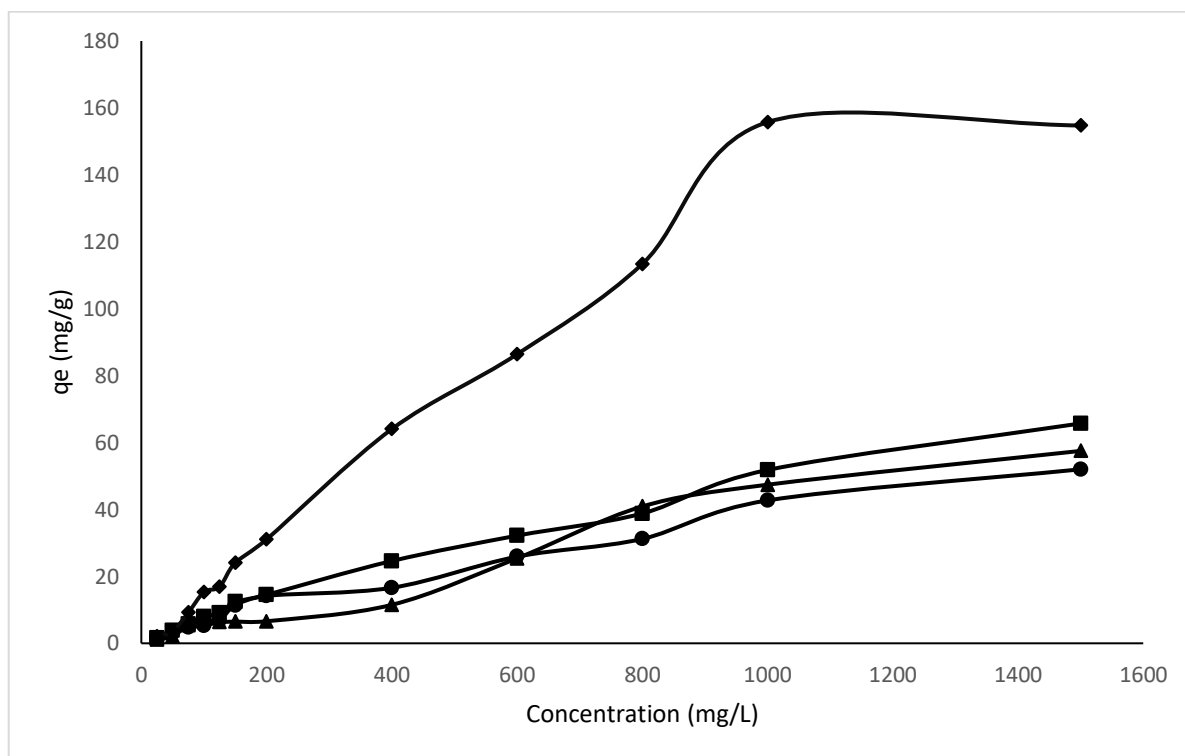


Figure 6. Effect of Hg (II) and As (III) ions concentration on the adsorption by APS, PS, PS + FeCl₃, PS + NaOH + FeCl₃ (0.10±0.02 g of APS, 0.5 g of MPS)
 (●: PS, ▲: FeCl₃ + PS, ■: FeCl₃ + NaOH + PS, ◆: APS)

Compliance with the Freundlich isotherm indicates that the adsorbate is heterogeneously coated on the surface [27-29]. The equations for Freundlich, and the calculated parameters are given in Table 1. Since the correlation coefficient of the plot of Freundlich model plot is higher than that of Langmuir, it can be said that the Freundlich type adsorption isotherm is suitable for Hg adsorption. In concentration change studies for As (III) and Hg (II) adsorption, values of 20, 50, 100, 200, 400, 800, 1000 and 1500 mg L⁻¹ were determined. As a result of the experiments and the isotherm graphs drawn, the Freundlich isotherm for PS, APS, FeCl₃+PS, and NaOH+FeCl₃+PS seems to be more appropriate than the Langmuir isotherm. It can be said that the adsorption has a heterogeneous structure for As (III) and Hg (II) ions.

Table 2. Some adsorbents in the literature and their capacities

Hg (II)		As (III)	
Adsorbent	Capacity	Adsorbent	Capacity
Cobalt ferrite	157.9 mg g ⁻¹ [30]	Iron pyrite [35]	571.7 μg g ⁻¹
4- Amino-5-methyl-1,2,4-triazole-3(4H)-thion-modified silica aerogel	142.85 mg g ⁻¹ [31]	Hydrated zirconium oxide (ZrO(OH) ₂) nanoparticles modified with graphene oxide (GO-ZrO(OH) ₂) [36]	95.15 mg g ⁻¹
n-(2- aminoethyl)-3-aminopropyl-trimethoxysilane	590 μg g ⁻¹ 131.7 mg g ⁻¹ [32]	Inorganicorganic iron chitosan nanoparticles (CIN)[37]	94±1.5 mg g ⁻¹
Oil shale	4.3mg g ⁻¹ [33]	αMnO ₂ [38]	4.64 mg g ⁻¹
Cellulose xanthate Xanthate	0.6 mg g ⁻¹ [34] 1.1mg g ⁻¹	CuO nanoparticles [39]	26.9 mg g ⁻¹
Activated pumice stone this work	155.75 mg g ⁻¹	Modified Pumice Stone (PS, PS + FeCl ₃ , PS + FeCl ₃ + NaOH	52.0 mg g ⁻¹ 57.5 mg g ⁻¹ 65.7 mg g ⁻¹

Table 2 shows the capacities of some adsorbents used for the adsorption of As (III) and Hg (II) ions from the literature. As can be seen, many adsorbents have been used. The pumice stone used in this study has the advantages of being widely available in nature and having a very good capacity.

3.6 Desorption and reusability studies

The percentage desorption of Hg(II) and As(III) from the sorbent is shown in Figure 7,8.

$$\text{Desorption ratio} = \frac{\text{Amount of metal ions desorbed}}{\text{Amount of metal ions adsorbed}} \times 100 \dots\dots\dots(6)$$

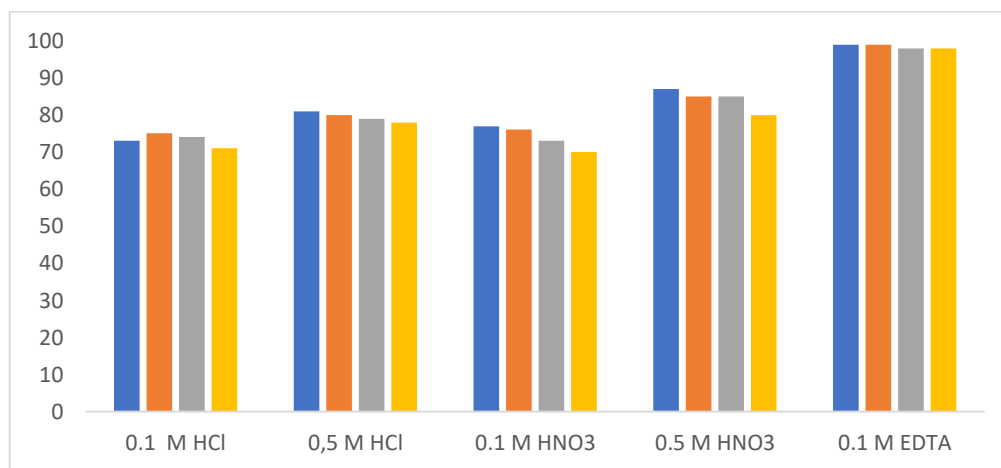


Figure 7. Desorption (%) results of Hg (II) ions from activated pumice stone by using different eluents (0.1 M HCl, 0.5 M HCl, 0.1 M HNO₃, 0.5 M HNO₃, 0.1 M EDTA)

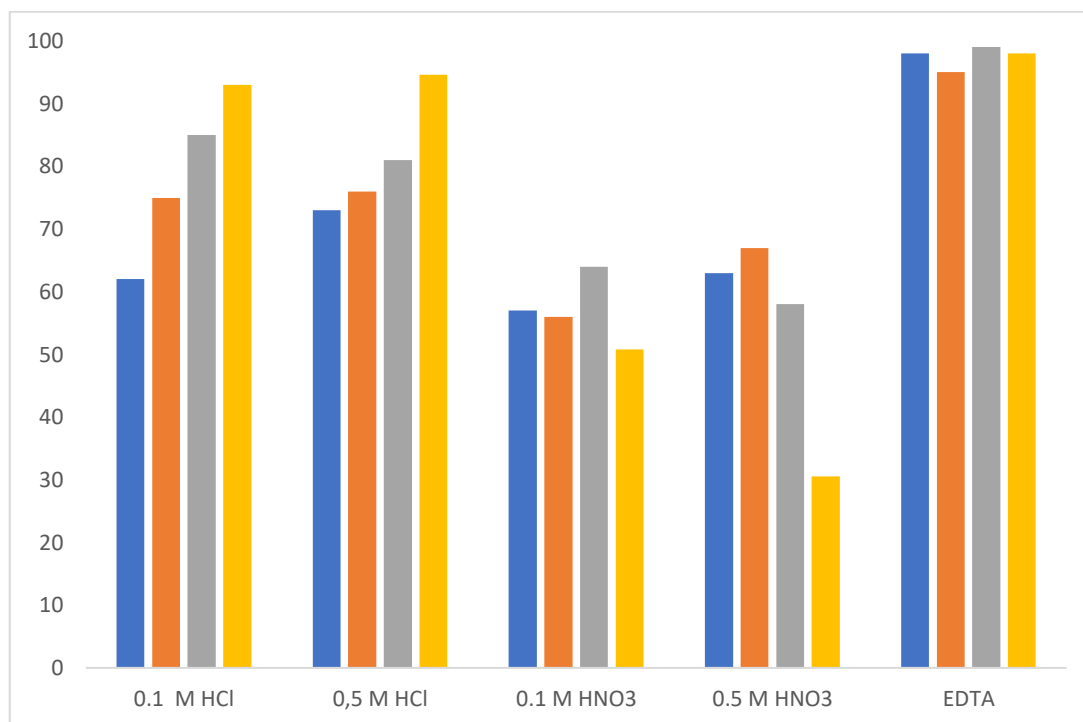


Figure 8. Desorption (%) results of As (III) ions from modified pumice stone by using different eluents (0.1 M HCl, 0.5 M HCl, 0.1 M HNO₃, 0.5 M HNO₃, 0.1 M EDTA)

Figures 7 and 8 show the results of 4 consecutive desorption treatments with 0.1 M and 0.5 M HCl, 0.1 M and 0.5 M HNO₃ and 0.1 M EDTA. 0.1 M EDTA seems to be suitable for both metal ions and has good reproducibility (% 99-98). 0.1 M EDTA is considered as a suitable eluent due to its tendency to form complexes with heavy metals. The fact that the desorbent still works with 98% efficiency even after 4 consecutive treatments is very important for the reusability of the desorbent.

4. Conclusion

In this study, APS and MPS were used to remove Hg (II) and As (III) ions from aqueous solution. APS and MPS could be effectively used to remove Hg (II) and As (III) ions. PS, FeCl₃ + PS, FeCl₃ + NaOH + PS adsorption capacities were found to be 52.0, 57.5, 65.7 mg g⁻¹ for As (III) ions respectively, and APS adsorption capacity was found to be 155.75 mg g⁻¹ for Hg (II) ions, respectively. The adsorption capacities of PS and FeCl₃ + PS are close to each other. When the adsorption capacities of PS, FeCl₃ + PS, FeCl₃ + NaOH + PS were examined, it was found that the adsorption capacity of FeCl₃ + NaOH + PS was higher. Since metals can be recovered with EDTA, pumice stone is very advantageous in terms of reusability. Pumice stone is an economical adsorbent low cost and effective adsorbent for the removal of Hg (II) and As (III) ions from water. The use of pumice stone, which is very common and abundant in nature, as an adsorbent in the removal of As (III) and Hg (II), which are highly toxic metals, from aqueous environments can be recommended as an economical and simple adsorption method.

Ethics in Publishing

There are no ethical issues regarding the publication of this study

Author Contributions

Vedia Nüket Tirtom: Designed and wrote the manuscript, carried out the experimental studies, conclusions and interpretation of the experiment.

References

- [1] Tirtom, VN., Goulding, Ş., Henden, E. (2008) Application of a wool column for flow injection online preconcentration of inorganic mercury(II) and methyl mercury species prior to atomic fluorescence measurement. *Talanta*, 76, 1212-1217.
- [2] Bhattacharyya, A., Dutta, S., De, P., Ray, P., Basu, S. (2010) Removal of mercury (II) from aqueous solution using papain immobilized on alginate bead: Optimization of immobilization condition and modeling of removal study. *Bioresource Technology*, 101(24), 9421-9428.
- [3] Natale, F., Di, Lancia, A., Molino, A., Di Natale, M., Karatza, D., Musmarra, D. (2006) Capture of mercury ions by natural and industrial materials. *Journal of Hazardous Materials B*, 132: 220-225.
- [4] Ma, Rao., M, K, Reddy, DHK., Venkateswarlu, P., Seshaiyah, K. (2009) Removal of mercury from aqueous solutions using activated carbon prepared from agricultural by-product/waste. *Journal of Environmental Management*, 90: 634-643.
- [5] Yardim, MF., Budinova, T., Ekinci, E., Petrov, N., Razvigorova, M., Minkova, V. (2003) Removal of mercury(II) from aqueous solution by activated carbon obtained from furfural. *Chemosphere*, 52(5): 835-841.
- [6] Kumar, D., Tomar, V. (2014) New generation material for the removal of arsenic from water. *Advanced Materials For Agriculture, Food, And Environmental Safety*, 3: 61-85.
- [7] Imran, A., Tabrez AK., Asım, M. (2011) Removal of arsenic from water by electrocoagulation and electrodialysis techniques. *Separation & Purification Reviews*; 40: 25-42.
- [8] Wang, Y., Yu, J., Wang, Z., Liu, Y., Zhao, Y. (2021) A review on arsenic removal from coal combustion: Advances, challenges and opportunities. *Chemical Engineering Journal*, 414: 128785.
- [9] Kaçar, E., (2022) Relationship of concentrations of some heavy metals with fish size in muscle tissue of *carassius gibelio* (Bloch, 1782) from the Tigris River (Turkey), *Erzincan University Journal of Science and Technology*, 15(2): 475-484.

- [10] SALTAN, G. M., (2023) Synthesis and characterization of terpolymer adsorbents using photopolymerization: investigation of heavy metal adsorption capacity, *Erzincan University Journal of Science and Technology*, 16(2): 528-547
- [11] Kannan, N., Malar, SJS. (2005) Removal mercury(II) ions by adsorption onto dates nut and commercial activated carbons: a comparative study. *Indian Journal of Chemical Technology*, 12: 522-527.
- [12] Hassan, SSM., Awwad, NS, Aboterik, AHA. (2008). Removal of mercury(II) from wastewater using camel bone charcoal. *Journal of Hazardous Materials*, 154(1–3): 992-997.
- [13] Akbal, FÖ., Akdemir, N., Onar, AN. (2000) FT-IR spectroscopic detection of pesticide after sorption onto modified pumice. *Talanta*, 53:131-135.
- [14] Akbal, F. (2005) Adsorption of basic dyes from aqueous solution onto pumice powder. *Journal of Colloid Interface Science*, 286: 455–458.
- [15] Asgari, G., Roshani, B., Ghanizadehc, G. (2012) The investigation of kinetic and isotherm of fluoride adsorption onto functionalize pumice stone. *Journal of Hazardous Material*, 217–218: 123-132.
- [16] Ersoy, B., Sariisik, A., Dikmen, Sariisik, G. (2010) Characterization of acidic pumice and determination of its electrokinetic properties in water. *Powder Technology*, 197:129–135.
- [17] Erdem, F., Ergun, Mübecel., (2020) Application of response surface methodology for removal of remazol yellow (rr) by immobilised *s. cerevisiae* on pumice stone. *Iranian Journal of Chemistry and Chemical Engineering*, 39(3): 175-187.
- [18] Güler, Ülkü, Aslı., Sarioglu, Meltem., (2014) Removal of tetracycline from wastewater using pumice stone: equilibrium, kinetic and thermodynamic studies. *Journal of Environmental Health Science & Engineering*, 12:79
- [19] Ilhan, S., Iscen, C., Caner, FN., Kiran, I. (2008) Biosorption potential of dried penicillium restrictum for reactive orange 122: isotherm, kinetic and thermodynamic studies. *Journal of Chemical Technology & Biotechnology*, 83(4): 569-575.
- [20] Kargi, F., Cikla, S. (2006) Zinc(II) ion recovery by biosorption onto powdered waste sludge (PWS): effects of operating conditions. *Journal of Chemical Technology & Biotechnology*, 81(10):1661-1668.
- [21] Arcibar-Orozco, J.A., Josue, D., Rios-Hurtado, J.C., Rangel- Mendez, J.R. (2014) Influence of iron content, surface area and charge distribution in the arsenic removal by activated carbons, *Chemical Engineering Journal*, 249: 201–209.

- [22] Zhang, F.S., Nriagu, JO., Itoh, H. (2005) Mercury removal from water using activated carbons derived from organic sewage sludge. *Water Research*, 39: 389-395.
- [23] Bayramoglu, G., Tuzun, I., Celik, G., Yilmaz, M., Arica, Y., (2006) Biosorption of mercury(II), cadmium(II) and lead(II) ions from aqueous system by microalgae *Chlamydomonas reinhardtii* immobilized in alginate beads. *International Journal of Mineral Processing*, 81: 35-43.
- [24] Inbaraj, BS., Sulochana, N. (2006) Mercury adsorption on a carbon sorbent derived from fruit shell of *Terminalia catappa*. *Journal of Hazardous Materials*; 133: 283-290.
- [25] Zeroual, Y., Moutaouakkil, A., Dzairi, FZ., Talbi, M., Park, UC., Lee, K., Blaghen, M. (2003) Biosorption of mercury from aqueous solution by *Ulva lactuca* biomass. *Bioresource Technology*, 90(3): 349-351.
- [26] Wan, M., W, Kan, CC., Rogel, BD., Dalida, MLP. (2010) Adsorption of copper (II) and lead (II) ions from aqueous solution on chitosan-coated sand. *Carbohydrate Polymers*, 80: 891-899.
- [27] Chatterjee, S., Chatterjee, S., Chatterjee, BP., Guha, AK. (2007) Adsorptive removal of Congo red, a carcinogenic textile dye by chitosan hydrobeads: binding mechanism, equilibrium and kinetics. *Colloids and Surfaces A; Physicochemical and Engineering Aspects*, 299(1):146-152.
- [28] Ng, JCY., Cheung, WH., McKay G. (2003) Equilibrium studies for the sorption of lead from effluents using chitosan. *Chemosphere*, 52:1021-1030.
- [28] Freundlich, HMF. 1906. Uber die adsorption in lasungen, *Zeitschrift für Physikalische Chemie*: 57, 385-470.
- [30] Zhang, YK., Yan LG., Xu WY., Guo XY., Cui LM., Gao L., Wei Q., Du, B. (2014) Adsorption of Pb(II) and Hg(II) from aqueous solution using magnetic CoFe_2O_4 -reduced graphene oxide. *Journal of Molecular Liquids*, 191; 177–182.
- [31] Tadayon, F., Saber-Tehrani, M., Motahar, S. (2013) Selective removal mercury (II) from aqueous solution using silica aerogel modified with 4- amino-5-methyl-1,2,4-triazole-3(4H)-thion. *Korean Journal of Chemical Engineering*, 30; 642–648.
- [32] Yu, Y., Addai-Mensah, J., Losic, D. (2012) Functionalized diatom silica microparticles for removal of mercury ions. *Science and Technology of Advanced Materials*, 13: 015008
- [33] Daifullah, AAM., Awwad, NS., Al-Azhar. (2003) *Bulletin of Science*; in: *Proceeding of 5th Int. Sci. Conf*: 25–27 March, 57.
- [34] Bricka, RM., Hill D.O. in: P.L. Cote, T.M. (1989) Gilliam (Eds.), *ASTM STP 1033*, American Society for Testing and Materials, 257, Philadelphia.

- [35] Jat Baloch MY., Su C., Talpur, SA., Iqbal, J., Bajwa, K. (2023) Arsenic Removal from groundwater using iron pyrite: influence factors and removal mechanism, *Journal of Earth Science* XX, 1-11.
- [36] Habuda-Stanić, M., Nujić, M. (2015) Arsenic removal by nanoparticles: a review, *Environ Science and Pollution Research International*, 22: 8094–8123.
- [37] Gupta, A., Yunus, M., Sankararamkrishnan, N. 2012. Zerovalent iron encapsulated chitosan nanospheres—a novel adsorbent for the removal of total inorganic arsenic from aqueous systems. *Chemosphere*, 86:150–155.
- [38] Nguyen, Thanh, D., Singh, M., Ulbrich, P., Strnadova, N., Štěpánek, F. (2011) Perlite incorporating γ -Fe₂O₃ and α -MnO₂ nanomaterials: preparation and evaluation of a new adsorbent for As(V) removal. *Separation & Purification Technology*, 82: 93–10.
- [39] Martinson, CA., Reddy, KJ. (2009) Adsorption of arsenic(III) and arsenic(V) by cupric oxide nanoparticles. *Journal of Colloid Interface Science*, 336, 406–411.

Exploring the Impact of *Gypsophila perfoliata* L. Root Extract on Germination and Seedling Growth Parameters of Sweet Sorghum and Hungarian Vetch

Muhammet İslam Işık¹, *, Aslı Güleç², Aras Türkoğlu¹, Metin Armağan¹

¹Department of Field Crops, Faculty of Agriculture, Necmettin Erbakan University, Konya, Türkiye

² Department of Farm Buildings and Irrigation, Faculty of Agriculture, Selcuk University, Konya, Türkiye

Received: 22/11/2023, Revised: 02/04/2024, Accepted: 04/04/2024, Published: 31/08/2024

Abstract

In recent years, there has been a growing emphasis on exploring alternative approaches, such as the utilization of medicinal plant extracts and essential oils, to address potential limitations in germination and emergence, as opposed to traditional chemical methods. Biochemicals synthesized in medicinal and aromatic plants can elicit either stimulating or inhibitory effects on the growth and development of other plants. This study aimed to investigate the impact of gypsophila plant root extract on the germination and seedling development of vetch and sorghum, assessing different concentrations of the extract (0%, 5%, and 10%). Upon evaluating the results, it was observed that the sorghum plant exhibited the highest germination rate, mean germination time, germination vigor index, root and shoot length, as well as root and shoot fresh weight when subjected to the control concentration. In contrast, the vetch plant demonstrated optimal results at the 5% concentration. In conclusion, the inhibitory effect of the gypsophila plant root extract on germination and seedling development was more pronounced in the sorghum plant compared to the vetch plant. This suggests that the impact of the extract varies among different plant species, highlighting the need for species-specific considerations when implementing such alternative approaches in agricultural practices.

Keywords: Root extract, gypsophila, vetch, sorghum, germination

Çöven (*Gypsophila perfoliata* L.) Kök Ekstraktının Tatlı Sorgum (*Sorghum bicolor* L.) ve Macar Fiğ (*Vicia sativa* L.) Tohumlarının Çimlenme ve Fide İle İlgili Parametreler Üzerine Etkisi

Öz

Son yıllarda, geleneksel kimyasal yöntemlerin aksine, çimlenme ve ortaya çıkmadaki potansiyel sınırlamaları ele almak için tıbbi bitki ekstraktlarının ve uçucu yağların kullanımı gibi alternatif yaklaşımların araştırılmasına artan bir vurgu yapılmıştır. Tıbbi ve aromatik bitkilerde sentezlenen biyokimyasallar, diğer bitkilerin büyüme ve gelişmesi üzerinde uyarıcı veya engelleyici etkiler ortaya çıkarabilir. Bu çalışma, çöven bitkisi kök ekstraktının fiğ ve sorgumun çimlenmesi ve fide gelişimi üzerindeki etkisini, ekstraktın farklı konsantrasyonlarını (%0, %5 ve %10) değerlendirerek araştırmayı amaçlamıştır. Sonuçlar değerlendirildiğinde sorgum bitkisinin kontrol konsantrasyonunda en yüksek çimlenme oranı, ortalama çimlenme zamanı, çimlenme gücü indeksi, kök ve sürgün uzunluğu ile kök ve sürgün yaş ağırlığına sahip olduğu saptanmıştır. Buna karşılık, fiğ bitkisi %5 konsantrasyonda optimal sonuçlar göstermiştir. Sonuç olarak, çöven bitkisi kök ekstraktının çimlenme ve fide gelişimi üzerindeki inhibitör etkisi sorgum bitkisinde fiğ bitkisine göre daha belirgin olmuştur. Bu sonuç, ekstraktın etkisinin farklı bitki türleri arasında değiştiğini ve tarımsal uygulamalarda bu tür alternatif yaklaşımların uygulanmasında türe özgü değerlendirmelerin daha önemli olduğunu göstermektedir.

Anahtar Kelimeler: Kök özütü, çöven, fiğ, sorgum, çimlenme

*Corresponding Author: muhammetislam.isik@erbakan.edu.tr

1. Introduction

Forage crop production holds immense significance on international and domestic fronts as it provides a sustainable means to feed animals and supports livestock farming at a reasonable cost [1]. Legumes and cereals are particularly crucial among the plant types cultivated for animal feeding purposes globally. Vetch (*Vicia sativa* L.), a member of the Fabaceae family, stands out as one of the major genera, encompassing 247 taxa worldwide [2], with approximately 100 taxa found in Türkiye [3]. Vetch serves diverse purposes, including the production of green and dry forage, grain, green manure, and as a source for livestock grazing, owing to its high-quality forage attributes [4]. Its notable forage quality not only makes it a valuable resource for various agricultural purposes but also contributes to reducing the overall costs associated with livestock feeding [5]. Sorghum (*Sorghum bicolor* L.), belonging to the Poaceae family within the Sorghum Moench genus, holds the distinction of being the fifth most important C4 plant globally. Cultivated for various purposes such as fuel, forage, roughage, and food, sorghum stands out due to its versatility [6; 7]. The cultivation of sorghum plays a significant role in meeting diverse agricultural needs, making it a valuable and adaptable resource on a global scale.

The challenges posed by water scarcity, drought, and difficulties in accessing food, compounded by the negative impacts of global warming, are becoming increasingly pronounced with the growing world population [8]. Consequently, there is a pressing need to cultivate plants that exhibit water efficiency, drought tolerance, and high productivity. In semi-arid regions, low humidity levels during germination becomes a limiting factor [9], turning the germination period into a critical phase that significantly influences both yield and quality in agricultural production [10]. Various phytohormones, including brassinosteroids, auxins, ethylene, cytokinins, salicylic acid, jasmonic acid, and strigolactones, along with specific compounds such as karrikins and reactive oxygen species, play a crucial role in dormancy and germination processes [11]. Natural methods that promote germination, such as seaweed, medicinal plant extracts, vinegar, and essential oils, offer environmentally friendly alternatives [12]. However, the conventional use of chemicals in agriculture raises input costs and contributes to environmental pollution. Therefore, there is a growing emphasis on adopting sustainable and eco-friendly practices in agriculture to address these challenges and promote the long-term health of both the agricultural ecosystem and the environment.

Indeed, contemporary agricultural practices need to prioritize techniques that not only enhance the yield and quality of seeds or seedlings but also reduce costs and minimize environmental pollution. Plant-synthesized biochemicals emerge as pivotal players in promoting or inhibiting various plants' growth and development [13]. These secondary metabolites, characterized by their diverse structures, carry significant economic value due to their wide-ranging applications in medicine, antibiotics, antioxidants, flavor sources, food additives, allelochemicals, antifungals, insecticides, fertilization stimulants, and growth regulators [14]. The concept of allelopathy is crucial in this context, referring to the phenomenon whereby plants influence the growth and development of other plants, either positively or negatively, through the synthesis or decomposition of specific compounds [15]. Harnessing the potential of allelopathic interactions and plant-synthesized biochemicals provides an avenue for sustainable agricultural

practices that optimize productivity and contribute to environmental conservation and the overall health of agroecosystems. As we navigate the challenges of a changing climate and a growing global population, these approaches become increasingly important in creating resilient and sustainable agricultural systems.

Gypsophila, categorized among medicinal and aromatic plants, possesses diverse features that have captured the interest of various scientific disciplines. The species within the *Gypsophila* genus, characterized by significant levels of saponins, find application as additives in medicine, cleaning products, and food items. The roots of this plant have been a source of saponins for centuries, valued for their antibiotic, antifungal, and pharmacological effects [16]. Saponins, primarily synthesized by plants, are broadly classified into steroidal and triterpenoid glycoside compounds [17]. These compounds are believed to protect plants against certain insects owing to their antimicrobial properties and enhance resistance in specific plant parts [18]. Furthermore, saponin compounds exhibit high biological activity in plants, fungi, insects, and microorganisms. While low concentrations play a regulatory role in plant rooting, elevated concentrations are reported to inhibit root growth [19]. Therefore, a comprehensive exploration of the detailed physiological effects of saponins and saponin-rich materials on plants remains an open area of research. Soliman et al. [20] demonstrated that priming soybean seeds with 5% and 10% concentrations of saponin effectively alleviated salinity stress. In a study conducted by Yang et al. [21], seven different concentrations of saponin priming were applied to quinoa seeds to mitigate the adverse effects of salinity stress. These findings highlight the potential of saponins in enhancing stress tolerance in plants, opening avenues for further research into their applications in sustainable agriculture, especially in mitigating environmental stresses that can impact crop productivity.

The current research represents a pioneering study aiming to address a gap in the existing literature by investigating the effects of *Gypsophila* extract on the germination and seedling growth patterns of vetch and sorghum plants. The study was conducted by applying *Gypsophila* extract to sweet sorghum and Hungarian vetch seeds to determine its effects on germination and seedling growth-related traits.

2. Material and Methods

In this study, the Helvacı *Gypsophila* (*Gypsophila perfoliata*) plant material was used to determine its impact on germination and seedling-related traits in Cowley sweet sorghum (*Sorghum bicolor*) and Aygün hungarian vetch (*Vicia pannonica* Crantz). Seeds were initially washed with tap water for surface sterilization, followed by soaking in a 10% sodium hypochlorite (NaClO₄) solution for 25 minutes. Subsequently, the seeds were rinsed three times with sterile distilled water, immersed in a 70% ethyl alcohol solution for 5 minutes. They washed three more times with sterile distilled water to complete the sterilization process. *Gypsophila perfoliata*, a commercially significant species, was used in three concentrations (0%, 5%, and 10%) according to a completely randomized design with three replications. *Gypsophila* roots, collected from Adabağ village in Ereğli (Konya), were dried in a dust-free environment without direct sunlight for seven days in the Laboratory of the Department of Field Crops at Necmettin Erbakan University, Ereğli Faculty of Agriculture. Before extraction, the

Gypsophila roots were finely divided into small pieces. For the 10% concentration, 100 grams of dried Gypsophila roots were boiled in 1 liter of distilled water for 20 minutes and then cooled to room temperature. The resulting extract was filtered and stored in a refrigerator (+4°C) during the experiment.

In the trials, containers with base dimensions of 7.5 mm width and 12 mm length were prepared by placing two layers of germination paper (Whatman filter paper No. 1) on the base, and 25 seeds were placed on top. Application groups were treated with 5 ml of Gypsophila root extract, while control groups received 5 ml of distilled water. The seeds were germinated in a 16:8-hour light:dark photoperiod at 24-26°C room temperature over a 14-day period. Germination-related parameters were recorded by counting the seeds each day during this period. Germination rate (GR) (%), germination rate coefficient (GRC), germination rate index (GRI), mean germination time (MGT), and germination vigor index (GVI) were calculated according to Türkoğlu et al. [22]. Seeds with a root length of 1 mm or longer were considered germinated. On the 14th day of the study, five seedlings were randomly selected from each treatment, and root and shoot lengths were measured using a metric ruler, while root and shoot fresh weights were measured using a precision balance [23].

The statistical analysis of the data was subjected to a factorial design variance analysis with plant (2) and application concentration (3) as factors, following a completely randomized trial plan with four replications (SPSS 26 software, SPSS Inc., IBM). The Duncan test determined differences between means for these parameters at a 5% significance level.

3. Results and Discussion

Germination-Related Traits

The seeds placed in the environment at different concentrations germinated within approximately 1-2 days, and their development was ensured over the 14 days.

Germination Rate (GR)

The plant and plant x concentration interaction had a highly significant effect ($p \leq 0.01$) on the germination rate, while the concentration was not significant ($p \geq 0.05$) (Table 1). The mean germination rate data shows that the highest germination rate was observed in the sorghum plant at 88.89%, while the lowest amount was observed in the vetch plant at 56.00% (Table 2). Considering the means of concentrations, the highest germination rate without a significant difference was obtained at the 10% concentration of Gypsophila root extract (Table 2). Looking at the means of the plant x concentration interaction data, the highest germination rate in the sorghum plant was achieved at 96.00% with the control dose of Gypsophila extract, and the lowest germination rate was 44.00% with the control dose in the vetch plant.

Table 1. Analysis of variance results of different concentrations of gypsophila root extract applied to vetch and sorghum plants for the studied traits.

Source of Variation	Mean of squares					
	SD	GR	GRC	GRI	MGT	GVI
Plant (P)	1	4867,56** ¹	4756,85**	0,03**	17,42**	146008985,74**
Concentration (C) (%)	2	27,56 ^{ns}	143,36**	0,00 ^{ns}	0,66**	28440373,23**
P×C	2	491,56**	1306,53**	0,00**	2,72**	52349984,46**
Error	12	43,56	130,51	0,00	0,02	317478,93
Total	18					

1 : **: significant at $p \leq 0.01$., ns: non-significant at $p \geq 0.05$. GR (%): Germination rate; GRC: Germination rate coefficient; GRI: Germination rate index; MGT: Mean germination time; GVI: Germination vigor index.

Table 2. Means of different concentrations of gypsophila root extract applied to vetch and sorghum plants for the studied traits.

Plant	Concentrations	GR%	GRC	GRI	MGT (day)	GVI
Vetch	0.00%	44,00±0,00 ^{b1}	35,48±0,00 ^a	0,10±0,00 ^b	2,82±0,00 ^b	888,80±0,00 ^b
	5.00%	65,33±10,07 ^a	21,00±1,13 ^c	0,16±0,02 ^a	4,77±0,25 ^a	3366,13±280,56 ^a
	10.00%	58,67±2,31 ^a	29,57±1,17 ^b	0,14±0,01 ^a	3,39±0,14 ^b	1778,40±318,51 ^a
	Mean	56,00±10,77 ^B	28,68±6,36 ^B	0,13±0,03 ^B	3,66±0,88 ^A	2011,11±1107,35 ^B
Sorghum	0.00%	96,00±0,00 ^a	51,06±0,00 ^b	0,23±0,00 ^a	1,96±0,00 ^a	13401,60±0,00 ^a
	5.00%	81,33±9,24 ^a	76,83±5,41 ^a	0,19±0,02 ^a	1,31±0,09 ^b	5878,13±1281,84 ^b
	10.00%	89,33±8,33 ^a	55,70±5,77 ^b	0,21±0,02 ^a	1,81±0,19 ^a	3842,13±285,67 ^a
	Mean	88,89±8,89 ^A	61,20±12,53 ^A	0,21±0,02 ^A	1,69±0,31 ^B	7707,29±4409,94 ^A
Gypsophila root extract	0.00%	70,00±28,48 ^A	43,27±8,53 ^B	0,17±0,07 ^A	2,39±0,47 ^C	7145,20±6853,54 ^A
	5.00%	73,33±12,31 ^A	48,91±30,78 ^A	0,17±0,03 ^A	3,04±1,91 ^A	4622,13±1606,79 ^B
	10.00%	74,00±17,66 ^A	42,63±14,79 ^B	0,18±0,04 ^A	2,60±0,88 ^B	2810,27±1162,29 ^C

¹Numbers indicated with similar letters within the same column are statistically indistinguishable within a 1% margin of error according to the Duncan test. GR (%): Germination rate; GRC: Germination rate coefficient; GRI: Germination rate index; MGT: Mean germination time; GVI: Germination vigor index.

Germination Rate Coefficient

The plant, concentration, and plant x concentration interaction had a statistically significant effect ($p \leq 0.01$) on the germination rate coefficient (GRC) (Table 1). According to the mean statistical data, the highest germination rate coefficient was determined in the sorghum plant at 61.20, while the lowest was recorded in the vetch plant at 28.68 (Table 2). Evaluating the mean data of concentrations, the germination rate coefficient at the 5% dose was significant at 48.91 (Table 2). Looking at the mean data of the plant x concentration interaction, the highest germination rate coefficient in the sorghum plant was 76.83 at the 5% concentration, while the lowest in the vetch plant was 21.00 at the 5% concentration (Table 2).

Germination Rate Index

Statistically, the plant and plant x concentration interaction had a highly significant effect ($p \leq 0.01$) on the germination rate index (GRI), while the concentration's effect was found to be insignificant ($p \geq 0.05$) (Table 1). According to the mean data, the highest value in the germination rate index was 0.21 in the sorghum plant, and 0.13 in the vetch plant (Table 2). Evaluating the mean data of concentrations, there was no statistically significant difference, and the highest result, 0.18, was obtained at the 10% concentration (Table 2). Looking at the plant x concentration interaction, the germination rate index was highest in the sorghum plant at 0.23 in the control dose and lowest in the vetch plant at 0.10, again in the control dose (Table 2).

Mean Germination Time

According to the statistical data, the plant, concentration, and plant x concentration interaction had a highly significant effect ($p \leq 0.01$) on the mean germination time (MGT) (Table 1). Looking at the mean data, the mean germination time was highest in the vetch plant at 3.66 and lowest in the sorghum plant at 1.69 (Table 2). Evaluating the mean data of concentrations, the highest mean germination time was 3.04 at the 5% *Gypsophila* root extract concentration, and the lowest was 2.39 in the control (Table 2). Looking at the plant x concentration interaction data, vetch had the highest mean germination time at 4.77 at the 5% concentration, while sorghum had the lowest value at 1.31 at the 5% concentration (Table 2).

Germination Vigor Index

According to the variance analysis results, concentration and plant x concentration interaction had a highly significant effect ($p \leq 0.01$) on the germination vigor index (GVI) (Table 1). According to the mean data, the germination vigor index was highest in the sorghum plant at 7707.29 and lowest in the vetch plant at 2011.11 (Table 2). Evaluating the mean data of concentrations, the control concentration was significant at 7145.20 (Table 2). Looking at the plant x concentration interaction, the highest value was observed in the sorghum plant at 13401.60 in the control concentration, while the lowest was in the vetch plant at 888.80, again in the control concentration (Table 2).

Seedling-Related Characteristics

Root Length

Root length was found to be statistically significant ($p \leq 0.01$) concerning plant concentration and plant x concentration interaction (Table 3). Looking at the mean data, the highest root length was recorded in the sorghum plant at 3.81 cm, while the lowest was in the vetch plant at 0.97 cm (Table 4). According to the concentration statistical results, the highest, 3.68 cm, was obtained in the control concentration (Table 4). Regarding the plant x concentration interaction, the highest root length was 6.54 cm in the sorghum plant at the control concentration, and the lowest was 0.76 cm in the vetch plant at the 10% concentration prepared (Table 4).

Table 3. Variance analysis results for different *Gypsophila* root extract concentrations applied to vetch and sorghum plants for the studied traits.

Source of Variation	Mean of squares				
	SD	RL	SL	RFW	SFW
Plant (P)	1	3618,17** ¹	2266,89**	0,01**	0,01**
Concentration (C) (%)	2	951,27**	519,96**	0,00*	0,00*
P×C	2	987,63**	1787,95**	0,00*	0,02**
Error	12	2,64	28,93	0,00	0,00
Total	18				

1 : **: significant at $p \leq 0.01$., ns: non-significant at $p \geq 0.05$. RL (cm): Root length; SL (cm): Shoot length; RFW (g): Root fresh weight; SFW (g): Shoot fresh weight.

Table 4. Means of different *Gypsophila* root extract concentrations applied to vetch and sorghum plants for the studied traits.

Plant	Concentrations	RL (cm)	SL (cm)	RFW (gr)	SFW (gr)
Vetch	0.00%	8,20±0,00 ^{b1}	12,00±0,00 ^a	0,0200±0,0000 ^a	0,0100±0,0000 ^b
	5.00%	13,53±2,34 ^a	38,47±7,20 ^a	0,0400±0,0100 ^a	0,1000±0,0100 ^a
	10.00%	7,60±1,31 ^b	22,60±5,60 ^b	0,0233±0,0153 ^a	0,0533±0,0379 ^b
	Mean	9,78±3,1 ^B	24,36±12,41 ^B	0,0278±0,0130 ^B	0,0544±0,0436 ^B
Sorghum	0.00%	65,40±0,00 ^a	74,20±0,00 ^a	0,1000±0,0000 ^a	0,1800±0,0000 ^a
	5.00%	33,33±1,96 ^b	38,47±7,20 ^b	0,0800±0,0400 ^b	0,0833±0,0252 ^b
	10.00%	15,67±2,19 ^c	27,73±6,20 ^b	0,0400±0,0200 ^b	0,0633±0,0404 ^b
	Mean	38,13±21,88 ^A	46,80±21,60 ^A	0,0733±0,0346 ^A	0,1089±0,0590 ^A
Gypsophila root extract	0.00%	36,80±31,33 ^A	43,10±34,07 ^A	0,0600±0,0438 ^A	0,0950±0,0931 ^A
	5.00%	23,43±11,02 ^B	38,47±6,44 ^A	0,0600±0,0341 ^A	0,0917±0,0194 ^A
	10.00%	11,63±4,70 ^C	25,17±5,99 ^B	0,0317±0,0183 ^B	0,0583±0,0354 ^B

¹Numbers indicated with similar letters within the same column are statistically indistinguishable within a 1% margin of error according to the Duncan test. RL (cm): Root length; SL (cm): Shoot length; RFW (g): Root fresh weight; SFW (g): Shoot fresh weight.

Shoot Length

Statistical analysis, considering plant, concentration, and plant x concentration interaction, revealed significant effects ($p \leq 0.01$) (Table 3). The mean shoot length was highest in sorghum plants, recorded as 4.68 cm, and lowest in vetch plants, measured at 2.43 cm (Table 4). According to concentration data, control concentration and the concentration prepared at 5% produced the most extended shoots, measuring 4.31 cm and 3.84 cm, respectively (Table 4). Examining the results of plant x concentration interaction, it was found that the highest value was 7.42 cm in sorghum plants at the control concentration, and the lowest was 1.20 cm in vetch plants at the control concentration (Table 4).

Root Fresh Weight

The statistical evaluation of root fresh weight showed significance for plant ($p \leq 0.01$), concentration, and plant x concentration interaction (Table 3). Analyzing the mean values revealed that the highest root fresh weight was 0.0733 g in sorghum plants, and the lowest was 0.0278 g in vetch plants (Table 4). Concentration-wise, control and 5% concentrations showed the highest values without significant differences, both measuring 0.600 g (Table 4). Plant x

concentration interaction indicated that sorghum plants had the highest root fresh weight at the control concentration, measuring 0.1000 g. In contrast, vetch plants had the lowest at the control concentration, recording 0.200 g (Table 4).

Shoot Fresh Weight

The statistical analysis revealed the significance of both plant and plant x concentration interaction ($p \leq 0.01$), while concentration showed significance as well (Table 3). The highest shoot fresh weight was obtained in sorghum plants, reaching 0.1089 g, whereas the lowest was recorded in vetch plants at 0.0544 g (Table 4). According to mean values, control and 5% concentrations yielded the highest values, measuring 0.950 g and 0.917 g, respectively (Table 4). Plant x concentration interaction showed that sorghum plants had the highest shoot fresh weight at the control concentration, recording 0.1800 g, while vetch plants had the lowest at the control concentration, with a value of 0.0100 g (Table 4).

4. Conclusion

Over centuries, medicinal and aromatic plants have played an integral role globally in Daily life and culture [24]. These plants harbor bioactive secondary metabolites, including steroids, flavonoids, saponins, alkaloids, terpenes, and phenolic compounds, which exhibit a diverse array of properties such as antimicrobial, antifungal, antiallergic, antidiabetic, cardiovascular protective, antioxidant, anticancer, antithyroid, antihistaminic, antimalarial, anthelmintic, anti-inflammatory, antihypertensive, antispasmodic, and analgesic [25]. This study delves into the effects of *Gypsophila* plant extract, within the realm of medicinal and aromatic plants, on the germination and seedling-related traits of vetch and sorghum seeds. Upon evaluating the mean values, we observed that the control concentration exhibited the highest germination rate, mean germination time, germination vigor index, root and shoot length, and root and shoot fresh weight in sorghum. The highest values were observed in the 5% concentration of *Gypsophila* extract in vetch. The existing literature has explored the effects of extracts from various medicinal and aromatic plants on cultivated plants' germination and seedling development [13]. While many studies emphasize the inhibitory effects of plant extracts on germination and seedling development, dependent on factors such as plant species, chemical compound type, and dosage [26; 27], there are also findings indicating stimulatory effects of plant extracts on germination and seedling development [28]. For example, Türkmen and Işık [29] investigated the impact of extracts from different vetch species on germination. The results indicated that extracts from certain vetch species completely inhibited germination at specific doses. Another study by Day [30] explored the effects of extracts from the stem and roots of the ragweed plant on the germination and seedling development of wheat, barley, sunflower, and chickpea seeds, revealing variable effects on different crops. In conclusion, the findings from this research suggest that the root extract obtained from the *Gypsophila* plant has a more inhibitory effect on germination and seedling development in sorghum plants compared to vetch plants. This adds valuable insights to the existing knowledge on the interactions between medicinal plant extracts and different crop species, emphasizing the need for species-specific considerations in agricultural practices.

Ethics in Publishing

There are no ethical issues regarding the publication of this study.

Author Contributions

Türkoğlu, A. concept; Armağan, M. and Türkoğlu, A. design; Işık, M. I. and Genç, A. resources; Işık, M. I. and Armağan, M. materials; Türkoğlu, A. and Genç, A. data collection and processing; Türkoğlu, A. data validation; Türkoğlu, A. analysis and interpretation; Türkoğlu, A. and Işık, M. I. literature search; Türkoğlu, A. and Işık, M. I. writing; Türkoğlu, A. and Armağan, M. critical reviews. All authors have read and agreed to the published version of the manuscript.

References

- [1] Hayta, M., & Koca, H., (2023). Erzurum Ovası'nda yem bitkileri tarımı ve coğrafi esasları. Ağrı İbrahim Çeçen Üniversitesi Sosyal Bilimler Enstitüsü Dergisi, 9(1), 68-100.
- [2] POWO (2023+). Plants of the World Online. Facilitated by the Royal Botanic Gardens, Kew. Available from: <http://www.plantsoftheworldonline.org/> [23.10.2023].
- [3] Ertekin, A.S. (2012). *Vicia*. Şu sitede: Bizimbitkiler (2013). <<http://www.bizimbitkiler.org.tr>>, [er. tar.: 23 10 2023].
- [4] Rubiales, D., Sillero J.C., Emeran, A.A., (2013). Response of vetches (*Vicia* spp.) to speciallized froms *Uramuces vicia-fabae* and to *Uromyces pisi*. Crop Production, 46, 38–43.
- [5] Atılğan, G. B. (2023). Pamuk tarımı yapılan arazilerde ikinci ürün olarak yetiştirilen fiğ ve arpa karışımlarına farklı silaj katkıları ilavesinin silaj kalitesi üzerine etkisinin araştırılması (Doctoral dissertation).
- [6] Duff, J., Bice, D., Hoeffner, I., Weinheimer, J., (2019). The sorghum industry and its market perspective. In Agronomy Monographs, pp. 503–514. Soil Science Society of America.
- [7] Mundia, C.W., Secchi, S., Akamani, K., Wang, G., (2019). A regional comparison of factors affecting global sorghum production: The case of North America, Asia and Africa's Sahel. Sustain.: Sci. Pract. Policy, 11(7), 2135.
- [8] Arııcı, R.Ç., & Avcı, M.A., (2022). Determination of forage yield and some quality characteristics of silage Sorghum Genotypes at different water stress levels. Selcuk Journal of Agriculture and Food Sciences, 36(1): 1-7.
- [9] Pour, A. H., Aydın, M., Tosun, M., Haliloğlu, K. (2013). Buğdayda Kuraklık ve Putresin Uygulamasının Tohum Çimlenmesi Üzerine Etkileri.

- [10] Emiralioglu, İ., & Acar, R. (2022). Tohumculuk Açısından Priming Uygulamalarının Önemi. *International Journal of Eastern Mediterranean Agricultural Research*, 5(1), 20-36.
- [11] Villedieu-Percheron, E., Lachia, M., Jung, P. M., Screpanti, C., Fonné-Pfister, R., Wendeborn, S., De Mesmaeker, A., (2014). Chemicals inducing seed germination and early seedling development. *Chimia*, 68(9), 654-654.
- [12] Kenanoğlu, B. B. (2016). Tohumların Çimlendirilmesinde Farklı Organik Ön Çimlendirme (Ozmotik Koşullandırma) Uygulamalarının Kullanımı. *Yüzüncü Yıl Üniversitesi Fen Bilimleri Enstitüsü Dergisi*, 21(2), 124-134.
- [13] Yıldız, E. (2019). Bazı Tıbbi ve Aromatik Bitki Ekstraktlarının Allelopatik Etkisi (Master's thesis, Fen Bilimleri Enstitüsü).
- [14] Binbir U., Türkmen C., Çıkkılı Y., Coşkun Y., Taş İ. (2021) Lavandin (*Lavandula x intermedia*) Uçucu Yağının Mısır (*Zea mays* L.)'ın Çimlenme ve Fide Gelişimine Etkileri, *ÇOMÜ Zir. Fak. Derg. COMU J. Agric. Fac.* 9 (1): 89 – 95.
- [15] Kuru, A. (2016). Entansif tarımda kullanılan jojoba ve lavanta bitkilerinin allelopatik potansiyellerinin araştırılması (Master's thesis, Pamukkale Üniversitesi Fen Bilimleri Enstitüsü).
- [16] Arslan D., Bayraktar Ö. V., (2022). Arslan H., Bazı Önemli Tıbbi ve Aromatik Bitkilerin Siirt İlinde Tarımının Yaygınlaştırılması.
- [17] Aganga, A. A., Tshwenyane, O. S. (2003), Feeding Values and Anti Nutrutive Factors of Forage Tree Legumes, *Pakistan Journal of Nutrition* 2(3): 170- 177, 2003.
- [18] İnan, M. (2006), Çukurova Koşullarında Farklı Kökenli Çöven (*Gypsophila* sp.) Türlerinde Kök Verimleri ve Saponin İçeriklerinin Araştırılması, Doktora Tezi. Çukurova Üniversitesi, Fen Bilimleri Enstitüsü, Tarla Bitkileri Anabilim Dalı, 90 s. Adana.
- [19] Gülören Ö.T. (2021), Bazı *Gypsophila* L. (*Caryophyllaceae*) Türlerinin Antimikrobiyal ve Genotoksik Aktiviteleri, Eskişehir Osmangazi Üniversitesi Fen Bilimleri Enstitüsü Doktora Tezi.
- [20] Soliman M.H., Abdulmajeed A.M., Alhaithloul H., Alharbi B.M., El-Esawi M.A., Hasanuzzaman M., Elkelish A., (2020). Saponin biopriming positively stimulates antioxidants defense, osmolytes metabolism and ionic status to confer salt stress tolerance in soybean, *Acta Physiologiae Plantarum* 42:114.
- [21] Yang A., Akhtar S.S., Iqbal S., (2018). Saponin seed priming improves salt tolerance in quinoa. *J Agron Crop Sci* 204:31–39.
- [22] Türkoğlu, A., Tosun, M., Haliloğlu, K., & Karagöz, H. Effects of Early Drought Stress on Germination and Seedling Growth Parameters of Kırık Bread Wheat (*Triticum aestivum* L.). *Journal of Agricultural Science*, 2(2), 75-80.

- [23] Halilođlu, K., Türkođlu, A., Aydın, M., (2022). Determination of Imazamox Herbicide Dose in in vivo Selection in Wheat (*Triticum aestivum* L.). Eregli journal of Agricultural Science.
- [24] Varlı, M., Hancı, H., Kalafat, G., (2020). Tıbbi ve aromatik bitkilerin üretim potansiyeli ve biyoyararlılıđı. Research Journal of Biomedical and Biotechnology, 1(1), 24-32.
- [25] Aftab, T. (2019). A review of medicinal and aromatic plants and their secondary metabolites status under abiotic stress. Journal of Medicinal Plants, 7(3), 99-106.
- [26] Zeren, H. (2015). Bazı tıbbi bitki ekstraktlarının ekmeklik buđday (*Triticum aestivum* l.) tohumlarının çimlenme ve gelişmeleri üzerine allelopatik etkileri. Yüksel Lisans Tezi, Gaziantep Üniversitesi, Fen Bilimleri Enstitüsü, Biyoloji Anabilim Dalı, Gaziantep.
- [27] Özen, F., Yaldız, G., Çamlıca, M., (2017). Yabancı ot mücadelesinde bazı aromatik bitkilerinin uçucu yağlarının allelopatik etkisi. Uluslararası Tarım ve Yaban Hayatı Bilimleri Dergisi, 3 (1), 40 – 48.
- [28] Öner, E.K., Kara, Ş.M., Açıkgöz, M.A., Özcan, M.M., (2017). Bazı Yem Bitkisi Tohumlarına Uygulanan Uçucu Yağların Çimlenme Üzerine Etkilerinin Belirlenmesi. Ordu Üniversitesi Bilimsel Araştırma Projeleri (BAP) Koordinasyon Birimi, Sonuç Raporu No: AR-1640, Ordu.
- [29] Türkmen, G., & Işık, D., (2016). Bazı fiğ türlerinin *Amaranthus retroflexus* l. tohumlarının çimlenmesi üzerine etkilerinin araştırılması. Uluslararası Katılımlı Türkiye VI. Bitki Koruma Kongresi, 5-8 Eylül, Konya.
- [30] Day, S. (2016). Aspir sap ve köklerinden elde edilen uçucu yağların buđday, arpa, ayçiçeđi ve nohutun çimlenme ve fide gelişimine etkileri. Türk Tarım–Gıda Bilim ve Teknoloji Dergisi, 4(8), 706-711.

A Generalization of Curve Mates: Normal Mate of a Curve

Oğuzhan Çelik^{1*}

¹Pamukkale University, Department of Banking-Finance and Insurance, Bekilli Vocational High School,
20930 Denizli, Türkiye

Received: 27/11/2024, **Revised:** 21/06/2024, **Accepted:** 08/08/2024, **Published:** 31/08/2024

Abstract

This paper, a new curve pair is defined that generalizes some pairs of curves well known as Mannheim and Bertrand curve pairs. A normal curve pair is defined in such a way that a vector \vec{w} obtained by overlapping the normal planes of the P and P^* curves makes the Γ angle as the binormals of these curves. The relationship between torsions and curvatures of curve pairs was analyzed. Moreover, a unit quaternion q was defined corresponding to the rotation matrix between the Frenet vectors of the curves. In the conclusion, it is expressed which famous curve pairs will be obtained in which particular case.

Keywords: Normal mate, Curve mates, Mannheim mate, Quaternion.

Eğri Çiftlerinin Genelleştirilmesi: Bir Eğrinin Normal Eğri Çifti

Öz

Bu çalışmada Bertrand ve Mannheim gibi çok bilinen eğri çiftlerini genelleştiren yeni bir eğri çifti tanımlanmıştır. Normal eğri çifti, P ve P^* eğrilerinin normal düzlemlerinin kesişimleri ile elde edilen bir \vec{w} vektörünün bu eğrilerin binormalleri ile Γ açısı yapacak şekilde tanımlanır. Eğri çiftlerinin eğrilikleri ve burulmaları arasındaki ilişki analiz edilmiştir. Ayrıca, eğrilerin Frenet vektörleri arasındaki dönme matrisine karşılık gelen birim q kuaterniyonu tanımlanmıştır. Sonuç olarak, hangi özel durumda hangi ünlü eğri çiftinin elde edileceğini ifade edilmiştir.

Anahtar Kelimeler: Normal eğri çifti, Eğri çiftleri, Mannheim eğri çifti, Kuaterniyon.

1. Introduction

Establishing a connection between two points corresponding to two curves and defining a new curve pair from these curves has been a subject that has attracted the attention of many researchers in classical differential geometry. These curve pairs have applications in fields like robotics, computer-aided geometric design and planning of paths. Some of the famous curve pairs are like Parallel, Evolute, Involute, Bertrand, Natural and Mannheim mates. Some properties and basic definitions of these curve pairs can be found in various papers [1,3,5,9,10,11,17,21,23,24,28,33,36]. These curves have been studied by many authors and some have been generalized to larger dimensions [8,14,16,25,32]. Moreover, Curve pairs in Lorentzian space have also been studied by many researchers [2,13,15,18,22,31,34,35,37]. The aim of the authors in this study is to express these curves in three-dimensional Euclidean space and make a new generalization and to investigate whether they give one of them by examining the special cases in the general definition. For this, A new pair of curves called normal mate is defined. If a vector obtained by overlapping normal planes makes the same angle as the binormals of the curves, the pair of curves formed by these curves is called normal mates. In this paper, we'll only analyze the normal mate. Moreover, we'll also expressed firstly the states between the Frenet vectors of curves of P and P^* . Then the states between their curvatures and torsions of curves of P and P^* . In the result section, it will be given which specific result represents which well-known curve.

If the tangent of a regular α curve with curvature different from zero at each point is the normal of an I curve, the involute curve of the α curve is expressed as the I curve. Evolute of a curve is defined as the place of the centers of curvatures of the curve. The evolute of an involute is the original curve. The definitions of involute and evolute were introduced by the Dutch mathematician Christian Huygens.

If the points on the curves that correspond to each other are also in the same direction as the normal of one curve and the normal of another these two curves are called the Bertrand curve pair. Moreover, a Bertrand curve is defined as a space curve B whose normal vector is identical to the normal vector of another curve B^* , known as its Bertrand mate. If λ is nonzero constant B^* and B are Bertrand mates as

$$B^*(s) = B(s) + \lambda \mathbf{N}(s) \text{ and } \mathbf{N}^*(s) = \pm \mathbf{N}(s)$$

for all $s \in I$. Bertrand curves stated by Bertrand in 1850 [1,5,17,21,24].

If the points on the curves that correspond to each other are also in the same direction as the normal of one curve and the binormal of another these two curves are called the Mannheim curve pair. Moreover, a Mannheim curve is defined as a space curve M whose normal vector is identical to the binormal vector of another curve M^* , known as its Mannheim mate. If λ is nonzero constant M^* and M are Mannheim mates as

$$M^*(s) = M(s) + \lambda \mathbf{N}(s) \text{ and } \mathbf{B}^*(s) = \pm \mathbf{N}(s)$$

for all $s \in I$. It was stated by A. Mannheim in 1878 [17,23,28].

We define curve pairs resulting from a Backlund transformation as pairs of constant torsion curves, which we will refer to as Backlund curves in this study. In classical differential geometry, a Backlund map transforms a surface with constant negative Gauss curvature into another surface with the same constant negative Gauss curvature. Moreover, the Backlund transformation can be restricted to produce a transformation that maps constant torsion curves to other constant torsion curves [6]. Let β and β^* be a smooth curves and Frenet vector fields of the curves β be $\{\mathbf{T}, \mathbf{N}, \mathbf{B}\}$. C is constant, τ is torsion and κ is curvature of β . It can be given the relation

$$\beta^*(s) = \beta(s) + ((2C)/(C^2 + \tau^2))((\cos\Gamma)\mathbf{T} + (\sin\Gamma)\mathbf{N})$$

where, $\beta' = C\sin\Gamma - \kappa$. The τ and τ^* torsions of β and β^* respectively constant and are

$$\tau^* = \tau = \frac{\sin\Phi}{\lambda}$$

in the above equation λ is the distance between these points and Φ is the angle between binormals of points on the curves that correspond to each other. Studies about Backlund mates can be found in the following articles: [6,26,27].

Our study will involve curve pairs where the vectors connecting corresponding points are always situated in the normal plane. Since we should not confuse these curves with the concepts of normal curves found in the literature, we will refer to these curves as normal pairs.

2. Preliminaries

Now, shortly reminding the Frenet elements of curves. Let's $\delta: I \rightarrow E^3$ a regular curve, $v = \|\delta'\| \neq 0$. The tangent, binormal and normal vector fields of δ are expressed as follows

$$\mathbf{T} = \frac{\delta'}{v}, \quad \mathbf{B} = \frac{\delta' \times \delta''}{\|\delta' \times \delta''\|} \text{ and } \mathbf{N} = \mathbf{B} \times \mathbf{T}$$

in order of. Additionally, curvature and torsion of the curve δ are

$$\kappa = \frac{\|\delta' \times \delta''\|}{\|\delta'\|^3} \text{ and } \tau = \frac{\det(\delta', \delta'', \delta''')}{\|\delta' \times \delta''\|^2}.$$

Frenet-Serret formula for the curve δ is

$$\begin{bmatrix} \mathbf{T}' \\ \mathbf{N}' \\ \mathbf{B}' \end{bmatrix} = \begin{bmatrix} 0 & v\kappa & 0 \\ -v\kappa & 0 & v\tau \\ 0 & -v\tau & 0 \end{bmatrix} \begin{bmatrix} \mathbf{T} \\ \mathbf{N} \\ \mathbf{B} \end{bmatrix}.$$

The planes spanned by $\{\mathbf{N}, \mathbf{B}\}$, $\{\mathbf{T}, \mathbf{B}\}$ and $\{\mathbf{T}, \mathbf{N}\}$ are called respectively the normal, rectifying and osculating plane at each point of a curve. The focus of this paper is on curve pairs, where lines connecting corresponding points are found within their normal planes.

Main Theorem and Proof

In this section, we will introduce a new curve pairs that can generalize the famous curve pairs briefly expressed in the previous sections.

3.1. Normal Mates in the Euclidean 3-space

Definition 3.1. Let's map the corresponding points of the curves P and P^* given on the space E^3 and define the curve

$$P^*(s) = P(s) + \lambda(s)\vec{\mathbf{w}}(s)$$

where $\vec{\mathbf{w}}$ is a unit vector and λ is the distance function.

The vector $\vec{\mathbf{w}}$ lies on the line where the normal planes of the curves P and P^* intersect. If the vector $\vec{\mathbf{w}}$ makes an angle Γ with the binormal vector fields at points on the curves P and P^* that correspond to each other, then the pair of curves $\{P, P^*\}$ is termed the Normal pair of curve or Normal mates. In this place, P and P^* are called normal curve and equinormal curve, in order of. Moreover, $P^*(s)$ is expressed as the normal mate of $P(s)$

Theorem 3.2. Let $\{P, P^*\}$ be the Normal mate. $\mathbf{B}(s)$ and $\mathbf{N}(s)$ being the binormal and normal vector fields of the curve $P(s)$, in order of. It is written as follows

$$P^*(s) = P(s) + \lambda(s)((\cos\Gamma(s))\mathbf{B}(s) + (\sin\Gamma(s))\mathbf{N}(s)) \tag{3.1}$$

where $\lambda(s) \neq 0$ is the distance function between curves P and P^* . Hence, the following equation is obtained

$$0 = \lambda' \tag{3.2}$$

to be $v = \|P'\|$, $v^* = \|P^{*'}\|$.

Proof If P, P^* is an Normal curve mate, then the vector $\lambda\mathbf{w}(s) = P^*(s) - P(s)$ will make an angle $\Gamma(s)$ with binormal vector fields $\mathbf{B}(s)$ and $\mathbf{B}^*(s)$ along the curves P and P^* . Moreover, given that the unit vector $\mathbf{w}(s)$ is in the normal plane. We can express the following equations

$$\vec{\mathbf{w}} = (\cos\Gamma)\mathbf{B} + (\sin\Gamma)\mathbf{N}$$

and

$$P^* = P + \lambda((\cos\Gamma)\mathbf{B} + (\sin\Gamma)\mathbf{N}).$$

Now let's take the derivative of equation (3.1). Then we find the following equation

$$\begin{aligned}
 v^* \mathbf{T}^* &= v \mathbf{T} + \lambda'((\cos \Gamma) \mathbf{B} + (\sin \Gamma) \mathbf{N}) \\
 &\quad + \lambda(\Gamma'(-\sin \Gamma) \mathbf{B} + (\cos \Gamma)(-\tau v \mathbf{N}) + \Gamma'(\cos \Gamma) \mathbf{N} + (\sin \Gamma)(-\kappa v \mathbf{T} + \tau v \mathbf{B}))
 \end{aligned} \tag{3.3}$$

$$\begin{aligned}
 v^* \mathbf{T}^* &= (v - \kappa v \sin \Gamma) \mathbf{T} \\
 &\quad + (\lambda' \sin \Gamma - \lambda v \tau \cos \Gamma + \lambda \Gamma' \cos \Gamma) \mathbf{N} \\
 &\quad + (\lambda' \cos \Gamma - \lambda \Gamma' \sin \Gamma + \lambda v \tau \sin \Gamma) \mathbf{B}.
 \end{aligned} \tag{3.4}$$

If we take the inner product of both sides of equation (3.4) with the vector \vec{w} , we get

$$0 = (\lambda' \cos \Gamma - \lambda \Gamma' \sin \Gamma + \lambda v \tau \sin \Gamma) \cos \Gamma + (\lambda' \sin \Gamma - \lambda v \tau \cos \Gamma + \lambda \Gamma' \cos \Gamma) \sin \Gamma$$

$$0 = \lambda'.$$

Consequently, we obtain the equality

$$0 = \lambda'.$$

3.2. The Relations Between Frenet Apparatus of Pair of Normal Curves

In this section, we will begin by exploring the relationship both between Frenet frames of normal curve and their mates, as well as the curvature and the torsion of these curves. Moreover, we'll analyze whether distance function between the points on the curves P and P^* that correspond to each other is constant or not. Furthermore, we will discuss whether the angle Γ remains constant, considering special cases such as when Γ is constant, $\Gamma = \pi/2$ or $\Gamma = 0$. We will investigate under which specific conditions we can obtain curve pairs that are either in Mannheim curves, Bertrand curves or other type.

Theorem 3.3. Let P and P^* respectively be a regular curves and normal mates of given by the equation

$$P^* = P + \lambda((\cos \Gamma) \mathbf{B} + (\sin \Gamma) \mathbf{N}). \tag{4.1}$$

Let $\{\mathbf{T}, \mathbf{N}, \mathbf{B}\}$ and $\{\mathbf{T}^*, \mathbf{N}^*, \mathbf{B}^*\}$ be Frenet vector fields of curves P and P^* , in order of. Provided that the angle Φ is between the opposite tangent of the curves, $\mu = 1 - \cos \Phi$. We obtain the matrix equation

$$\begin{bmatrix} \mathbf{T}^* \\ \mathbf{N}^* \\ \mathbf{B}^* \end{bmatrix} = \begin{bmatrix} \cos \Phi & -\sin \Phi \cos \Gamma & \sin \Phi \sin \Gamma \\ \cos \Gamma \sin \Phi & 1 - \mu \cos^2 \Gamma & \mu \cos \Gamma \sin \Gamma \\ -\sin \Gamma \sin \Phi & \mu \sin \Gamma \cos \Gamma & 1 - \mu \sin^2 \Gamma \end{bmatrix} \begin{bmatrix} \mathbf{T} \\ \mathbf{N} \\ \mathbf{B} \end{bmatrix} \tag{4.2}$$

Proof Since the vector field

$$\vec{w} = (\cos \Gamma) \mathbf{B} + (\sin \Gamma) \mathbf{N}$$

lying on the normal plane, this vector is perpendicular to the tangent vector fields \mathbf{T} and \mathbf{T}^* . Hence, $\mathbf{v} = \mathbf{T} \times \mathbf{w}$ and $\mathbf{v}^* = \mathbf{T}^* \times \mathbf{w}$ lies on the normal planes of the curves. Thus, every one of the collections $\{\mathbf{w}, \mathbf{v}^*, \mathbf{T}^*\}$ and $\{\mathbf{w}, \mathbf{v}, \mathbf{T}\}$ forms an orthonormal frame for the curves P and P^* , respectively. The following Matrix equations can be obtained

$$\begin{bmatrix} \vec{\mathbf{w}} \\ \vec{\mathbf{v}} \end{bmatrix} = \begin{bmatrix} \cos\Gamma & \sin\Gamma \\ -\sin\Gamma & \cos\Gamma \end{bmatrix} \begin{bmatrix} \mathbf{B}^* \\ \mathbf{N}^* \end{bmatrix} \quad (4.3)$$

and

$$\begin{bmatrix} \vec{\mathbf{w}} \\ \vec{\mathbf{v}}^* \end{bmatrix} = \begin{bmatrix} \cos\Gamma & \sin\Gamma \\ -\sin\Gamma & \cos\Gamma \end{bmatrix} \begin{bmatrix} \mathbf{B} \\ \mathbf{N} \end{bmatrix}. \quad (4.4)$$

Let Φ be the angle between \mathbf{T}^* and \mathbf{T} . Since all of the vectors \mathbf{T}^* , $\vec{\mathbf{v}}^*$, \mathbf{T} , $\vec{\mathbf{v}}$ are perpendicular to the $\vec{\mathbf{w}}$. Provided that the equation (4.3) was used, we get

$$\begin{aligned} \mathbf{T}^* &= (\sin\Phi)\vec{\mathbf{v}} + (\cos\Phi)\mathbf{T} \\ &= (\cos\Phi)\mathbf{T} - (\sin\Phi\cos\Gamma)\mathbf{N} + (\sin\Phi\sin\Gamma)\mathbf{B} \end{aligned}$$

and

$$\begin{aligned} \vec{\mathbf{v}}^* &= (\cos\Phi)\vec{\mathbf{v}} + (\sin\Phi)\mathbf{B} \\ &= (\sin\Phi)\mathbf{T} + (\cos\Phi\cos\Gamma)\mathbf{N} - \cos\Phi\sin\Gamma\mathbf{B}. \end{aligned}$$

Thus, using the equalities (4.4) and (4.3) we have

$$\begin{aligned} \begin{bmatrix} \mathbf{B}^* \\ \mathbf{N}^* \end{bmatrix} &= \begin{bmatrix} \cos\Gamma & -\sin\Gamma \\ \sin\Gamma & \cos\Gamma \end{bmatrix} \begin{bmatrix} \vec{\mathbf{w}} \\ \vec{\mathbf{v}} \end{bmatrix} \\ &= \begin{bmatrix} -(\sin\Gamma\sin\Phi)\mathbf{T} + \sin\Gamma\cos\Gamma(1 - \cos\Phi)\mathbf{N} + (1 + \sin^2\Gamma(\cos\Phi - 1))\mathbf{B} \\ (\cos\Gamma\sin\Phi)\mathbf{T} + (1 + \cos^2\Gamma(\cos\Phi - 1))\mathbf{N} + (\sin\Gamma\cos\Gamma)(1 - \cos\Phi)\mathbf{B} \end{bmatrix}. \end{aligned}$$

As a result, (4.2) equality is obtained where $1 - \mu = \cos\Phi$.

3.3. Curvature and Torsion of The Normal Curve P

Theorem 3.4. Let P and P^* respectively be a regular curves and normal mates with the relation $P^* = P + \lambda((\cos\Gamma)\mathbf{B} + (\sin\Gamma)\mathbf{N})$ where $\Gamma \neq 0, \Gamma \neq \pi/2$ and the distance function λ . Provided that the angle $\Phi \neq 0$ is between binormal of the corresponding points of P and P^* , in this case the curvature and torsion of the $P(s)$ curve is

$$\begin{aligned} \kappa &= \frac{v - v^*\cos\Phi}{\lambda v \sin\Gamma} \\ \tau &= \frac{v^*\sin\Phi + \Gamma'\lambda}{\lambda v} \end{aligned} \quad (4.5)$$

respectively, where $\mu = 1 - \cos\Phi$.

Proof If we compare the equality (3.4) and (4.1)

$$\begin{aligned} v^*\mathbf{T}^* &= (v - \lambda\kappa v \sin\Gamma)\mathbf{T} \\ &+ (\lambda' \sin\Gamma - \lambda\nu\tau \cos\Gamma + \lambda\Gamma' \cos\Gamma)\mathbf{N} \\ &+ (\lambda' \cos\Gamma - \lambda\Gamma' \sin\Gamma + \lambda\nu\tau \sin\Gamma)\mathbf{B}. \end{aligned}$$

Let's take the inner product of both sides of the above equation with \mathbf{T} , \mathbf{N} and \mathbf{B} respectively, then the following equality is obtained

$$\begin{aligned} v^*(\cos\Phi) &= (v - \lambda\kappa v \sin\Gamma) \\ -v^* \sin\Phi \cos\Gamma &= (\lambda' \sin\Gamma - \lambda\nu\tau \cos\Gamma + \lambda\Gamma' \cos\Gamma) \\ v^* \sin\Phi \sin\Gamma &= (\lambda' \cos\Gamma - \lambda\Gamma' \sin\Gamma + \lambda\nu\tau \sin\Gamma). \end{aligned} \tag{4.6}$$

In terms of $\Gamma \neq 0, \pi/2$, thinking $0 = \lambda'$ and $\mu = 1 - \cos\Phi$, we find

$$-v^* \sin\Phi \cos\Gamma = (\lambda' \sin\Gamma - \lambda\nu\tau \cos\Gamma + \lambda\Gamma' \cos\Gamma)$$

$$\tau = \frac{v^* \sin\Phi + \Gamma' \lambda}{\lambda\nu}$$

and

$$v^*(\cos\Phi) = (v - \lambda\kappa v \sin\Gamma)$$

$$\kappa = \frac{v - v^* \cos\Phi}{\lambda v \sin\Gamma}.$$

Proposition 3.5. Let it be

$$R_\Phi = \begin{bmatrix} \cos\Phi & -\cos\Gamma \sin\Phi & \sin\Gamma \sin\Phi \\ \cos\Gamma \sin\Phi & 1 - \mu \cos^2\Gamma & \mu \cos\Gamma \sin\Gamma \\ -\sin\Gamma \sin\Phi & \mu \sin\Gamma \cos\Gamma & 1 - \mu \sin^2\Gamma \end{bmatrix}$$

is a rotation matrix for any normal pair of the curves. R_Φ rotates a vector through the angle Φ around the axis $\vec{\mathbf{u}} = (0, \sin\Gamma, \cos\Gamma)$. The unit quaternion q corresponds to R_Φ . Then

$$q = \cos \frac{\Phi}{2} + \sin\Gamma \sin \frac{\Phi}{2} \mathbf{j} + \cos\Gamma \sin \frac{\Phi}{2} \mathbf{k}.$$

Proof

$$R_\phi = \begin{bmatrix} 1 - 2(1 - a^2)\sin^2\frac{\phi}{2} & ab(1 - \cos\phi) - c\sin\phi & b\sin\phi + ac(1 - \cos\phi) \\ ab(1 - \cos\phi) + c\sin\phi & 1 - 2(1 - b^2)\sin^2\frac{\phi}{2} & -a\sin\phi + bc(1 - \cos\phi) \\ -b\sin\phi + ac(1 - \cos\phi) & a\sin\phi + bc(1 - \cos\phi) & 1 - 2(1 - c^2)\sin^2\frac{\phi}{2} \end{bmatrix}$$

is a rotation matrix. R_ϕ rotates a vector through the angle ϕ around the axis $\vec{u} = (a, b, c)$ and the unit quaternion q corresponds to R_ϕ is

$$q = \cos\frac{\phi}{2} + (a\mathbf{i} + b\mathbf{j} + c\mathbf{k})\sin\frac{\phi}{2} \quad [31].$$

If we have $\vec{u} = (0, \sin\Gamma, \cos\Gamma)$ the rotation matrix is

$$R_\phi = \begin{bmatrix} \cos\phi & -\cos\Gamma\sin\phi & \sin\Gamma\sin\phi \\ \cos\Gamma\sin\phi & 1 - \mu\cos^2\Gamma & \mu\sin\Gamma\cos\Gamma \\ -\sin\Gamma\sin\phi & \mu\cos\Gamma\sin\Gamma & 1 - \mu\sin^2\Gamma \end{bmatrix}$$

and the unit quaternion q corresponds to R_ϕ . Then

$$q = \cos\frac{\phi}{2} + \sin\Gamma\sin\frac{\phi}{2}\mathbf{j} + \cos\Gamma\sin\frac{\phi}{2}\mathbf{k}.$$

Theorem 3.6. Let P and P^* respectively be a regular curves and normal mates with the relation $P^* = P + \lambda((\cos\Gamma)\mathbf{B} + (\sin\Gamma)\mathbf{N})$ where $\Gamma \neq 0, \pi/2$ and the distance function λ . Provided that the angle $\phi \neq 0$ between tangent of the corresponding points of P and P^* , in this case the curvature and torsion of the $P^*(s)$ curve is

$$\begin{aligned} \kappa^* &= \frac{v - v^*\cos\phi}{v^*\sin\Gamma} - \frac{\phi'}{v^*\cos\Gamma}, \\ \tau^* &= \frac{\Gamma' + \phi'\tan\Gamma\cot\phi}{v^*} - \frac{v\kappa\sin\Gamma}{v^*\sin\phi} \end{aligned} \quad (4.7)$$

respectively, where $\mu = 1 - \cos\phi$.

Proof Now let's take the derivative of \mathbf{T}^* in equation (4.2). Then we find the following equation

$$\mathbf{T}^* = (\cos\phi)\mathbf{T} - \sin\phi\cos\Gamma\mathbf{N} + (\sin\phi\sin\Gamma)\mathbf{B}$$

$$v^*\kappa^*\mathbf{N}^* = (-\phi'\sin\phi + v\kappa\sin\phi\cos\Gamma)\mathbf{T}$$

$$+ (v\kappa\cos\phi - \phi'\cos\phi\cos\Gamma + \Gamma'\sin\phi\sin\Gamma - v\tau\sin\phi\sin\Gamma)\mathbf{N} \quad (4.8)$$

$$+ (-v\tau\sin\phi\cos\Gamma + \phi'\cos\phi\sin\Gamma + \Gamma'\sin\phi\cos\Gamma)\mathbf{B}.$$

Let's the inner product of both sides of equation (4.8) with the \mathbf{T} , we get

$$v^*\kappa^*\cos\Gamma = (-\Phi' + v\kappa\cos\Gamma) \tag{4.9}$$

since $\langle \mathbf{N}^*, \mathbf{T} \rangle = \sin\Phi\cos\Gamma$. Thus, we get

$$v^*\kappa^* = v\kappa - \frac{\Phi'}{\cos\Gamma}$$

or $\Gamma \neq 0$ and $\Gamma \neq \pi/2$. Moreover, in terms of $\Phi \neq 0$, we write $\mu = 1 - \cos\Phi$. Hence $\mu' = \Phi'\sin\Phi$ and

$$\frac{\mu'}{\mu} = \frac{\Phi'\sin\Phi}{1 - \cos\Phi} = \frac{\Phi'(1 + \cos\Phi)}{\sin\Phi}.$$

Using these equalities, we obtain

$$v^*\kappa^* = v\kappa - \frac{\Phi'}{\cos\Gamma} \tag{4.10}$$

$$\kappa^* = \frac{v\kappa}{v^*} - \frac{\Phi'}{v^*\cos\Gamma} \tag{4.11}$$

$$\kappa^* = \frac{v - v^*\cos\Phi}{v^*\lambda\sin\Gamma} - \frac{\Phi'}{v^*\cos\Gamma}. \tag{4.12}$$

Let's the inner product of both sides of equation (4.8) with the \mathbf{B} , we get

$$v^*\kappa^*\mu\cos\Gamma\sin\Gamma = -v\tau\sin\Phi\cos\Gamma + \Phi'\cos\Phi\sin\Gamma + \Gamma'\sin\Phi\cos\Gamma$$

$$v^*\kappa^* = \frac{-v\tau\sin\Phi + \Phi'\cos\Phi\tan\Gamma + \Gamma'\sin\Phi}{\mu\sin\Gamma}$$

since $\langle \mathbf{N}^*, \mathbf{B} \rangle = \mu\cos\Gamma\sin\Gamma$. Let's write $\tau = \frac{v^*\sin\Phi + \Gamma'\lambda}{v\lambda}$ in this equation. Thus, we have

$$v^*\kappa^* = \frac{-v\tau\sin\Phi + \Phi'\cos\Phi\tan\Gamma + \Gamma'\sin\Phi}{\mu\sin\Gamma} \tag{4.13}$$

$$\kappa^* = \frac{-v\tau\sin\Phi + \Phi'\cos\Phi\tan\Gamma + \Gamma'\sin\Phi}{v^*\mu\sin\Gamma}. \tag{4.14}$$

Additionally, by using equations (4.10) and (4.13) we obtain the following equation

$$\frac{v - v^*\cos\Phi}{v^*\lambda\sin\Gamma} - \frac{\Phi'}{v^*\cos\Gamma} = \frac{-v\tau\sin\Phi + \Phi'\cos\Phi\tan\Gamma + \Gamma'\sin\Phi}{v^*\mu\sin\Gamma}$$

$$\mu v - \mu v^*\cos\Phi - \mu\Phi'\tan\Gamma = -\frac{v^*\sin\Phi + \Gamma'\lambda}{\lambda}\sin\Phi + \Phi'\cos\Phi\tan\Gamma + \Gamma'\sin\Phi.$$

If we substitute the κ curvature expressed in Theorem 4.2 into the equation above, we obtain the following equation

$$\frac{\lambda\Phi'}{\sin\Phi} = (v^* - v)\cos\Gamma.$$

Thus, considering the equality $0 = \lambda'$ we find

$$\lambda = -\frac{v^*\sin\Phi}{v - v^*\cos\Phi + \mu\Phi'\tan\Gamma} + c \tag{4.15}$$

with $c \in \mathbb{R}$. The equation (4.15) shows that when Φ is constant, λ will also be constant. If we write equation (4.15) into equation (4.1), we obtain

$$P^* = P + \left(-\frac{v^*\sin\Phi}{v - v^*\cos\Phi + \mu\Phi'\tan\Gamma} + c\right)((\cos\Gamma)\mathbf{B} + (\sin\Gamma)\mathbf{N}). \tag{4.16}$$

If take derivative of \mathbf{B}^* expressed in (4.2). Then, we obtain

$$\begin{aligned} \mathbf{B}^* &= -(\sin\Gamma\sin\Phi)\mathbf{T} + \mu\sin\Gamma\cos\Gamma\mathbf{N} + (1 - \mu\sin^2\Gamma)\mathbf{B} \\ -v^*\tau^*\mathbf{N}^* &= -(\Gamma'\cos\Gamma\sin\Phi + \Phi'\sin\Gamma\cos\Phi + v\kappa\mu\sin\Gamma\cos\Gamma)\mathbf{T} \\ &\quad (-v\kappa\sin\Gamma\sin\Phi + \mu'\sin\Gamma\cos\Gamma + \mu\Gamma'\cos^2\Gamma - \mu\Gamma'\sin^2\Gamma - v\tau(1 - \mu\sin^2\Gamma))\mathbf{N} \\ &\quad (v\tau\mu\sin\Gamma\cos\Gamma - \mu'\sin^2\Gamma - 2\mu\Gamma'\sin\Gamma\cos\Gamma)\mathbf{B}. \end{aligned}$$

Using the equality $\langle \mathbf{N}^*, \mathbf{T} \rangle = \cos\Gamma\sin\Phi$ we obtain

$$v^*\tau^*\cos\Gamma\sin\Phi = \Gamma'\cos\Gamma\sin\Phi + \Phi'\sin\Gamma\cos\Phi + v\kappa\mu\sin\Gamma\cos\Gamma$$

$$v^*\tau^* = \Gamma' + \Phi'\tan\Gamma\cot\Phi + \frac{v\kappa\mu\sin\Gamma}{v^*\sin\Phi}$$

$$\tau^* = \frac{\Gamma'}{v^*} + \frac{\Phi'\tan\Gamma\cot\Phi}{v^*} + \frac{v\kappa\mu\sin\Gamma}{v^*\sin\Phi}$$

for $\Phi \neq 0$.

4. Conclusion

4.1. Both Φ and Γ are non-constant

Let $\{P, P^*\}$ be an Normal mate of curves. Provided that the angle $\Phi \neq 0$ between binormal of the corresponding points of P and P^* , we have the equation (4.16) for $\Gamma \neq 0, \pi/2$. The curvatures and torsions of P and P^* are

$$\begin{aligned} \tau &= \frac{v^* \sin\Phi + \Gamma'\lambda}{v\lambda}, & \tau^* &= \frac{\Gamma' + \Phi' \tan\Gamma \cot\Phi}{v^*} - \frac{v\kappa \sin\Gamma}{v^* \sin\Phi}, \\ \kappa &= \frac{v - v^* \cos\Phi}{\lambda v \sin\Gamma}, & \kappa^* &= \frac{v\kappa}{v^*} - \frac{\Phi'}{v^* \cos\Gamma}. \end{aligned}$$

Now, let's analyze special cases.

4.2. Φ is constant and Γ is non-constant with $\Gamma \neq 0, \Gamma \neq \pi/2$.

If Φ is constant, $\lambda = -\frac{v^* \sin\Phi}{v - v^* \cos\Phi + \mu\Phi' \tan\Gamma} + c$ and λ will also be constant. So, if $\Gamma \neq \pi/2$, the equality $0 = \lambda'$. In this case the curvatures and torsions of P and P^* are

$$\begin{aligned} \tau &= \frac{v^* \sin\Phi + \Gamma'\lambda}{v\lambda}, & \tau^* &= \frac{\Gamma'}{v^*} - \frac{v\kappa \sin\Gamma}{v^* \sin\Phi}, \\ \kappa &= \frac{v - v^* \cos\Phi}{\lambda v \sin\Gamma}, & \kappa^* &= \frac{v\kappa}{v^*}. \end{aligned} \tag{4.17}$$

4.3. Φ is non-constant and Γ are constant

Let $\{P, P^*\}$ be a Normal mate of curves. Provided that the angle $\Phi \neq 0$ between binormal of the corresponding points of P and P^* , we have the equation (4.16) for $\Gamma \neq 0, \pi/2$. The curvatures and torsions of P and P^* are

$$\begin{aligned} \tau &= \frac{v^* \sin\Phi}{v\lambda}, & \tau^* &= \frac{\Phi' \tan\Gamma \cot\Phi}{v^*} - \frac{v\kappa \sin\Gamma}{v^* \sin\Phi}, \\ \kappa &= \frac{v - v^* \cos\Phi}{\lambda v \sin\Gamma}, & \kappa^* &= \frac{v\kappa}{v^*} - \frac{\Phi'}{v^* \cos\Gamma}. \end{aligned} \tag{4.18}$$

4.4. Both Φ and Γ are constant

Let $\{P, P^*\}$ be an Normal mate of curves. Provided that the angle $\Phi \neq 0, \pi/2$ between binormal of the corresponding points of P and P^* , we have the equation (4.16) for $\Gamma \neq 0, \pi/2$. The curvatures and torsions of P and P^* are

$$\begin{aligned} \tau &= \frac{v^* \sin\Phi + \Gamma'\lambda}{v\lambda}, & \tau^* &= -\frac{v\kappa \sin\Gamma}{v^* \sin\Phi}, \\ \kappa &= \frac{v - v^* \cos\Phi}{\lambda v \sin\Gamma}, & \kappa^* &= \frac{v\kappa}{v^*}. \end{aligned} \tag{4.19}$$

Now, let's analyze special cases.

4.4.1. $\Phi \neq 0, \pi/2$ and $\Gamma = 0$ case

From (4.19) we have

$$\tau = \frac{v^* \sin\Phi + \Gamma'\lambda}{v\lambda}, \quad \tau^* = 0,$$

$$\kappa^* = \frac{v\kappa}{v^*}.$$

4.4.2. $\Phi \neq 0, \pi/2$ and $\Gamma = \pi/2$. (In the case $\{P, P^*\}$ is a Mannheim mate)

λ is constant, then

$$P^* = P + \lambda N.$$

Moreover, with respect to the equality (3.4) and (4.2) we obtain

$$v^* \mathbf{T}^* = (v - v\kappa\lambda) \mathbf{T} + v\lambda\tau \mathbf{B}$$

$$\begin{bmatrix} \mathbf{T}^* \\ \mathbf{N}^* \\ \mathbf{B}^* \end{bmatrix} = \begin{bmatrix} \cos\Phi & 0 & \sin\Phi \\ 0 & 1 & 0 \\ -\sin\Phi & 0 & \cos\Phi \end{bmatrix} \begin{bmatrix} \mathbf{T} \\ \mathbf{N} \\ \mathbf{B} \end{bmatrix}.$$

Thus, since $P^* = P + \lambda N$, $\lambda \in \mathbb{R}$ $\{P, P^*\}$ is a Mannheim mate. So, using the special case given above, we express

$$\tau = \frac{v^* \sin\Phi}{v\lambda}, \quad \tau^* = -\frac{v\kappa}{v^* \sin\Phi},$$

$$\kappa = \frac{v - v^* \cos\Phi}{\lambda v}, \quad \kappa^* = \frac{v\kappa}{v^*}. \tag{4.20}$$

for Mannheim curve P .

Therefore, from equations (4.20) we obtain the following expressions for Mannheim mates

- The product of the twist torsions of Mannheim curves points on the curves P and P^* that correspond to each other must be constant, hence

$$\tau\tau^* = \frac{\kappa}{\lambda}$$

from (4.20).

- If a and b are non-zero constants and $a\kappa + b\tau = 1$, this curve is a Mannheim curve. Hence

$$\cot\Phi = \frac{1 - \kappa\lambda}{\tau\lambda} \Leftrightarrow \kappa\lambda + (\cot\Phi)\lambda\tau = 1$$

from (4.20). It means that, $a = \lambda$ and $b = \lambda\cot\Phi$.

4.4.3. $\Phi = \pi/2$ and $\Gamma \neq 0, \pi/2$ case

From (4.19) and λ is constant we have

$$\begin{aligned} \tau &= \frac{v^*}{v\lambda}, & \tau^* &= -\frac{v}{\lambda v^*}, \\ \kappa &= \frac{1}{\lambda \sin \Gamma}, & \kappa^* &= \frac{v}{v^* \lambda \sin \Gamma}. \end{aligned}$$

4.4.4. $\Phi = \pi/2$ and $\Gamma = \pi/2$ case

From (3.1) we have

$$P^* = P + \lambda N.$$

From (4.19) we have

$$\begin{aligned} \tau &= \frac{v^*}{v\lambda}, & \tau^* &= -\frac{v}{\lambda v^*}, \\ \kappa &= \frac{1}{\lambda}, & \kappa^* &= \frac{v\kappa}{v^*}. \end{aligned}$$

$$\tau\tau^* = -\frac{1}{\lambda^2}, \lambda\kappa + \mu\tau = 1.$$

Ethics in publishing

There are no ethical issues regarding the publication of this study.

References

- [1] Babaarslan, M., Yayli, Y., (2013) On helices and Bertrand curves in Euclidean 3-space, *Mathematical and Computational Applications*, 18 (1) 1 - 11.
- [2] Balgetir, H., Bektas, M., Inoguchi, J. I., (2004) Null Bertrand curves in Minkowski 3-space and their characterizations, *Note di matematica*, 23 (1) 7 - 13.
- [3] Bektaş, Ö., (2018) Normal curves in n-dimensional Euclidean Space, *Advances in Difference Equations*, 2018 456.
- [4] Bukcu, B., Karacan, M. K., Yuksel, N., (2011) New Characterizations for Bertrand Curves in Minkowski 3-Space, *Mathematical Combinatorics*, 2 98-103.
- [5] Burke, J. F., (1960) Bertrand curves associated with a pair of curves, *Mathematics Magazine*, 34 (1) 60 - 62.
- [6] Calini, A., Ivey, T., (1998) Backlund transformations and knots of constant torsion, *Journal of Knot Theory and Its Ramifications*, 7 (06) 719 - 746.
- [7] Çelik, O., Özdemir, M., (2022) A New Generalization of Some Curve Pairs, *International Electronic Journal of Geometry*, 15 (2) 214 - 224.

- [8] Cheng, Y. M., Lini, C. C., (2010) On the Generalized Bertrand Curves in Euclidean-spaces, *Note di Matematica*, 29 (2) 33 - 39.
- [9] Choi, J. H., Kim, Y. H., (2012) Associated curves of a Frenet curve and their applications, *Applied Mathematics and Computation*, 218 (18) 9116 - 9124.
- [10] Dede, M., Ekici, C., (2018) Directional Bertrand curves, *Gazi University Journal of Science*, 31 (1) 202 - 211.
- [11] Deshmukh S, Chen B. Y., (2018) Alghanemi A, Natural mates of Frenet curves in Euclidean 3-space. *Turkish Journal of Mathematics*, 42 (5) 2826 - 2840.
- [12] Ekmekci, N., Ilarslan, K., (2001) On Bertrand curves and their characterization, *Differ. Geom. Dyn. Syst.*, 3 (2) 17 - 24.
- [13] Gok, I., Nurkan, S. K., Ilarslan, K., (2014) On pseudo null Bertrand curves in Minkowski space-time, *Kyungpook Mathematical Journal*, 54 (4) 685-697.
- [14] Görgülü, A., Özdamar, E., (1986)“A generalization of the Bertrand curves as general inclined curves in E^n , *Commun. Fac. Sci. Univ. Ank., Series A1* (35) 53 - 60.
- [15] Güner G., Ekmekci, N., (2012) On the spherical curves and Bertrand curves in Minkowski-3 space, *J. Math. Comput. Sci.*, 2 (4) 898 - 906.
- [16] Hanif, M., Hou, Z. H., (2018) Generalized involute and evolute curve-couple In Euclidean space, *Int. J. Open Problems Compt. Math.*, 11 (2).
- [17] Honda, S. I., Takahashi, M., (2020) Bertrand and Mannheim curves of framed curves in the 3-dimensional Euclidean space, *Turkish Journal of Mathematics*, 44 (3) 883 – 899.
- [18] Ilarslan, K., Aslan, N. K., (2016) On Spacelike Bertrand Curves in Minkowski 3-Space, *Konuralp Journal of Mathematics*, 5 (1) 214 - 222.
- [19] Ilarslan, K., (2005) Timelike and null normal curves in Minkowski space $E(1,3)$. *Turk. J.Math.*, 29 (1) 53 - 63.
- [20] Ilarslan, K., Nesovic, E., (2009) Spacelike and timelike normal curves in Minkowski space-time, *Publ. Inst. Math.*, 85 (99) 111 - 118.
- [21] Izumiya, S., Takeuchi, N., (2002) Generic properties of helices and Bertrand curves, *Journal of Geometry*, 74 (1-2) 97 - 109.
- [22] Karacan, M. K., Tunçer, Y., (2012) Backlund transformations according to bishop frame in Euclidean 3-space, *In Siauliai Mathematical Seminar*, 7 (15).
- [23] Liu, H., Wang, F., (2008) Mannheim partner curves in 3-space, *Journal of Geometry*, 88 (1-2) 120 - 126.

- [24] Matsuda, H., Yorozu, S., (2003) Notes on Bertrand Curves, *Yokohama Mathematical Journal*, 50 (1) 41 - 58.
- [25] Matsuda, H., Yorozu, S., (2009) On generalized Mannheim curves in Euclidean 4-space, *Nihonkai Mathematical Journal*, 20 (1) 33 - 56.
- [26] Nemeth, S. Z., (2000) Backlund transformations of constant torsion curves in 3 dimensional constant curvature spaces, *Italian Journal of Pure and Applied Mathematics*, (7) 125 - 138.
- [27] Nemeth, S. Z., (1998) Backlund transformations of n-dimensional constant torsion curves, *Publicationes Mathematicae Debrecen*, 53 (3-4) 271 - 279.
- [28] Orbay, K., Kasap, E., (2009) On Mannheim partner curves in E^3 , *International Journal of Physical Sciences*, 4 (5) 261 - 264.
- [29] Önder, M., (2019) Construction of curve pairs and their application, *Proceedings of the National Academy of Sciences, India Section A: Physical Sciences*:1-8.
- [30] Özdemir, M., Çöken, A. C., (2009) Backlund transformation for non-lightlike curves in Minkowski 3-space, *Chaos, Solitons & Fractals*, 42 (4) 2540 - 2545.
- [31] Özdemir, M., (2020) *Kuaterniyonlar ve Geometri*, (72). Altın Nokta Yayınları, İzmir.
- [32] Öztekin, H. B., Bektas, M., (2020) Representation formulae for Bertrand curves in the Minkowski 3-space, *Scientia Magna*, 6 (1) 89.
- [33] Ozturk, G., Arslan, K., Bulca, B., (2018) A Characterization of Involutes and Evolutes of a Given Curve in E^n , *Kyungpook Mathematical Journal*, 58 (1) 117 - 135.
- [34] Tunçer, Y., Ünal, S., (2012) New representations of Bertrand pairs in Euclidean 3-space, *Applied Mathematics and Computation*, 219 (4) 1833 - 1842.
- [35] Uçum, A., İlarıslan, K., (2016) On timelike Bertrand Curves in Minkowski 3-space, *Honam Mathematical Journal*, 38 (3) 467 - 477.
- [36] Uçum, A., Keçiliođlu, O., İlarıslan, K., (2016) Generalized Bertrand Curves with Spacelike (1,3) Normal Plane in Minkowski Space-Time, *Turkish Journal of Mathematics*, 40 (3) 487 – 505.
- [37] Wang, F., Liu, H., (2007) Mannheim Partner Curve in 3-Euclidean Space, *Mathematics in Practice and Theory*, 37 141 - 143.
- [38] Zhang, C., Pei, D., (2020) Generalized Bertrand Curves in Minkowski 3-Space, *Mathematics*, 8 (12) 21 - 99.

Determination of Some Antioxidant Activity Values in Wines of *Vitis vinifera* L. Karalahna, Karasakız and Çavuş Grape Varieties Produced in Bozcaada

Tuğba GÜNGÖR ERTUĞRAL¹*, Gülen TÜRKER¹

¹Department of Food Technology, Faculty of Canakkale Applied Sciences, Canakkale Onsekiz Mart University, Türkiye

Received: 05/12/2023, Revised: 27/05/2024, Accepted: 27/05/2024, Published: 31/08/2024

Abstract

Çanakkale Bozcaada region, which has witnessed different cultures in different periods for centuries due to its strategic location and wines obtained from grapes belonging to the *Vitis vinifera* L. species, whose traditional names are Karalahna, Çavuş and Karasakız, have been consumed by the local people for years. Wine is a traditional fermented beverage rich in phenolic substances and antioxidant properties, due to the production process, especially during maceration stage, where grape berries are processed with their skins. The geographical structure, plant flora and climate of the region where the grapes grow can create different quality characteristics in grapes, and this affects the quality of the wine through wine processing methods. In this study, to determine some antioxidant activity values of wines produced from Karalahna, Karasakız, and Çavuş grapes grown in Bozcaada. 2, 2-Diphenyl-1-picryl-hydrazyl (DPPH·) free radical scavenging activity, total phenolic substance (Folin-Ciocalteu), reducing power, total flavonoid, anthocyanin, and condensed tannin amounts were measured. DPPH·% Inhibition value of Karalahna wine was found to be 90.6±1.14, condensed tannin was 54.22±0.612 µg CE/g, anthocyanin was found to be 2.46±0.09 mg cyanidin-3-glucoside/g. The results obtained were examined by comparing them with other wine samples.

Keywords: Wine, flavonoids antioxidant, reducing power, phenolic substance.

Bozcaada'da Üretilen *Vitis vinifera* L.'nin Karalahna, Karasakız ve Çavuş üzüm Çeşitlerine Ait Şaraplarda Bazı Antioksidan Aktivite Değerlerinin Belirlenmesi

Öz

Stratejik konumu nedeniyle yüzyıllardır farklı dönemlerde farklı kültürlerle tanıklık eden Çanakkale Bozcaada bölgesi, geleneksel isimleri Karalahna, Çavuş ve Karasakız olan *Vitis vinifera* L. türüne ait üzümlerden elde edilen şaraplar yöre halkı tarafından yıllarca tüketilmektedir. Şarap, üretim süreci nedeniyle ve özellikle de maserasyon aşamasında üzüm tanelerinin kabuklarıyla birlikte işleme alındığı, fenolik maddeler ve antioksidan özellikler açısından zengin, geleneksel fermente bir içecektir. Yetiştirildiği bölgenin coğrafi yapısı, bitki florası ve iklimi üzümlerde farklı kalite özellikleri oluşturabilmekte ve bu durum şarap işleme yöntemleri ile şarapta kaliteyi etkilemektedir. Bu çalışmada, Bozcaada'da yetiştirilen Karalahna, Karasakız ve Çavuş üzümlerinden üretilen şarapların bazı antioksidan aktivite değerlerinin belirlenmesi amacıyla 2,2-Difenil-1-pikril-hidrazil (DPPH·) serbest radikal temizleme aktivitesi, toplam fenolik madde (Folin-Ciocalteu), indirgeme gücü, toplam flavonoid, antosiyanin, yoğunlaştırılmış tanen miktarları belirlenmiştir. Karalahna şarabının DPPH % inhibisyon değeri 90.6±1.14, kondense tanin 54.22±0.612 µg CE/g ve antosiyanin 2.46±0.09 mg siyanidin-3-glikozit/g olarak bulunmuştur. Elde edilen sonuçlar diğer şarap örnekleri ile karşılaştırılarak incelenmiştir.

Anahtar Kelimeler: Şarap, flavonoid, antioksidan, indirgeme gücü, fenolik madde.

1. Introduction

Wine is a traditional beverage consumed by human beings for centuries. Spontaneous alcohol fermentation in grape must is defined as a complex process in which different yeast genera and species, other than *Saccharomyces cerevisiae*, which is considered the main wine yeast, are present in grapes, must, and wine and contribute to wine aroma, sequentially participate [1] and sulfurization process is one of them [2]. Terroir, which is an important factor in the quality and style of wine, defines the geographical, topographical, and climatic structure of the region where the grape grows and its relationship with the sun [3]. The amount of phenolic compounds in grapes is important for wine quality. Grape grows region can be effective in determining the phenolic compound and aroma level of the grape [4].

Wine is also rich in phenolic compounds, which contain alcohol, polysaccharides, polyphenols, proteins, organic acids, and minerals [5, 6, 7, 8], and grape skins, pulp, and seeds are partially removed from the must [9]. During fermentation, total phenolic compound, total anthocyanin, and antioxidant values in red grape varieties can reach their maximum level when the maceration is completed on the 10th day [10]. However, maceration is not applied to white grape wines and the must has a low amount of phenolic compounds [11]. Polyphenolic composition varies in wine production depending on grape variety, weather, viticulture, and wine process techniques [12, 13]. Phenolic compounds are among the most important quality criteria for wine and create a unique taste in wine [14]. Around the world, the main determining factor of polyphenolic amount variation in red wine may have a period of exposure to sunlight during planting. Additionally, considering the type and geographical origin of the wine sample, differentiation, and classification may occur depending on flavanols, and trans-resveratrol concentrations [15]. Polyphenols can positively affect our health with their antioxidant activity [16], and polyphenol antioxidants such as resveratrol, catechin, epicatechin and quercetin, especially found in red wines, may have an inhibitory effect on cell growth in the fight against prostate cancer [17]. Resveratrol, found in high concentrations in grape skins [18] and it has been analyzed in over 70 plant species [19]. Diets containing high amounts of grapes and resveratrol containing grape powder have been observed to reduce the pathogenesis of heart failure in Dahl-Salt-Sensitive mice, a model of hypertension and diastolic dysfunction [20]. In addition, resveratrol polyphenol has positive effects in preventing cancer and protecting the heart [21]. In France, high consumption of saturated fat and moderate consumption of red wine positively improved coronary heart disease [22].

Karalahna grape, one of the famous local grape varieties from Bozcaada (Tenedos) in Çanakkale, is used for wine production which is a unique dark color [23]. Çavuş grape is grown almost everywhere in Turkey, especially in Bozcaada Çanakkale, Marmara, Central Anatolia, Central Western Black Sea, and Aegean Regions [24,25,26,27,28]. However, it is known as Bozcaada Çavuşu and has grown most intensively in Bozcaada [29,30]. The effect of the island's soil, climate, and topography characteristics (terroir elements) and differences in pollinator varieties have caused Bozcaada Çavuş Grape to gain distinctive characteristics compared to the Çavuş grape variety grown in other regions and regions [30]. Karasakız grape has become a variety whose cultivation is given more importance due to the Çanakkale Tekel

Wine and Brandy Factory established in 1960 [31]. Even though separate studies have been conducted for Karasakız, Karalahna, and Çavuş grapes, no study has been found targeting the region in terms of wine specific to the Bozcaada region.

In this study, total flavonoids, total anthocyanins, reducing power, chelating capacity, and total phenolic properties were determined to determine some antioxidant properties of red and white wines obtained from local grape species grown in Bozcaada.

2. Materials and Methods

In the study, wines obtained from Karalahna, Çavuş, and Karasakız grapes from the 2020-2021 Bozcaada harvest period were purchased commercially from the winery in Bozcaada, Turkey. Sodium thiocyanate, butylated hydroxytoluene (BHT), routine, gallic acid, and catechin were from Fluka Chemical Co. (Buchs, Switzerland), 2,2-diphenyl-1-picryl-hydrazyl (DPPH) was obtained from Sigma Chemical Co. (St. Louis, MO). Potassium ferricyanide, trichloroacetic acid (TCA), AlCl₃, FeCl₃, Vanillin, Der. Hydrochloric acid was obtained from Merck and all other reagents were analytical grade. In the quality analysis of antioxidant activity values, 30 wine samples were taken for each wine type.

2.1. Determination of total phenolic compounds

Total phenolic compounds were determined according to the Folin-Ciocalteu method according to the method of Slinkard and Singleton (1977) with some modifications [32]. Absorbances were measured using a Shimadzu 1208 UV-Vis spectrophotometer (Shimadzu Corporation, Kyoto, Japan). The amount of total phenolic compounds was calculated as mg gallic acid equivalents (GAE) from the calibration curve of the gallic acid standard solution and expressed as mg GAE/ml.

2.2. Determination of total flavonoid content

Total flavonoid content was determined using a modified version of a method described by Whiskey and Salatino (1998) [33] Wine samples were diluted 1/20. Mean (±SD) results of triplicate analyzes were expressed as mg Rutin/ml of Rutin equivalents of total extractable compounds.

2.3. DPPH radical scavenging activity

Wine samples were diluted 1/20, then 2,2-diphenyl-1-picrylhydrazyl (DPPH) was used, a modified version of method used by Brand-Williams et al. in 1995 [34]. Samples prepared at different concentrations were calculated using $6 \cdot 10^{-5}$ DPPH•, according to following formula, after measuring absorbance at 515 nm after a waiting period of 30 minutes:

$$\%Inh = \frac{A_0 - (A - A_b)}{A_0} \times 100$$

A₀: absorbance of DPPH•

A: Absorbance of the substance

A_b: Blank absorbance

IC₅₀ for sample extracts, expressed as micrograms of material equivalents per milliliter (extract concentrations providing inhibition values are the concentration of compounds capable of inhibiting 50% of total DPPH radicals) were calculated by non-linear regression via graph plotting and BHT was the positive control. Lower IC₅₀ values indicate higher antioxidant activity and vice versa.

2.4. Reducing power

The Reducing powers of wines at different concentrations were determined according to method described by Oyaizu et al. [35]. From each sample (0.25;0.5;1 mg/ml), BHT (0.25;0.5;1 mg/ml) was mixed with an equal volume of 0.2 M phosphate buffer (pH 6.6) and 1% potassium ferricyanide followed by incubation at 50 °C was incubated for 30 minutes. To stop reaction, 1% trichloroacetic acid (TCA) was added to mixture than mixture was centrifuged at 1000 rpm. Supernatant, distilled water and 0.1% FeCl₃ were added, then reducing powers of tested samples were measured by absorbance values by reading at 700 nm (Table 1).

2.5. Amount of condensed tannin

Condensed tannin content was determined using 4% vanillin solution [36]. After adding 4% vanillin solution and 1% HCl to samples prepared at different concentrations, they were placed in a water bath at 30 °C with constant shaking for 20 minutes. After incubation, samples were centrifuged. Absorbance was then measured at 500 nm using a UV-Vis spectrophotometer (Thermo Aquamate). Results were expressed as microgram catechin equivalents (µg CE/g).

2.6. Determination of total anthocyanin

Anthocyanin content was calculated using technique developed by Padmawati, Sakthivel, Thara and Reddy in 1997 [37], modified by Chung et al. 2005 [38]. The total anthocyanin content was estimated as cyanidin-3-glucoside equivalents in milligrams per gram wine sample. The sample was kept in the dark at room temperature for 2 hours with methanol acidified with 1% HCl, then centrifuged at 1000 rpm and measured at 653 nm and 530 nm, and then it was calculated according to following formula;

$$\text{Anthocyanin content (mg cyanidin-3-glycoside/ g wine)} = A_{530} - (0,24 \times A_{653})$$

2.7. Statistical analysis

The SPSS version 18 software [Statistical Packages for the Social Sciences (SPSS) version 18 commercial software (IBM Corp.; Armonk, NY, USA)] was utilized for data analysis in the study. Descriptive analyses were conducted to provide information about the general characteristics of the groups. Data pertaining to continuous variables were summarized as Mean ± Standard deviation. Normality tests for numerical variables were performed using the Kolmogorov-Smirnov test and examined through measures of kurtosis and skewness. Differences between means were compared using one-way analysis of variance (ANOVA).

Following the analysis of variance, DUNCAN multiple comparison tests (Post-hoc tests) were applied. Values with $p < 0.05$ were considered statistically significant.

3. Result and Discussion

Table 1. Reducing power of grape samples at different concentrations

Concentration (mg/ml)	Wines			F	p
	Karasakız	Karalahna	Çavuş		
0.25	0.83 ± 0.011^a	0.99 ± 0.012^b	0.34 ± 0.005^c	30372.90	<.001
0.5	1.28 ± 0.008^a	1.26 ± 0.013^b	0.39 ± 0.002^c	133074.61	<.001
1	1.55 ± 0.010^a	1.81 ± 0.001^b	0.49 ± 0.009^c	212229.83	<.001

\bar{X} : Mean SD: standard deviation ^{a-c}: There is no difference between values with the same letter.

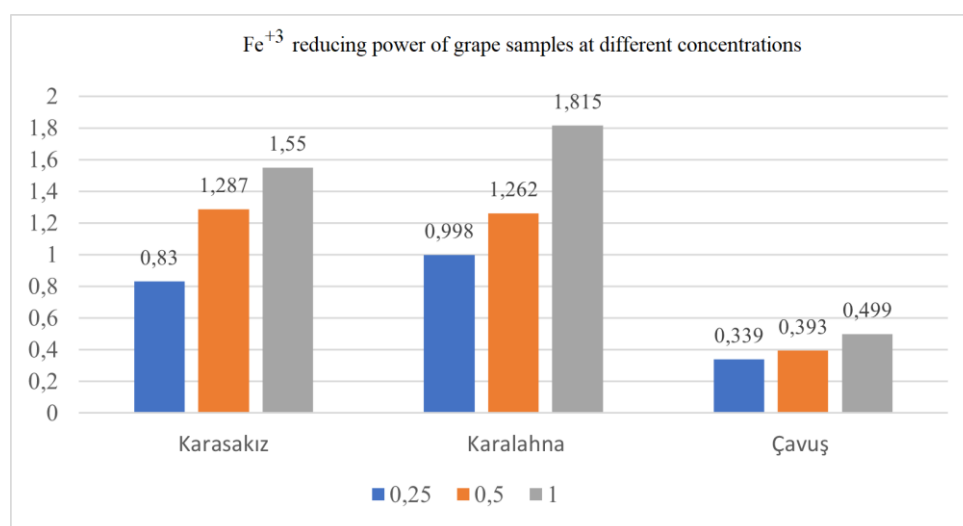


Figure 1. Reducing power of grape samples at different concentrations

Table 2. Spectrophotometric properties wines of the Karasakız, Karalahna and Çavuş grapes

	Wines			F	p	BHT
	Karasakız	Karalahna	Çavuş			
	$\bar{X} \pm SD$	$\bar{X} \pm SD$	$\bar{X} \pm SD$			$\bar{X} \pm SD$
Condensed tannin ($\mu\text{g CE/g}$)	48.44 ± 0.483^a	54.22 ± 0.612^b	15.58 ± 0.179^c	67359.28	<.001	
DPPH· IC ₅₀ ($\mu\text{g/ml}$)	1.7 ± 0.125^a	1.6 ± 0.157^a	2.07 ± 0.142^b	77.96	<.001	1.34 ± 0.710
DPPH· % inhibition	89.6 ± 1.14^a	90.6 ± 1.14^b	84.8 ± 0.837^c	196.85	<.001	96.5 ± 0.930
Total flavonoids ($\mu\text{g rutin/ml}$)	2927.58 ± 0.531^a	2887.3 ± 8.367^b	2714.64 ± 2.016^c	11918.19	<.001	
Anthocyanin (mg cyanidin-3-glucoside/g wine)	1.98 ± 0.007^a	2.46 ± 0.09^b	0.74 ± 0.005^c	396731.76	<.001	
Total phenolics ($\mu\text{g GAE /ml}$)	2519.34 ± 0.786^a	2026.4 ± 0.894^b	434.52 ± 0.705^c	45790710.4	<.001	

\bar{X} : Mean SD: standard deviation ^{a-c}: There is no difference between values with the same letter.

The amount of condensed tannin in Karalahna grape wine was measured as 54.62%, and the free radical scavenging activity was measured as 97% anthocyanin value is 2.46 (mg cyanidin-3-glucoside/g wine) (Table 2). According to these data, the antioxidant power of Karalahna grape wine is higher than Çavuş, and Karasakız grape wines. The high values in Karasakız and Karalahna grape wines, which have antioxidant effect values close to vitamin C, are related to the amount of anthocyanins and condensed tannins. Additionally, anthocyanin, condensed tannin and DPPH free radical scavenging activity in Karalahna grape wine is higher than Karasakız and Çavuş grape wines. In previous studies, the total phenolic contents of Karasakız and Karalahna wines were 1497.45 mg GAE/L, 1702.91 mg GAE/L [40], and 3052.42 mg GAE/L [41]. In this study, the total phenolic contents of Karasakız grape wines were 2519.34 µg GAE /ml and the high reducing power observed in Karalahna grape wine depends on the total amount of polyphenolics and anthocyanins (Table 1). On the other hand, when the results are evaluated, a statistically significant difference was observed between the antioxidant values of all samples of wine.

In addition, the total phenolic substance in Vasilaki grape wine grown in Bozcaada is 478 mg/L in terms of gallic acid [42], and Çavuş grape wine was content approximately 434.52 (µg GAE / ml). The total amount of phenolic substances in white grape wines produced from the Narince grape variety in Tokat is 345 mg GAE/L [43] and 1090 mg GAE/L in Muscatel grape wines was determined [44]. While wines made from Riesling grapes had the lowest total phenol content with 250 mg GAE/L, wines produced from Cabernet Sauvignon grapes reached 2005 mg GAE/L [45]. In the analyses conducted on white and red wine produced in the Czech Republic in 2006, the total phenolic compound amount was found to be in the range of 90–118 mg GAE/L in white wines and in the range of 874–2262 mg GAE/L in red wines [46]. In addition, the total amount of phenolic compounds is 406.9 mg GAE/L in white wine and 1787 mg GAE/L in red wine [47]. Cabernet Sauvignon, Boğazkere, Öküzgözü, Papazkarası, Shiraz, Merlot, Kalecik Karası, Kuntra (Karasakız), and Karalahna grape varieties are 1412-3183 mg GAE/L (2007) and between 1119-4285 mg GAE/L (2008) [48].

The total amount of flavonoids in white wine, in terms of catechin, is 33.12 mg/L for Narince grape wine and 43.84 mg/L for Emir grape wine [49]. Just as the total phenolic compound value is higher than the wines made from black grapes grown in the Tokat region when compared to total phenolic values of Kuntra (Karasakız) and Karalahna wines grown in the Tokat region, Bozcaada Karalahna and Karasakız grape wines were found to have a higher phenolic substance content. The total amount of flavonoids in Çavuş grape wine, also grown in Bozcaada, is approximately Emir and Narince grape wines. Öküzgözü grape is a quality wine grape variety. The anthocyanin amount in Öküzgözü grape wine was determined to be 2.17 (cyanidin-3-glycosides) in previous studies [50]. In this study, Karalahna wine was measured as 2.46 (cyanidin-3-glycosides), a higher value than Özküzgözü grape wine. The phenolic content of grapes and wines varies depending on the region and may vary from year to year [51], however, it is also known that phenolic compounds are affected by terroir properties [52, 53].

4. Conclusion

In this study, some spectrophotometric quality characteristics of factory wines obtained from Karasakız, Karalahna and Çavuş grape varieties in Bozcaada were determined to investigate the antioxidant capacity of wine.

The amount of condensed tannin in Karalahna grape wine was measured as 54.22 µg CE/g, and the total flavonoid amount in Karasakız grape wine was determined as 2927.58 µg routine/ml. In free radical scavenging activity (DPPH·), the lower the IC₅₀ values, the higher the % inhibition value. According to the results, the free radical scavenging activity and antioxidant capacity of Karalahna grape wine was higher. The total phenolic amount in Çavuş grape variety white wine was lower than in red wines. The antioxidant effect in the factory red wine obtained from the Karalahna grape variety grown in the Bozcaada region is stronger and the anthocyanin value is higher than in the Karasakız and Çavuş grape wines of the same region.

Ethics in Publishing

There are no ethical issues regarding the publication of this study.

Author Contributions

Designing study, evaluating results, writing article and performing analysis: Tuğba Güngör Ertuğral; Conducting analyses: Gülen Türker

References

- [1] Romano, P., Fiore, C., Paraggio, M., Caruso, M., ve Capece, A. (2003). Function of yeast species and strains in wine flavour. *International journal of food microbiology*, 86(1-2), 169-180.
- [2] Ribéreau-Gayon, P., Dubourdiou, D., Doneche, B., ve Lonvaud, A. (2006). The use of sulfur dioxide in must and wine treatment. *Handbook of Enology. The Microbiology of Wine and Vinifications*, 193-197.
- [3] Bayram, M., Kayalar, M., Cemal, K. A. Y. A., & Topuz, S. (2016). Şarapta fenolik ve aroma bileşikleri üzerine 'Teruar'ın etkisi. *Gaziosmanpaşa Bilimsel Araştırma Dergisi*, (13), 35-46.
- [4] Van Leeuwen, C., Friant, P., Chone, X., Tregoat, O., Koundouras, S., & Dubourdiou, D. (2004). Influence of climate, soil, and cultivar on terroir. *American Journal of Enology and Viticulture*, 55(3), 207-217.
- [5] Arvisenet, G., Ballester, J., Ayed, C., Sémon, E., Andriot, I., Le Quere, J. L. ve Guichard, E. (2019). Effect of sugar and acid composition, aroma release, and assessment conditions on aroma enhancement by taste in model wines. *Food Quality and Preference*, 71, 172-180.

- [6] Baker, A. K., ve Ross, C. F. (2014). Sensory evaluation of impact of wine matrix on red wine finish: a preliminary study. *Journal of Sensory Studies*, 29(2), 139-148.
- [7] Zhang, B., Shi, X., Zhang, Y., Wang, Q., Zhou, P. P., Li, Y. K. ve Tao, Y. S. (2022). The implication of phenolic acid matrix effect on the volatility of ethyl acetate in alcohol-free wine model: Investigations with experimental and theoretical methods. *Food Chemistry*, 378, 132114.
- [8] Rousserie, P., Rabot, A. ve Geny-Denis, L. (2019). From flavanols biosynthesis to wine tannins: What place for grape seeds?. *Journal of agricultural and food chemistry*, 67(5), 1325-1343.
- [9] Jackson RS. (1994). *Wine science: principles and applications*. New York: Academic Press.
- [10] Tahmaz, H. ve Söylemezoğlu, G. (2019). Karaoğlan (*Vitis vinifera* L.) Üzüm Çeşidinin Şarap Fermantasyon Sürecinde Fenolik Bileşik ve Antioksidan İçeriğinin Belirlenmesi. *Türk Tarım ve Doğa Bilimleri Dergisi*, 6(4), 671-677.
- [11] Ramos, R., Andrade, P. B., Seabra, R. M., Pereira, C., Ferreira, M. A. ve Faia, M. A. (1999). A preliminary study of non-coloured phenolics in wines of varietal white grapes (códega, gouveio and malvasia fina): effects of grape variety, grape maturation and technology of winemaking. *Food Chemistry*, 67(1), 39-44.
- [12] Mazza, G., Fukumoto, L., Delaquis, P., Girard, B., & Ewert, B. (1999). Anthocyanins, phenolics, and color of Cabernet franc, Merlot, and Pinot noir wines from British Columbia. *Journal of agricultural and food chemistry*, 47(10), 4009-4017.
- [13] Rodríguez-Delgado, M. Á., González-Hernández, G., Conde-González, J. E., & Pérez-Trujillo, J. P. (2002). Principal component analysis of the polyphenol content in young red wines. *Food Chemistry*, 78(4), 523-532.
- [14] Proestos, C. (2004). High performance liquid chromatography analysis of phenolic substances in Greek wines.
- [15] Howard, A., Chopra, M., Thurnham, D. I., Strain, J. J., Fuhrman, B., & Aviram, M. (2002). Red wine consumption and inhibition of LDL oxidation: what are the important components?. *Medical hypotheses*, 59(1), 101-104.
- [16] Yoo, Y. J., Saliba, A. J. ve Prenzler, P. D. (2010). Should red wine be considered a functional food?. *Comprehensive Reviews in Food Science and Food Safety*, 9(5), 530-551.
- [17] Kampa, M., Hatzoglou, A., Notas, G., Damianaki, A., Bakogeorgou, E., Gemetzi, C., ve Castanas, E. (2000). Wine antioxidant polyphenols inhibit the proliferation of human prostate cancer cell lines. *Nutrition and cancer*, 37(2), 223-233.

- [18]Guerrero, R. F., Puertas, B., Jiménez, M. J., Cacho, J. ve Cantos-Villar, E.(2010). Monitoring the process to obtain red wine enriched in resveratrol and piceatannol without quality loss. Food chemistry, 122(1), 195-202.
- [19]Singh, C. K., Liu, X. ve Ahmad, N. (2015). Resveratrol, in its natural combination in whole grape, for health promotion and disease management. Annals of the New York Academy of Sciences, 1348(1), 150-160.
- [20]Seymour, E. M., Singer, A. A. M., Kirakosyan, A., Kaufman, P. B., Warber, S. ev Bolling, S. F. (2008). Tart cherry-enriched diets reduce hepatic lipid content, hepatic PPAR expression, metabolic syndrome and oxidative stress in Dahl-SS rats. Journal of medicinal food, 11(2), 252-259.
- [21]Bertelli, A. A. ve Das, D. K. (2009). Grapes, wines, resveratrol, and heart health. Journal of cardiovascular pharmacology, 54(6), 468-476.
- [22]Renaud, S. D. ve de Lorgeril, M. (1992). Wine, alcohol, platelets, and the French paradox for coronary heart disease. The Lancet, 339(8808), 1523-1526.
- [23]Çelebi Uzkuç, N. M., Şişli, B., Ay, M., Togay, S. Ö., Karagül Yüceer, Y., Bayhan, A. ve Kırca Toklucu, A. (2020). Effects of spontaneous fermentation on Karalahna and Cabernet Sauvignon young red wines: Volatile compounds, sensory profiles and identification of autochthonous yeasts. European Food Research and Technology, 246, 81-92.
- [24]Tangolar, S., Ergenoğlu, F. ve Gök, S. (1996). Çukurova Üniversitesi Ziraat Fakültesi Bahçe Bitkileri Bölümü Araştırma Bazı Üzüm Çeşitleri Kataloğu. Çukurova Üniversitesi Ziraat Fakültesi Ofset Atölyesi. Adana, 94 s.
- [25]Anonim.(1997). T.C. ethanol Üzüm Çeşitleri Kataloğu. Tarım ve Köyişleri Bakanlığı Tarımsal Üretim ve Geliştirme Genel Müdürlüğü. Ankara. 88 s.
- [26]Uslu, İ., Samancı, H, (1997a). Marmara Bölgesi üzüm çeşitlerinde klon seleksiyonu çalışmaları. Atatürk Bahçe Kültürleri Merkez Araştırma Enstitüsü. Bilimsel Araştırma ve İncelemeler, Yayın No: 95. 23 s. Yalova.
- [27]Kiracı, N.A., Bayraktar, H., Usta, K., Özışık, S. ve Gürnil, K. (2002). Bozcaada Çavuşu, Kozak Beyazı, Karasakız ve Amasya Beyazı üzüm çeşitlerinde klon seleksiyonu çalışmaları. Türkiye V. Bağcılık ve Şarapçılık Sempozyumu, Nevşehir, Türkiye, 5–9 Ekim. 97–102.
- [28]Dardeniz, A. (2002). Bozcaada bağcılığının mevcut durumu, sorunları ve bağcılığın geliştirilmesine yönelik öneriler. Türk-Koop Ekin, 20, 77-84.
- [29]Uslu, İ., Samancı, H, (1997b). Beyaz Çavuş ve Hamburg Misketi üzüm çeşitleri için uygun telli terbiye şekillerinin saptanması. Atatürk Bahçe Kültürleri Merkez Araştırma Enstitüsü. Bilimsel Araştırma ve İncelemeler, Yayın No: 96. 31 s. Yalova

- [30] Türk Patent Enstitüsü. Coğrafi işaretler. “<https://ci.turkpatent.gov.tr/cografi-isaretler/detay/38630>”. (Erişim tarihi: 24.05.2023)
- [31] Dardeniz, A. ve Güven, S. (2003). Karasakız üzüm çeşidinin Çanakkale ekonomisindeki yeri ve önemi ile başlıca değerlendirilme şekilleri. *Türk-Koop Ekin*, 26, 62-68.
- [32] Slinkard, K., & Singleton, V. L. (1977). Total phenol analysis: automation and comparison with manual methods. *American journal of enology and viticulture*, 28(1), 49-55.
- [33] Whisky, R. ve Salatino A. (1998). Analysis of propolis: some parameters and procedures for chemical quality control. *Journal of Apicultural Research*, 37 (2): 99–105.
- [34] Brand-Williams, W., Cuvelier, M. E. ve Berset, C. L. W. T. (1995). Use of a free radical method to evaluate antioxidant activity. *LWT-Food science and Technology*, 28(1), 25-30.
- [35] Oyaizu, M. (1986). Studies on products of browning reaction antioxidative activities of products of browning reaction prepared from glucosamine. *The Japanese journal of nutrition and dietetics*, 44(6), 307-315.
- [36] Julkunen-Tiitto, R. (1985). Phenolic constituents in the leaves of northern willows: methods for the analysis of certain phenolics. *Journal of agricultural and food chemistry*, 33(2), 213-217.
- [37] Padmavati, M., Sakthivel, N., Thara, K. V. ve Reddy, A. R. (1997). Differential sensitivity of rice pathogens to growth inhibition by flavonoids. *Phytochemistry*, 46(3), 499-502.
- [38] Chung, Y. C., Chen, S. J., Hsu, C. K., Chang, C. T. ve Chou, S. T. (2005). Studies on the antioxidative activity of *Graptopetalum paraguayense* E. Walther. *Food Chemistry*, 91(3), 419-424.
- [39] Lee, K. W., Kim, Y. J., Kim, D. O., Lee, H. J., & Lee, C. Y. (2003). Major phenolics in apple and their contribution to the total antioxidant capacity. *Journal of agricultural and food chemistry*, 51(22), 6516-6520.
- [40] Erkan, S. (2020). Çanakkalede üretilen endüstriyel ve ev yapımı kırmızı şarapların metanol içerikleri ve bazı kimyasal özelliklerinin belirlenmesi (Master's thesis, Fen Bilimleri Enstitüsü).
- [41] Şişli, B., Uzkuç, N. M. Ç., Bayhan, A., ve Toklucu, A. K. (2023). Karalahna şaraplarının fenolik bileşenleri üzerine fermantasyon tekniği ve şişede depolamanın etkisi. *Gıda*, 48(1), 130-143.
- [42] Özkan, Ö. (2017). Bozcaadada yetiştirilen vasilaki üzümlerinden spontan ve saf maya fermantasyonuyla üretilen beyaz şarapların karakteristik özellikleri (Master's thesis, Fen Bilimleri Enstitüsü).

- [43] Şen, I., (2014). Characterization and Classification of Wines from Grape Varieties Grown in Turkey. (Doctor Of Philosophy), A Thesis Submitted to The Graduate School of Engineering and Sciences of İzmir Institute of Technology in Partial Fulfillment of The Requirements in Food Engineering. İzmir.
- [44] Silva, S.D., Feliciano, R.P., Boas, L.V. ve Bronze, M.R., (2014). Application of FTIRATR to Moscatel Dessert Wines for Prediction of Total Phenolic and Flavonoid Contents and Antioxidant Capacity. *Food Chemistry* 150 (2014) 489–493.
- [45] Walzem R.L., (2008). Wine and Health: State of Proofs and Research Needs. *Inflammopharmacology*, 16 (2008): 265–271.
- [46] Stratil, P., Kuban V. ve Fojtova, J., (2008). Comparisan of the Phenolic Content and Total Antioxidant Activity in Wines as Determined by Spectrophotometric Methods. *Czech Journal of Food Sciences*, 26 (4): 242–253.
- [47] Yıldırım, H.K., Akçay, Y.D., Güvenç, U., Altındışli, A. ve Sözmen, E.Y., (2005). Antioxidant Activities of Organic Grape, Pomace, Juice, Must, Wine and Their Correlation with Phenolic Content. *International Journal of Food Science and Technology*, 2005, 40, 133–142.
- [48] Aksoy, M., (2010). Bazı Kırmızı Şarapların Fenolik Madde Profilleri Üzerine Araştırmalar. (Yüksek Lisans Tezi), Çanakkale Onsekiz Mart Üniversitesi, Fen Bilimleri Enstitüsü, Gıda Mühendisliği Anabilim Dalı, Çanakkale.
- [49] Aras, Ö., (2006). Üzüm ve Üzüm Ürünlerinin Toplam Karbonhidrat, Protein, Mineral Madde ve Fenolik Bileşik İçeriklerinin Belirlenmesi. (Yüksek Lisans Tezi), Süleyman Demirel Üniversitesi, Fen Bilimleri Enstitüsü, Bahçe Bitkileri Anabilim Dalı, Isparta.
- [50] Kelebek, H. (2010). Öküzgözü üzümlerinden kırmızı şarap üretiminde soğuk maserasyon uygulamasının antosiyaninler üzerine etkisi. *Journal of Agricultural Sciences*, 16(4).
- [51] Kumšta, M., Pavloušek, P. ve Kupsa, J., (2012). Influence of Terroir on The Concentration of Selected Stilbenes in Wines of the cv. Riesling in The Czech Republic. *Hort. Sci. (Prague)*, 39 (1), 38–46.
- [52] Šeruga, M., Novak, I. and Jakobek, L., (2011). Determination of Polyphenols Content and Antioxidant Activity of Some Red Wines by Differential Pulse Voltammetry, HPLC and Spectrophotometric Methods. *Food Chemistry*, (124), 1208-1216.
- [53] Lampiř L. ve Pavloušek P. (2013). Influence of Locality on Content of Phenolic compounds in White Wines. *Czech J. Food Sci.*, (31), 619–626.

Synthesis, characterization and investigation of biological activities of Schiff Base and its Ni(II) complex obtained from 2-Benzoylpyridine and 3-Hydroxy-2-naphthoic hydrazide

Murat Çınarlı ^{1*}

¹Kırşehir Ahi Evran University, Vocational School of Health Services, Kırşehir, Türkiye

Received: 25/01/2023, **Revised:** 29/06/2024, **Accepted:** 01/07/2024, **Published:** 31/08/2024

Abstract

In this paper, a new aryl hydrazone and its Nickel (II) complex were synthesized from 2-benzoylpyridine and 3-Hydroxy-2-naphthoic hydrazide. The synthesized compounds were characterized by elemental analysis, UV-Visible, IR, ¹H and ¹³C-NMR spectral studies and mass spectra.

Elemental analysis data show that the metal atom is coordinated by two ligands. Considering all the data, the ligand coordinates to the metal atom through carbonyl-O, azomethine-N and pyridyl-N atoms. This shows that the [NiL₂] complex is octahedral. When tested against various reference bacterial strains and clinical isolates, it was discovered that the antibacterial activity of the [NiL₂] complex was more effective than the ligand.

Keywords: Aryl hydrazone, Metal Complexes, Antimicrobial Studies, NNO Donor

2-Benzoilpiridin ve 3-Hidroksi-2-naftoik hidrazitten elde edilen Schiff bazı ve Ni(II) kompleksinin sentezi, karakterizasyonu ve biyolojik aktivitelerinin araştırılması

Öz

Bu yazıda, 2-Benzoilpiridin ve 3-Hidroksi-2-naftoik hidrazitten yeni bir aril hidrazon ve onun Nikel (II) kompleksi sentezlendi. Sentezlenen bileşikler element analiz, UV-Visible, IR, ¹H ve ¹³C-NMR spektral çalışmaları ve kütle spektrumları ile karakterize edildi.

Element analizi verileri, metal atomunun iki ligand tarafından koordine edildiğini göstermektedir. Tüm veriler göz önüne alındığında ligandın metal atomuna karbonil-O, azometin-N ve piridil-N atomları aracılığıyla koordine olduğu görülmektedir. Bu, [NiL₂] kompleksinin oktahedral olduğunu gösterir. Çeşitli referans bakteri suşlarına ve klinik izolatlara karşı test edildiğinde, [NiL₂] kompleksinin antibakteriyel aktivitesinin ligandan daha etkili olduğu keşfedildi.

Anahtar Kelimeler: Aril Hidrazon, Metal Kompleksleri, Antimikrobiyal Çalışmalar, NNO Donör

1. Introduction

Arylhydrazones exhibit a broad spectrum of biological activity properties and pronounced binding modifications to transition metal complexes. Therefore, the importance of these molecules in coordination chemistry is increasing. It is also recognized that arylhydrazone transition metal complexes provide a good model for elucidating their crucial biological functions [1]. Arylhydrazone metal complexes have been associated with a variety of biological effects, including antibacterial [2, 3], anticonvulsant [4], anti-tuberculosis [5], and anti-proliferation [6]. Due to keto-enol tautomerization, 2-benzoylpyridine arylhydrazone derivatives behave as a neutral or tridentate monobasic ligand. These ligands are capable of generating six coordinated octahedral geometries due to their tridentate binding modes. Furthermore, the heterocyclic ring in these ligands provides an additional binding site for metal ions, enhancing the pharmacological properties of the synthesized compounds [7]. The structural characteristics, biological functions, and cytotoxic effects of 2-benzoylpyridine Schiff metal complexes are all still being studied in depth.

In this study, we describe the synthesis, characterization, and biological activity of the new arylhydrazone **HL**, a novel 3-hydroxy-2-naphthoic acid hydrazide derivative, and its Ni(II) complex. The molecular structures of the **HL** ligand and the $[\text{NiL}_2]$ complex were identified by IR, UV-Visible, ^1H and ^{13}C -NMR studies, elemental analyses, and mass spectra. The antibacterial activity of the compounds was investigated using yeast, Gram-positive, and Gram-negative bacteria as test organisms.

2. Material and Method

2.1. Chemicals and instrumentations

All chemicals used in this study were purchased from commercial suppliers (Sigma/Aldrich). All chemicals purchased from commercial suppliers were of reagent grade and were used immediately.

Elemental analyses were performed using the Thermo Flash 2000 CHNS Analyzer. A Thermo Scientific GENESYS 10S UV-Visible spectrophotometer operating between 200 and 1100 nm was used to record the UV spectra of the synthesized compounds in DMSO solution. The MX1 instrument from Sherwood Scientific was used to identify the magnetic moment of the $[\text{NiL}_2]$ complex at room temperature as Bohr Magneton (BM). Infrared spectra were recorded with the Thermo Scientific Nicolet iS10 using ATR. The ^1H and ^{13}C -NMR spectra of the ligand dissolved in DMSO- d_6 was recorded using an Agilent Premium Compact 600 MHz spectrometer. Mass spectra were collected using a Thermo Scientific TSQ Quantum Access Max.

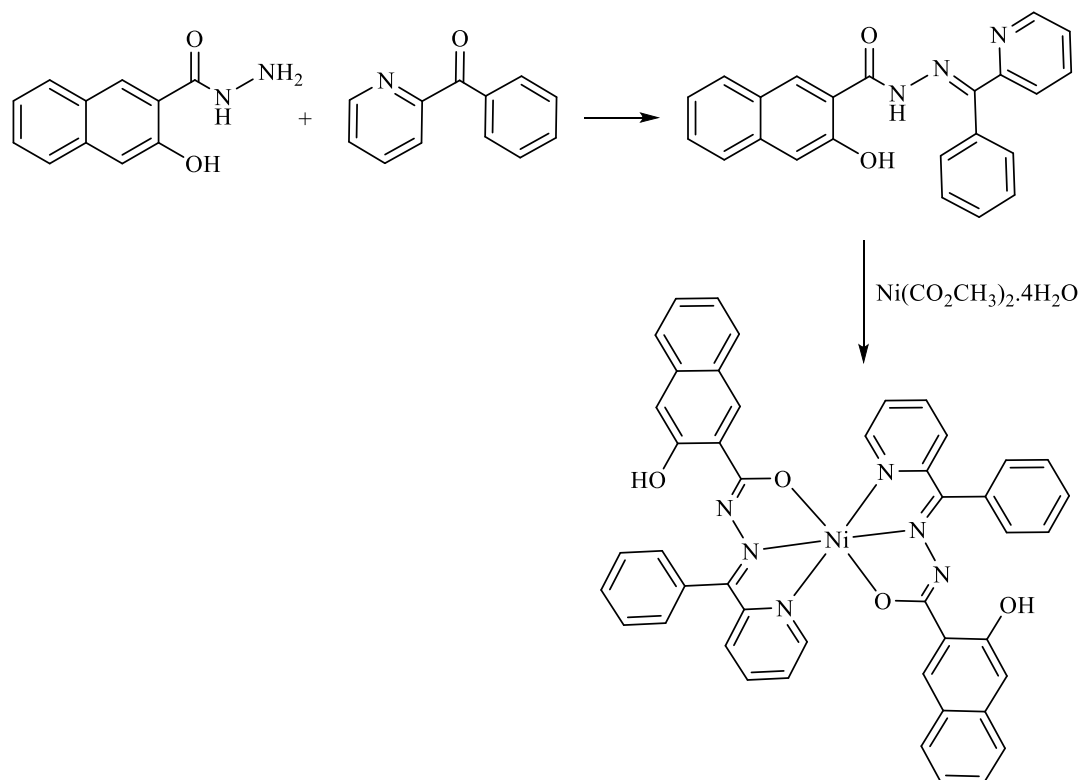
2.2. Preparation of the compounds

2.2.1. Synthesis of HL

To a solution of 3-hydroxy-2-naphthoic hydrazide (0.202 g, 1 mmol) in ethanol (20 mL) was added 2-benzoylpyridine solution (0.183 g, 1 mmol) dissolved in ethanol (20 mL) and refluxed for 4-5 hours. The filtered and ethanol-washed yellow product was dried in the air. Yield: 77%, Mp: 145 °C. Elemental Anal. Calcd. for $C_{23}H_{17}N_3O_2$ ($367.41 \text{ g}\cdot\text{mol}^{-1}$): C, 75.19; H, 4.66; N, 11.44; found: C, 74.25; H, 5.03; N, 10.31. $^1\text{H-NMR}$ (600 MHz, ppm, DMSO- d_6) δ =13.27 (Z), 11.61 (E) [O-H], 11.22 (Z), 11.07 (E) [N-H]. $^{13}\text{C-NMR}$ (600 MHz, solvent) δ = 162.05 (Z), 161.53 (E) [C13 (Z and E isomers)]; 154.23 (Z), 152.98 (E) [C5 (Z and E isomers)]; 152.69 (Z), 152.08 (E) [C6 (Z and E isomers)]; 150.21 (Z), 149.24 (E) [C1 (Z and E isomers)]; 138.48 (Z), 137.55 (E) [C3 (Z and E isomers)]; 137.18 (Z), 136.16 (E) [C4 (Z and E isomers)]; 133.60 (Z), 133.44 (E) [C5 (Z and E isomers)]. LC-MS/MS, m/z = 368.06 $[\text{M}+\text{H}]^+$, 391.11 $[\text{M}+\text{Na}]^+$.

2.2.2. Synthesis of $[\text{NiL}_2]$

A heated ethanolic solution of HL (0.734 g, 2 mmol) (20 mL) was added to a ethanolic solution of $\text{Ni}(\text{CO}_2\text{CH}_3)_2 \cdot 4\text{H}_2\text{O}$ (0.248 g, 1 mmol) (10 mL). For 3 to 4 hours, the reaction mixture was refluxed. Filtering and air drying were done on the precipitated dark brown product. Yield: 62 %, M.P. Decomposition: 297 °C. Elemental Anal. Calcd. for $C_{46}H_{32}N_6O_4\text{Ni}$ ($791.49 \text{ g}\cdot\text{mol}^{-1}$): C, 69.81; H, 4.08; N, 10.62; found: C, 69.09; H, 4.26; N, 9.61. LC-MS/MS, m/z = 792.97 $[\text{M}+\text{H}]^+$. Proposed structures of HL and $[\text{NiL}_2]$ were given Scheme 1.



Scheme 1. Proposed structures of HL and $[\text{NiL}_2]$

2.3. Detection of antimicrobial activity

The minimum inhibitory concentration (MIC) was determined according to the previously mentioned method [8]. Clinical samples of *S. aureus* ATCC 25923, *E. coli* ATCC 25922, *P. aeruginosa* ATCC 27853, *L. monocytogenes* ATCC 19115, *B. cereus* ATCC 14579, *E. aerogenes* ATCC 1304 and *S.dysentery* ATCC from patients in the intensive care unit of the hospital were used in the study. These clinical strains are *Escherichia coli*, *Klebsiella pneumoniae*, *Pseudomonas aeruginosa*, *Enterococcus faecalis* and methicillin-resistant *Staphylococcus aureus* (MRSA). Clinical and type strains were developed using tryptone soy broth (TSB). Cultures were diluted to 1×10^6 CFU/mL after one night of incubation at 37 °C. **HL** and [**NiL**₂] were diluted 2-fold to a final concentration of 256-2 μM after dissolution in dimethyl sulfoxide (DMSO). The 96-well plate was then filled with an equivalent volume of the bacterial suspension and 50 μL of different concentrations of **HL** and [**NiL**₂] and incubated at 37 °C for 18 hours.

The lowest concentration at which no significant bacterial growth occurred was designated as MIC. In addition to gentamicin and ciprofloxacin, media containing metal-free bacteria was used as a negative control (Sigma Aldrich, USA) as a positive control [9].

3. Results and Discussion

3.1. NMR Spectra of HL

In the ¹H and ¹³C-NMR spectra of **HL**, the signals of all hydrogens and carbons are duplicated, suggesting the existence of the E and Z configurations in DMSO-d₆ solution. Two signals of the azomethine proton (NH) group were observed at δ 11.22 and 11.07, which were attributed to the Z and E forms, respectively. Also, multiple signals may be seen in the ¹H-NMR spectrum of **HL** ligand in the 7.20-8.90 ppm range, which are indicative of aromatic ring protons of the E and Z isomers (Scheme 2) (Figure 1). Similarly, the signals of C13=O at δ 162.05 and 161.53 were attributed to the Z and E isomers, respectively. From the study of the ¹³C-NMR spectrum of the **HL** ligand, C6=N signals were observed at δ 152.69 and 152.08 for the Z and E isomers, respectively (Figure 2) [10-13].

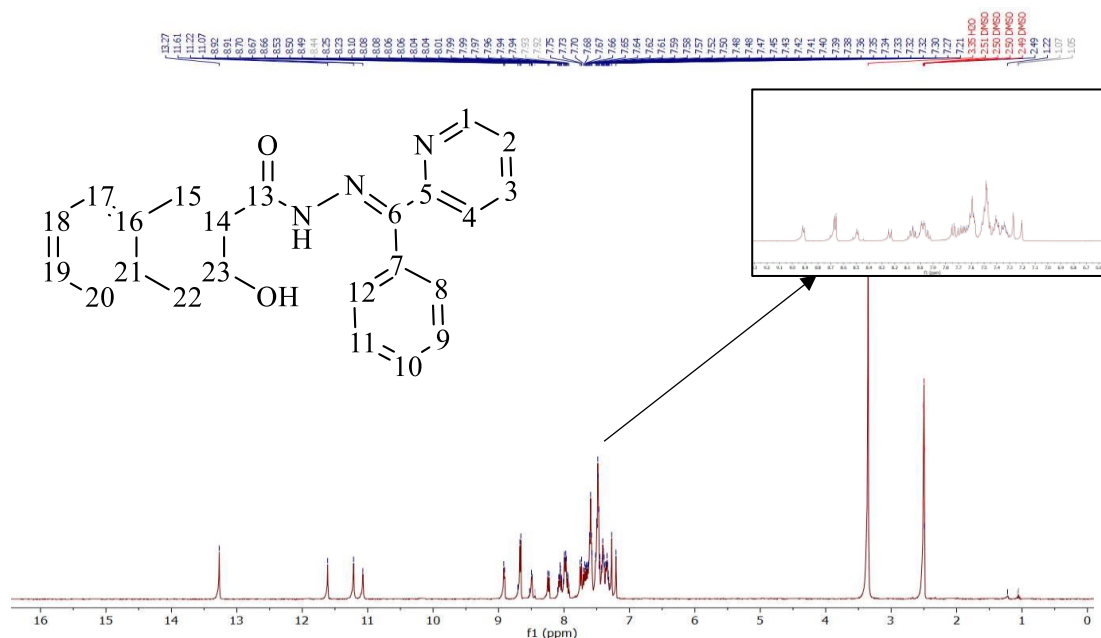


Figure 1. ¹H-NMR spectrum of the HL

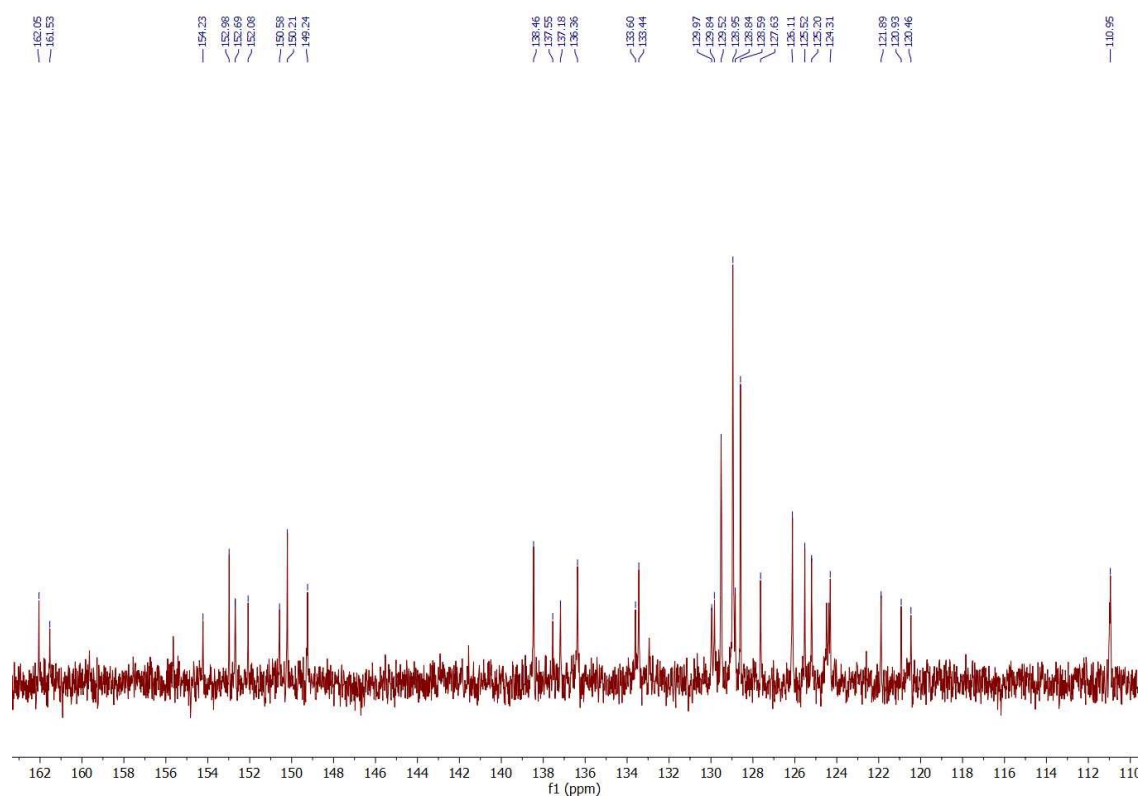
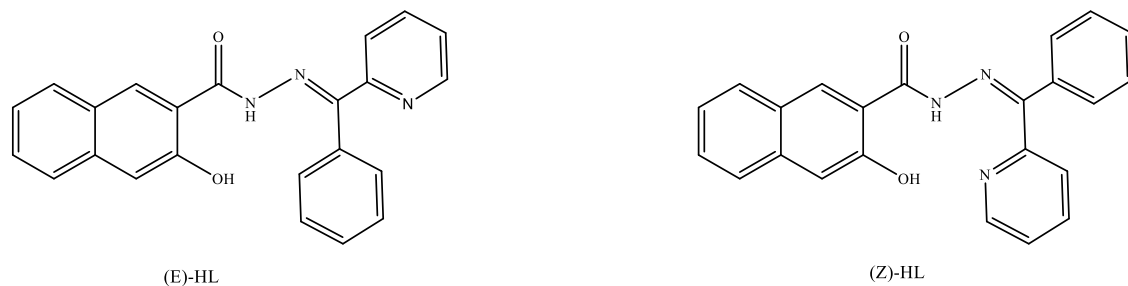


Figure 2. ¹³C-NMR spectrum of the HL



Scheme 2. E and Z isomers of the HL

3.2. IR Studies of HL and [NiL₂]

The bands at 3415 cm^{-1} and 3216 cm^{-1} in the IR spectrum of HL are caused by (O-H) and (N-H), respectively. The complex spectrum did not contain the (N-H) band. For [NiL₂], the OH band was seen at 3452 cm^{-1} . This shows that the OH group is uncoordinated and the NH group is coordinated with the metal ion. The IR spectrum of the HL exhibits three absorption bands with wavenumbers of 1650 , 1623 , and 1513 cm^{-1} that are caused, respectively, by $\nu(\text{C}=\text{O})$, $(\text{C}=\text{N})_{\text{imine}}$, and $(\text{C}=\text{N})_{\text{pyridine}}$. In comparison to the ligand, the IR spectrum of [NiL₂] complex shows considerable modifications. The (C-O) band was recorded in 1360 cm^{-1} for the complex spectrum, but the (C=O) band was not seen. And also new band due to the conjugate system $\nu(>\text{C}=\text{N}-\text{N}=\text{C}<)$ appeared at 1575 cm^{-1} , for [NiL₂] (Figure 3) [14].

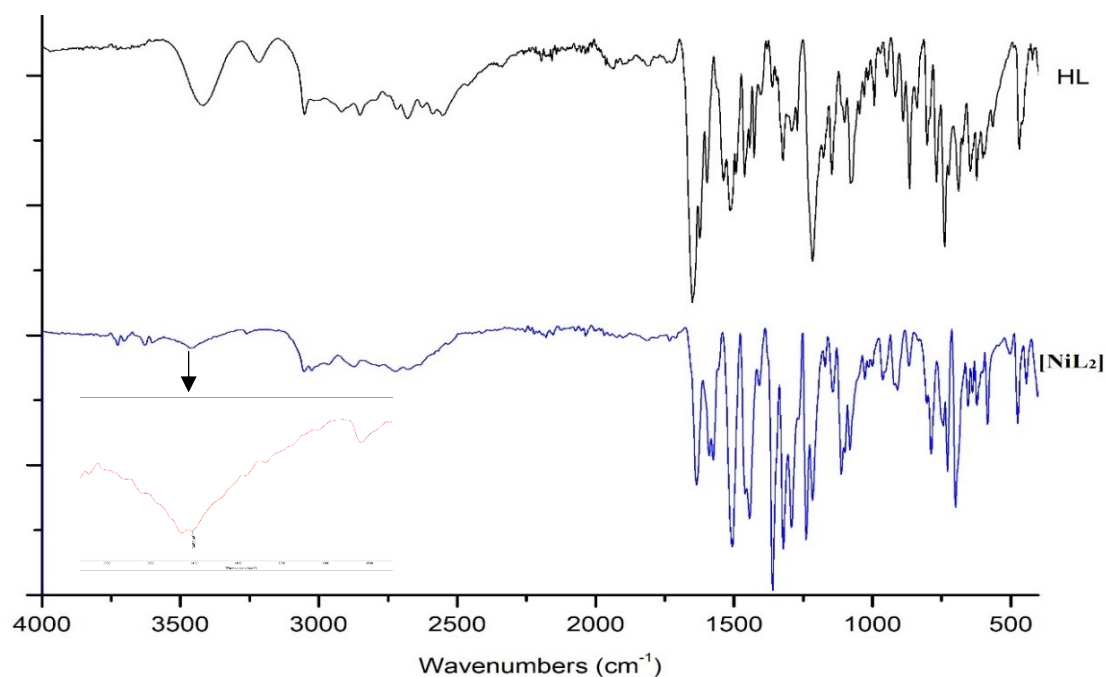


Figure 3. Infrared spectra of the HL and [NiL₂]

3.3. UV-Visible and magnetic measurement studies

In DMSO (10^{-4} M), the electronic spectrum of **HL** (Figure 4) shows a band at 318 nm associated with the $n \rightarrow \pi^*$ transition of the carbonyl group. The aromatic rings and azomethine moiety are attributed to the $\pi \rightarrow \pi^*$ transitions that are seen as a band and a shoulder at 289 nm. There is a slight shift in these bands during complexation. In the UV-Visible spectrum of the **[NiL₂]** complex (Figure 5), charge-transfer transitions for the **[NiL₂]** complex were observed at 393 nm. Two electronic absorption bands at 413 and 826 nm, which stand for the ${}^3A_{2g}(F) \rightarrow {}^3T_{1g}(F)(\nu_2)$ and ${}^3A_{2g}(F) \rightarrow {}^3T_{1g}(P)(\nu_2)$ transitions, respectively, were visible in the electronic spectra of the synthesized **[NiL₂]** complex [15]. These transitions demonstrated the octahedral geometry of the **[NiL₂]** complex. The **[NiL₂]** complex showed the magnetic moment value 3.5 BM. This value is consistent with the values expected for Ni(II) cations in octahedral geometries with two unpaired electrons [15, 16].

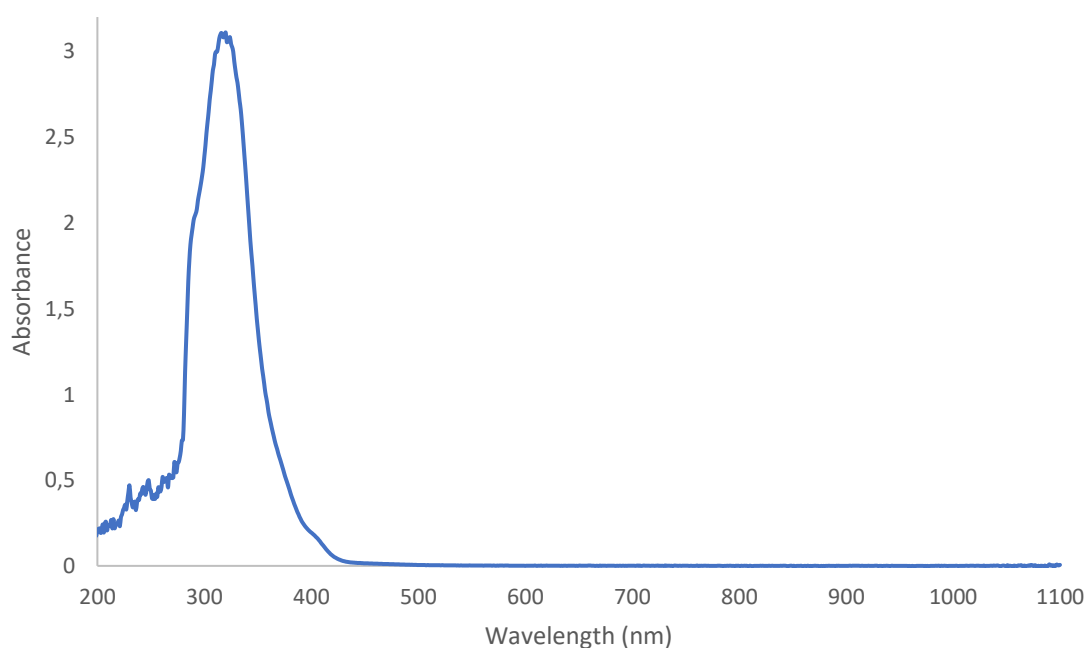


Figure 4. Absorption spectrum of the **HL**

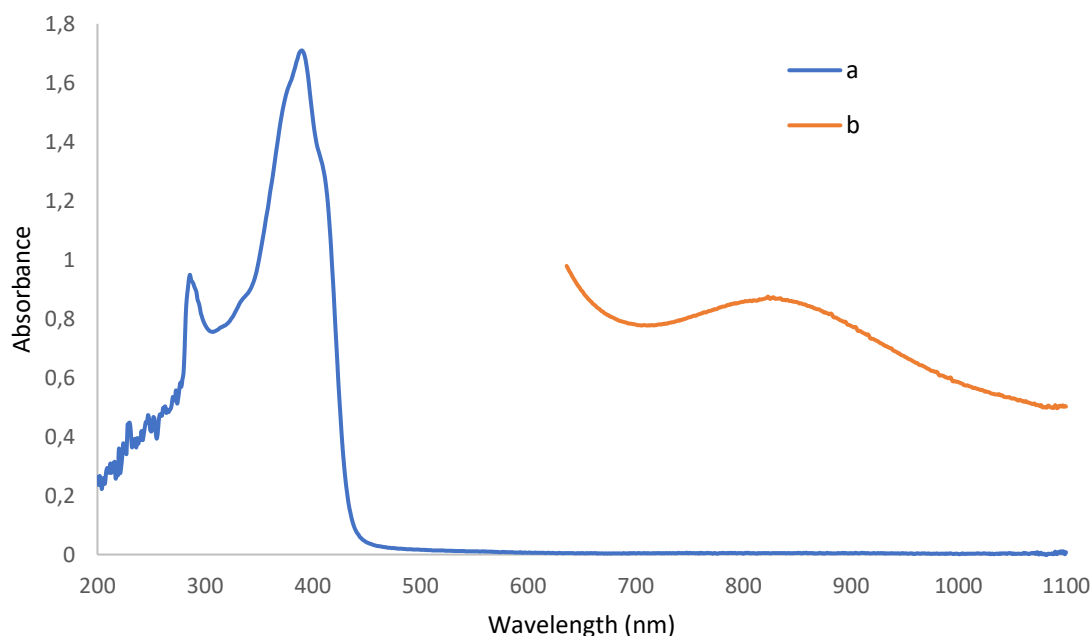


Figure 5. Absorption spectra of [NiL₂] complex a) 10⁻⁴ M, b) 10⁻² M

3.4. Mass spectral analysis of HL and [NiL₂]

The ESI-MS spectra of the **HL** and [NiL₂] complex are presented Figure 6. The mass spectra of **HL** and [NiL₂] complex confirmed the identity of the structures. The **HL** ligand spectrum gave two m/z signals of 368.06 and 391.11 for [M+H]⁺, [M+Na]⁺, respectively, which were in agreement with the calculated values of 368.42 and 390.40. ESI-MS of the [NiL₂] complex gave m/z signal at 790.85 which corresponded to the calculated value of 792.50 for [NiL₂+H]⁺. The mass spectrum of the Ni(II) complex was evidence for the chelation of the two ligand molecules to the Ni (II) center.

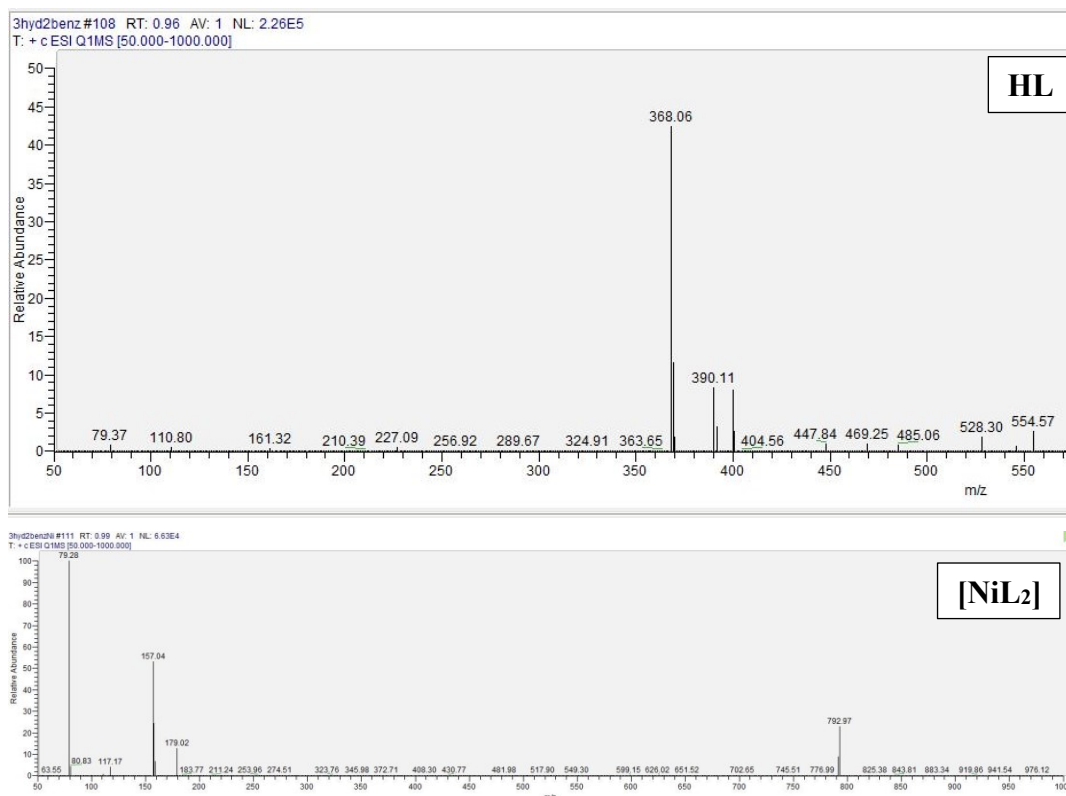


Figure 6. Mass spectra of the HL and [NiL₂]

3.5. Biological activity of HL and [NiL₂]

The antibacterial activity of the newly synthesized compounds HL and [NiL₂] was evaluated using broth microdilution technique against various reference bacterial strains and clinical isolates. The outcomes demonstrated that these substances have potent antibacterial action.

The data presented in Table 1 show that between both novel compounds, the [NiL₂] complex has higher antibacterial activity compared to the HL ligand. However, it can be said that [NiL₂] complex is more active on *S. aureus* 25923 and *E. faecalis* bacteria. When the Minimum Inhibitory Concentration (MIC) values of the compounds tested with positive control substances such as gentamicin and streptomycin are compared in the study, it is observed that these values are similar. MIC values indicate that the [NiL₂] complex is active at a lower concentration than the HL ligand. The data as a whole indicate that the test chemicals were more effective at killing Gram-negative bacteria than Gram-positive bacteria [17,18].

Table 1. Minimum inhibitory concentration with antimicrobial activity of HL and [NiL₂]

Compounds	Antimicrobial zone diameters												
	Gram-negative						Gram-positive						
	<i>E. coli</i> 25922	<i>E. coli</i>	<i>PA</i> 27853	<i>PA</i>	<i>KP</i>	<i>EA</i> 1304	<i>SD</i> 11456b		<i>LM</i> 19115	<i>S. aureus</i> 25923	<i>S. aureus</i> (MRSA)	<i>B. cereus</i> 14579	<i>E. faecalis</i>
[NiL ₂]	16	15	15	17	14	17	15		14	16	16	17	17
HL	12	13	n.d ^b	n.d.	13	12	14		11	14	n.d.	14	n.d.
GN	19	18	15	16	18	21	19		n.d.	18	19	23	n.d.
CIP	22	24	25	27	22	18	21		n.d.	22	21	19	20
	MIC ^a (μM)												
[NiL ₂]	32	16	8	16	8	8	16		64	8	16	32	8
HL	64	128	n.d ^b	n.d.	2	64	32		>256	64	64	8	n.d.
GN	1	2	1	2	1	0.5			n.d.	1		2	n.d.
CIP	0.5	0.5	1	0.5	0.5	2	0.5		n.d.	0.5	1	0.5	0.5

^aThe lowest peptide concentration that prevented bacterial growth was identified as the minimum inhibitory concentration (MIC) in three separate experiments carried out in triplicate. Abbreviations: PA: *P. aeruginosa*, KP: *Klebsiella pneumoniae*, EA: *Enterobacter aerogenes*, SD: *Shigella dysenteriae*, LM: *Listeria monocytogenes*, GN: Gentamisin, CIP: Siprofloksasin.

^bn.d: Not detected

4. Conclusion

In this work, the synthesis and characterization of a novel 3-hydroxy-2-naphthoic acid hydrazide derivative, the hydrazone ligand **HL** and its Ni(II) complex was reported. Elemental analyzes, spectroscopic studies and magnetic measurements were performed to characterize the structural properties of the prepared compounds. $^1\text{H-NMR}$ and $^{13}\text{C-NMR}$ confirmed the structure of **HL**. The metal-to-ligand ratio of the $[\text{NiL}_2]$ complex, determined by elemental analysis and mass spectra, was 1:2. The O-H and C=O bands observed in the IR spectrum of **HL** were not observed in the spectrum of the complex. In addition, shifts in the $(\text{C}=\text{N})_{\text{imine}}$ and $(\text{C}=\text{N})_{\text{pyridine}}$ bands were observed. The duplicating of the signals in the $^1\text{H-NMR}$ and $^{13}\text{C-NMR}$ spectra of the ligand indicates the presence of E and Z isomers of the ligand in DMSO- d_6 solution. These data show that the ligand in the E-isomer form coordinates to the metal atom via carbonyl-O, azomethine-N, and pyridyl-N atoms. When the antibacterial activity of the newly synthesized **HL** and $[\text{NiL}_2]$ was tested on clinically important isolates and pathogenic strains, it was found that the $[\text{NiL}_2]$ complex exhibited a wider zone width than the ligand in all microorganisms tested. It is of crucial importance for clinical microbiology as it has a stronger antibacterial effect against Gram-negative bacteria than against Gram-positive bacteria and also plays an effective role against resistant germs. The fact that the tested compounds have strong antimicrobial activity against microorganisms such as *E. coli*, *P. aeruginosa*, and *S. aureus*, which cause serious diseases in outpatient groups and cause death in intensive care patients, as well as resistant microorganisms such as methicillin-resistant *Staphylococcus aureus* (MRSA), indicates that they may be antibiotic alternatives in the future. Furthermore, the chemicals examined have strong antibacterial action against *E. faecalis*, a Gram-positive bacteria prevalent in the gastrointestinal system. When the antibacterial activity of the new synthesized products are compared to the antibiotics utilized as positive controls, the compounds show promise as an alternative to antibiotics.

Ethics in Publishing

There are no ethical issues regarding the publication of this study.

Acknowledgements

The Coordination Unit for Scientific Research Projects at Kırşehir Ahi Evran University provided funding for this work (Project ID: AHİLAB.A4.23.002). Dr. Esin Kıray (Kırşehir Ahi Evran University) is sincerely appreciated by the authors.

References

- [1] Adjissi, L., Chafai, N., Benbouguerra, K., Kirouani, I., Hellal, A., Layaida, H., ... & Chafaa, S. (2023). New aromatic hydrazones: Synthesis, structural analysis, DFT study, biological activity, ADME-T properties and in silico evaluation of their inhibition of SAS-CoV-2 main protease. *Journal of Molecular Structure*, 1279, 134997.
- [2] Boora, A., Devi, J., Rom, T., & Paul, A. K. (2023). Synthesis, characterization, single crystal structure, biological evaluation of ONO donor hydrazones and their diorganotin (IV) complexes. *Journal of Molecular Structure*, 1284, 135386.
- [3] Sinha, R., Singh, U. V. S., Khosa, R. L., & Jain, J. (2018). Anticonvulsant Activity of Isonicotinic Acid Hydrazone Derivatives Using MES, scPTZ and Rotorod Neurotoxicity Models. *Journal of Applied Pharmaceutical Sciences and Research*, 1(1):16-22.
- [4] Sail, B. S., Naik, V. H., Prasanna, B. M., Ahmad, N., Khan, M. R., Jagadeesh, M. R., & Cheedarala, R. (2023). Synthesis, characterization and pharmacological studies of cobalt (II), nickel (II) and copper (II) complexes of thiazole schiff bases. *Journal of Molecular Structure*, 1288, 135748.
- [5] Rohane, S. H., Redasani, V. K., Fuloria, N. K., & Fuloria, S. (2023). Synthesis, molecular docking and anti-inflammatory potential of novel hydrazones of eugenol in tuberculosis treatment. *Indian Journal of Chemistry (IJC)*, 62(6), 551-558.
- [6] Mohamed-Ezzat, R. A., Kariuki, B. M., & Elgemeie, G. H. (2023). Unexpected products of the reaction of cyanoacetylhydrazones of aryl/heteryl ketones with hydrazine: a new route to aryl/heteryl hydrazones, x-ray structure, and in vitro anti-proliferative activity against nci 60-cell line panel. *Egyptian Journal of Chemistry*, 66(13), 225-239.
- [7] Kumar, R., Singh, A. A., Kumar, U., Jain, P., Sharma, A. K., Kant, C., & Faizi, M. S. H. (2023). Recent advances in synthesis of heterocyclic Schiff base transition metal complexes and their antimicrobial activities especially antibacterial and antifungal. *Journal of Molecular Structure*, 1294, 136346.
- [8] Kiray, E. (2023). Cinnamomum verum Uçucu Yağının Pseudomonas aeruginosa ve Acinetobacter baumannii Üzerindeki Anti-biyofilm ve Anti-quorum Sensing Aktivitesi. *Balikesir Sağlık Bilimleri Dergisi*, 12(1), 169-176.
- [9] İnce, U. and Han, M.İ., (2023). Ufuk, İ. N. C. E., & Han, M. İ. (2023). Investigation of Antimicrobial Activity of Some Ethylparaben Hydrazone-Hydrazone Derivatives. *Turkish Journal of Pharmaceutical Sciences*, 20(1), 35.
- [10] Kamboj, S., Thakral, S., Kumar, S., & Singh, V. (2023). Synthesis, Biological Evaluation and in Silico Studies of 3-Hydroxy-N-(2-(substituted phenyl)-4-oxothiazolidin-3-yl)-2-naphthamide Derivatives. *Chemistry & Biodiversity*, 20(6), e202200976.

- [11] Al-Hazmi, G. H. (2023). Synthesis, spectroscopic characterizations and cytotoxic activities of some novel 1, 2-bis-(tetrasubstituted-benzylidene) hydrazine analogues. *Bulletin of the Chemical Society of Ethiopia*, 37(6), 1503-1520.
- [12] Despaigne, A. A. R., Da Silva, J. G., do Carmo, A. C. M., Piro, O. E., Castellano, E. E., & Beraldo, H. (2009). Structural studies on zinc (II) complexes with 2-benzoylpyridine-derived hydrazones. *Inorganica Chimica Acta*, 362(7), 2117-2122.
- [13] Despaigne, A. A. R., Da Silva, J. G., Do Carmo, A. C. M., Piro, O. E., Castellano, E. E., & Beraldo, H. (2009). Copper (II) and zinc (II) complexes with 2-benzoylpyridine-methyl hydrazone. *Journal of Molecular Structure*, 920(1-3), 97-102.
- [14] Meenatchi, V., Zo, S. M., Won, S. Y., Nam, J. W., Cheng, L., & Han, S. S. (2023). Cuminaldehyde-3-hydroxy-2-naphthoichydrazone: Synthesis, effect of solvents, nonlinear optical activity, antioxidant activity, antimicrobial activity, and DFT analysis. *Spectrochimica Acta Part A: Molecular and Biomolecular Spectroscopy*, 302, 123071.
- [15] Patil, S. A., Naik, V. H., Kulkarni, A. D., & Badami, P. S. (2010). DNA cleavage, antimicrobial, spectroscopic and fluorescence studies of Co (II), Ni (II) and Cu (II) complexes with SNO donor coumarin Schiff bases. *Spectrochimica Acta Part A: Molecular and Biomolecular Spectroscopy*, 75(1), 347-354.
- [16] Baul, T. S. B., Nongsiej, K., Ka-Ot, A. L., Joshi, S. R., Rocha, B. G., & da Silva, M. F. C. G. (2020). Synthesis, crystal structures, magnetic properties and antimicrobial screening of octahedral nickel (II) complexes with substituted quinolin-8-olates and pyridine ligands. *Journal of Molecular Structure*, 1200, 127106.
- [17] Maia, D. O., Santos, V. F., Barbosa, C. R., Fróes, Y. N., Muniz, D. F., Santos, A. L., ... & Teixeira, C. S. (2022). Nickel (II) chloride Schiff base complex: Synthesis, characterization, toxicity, antibacterial and leishmanicidal activity. *Chemico-Biological Interactions*, 351, 109714.
- [18] Roy, T. G. (2020). Synthesis, characterization and antibacterial evaluation of some new nickel (II) complexes of a tetraazamacrocyclic. *Acta Scientific Pharmaceutical Sciences*, 5, 60-69.

***MEFV* Gene Mutations in Familial Mediterranean Fever Patients: Erzincan Experience**

Abdussamed Yasin DEMİR^{1*}, Özlem ADMIŞ²

¹ Erzincan Binali Yıldırım University, Faculty of Medicine, Medical Genetics

² Erzincan Binali Yıldırım University - Mengücek Gazi Training and Research Hospital, Medical Biochemistry

Received: 06/02/2024, **Revised:** 15/05/2024, **Accepted:** 16/05/2024, **Published:** 31/05/2024

Abstract

Familial Mediterranean Fever is an autosomal recessive autoinflammatory multisystemic genetic disease caused by mutations in the *MEFV* gene. Although it is a common disease in our country, the type and frequency of mutations that cause the disease vary regionally. This study aimed to determine the types and frequencies of *MEFV* gene mutations in patients with a preliminary diagnosis of Familial Mediterranean Fever in our city. 303 patients who were referred to our laboratory with a preliminary diagnosis of Familial Mediterranean Fever were included in the study. The findings of the patients analyzed for common mutations in the *MEFV* gene using the Real-Time PCR method were evaluated retrospectively. While mutations in the *MEFV* gene were detected in 44.8% of the patients included in the study, no mutations related to the investigated regions were detected in 55.2%. In patients with detected mutations; the frequency percentages of the most frequently detected genotypes are M694V/- (36.4%), E148Q/- (18.3%), M694V/M694V (7.3%); the frequency percentages of the alleles were determined as M694V (48.3%), E148Q (22.2%), M680I (10.8%), V726A (10.3%). The results of the study support the heterogeneity in *MEFV* gene mutations seen in Familial Mediterranean Fever patients. Although minor differences are observed in terms of mutation types and frequencies detected in the *MEFV* gene, the findings are compatible with the results of other studies conducted in the Turkish population. Current data on the genotype distribution of Familial Mediterranean Fever patients in our city will contribute to the literature.

Keywords: Familial Mediterranean Fever, *MEFV* Gene, Mutation, Pathogenic, Real-Time PCR

Ailesel Akdeniz Ateşi Hastalarında *MEFV* Gen Mutasyonları: Erzincan Deneyimi

Ailesel Akdeniz Ateşi, *MEFV* geninde meydana gelen mutasyonların yol açtığı otozomal resesif geçişli otoinflamatuar multisistemik genetik bir hastalıktır. Ülkemizde sık görülen bir hastalık olmakla birlikte hastalığa sebep olan mutasyonların tipi ve sıklıkları bölgesel olarak farklılık göstermektedir. Bu çalışmada, ilimizde Ailesel Akdeniz Ateşi ön tanısı alan hastalarda *MEFV* gen mutasyonlarının tiplerinin ve sıklıklarının belirlenmesi amaçlanmıştır. Ailesel Akdeniz Ateşi ön tanısı ile laboratuvarımıza yönlendirilen 303 hasta çalışmaya dahil edildi. Real-Time PCR yöntemi ile *MEFV* geninde sık görülen mutasyonlar açısından analiz edilen hastaların bulguları retrospektif olarak değerlendirildi. Çalışmaya dahil edilen hastaların %44.8'inde *MEFV* geninde mutasyon saptanırken %55.2'sinde ise araştırılan bölgelere ilişkin mutasyon saptanmadı. Mutasyon tespit edilen hastalarda en sık saptanan genotiplerin frekans yüzdeleri; M694V/- (%36.4), E148Q/- (%18.3), M694V/M694V (%7.3); alellerin frekans yüzdeleri ise M694V (%48.3), E148Q (%22.2), M680I (%10.8), V726A (%10.3) olarak tespit edildi. Çalışmanın sonuçları Ailesel Akdeniz Ateşi hastalarında görülen *MEFV* gen mutasyonlarındaki heterojeniteyi desteklemektedir. *MEFV* geninde saptanan mutasyon tipleri ve sıklıkları bakımından minör farklılıklar gözlemlense de elde edilen bulgular Türk popülasyonunda gerçekleştirilen diğer çalışmaların sonuçları ile uyumludur. İlimizdeki Ailesel Akdeniz Ateşi hastalarının genotip dağılımlarının güncel verileri literatüre katkı sağlayacaktır.

Anahtar Kelimeler: Ailesel Akdeniz Ateşi, *MEFV* Geni, Mutasyon, Patojenik, Real-Time PCR

1. Introduction

Familial Mediterranean Fever (FMF) (OMIM #249100) is the earliest identified and most common autosomal recessive hereditary autoinflammatory disease [1-2]. FMF is characterized by recurrent short-term fever, abdominal, chest and joint pain, and erythema-like skin lesions [3]. The period and type of attacks vary according to mutation type, ethnicity and colchicine use, as well as age and gender [4]. Complications of the disease can range from simple skin lesions to life-threatening amyloidosis [5-6].

Although FMF is especially common in populations originating from the Mediterranean basin such as Turks, Jews, Arabs and Armenians, it seen worldwide due to increased travel and migration in recent years [7-8]. It has been reported that the frequency of the disease in our country is approximately 1/1000 and the carrier rate is 1/5 [1]. Due to the high carrier rate in our country, determining Mediterranean Fever (*MEFV*) gene mutations is important in detecting patients as well as other family members carrying the disease, initiating treatment and providing genetic counseling.

The *MEFV* gene responsible for the disease is located on the short arm of chromosome 16 (16p13.3) [9]. This gene, which has 10 exons, encodes the protein called pyrin, which consists of 781 amino acids [10]. This immune regulatory protein functions as an innate immune sensor that triggers inflammation and enables the production of inflammatory mediators [11]. Pyrin is mostly expressed in neutrophils, eosinophils, monocytes, dendritic cells and fibroblasts and plays a role in the regulation of apoptosis, inflammation and cytokine production [12]. Changes in the structure of this protein cause uncontrolled interleukin-1 (IL-1) secretion and an increase in the inflammatory response [12].

The variability in clinical findings and disease severity in FMF patients can be explained by different mutations in the *MEFV* gene. According to the INFEVERS database, 340 different mutations have been identified in the *MEFV* gene [13]. It has been shown that the majority of these nucleotide changes that cause the disease are in exons 2 and 10 [7, 14]. Knowing the mutation types is important in terms of approaching the patient. As far as we know, there is no study on the mutation types of FMF patients in our province. Therefore, our current study aimed to determine the common mutation types in the *MEFV* gene in patients sent to our laboratory with a preliminary diagnosis of FMF.

2. Material and Methods

In our study, the results of 303 patients who were referred from different units of our hospital with a preliminary diagnosis of FMF between 10.10.2022 and 10.10.2023 and were analyzed for *MEFV* gene mutations in our laboratory were evaluated retrospectively. Consent forms were obtained during the outpatient clinic examination. This study was carried out taking into account ethical responsibilities according to the World Medical Association and the Declaration of Helsinki, and ethics committee approval was received from Erzincan Binali Yıldırım

University Non-Interventional Clinical Research Ethics Committee with decision number 2023-18/17.

For *MEFV* gene analysis, 2 ml peripheral venous blood samples were taken from the patients and placed in ethylene diamine tetra acetic acid (EDTA) tubes. Genomic material was isolated with the QIAmp DNA Mini Kit (Qiagen GmbH). The concentration and quality of the obtained DNAs were measured with a Nanodrop spectrophotometer (Thermo Scientific, USA). DNAs with appropriate purity and concentration (OD260/OD280, 1.8-2.0) for analysis were included in the study. The DNA samples obtained were analyzed for mutations common in FMF disease (M694V, E148Q, M680I, V726A, P369S, M694I) with the Real-Time PCR method (Roche Cobas Z 480). Individuals in which mutant and wild type bands were observed together were considered heterozygous, individuals in which only mutant bands were observed were considered homozygous mutant, and individuals in which only wild type peaks were observed were considered normal.

For statistical analysis of the data, SPSS (Statistical Package for Social Sciences for Windows v22.0) program was used. Descriptive statistics; it was calculated as mean ± standard deviation for numerical variables, and as frequency distribution and percentage for heterogenic variables.

3. Results and Discussion

While mutation was detected in 44.8% of 303 patients who were referred to our laboratory with a preliminary diagnosis of FMF disease and included in the study, no mutation was detected in 55.2% of the investigated regions. Detailed molecular and clinical classification of the detected mutations is shown in Table 1.

Table 1: Molecular and clinical information on *MEFV* mutations.

Mutation	Exonic Location	Nucleotide Change	Protein Change	ACMG Classification
E148Q	2	c.442G>C	p.Glu148Gln	Uncertain Significance
P369S	3	c.1105C>T	p.Pro369Ser	Uncertain Significance
M694V	10	c.2080A>G	p.Met694Val	Pathogenic
M680I	10	c.2040G>A	p.Met680Ile	Pathogenic
V726A	10	c.2177T>C	p.Val726Ala	Pathogenic
M694I	10	c.2082G>A	p.Met694Ile	Pathogenic

It was determined that 70.1% of the patients with a mutation were heterozygous, 16.8% were compound heterozygous, and 13.1 were homozygous (Table 2).

Table 2: Distribution of genotypes in patients with detected mutations.

Mutation type	Number of patients (n)	Percentage (%)
Heterozygous	95	70.1
Compound Heterozygous	23	16.8
Homozygous	18	13.1
Total	136	100

The most frequent genotype in patients with a mutation was M694V/- (36.4%). This is followed by E148Q/- (18.3%) and M694V/M694V (7.3%) genotypes, respectively. Other genotypes observed in the patients are shown in Table 3.

Table 3: Distribution and frequencies of mutations detected in the *MEFV* gene.

Mutation type	Genotype	Number of patients (n)	Percentage (%)
Heterozygous	M694V/-	49	36.4
	E148Q/-	25	18.3
	P369S/-	9	6.6
	V726A/-	8	5.9
	M680I/-	3	2.2
	M694I/-	1	0.7
	Total	95	70.1
Compound Heterozygous	M694V/M680I	6	4.4
	M694V/E148Q	6	4.4
	M694V/V726A	4	2.9
	M680I/V726A	4	2.9
	E148Q/P369S	2	1.5
	V726A/P369S	1	0.7
	Total	23	16.8
Homozygous	M694V	10	7.3
	M680I	3	2.2
	E148Q	3	2.2
	V726A	1	0.7
	P369S	1	0.7
	Total	18	13.1
General Total	136	100	

When the allele frequencies mutations are examined, the most common mutation is M694V with 48.3%. This mutation is followed by E148Q (22.2%) and M680I (10.8%), respectively. The allele frequency distribution of the mutations in the patients is shown in Table 4.

Table 4: Allele frequency distribution of mutations in patients.

Mutation	Number of Alleles	Percentage (%)
M694V	85	48.3
E148Q	39	22.2
M680I	19	10.8
V726A	18	10.3
P369S	14	7.9
M694I	1	0.5
Total	176	100

FMF is an autosomal recessive systemic inflammatory disease that is more common in the Middle East and Mediterranean countries. The most important symptoms of the disease are fever, abdominal pain, joint pain and skin lesions [15]. The diagnosis of FMF can be made by observing characteristic attacks in patients with typical clinical findings. On the other hand, in atypical cases such as patients with amyloidosis or cases that cannot be distinguished from other periodic fever syndromes, genetic examination comes to the fore as an approach to diagnosis and treatment [11]. It is known that mutations in the *MEFV* gene located on the short arm of chromosome 16 (16p13.3) cause FMF disease [2]. The variability in clinical findings and severity of the disease is explained by different mutations in the *MEFV* gene [15]. Different methods such as sanger sequencing, pyrosequencing, real-time polymerase reaction and next-generation sequencing are used to detect these mutations responsible for the pathogenesis of the disease. In our current study, patients sent to our laboratory with a preliminary diagnosis of FMF were examined using the real-time polymerase reaction method for 5 common mutations in the *MEFV* gene.

Mutations were detected in 136 (44.8%) of the 303 patients included in our study. In studies conducted on the observed mutations in the *MEFV* gene, Çilingir et al. [15] detected mutations in 47.5% of the patients, Yeşilada et al. [3] in 47.21% of the patients, and Dönder et al. [5] in 42.85% of the patients. The results we obtained are similar to the results of these studies.

Among the cases with mutations in our study, the heterozygosity rate was found to be 70.1%, the compound heterozygosity rate was 16.8%, and the homozygosity rate was 13.1%. In a study conducted by Binici et al. in the southeastern region, the *MEFV* gene was analyzed for frequent regions using the pyrosequencing method [1]. In this study, they revealed that 74.13% of the patients were heterozygous, 16.43% were compound heterozygous, and 9.44% were homozygous. In another study by Çilingir et al. in a large patient group using the pyrosequencing method, the heterozygosity rate was found to be 60.77%, the compound heterozygosity rate was 22.56%, and the homozygosity rate was 16.65% [15]. The results we obtained are in agreement with the results of similar studies, especially in terms of the distribution of genotypes. Additionally, the heterozygous mutation rate of 70.1% obtained in our study was found to be higher than most of the studies in our country.

The frequencies of the mutations we detected in our study were determined as M694V/- (36.4%), E148Q/- (18.3%) and M694V/M694V (7.3%), respectively. According to the results

of the study by the Turkish FMF working group in 2005, the most frequently observed mutations were reported as M694V (51.4%), M680I (14.4%), V726A (8.6%), respectively [16]. In the study carried out by Bayrak et al. using the next generation sequencing method, the common mutations were found to be M694V (34.9%), E148Q (26%), V726A (16%) [13]. Taşdemir et al., in their study conducted in the Konya region, stated that they found the mutation frequencies as M694V (22.3%), E148Q (12.9%), and M680I(C) (9.7%) [7]. Teker and Öz, in their study where they examined all coding regions and exon-intron junctions of the *MEFV* gene with the next generation sequencing method, reported the most frequent mutations as M694V (46.6%), V726A (14.5%), and M680I (14%), respectively [12].

The allele frequencies of the mutations in our study were found as M694V (48.3%), E148Q (22.2%), M680I (10.8%) and V726A (10.3%). Özemri et al. found the allele frequencies in 350 patients in which they detected mutations in the *MEFV* gene as M694V (38.1%), E148Q (20.4%), V726A (8.9%) and M680I (6.8%) [17]. In a similar study, Çilingir et al. reported the allele frequencies as M694V (40.13%), E148Q (24.43%), V726A (11.57%) [15]. Similar to studies in the literature, the M694I mutation was found at low frequency in our study [1, 5, 11]. When the data of our study and similar studies in our country are evaluated together, it is concluded that M694V, V726A, M680I(C), E148Q mutations are the most frequently observed mutations in most of the studies and that there are generally differences in terms of *MEFV* gene mutation allele frequencies between regions.

4. Conclusion

In conclusion, the findings this study show that the distribution and allele frequencies of *MEFV* gene mutations in our patients evaluated with a preliminary diagnosis of FMF were compatible with previously reported data in FMF patients in our country. Detection of FMF mutations allows the clinical diagnosis to be confirmed, colchicine treatment to be started without delay, and the patient's relatives to be evaluated in terms of the determined mutation in our country where the carrier rate is high. Apart from the common mutations in FMF disease, it is known that some other mutations may also cause the disease. Therefore, although it has a higher cost compared to other methods, analyzing the *MEFV* gene with the next generation sequencing method, especially in countries with a high prevalence of FMF disease, will contribute to the detection of common, rare or unknown mutations.

The most important limitations of our study are the small number of cases and the fact that it is a single-center study. Another important limitation of the study is that since it was a retrospective study, the relationship between mutation types and the clinic could not be examined.

Ethics in Publishing

Ethics committee approval was received from Erzincan Binali Yıldırım University Non-invasive Clinical Research Ethics Committee on 19.10.2023 with the decision numbered 2023-18/17.

Author Contributions

Main Idea/Planning: AYD, ÖA; Analysis/Comment: AYD, ÖA; Providing Data: ÖA; Writing: AYD; Review and Correction: AYD, ÖA; Confirmation: AYD, ÖA

Conflicts of Interests

There is no conflict of interest between the authors.

References

- [1] Binici, M., Tekeş, S., Balkan, M., Oral, D., Yücel, İ., Tunç, Ş. (2022) Çocuk Ailesel Akdeniz Ateşi hastalarında *MEFV* mutasyonlarının dağılımı: Türkiye'nin güneydoğusunda tek merkezli çalışma. *Dicle Tıp Dergisi*. 49(2):361-6.
- [2] Kırmaz, B., Gezgin, Y., Berdeli A. (2022) *MEFV* gene allele frequency and genotype distribution in 3230 patients' analyses by next generation sequencing methods. *Gene*. Jun 15;827:146447. doi: 10.1016/j.gene.2022.146447.
- [3] Yeşilada, E., Savaci, S., Yüksel, Ş., Gülbay, G., Otlu, G., Kaygusuzoğlu, E. (2005) Ailesel Akdeniz Ateşi (FMF) düşünülen olgularda *MEFV* gen mutasyonları. *İnönü Üniversitesi Tıp Fakültesi Dergisi*. 12(4):235-8.
- [4] Erden, G., Bal, C., Torun, G.O., Uğuz, N., Yıldırımkaaya, M.M. (2008) Ailesel Akdeniz Ateşi (FMF) düşünülen olgularda *MEFV* gen mutasyonları sıklığının incelenmesi. *Türk Hijyen ve Deneysel Biyoloji Dergisi*. 65(1):1-5.
- [5] Dönder, A., Dülger, H., Balahoroğlu, R., Çokluk, E., Şekeroğlu, M.R. (2012) Retrospektif moleküler bir çalışma: FMF ön tanısı alan hastalarda *MEFV* gen mutasyonları. *Tıp Araştırmaları Dergisi*. 10(3):94-8.
- [6] Ülgenalp, A. (2009) DEGETAM'a Yönlendirilen hastalardaki *MEFV* geni mutasyonlarının dağılımı. *DEÜ Tıp Fakültesi Dergisi*. 23(2):53-8.
- [7] Taşdemir, P. (2018) Konya Bölgesi'nde *MEFV* Gen mutasyonlarının sıklığı ve dağılımı. *Bozok Tıp Dergisi*. (3):35-9.
- [8] Evliyaoglu, O., Bilici, S., Yolbas, İ., Kelekçi, S., Sen, V. (2009) Diyarbakır yöresi Ailevi Akdeniz Ateşli çocuklarda *MEFV* gen mutasyon sıklıkları. *Dicle Tıp Dergisi*. 36(2):80-4.
- [9] Köçeroğlu, R., Şekeroğlu, M.R., Balahoroğlu, R., Çokluk, E., Dülger, H. (2014) Van ve çevresindeki çocuklarda ailesel Akdeniz Ateşi gen mutasyonlarının sıklığı. *Türk Klinik Biyokimya Dergisi*. 12(3):125-30.
- [10] Bozkaya, G., Örmən, M., Bilgili, S., Akşit, M. (2016) İzmir'de *MEFV* gen mutasyonlarının sıklığının araştırılması. *Türk Klinik Biyokimya Dergisi*. 14(2):94-9.

- [11] Torun, D., Tekgöz, E., Kavuş, H., Öztuna, A., Akar, H., Çınar, M., ve ark. (2017) FMF hastalarındaki *MEFV* gen mutasyon sıklığı ve mutasyonların dağılımı: Tek bir merkezden geniş bir hasta grubunun analizi. *Gülhane Tıp Dergisi*. 59(1):247.
- [12] Düzkale, T.N., Öz. Ö. (2020) Ailevi Akdeniz Ateşi hastalarında *MEFV* geninin NGS ile analizi: Tek merkez deneyimi. *Harran Üniversitesi Tıp Fakültesi Dergisi*. 17(3):454-9.
- [13] Bayrak, M., Çadircı, K., Yaralı, O. (2019) Bölgemizdeki ailesel Akdeniz Ateşi hastalarının *MEFV* gen mutasyon tiplerinin sıklığı. *Kırıkkale Üniversitesi Tıp Fakültesi Dergisi*. 21(2):254-60.
- [14] Tokgün, O., Türel, S., Tokgün, P.E., Durak, T., Karagenç, N., Demiray, A., Akça, H. (2021) Ailesel akdeniz ateşi ön tanılı hastalarda *MEFV* mutasyonlarının gerçek zamanlı polimeraz zincir reaksiyonu ve yeni nesil dizileme ile karşılaştırmalı analizi-tek merkez deneyimi. *Pamukkale Tıp Dergisi*. 14:638-644.
- [15] Çilingir, O., Durak, A.B., Arslan, S., Kutlay, Ö., Erzurumluoğlu, E., Kocagil, S., ve ark. (2018) Ailesel Akdeniz Ateşi tanısı alan olgularda *MEFV* geni mutasyonlarının ve allel frekanslarının dağılımı - Tek Merkez Deneyimi. *Osmangazi Journal of Medicine*. 40(2):39-46.
- [16] Group TFS. (2005) Familial Mediterranean fever (FMF) in Turkey: results of a nationwide multicenter study. *Medicine*. 84(1):1-11.
- [17] Özemri, S.Ş., Alemdar, A., Aliyeva, L., Kaya, N., Temel, Ş.G. (2021) Frequency and Distribution of *MEFV* Gene Mutation in Familial Mediterranean Fever Patients: A Single Center Experience. *SDU Medical Faculty Journal* 28(1):85-91.

Biosynthesis of Naringenin@Cu (II), Zn (II) Hybrid Nanoflower: Anticancer Activity

Assay process

Burcu SOMTÜRK YILMAZ¹*

¹Drug Application and Research Center, Erciyes University, 38280 Kayseri, Turkey

Received: 09/02/2024, Revised: 03/05/2024, Accepted: 16/05/2024, Published: 31/08/2024

Abstract

In the study, the synthesis of organic-inorganic hybrid nanoflowers, which have a flower-like structure and are called nanoflowers, was carried out. For this purpose, hybrid nanoflower synthesis was carried out using naringenin as the organic part and different metal ions (Cu and Zn) as the inorganic part. Various analyzes were carried out to characterize the synthesized nanoflowers (such as SEM, EDX, FTIR, XRD). In addition, the anticancer activities of hybrid nanoflowers were tested on the MCF7 (breast cancer) cell line. Naringenin-ZnhNFs killed MCF7 cells at a rate of approximately 76%, while Naringenin CuhNFs caused cell death at a rate of 68%. Naringenin caused 45% cell death. It was concluded that there was a good increase in anticancer activity when naringenin was converted into hybrid nanoflower form. In particular, the anticancer activity of hybrid nanoflowers synthesized with Zn metal ion was quite excellent. This means that Zn hybrid nanoflowers may be a safer therapeutic alternative than others.

Keywords: nanoflower, anticancer, naringenin

Naringenin@Cu (II), Zn (II) Hibrit Nanoçiçeğinin Biyosentezi: Antikanser Aktivite Testi süreci

Öz

Çalışmada çiçeğe benzer bir yapıya sahip olan ve nanoçiçek olarak adlandırılan organik-inorganik hibrit nanoçiçeklerin sentezi gerçekleştirildi. Bu amaçla organik kısım olarak naringenin, inorganik kısım olarak ise farklı metal iyonları (Cu ve Zn) kullanılarak hibrit nanoçiçek sentezi gerçekleştirilmiştir. Sentezlenen nanoçiçekleri (SEM, EDX, FTIR, XRD gibi) karakterize etmek için çeşitli analizler yapıldı. Ayrıca hibrit nanoçiçeklerin antikanser aktiviteleri MCF7 (meme kanseri) hücre hattı üzerinde test edildi. Naringenin-ZnhNF'ler MCF7 hücrelerini yaklaşık %76 oranında öldürürken Naringenin CuhNF'ler %68 oranında hücre ölümüne neden oldu. Naringenin %45 hücre ölümüne neden oldu. Naringenin hibrit nanoçiçek formuna dönüştürüldüğünde antikanser aktivitesinde iyi bir artış olduğu sonucuna varıldı. Özellikle Zn metal iyonu ile sentezlenen hibrit nanoçiçeklerin antikanser aktivitesi oldukça mükemmeldi. Bu, Zn hibrid nano çiçeklerinin diğerlerinden daha güvenli bir terapötik alternatif olabileceği anlamına gelir.

Anahtar Kelimeler: nanoçiçek, antikanser, naringenin

1. Introduction

Flower-shaped nanoflowers, which are the most striking member of nanoparticles today, are called nanoflowers because they have a flower-like structure. Hybrid nanoflowers consist of two parts: organic and inorganic. While proteins and enzymes containing nitrogen groups are preferred as the organic part, various metal ions (such as Zn(II), Cu(II), Mn(II) and Co(II)) are preferred as the inorganic part. However, today, it has been proven in many studies that nanoflower synthesis can be achieved with organic molecules or plant extracts containing hydroxyl and carboxyl groups other than nitrogen groups. For example, Somtürk et al. (2024) synthesized hybrid nanoflowers using *Tribulus Terrestris L.* plant extract as the organic part and different metal ions (Cu, Co and Zn) as the inorganic part, and examined the anticancer activities of the nanoflowers they synthesized. [1]. Uras et al. synthesized hybrid nanoflowers using *Aspergillus terreus* extract as the organic part and examined the antimicrobial activities of the hybrid nanoflowers they synthesized. [2]. Dadi and colleagues (2020) synthesized hybrid nanoflowers using gallic acid and examined its peroxidase-like activity [3]. Hybrid nanoflowers have excellent properties. These can be listed as having good stability, high stability and very good activity. The reason for this may be due to its morphology. Because it has a flower structure, it has a very large surface area. This is why it has such unique features. Although the formation mechanism of hybrid nanoflowers has not yet been fully elucidated, it can be explained as follows when the literature is examined. It can only be said that metal ions primarily form metal phosphate crystals in a buffered environment. Then, the metal phosphate crystals are bonded with the nitrogen groups in the enzyme or protein in the environment with a coordination bond, and it is predicted that hybrid nanoflowers are formed in this way. Naringenin, a flavanone, was preferred in the study. Naringenin has anticancer, antimutagenic, anti-inflammatory and antiatherogenic activities. Naringenin (5,7,4'-trihidroksiflavanonis) is found in orange, grapefruit, grape, tangerine and lemon peel [4-7]. Moreover, it is easily soluble in solvents such as ethanol and dimethyl sulfoxide. However, it has very little solubility in aqueous buffer systems. However, the poor water solubility of naringenin limits its use [8-12]. To overcome such limitations, strategies such as nanosized tools have been developed. In this context, organic-inorganic hybrid nanomaterials may be promising candidates [13-17]. There are not many studies on the anticancer activities of nanoflowers. In recent years, the anticancer effectiveness of hybrid nanoflowers was evaluated by Somturk and his group (2024) and they observed that the effectiveness of nanoflowers was very good [1]. Based on these studies, our study aimed to synthesize hybrid nanoflowers by considering the naringenin molecule, which has anticancer activity. Hybrid nanoflower synthesis was carried out using naringenin as the organic part and various metal ions (Cu and Zn) as the inorganic part. After characterization, anticancer activities were evaluated on the MCF7 cell line.

2. Material and Methods

Synthesis of Naringenin-CuhNFs

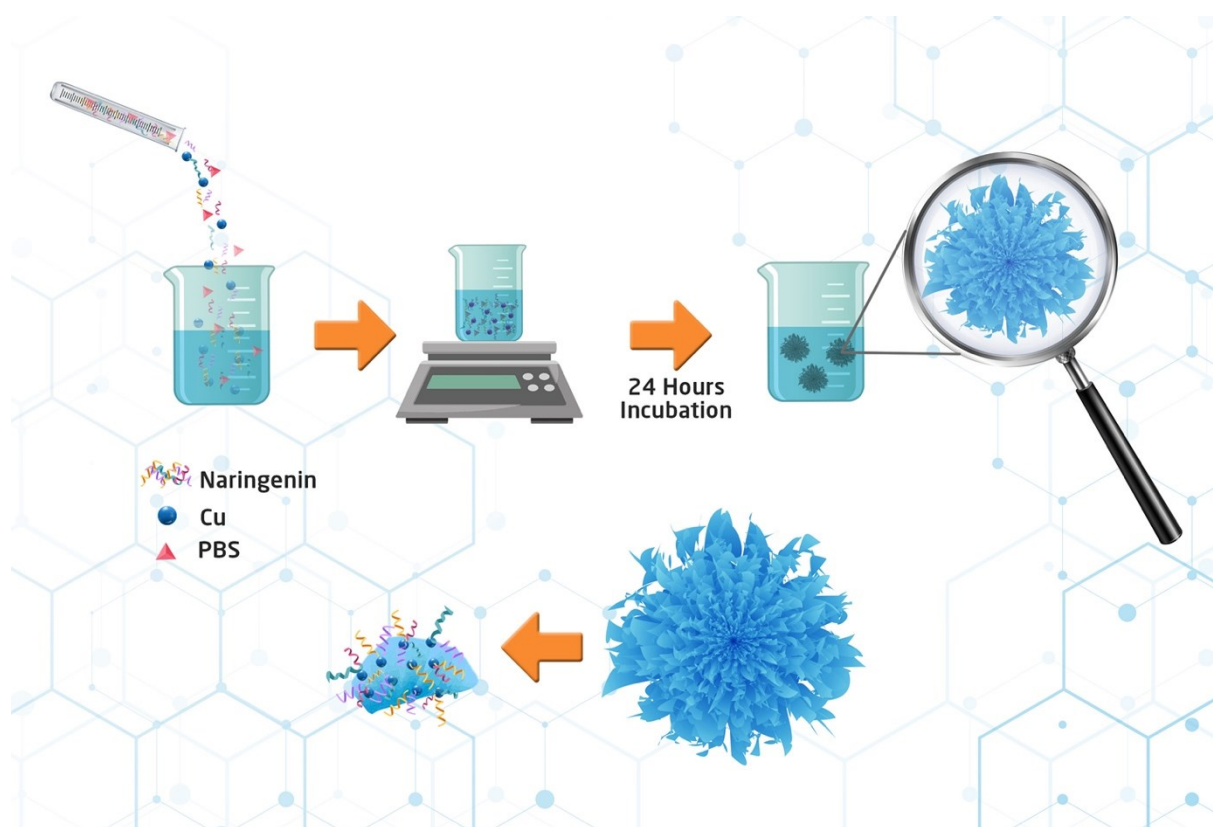


Figure 1. Naringenin-CuhNFs synthesis scheme

Synthesis of Naringenin-Cu(II) hybrid nanoflowers was synthesized using a method previously reported by Somturk et al. [18-20]. In this method, first 333 microliters of copper sulfate solution was added into 50 mL of PBS buffer. Then, Naringenin was added to the medium at a certain concentration. It is then centrifuged at 10,000 rpm for 25 minutes and left to dry. Naringenin-CuhNFs synthesis scheme is given in Figure 1.

Synthesis of Naringenin-ZnhNFs

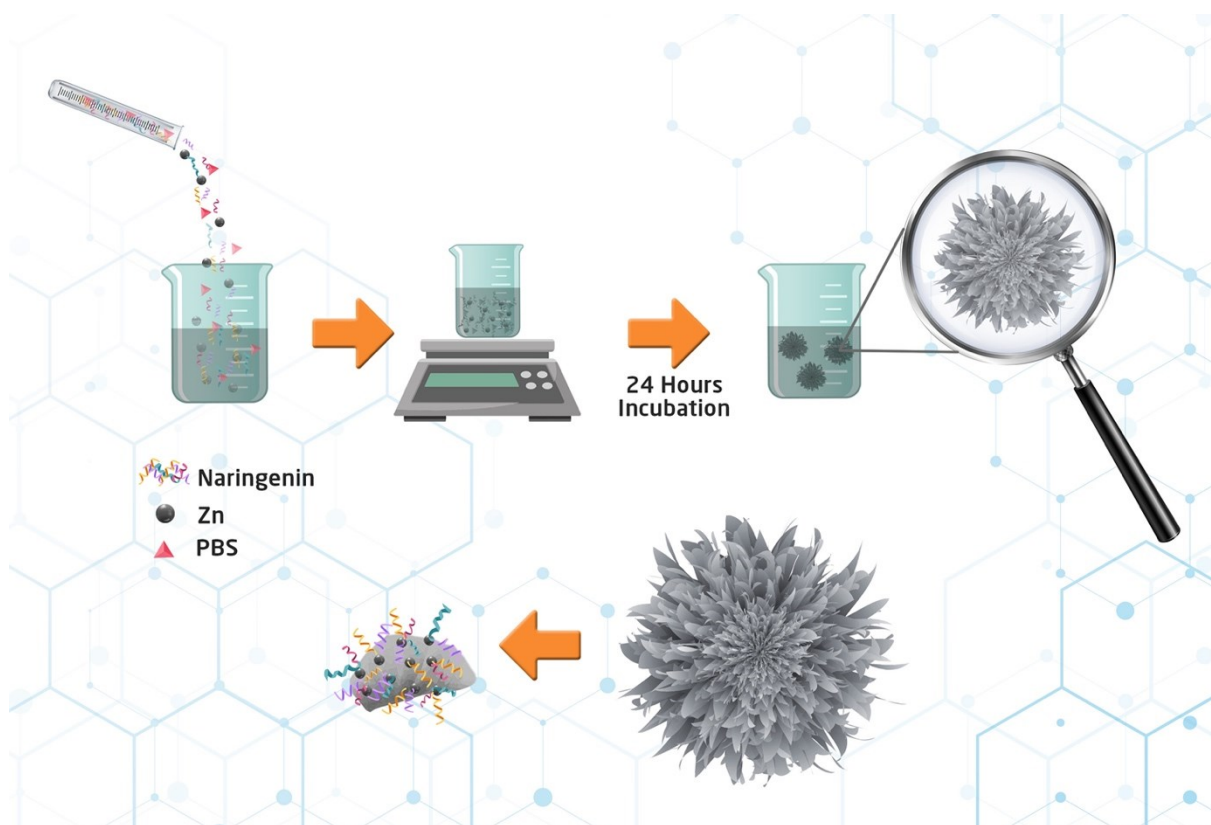


Figure 2. Naringenin-ZnhNFs synthesis scheme

Synthesis of Naringenin-Zn(II) hybrid nanoflowers was synthesized according to a method previously reported by Somturk et al. [21]. In this method, 1.6 mL of zinc acetate solution is added into 20 mL of phosphate buffer saline and then naringenin is added to the medium at a certain concentration. It is then centrifuged at 10,000 rpm for 25 minutes and left to dry. Naringenin-ZnhNFs synthesis scheme is given in Figure 2.

Characterization of Naringenin-CuhNFs and Naringenin-ZnhNFs

The morphologies of the hNFs were determined using the SEM device (FESEM, Zeiss GeminiSEM 500). Additionally, the metal ions contained in the hybrid nanoflowers were illuminated with EDX. While the crystal structures were determined using XRD, the chemical structure of the hNFs was determined by FTIR.

Cytotoxicity assessment (MTT assay)

The anticancer activity of Naringenin, Naringenin-CuhNFs and Naringenin-ZnhNFs were determined using the MCF7 (breast cancer) cell line and the MTT method. MCF7 cells were incubated in Dulbecco's Modified Eagle's Medium (DMEM)/ High Glucose supplemented with 10% fetal bovine serum and 1% penicillin-streptomycin in an atmosphere of 5% CO₂ at 37 °C. For cell culture analysis, stock solutions of Naringenin, Naringenin-CuhNFs and Naringenin-ZnhNFs were prepared and applied at 7 dilutions to cell lines grown in 96-well plates. It was then incubated for 24 hours. MTT([3-(4,5-dimethylthiazol-2-yl)-2,5 diphenyltrazolium bromide]) test was applied to reveal the possible cytotoxic effects of synthesized hybrid nanoflowers and to determine the concentrations that can be used in genotoxicity studies. For this purpose, MCF-7 cell was seeded at a density of 5000 cells/well and incubated overnight. Concentrations used in the MTT test were gradually reduced starting from the highest concentration. In this context, Naringenin, Naringenin-CuhNFs and Naringenin-ZnhNFs in the concentration range of 7.875-500 µg/mL were added to the culture medium. It was then subjected to incubation and after the staining process was performed, absorbance was read at 572 nm in a microplate reader (FilterMax F5, Molecular Devices, USA).

3. Results and discussion

SEM analysis

The morphologies of hNFs synthesized at pH 7.4 at +4 °C were determined by FESEM. As seen from the SEM images, the structures were confirmed to be flower-like (Figure 3). As the metal ion content changed, there was a visible difference in nanoflower formation. It was observed that the leaves were lighter in morphology when synthesized with Cu metal ion, and the formation of spiny leaves was observed when synthesized with Zn metal ion.

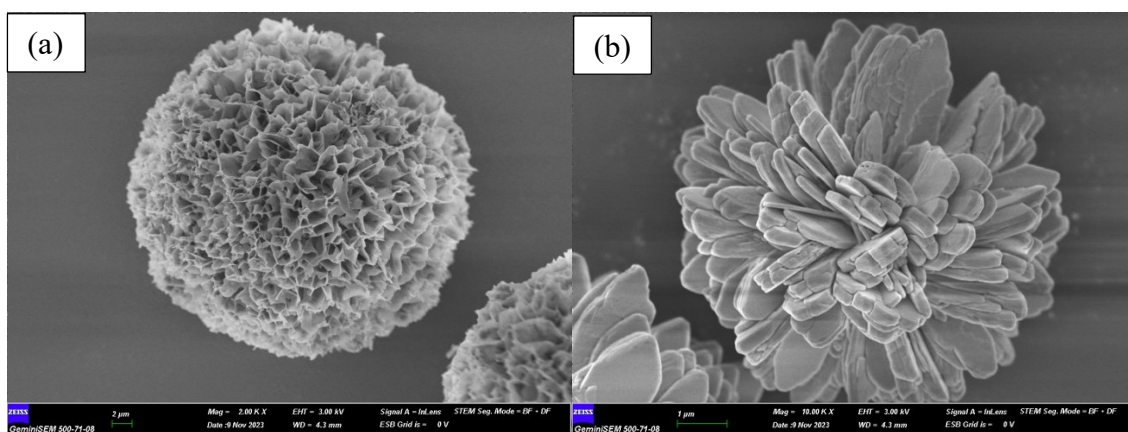


Figure 3. SEM images of Naringenin hybrid nanoflowers a) naringenin-Cu(II) hybrid nanoflower (2.00KX), b) naringenin-Zn(II) hybrid nanoflower (10.00 KX)

EDX Analysis

EDX analysis was performed to elucidate the metal content in hybrid nanoflowers. The EDX spectrum of synthesized hNFs is given in Figures 4-5. The elements Cu, Zn, O and P found in the spectrum come from the $\text{Cu}_3(\text{PO}_4)_2 \cdot 3\text{H}_2\text{O}$ and $\text{Zn}_3(\text{PO}_4)_2 \cdot 4\text{H}_2\text{O}$ nanocrystalline.

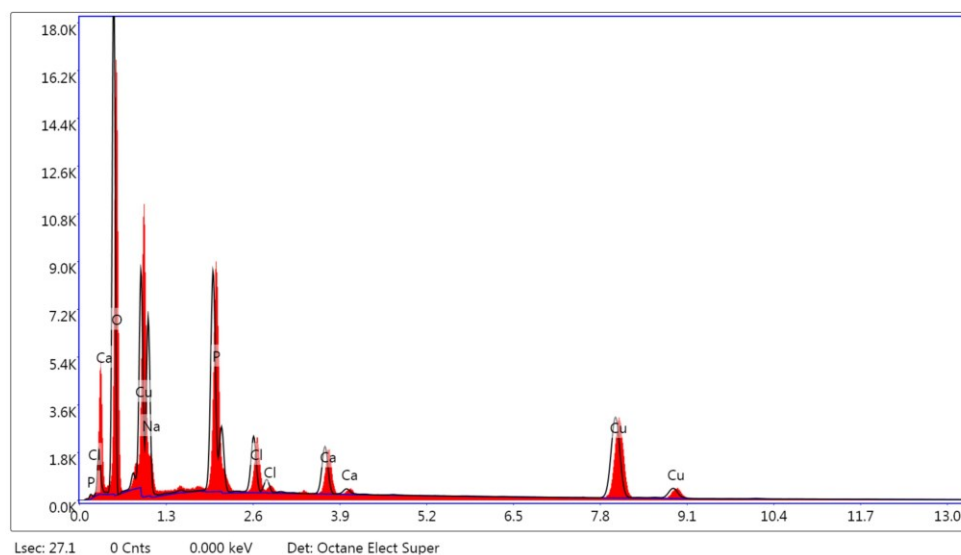


Figure 4. EDX analysis of Naringenin-CuhNFs

Table 1. Weight and atomic percentage of Naringenin-CuhNFs

Element	Weight %	Atomic %	Net Int.
O K	36.73	56.58	4173.98
NaK	17.81	19.09	1534.62
PK	11.9	9.47	2631.34
ClK	3.13	2.18	708.69
CaK	3.9	2.4	739.25
CuK	26.53	10.29	1840.83

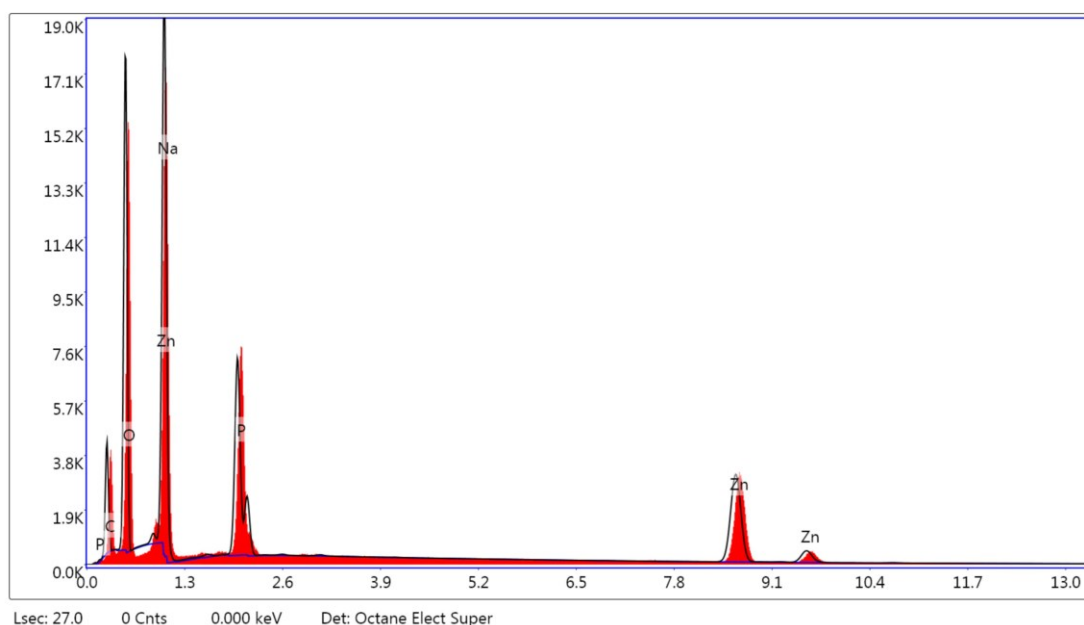


Figure 5. EDX analysis of Naringenin-ZnhNFs

Table 2. Weight and atomic percentage of Naringenin-ZnhNFs

Element	Weight %	Atomic %	Net Int.
C K	19.16	32.29	721.69
O K	27.61	34.93	3812.58
NaK	24.56	21.63	4644.73
P K	6.62	4.33	2149.98
ZnK	22.05	6.83	1899.62

Elemental mapping

Base mapping of Naringenin-CuhNFs and Naringenin-ZnhNFs were carried out. The homogeneous distribution of the metals was equal as seen in Figures 6-7.

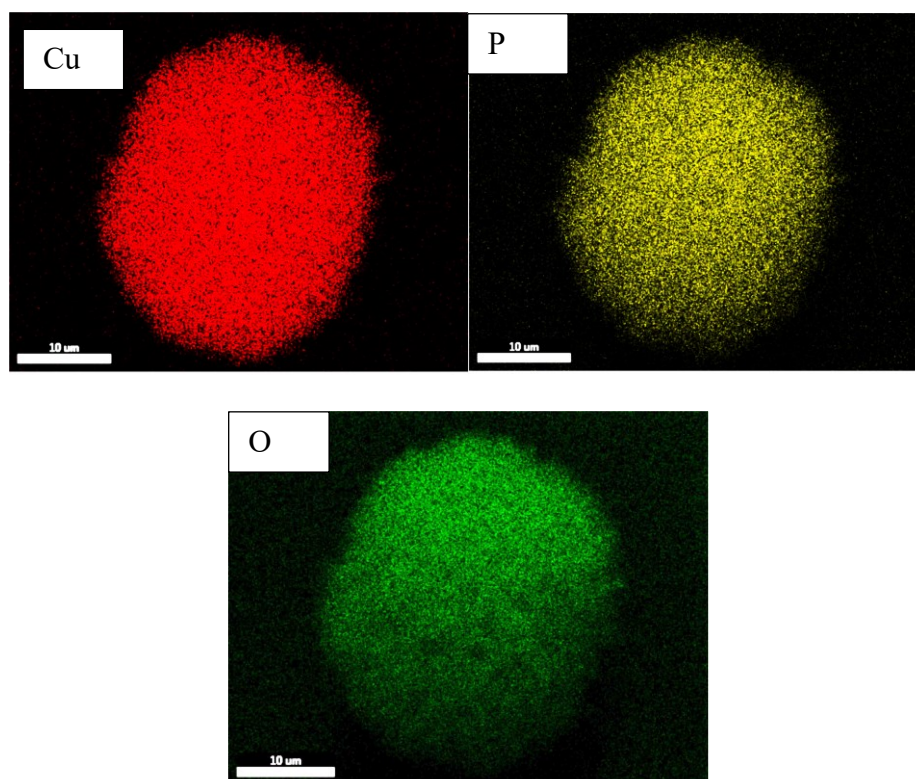


Figure 6. Elemental mapping (Cu,P, O) of Naringenin-Cu hNFs.

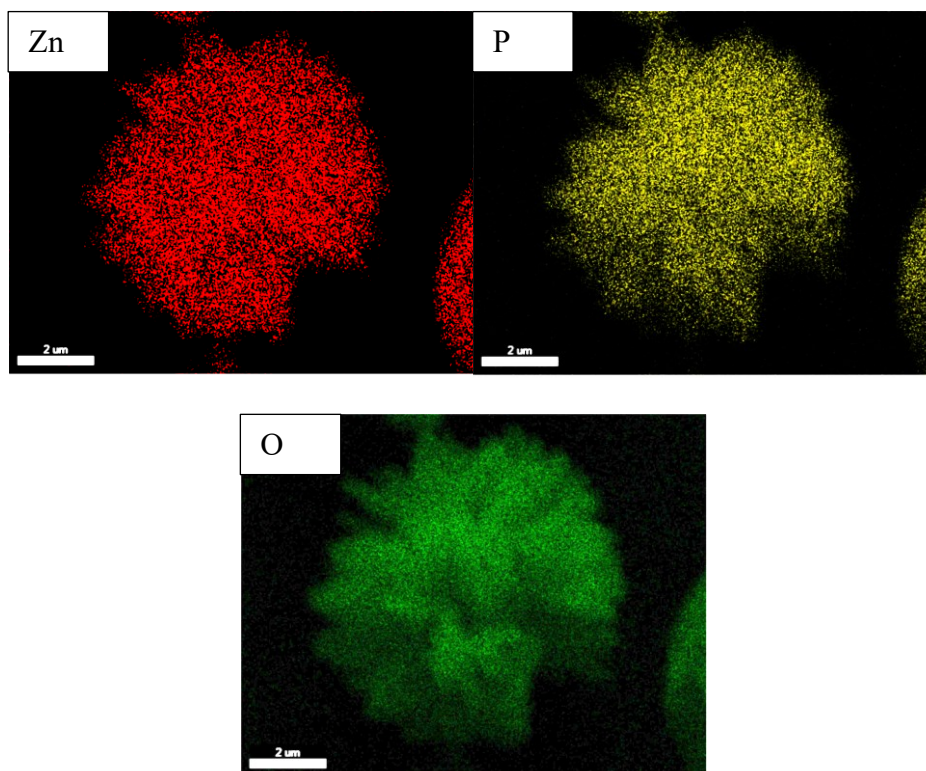
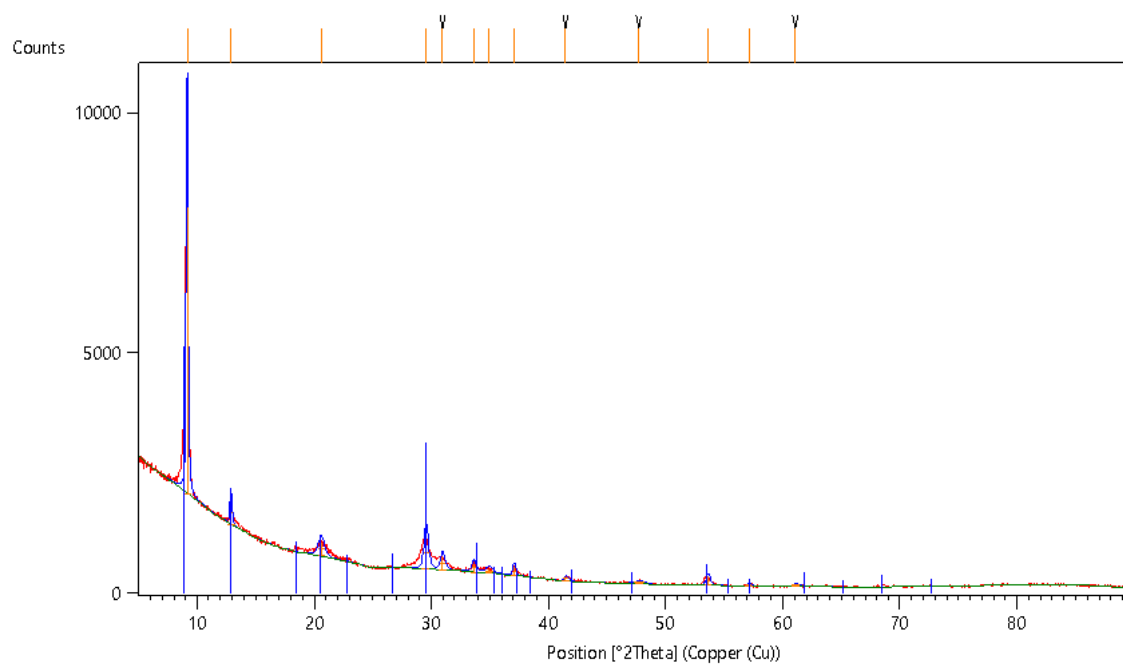


Figure 7. Elemental mapping (Zn, P, O) of Naringenin-Zn hNFs.

XRD analysis

XRD analysis was carried out to determine the crystal structure of hNFs. (Figure 8). The peaks for hNFs as follows: for Naringenin-CuhNFs, XRD: 9.10° , 12.96° , 18.79° , 20.87° , 27.38° , 29.48° , 30.64° , 31.74° , 33.71° , 37.21° , 41.59° , 45.48° , 47.74° , 53.46° , 56.48° , 61.10° , 63.57° , 66.22° , 68.19° , 71.42° , 75.26° , 79.06° , 83.95° in Fig. 8(a) in comparison with JCPDS (00-022-0548), and for Naringenin-ZnhNFs, XRD: 9.68° , 16.83° , 17.54° , 18.35° , 19.45° , 20.21° , 22.21° , 22.99° , 24.55° , 25.83° , 26.36° , 27.46° , 28.67° , 31.48° , 33.95° , 34.45° , 35.79° , 37.18° , 38.49° , 39.73° , 41.20° , 41.99° , 43.12° , 45.47° , 46.92° , 50.07° , 52.99° , 54.23° , 55.06° , 56.37° , 57.87° , 59.11° , 60.60° , 61.34° , 66.12° , 69.35° , 71.42° , 75.07° , 77.07° , 82.11° in Figure 8(b) in comparison with JCPDS (01-076-0896)

(a)



(b)

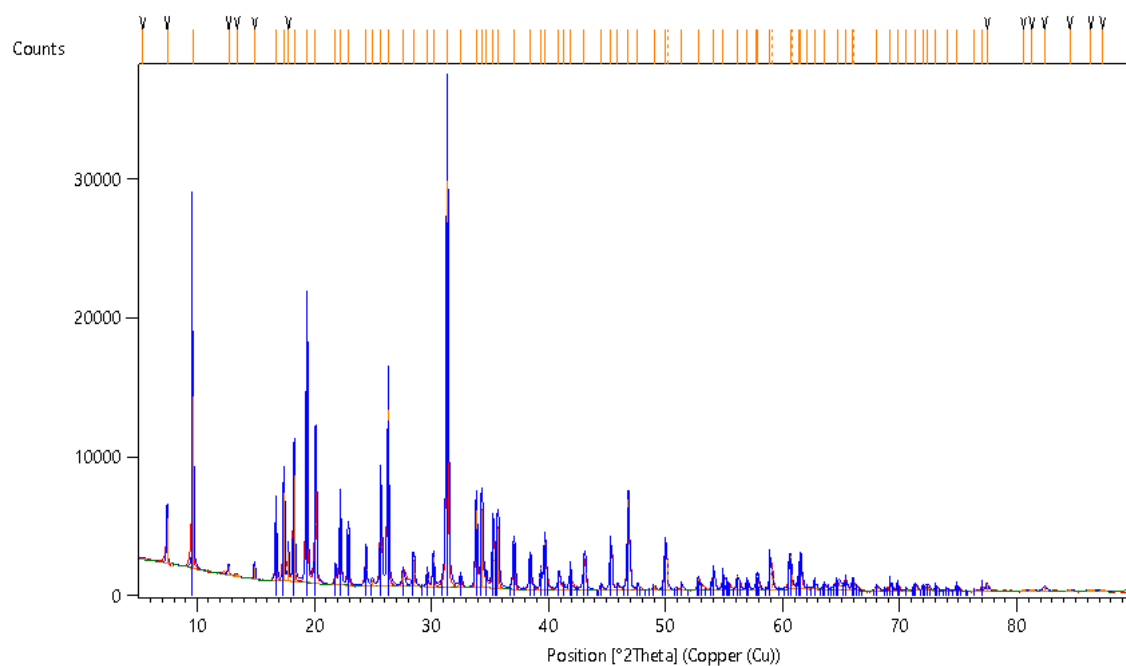


Figure 8. XRD analysis of Naringenin-CuhNFs (red line). This analysis complies with the JCPDS (00-022-0548) standard (blue line), b) XRD analysis of Naringenin-ZnhNFs (red line). This analysis complies with the JCPDS (01-076-0896) standard (blue line)

FTIR analysis

As seen in Figure 9, the peaks of hybrid nano flowers are as follows: For Naringenin- CuhNFs, FT-IR (cm^{-1}): 3592 (N-H and O-H stretching), 3311 (Ar-H and C-H stretching), 2939 (C-H, stretching), 2018, 1674, 1556, 1176 (P=O), 1088, 975 (P-O), 645, 568(O=P=O) . For Naringenin-ZnhNFs, FT-IR (cm^{-1}): 3758 (N-H and O-H stretching), 2968 (Ar-H, stretching), 2653 (Ar-H, stretching), 2346, 2043 (C-H, stretching), 1548, 1335, 1139, (P=O), 993 (P=O), 930 (P-O), 648, 587 (O=P=O).

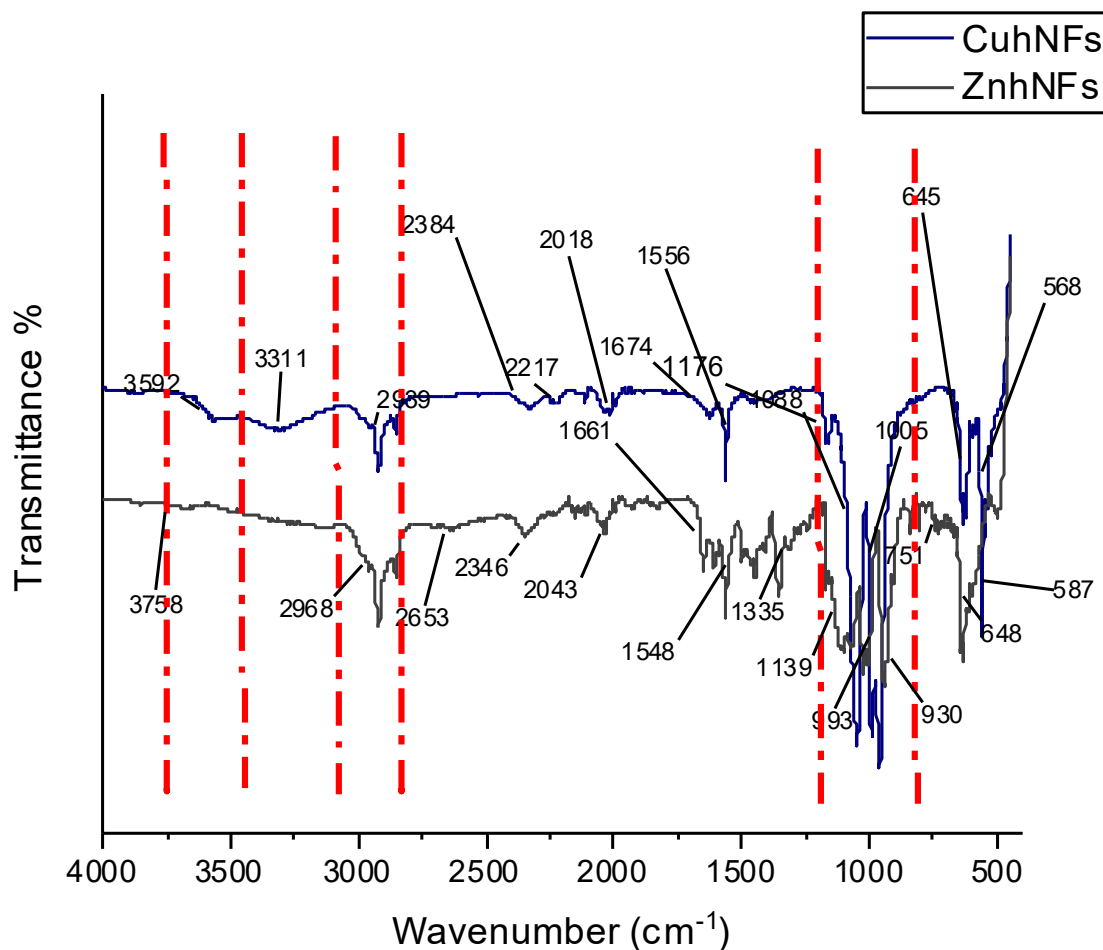


Figure 9. FT-IR spectrum of Naringenin-CuhNFs, Naringenin-ZnhNFs

Cytotoxicity assessment

The cytotoxic effect of Naringenin, Naringenin-CuhNFs and Naringenin-ZnhNFs on the MCF7 cell line is given in Figure 10. As seen in Figure 10, it was observed that Naringenin had a very good anticancer activity on the MCF7 cell line when converted into hybrid nanoflower form. As can be seen, Naringenin-ZnhNFs killed MCF7 cells at a rate of approximately 76%, while Naringenin CuhNFs caused cell death at a rate of 68%. Naringenin caused 45% cell death. As can be concluded from the results, when Naringenin was converted into hybrid nanoflower form, its effectiveness in the MCF7 cell line was greatly increased. CuhNFs synthesized according to ISO 10993-5 criteria were classified as non-cytotoxic

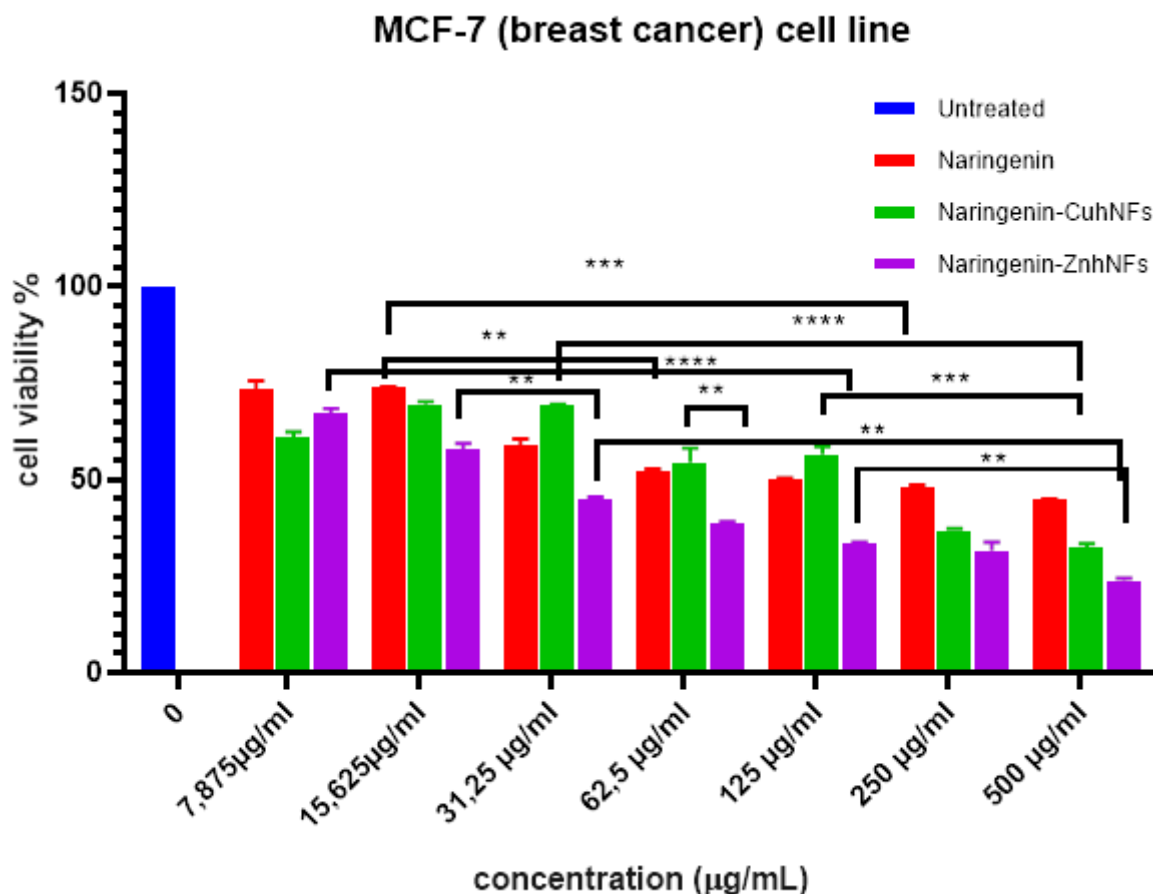


Figure 10. Cytotoxicity of CuhNFs, ZnhNFs and naringenin on MCF7 cells lines. Data were presented as mean \pm SD. ** $p < 0.01$, *** $p < 0.001$, **** $p < 0.0001$

Many studies have been conducted on plants and similar hybrid nanoflowers in the literature. Bor et al. [22] synthesized Cu and Zn hybrid nanoflowers using the *Persea americana Mill.* leaves extract. They applied the cytotoxic effects of the metal nanoflowers they synthesized to the L929-mouse fibroblast cell line. They found that the anticancer activity of hybrid nanoflowers synthesized with Cu was higher than that of plant extract. Somturk et al. [1] synthesized hybrid nanoflowers using *Tribulus Terrestris L* extract and Cu, Co and Zn metal ions. The anticancer activities of these synthesized hybrid nanoflowers were applied to the A549 cell line. They observed that when the plant extract was converted into a hybrid nanoflower, its anticancer activity was greatly increased. They concluded that the effectiveness of hybrid nanoflowers especially synthesized with Co metal ion was better than others.

4. Conclusion

As a result, nanoflower synthesis was carried out using Naringenin as the organic part and Cu (II) and Zn (II) metal ions as the inorganic part. The structures of the synthesized nanoflowers were elucidated using SEM, EDX, FTIR, XRD and elemental mapping. Next, cytotoxic effects were evaluated using MCF7 cells. When the CuhNFs, ZnhNFs and Naringenin were applied to the MCF7 cell line, an increase in cell death occurred depending on the concentration. Additionally, an increase in cell death occurred when naringenin was converted into its hybrid

nanoflower form. In particular, it was observed that hybrid nanoflowers synthesized with Zn metal ion killed breast cancer cells by 76%. It was observed that hybrid nanoflowers synthesized with Cu metal ion caused 68% cell death. This means that it can be said that Zn metal ion is more effective than naringenin and the hybrid nanoflower synthesized with Cu metal ion.

Author Contributions

B.S.Y. performed all experiments. B.S.Y. conceived the original idea and designed the project. B.S.Y. wrote the manuscript.

Acknowledgements

The author would like to thank Erciyes University, Drug Application and Research Center (ERFARMA) for laboratory and device support.

References

- [1] Somturk Yilmaz, B., Bekci, H., Altiparmak, A., Uysal, S., Şenkardeş, İ., Zengin, G. 2024. Determination of anticancer activity and biosynthesis of Cu, Zn, and Co hybrid nanoflowers with *Tribulus terrestris* L. extract. *Process Biochemistry*. 138: 14-22
- [2] Uras, I.S, Karşlı, B., Konuklugil, B., Ocsoy, I., Demirbas, A. 2023. Organic–Inorganic Nanocomposites of *Aspergillus terreus* Extract and Its Compounds with Antimicrobial Properties. *Sustainability* 2023, 15(5), 4638; <https://doi.org/10.3390/su15054638>
- [3] Dadi, S., Celik, C., Ocsoy, I., 2020. Gallic acid nanoflower immobilized membrane with peroxidase-like activity for m-cresol detection. Gallic acid nanoflower immobilized membrane with peroxidase-like activity for m-cresol detection. *Scientific Reports*. 10:16765
- [4] Yoshida, H., Takamura, N., Shuto, T., Ogata, K., Tokunaga, J. ve Kawai, K., 2010, The citrus flavonoids hesperetin and naringenin block the lipolytic actions of TNF- α in mouse adipocytes, *Biochemical and Biophysical Research Communications*, 394, 728-732.
- [5] Zeng, W., Jin, L., Zhang, F., Zhang, C. ve Liang, W., 2018, Naringenin as a potential immunomodulator in therapeutics, *Pharmacological Research*, 135 (2018), 122–126.
- [6] Zhang, J.J., Dong, X., Cao, Y.Y., Yuan, Y. D., Yang, Y.B., Yan, Y.Q., vd., 2020, Clinical characteristics of 140 patients infected with SARS-CoV-2 in Wuhan, China, *Allergy*, 75, 1730–41. doi: 10.1111/all. 14238.
- [7] Zhang, L., Song, L., Zhang, P., Liu, T., Zhou, L., Yang, G., Lin, R. ve Zhang, J., 2015, Solubilities of naringin and naringenin in different solvents and dissociation constants of naringenin, *Journal of Chemical & Engineering Data*, 60(3), 932-40. <https://doi.org/10.1021/je501004g>.

[8]Wang, M.J., Chao, P.D., Hou, Y.C. ve Hsiu, S.L., 2006, Pharmacokinetics and conjugation metabolism of naringin and naringenin in rats after single dose and multiple dose administrations, *Journal of Food and Drug Analysis*, 14(3), 247-253.

[9]Wang, N., Li, D., Lu, N.H., Yi, L., Huang, X.W. ve Gao, Z.H., 2010, Peroxynitrite and hemoglobinmediated nitrative/oxidative modification of human plasma protein: effects of some flavonoids, *Journal of Asian Natural Products Research*, 12(4), 257-64. <https://doi.org/10.1080/10286021003620226>.

[10]Wang, Y., Wang, S., Firempong, C.K., Zhang, H., Wang, M., Zhang, Y., Zhu, Y., Yu, J., Xu, X., 2017, Enhanced solubility and bioavailability of naringenin via liposomal nanoformulation: preparation and in vitro and in vivo evaluations, *AAPS PharmSciTech*, (2017) 18, 586–94. doi: 10.1208/s12249-016-0537-8.

[11]Wang, Z., Wang, S., Zhao, J., Yu, C., Hu, Y., Tu, Y., Yang, Z., Zheng, J., Wang, Y., Gao, Y., 2019, Naringenin ameliorates renovascular hypertensive renal damage by normalizing the balance of reninangiotensin system components in rats, *International Journal of Medical Sciences*, 16, 644– 53. doi: 10.7150/ijms.31075.

[12]Wilcox, L.J., Borradaile, N.M. ve Huff, M.W., 1999, Antiatherogenic properties of naringenin, a citrus flavonoid, *Cardiovascular Drug Reviews*, 17:160-178.

[13]Yao, L.H., Jiang, Y.M., Shi, J., Tomas-Barberan, F.A., Datta N., Singanusong, R., Chen, S. S., 2004, Flavonoids in food and their health benefits, *Plant Foods for Human Nutrition*, 59(3), 113-22. <https://doi.org/10.1007/s11130-004-0049-7>.

[14]Alam, M.A., Subhan, N., Rahman, M.M., Uddin, S.J., Reza, H.M. ve Sarker, S.D., 2014, Effect of citrus flavonoids, naringin and naringenin on metabolic syndrome and their mechanisms of action, *Advances and Nutrition*, 5(4), 404- 17. <https://doi.org/10.3945/an.113.005603>.

[15]Alberca, R.W., Teixeira, F.M.E., Beserra, D.R., de Oliveira, E.A., de Andrade, M.M.S., Pietrobon, A.J. ve Sato, M.N., 2020, Perspective: the potential effects of naringenin in COVID19, *Frontiers in Immunology*, (2020) 11, 1.

[16]Bourian, M., Runkel, M., Krisp, A., Tegtmeier, M., Freudenstein, J. ve Legrum, W., 1999, Naringenin and interindividual variability in interaction of coumarin with grapefruit juice, *Experimental and Toxicologic Pathology*, (1999) 51, 289–93. doi: 10.1016/S0940-2993(99)80008-6.

[17]Breinholt, V.M., Svendsen, G.W., Dragsted, L.O. ve Hossaini, A., 2008, The citrus-derived flavonoid naringenin exerts uterotrophic effects in female mice at human relevant doses, *Basic and Clinical Pharmacology and Toxicology*, (2008) 94, 30–6. doi: 10.1111/j.1742-7843.2004.pto_940106.x.

[18] Somturk B, Yilmaz I, Altinkaynak C, Karatepe A, Özdemir N, Ocsoy I (2016) Synthesis of urease hybrid nanoflowers and their enhanced catalytic properties. *Enzyme Microb Technol* 86:134–142. doi:10.1016/j.enzmictec.2015.09.005

[19] Somturk B, Hançer M, Öcsoy İ, Ozdemir N (2015). Synthesis of copper ion incorporated horseradish peroxidase based hybrid nanoflowers for enhanced catalytic activity and stability. *Dalton Trans.*, 44(31):13845-13852. doi:10.1039/c5dt01250c

[20] Noma, S.A., Somturk Yilmaz, B., Ulu, A., Ozdemir, N., Ateş, B. Development of l-asparaginase@hybrid Nanoflowers (ASNase@HNFs) Reactor System with Enhanced Enzymatic Reusability and Stability *Catalysis Letters*. 2021,151:1191-1201 DOI:10.1007/s10562-020-03362-1

[21] Somturk B, Dayan S, Ozdemir N, Kalaycıoğlu Özpozan N (2022), Catalytic performance improvement with metal ion changes for efficient, stable, and reusable superoxide dismutase–metal phosphates hybrid nanoflowers, *Chem Pap* 76:4245–4260. <https://doi.org/10.1007/s11696-022-02179-z>

[22] E. Bor, U. Koca Caliskan, C. Anlas, G.D. Durbilmez, T. Bakirel, N. Ozdemir, Synthesis of *Persea americana* extract based hybrid nanoflowers as a new strategy to enhance hyaluronidase and gelatinase inhibitory activity and the evaluation of their toxicity potential, *Inorg. Nano-Met.* (2022) 1–3, <https://doi.org/10.1080/24701556.2022.2072342>.

Investigation of the Effect of Temperature on the Biofuel Performance of Hydrochar Obtained from Kidney Bean Shell

Zeynep YILDIZ UZUN^{1*}

¹Sinop University, Boyabat Vocational School, Department of Chemistry and Chemical Processing Technologies, Sinop, Turkey

Received: 07/03/2024, Revised: 15/06/2024, Accepted: 18/07/2024, Published: 31/08/2024

Abstract

In this study, hydrochar products were obtained from kidney bean shell biomass at different temperatures using the hydrothermal carbonization method. Hydrochar products were produced at three different temperatures (200, 220 and 240 °C) and a holding time of 90 minutes. Biomass/water ratio was taken as 1:10. Analysis techniques such as Thermogravimetric analysis, Ultimate analysis and Fourier Transform Infrared Spectroscopy were used in the characterization of raw materials and hydrochar products. In addition, the fuel properties (high heating value, energy yield and energy densification ratio) of raw KBS and hydrochar products were also investigated. As the hydrothermal carbonization temperature increases, the high heating value of hydrochar products increases. Among hydrochar products, the highest high heating value belongs to the product obtained at 240 °C. The combustion behavior of raw and hydrochar a product was examined using the thermogravimetric analysis method and combustion parameters (T_i , T_b and T_m) were determined. As a result, this study has shown that the hydrochar product produced from kidney bean shell by hydrothermal carbonization method can be used as a biofuel material.

Keywords: Hydrothermal carbonization, hydrochar, biofuel, kidney bean shell

Barbunya Kabuğundan Elde Edilen Hydrochar Ürünlerinin Biyoyakıt Performansına Sıcaklığın Etkisinin Araştırılması

Öz

Bu çalışmada, hidrotermal karbonizasyon yöntemi kullanılarak barbunya fasulyesi kabuğu biyokütlesinden farklı sıcaklıklarda hydrochar ürünleri elde edilmiştir. Hydrochar ürünleri üç farklı sıcaklıkta (200, 220 ve 240 °C) ve 90 dakika bekleme süresinde üretilmiştir. Biyokütle/su oranı 1:10 olarak alınmıştır. Ham madde ve hydrochar ürünlerinin karakterizasyonu için Termogravimetrik analiz, Elementel analiz ve Fourier Dönüşümü Kızılötesi Spektroskopisi gibi analiz teknikleri kullanılmıştır. Ham madde ve farklı sıcaklıklarda elde edilen hydrochar ürünlerinin yakıt özellikleri de (yüksek ısıl değeri, enerji verimi ve enerji yoğunlaşma oranı) araştırılmıştır. Hidrotermal karbonizasyon sıcaklığı arttıkça hydrochar ürünlerinin de ısıl değerleri artmıştır. En yüksek ısıl değere (18,19 MJ/kg) sahip hydrochar ürünü 240 °C sıcaklığında elde edilmiştir. Termogravimetrik analiz yöntemi kullanılarak ham madde ve hydrochar ürünlerinin yanma davranışları incelenmiş ve yanma parametreleri (T_i , T_b ve T_m) belirlenmiştir. Sonuçlar barbunya fasulyesi kabuğundan hidrotermal karbonizasyon yöntemiyle üretilen hydrochar ürününün biyoyakıt malzemesi olarak kullanılabilceğini göstermiştir.

Anahtar Kelimeler: Hidrotermal karbonizasyon, hydrochar, biyoyakıt, barbunya fasulyesi kabuğu

1. Introduction

Due to the increase in energy demand and the rapid depletion of fossil fuels, the demand for new energy sources that are sustainable and more environmentally friendly is increasing. Biomass energy is a powerful energy source and is the fourth largest energy source after coal, oil and natural gas [1]. In addition, biomass is considered neutral (in terms of carbon dioxide) and is known for its low greenhouse gas emissions [2]. For this reason, research on the use of biomass as an alternative energy source has been increasing rapidly in recent years. Particularly lignocellulose biomass is known as a sustainable energy source due to its high efficiency [3]. Biological, thermochemical and physical techniques are used to convert biomass into fuels. Thermochemical processes can be classified as combustion, gasification, pyrolysis and hydrothermal carbonization [2]. Hydrothermal carbonization method, which is among the thermochemical processes, has attracted great attention in recent years [4]. Hydrothermal carbonization (HTC) is a cheap and effective method that increases the high heating value and energy density of biomass [5]. In HTC, biomass is heated in a closed system at high temperature and under self-generated pressure. Depending on the chemical properties of the raw material, different chemical reactions such as dissolution, dehydration/decarboxylation, polymerization and condensation may occur [6]. In addition, hydrothermal carbonization (HTC) occurs with water at moderate temperatures ranging from 150-300 °C [7]. Many studies have been conducted in the literature on the production of biofuel from biomass using the hydrothermal carbonization method. For example, it has been reported that the high heating values of hydrochar products obtained from turfgrass at different temperatures (180-220 °C) are in the range of 17.67–20.43 MJ/kg [9]. Hydrochar products were obtained from macadamia nut shell by hydrothermal carbonization method at different temperatures (170, 200 and 230 °C) and different biomass/water ratios. [8]. It has been reported that the high heating values of hydrochar products vary between 22.22–27.29 MJ/kg. In another study, the high heating values of hydrochar products produced from wheat straw biomass at different temperatures (180, 220 and 260 °C) and for different times (10, 20 and 30 min) were measured. It has been reported that hydrochar with the highest high heating value was obtained in 30 minutes and at 260 °C [10]. In this study, hydrochar products were produced from kidney bean shells (KBS) at different temperatures (200, 220 and 240 °C) using the Hydrothermal carbonization (HTC) method. The effect of temperature on the fuel properties of hydrochar products was investigated. For this, first the raw material was characterized using different techniques (Thermogravimetric analysis, Ultimate Analysis, Fourier Transform Infrared Spectroscopy). Then, the fuel performance (mass yield, energy yield, and High heating value) of the obtained hydrochar products was investigated. The hydrochar product with the highest high heating value was obtained at 240 °C and the high heating value was calculated as 18.19 MJ/kg. According to the results, the fuel properties of KBS were improved with HTC and the resulting hydrochar products can be used as biofuel materials.

Studies on the investigation of fuel potentials of hydrochar samples obtained from kidney bean shells and the determination of fuel potential values are insufficient in the literature. Determining the fuel properties of hydrochar products obtained from this type of raw material adds innovation and originality to this study. In addition, considering the issues such as climate

change and global warming that have occurred in recent years, the fact that hydrochar products enable the production of more sustainable biofuels reveals another unique aspect of the study.

2. Materials and Methods

2.1 Preparation of raw materials

Raw KBS was purchased from local markets in Samsun, Turkey. Before starting the experiments, the raw materials were dried at 70 °C for 12 hours. After the KBS was dried, it was ground using a blender. The ground samples were used in experiments.

2.2 Hydrothermal carbonization

After mixing 0.5 g KBS and 5 mL deionized water, the mixture was placed in a 40 mL steel reactor. The samples were kept in the oven at different temperatures (200, 220 and 240 °C) for 90 minute. At the end of the carbonization process, the reactor was cooled and the solid product was collected and the yield was calculated. The hydrochars obtained from the KBS was labeled as HC₂₀₀, HC₂₂₀ and HC₂₄₀.

2.3 Characterization of KBS and hydrochars

Fourier Transform Infrared Spectroscopy (FT-IR), Ultimate Analysis and Thermogravimetric (TG) Analysis techniques were used for the characterization of raw KBS and hydrochars produced at different temperatures. Fourier Transform Infrared Spectrometer (Mattson 1000) device was used for FT-IR analysis. FTIR spectra of KBS and hydrochars were drawn in the wavenumber range of 650 cm⁻¹ and 4000 cm⁻¹. The % C, N, H and S amounts were measured simultaneously, and the oxygen content was calculated from the percentage difference. High heating value (HHV), energy and mass yields and energy densification ratio of raw KBS and hydrochar products were calculated using the equations given below [11,12].

$$\text{HHV} = 0.338 \times C + 1.428 \times (H - O/8) + (0.095 \times S) \quad (1)$$

$$\text{Energy densification ratio} = (\text{HHV of hydrochar}) / (\text{HHV of KBS}) \quad (2)$$

$$\text{Energy yield (\%)} = \text{Mass yield} \times \text{Energy densification} \quad (3)$$

2.4 Thermogravimetric analysis

Combustion analysis of the products was carried out in air atmosphere using a thermogravimetric analyzer (DTG-60). Approximately 10 mg of material was used in each measurement. Samples were heated from 20 °C to 800 °C at a constant heating rate of 20 °C/min. S determines the quality of combustion. Within the scope of this study, the combustibility index S was determined using the following equation [21].

$$S = (R_{\max} \times R_{\text{mean}})/(T_i^2 \times T_b) \quad (4)$$

where T_i is the ignition temperature, T_b is the burnout temperature, R_{\max} and R_{mean} are maximum and mean decomposition rate.

3. Results and Discussion

3.1 Characterization of KBS and hydrochars

Ultimate analysis results of raw KBS and hydrochar product are shown in Table 1. In the characterization of raw biomass, ash determination was first made. In the literature, the ash content is between 0.2-22.5% [13]. As can be seen from the results, it can be said that the ash amount of KBS is compatible with the literature. Ultimate analysis and HHV analysis results of some biomass wastes have been reported in the literature. According to the results of ultimate analysis, Nitrogen (N) and Sulfur (S) values of biomasses vary between 0-8.14% and 0-0.86%, respectively [14]. Sulfur (S) and Nitrogen (N) values in biomass are expected to be low in order not to create greenhouse gases. As can be seen from the results, there is no sulfur (S) in the structure of KBS. The amount of Nitrogen (N) is compatible with the literature. The HHV of KBS was calculated as 13.05 MJ/kg. In addition, the fuel properties of the hydrochars (especially the HHV value) are calculated. When Table 1 is examined, the elemental analysis results of KBS have changed significantly after the HTC process. With the increase of HTC temperature, there was a significant increase in the %C content. The hydrochar product with the highest carbon content was obtained at 240 °C temperatures. The %C value of raw KBS and HC₂₄₀ samples was measured as 41.26% and 51.69%. Increasing carbon value allows hydrochar products to increase their high heating value and be used as an alternative fuel material [19, 20]. HHV is a crucial parameter of solid biofuels, such as biomass and its derived hydrochars, as it embodies the total attainable energy in the biomass [22]. As a result, the product with the highest HHV among hydrochar products is HC₂₄₀. The mass yield values of HC₂₀₀, HC₂₂₀ and HC₂₄₀ hydrochar products were determined as 75.7%, 71.6% and 68.4%, respectively. As seen in Table 1, energy yield increased significantly with increasing temperature and reached 95.08% for HC₂₄₀.

Hydrothermal carbonization method and process conditions (temperature, time, biomass water ratio etc.) are very important to obtain hydrochar products with high energy value. In particular, temperature is a critical factor in determining the reaction intensity and has a decisive effect on the transformation pathways of the raw material [23].

Studies in the literature show that as temperature increases, yield decreases and high heating value increases [24]. As the temperature increases, the Hydrogen (H) and Oxygen (O) content

in the hydrochar structure decreases, while the Carbon (C) content increases. A high carbon value causes an increase in high heating value (Pauline, 2020). For example, it has been reported in the literature that the high heating value of hydrochar products obtained from tobacco stem biomass at 260 °C reaches from 26.1 MJ/kg to 27.2 MJ/kg [25]. In addition, the HHV results of hydrochar samples obtained from lignocellulosic biomass such as walnut shell, tea stalk, olive pomace were reported as 21.46, 22.53, 25.56 MJ/kg, respectively [26].

Table 1. Characterization of KBS and hydrochars

Materials	Ultimate Analiz (%)					Ash (%)	HHV (MJ/kg)	Energy densification	Energy yield (%)
	C	H	N	S	O				
KBS	41.26	5.91	0.52	-	52.31	5.97	13.05	-	-
HC ₂₀₀	45.51	5.87	0.39	-	48.23	2.78	15.16	1.16	87.81
HC ₂₂₀	48.82	5.74	0.63	-	44.81	5.23	16.70	1.28	91.65
HC ₂₄₀	51.69	5.76	0.50	-	42.05	3.42	18.19	1.39	95.08

FT-IR spectra of KBS and hydrochar products were examined and presented in Figure 1. The vibration peak seen at 3362 cm⁻¹ in the raw KBS is the O-H stretching of water. However, as the HTC temperature increases, the O-H bond in the structure of hydrochar products gradually weakens. This is due to dehydration and decarboxylation reactions during the HTC process [17]. The peaks observed around 2960-2872 cm⁻¹ in raw and hydrochar samples are C-H stretching vibrations arising from aliphatic hydrocarbons. C=O asymmetric stretching vibrations are seen at approximately 1650 cm⁻¹ in all products. This peak may belong to compounds derived from ketones, aldehydes, esters and carboxylic acids, for example [17]. The peaks seen in the spectra at approximately 1000-1500 cm⁻¹ may belong to C-O, C-C stretching vibrations [15,18].

Hydrochar is a low-cost adsorbent used to adsorb pollutants in water due to the rich functional group structure on its surface [28]. It has been reported in the literature that hydrochar products obtained from different biomass are used in adsorption applications. For example, it has been reported in the literature that hydrochar products obtained by HTC are used as adsorbents in the removal of heavy metals and antibiotics after modification [27]. As another example, it has been reported in the literature that hydrochar products obtained from oak sawdust biomass by hydrothermal carbonization method at different temperatures (175, 200, 225 °C) and times (12, 24, 48, 60, 72 h) contain oxygen-rich functional groups [16].

According to literature results; It can be said that the hydrochar samples obtained in this study can be used in adsorption studies because they contain oxygen-rich functional groups (C=O, C-O).

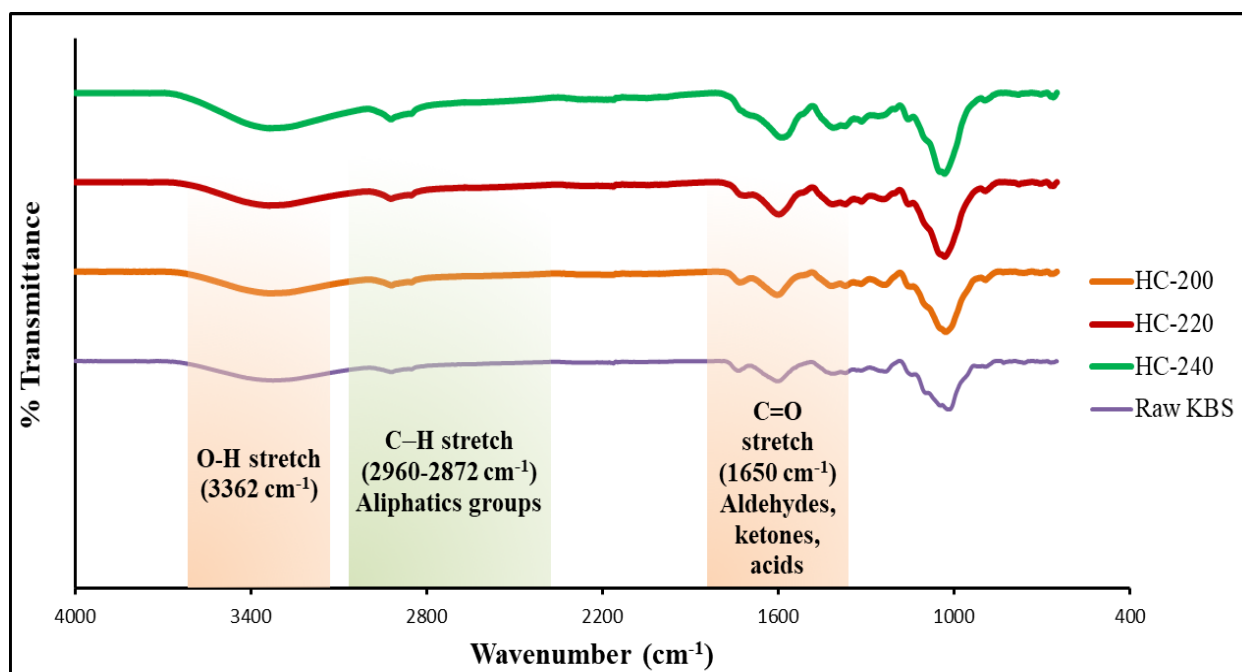
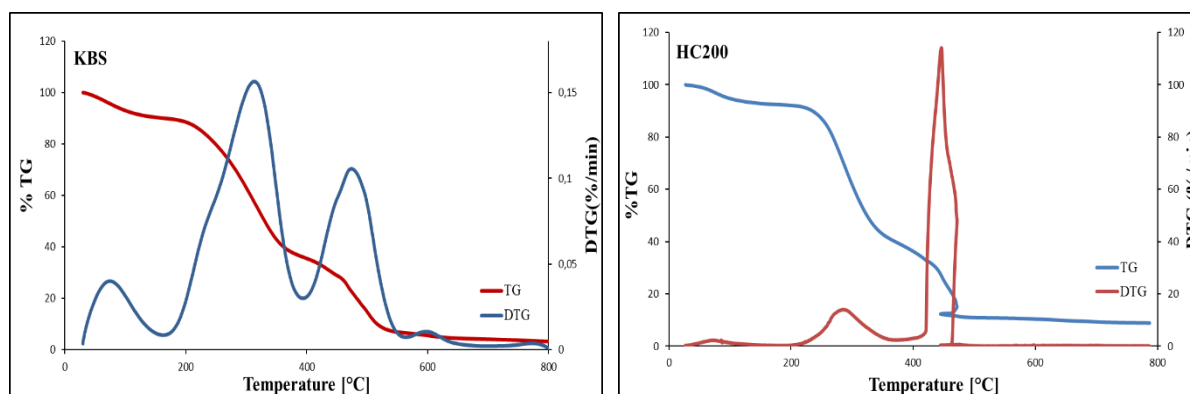


Figure 1. FT-IR spectra of raw KBS and hydrochars

3.2 Thermogravimetric analysis and combustion characteristics

TG and DTG curves of the thermal decomposition of raw KBS and hydrochars are shown in Figure 2. According to the DTG curve; the decomposition of the crude KBS product occurs in 3 steps. The first decomposition is in the temperature range of 31-152 °C and volatile components are separated from the structure. This step is a decomposition that represents moisture loss in KBS. (It appears as a small peak on the DTG curve). The second decomposition is in the temperature range of 163-384 °C and the weight loss is 53.62%. The final decomposition is in the temperature range of 392-793 °C and the weight loss is 32.78%. Similar thermogravimetric curves were observed in studies reported in the literature. For example; according to the thermogravimetric analysis results of KBS biomass, decomposition occurred in three steps [1].



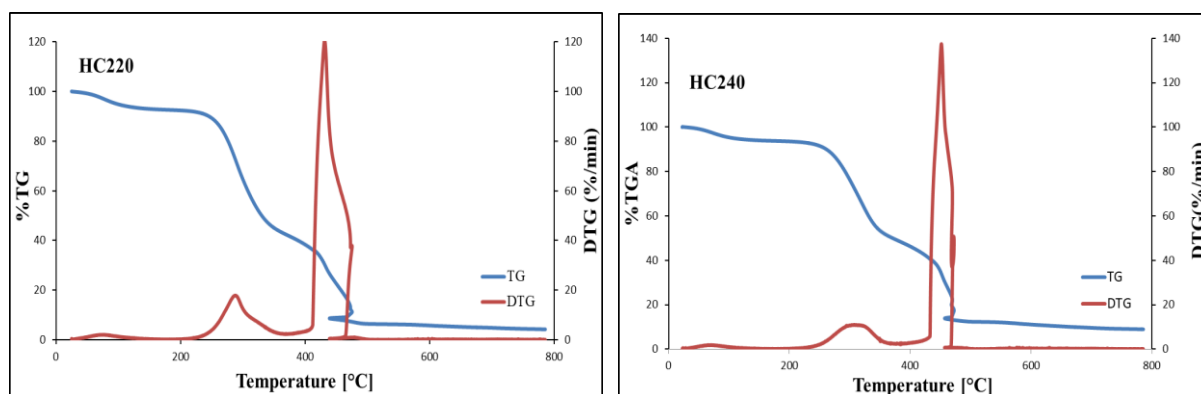


Figure 2. TG-DTG curves of KBS and hydrochars

When the DTG curves of the hydrochar samples were examined, two stages were observed for thermal decomposition in the temperature range of 25-800 °C under the air atmosphere. In the first stage, all hydrochar samples decompose at approximately 220-350 °C. In the second stage, the degradation of the samples is in the temperature range of 400-450 °C. At this stage, a weight loss of 66.91, 80.57 and 71.49% is observed in HC₂₀₀, HC₂₂₀ and HC₂₄₀ samples, respectively. Compared to HCs, raw KBS has the highest weight loss and shows less stability.

Table 2. Combustion parameters of KBS and hydrochars

Sample	T _i (°C)	T _b (°C)	T _m (°C)	-ΔTG _{max} (%/min)	-ΔTG _{mean} (%/min)	S (% ² /°C ³ .min ²)
KBS	163	793	305	0.154	0.03	2.19×10 ⁻¹⁰
HC ₂₀₀	231	478	444	112.19	2.35	1.03×10 ⁻⁵
HC ₂₂₀	232	492	431	120.63	2.47	1.12×10 ⁻⁵
HC ₂₄₀	243	484	451	137.45	2.34	1.13×10 ⁻⁵

Combustion parameters (T_i, T_b, and T_m) of KBS and hydrochar products were estimated using TG and DTG curves. A high T_i of the solid fuel can avoid the potential fire hazard which is favor for the safe handling, storing and transportation [20]. The combustion parameters of KBS and hydrochars are presented in Table 2. The T_i values of KBS, HC₂₀₀, HC₂₂₀ and HC₂₄₀ products are 163, 231, 232, and 243 °C, respectively. As can be seen, the T_i value of the HC₂₄₀ product is higher than raw biomass and other hydrochar samples. For example, similar to our study, it has been reported that the T_i value of hydrochar produced from waste ginkgo leaf residues is higher than that of raw biomass [21]. T_b (depletion temperature) values of KBS, HC₂₀₀, HC₂₂₀ and HC₂₄₀ products were determined as 793, 478, 492 and 484 °C, respectively. This result showed that the combustion process of KBS was longer than that of hydrochar products. As the hydrothermal temperature increased, the combustibility index S values showed a clear increasing trend. Compared with raw KBS, the S values of HC₂₀₀, HC₂₂₀, and HT₂₄₀

samples increased to 1.03×10^{-5} , 1.12×10^{-5} and 1.13×10^{-5} respectively, indicating superior combustion performance.

4. Conclusions

It is noteworthy that the fuel properties of hydrochar products obtained using KBS biomass was improved using the HTC method. All hydrochar products have higher carbon content and high heating value compared to the raw material. HTC method significantly increased the high heating value of hydrochar products. Among the hydrochar samples, the product obtained at 240 °C has the highest carbon value (51.69%) and HHV (18.19 MJ/kg). FT-IR results of hydrochar products showed that there are oxygen-rich functional groups in the structure. In a different study, the fuel properties of hydrochar products obtained from KBS at different times using the hydrothermal carbonization method can be investigated. As a result, The HC₂₄₀ product is rich in %C, has a higher HHV value and a higher energy yield, and is suitable for green energy and biofuel applications.

Ethics in Publishing

There are no ethical issues regarding the publication of this study.

References

- [1] Li, J., Yao, X., Ge, J., Yu, Y., Yang, D., Chen, S., Xu, K., Geng, L., (2022) Investigation on the pyrolysis process, products characteristics and BP neural network modelling of pine sawdust, cattle dung, kidney bean stalk and bamboo, *Process Safety and Environmental Protection*, 162:752–764.
- [2] Semaan, J.N., Belandria, V., Missaoui, A., Sarh, B., Gökalp, I., Bostyn, S., (2022) Energy analysis of olive pomace valorization via hydrothermal carbonization, *Biomass and Bioenergy*, 165, 106590.
- [3] Zhang, T., Kang, K., Nanda, S., Dalai, A. K., Xie, T., Zhao, Y., (2022) Comparative study on fuel characteristics and pyrolysis kinetics of corn residue-based hydrochar produced via microwave hydrothermal carbonization, *Chemosphere*, 291, 132787.
- [4] Sangare, D., Chartier, A., Santillan, M. M., Gökalp, I., Bostyn, S., (2022) Kinetic studies of hydrothermal carbonization of avocado stone and analysis of the polycyclic aromatic hydrocarbon contents in the hydrochars produced, *Fuel*, 316, 123163.
- [5] Wang, Q., Li, Y., Yu, Z., Li, X., Yin, S., Ji, W., Hu, Y., Cai, W., Wang, X., (2023) Highly porous carbon derived from hydrothermal-pyrolysis synergistic carbonization of biomass for

enhanced CO₂ capture, *Colloids and Surfaces A: Physicochemical and Engineering Aspects*, 673, 131787.

[6] Malhotra, M., Garg, A., (2023) Hydrothermal carbonization of sewage sludge: Optimization of operating conditions using design of experiment approach and evaluation of resource recovery potential, *Journal of Environmental Chemical Engineering* 11, 109507.

[7] Zulkornain, M.F., Shamsuddin, A.H., Normanbhay, S., Saad, J. M., Zhang, Y. S., Samsuri, S., Ghani, W. A. W. A. K., (2021) Microwave-assisted Hydrothermal Carbonization for Solid Biofuel Application: A Brief Review, *Carbon Capture Science & Technology*, 1, 100014.

[8] Samaksaman, U., Pattaraprakorn, W., Neramittagapong, A., Kanchanatip, E., (2023) Solid fuel production from macadamia nut shell: effect of hydrothermal carbonization conditions on fuel characteristics, *Biomass Conversion and Biorefinery*, 13:2225–2232.

[9] Poomsawat, S., Poomsawat, W., (2022) Characterization and pyrolysis kinetics study of hydrochar derived from turfgrass (*Zoysia matrella*) using hydrothermal carbonization, *Biomass Conversion and Biorefinery*.

[10] Zhang, X., Gao, B., Zhao, S., Wu, P., Han, L., Liu, X., (2020) Optimization of a “coal-like” pelletization technique based on the sustainable biomass fuel of hydrothermal carbonization of wheat straw, *Journal of Cleaner Production*, 242, 118426.

[11] Lu, X., Ma, X., Qin, Z., Chen, X., Yue, W., (2022) Co-hydrothermal carbonization of sewage sludge and swine manure: Hydrochar properties and heavy metal chemical speciation, *Fuel*, 330, 125573.

[12] Ercan, B., Alper, K., Ucar, S., Karagoz, S., (2023) Comparative studies of hydrochars and biochars produced from lignocellulosic biomass via hydrothermal carbonization, torrefaction and pyrolysis, *Journal of the Energy Institute*, 109, 101298.

[13] Yin, C.Y., (2011) Prediction of higher heating values of biomass from proximate and ultimate analyses, *Fuel*, 90, 1128–1132.

[14] Wang, Q., Wu, S., Cui, D., Zhoua, H., Wu, D., Pana, S., Xu, F., Wang, Z., (2022) Co-hydrothermal carbonization of organic solid wastes to hydrochar as potential fuel: A review *Science of the Total Environment*, 850, 158034.

[15] Ding, Y., Guo, C., Wang, S. Q, B., Zhao, P., Cui, X., (2022) Effects of process water recirculation on yields and quality of hydrochar from hydrothermal carbonization process of rice husk, *Journal of Analytical and Applied Pyrolysis*, 166, 105618.

[16] Bağ, Ö. and Tekin, K. (2020) Production and characterization of hydrothermal carbon from waste lignocellulosic biomass, *Journal of the Faculty of Engineering and Architecture of Gazi University* 35:2, 1063-1076.

[17] Liang, W., Wang, G., Xu, R., Ning, X., Zhang, J., Guo, X., Ye, L., Li, J., Jiang, C., Wang, P., Wang, C., (2022) Hydrothermal carbonization of forest waste into solid fuel: Mechanism and combustion behavior, *Energy*, 246, 123343.

- [18] Zhi, Y., Xu, D., Jiang, G., Yang, W., Chen, Z., Duan, P., Zhang, J., (2024) A review of hydrothermal carbonization of municipal sludge: Process conditions, physicochemical properties, methods coupling, energy balances and life cycle analyses, *Fuel Processing Technology*, 254, 107943.
- [19] Sharma, H.B., Sarmah, A. K., Dubey, B., (2020) Hydrothermal carbonization of renewable waste biomass for solid biofuel production: A discussion on process mechanism, the influence of process parameters, environmental performance and fuel properties of hydrochar, *Renewable and Sustainable Energy Reviews*, 123, 109761.
- [20] Zhang, Z., Yang, J., Qian, J., Zhao, Y., Wang, T., Zhai, Y., (2021) Biowaste hydrothermal carbonization for hydrochar valorization: Skeleton structure, conversion pathways and clean biofuel applications, *Bioresource Technology* 324, 124686.
- [21] Yu, Y., Guo, Y., Wang, G., El-Kassaby, Y. A., Sokhansanj, S., (2022) Hydrothermal carbonization of waste ginkgo leaf residues for solid biofuel production: Hydrochar characterization and its pelletization, *Fuel* 324, 124341.
- [22] Ahmad, S., Zhu, X., Wei, X., Zhang, S., (2021) Influence of process parameters on hydrothermal modification of soybean residue: Insight into the nutrient, solid biofuel, and thermal properties of hydrochars, *Journal of Environmental Management* 283, 111981.
- [23] Zhang, Z., Yang, J., Qian, J., Zhao, Y., Wang, T., Zhai, Y., (2021) Biowaste hydrothermal carbonization for hydrochar valorization: Skeleton structure, conversion pathways and clean biofuel applications, *Bioresource Technology*, 324, 124686
- [24] Pauline A. L., Joseph K., (2020) Hydrothermal carbonization of organic wastes to carbonaceous solid fuel –A review of mechanisms and process parameters, *Fuel*, 279, 118472.
- [25] Cai, J., Li, B., Chen, C., Wang, J., Zhao, M., Zhang K., (2016) Hydrothermal carbonization of tobacco stalk for fuel application, *Bioresource Technology*, 220, 305–311.
- [26] Kabakci, S.B., Baran, S.S., (2019) Hydrothermal carbonization of various lignocellulosics: Fuel characteristics of hydrochars and surface characteristics of activated hydrochars, *Waste Management*, 100, 259–268.
- [27] Qin, X., Meng, W., Cheng, S., Xing, B., Shi, C., Nie, Y., Wang, Q., Xia, H., (2023) Efficient removal of heavy metal and antibiotics from wastewater by phosphate-modified hydrochar, *Chemosphere*, 345, 140484.
- [28] Yang, J., Zhang, Z., Wang, J., Zhao, X., Zhao, Y., Qiana, J., Wang, T., (2023) Pyrolysis and hydrothermal carbonization of biowaste: A comparative review on the conversion pathways and potential applications of char product, *Sustainable Chemistry and Pharmacy* 33, 101106.

Evaluation of Pro-Drug Properties in a Novel Schiff Base-Incorporated Pt(II) Complex

Salih Günnaz¹, Khan Mohammad Rahmat¹, Sevil İrişli^{1*}

¹ Department of Chemistry, Ege University, Bornova, İzmir, Türkiye

Received: 11/03/2024, Revised: 14/06/2024, Accepted: 28/06/2024, Published: 31/08/2024

Abstract

The present investigation involved the synthesis of a new Schiff base and its platinum complex. The chemical structures of both the ligand and the complex were determined using various analytical techniques, including ¹H-NMR, ¹³C-NMR, FT-IR, and elemental analysis. Moreover, the interaction between the synthesized complex and Amyloid-Beta, a crucial factor in the pathogenesis of Alzheimer's disease, was explored. This interaction was assessed by employing fluorescence spectrophotometry. Additionally, the influence of the histidine amino acid, which has been reported in the literature to play a significant role in the interaction between Amyloid-Beta and coordination compounds, was monitored using ¹H-NMR. These investigations could improve our comprehension of ligands and complexes' chemical structure and biological effects. Furthermore, they may contribute to the advancement of knowledge regarding important neurodegenerative disorders such as Alzheimer's disease, as well as the development of potential therapeutic strategies.

Keywords: Alzheimer's Disease, Amyloid Beta, Platinum Complexes, Schiff Bases, Cytotoxic Activity.

Yeni Schiff Bazı İçeren Pt(II) Kompleksinin Pro-İlaç Özelliklerinin Değerlendirilmesi

Öz

Bu çalışma, yeni bir Schiff bazının sentezi ve platin kompleksinin incelenmesini içermiştir. Hem ligandın hem de kompleksin kimyasal yapıları, ¹H-NMR, ¹³C-NMR, FT-IR ve elementel analiz gibi çeşitli analitik teknikler kullanılarak belirlenmiştir. Ayrıca, Alzheimer hastalığının patogeneğinde önemli bir faktör olan Amiloid-Beta ile sentezlenen kompleks arasındaki etkileşim araştırılmıştır. Bu etkileşim, floresan spektrofotometre kullanılarak değerlendirilmiştir. Ek olarak, Amiloid-Beta ve koordinasyon bileşikleri arasındaki etkileşimde önemli bir rol oynadığı literatürde bildirilen histidin amino asidinin etkisi, ¹H-NMR kullanılarak izlenmiştir. Bu araştırmalar, ligand ve komplekslerin kimyasal yapıları ve biyolojik etkileri hakkındaki anlayışımızı artırma potansiyeline sahiptir. Ayrıca, Alzheimer hastalığı gibi önemli nörodejeneratif bozukluklar hakkındaki bilgi ilerlemesine ve potansiyel terapötik stratejilerin geliştirilmesine katkıda bulunabilir.

Anahtar Kelimeler: Alzheimer Hastalığı, Amiloid Beta, Platin Kompleksleri, Schiff Bazları, Sitotoksik Aktivite.

*Corresponding Author: salih.gunnaz@ege.edu.tr

Salih Günnaz: <https://orcid.org/0000-0002-7422-6593>

Khan Mohammad Rahmat: <https://orcid.org/0000-0002-8019-8859>

Sevil İrişli: <https://orcid.org/0000-0002-3727-2216>

1. Introduction

Schiff Bases are a class of compounds that follow the general formula $RR'C=NR''$ (where R represents an aryl group, R' represents a hydrogen atom, and R'' represents an alkyl or aryl group). Interestingly, even when R'' is an alkyl or aryl group and R' is an alkyl or aromatic group, the compound is still referred to as a Schiff Base. These compounds exhibit versatility due to the presence of different substituents and the potential inclusion of N-N' bridges or the absence of bridges altogether.

The synthesis of Schiff Bases can be achieved through various reaction methods, with the most employed method being the acid-catalyzed condensation reaction between an amine and an aldehyde or ketone under reflux conditions. In the initial step of this reaction, the nitrogen atom of the amine undergoes a nucleophilic attack on the carbonyl carbon, resulting in the formation of an unstable carbinolamine intermediate. It is worth noting that the starting materials can be interchanged in this reaction. Upon elimination of water, a C=N bond is formed. These bases are typically synthesized from carbonyl compounds such as aldehydes and ketones, along with aromatic amines. The process involves nucleophilic addition, semi-aminal formation, and subsequent dehydration, ultimately leading to the formation of an imine [1].

The pH dependence of imine formation is a crucial factor to consider. In the initial step, non-protonated free amines are added to carbonyl groups. If the solution becomes excessively acidic, the concentration of amines decreases, resulting in a slowdown of the normally rapid step. This step plays a significant role in determining the overall reaction rate. In the subsequent step, protonated groups, such as OH, are eliminated. Consequently, a decrease in acidic concentration promotes the progression of the second step, facilitating the easy elimination of H₂O. Under acidic conditions, basic amines are typically protonated, making them non-nucleophilic and impeding the reaction's advancement. Moreover, the reaction is hindered under highly basic conditions. For instance, there is a lack of suitable protons available to catalyze the separation of the hydroxyl group in carbinolamine. In general, the reactivity of aldehyde is more than ketone in the formation of Schiff base.

Schiff bases are a class of ligands that play a crucial role in chemistry [2]. They are highly versatile and can be easily prepared, making them valuable in transition metal coordination chemistry. In recent years, there have been significant advancements in the chemistry of transition metal complexes with metallo-rings [3]. Bidentate N-donor ligands form chelate complexes by coordinating with one of the metal centers using each nitrogen atom. These metalochelates are commonly used in regiospecific organic and organometallic syntheses, including addition reactions and catalytic materials. Ruthenium complexes containing bidentate Schiff bases are particularly useful in catalytic processes such as Kharasch addition, enol-ester synthesis, alkyne dimerization, olefin metathesis, and polymerization. Chiral Schiff base metal complexes are employed for achieving stereoselective organic transformations. Tetradentate Schiff base complexes of oxovanadium exhibit potential for multi-electron transfer. Schiff bases have shown potential as anticancer agents, but their activity is further enhanced when

they form metal complexes. Schiff bases with an azomethine bridge have been found to possess antitumor, antibacterial, and antifungal properties. In drug research, it has been observed that small molecules interacting with DNA can cause DNA damage, leading to cell death. Therefore, compounds with anticancer, antiviral, and antiseptic properties often exhibit biological activity by interacting with DNA. Numerous studies have demonstrated that transition metal complexes can bind to DNA through intercalation.

Alzheimer's disease (AD) is a prevalent form of dementia, accounting for approximately 60-80% of dementia cases. Dementia is a neurodegenerative condition that impacts various cognitive functions such as memory, language, attention, problem-solving, and decision-making. This impairment arises from brain damage. Alzheimer's disease poses significant challenges globally, requiring costly and labor-intensive treatment, second only to heart and cancer diseases. The primary culprit behind this disease is believed to be the accumulation of $A\beta_{1-42}$, resulting in the formation of insoluble plaques. These plaques consist of amyloid- β ($A\beta$) peptides and are thought to disrupt neuronal communication between cells. In the pursuit of effective treatment, organic molecules with aromatic rings and suitable chelating ligands containing nitrogen donors play a crucial role. The development of these ligands and the synthesis of coordination compounds formed with them are essential for combating Alzheimer's disease.

Despite the numerous Schiff base-Pt complexes that have been reported [5-11], their impact on Alzheimer's disease has not yet been explored. In a recent study, F. Collin and colleagues [12] synthesized several Pt complexes, including $Pt(\Phi\text{-MePy})(\text{DMSO})\text{Cl}$, $Pt(\text{DMSO})_2\text{Cl}_2$, $Pt(\text{bpy})\text{Cl}_2$, $Pt(\text{Phen})\text{Cl}_2$, and $Pt(\Phi\text{-Phen})\text{Cl}_2$, with the aim of reducing the interaction of Zn and Cu with $A\beta$ aggregation and ROS production, respectively. The structures of these complexes were elucidated, and their interaction with the $A\beta_{28}$ peptide was examined. Similarly, Sasaki and colleagues [13] investigated the interaction of $Pt(\Phi\text{-MePy})(\text{DMSO})\text{Cl}$ and $Pt(\text{DMSO})_2\text{Cl}_2$ complexes with $\text{Cu(II)-}A\beta_{28}$ using EPR measurements. The results indicated that the Pt complex did not displace Cu(II) , but it did bind to specific regions of the $A\beta$ peptide. In another study, Kenche and colleagues [14] determined the structure of a complex formed between an N,N -dimethyl-2-[2-(quinolin-8-yl)-1H-benzimidazol-1-yl] ligand and $Pt(\text{dmsO})_2\text{Cl}_2$. They then investigated the interaction of this complex with mouse $A\beta$ fibrils and found that it inhibited aggregation. Additionally, Satra synthesized a Pt(IV) complex with the same ligand and demonstrated that its efficacy was higher than that of the Pt(II) complex. Based on these findings, our study aims to synthesize a new Schiff base and characterize its four-coordinated Pt(II) complexes. Furthermore, we plan to investigate the interactions of these complexes with histidine.

2. Materials And Methods

2.1. Chemicals

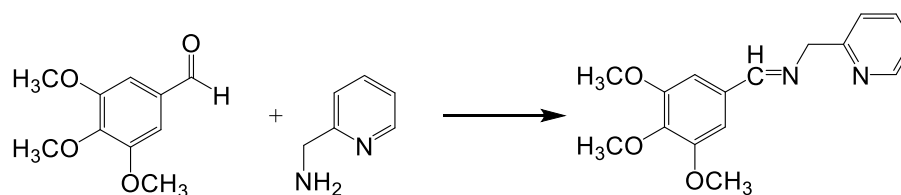
To synthesize the Schiff base, 2-picolamine and 3,4,5-trimethoxybenzaldehyde were obtained from Sigma Aldrich and Alfa Easer companies. L-Histidine, PBS buffer (phosphate buffer), and Tioflavin-T were also acquired from the same suppliers. The A β ₁₋₄₂ fluorescent kit was purchased from Anaspec. The starting complex Pt(DMSO)₂Cl₂ was synthesized based on the literature data [15].

2.2. Instrumentations

¹H NMR and ¹³C NMR spectra were recorded on the Vairian AS 400 NMR spectrometer in CDCl₃ and DMSO-d₆ with tetramethylsilane (TMS) as an internal reference. Chemical shifts are reported in ppm (δ). Coupling constants, *J*, are reported in Hz. FT-IR analyses were conducted using the Perkin Elmer Spectrum 100 FTIR spectrophotometer with CsI (4000-250 cm⁻¹). Furthermore, the facilities at İnönü University were utilized for elemental analysis.

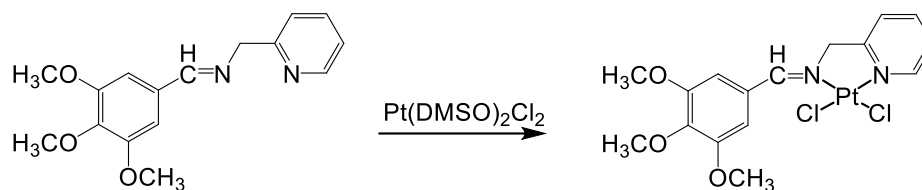
2.3. Synthesis of Ligand and its Platinum Complex

2.3.1. Synthesis of Ligand



The synthesis was carried out using the melting technique at a temperature of 80°C in the presence of N₂ gas, without a solvent. The reactants used were 3,4,5-trimethoxybenzaldehyde (36 mg; 0.184 mmol) and 2-picolamine (20 mg; 0.184 mmol). The reaction occurred in an oil bath for approximately 15 minutes. After the reaction was complete, a yellow-colored oil-like product was obtained. The volatile components were then removed under vacuum. The overall yield of the reaction was determined to be 80%. FT-IR (U, cm⁻¹): 1586.1 (C=N). ¹H (400 MHz, CDCl₃) δ (ppm): 8.48 (d, 1H, *J*=4.7 Hz, Py-*H*), 8.29 (s, 1H, N=CH), 7.58 (t, 1H, *J*=7.7 Hz, Py-*H*), 7.32 (d, 1H, *J*=7.8 Hz, Py-*H*), 7.09 (t, 1H, *J*=6.0 Hz, Py-*H*), 6.99 (s, 2H, Ar-*H*), 4.86 (s, 2H, N-CH₂), 3.81 (s, 6H, OCH₃), 3.80 (s, 3H, OCH₃). ¹³C (100 MHz, CDCl₃) δ (ppm): 162.7 (C=N), 159.1 (Py-C), 153.4 (Ar-C), 149.2 (Py-C), 140.5 (Ar-C), 136.6 (Py-C), 131.5 (Ar-C), 122.2 (Py-C), 122.0 (Py-C), 105.4 (Ar-C), 66.5 (N-CH₂), 60.8 (OCH₃), 56.1 (OCH₃).

2.3.2. Synthesis of Complex (Pt-L)



L (20.3 mg; 0.071 mmol) was refluxed with $\text{Pt}(\text{DMSO})_2\text{Cl}_2$ (30 mg; 0.071 mmol) in a 1:1 molar ratio in chloroform for 2 hours. At the end of this period, a dark yellow-orange precipitate formed, which was separated and washed with diethyl ether. The resulting material was dried under vacuum to obtain a yellow-orange solid product. Yield: 52%, Decomposition Point: 220-240°C. Elemental analysis: Calculated ($\text{C}_{16}\text{H}_{18}\text{Cl}_2\text{N}_2\text{O}_3\text{Pt}$, 552.32): C, 34.79; H, 3.28; N, 5.07; Found: C, 33.98; H, 3.16; N, 5.07. FT-IR (U, cm^{-1}): 1647.0 (C=N), 322-293 (Pt-Cl). ^1H (400 MHz, DMSO-d_6) δ (ppm): 9.07 (d, 1H, $J=5.9$ Hz, Py-H), 8.92 (s, 1H, N=CH), 8.10 (t, 1H, $J=7.7$ Hz, Py-H), 7.62 (d, 1H, $J=7.9$ Hz, Py-H), 7.46 (t, 1H, $J=6.7$ Hz, Py-H), 7.40 (s, 2H, Ar-H), 6.16 (s, 2H, N-CH₂), 4.08 (s, 3H, OCH₃), 4.06 (s, 6H, OCH₃). ^{13}C (100 MHz, DMSO-d_6) δ (ppm): 166.0 (C=N), 162.4 (Py-C), 156.7 (Ar-C), 152.5 (Py-C), 143.8 (Ar-C), 139.9 (Py-C), 134.9 (Ar-C), 125.6 (Py-C), 125.3 (Py-C), 108.7 (Ar-C), 69.9 (N-CH₂), 61.4 (OCH₃), 59.5 (OCH₃).

2.4. NMR Measurement of Pt(L)Cl₂-Histidine Interaction

The $\text{Pt}(\text{L})\text{Cl}_2$ complex underwent solvolysis through vigorous stirring in a mixture of DMSO and H_2O with a ratio of 2:1 for a duration of 15 minutes. Subsequently, histidine was meticulously weighed and combined with the complex solution in a molar ratio of 1:2 (complex to histidine) in the presence of HCl. The resulting mixture was then incubated at a temperature of 37°C for 15 minutes, while PBS buffer was added. Following this, the ^1H -NMR spectrum of the sample was acquired, revealing discernible differences in the signals resulting from the interaction.

2.5. Fluorescence Measurements

The $\text{A}\beta_{1-42}$, ThT, and the complex formed with 1% DMSO in water were initially diluted to the desired concentration (final concentration 10 micromolar) using the provided assay buffer. To conduct fluorescence measurements, a black well plate was used, with each well adjusted to a volume of 100 μl . The aggregation inhibition of the complex was evaluated by adding $\text{A}\beta_{1-42}$ to the system both individually and in combination with the complex. Additionally, the fluorescence properties of the complex alone and the assay buffer were examined. Measurements were recorded using the Thermo Fisher Scientific Varioskan Flash microplate reader, with excitation at 480 nm and emission at 484 nm.

3. Results and Discussion

3.1. NMR Evolution

Figures 1 and 2 present the ^1H -NMR and ^{13}C -NMR spectra, respectively, of the L ligand. The imine proton of the ligand is detected as a singlet at 8.29 ppm. The $-\text{OCH}_3$ groups exhibit multiplet signals at 3.81 and 3.80 ppm. Additionally, the ^{13}C -NMR values of the ligand align with the anticipated structure. The imine carbon is observed at 162.7 ppm and the carbons of the methoxy group at 60.8 and 56.1 ppm.

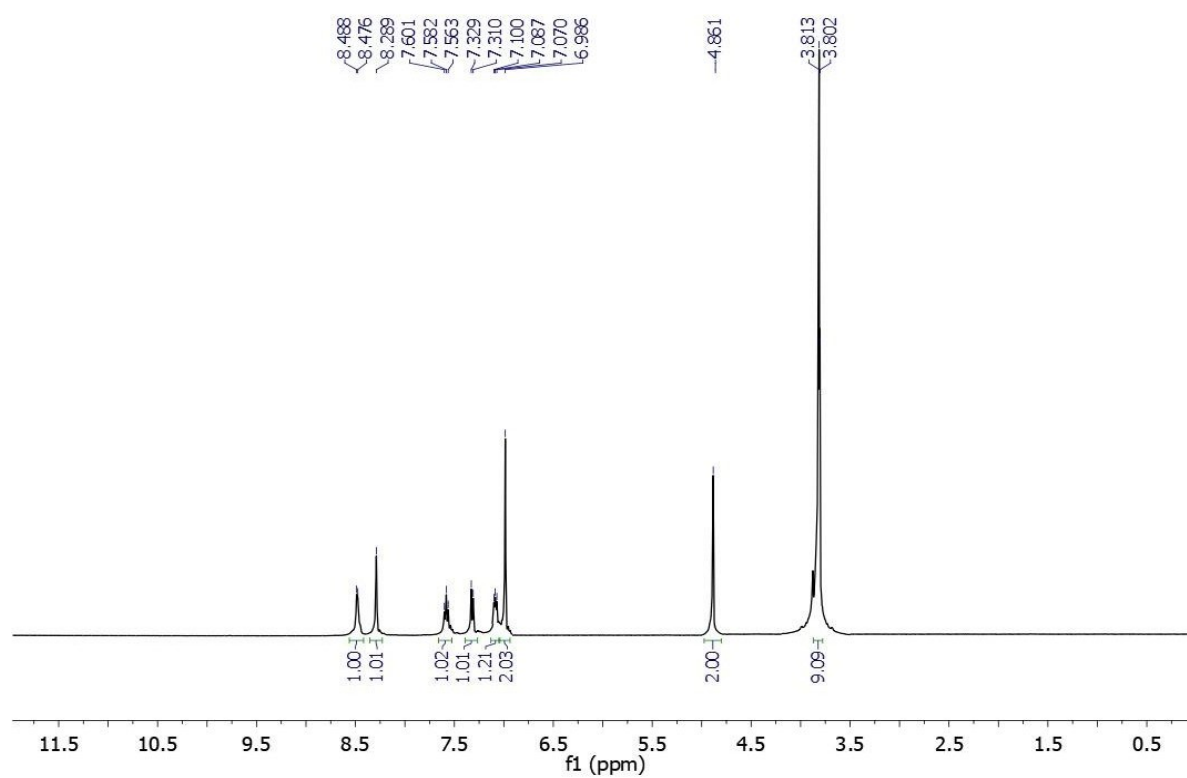


Figure 1. ^1H -NMR Spectrum of L.

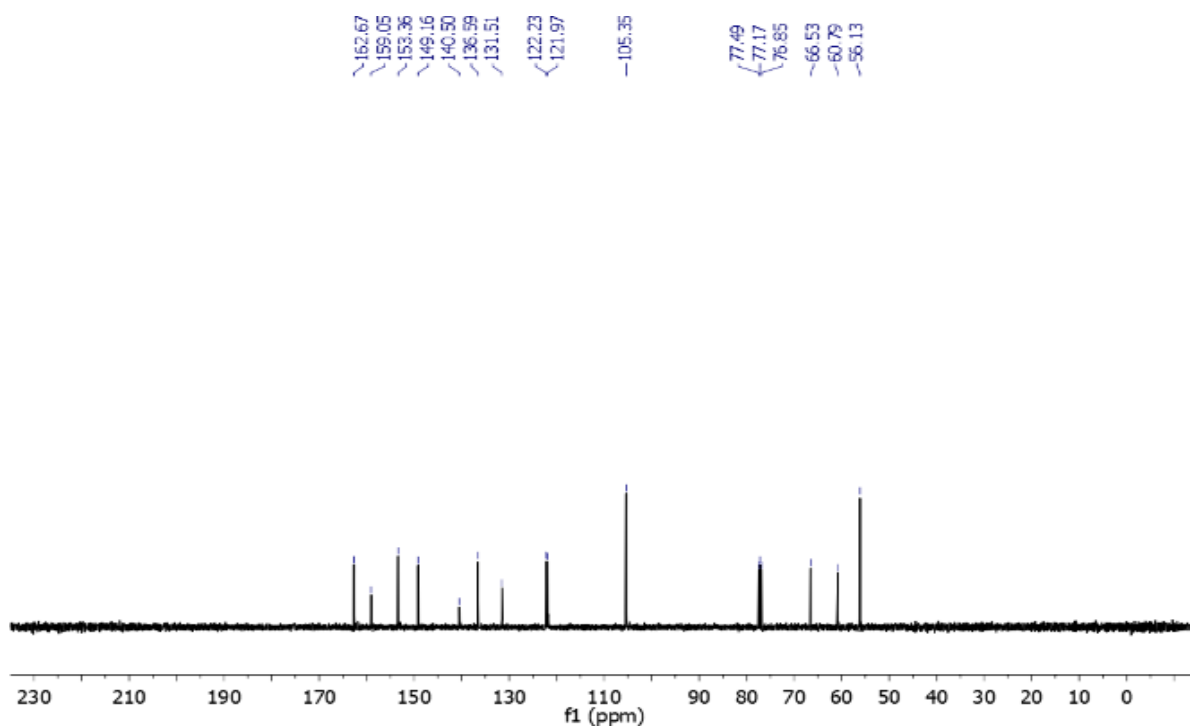


Figure 2. ^{13}C -NMR Spectrum of L.

The ^1H -NMR and ^{13}C -NMR spectra of the synthesized $\text{Pt}(\text{L})\text{Cl}_2$ complex are given in Figures 4 and 5. NMR data related to the ligand and complexes are shown in Table 1.

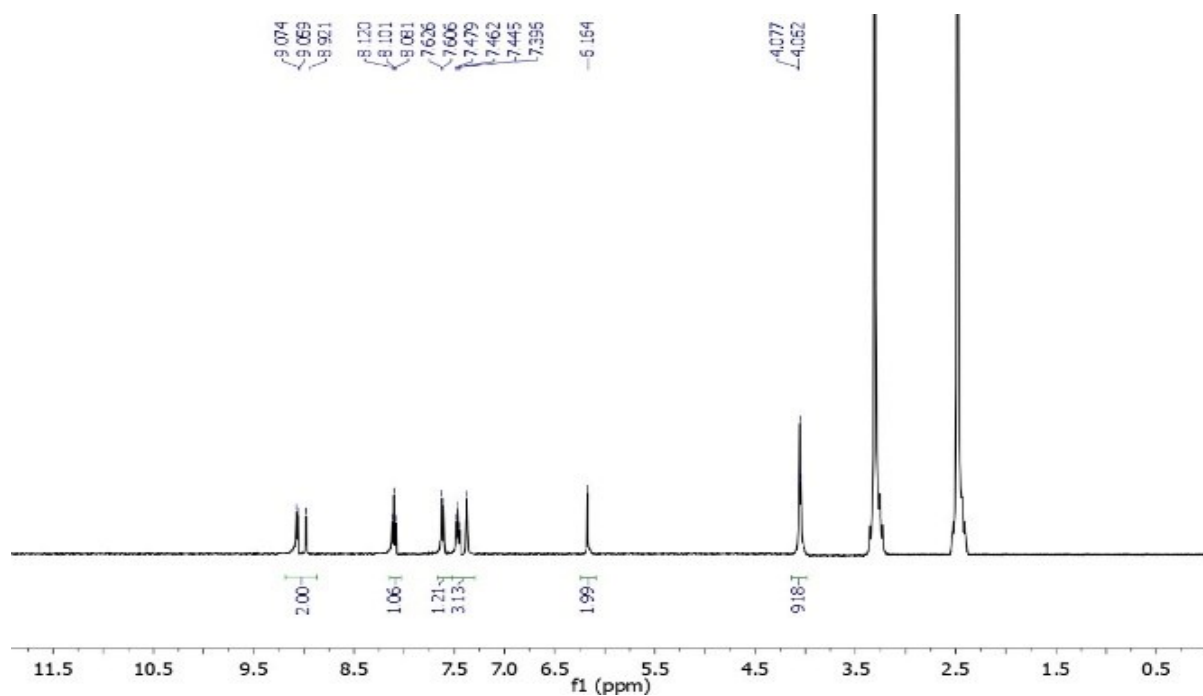


Figure 3. ^1H -NMR Spectrum of $\text{Pt}(\text{L})\text{Cl}_2$.

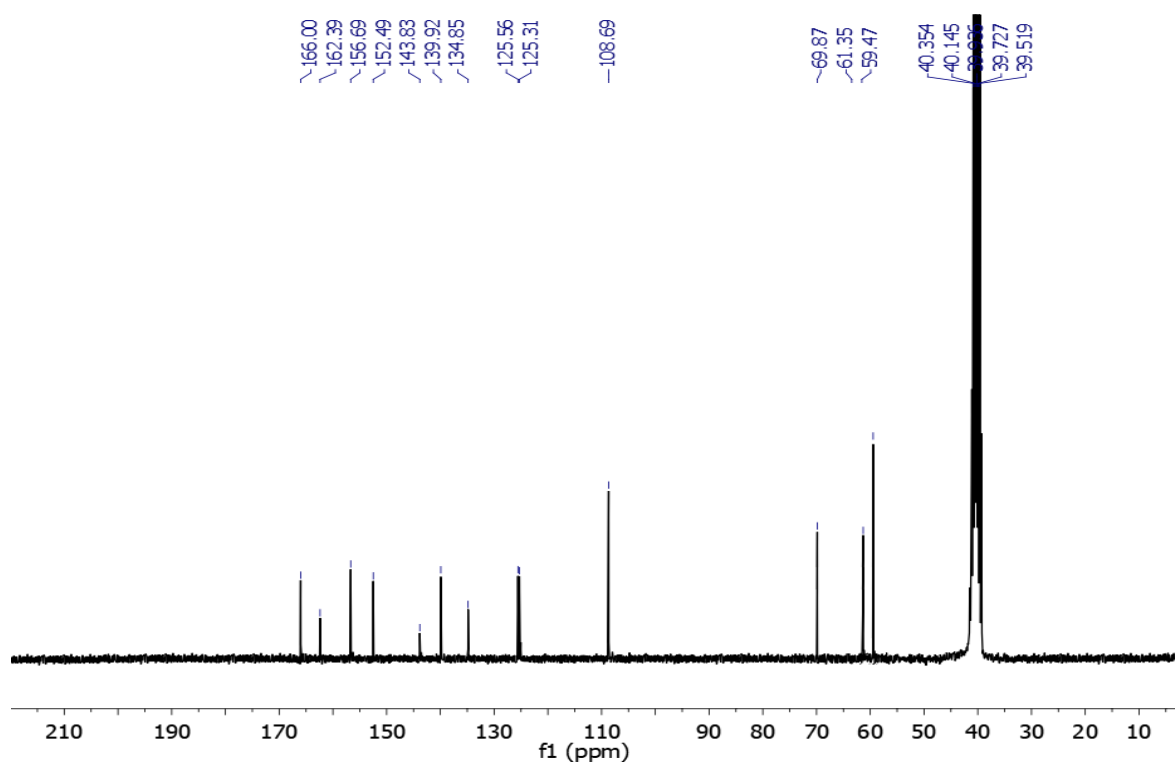
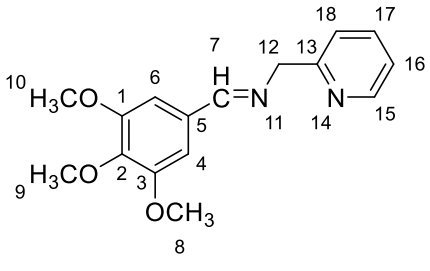
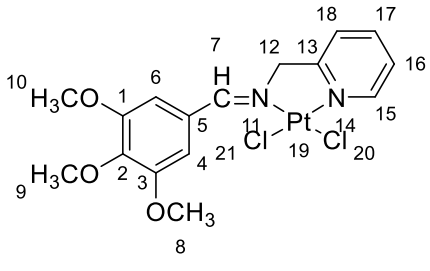


Figure 4. ^{13}C -NMR Spectrum of $\text{Pt}(\text{L})\text{Cl}_2$.

Table 1: ^1H - and ^{13}C -NMR Peak Assignments for Ligand and Complex

 Ligand (L)		 complex (Pt-L)	
^1H -NMR			
Number	ppm	Number	ppm
15	8.48 (d)	15	9.07 (d)
7	8.29 (s)	7	8.92 (s)
16	7.58 (t)	16	8.10 (t)
18	7.32 (d)	18	7.62 (d)
17	7.09 (t)	17	7.46 (t)
4, 6	6.99 (s)	4, 6	7.40 (s)
12	4.86 (s)	12	6.16 (s)
8, 10	3.81 (s)	8, 10	4.06 (s)
9	3.80 (s)	9	4.08 (s)
^{13}C -NMR			
Number	ppm	Number	ppm
7	162.7	7	166.0
13	159.1	13	162.4
1, 3	153.4	1, 3	156.7
15	149.2	15	152.5
2	140.5	2	143.8
17	136.6	17	139.9
5	131.5	5	134.
16	122.2	16	125.6
18	122.0	18	125.3
4,6	105.4	4,6	108.7
12	66.5	12	69.9
9	60.8	9	61.4
8, 10	56.1	8, 10	59.5

*s: singlet; d: doublet; t: triplet; m: multiplet; bs: broad singlet

The imine group in the complex exhibits a shift to 8.92 ppm in the ^1H -NMR spectrum, indicating its binding. Conversely, when the pyridylamine's N end binds, it causes a significant shift in the adjacent aromatic ring's protons. Specifically, these protons experience a shift to a

weaker field during complexation, with the proton adjacent to N shifting from 8.49 ppm to 9.07 ppm. Furthermore, the ^{13}C spectrum shows a weak-field shift in the imine group's C atom compared to the ligand spectrum (166.0 ppm) [9, 17].

3.2. FT-IR spectra

The FT-IR spectrum of the ligand is given in figure 5. The characteristic vibration signal of the imine group is observed at 1586.1 cm^{-1} . It is observed that the signal related to the carbonyl group in the aldehyde disappears. These assessments collectively confirm the successful synthesis of the ligands. These findings are corroborated by the weak-field shift observed in the imine group vibrations in the FT-IR spectrum of the complex (Fig.6) as well as the elemental analysis results [18, 19]. Additionally, the presence of Pt-Cl stretching vibrations in the FT-IR spectrum of the complex, appearing as a doublet and shifting compared to the starting complex, confirms the occurrence of the anticipated interaction [20]. It was also observed that the signals related to the DMSO group in the initial complex disappeared in the complex spectrum.

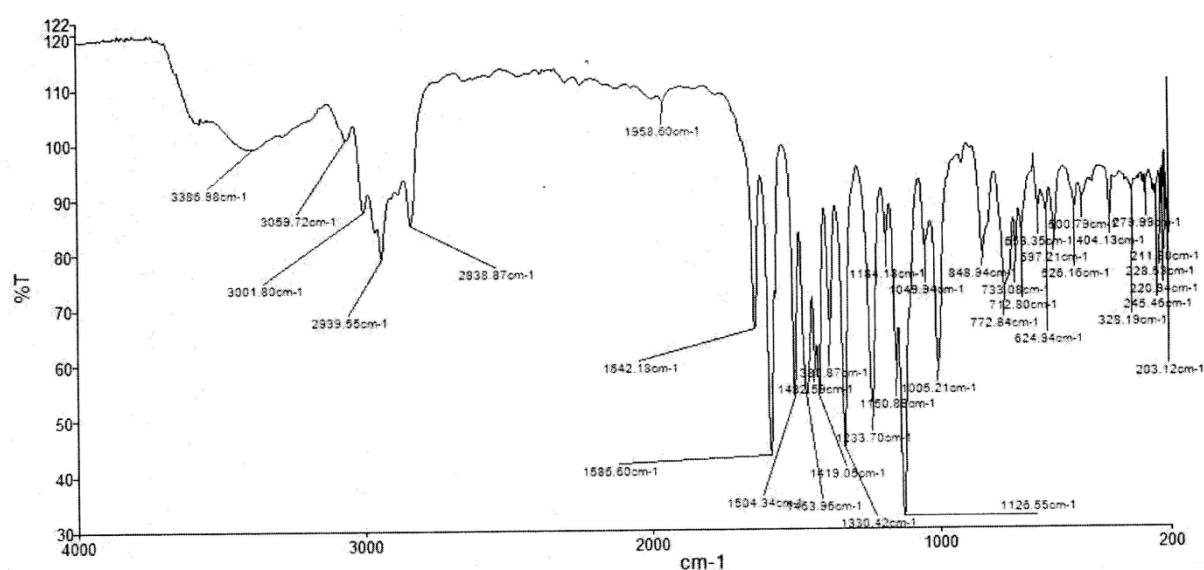


Figure 5. FT-IR spectrum of the Ligand

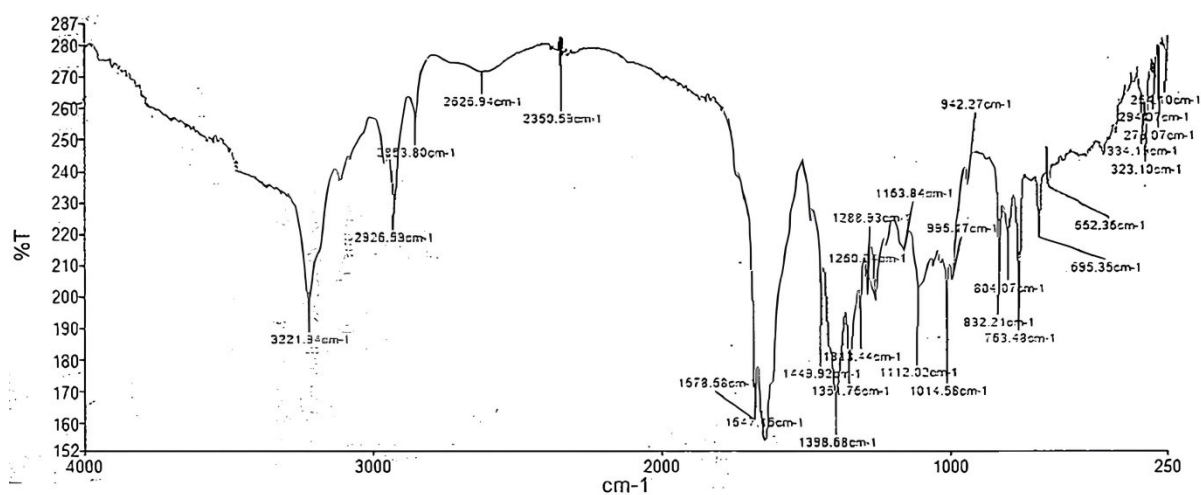


Figure 6. FT-IR spectrum of the Pt(L)Cl₂

3.3. Evaluation of Pt(L)Cl₂ -Histidine Interaction by NMR Measurements

The determination of the environment for measuring the complex with Histidine was carried out in accordance with the existing literature. To measure the biological activity, it is necessary to first hydrolyze or solvolysis the complex. Initially, an attempt was made to use H₂O, and if the solubility was low, mixtures of DMSO/H₂O were tested [16]. Due to the low solubility of the synthesized complex in water, it was solvolysis with DMSO and then examined for its interaction with Histidine in a DMSO: H₂O (2:1) mixture. Consequently, the spectrum for the complex was initially obtained in DMSO-d₆. Upon examination of the spectrum obtained for the complex in DMSO-d₆, the peak corresponding to the imine proton was observed at 8.92 ppm. Additionally, the ¹H-NMR spectrum of free Histidine in a DMSO/H₂O environment was acquired, revealing the presence of the aromatic protons (Ar-CH) of Histidine hydrochloride (two protons) at 8.57 ppm and 7.27 ppm. The solvolysis complex and Histidine were then incubated in a PBS buffer for 15 minutes at 37°C, and the ¹H-NMR spectrum was recorded. The expectation was that one or two solvent molecules would be displaced by Histidine from the solvolysis product. In the resulting spectrum of the interaction, the imine peak associated with the Histidine-bound complex was observed at 8.65 ppm. Furthermore, the (Ar-CH) protons of Histidine shifted to 8.41 ppm and 7.12 ppm due to the interaction with the complex. Based on the observed chemical shift values, it can be inferred that there is an interaction between the complex and histidine. This is further supported by Figure 5, which shows the shift of the imine proton and the shifts in the Histidine peaks during the interaction between the Complex and Histidine. Additionally, according to the literature, the solvolysis of such complexes can result in the formation of numerous adduct products in the interaction with Histidine, indicating interactions with different molar ratios of Histidine [16, 21].

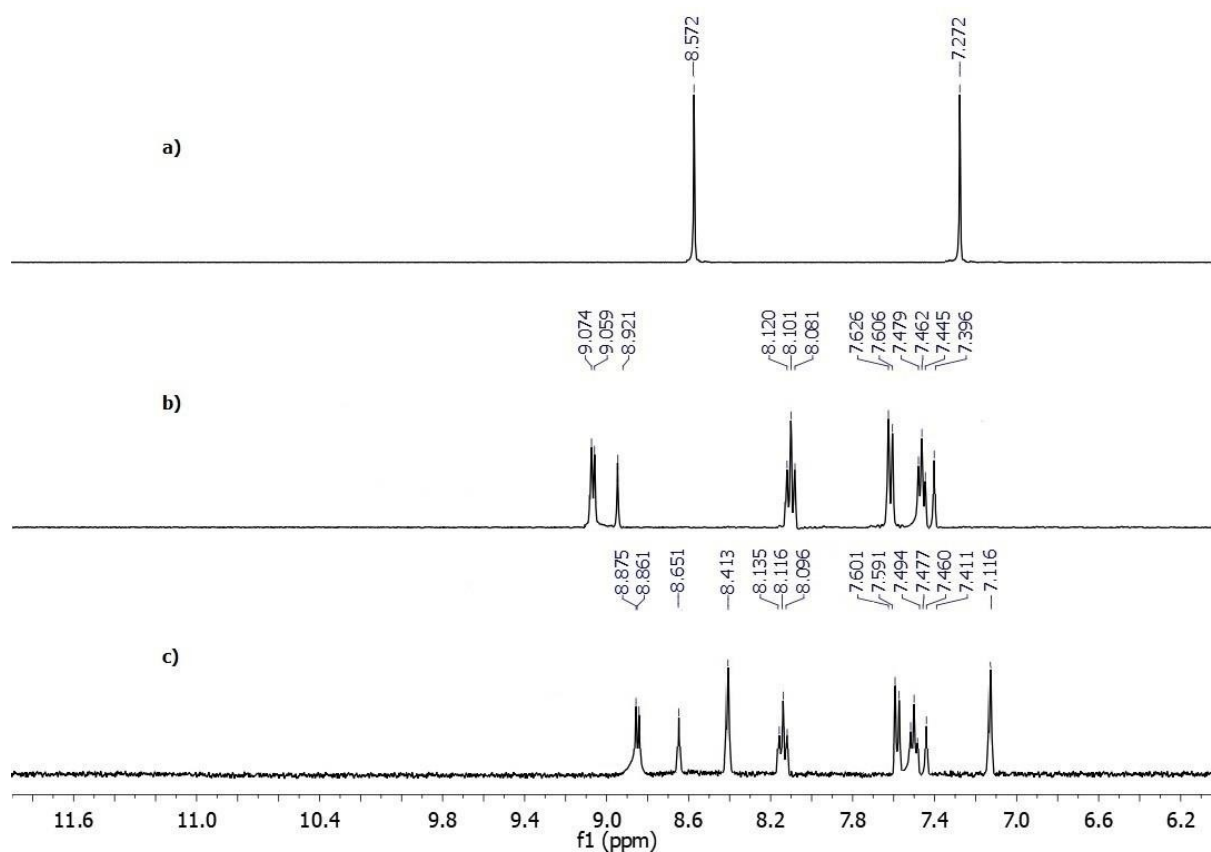


Figure 5. a) ¹H-NMR spectrum of Histidine hydrochloride (blind), b) ¹H-NMR spectrum of Pt(L)Cl₂ complex in DMSO environment, c) ¹H-NMR spectrum obtained after 15 minutes of incubation at 37 °C in a 1:2 ratio of complex to Histidine at pH 7.4.

3.4. Evaluation of Fluorescence Measurements

Although Thioflavin T does not emit fluorescence when it is in its monomeric form and in the presence of A β ₁₋₄₂, it does produce a signal when it is in the presence of aggregated amyloid with ThT (Excitation: 440 nm, Emission: 484 nm). It is anticipated that the complex formed by Thioflavin T and A β ₁₋₄₂ will diminish this signal. The measurement results indicate that the Pt(L)Cl₂ complex interacts with A β ₁₋₄₂ in a 1:1 molar ratio (Figure 6). The decrease in fluorescence values observed when interacting with Amyloid Beta provides evidence that the synthesized compound indeed interacts with Amyloid Beta.

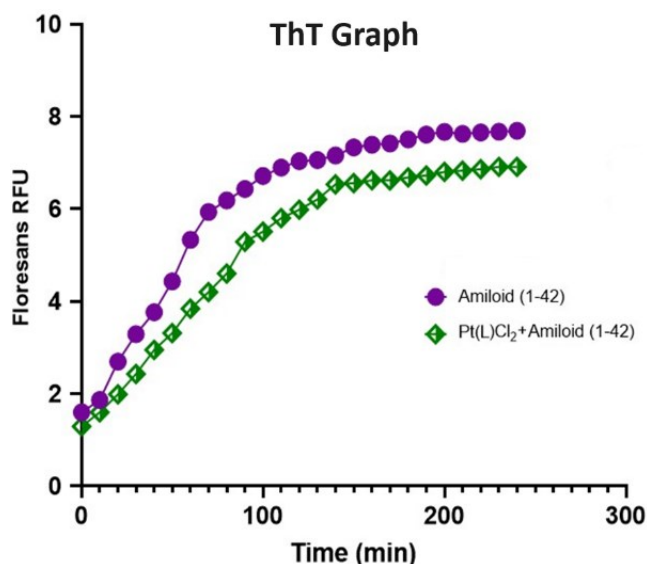


Figure 6. Fluorescence Measurement Graph of Pt(L)Cl₂ Complex.

The decrease in the fluorescence intensity of amyloid in the presence of the complex during interaction with Thioflavin T indicates the occurrence of interaction.

4. Conclusion

A Schiff base compound of a novel nature has been successfully synthesized, followed by the synthesis of its platinum complex. The structures of both the ligand and the complex have been thoroughly elucidated through the utilization of various spectroscopic techniques. In the subsequent phase of the research, the compound's potential to exhibit activity against Alzheimer's disease has been investigated by studying its interaction with Amyloid beta in a 1:1 molar ratio. To assess the compound's efficacy, fluorescence measurements have been conducted. Notably, the synthesized complex has displayed significant activity against Alzheimer's disease. Moreover, the interaction between the complex and Histidine, an amino acid predominantly found in Amyloid beta and commonly targeted by coordination compounds, has been meticulously examined. As a result, the study has uncovered the formation of solvolysis products at different molar ratios when one mole of the complex interacts with two moles of Histidine.

Ethics in Publishing

There are no ethical issues regarding the publication of this manuscript.

Author Contributions

Salih Günnaz: Conducted the experiment, analyzed the results, and composed the manuscript.

Khan Mohammad Rahmat: Conducted the experiment.

Sevil İrişli: Oversaw the advancement of the trial, managed the experiment, analyzed the findings, and drafted the written report.

Acknowledgement

Financial support from Ege University (Project FYL-2019-20437) is gratefully acknowledged.

References

- [1] Ganjali, MR, Tavakoli, M, Faridbod, F, Riahi, S, Norouzi, P, Niassari, MS. 2008. Interaction Study of a new Bis-Bidentate Schiff's Base with some Metal Ions and its Application in Fabrication of Sm(III) Potentiometric Membrane Sensor. *International Journal of Electrochemical Science*, 3: 1559-1573.
- [2] Vigato, PA, Magro PA, Crociani, L, Prinziavalli, C, Zanonato, L, Tamburini, S. 2014. Coordination ability of free or silica immobilized Schiff bases towards Hg(II), Cd(II) and Pb(II) ions. *Inorganica Chimica Acta*, 410: 29-38.
- [3] Ramírez, P, Contreras, R, Valderrama, M, Carmona, D, Lahoz, FJ, Balana, AI. 2008. Cyclometallated platinum (II) complexes containing the chiral ligand [2-(diphenylphosphanyl)-benzylidene]-(1-phenyl-ethyl)-amine: Synthesis and molecular structures of the compounds $[\text{PtCl}(\text{Me})\{\kappa^2\text{-(R)-Ph}_2\text{P}(\text{C}_6\text{H}_4)=\text{NCH}(\text{Ph})\text{Me-P,N}\}]$ and $[\text{Pt}\{\kappa^3\text{-(S)-Ph}_2\text{P}(\text{C}_6\text{H}_4)\text{CH}=\text{NCH}(\text{C}_6\text{H}_4)\text{Me-P,N,C}\}\text{Py}]\text{BF}_4$. *Journal of Organometallic Chemistry*; 693(2): 349-356.
- [4] Hayne, DJ, Lim, S, Donnelly, PS. 2014. Metal complexes designed to bind to amyloid- β for the diagnosis and treatment of Alzheimer's disease. *Chemical Society Reviews*; 43: 6701-6715.
- [5] Khalaji, AD, Jian, FF, Xiao, H, Mojdekanlou, S. 2008. Crystal Structure of N,N'-Bis(3,4,5-trimethoxybenzylidene)ethylenediaminediiodo zinc(II). *Analytical Sciences*, 24: x91-x92.
- [6] Ghosh, K, Roy, S, Ghosh, S, Banerjee, A, Bauzá, A. 2016. A combined experimental and theoretical study on supramolecular assemblies in octahedral cobalt(III) salicylaldimine complexes having pendant side arms. *Polyhedron*; 112: 86-95.
- [7] Khalaji, AD, Brad, K, and Zhang, Y. 2008. Diacetonitrile[N,N'-bis(3,4,5-trimethoxybenzylidene)ethylenediamine]copper(I) perchlorate. *Acta Crystallographica Section E*; 64: m189.
- [8] Subbaraj, P, Ramu, A, Raman, N, Dharmaraja, J. 2015. Synthesis, characterization, DNA interaction and pharmacological studies of substituted benzophenone derived Schiff base metal (II) complexes, *Journal of Saudi Chemical Society*; 19: 207-216.
- [9] Raman, N, Selvan, A, Sudharsan, S. 2011. Metallation of ethylenediamine based Schiff base with biologically active Cu (II), Ni (II) and Zn (II) ions: synthesis, spectroscopic characterization, electrochemical behaviour, DNA binding, photonuclease activity and in vitro antimicrobial efficacy, *Spectrochimica Acta Part A*; 79: 873-883.
- [10] Chandra, S, Gautam, S, Rajor, HK, Bhatia, R, 2015. Syntheses, spectroscopic characterization, thermal study, molecular modeling, and biological evaluation of novel Schiff's base benzil bis(5-amino-1,3,4-thiadiazole-2-thiol) with Ni(II), and Cu(II) metal complexes. *Spectrochimica Acta Part A: Molecular and Biomolecular Spectroscopy*; 137: 749-760.

- [11] Reddy, PR, Rajeshwar, S, Satyanarayana, B. 2016. Synthesis, characterization of new copper (ii) Schiff base and 1,10 phenanthroline complexes and study of their bioproperties, *Journal of Photochemistry & Photobiology, B: Biology*;160: 217-224.
- [12] Collin, F, Sasaki, I, Eury, H, Fuller, P, Hureau, C. 2013. Pt(II) compounds interplay with Cu(II) and Zn(II) coordination to the amyloid- β peptide has metal specific consequences on deleterious processes associated to Alzheimer's disease, *Chemical Communications*; 49: 2130-2132.
- [13] Sasaki, I, Bijani, C, Ladeira, S, bourdon, V, Faller, P, Hureau C. 2012. Interference of a new cyclometallated Pt compound with Cu binding to amyloid- β peptide, *Dalton Transactions*; 41(12): 6404-6407.
- [14] McColl G, Roberts BR, Pukala TL, Kenche VB, Roberts CM, Link CD, Ryan TM, Masters CL, Barnham KJ, Bush AI, Cherny RA. 2012. Utility of an improved model of amyloid-beta ($A\beta_{1-42}$) toxicity in *Caenorhabditis elegans* for drug screening for Alzheimer's disease, *Molecular Neurodegeneration*; 7: 57.
- [15] Price, JH, Williamson, AN, Schramm, R.F, Wayland, BB. 1972. Palladium(II) and platinum(II) alkyl sulfoxide complexes. Examples of sulfur-bonded, mixed sulfur- and oxygen-bonded, and totally oxygen-bonded complexes, *Inorganic Chemistry*; 11(6): 1280-1284.
- [16] Ma, G, Huang, F, Pu, X, Jia, L, Jiang, T, Li, L, Liu, Y. 2011. Identification of [PtCl₂(phen)] Binding Modes in Amyloid- β Peptide and the Mechanism of Aggregation Inhibition, *Chemistry A European Journal*; 17: 11657-11666.
- [17] Zhang, XL. 2016. Copper(II) Complexes With Bis-Schiff Bases: Synthesis, Crystal Structures, and Antibacterial Activities, *Metal-Organic, and Nano-Metal Chemistry*; 46: 1848-1853.
- [18] Bekhit, AA, El-Sayed, OA, Al-Allaf, TAK, Aboul-Enein, HY, Kunhi M, Pulicat, SM, Al-Hussain, K, Al Khodairy, F, Arif, J. 2004. Synthesis, characterization and cytotoxicity evaluation of some new platinum(II) complexes of tetrazolo[1,5-a]quinolines, *European Journal of Medicinal Chemistry*; 39: 499-505.
- [19] Miles, BA, Patterson, AE, Vogels, CM, Decken, A, Waller, JC, Morin, PJ, Westcott, SA. 2016. Synthesis, characterization, and anticancer activities of lipophilic pyridinecarboxaldimine platinum(II) complexes, *Polyhedron*; 108: 23-29.
- [20] Gümüş, F, Eren, G, Açıık, L, Çelebi, A, Öztürk, F, Yılmaz, Ş, Sağkan, RI, Gür, S, Özkul, A, Elmalı, A, Elerman, Y.2009. Synthesis, Cytotoxicity, and DNA Interactions of New Cisplatin Analogues Containing Substituted Benzimidazole Ligands, *Journal of Medicinal Chemistry*; 52(5): 1345-1357.

[21] Jin, L, Sakiyan, İ, Gonzales, NS, Lane, D, Cherala, S. 2014, Synthesis, characterization and Cu²⁺ binding studies of 1-histidine ester of 8-hydroxyquinoline, *Inorganica Chimica Acta*; 423: 72-78.

Energy Production From Flue Gas of Sinter Plant Circular Coolers

Tuba Nur AKÇALI ¹, Yıldız KOÇ ^{2*}, Özkan KÖSE ²

¹Iskenderun Technical University, Institute of Engineering and Science, Hatay, Türkiye

²Iskenderun Technical University, Hatay, Türkiye

Received: 05/04/2024, Revised: 10/06/2024, Accepted: 11/06/2024, Published: 31/08/2024

Abstract

This study aims to utilise from the env-friendly recovery technologies for the waste heat released from circular coolers of energy-intensive systems to the atmosphere in the sinter plant due to reaching carbon emissions to critical levels and decreasing fossil fuel sources. For sinter plant energy waste heat recovery, the organic Rankine cycle (ORC) is selected. The performance metrics, including mass flow rates, gross power, power consumption of the pump and net power output in the study scope are evaluated considering variations in exhaust gas throughout a year. The system underwent energy and exergy analyses, determining the maximum performance values for each month. This was achieved by utilizing R123 as the organic fluid within the ORC, operating between pressures ranging from 7.5 bar to 36 bar. As a result, the highest net power was achieved in August, and the efficiency of exergy was determined to be 63%. Recycling of waste energy not only meets the electricity consumption of the sinter cooler system fans but also leaves 62% excess electrical energy. Furthermore, this value corresponds to approximately 18.3% of the annual energy requirement of the entire sinter plant.

Keywords: Sinter, waste heat, organic Rankine cycle, energy, exergy

Sinter Fabrikası Dairesel Soğutucu Baca Gazından Enerji Üretimi

Öz

Bu çalışmada karbon emisyonlarının kritik seviyelere ulaşması ve fosil yakıt kaynaklarının azalması nedeniyle sinter tesisinde enerji yoğun sistemlerin dairesel soğutucularından atmosfere salınan atık ısının çevre dostu geri kazanım teknolojilerinden faydalanılması amaçlanmaktadır. Sinter tesisi enerji atık ısısının geri kazanımı için organik Rankine çevrimi (ORC) seçilmiştir. Çalışma kapsamındaki kütle akış hızları, brüt güç, pompanın güç tüketimi ve net güç çıkışını içeren performans metrikleri, bir yıl boyunca egzoz gazındaki değişimler dikkate alınarak değerlendirilmektedir. Sistemin enerji ve ekserji analizleri yapılarak her ay için maksimum performans değerleri belirlendi. Bu, 7,5 bar ile 36 bar arasında değişen basınçlar arasında çalışan, ORC içerisinde organik sıvı olarak R123 kullanılarak elde edildi. Sonuç olarak en yüksek net güce ağustos ayında ulaşılmış ve ekserji verimi %63 olarak belirlenmiştir. Atık enerjinin geri dönüşümü, sinter soğutucu sistem fanlarının elektrik tüketimini karşılamanın yanı sıra, geriye %62 oranında elektrik enerji fazlası bırakılmaktadır. Ayrıca bu değer tüm sinter tesisinin yıllık enerji ihtiyacının yaklaşık %18,3'üne karşılık gelmektedir.

Anahtar Kelimeler: Sinter, atık ısı, organik Rankine çevrimi, enerji, ekserji

*Corresponding Author: yildiz.koc@iste.edu.tr
Tuba Nur AKÇALI, <https://orcid.org/0009-0003-6835-3347>
Yıldız KOÇ, <https://orcid.org/0000-0002-2219-645X>
Özkan KÖSE, <https://orcid.org/0000-0002-9069-1989>

1. Introduction

Due to rising energy requirements driven by factors such as technological advancements, industrialization, economic growth, population increases, and urbanization, there's a consistent upward trend in energy demand in our era. The surge in global population and evolving lifestyle patterns have led to unprecedented energy needs. Moreover, challenges like inter-country conflicts, natural calamities, and erratic weather phenomena pose substantial threats to energy security. However, despite these challenges, a significant portion of heat, serving as the primary energy source for numerous industrial processes, is often generated excessively and released into the atmosphere without being harnessed [1-3]. Given the escalating demand, technologies for recovering waste heat hold paramount importance in the industrial sector owing to the substantial energy potential of waste heat. Additionally, surplus heat generated in energy-intensive operations should be actively converted into usable electricity through eco-friendly waste heat recycling technologies [4-7]. Despite the world's daily consumption of approximately 76 million barrels of fossil fuels, over fifty percent of the generated energy is dissipated as residual heat, usually falling within the temperature range of 100 to 220°C. [8-11]. This pattern is on the rise in correlation with the world population growth and the development of economies. Therefore, by incorporating practical methods and maximizing the utilization of waste heat, it is possible to reduce fuel consumption in existing energy production systems substantially. Furthermore, this approach aids in mitigating the adverse effects of several critical challenges related to the environment, including changes in the climate, the increase in Earth's average surface temperature, the reduction of ozone molecules in the Earth's stratosphere, and contamination of the air [12]. Despite challenges, there are promising indications of a shift towards clean energy gaining momentum. Both global and national initiatives for achieving net zero emissions are anticipated to result in a 1.2% decline in primary energy consumption by 2030, with projections extending to 2050 [13]. This underscores the significance of waste energy recycling technologies, highlighting the need to enhance current systems rather than building new energy production facilities. Traditional conversion of energy techniques like steam turbine processes struggles to harness waste heat at lower and moderate temperatures effectively due to their reliance on high temperatures. Consequently, several environmentally friendly technologies for converting energy, similar to the Kalina and ORC systems, have been developed to enhance energy production efficiency and decrease the usage of fuel to a certain degree [14-17].

A research indicates that cycle performance is greatly influenced by factors including the heat source, choosing the appropriate fluid used in the process, and operating conditions [18]. It is asserted that ORC is particularly well-suited for lower-temperature heat sources when contrasted with alternative cycles such as Kalina cycles [19, 20]. Also, numerous articles have been dedicated to systems utilizing waste heat. Yang et al. performed the energy and power optimization of the supercritical ORC system. The highest power output was achieved when R143 organic fluid was used. Also, as a result of optimization, thermal efficiency and power output were increased by 7.13% and 39.45% respectively [21].

Quoilin et al. [22] and Calise et al. [23] studied the optimization and efficiency of a solar-powered ORC system. Meanwhile, Liu et al. [24] focused on designing, analysing, and optimizing a third-generation system based on biomass, exploring the integration of electricity, heating, and freshwater production. Their research employed optimization techniques for multiple objectives using particle swarm optimization to identify the optimal operational parameters of the system across various optimization scenarios. In their research, Liu et al. [25] examined systems employing three different energy cycles: Supercritical Rankine Cycle (SRC), ORC, and Supercritical Brayton Cycle (SBC). Through their investigation, they highlighted the specific pros and cons of each cycle. Their findings suggest that ORC is best suited for recovering waste heat at low temperatures, and SRC is ideal for tasks involving moderate temperatures. In contrast, SBC is most effective for producing energy under high-temperature conditions. Yu et al. [26] have developed a simplified theoretical approach to predict the thermal degradation temperatures of organic process fluid, aiming to enhance the effectiveness and safety of ORC systems. Their analysis indicates that calculating the primary reactions identified can reduce costs while maintaining prediction accuracy. In their research, Feng et al. [27] suggest that utilizing low-quality sinter cooling flue gas employing an ORC cycle utilizing R245 fluid and a single heat source can significantly boost the thermal energy recovery rate of sinter waste. They propose that effective energy conservation can be achieved by determining optimal temperature and thermal parameters. By employing these optimal parameters, the energy recovery rate from sinter waste can increase up to 64.86%. Akkaya et al. [28] conducted an assessment of the energy efficiency of integrated power generation systems based on fuel cells and ORC. Their study revealed that integrating waste heat from fuel cells enhanced the overall energy efficiency of the integrated system by approximately 14% to 25%. The selection of operational media is a critical factor impacting the thermodynamic efficiency of the ORC system. Although ORC systems can employ various organic fluids as process media, selecting the optimal one requires a thorough analysis considering both environmental impacts and the performance of the system. Wang et al. [29] proposed a multi-criteria optimization framework to evaluate the influence of process fluids on ORC performance. Thirteen fluids were examined, with R123 identified as the best option for source temperatures ranging from 100 to 180 degrees Celsius, while R141b was deemed optimal for temperatures exceeding 180 degrees Celsius. However, they highlighted that the ORC cycle would not be economically feasible if the source temperature falls below 100 degrees Celsius. Xu et al. [30] discussed the effects of 30 different fluids on the maximum achievable thermal efficiency and its constraints on thermodynamic excellence in both basic and regenerative ORCs, which vary based on the working temperatures. They developed charts to aid in selecting suitable process fluids for both s-ORC and r-ORC setups. Haervig et al. [31] offered guidelines for choosing the optimal process media for ORC systems, examining twenty-six process fluids employed in ORC systems with temperatures of the heat source ranging from 50 to 280°C. They found that process fluids containing isopentane, pentane, and ethanol, such as R124, R245FA, R23, R123, R7146, R141b, R218, R236EA and R227EA yielded the utmost power generation over the temperature span of 50 to 280°C. Jeong et al. [32] investigated many organic working fluids. They obtained more power output (250 kW) from R245ca compared to R245fa. However, they asserted that R245fa notably drew attention due to its lower compact turbine size. Elmailhy et al. [33] examined the ORC system for utilizing the cooling water released into the atmosphere through

the car engine. They analyzed 16 working fluids. The best thermal efficiencies were calculated as 7.49 and 7.76% when using R123 and R245fa in the ORC system, respectively.

Above, many studies have been carried out on organic Rankine cycles and working fluids. However, there are almost no studies examining the thermodynamic performances of the ORC cycle using R123 fluid to evaluate the flue waste gas of the sintering system operating with coke gas. In addition, there is almost no study that analyses the performance of the waste heat recycling system by measuring the exhaust gas temperature of the sintering system from a facility separately for each month throughout the year.

In this study, sintering system facility cooler chimney exhaust gas temperature values were measured for every month throughout the year. The actual exhaust gas chemical content was then determined. Then, an organic fluid that could operate between these temperatures was determined. ORC, which uses R123 as the working fluid, was examined between 7.5 bar and 36 bar turbine inlet pressures, and the values showing maximum performance were calculated for each month. Moreover, energy and exergy analyzes of the system were carried out.

2. Material and Methods

2.1. System Description

The objective of this study is to assess the thermodynamic performance of the exhaust gas of a Sinter cooler system operating in a sinter facility in Türkiye. This research aims to enhance heat recovery efficiency by integrating the exhaust gas released into the air with an ORC. Figure 1 illustrates the schematic layout of the system for recovering waste heat, planned for the facility.

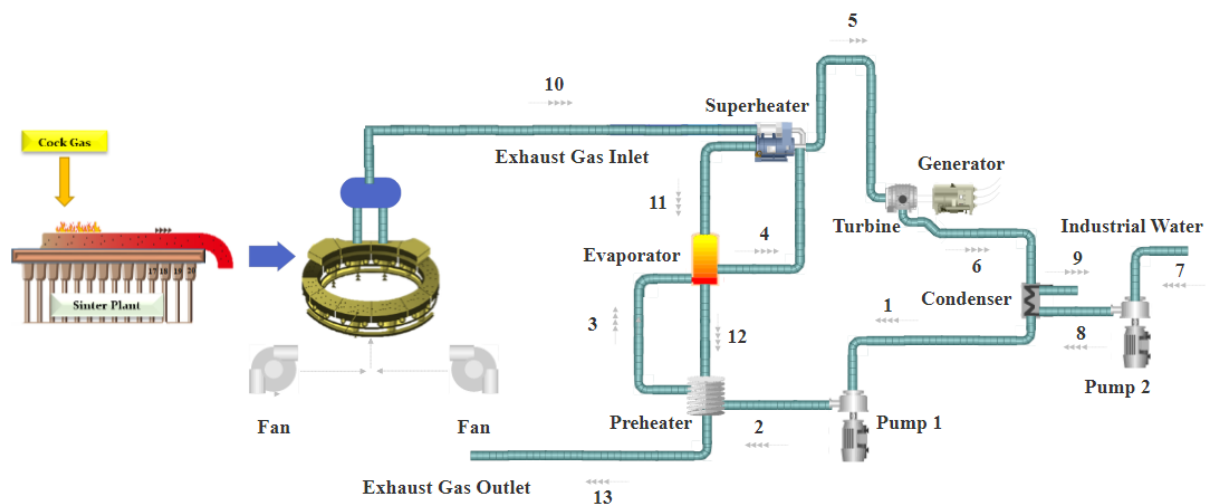


Figure 1. ORC cycle energy production from the waste heat of the circular coolers of the sinter system

As well known, the operational principle of the ORC system appears to be similar to that of the traditional Rankine cycle, there exist notable distinctions between the two cycles, particularly in terms of the process media. Figure 1 depicts an ORC system utilizing an organic process media. The exhaust gas from the Circular Cooler Stack of the Sintering Plant enters the ORC

system (Point 10) at varying temperatures each month throughout the year, and after thermal energy exchange occurs in the superheater, evaporator, and preheater (10 → 13), it is released into the atmosphere from the stack. Once the system is pressurized using the pump (1 → 2), the organic media vaporized by the preheater (2 → 3), evaporator (3 → 4), and superheater (4 → 5) is transmitted to the ORC turbine and generator, which produce mechanical energy and electricity (5 → 6). The process media undergoes cooling in the condenser, causing it to transition from gas to liquid phase as it exits the ORC turbine (6 → 1). Approximately 20°C water from the factory service water line, at a pressure of 3 bars, is pressurized by the pump (7 → 8) and facilitates heat transfer with entry and exit to the condenser (8 → 9). Thus, the organic fluid undergoes a phase change from gas to liquid (6 → 1). A hybrid cycle has been engineered and optimized to recuperate excess heat emitted by gases released from the Circular Cooler Stacks of the Sintering Plant. The aim is to enhance the overall system effectiveness through this approach. The specified nominal parameters for the designed ORC are outlined in Table 1.

Table 1. Nominal parameters for the designed ORC

Parameter	Value	Unit
$\eta_{Pum;is}$	80	%
$\eta_{Tur;is}$	88	%
$T_{CW;in}$	20	°C
$T_{CW;out}$	25	°C
$\dot{m}_{sin;exh}$	803662	kg/h
$P_{sin;exh}$	2	bar
$T_{sin;exh,in}$	137-235	°C
$T_{sin;exh,out}$	90-165	°C
T_{Pinch}	10	°C
Fuel Type	Coke gas	-

2.2. Mathematical Model

An ORC system has been incorporated into the Circular Cooler exhaust gas system of the Sintering Plant to efficiently harness the waste heat. ORC systems employ organic process media, and it's widely recognized that the selection of these fluids significantly influences the ORC system's performance. Hence, this study undertook an in-depth examination of the energy and exergy analyses of the system, grounded in the fundamental principles of thermodynamics. The aim was to observe the thorough impacts of the chosen process media on the entire system. The data utilized in this analysis were sourced from Steag GmbH's EBSILON® Professional software. The energy and exergy equations for the ORC design are outlined below [34-43].

General mass, energy and exergy equations are provided below:

The equation for mass balance utilized in these calculations is as follows:

$$\sum \dot{m}_{in} = \sum \dot{m}_{out} \quad (1)$$

The equation for energy balance employed in these calculations is as follows:

$$\dot{Q} + \dot{W} = \sum \dot{m}_{out} h_{out} - \sum \dot{m}_{in} h_{in} \quad (2)$$

Within this equation, \dot{Q} and \dot{W} represent heat and power generation, respectively. The equation for exergy balance utilized in these computations is as follows:

$$\dot{E}_{in} = \dot{E}_{out} + \dot{E}_{dest} \quad (3)$$

Exergy flow is represented by \dot{E} , with subscripts "in", "out", and "dest" denoting exergy in, exergy out, and exergy destruction, respectively. Exergy flow is calculated as follows:

$$\dot{E} = \dot{m}\psi \quad (4)$$

The symbol for specific exergy is ψ , which can be ascertained utilizing the subsequent expression:

$$\psi = (h - h_0) - T_0(s - s_0) \quad (5)$$

Exergy represents utilisable work. Therefore, the exergetic work is assumed to be 100%. However, the exergetic efficiency for heat is typically less than 100%. The calculation for the exergy flow related to heat is as follows:

$$\dot{E} = \left(1 - \frac{T_0}{T_{sur}}\right) \dot{Q} \quad (6)$$

In this context, T_0 stands for the ambient temperature, while T_{sur} indicates the temperature of the surface engaged in transferring heat. While computing, the average value of the inlet and outlet temperatures of an element is considered as the temperature of the heat transfer surface. T_0 is assumed to reflect the average ambient temperature, set at 20°C.

The equations for energy and exergy in the ORC can be presented as follows:

The evaluation of the ORC based on energy and exergy principles is implemented for both the entire cycle and individual components. The overall heat exchange from the exhaust to the organic process media is derived as follows:

$$\dot{Q}_{in;ORC} = \dot{m}_{exh}(h_{10} - h_{13}) = \dot{m}_{ORC}(h_5 - h_2) \quad (7)$$

In this context, represents the rate of mass flow of the organic process media within the ORC. The computation for the resultant power generated by the ORC is expressed as follows:

$$\dot{W}_{net;ORC} = \dot{W}_{Tur;ORC} - \dot{W}_{Pum;ORC} \quad (8)$$

Here, $\dot{W}_{Tur;ORC}$, the power output from the ORC turbine, and $\dot{W}_{Pum;ORC}$, is the power utilized by the ORC pump. The exergy input to the ORC from the exhaust is calculated as follows:

$$\dot{E}_{in;ORC} = \dot{m}_{exh}(\psi_{10} - \psi_{13}) \quad (9)$$

The thermal and exergetic efficiencies of the ORC system are established using the subsequent formulations:

$$\eta_{ORC} = \frac{\dot{W}_{net,ORC}}{\dot{Q}_{in,ORC}} \quad (10)$$

$$\varepsilon_{ORC} = \frac{\dot{W}_{net,ORC}}{\dot{E}_{in,ORC}} \quad (11)$$

In the computations, steady-state conditions are presumed, and kinetic and potential energies are disregarded. The surrounding temperature of 20°C is taken into account.

2.3. Working Fluid

The choice of process media has a substantial impact on the efficiency in terms of heat utilization of ORC systems [43,44]. Choosing the right process media can minimize thermodynamic inefficiencies, allowing for increased enhanced efficiency in converting energy and reduced initial investment requirements [45]. Consequently, the selected media should exhibit ideal thermodynamic and transport characteristics under suitable temperature and pressure conditions, while also meeting requirements such as non-toxicity, cost-effectiveness, environmental compatibility, safety, non-flammability and enabling efficient energy utilization from available heat sources [46,47]. Moreover, the gradient of the fluid's saturation curve is vital for ORC system design, cost, and performance. Wet fluids may cause inefficiencies at certain operating conditions, while dry or isentropic fluids tend to offer more consistent performance. Therefore, careful consideration of the process media is pivotal as it directly impacts ORC system efficiency and reliability [43]. In this study, dichlorotrifluoroethane (R123, CF₃CHCL₂) is employed as the process media, possessing a molar mass of 152.9 g/mole, a normal boiling point of 300.97 K at 1 atmosphere, a pivotal temperature of 456.8 K, and a pivotal pressure of 3.66 MPa.

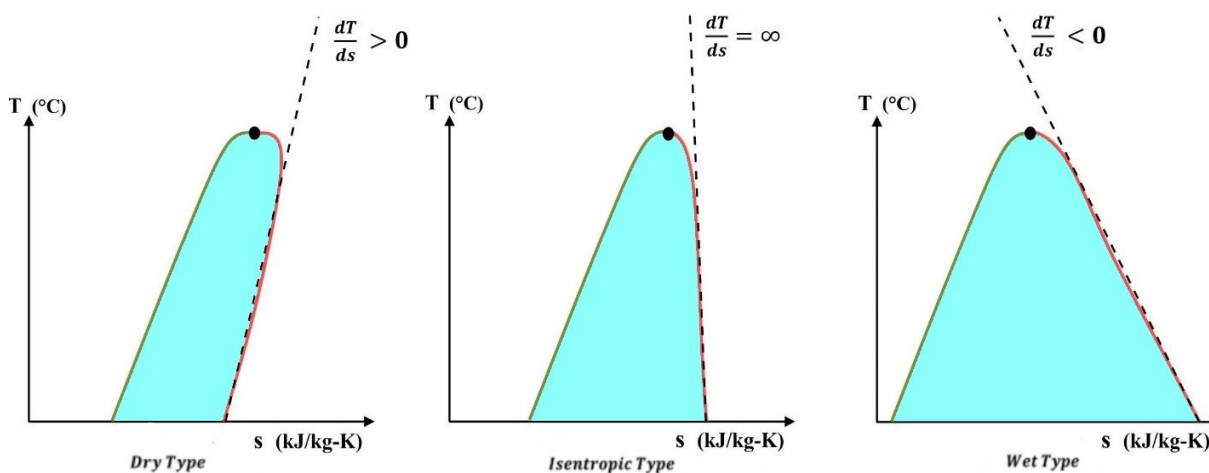


Figure 2. Temperature-entropy (T-s) diagram illustrates the thermodynamic properties of organic fluids in various states

When a process media demonstrates high performance values, its environmental repercussions can become significant. Conversely, a process media with low performance may lead to

substantial environmental drawbacks. To evaluate environmental impact, factors like Ozone Depletion Potential (ODP) and Global Warming Potential (GWP) must be considered. ODP, originally outlined in the Montreal Protocol, is determined by comparing the process media to R11 [48]. GWP represents the impact ratio over a 100-year period compared to CO₂. Given these definitions and criteria, an ideal organic fluid should exhibit high thermodynamic performance while maintaining ODP values close to zero and GWP values below 200 for environmental sustainability [48]. In this study, the proposed process media, R123, has an ODP value of 0.020 and a GWP of 77 [49]. Consequently, it is evident that R123 poses a significantly low environmental impact as a process media.

3. Result and Discussion

The most effective approach to assess a system's performance is to consider parameters derived from both the principles of the first and second laws of thermodynamics. This method offers crucial insights into the system's current status. Therefore, it's highly important to conduct both energy and exergy analyses based on operating pressure and temperature to make well-informed decisions. This section presents a thorough parametric optimization of the ORC, concentrating on pressure and temperature at the inlet of the turbine. The optimization includes a spectrum of pressures, from 7.5 to 36 bar, and temperatures ranging from 99°C to 225°C. Variations in the maximum thermodynamic performance metrics resulting from the parametric optimization of the ORC were examined for each month throughout the year. Subsequently, the maximum performance values for each month were compared based on the measured waste heat value. The variation of the temperature and pressure at the inlet of the turbine, at maximum performance for each month throughout the year is depicted in Figure 3.

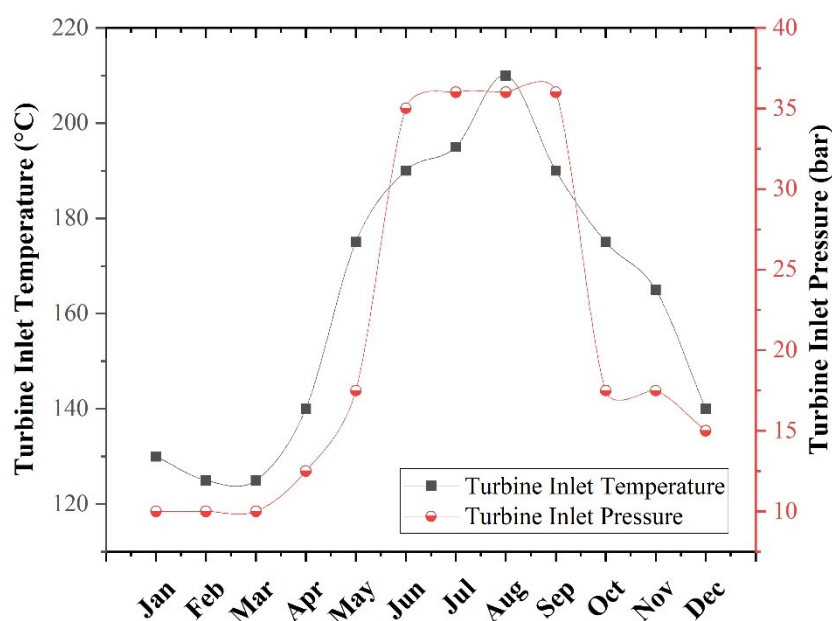


Figure 3. The Changes in the turbine inlet temperature and pressure of the ORC at maximum performance for each month throughout the year

The temperature at the turbine inlet is observed to be unstable, peaking during the summer months. This instability in the exhaust gas temperature of the sintering machine's cooling stack is attributed to the variability of parameters such as the chemical and physical properties of the bed material during the sintering process, material temperature, ore layer thickness, sinter machine speed, coke powder ratio, amount of water supplied for moistening, and most importantly, cooling efficiency, alongside the variability in weather conditions. Additionally, due to inevitable uncertainties in operating parameters within the sinter cooling process, such as flow and temperature fields, the performance of sinter cooling processes can exhibit uncertainties. Several parameters affect the exhaust gas outlet temperature of the sinter cooling stack every month, with weather conditions being one of the most notable. The minimum turbine inlet temperature is 125°C in February and March, with sinter production being 56,336 tons in February and 75,532 tons in March. The maximum turbine inlet temperature is 210°C in August, with sinter production reaching 336,376 tons in that month. Dry fluids tend to perform at their maximum near-saturation temperature. In January, February, and March, the turbine's inlet temperature ranges from 125°C at its lowest to 130°C at its highest, with a turbine inlet pressure of 10 bars for all three months. The point where maximum performance is achieved is at 36 bars. As the inlet temperature increases, the pressure at which maximum performance is achieved varies, attributed to the fluid being dry. Figure 4 illustrates the fluctuations in mass flow rate and power consumption of the pump within the ORC system across each month of the year.

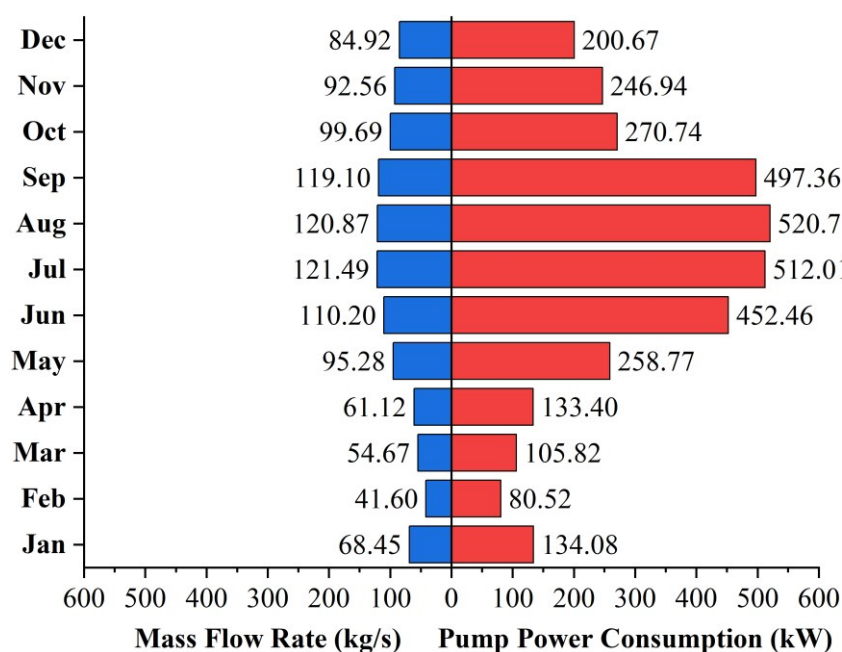


Figure 4. The variation in mass flow rate and pump power consumption within the ORC system at its maximum efficiency for the course of each month throughout the year

The amount of power consumed by the pump exhibits fluctuations throughout the year, with peaks observed in July, August, and September, as depicted in the graph. For example, the power consumption of the pump was found to be 512 kW when the rate at which mass flows through a system was 121.49 kg/s, 520.7 kW when the mass flow rate decreased to 120.87 kg/s,

and subsequently reduced to 497.36 kW when the mass flow rate further decreased to 119.1 kg/s. The fluctuation in exhaust gas inlet temperature over the course of the year has a notable impact on both the mass flow rate and pump power consumption. The exergy destruction of the utilized equipment in the ORC system at maximum performance for each month throughout the year is depicted in Figure 5.

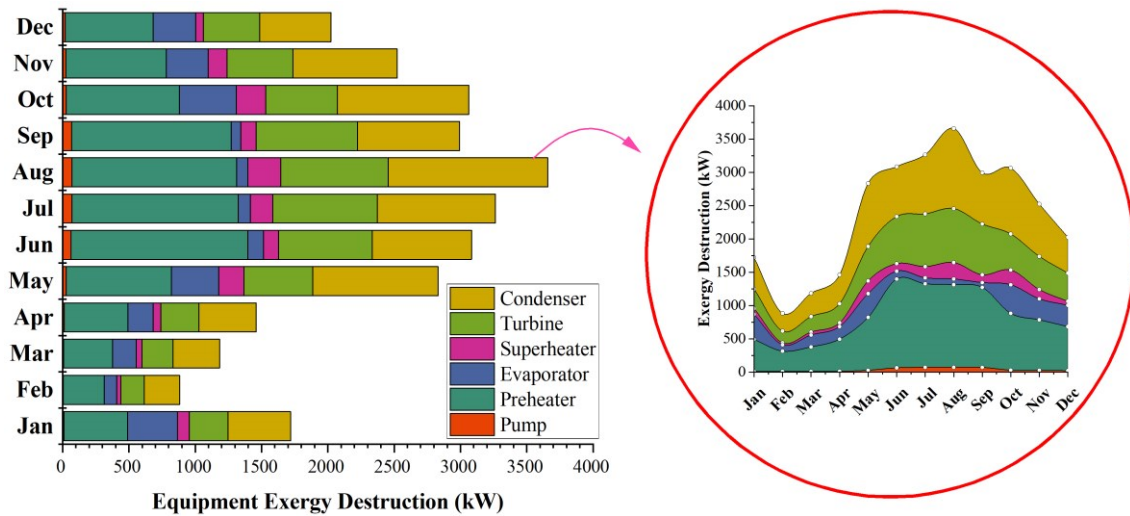


Figure 5. The exergy destruction of the equipment utilized in the ORC system at its maximum performance for each month throughout the year

Throughout the year, the preheater equipment showed the highest exergy destruction among all components within the ORC system, with a magnitude of 1333 kW, while the lowest exergy destruction was in the pump equipment, with a magnitude of 6 kW. The condenser equipment followed closely behind, ranking second in terms of notable exergy degradation, with a magnitude of 1204 kW. Hence, it is evident from the calculation results that there is considerable potential for improvement in the preheater and condenser equipment. The exergy efficiency of the equipment used in the ORC system at maximum performance for each month over the course of the year is depicted in Figure 6.

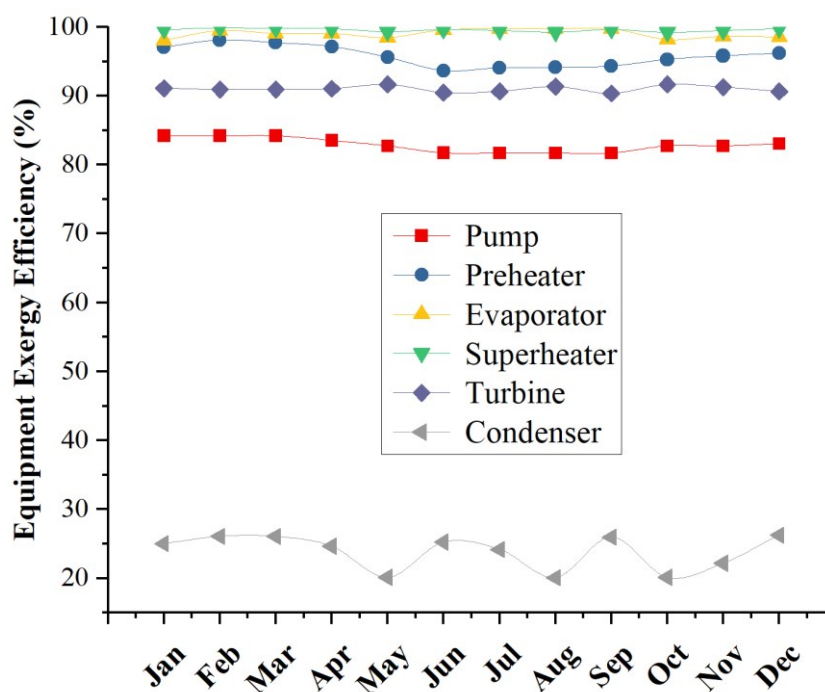


Figure 6. The equipment's exergy efficiency at its maximum performance for each month throughout the year

Throughout the year, it is observed that the exergy efficiencies of the pump, preheater, evaporator, superheater, and turbine do not undergo significant fluctuations, indicating that the system operates as desired. However, it is noted that the condenser exhibits notably lower exergy efficiency and exhibits more variability compared to the efficiencies of other equipment. Therefore, there appears to be more potential for improvement in the condenser equipment, offering the possibility of making the system more efficient. Additionally, decreases in exergy efficiency are observed in May, August, and October, with efficiency values of 20.13%, 20.10%, and 20.13%, respectively. The efficiencies of the evaporator and superheater are found to be very close to each other on a monthly basis. The superheater demonstrates a maximum efficiency of 99.84% throughout the year, whereas the evaporator reaches a maximum efficiency of 99.73%. The overall power produced by the ORC system and the exhaust gas heat input from the sinter cooler stack at maximum performance for every month across the year is depicted in Figure 7.

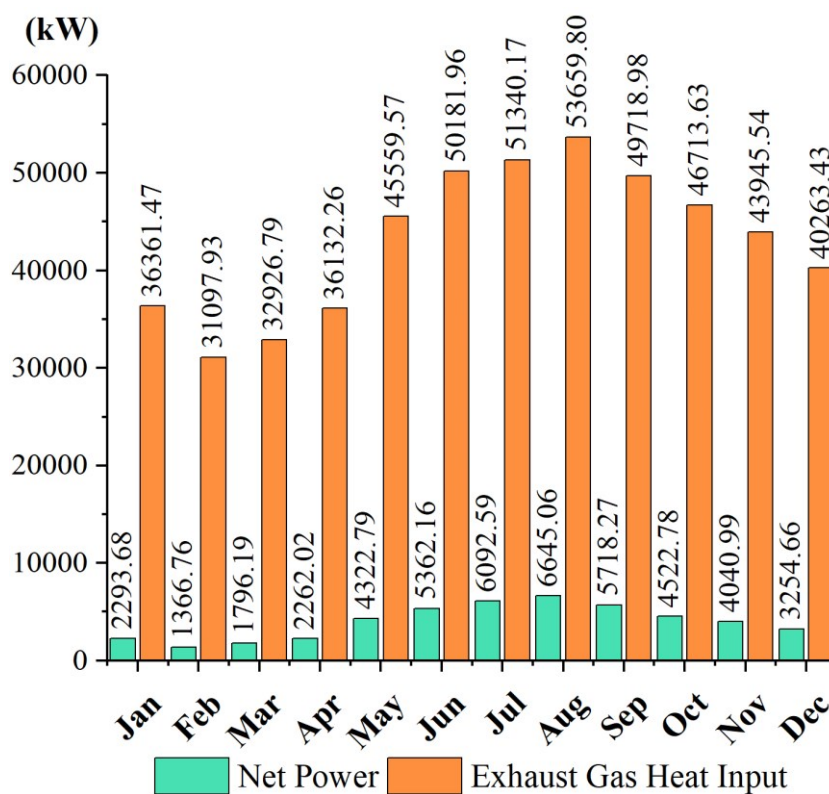


Figure 7. The net power of the ORC system and the exhaust gas heat input from the sinter cooler stack at maximum performance for every month across the year

From the graph, it was noted that as the exhaust gas heat input from the sintering system's cooler stack increases, there is a linear rise in the overall power output. In August, a peak in both heat input and variations in the net power were noticed owing to climatic conditions. The highest achievable net power output of the ORC system at peak performance was 6645 kW in August and 1367 kW in February. Throughout the year, the highest net power was obtained in July, August, and September, while the lowest was in February, March, and April. With this system, a total of 33374.563 MW of annual waste heat was recovered from the exhaust gases, out of a total of 362531.076 MW released from the sinter cooler stack to the atmosphere over the year. The average annual power consumption of the sinter plant's cooler system fans was calculated to be 20539.400 MW. Waste energy recovery not only meets the electricity consumption of the sinter cooler system fans but also leaves an excess of 62%, which accounts for approximately 18.3% of the sinter plant's annual energy demand. Therefore, the importance of heat recovery in sinter cooler stacks is crucial for systems to generate own energy consumption. Heat recovery in industrial facilities will contribute significantly to reducing emission rates and lowering new investment costs. The efficiency of thermal and exergy in the ORC system at peak performance for each month throughout the year is shown in Figure 8.

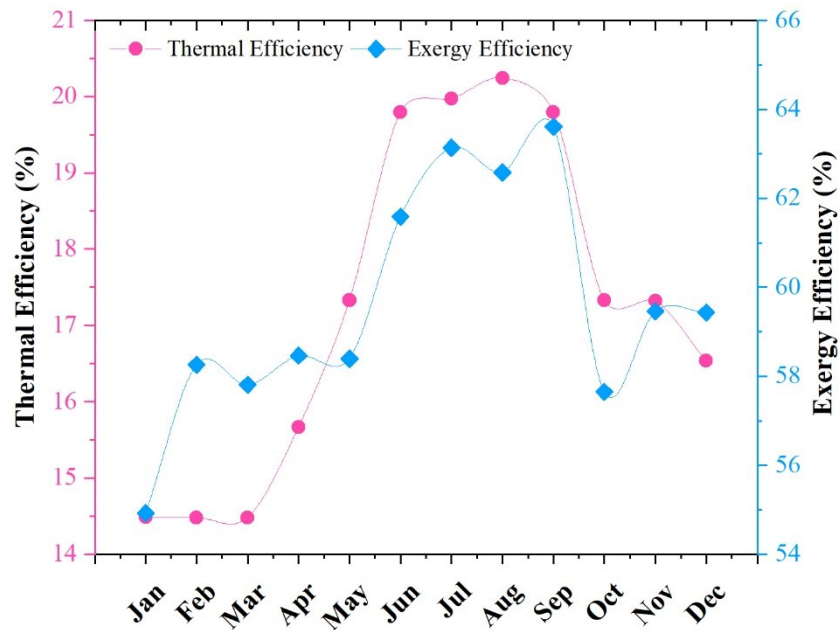


Figure 8. The thermal and exergy efficiency of the ORC system at its maximum performance for every month during the year

The maximum thermal and exergetic efficiencies of the ORC system performance for each month have been analysed throughout the year. It is observed from the graph that the efficiencies in both thermal and exergy are not constant and reach their highest levels during the summer months. Particularly in the summer months, the high exhaust gas temperature of the sintering system allows the turbine inlet pressure to reach higher levels due to the thermophysical characteristics of the fluid, significantly affecting thermal and exergy efficiency. The thermal efficiency peaks in August at 20.24%, while the exergy efficiency peaks in September, reaching its highest value at 64%. Conversely, the thermal efficiency is lowest in March at 14.48%, while the exergy efficiency is lowest in January at 54.92%.

4. Conclusion

As widely recognized, the choice of the process media employed in an ORC system is pivotal for its thermodynamic efficiency. Therefore, choosing the suitable process medium before system design can mitigate thermodynamic inefficiencies can lead to higher net power output with reduced capital expenditures. In this investigation, the R123 fluid, anticipated to exhibit optimal cycle conditions, has been employed. The research investigates multiple performance parameters of the ORC, covering exergy efficiency, net thermal efficiency, as well as metrics such as total power output, overall power, power consumed by the pump, and flow rates of mass. These are analysed across different turbine inlet pressures and temperatures. Thermodynamic parameters for each ORC component were sourced from Steag GmbH's EBSILON® Professional software utilized thereafter to compute performance metrics using thermodynamics' fundamental laws. This thorough optimization endeavour has produced several significant findings:

- When examining the variation in flow rate of mass and power consumed by the pump at maximum performance throughout the year for the ORC system, it's clear that the pump's power consumption fluctuates throughout the year, peaking in July, August, and September, as observed from the graph. Correspondingly, when the flow rate of mass is 121.49 kg/s, the pump power consumption is calculated to be 512 kW, while it reaches 520.7 kW when the mass flow rate is 120.87 kg/s. Furthermore, it was discovered that when the mass flow rate is 119.1 kg/s, the pump's power consumption measures 497.36 kW. The fluctuation in the exhaust inlet temperature throughout the year impacts both pump power consumption and the flow rates of mass.
- When examining the degradation of exergy within the equipment used in the ORC system at maximum performance throughout the year, it was noted that the preheater equipment experienced the highest level of exergy destruction. The condenser equipment followed closely behind, ranking second in terms of notable exergy degradation, with a magnitude of 1204 kW. In contrast, the pump equipment exhibited the lowest level of exergy destruction, with a magnitude of 6 kW. Therefore, it is evident from the calculation results that there is considerable potential for improvement in the preheater and condenser equipment.
- It has been determined that the condenser's exergy efficiency is considerably lower and more fluctuating compared to the efficiencies of other equipment. Therefore, it is observed that there is a greater potential for improvement in the condenser equipment, and there is a possibility of making the system more efficient.
- Throughout the year, it was observed from the graph that as the exhaust gas thermal input from the sintering system's cooling stack increased, there was a linear increase in the overall power output of the ORC system. The highest net power was obtained during July, August, and September, while the lowest was during February, March, and April. For one year, this system facilitated the recycling of 33,374.56 MW of waste heat out of a total of 362,531.08 MW released from the sinter cooling stack into the atmosphere. The average annual power consumption of the sinter plant's cooling system fans was calculated to be 20,539.40 MW. With waste energy recycling, not only does it cover the electricity consumption of the sinter cooling system fans, but there is also an excess of 62% electricity. Additionally, this amount corresponds to roughly 18.3% of the total yearly energy demand for the entire sinter plant.
- Throughout the year, the efficiencies in both thermal and exergetic domains within the ORC system at peak performance were examined for each month. It was observed from the graph that both thermal and exergy efficiencies were not constant and reached their highest levels during the summer months. Particularly in the summer months, the high exhaust gas temperature of the sintering system and the fluid's capability to raise the pressure at the turbine inlet to higher levels due to its thermophysical properties were found to significantly affect both thermal and exergy efficiency. August saw the peak thermal efficiency at 20.24%, whereas September marked the highest exergy efficiency at 64%. Conversely, the least thermal efficiency was observed in March, standing at 14.48%, whereas the lowest exergy efficiency was observed in January at 54.92%.

The ORC system is one of the most remarkable energy conversion systems among recovery systems with low waste heat. It has become widespread in the iron and steel industry. In this study, The analyzes were made considering that the sinter plant was operating continuously. However, in real industrial processes, downtimes can be long. In future studies, an assisted system will be designed and thermodynamic analysis of the ORC system will be carried out against undesirable situations.

Ethics in Publishing

There are no ethical issues regarding the publication of this study.

Author Contributions

Tuba Nur AKÇALI – Conceptualization; Methodology; Data collection; Formal analysis; Methodology; Writing – review & editing. Yıldız KOÇ – Conceptualization; Advisor; Data curation; Formal analysis; Investigation; Methodology; Resources; Software; Validation; Roles/Writing - original draft; Writing – review & editing. Özkan KÖSE - Conceptualization; Advisor; Software; Visualization Methodology; Data curation; Formal analysis; Methodology; Writing – review & editing.

Nomenclature

\dot{E}	exergy flow (kW)
GWP	global warming potential
h	enthalpy (kJ/kg)
\dot{m}	mass flow rate (kg/s)
ODP	ozone depletion potential
ORC	organic Rankine cycle
\dot{Q}	heat flow (kW)
P	pressure (bar)
s	entropy (kJ/kgK)
T_0	ambient temperature (°C)
T	temperature (°C)
\dot{W}	power (kW)

Greek letters

ψ	specific exergy (kJ/kg)
ε	exergetic efficiency (%)
η	thermal efficiency (%)

Subscripts

<i>boil</i>	boiling
<i>crit</i>	critical
<i>CW</i>	cooling water
<i>dest</i>	destruction
<i>exh</i>	exhaust gas

<i>in</i>	inlet
<i>max</i>	maximum
<i>out</i>	exit
<i>P_{um}</i>	pump
<i>sur</i>	heat transfer surface
<i>T_{ur}</i>	turbine

References

- [1] B. Dai, C. Liu, S. Liu, D. Wang, Q. Wang, T. Zou, X. Zhou, Life cycle techno-environmental assessment of dual-temperature evaporation transcritical CO₂ high-temperature heat pump systems for industrial waste heat recovery, *Appl. Therm. Eng.* 219 (2023), 119570.
- [2] H. Jouhara, N. Nieto, B. Egilegor, J. Zuazua, E. Gonz'alez, I. Yebra, A. Igesias, B. Delpech, S. Almahmoud, D. Brough, J. Malinauskaite, Waste heat recovery solution based on a heat pipe heat exchanger for the aluminium die casting industry, *Energy* 266 (2023), 126459.
- [3] Y. Zhang, L. Yu, K. Cui, H. Wang, T. Fu, Carbon capture and storage technology by steel-making slags: recent progress and future challenges, *Chem. Eng. J.* 455(2023), 140552.
- [4] Cheng, H., Liu, Y., Cao, F., Zhang, Q., & Ouyang, J. (2022). Integration of an electronic thermoelectric material with ionogels to harvest heat from both temperature gradient and temperature fluctuation. *Chemical Engineering Journal*, 450, 138433.
- [5] Shan, K., Luo, Q., Yun, P., Huang, L., Huang, K., Cao, B., ... & Jiang, H. (2023). All-day working photovoltaic cooling system for simultaneous generation of water and electricity by latent heat recycling. *Chemical Engineering Journal*, 457, 141283.
- [6] Luo, Q., He, A., Xu, S., Miao, M., Liu, T., Cao, B., ... & Jiang, H. (2023). Utilization of low-grade heat for desalination and electricity generation through thermal osmosis energy conversion process. *Chemical Engineering Journal*, 452, 139560.
- [7] C. Ononogbo, E.C. Nwosu, N.R. Nwakuba, G.N. Nwaji, O.C. Nwifo, O. C. Chukwuezie, M.M. Chukwu, E.E. Anyanwu, Opportunities of waste heat recovery from various sources: Review of technologies and implementation, *Heliyon*. (2023).
- [8] Mahmoudi A, Fazli M, Morad MR. A recent review of waste heat recovery by Organic Rankine Cycle. *Appl Therm Eng* 2018;143:660–75.
- [9] Koç A, Yağlı H, Koç Y, Uğurlu İ. Dünyada ve Türkiye’de Enerji Görünümünün Genel Değerlendirilmesi. *Eng Machin Mag* 2018;59(692).
- [10] Achinas S, Euverink GJW. Elevated biogas production from the anaerobic co-digestion of farmhouse waste: Insight into the process performance and kinetics. *Waste Manage Res* 2019. 0734242X19873383.
- [11] Achinas S, Krooneman J, Euverink GJW. Enhanced biogas production from the anaerobic batch treatment of banana peels. *Engineering* 2019.
- [12] Bao J, Zhao L. A review of working fluid and expander selections for organic Rankine cycle. *Renew Sustain Energy Rev* 2013;24:325–42.

- [13] İnternet: IEA, World Energy Outlook 2023, URL: World Energy Outlook 2023 – Analysis - IEA, Son Erişim Tarihi: 21.02.2024.
- [14] Yağlı, H., Koç, Y., Koç, A., Görgülü, A., & Tandiroğlu, A. (2016). Parametric optimization and exergetic analysis comparison of subcritical and supercritical organic Rankine cycle (ORC) for biogas fuelled combined heat and power (CHP) engine exhaust gas waste heat. *Energy*, 111, 923-932.
- [15] Yagli, H., Koc, A., Karakus, C., & Koc, Y. (2016). Comparison of toluene and cyclohexane as a working fluid of an organic Rankine cycle used for reheat furnace waste heat recovery. *International Journal of Exergy*, 19(3), 420-438.
- [16] Takleh, H. R., & Zare, V. (2019). Employing thermoelectric generator and booster compressor for performance improvement of a geothermal driven combined power and ejector-refrigeration cycle. *Energy Conversion and Management*, 186, 120-130.
- [17] Takleh, H. R., & Zare, V. (2019). Performance improvement of ejector expansion refrigeration cycles employing a booster compressor using different refrigerants: Thermodynamic analysis and optimization. *International Journal of Refrigeration*, 101, 56-70.
- [18] Bao, J., & Zhao, L. (2013). A review of working fluid and expander selections for organic Rankine cycle. *Renewable and sustainable energy reviews*, 24, 325-342
- [19] Chen, H., Goswami, D. Y., & Stefanakos, E. K. (2010). A review of thermodynamic cycles and working fluids for the conversion of low-grade heat. *Renewable and sustainable energy reviews*, 14(9), 3059-3067.
- [20] Sprouse III, C., & Depcik, C. (2013). Review of organic Rankine cycles for internal combustion engine exhaust waste heat recovery. *Applied thermal engineering*, 51(1-2), 711-722.
- [21] Yang, W., Feng, H., Chen, L., & Ge, Y. (2023). Power and efficiency optimizations of a simple irreversible supercritical organic Rankine cycle. *Energy*, 278, 127755.
- [22] Quoilin, S., Orosz, M., Hemond, H., & Lemort, V. (2011). Performance and design optimization of a low-cost solar organic Rankine cycle for remote power generation. *Solar energy*, 85(5), 955-966.
- [23] Calise, F., Capuozzo, C and Vanoli, L. (2013). Design and parametric optimization of an Organic Rankine Cycle powered by solar energy. *American Journal of Engineering and Applied Sciences*, 6(2), 178-204.
- [24] Liu, X., Hu, G., & Zeng, Z. (2022). Potential of biomass processing using digester in arrangement with a Brayton cycle, a Kalina cycle, and a multi-effect desalination; thermodynamic/environmental/financial study and MOPSO-based optimization. *Energy*, 261, 125222.
- [25] Liu, X., Hu, G., & Zeng, Z. (2023). Performance characterization and multi-objective optimization of integrating a biomass-fueled brayton cycle, a kalina cycle, and an organic rankine cycle with a claude hydrogen liquefaction cycle. *Energy*, 263, 125535.
- [26] Yu, W., Liu, C., Ban, X., Li, Z., Yan, T., Xin, L., & Wang, S. (2024). A novel method for predicting the thermal stabilization temperature of organic Rankine cycle system working fluids based on transition state theory. *Energy*, 130378.

- [27] Feng, J., Cheng, X., Wang, H., Zhao, L., Wang, H., & Dong, H. (2024). Performance analysis and multi-objective optimization of organic Rankine cycle for low-grade sinter waste heat recovery. *Case Studies in Thermal Engineering*, 53, 103915.
- [28] Akkaya, A. V., & Sahin, B. (2009). A study on performance of solid oxide fuel cell-organic Rankine cycle combined system. *International Journal of Energy Research*, 33(6), 553-564.
- [29] Wang, Z. Q., Zhou, N. J., Guo, J., & Wang, X. Y. (2012). Fluid selection and parametric optimization of organic Rankine cycle using low temperature waste heat. *Energy*, 40(1), 107-115.
- [30] Xu, W., Deng, S., Zhao, L., Su, W., Zhang, Y., Li, S., & Ma, M. (2018). How to quantitatively describe the role of the pure working fluids in subcritical organic Rankine cycle: A limitation on efficiency. *Energy conversion and management*, 172, 316-327.
- [31] Hærvig, J., Sørensen, K., & Condra, T. J. (2016). Guidelines for optimal selection of working fluid for an organic Rankine cycle in relation to waste heat recovery. *Energy*, 96, 592-602.
- [32] Jeong, Y. S., Park, K., Jang, Y. C., & Moon, S. J. (2024). Optimal working-fluid selection for organic Rankine cycle integrated into a combined cycle cogeneration plant. *Journal of Mechanical Science and Technology*, 38(4), 2073-2080.
- [33] Elmaihy, A., Rashad, A., Elweteedy, A., & Nessim, W. (2023). Energy and exergy analyses for organic Rankine cycle driven by cooling water of passenger car engine using sixteen working fluids. *Energy Conversion and Management: X*, 20, 100415.
- [34] Cengel, Y.A. and Boles, M.A. (2008) *Thermodynamics: an engineering approach*, McGraw-Hill Inc., 6th. Ed., New York, 2008.
- [35] Dincer, I., & Rosen, M. A. (2013). *Exergy: energy, environment and sustainable development*. Elsevier, 2nd. Ed., 2013.
- [36] Kotas, T. J. (2013). *The exergy method of thermal plant analysis*. Elsevier.
- [37] Safari, F., & Dincer, I. (2019). Development and analysis of a novel biomass-based integrated system for multigeneration with hydrogen production. *International Journal of Hydrogen Energy*, 44(7), 3511-3526.
- [38] Yağlı, H., Karakuş, C., Koç, Y., Çevik, M., Uğurlu, İ., & Koç, A. (2019). Designing and exergetic analysis of a solar power tower system for Iskenderun region. *International Journal of Exergy*, 28(1), 96-112.
- [39] Koç, Y., Yağlı, H., & Koç, A. (2019). Exergy Analysis and Performance Improvement of a Subcritical/Supercritical Organic Rankine Cycle (ORC) for Exhaust Gas Waste Heat Recovery in a Biogas Fuelled Combined Heat and Power (CHP) Engine Through the Use of Regeneration. *Energies*, 12(4), 575.
- [40] Koc, Y., Kose, O., & Yagli, H. (2019). Exergy analysis of a natural gas fuelled gas turbine based cogeneration cycle. *Int. J. Exergy*, 30, 103-125.
- [41] Ayub, A., Sheikh, N. A., Tariq, R., Khan, M. M., & Invernizzi, C. M. (2018). Exergetic optimization and comparison of combined gas turbine supercritical CO₂ power cycles. *Journal of Renewable and Sustainable Energy*, 10(4), 044703.
- [42] Abid, M., Adebayo, V. O., & Atikol, U. (2019). Energetic and exegetic analysis of a novel multi-generation system using solar power tower. *International Journal of Exergy*, 29(2-4), 211-235.

- [43] Vélez, F., Segovia, J. J., Martín, M. C., Antolín, G., Chejne, F., & Quijano, A. (2012). A technical, economical and market review of organic Rankine cycles for the conversion of low-grade heat for power generation. *Renewable and Sustainable Energy Reviews*, 16(6), 4175-4189
- [44] Andersen, W. C., & Bruno, T. J. (2005). Rapid screening of fluids for chemical stability in organic Rankine cycle applications. *Industrial & Engineering Chemistry Research*, 44(15), 5560-5566.
- [45] Pethurajan, V., Sivan, S., & Joy, G. C. (2018). Issues, comparisons, turbine selections and applications—An overview in organic Rankine cycle. *Energy conversion and management*, 166, 474-488.
- [46] Yang, A., Su, Y., Shen, W., Chien, I. L., & Ren, J. (2019). Multi-objective optimization of organic Rankine cycle system for the waste heat recovery in the heat pump assisted reactive dividing wall column. *Energy Conversion and Management*, 199, 112041.
- [47] Yang, A., Su, Y., Chien, I. L., Jin, S., Yan, C., & Shen, W. (2019). Investigation of an energy-saving double-thermally coupled extractive distillation for separating ternary system benzene/toluene/cyclohexane. *Energy*, 186, 115756.
- [48] Agromayor, R., & Nord, L. O. (2017). Fluid selection and thermodynamic optimization of organic Rankine cycles for waste heat recovery applications. *Energy Procedia*, 129, 527-534.
- [49] Shu, G., Zhao, M., Tian, H., Huo, Y., & Zhu, W. (2016). Experimental comparison of R123 and R245fa as working fluids for waste heat recovery from heavy-duty diesel engine. *Energy*, 115, 756-769.

Performance Analysis of NLP-Based Machine Learning Algorithms in Cyberbullying Detection

Funda AKAR^{1*}

¹Department of Computer Engineering, Faculty of Engineering and Architecture, Erzincan Binali Yıldırım University, Erzincan, Türkiye

Received: 26/04/2024, Revised: 25/06/2024, Accepted: 25/06/2024, Published: 31/08/2024

Abstract

In today's pervasive online landscape, the escalating threat of cyberbullying demands advanced detection and mitigation tools. This study utilizes Natural Language Processing (NLP) techniques to confront this imperative challenge, particularly in the dynamic realm of social media, focusing on tweets. A comprehensive NLP-based classification methods is deployed to uncover instances of cyberbullying. Nine prominent machine learning algorithms are meticulously evaluated: Logistic Regression, Decision Tree, Random Forest, Naive Bayes, K-Nearest Neighbor, Support Vector Machine, XGBoost, AdaBoost, and Gradient Boosting. Through the analysis, encompassing accuracy, precision, recall, and F1 score metrics, the study offers insights into the strengths and limitations of each approach. The findings carry profound implications for online user safeguarding and cyberbullying prevalence reduction. Notably, Random Forest and XGBoost classifiers emerge as pioneers with accuracy rates of 93.34% and 93.32%, respectively. This comparative research underscores the pivotal role of expert algorithmic choices in addressing the urgency of cyberbullying and has the potential to be a valuable resource for academics and practitioners engaged in combatting this pressing societal issue.

Keywords: Cyberbullying, Machine Learning, Multi-Class Classification, Natural Language Processing (NLP).

Siber Zorbalık Tespitinde NLP Tabanlı Makine Öğrenimi Algoritmalarının Performans Analizi

Öz

Günümüzün yaygın çevrimiçi ortamında, artan siber zorbalık tehdidi, gelişmiş tespit ve azaltma araçlarını gerektirmektedir. Bu çalışma, özellikle sosyal medyanın dinamik dünyasında, tweet'lere odaklanarak bu zorunlu zorlukla yüzleşmek için Doğal Dil İşleme (NLP) tekniklerinden yararlanmaktadır. Siber zorbalık örneklerini ortaya çıkarmak için kapsamlı NLP tabanlı sınıflandırma yöntemleri kullanılmıştır. Öne çıkan dokuz makine öğrenimi algoritması titizlikle değerlendirilmiştir: Lojistik Regresyon, Karar Ağacı, Rastgele Orman, Naive Bayes, K-En Yakın Komşu, Destek Vektör Makinesi, XGBoost, AdaBoost ve Gradient Boosting. Doğruluk, kesinlik, geri çağırma ve F1 puanı metriklerini kapsayan analiz aracılığıyla çalışma, her yaklaşımın güçlü yönlerine ve sınırlamalarına dair içgörüler sunmaktadır. Özellikle Random Forest ve XGBoost sınıflandırıcıları sırasıyla %93,34 ve %93,32 doğruluk oranlarıyla öncü olarak ortaya çıkmıştır. Bu karşılaştırmalı araştırma, siber zorbalığın aciliyetine değinerek güçlü algoritmik seçimlerin önemli rolünün altını çizmekte ve bu acil toplumsal sorunla mücadele eden akademisyenler ve uygulayıcılar için değerli bir kaynak olma potansiyeline sahiptir.

Anahtar Kelimeler: Siber Zorbalık, Makine Öğrenimi, Çok Sınıflı Sınıflandırma, Doğal Dil İşleme (DDİ).

1. Introduction

Bullying is any physical or verbal behavior that one person does to another person. This behavior is seen in almost every age group and is a serious social problem. On the other hand, Cyberbullying is the behavior done with various communication tools used on the internet. This type of behavior can be done in all kinds of social media, as well as frequently seen in social media [1]. Cyberbullying, which has increased a lot in recent years, has become difficult to prevent. Because the number of people using social media has increased considerably. Due to the increasing number of users and inadequate detection systems, this behavior, which annoys and humiliates other people, has unfortunately become unavoidable. There are two roles in cyberbullying. One of them is the person who is cyberbullying, and the other is the person who is suffering from this situation. Considering all types of cyberbullying, there may be various reasons behind the behavior of the person doing this job [2]. According to Xu et.al., there are many roles in cyberbullying: cyber bully, victim, accuser, advocate, reinforcer, bystander, reporter and the helper [3]. In order to solve this problem, automatic systems can be developed and relevant solutions can be created. Since written language is generally used in social media, the solution to the problem can be provided by natural language processing. It is very important to develop a system for detecting cyberbullying and for this system to prevent such bad events. Because the expanding number of social media users includes all kinds of people. In such systems, audits are usually carried out by a manager or a management team assigned to these tasks. However, it is really difficult to audit manually as it is a very large auditing environment [4].

One area that has seen extensive development over the years is natural language processing (NLP). Within the field of Natural Language Processing (NLP), diverse syntactic structures serve as pivotal tools for drawing conclusions or making assumptions in both multi-class and single-class research contexts, encompassing domains such as emotional states and textual representations of actions. Consequently, a myriad of scenarios emerges, each amenable to multiple methodological approaches. Accordingly, the employment of NLP based machine learning algorithms for classification purposes is deemed appropriate for scholarly inquiry. The comprehension of human language entails a nuanced progression through distinct stages akin to communicative interactions. These stages are systematically categorized to facilitate comprehensive analysis [5]. Numerous prominent corporations have successfully developed and implemented Natural Language Processing (NLP) systems, a trend that has witnessed widespread adoption within industrialized frameworks in recent years. Consequently, NLP has attained considerable reputation and effective, enabling the resolution of diverse challenges through automated systems, thereby obviating the necessity for traditional one-on-one customer service interactions and yielding notable time and cost savings. This paradigm shift has in turn allowed increased investment in research and the refinement of NLP system capabilities [6].

There has also been a lot of work on cyberbullying and cyber violence [7]–[12]. While conducting the literature research, the methods that can be considered as closer as possible were

emphasized with the study conducted in order to make comparisons. The study mainly includes datasets and the methods used, as well as performance evaluation.

In a study conducted for the detection of cyberbullying, 5453 tweets were tried to be made and a classification process was carried out by examining various variations such as baseline, personalities, emotion and sentiment. Values such as accuracy, f1-score, AUC were used as evaluation metrics. As a result of the study, about 90% success was achieved and the classification process was carried out. With the addition of an extended feature and the pre-processing processes applied, the result has been improved [13]. Another study conducted in 2019, dataset was taken from the site called Kaggle and the data obtained includes texts written on cyberbullying made on social media. The data was labelled and classified as cyberbullying or not cyberbullying, SVM and neural network were used for classification. It was determined that the neural network gave better results. Considering the scores obtained in the neural network in the 2-gram, 3-gram and 4-gram results, success rates above 90% were obtained [14]. Raza et al studied a dataset on the activities of PTA members on their website for cyberbullying in Japan. Using many machine learning methods for classification, the highest results were found with logistic regression to 82.7%. They then increased their success rate to 84.4% using supervised machine learning. In the study, it is stated that the main factor that leads to success is the voting classifier [15]. As another example of cyberbullying, pre-processing has been done for machine learning-based detection. Here, stop-word, repeating letters, punctuation, tokenization, Vector Space Model are used. In this way, the preliminary preparation necessary for the dataset to be evaluated, that is, for its classification, has been completed. The classification in the dataset has three classes that it is divided into positive, neutral and negative. Machine learning types used for classification are also SVM and Naive Bayes. As a result of the study, it is seen that the highest success rates are 89.54% in SVM and 73.03% in Naive Bayes [16]. Using multilingual data, [17] suggested a tailored deep network model to recognize and promote optimism in comments. Their approach obtained macro F1 scores of 75% for English, 62% for Tamil, and 67% for Malayalam using the CNN model by combining embedding from T5-Sentence. In another study the experiments made use of four deep learning models: RNN, LSTM, GRU, and BLSTM. In comparison to RNN, LSTM, and GRU, the BLSTM model was achieved the highest accuracy (82.18%) and the highest F1-measure score (88%) [18].

2. Material and Methods

Nine different machine learning algorithms were used in the study and the main purpose is to use too many algorithms and to determine which algorithm works better in such problems. It is inevitable to see what kind of results are obtained in a multi-class structure used in the dataset, and it will shed light when using it for other datasets. While evaluating the various classes in the dataset, both the display of weighted results and their performance on a class basis are shown. The dataset was taken from Twitter, which contains a large amount of data and is labeled. This data set has a 5-class structure and is multi-class. Since the classes are almost equal to each other, they are in a better position to give the results of the study. In the study, it

was used in pure form without any changes with the data. Then, using NLP methods, the texts in the dataset were made suitable for working with pre-processing.

After the pre-processing processes, a wide variety of machine learning methods were used to classify the dataset using machine learning methods. Here, a multi-class dataset has been classified using many machine learning methods and the methods have been compared. No parameter changes were made in the machine learning methods used here and default values were used. Better results are likely to be found by performing cross-validation. What is seen as important here is to show which machine learning method performs better.

The data set used in the study consists of tweets taken from Twitter. It contains 47 thousand tweets in total. The reason for choosing this data set is that multiple classes are evenly distributed in the data set. The dataset was accessed via the Kaggle site [19], [20]. Tweets related to cyberbullying were collected and labelled in the dataset. There is a balanced classification distribution, approximately 8 thousand of each class. You can see the percentage representation of the distribution in Figure 1.

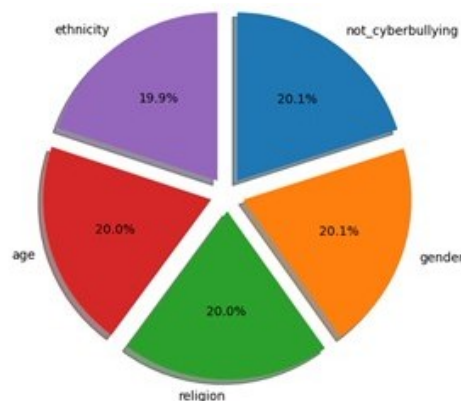


Figure 1. Distribution of classes in the dataset.

The dataset includes a total of 5 classes: ethnicity, religion, gender, age and not_cyberbullying. Since it is not appropriate to share the word cloud content in the data, it is not included in the article. Basic pre-processing techniques used in natural language processing are used. Then, this data was divided into train and test sets and tested with many different machine learning algorithms. The flowchart of the study is given in Figure 2.

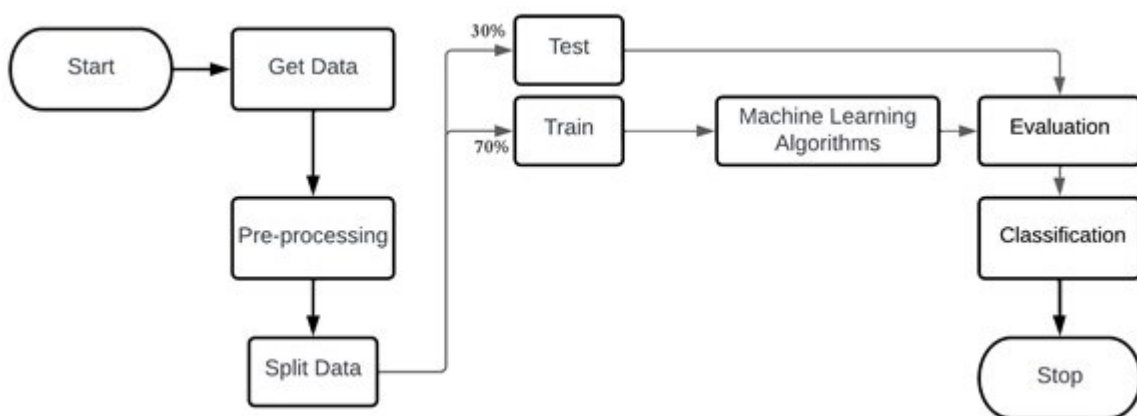


Figure 2. Flowchart of the study.

2.1. Pre-processing

This section employs classical natural language processing methods, as certain preliminary operations are requisite for accurate sentence classification within the dataset, thereby influencing the overall success of the classification endeavor. Specifically, the Natural Language Toolkit (NLTK) was employed for preprocessing tasks in the study [21]. NLTK, a comprehensive library, facilitates various operations including but not limited to eliminating redundant letters within sentences, performing lemmatization, and conducting tokenization procedures [22]. Due to its comprehensive features, NLTK is extensively utilized in various applications. The pre-processing methods employed in the study encompass:

- Lower text: Convert all text to lowercase. This is done to ensure uniformity and avoid the model treating uppercase and lowercase versions of the same word differently.
- Tokenize text [20] and remove punctuation: Tokenization involves breaking down the text into individual words or tokens. Punctuation removal involves eliminating punctuation marks from the text. This step helps in creating a clean and standardized set of words.
- Remove words that contain numbers: This step is often performed to focus on the textual content and remove any alphanumeric characters.
- Remove stop words: Stop words are common words (e.g., "and", "the", "is") that are often removed from text data because they don't carry significant meaning for certain types of analysis. Removing them can reduce noise in the data.
- Remove empty tokens: This step involves removing any empty tokens that might result from tokenization or other preprocessing steps. These empty tokens do not contribute to the analysis and need to be discarded.
- Lemmatized text: Lemmatization involves reducing words to their base or root form. For example, "running" would be lemmatized to "run." This step helps in reducing words to their core meaning and can improve the consistency of the dataset.
- Remove words with only one letter. Such words are often considered less informative and might not contribute much to the analysis.

These methods are commonly employed to clean and prepare text data for analysis. The pre-processing methods involved in preparing textual data prior to submitting it to machine learning techniques are intended to produce a purer and more uniform dataset, thereby enhancing its suitability for computational processing. These measures include removing unwanted characters, normalizing the text, and converting all words into lowercase. Depending on the unique features of the data and the objectives of the investigation, these methods may vary. To transform the text information into numerical vectors amenable to machine learning models, TFIDF (Term Frequency-Inverse Document Frequency) transformation is then applied before exporting the prepared data to the algorithm [14].

2.2. Machine Learning Algorithms

Machine learning algorithms have been broadened to be widely evaluated. While evaluating machine learning in the study, both class-based achievements and weighted average results were shared. Machine learning algorithms are concluded with default values. Therefore, it is likely that better performances will emerge if the studies to be carried out are worked on. The

main purpose here is to reveal which algorithms should be used to approach the results in this problem and to solve the problem. Machine learning algorithms used in the study:

- **Logistic Regression (LR):** Logistic Regression is a statistical and machine learning algorithm used for binary classification tasks, where the goal is to predict one of two possible outcomes (usually denoted as 0 and 1, or "negative" and "positive"). It's called "logistic" because it uses the logistic function (also known as the sigmoid function) to model the probability of the binary outcome. Logistic Regression is widely used in various fields, including healthcare (disease diagnosis), marketing (customer churn prediction), and natural language processing (sentiment analysis) [23]–[25].
- **Decision Tree Classifier (DTC):** Decision Trees are a popular machine learning algorithm used for both classification and regression tasks. They are a powerful and interpretable model that makes decisions by recursively splitting the data into subsets based on the most significant features. Each split is based on a decision rule, creating a tree-like structure, hence the name "Decision Tree" [26], [27].
- **Random Forest Classifier (RFC):** Random Forest is an ensemble machine learning algorithm that is widely used for both classification and regression tasks. It is built upon the foundation of Decision Trees and offers several advantages, including improved accuracy and reduced overfitting [28]–[31].
- **Naive Bayes (NB):** Naive Bayes is a simple yet effective probabilistic machine learning technique that is used for classification and, to a lesser extent, regression applications. It is founded on Bayes' theorem and makes the "naive" assumption of feature independence, which simplifies modeling and probability calculation [32]–[34].
- **K- Nearest Neighbor (K-NN):** A straightforward and user-friendly supervised machine learning technique for classification and regression applications is the k-Nearest Neighbors (K-NN) algorithm. Being a non-parametric method, it bases its predictions on how similar the data points in the training dataset are to one another. Based on the dominant class or average value of a data point's k-nearest neighbors, K-NN is used to categorize it or create a regression forecast [35], [36].
- **Extreme Gradient Boosting-XGBoost (XGB):** The class of gradient boosting algorithms includes sophisticated and extremely effective machine learning techniques like XGBoost. It is frequently employed for both classification and regression problems, and winning machine learning challenges on websites like Kaggle has often relied on it. XGBoost is renowned for its quickness, precision, and capacity for handling large, complicated datasets [37], [38].
- **Support Vector Machine (SVM):** An effective and flexible machine learning approach called SVM is utilized for both classification and regression problems. When needing to determine a distinct border (hyperplane) between two classes or making predictions using sparse data, SVMs are especially useful [39].
- **AdaBoost Classifier (ABC):** AdaBoost, which stands for Adaptive Boosting, is an ensemble learning method primarily used for classification tasks. AdaBoost is known for its ability to improve the accuracy of weak learners (classifiers with limited predictive power) by combining them into a strong ensemble model. The algorithm adapts and assigns more weight to data points that are misclassified by previous weak learners [40]–[42].

- Gradient Boosting Classifier (GBC): Gradient Boosting is an effective ensemble learning technique that may be utilized for classification and regression applications. Gradient Boosting Classifier, a subset of this approach, focuses on classification challenges. It creates a powerful ensemble model by pooling the predictions of numerous weak learners (usually decision trees). The term "gradient" refers to the optimization of a cost function by gradient descent [43], [44].

Since many articles on how the machine learning methods used work are given with their formulas and usage logic, in this study only the scanned publications are shown by citing the researched articles. For detailed information, you can refer to the related articles. Since all these methods are used in the study and a multi-class dataset is used, both the class-based performance results and the weighted total performances of all of them are given.

2.3. Evaluation Metrics

Some performance metrics are needed to see how well machine learning techniques are working in the study. In this way, it is possible to make a comparison about which method works better than which method. The method to be used may not always be the highest accuracy value. Different algorithms that are problem and result-oriented can also be selected. The metrics used in the study are as follows:

$$Accuracy = \frac{TP + TN}{TP + FP + TN + FN} \quad (1)$$

$$F1 - score = \frac{2 * Precision * Recall}{Precision + Recall} \quad (2)$$

$$Precision = \frac{TP}{TP + FP} \quad (3)$$

$$Recall = \frac{TP}{TP + FN} \quad (4)$$

Accuracy (1) measures the proportion of correct predictions out of all predictions made by the model. It is a straightforward and intuitive metric, but it may not be the best choice when dealing with imbalanced datasets (datasets where one class is much more frequent than the other). In imbalanced datasets, a high accuracy can be misleading because the model may simply predict the majority class most of the time. The harmonic mean of precision and recall values is expressed by the F1-score (2). When measuring a model's performance, it offers a fair assessment that considers both false positives and false negatives. When trying to balance recall and precision, the F1 Score is especially helpful. When the cost of false positives and false negatives differs, it is a useful metric to employ. Precision (3), also known as Positive Predictive Value, is the fraction of true positive predictions (positive instances properly predicted by the model) out of all positive instances projected by the model. Precision indicates how well your model performs when it predicts a positive class and aids in the reduction of false positives. In simple terms, it measures the accuracy of the model's positive predictions. Recall (4), also known as Sensitivity or True Positive Rate, measures the proportion of true positive predictions out of all actual positive instances in the dataset. Recall tells how well the model captures positive instances, and it helps to minimize false negatives. In other words, it is a measure of how effectively the model can find all the positive instances [45]. To calculate all these parameters, a Confusion Matrix must be developed. A classification model's performance can be evaluated using a crucial tool called a confusion matrix, which is a tabular representation of the model's predictions against the actual outcomes for a given dataset. The accuracy of the

model and its ability to distinguish between different classes are determined by analyzing this matrix. It's a critical tool for evaluating the effectiveness of a classification model and knowing how well it classifies data items. The confusion matrix gives information about the accuracy, precision, recall, and other performance measures of the model. Receiver Operating Characteristic (ROC) curve is a graphical representation used to assess the performance of binary classification models, particularly when determining the trade-off between the true positive rate and the false positive rate at different classification thresholds. ROC curves are commonly used in machine learning and statistics to comprehend a model's discriminative capability and to compare the performance of various classifiers.

3. Results and Discussion

Since many different machine learning methods were used in the study, instead of giving the results of all of them one by one, they were given in combination. The order of giving is random and independent of the height of success. The class labels shown in the study are as follows: not_cyberbullying: 0, gender: 1, religion: 2, age: 3, ethnicity: 4.

Table 1 displays the results of the evaluation metrics for each class and Figure 3 depicts the confusion matrices and ROC curves of nine machine learning methods employed in the study.

Table 1. Evaluation Metrics Results of Methods.

Classifier	Classes	Accuracy (%)	Precision (%)	Recall (%)	F1-Score (%)	Support
Logistic Regression	not-cyberbullying	88,93	78,75	88,93	83,53	2375
	gender	85,15	95,10	85,15	89,85	2371
	religion	94,51	96,28	94,51	95,39	2439
	age	96,08	96,28	96,08	96,18	2399
	ethnicity	97,72	98,09	97,72	97,90	2366
Decision Tree	not-cyberbullying	83,12	80,80	83,12	81,94	2375
	gender	87,05	88,81	87,05	87,92	2371
	religion	94,26	94,53	94,26	94,40	2439
	age	96,62	96,78	96,62	96,70	2399
	ethnicity	97,25	97,67	97,25	97,46	2366
Random Forest	not-cyberbullying	89,77	81,16	89,77	85,25	2375
	gender	84,23	94,55	84,23	89,09	2371
	religion	96,27	95,37	96,27	95,82	2439
	age	97,62	98,07	97,62	97,85	2399
	ethnicity	98,69	98,90	98,69	98,79	2366
Naïve Bayes	not-cyberbullying	88,93	77,42	88,93	82,77	2375
	gender	79,76	93,38	79,76	86,03	2371
	religion	94,38	93,01	94,38	93,69	2439
	age	96,71	96,95	96,71	96,83	2399
	ethnicity	94,72	96,22	94,72	95,46	2366
K-NN	not-cyberbullying	95,16	21,65	95,16	35,28	2375
	gender	16,87	48,37	16,87	25,02	2371
	religion	2,79	87,18	2,79	5,40	2439
	age	7,04	97,13	7,04	13,14	2399
	ethnicity	18,22	99,31	18,22	30,79	2366

XGBoost	not-cyberbullying	90,53	80,19	90,53	85,05	2375
	gender	85,20	94,75	85,20	89,72	2371
	religion	94,96	96,14	94,96	95,54	2439
	age	97,21	98,31	97,21	97,76	2399
	ethnicity	98,65	99,07	98,65	98,86	2366
SVM	not-cyberbullying	89,52	78,02	89,52	83,37	2375
	gender	83,55	95,79	83,55	89,25	2371
	religion	94,42	96,24	94,42	95,32	2439
	age	96,79	96,03	96,79	96,41	2399
	ethnicity	97,72	98,55	97,72	98,13	2366
AdaBoost	not-cyberbullying	88,34	72,87	88,34	79,86	2375
	gender	76,13	96,11	76,13	84,96	2371
	religion	92,91	94,89	92,91	93,89	2439
	age	96,96	95,29	96,96	96,12	2399
	ethnicity	97,55	97,63	97,55	97,59	2366
Gradient Boosting	not-cyberbullying	92,21	76,36	92,21	83,54	2375
	gender	82,58	95,89	82,58	88,74	2371
	religion	92,78	96,18	92,78	94,45	2439
	age	96,50	98,97	96,50	97,72	2399
	ethnicity	98,14	98,89	98,14	98,52	2366

There are deviations in the findings of the not_cyberbullying class in the Logistic Regression and Decision Tree classifier results. Other classes have obviously demonstrated significant levels of accomplishment. The confusion matrix and ROC curve of Logistic Regression and Decision Tree is given in Figure 3 (i) and (ii) respectively. Random Forest classifier outperforms all other classifiers in terms of accuracy with 93,34% (Figure 3 (iii)). Naive Bayes shows that while it is expected to give better results in statistical results, it can also give good results in this problem. It makes sense to think that this may have value in terms of statistical approach and can be used as a detail to consider when performing feature extraction. Naive Bayes' results are given in Table 1 and confusion matrix and ROC curve in Figure 3 (iv). Naive Bayes is often used in the solution of statistical data due to its speed and simple use. However, since there is not much statistical data in the study, it is a little behind. One of the reasons for using it in the study is the thought that it will be useful in comparison with other studies since it is a frequently preferred algorithm. Surprisingly, the KNN algorithm produced really poor results (Figure 3 (v)). The results were extremely poor, of a type that might produce almost entirely misleading results. This demonstrates that an algorithm must be employed to solve this problem. XGBoost, which is commonly employed because it produces good results in machine learning competitions, produced the highest and best outcomes of any machine learning algorithm utilized in the study. It was the algorithm with the second highest accuracy, earning a score of 93.32% (Figure 3 (vi)).

The Support Vector Machine algorithm was 92.42% accurate (Figure 3 (vii)). However, in terms of processing time, the model must be able to run for extended periods of time. This time is substantially shorter in other algorithms. As a result, instead of using this model, it would be more accurate to use other machine **learning** techniques. AdaBoost is a versatile and successful

method that is often utilized in real-world applications like face detection and text categorization. The findings of the not-cyberbullying class have lower results than other classes (Figure 3 (viii)). Gradient Boosting is a powerful ensemble method that often outperforms AdaBoost. The confusion matrix and ROC curve of Gradient Boosting is given in Figure 3 (ix).

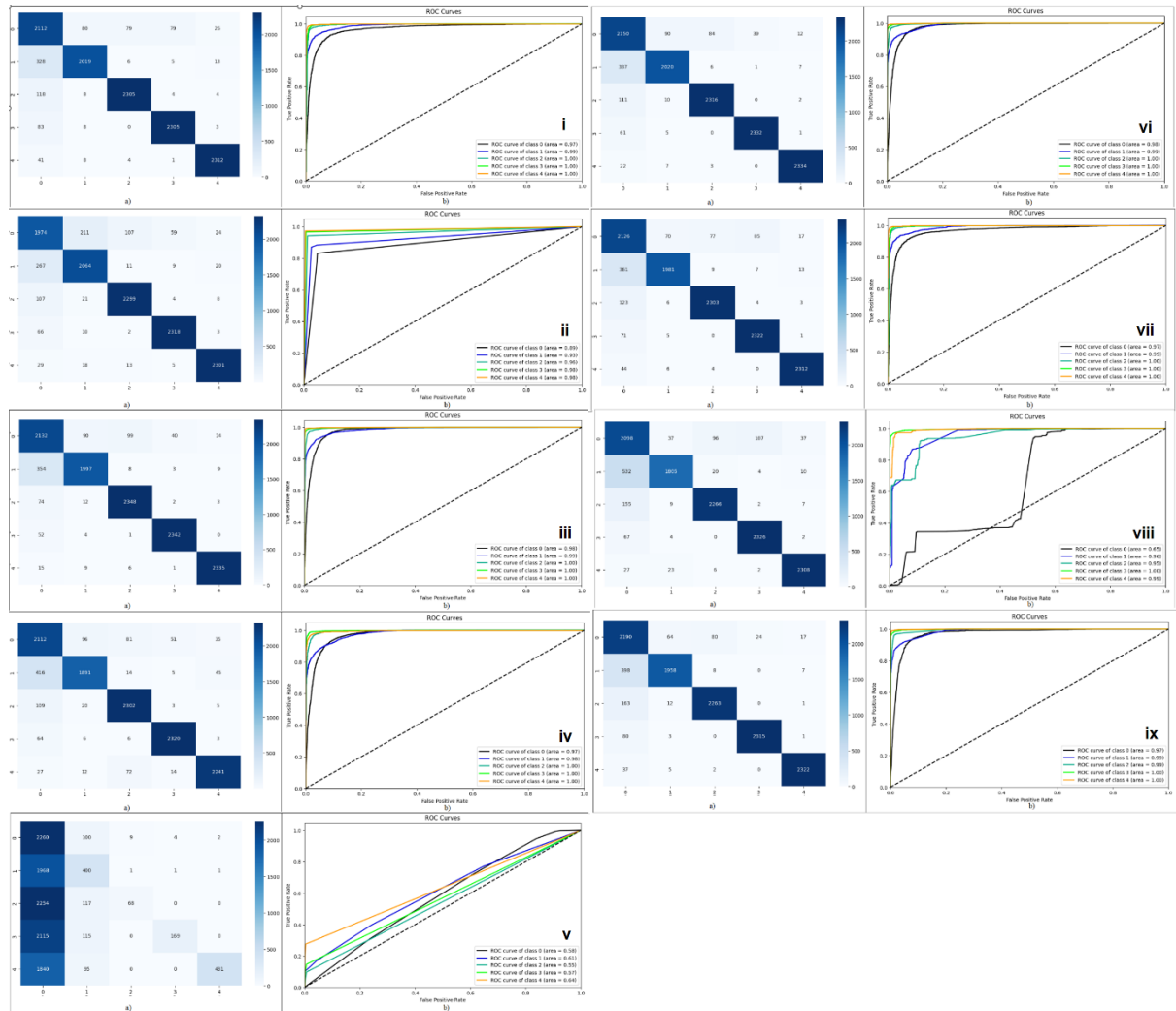


Figure 3. Confusion matrix (a) and ROC curve (b) of algorithms: (i) Logistic Regression, (ii) Decision Tree, (iii) Random Forest, (iv) Naïve Bayes, (v) K-NN, (vi) XGBoost, (vii) SVM, (viii) Adaboost, (ix) Gradient Boosting.

Table 1 previously provided the success metrics of the classifiers for five classes. Table 2 also displays the weighted metric findings for each classifier employed in the study. The authentic accuracy levels of all of the five classes are represented by these weighted metrics in Table 2. When all of the results are compared, the Random Forest and XGBoost algorithms yield the best accuracy. Due of its high success rate, XGBoost has been utilized a lot in recent years. Researchers frequently utilize it because of its capacity to classify large amounts of data quickly and efficiently. Weighted accuracy value was found 93,32% with XGBoost and 93,34% with Random Forest. The highest precision value was found in XGBoost, which is 93,71%. The highest recall value was on Random Forest at 93,34% and followed by XGBoost at 93.32%. The F1-Score metric shows the harmonic mean of precision and recall values. A high F1-Score indicates that both precision and recall are balanced. The XGBoost model has the highest F1-

Score with 93,40%. The method with the lowest results is KNN with 27.85% weighted accuracy.

In terms of F1-Score, XGBoost slightly outperforms Random Forest (93.40% vs. 93.38%). Because of its adaptability, speed, and performance, XGBoost has become a go-to solution for many machine learning practitioners. It is especially well-suited for structured data and is frequently utilized in real-world applications across multiple areas. Random Forest is a versatile and powerful algorithm that is widely employed in a wide range of applications.

Table 2. Weighted metric results of all classifiers.

Classifier	Accuracy (%)	Precision (%)	Recall (%)	F1-Score (%)
Logistic Regression	92,49	92,92	92,49	92,59
Decision Tree	91,68	91,74	91,68	91,71
Random Forest	93,34	93,62	93,34	93,38
Naïve Bayes	90,93	91,41	90,93	90,98
K-NN	27,85	70,85	27,85	21,81
XGBoost	93,32	93,71	93,32	93,40
SVM	92,42	92,94	92,42	92,52
AdaBoost	90,40	91,38	90,40	90,51
Gradient Boosting	92,45	93,28	92,45	92,61

Many machine learning algorithms have been included in the study and have been examined in many ways. The studies were aimed to find a result such as which one should be preferred for this problem. It sheds light on how subsequent similar problems should be solved with which algorithms. Default values were used intentionally in the study so that it was possible to observe which algorithm was better in a fundamental sense.

4. Conclusion

A large-scale dataset related to cyberbullying was discussed in the study. The dataset consists of five different classes. The distribution of the classes in the dataset is roughly equal. This makes it possible to more accurately assess how the study affected the overall success. There is no missing or unlabeled data in the dataset. As a result, neither additions nor subtraction were required. Feature extraction was done prior to the dataset being inserted into machine learning algorithms. For natural language processing tasks like tokenization and lower case, this procedure is widely utilized. It is a process that simplifies the tweets and ensures that the processes yield better results. It was then fed into machine learning algorithms after the required preparations were finished. Numerous machine learning algorithms were contrasted and discussed among themselves. It was determined that the Random Forest Classifier and XGBoost algorithms had the best success rates.

Random Forest is an ensemble learning model that trains many decision trees independently on subsets of the data. The final predictions are made by averaging or taking the majority of the predictions from individual trees. XGBoost similarly is an ensemble learning model, but it builds trees sequentially and focuses on correcting what previous trees have learned. It operates using the gradient boosting method and iteratively works to optimize the loss function. XGBoost tends to be faster than Random Forest. The sequential learning approach of gradient boosting can make the error reduction process more efficient. However, both models perform well on large datasets and in high-dimensional feature spaces. XGBoost provides more hyperparameter tuning options, allowing for better customization of the model. This provides flexibility but may require more attention. Random Forest generally requires fewer parameter adjustments and is simpler to use. Random Forest often exhibits a tendency towards overfitting, especially when including a large number of trees. XGBoost includes regularization terms and adjustments for tree size, providing better control over overfitting.

It was focused on vectorizing words, utilizing TFIDF to concentrate on the syntactic features of the words. However, future studies could enhance this approach by incorporating various word embedding methods such as word2vec, fastText, and GloVe, which consider the semantic properties of words. Additionally, integrating deep learning networks could provide more robust and comparable results. Similarly, the classification performance of large language models could be evaluated.

The goal of the study is to identify the optimal algorithmic technique for this particular problem, which is why numerous machine learning algorithms are used. This makes it possible to decide which algorithm to concentrate on when carrying out improvement experiments. Default parameters were utilized while applying machine learning methods. Based on weighted metrics, the Random Forest algorithm had the greatest Accuracy of 93,34% and the XGBoost algorithm had the highest F1 score of 93,4%. In general, all algorithms were discussed and the best one was revealed in the study.

In conclusion, both models demonstrate strong performance, but the choice between them depends on the specific application and dataset. While Random Forest may be simpler to use, XGBoost offers more parameter tuning options and often achieves higher performance.

Ethics in Publishing

There are no ethical issues regarding the publication of this study.

Author Contributions

Designing the research, collecting data, evaluating the results, writing articles, etc. transactions were made by Funda Akar.

References

- [1] A. Saravananaraj, J. I. Sheeba, and S. P. Devaneyan, "Automatic Detection of Cyberbullying From Twitter," *IRACST-International Journal of Computer Science and Information Technology & Security (IJCSITS)*, vol. 6, no. 6, pp. 2249–9555, 2019, [Online]. Available: <https://www.researchgate.net/publication/333320174>.
- [2] W. N. H. W. Ali, M. Mohd, and F. Fauzi, "Cyberbullying detection: an overview," in *2018 Cyber Resilience Conference (CRC)*, 2018, pp. 1–3.
- [3] J.-M. Xu, K.-S. Jun, X. Zhu, and A. Bellmore, "Learning from bullying traces in social media," in *Proceedings of the 2012 conference of the North American chapter of the association for computational linguistics: Human language technologies*, 2012, pp. 656–666.
- [4] M. Dadvar, F. M. G. de Jong, R. Ordelman, and D. Trieschnigg, "Improved cyberbullying detection using gender information," in *Proceedings of the Twelfth Dutch-Belgian Information Retrieval Workshop (DIR 2012)*, 2012, pp. 23–25.
- [5] D. Jurafsky, *Speech & language processing*. Pearson Education India, 2000.
- [6] T. P. Nagarhalli, V. Vaze, and N. K. Rana, "Impact of machine learning in natural language processing: A review," in *2021 third international conference on intelligent communication technologies and virtual mobile networks (ICICV)*, 2021, pp. 1529–1534.
- [7] J. Cheng, C. Danescu-Niculescu-Mizil, and J. Leskovec, "Antisocial behavior in online discussion communities," in *Proceedings of the international aaai conference on web and social media*, 2015, vol. 9, no. 1, pp. 61–70.
- [8] Z. Ghasem, I. Frommholz, and C. Maple, "Machine learning solutions for controlling cyberbullying and cyberstalking," *J Inf Secur Res*, vol. 6, no. 2, pp. 55–64, 2015.
- [9] S. Murnion, W. J. Buchanan, A. Smales, and G. Russell, "Machine learning and semantic analysis of in-game chat for cyberbullying," *Computers & Security*, vol. 76, pp. 197–213, 2018.
- [10] K. Reynolds, A. Kontostathis, and L. Edwards, "Using machine learning to detect cyberbullying," in *2011 10th International Conference on Machine learning and applications and workshops*, 2011, vol. 2, pp. 241–244.
- [11] D. Van Bruwaene, Q. Huang, and D. Inkpen, "A multi-platform dataset for detecting cyberbullying in social media," *Language Resources and Evaluation*, vol. 54, pp. 851–874, 2020.
- [12] J. Wang, R. J. Iannotti, and T. R. Nansel, "School bullying among adolescents in the United States: Physical, verbal, relational, and cyber," *Journal of Adolescent health*, vol. 45, no. 4, pp. 368–375, 2009.
- [13] V. Balakrishnan, S. Khan, and H. R. Arabnia, "Improving cyberbullying detection using Twitter users' psychological features and machine learning," *Computers & Security*, vol. 90, p. 101710, 2020.
- [14] J. Hani, N. Mohamed, M. Ahmed, Z. Emad, E. Amer, and M. Ammar, "Social media cyberbullying detection using machine learning," *International Journal of Advanced Computer Science and Applications*, vol. 10, no. 5, 2019.
- [15] M. O. Raza, M. Memon, S. Bhatti, and R. Bux, "Detecting cyberbullying in social

- commentary using supervised machine learning,” in *Advances in Information and Communication: Proceedings of the 2020 Future of Information and Communication Conference (FICC), Volume 2*, 2020, pp. 621–630.
- [16] M. Sintaha and M. Mostakim, “An empirical study and analysis of the machine learning algorithms used in detecting cyberbullying in social media,” in *2018 21st International Conference of Computer and Information Technology (ICCIT)*, 2018, pp. 1–6.
- [17] B. R. Chakravarthi, “Hope speech detection in YouTube comments,” *Social Network Analysis and Mining*, vol. 12, no. 1, p. 75, 2022.
- [18] C. Iwendi, G. Srivastava, S. Khan, and P. K. R. Maddikunta, “Cyberbullying detection solutions based on deep learning architectures,” *Multimedia Systems*, vol. 29, no. 3, pp. 1839–1852, 2023, doi: 10.1007/s00530-020-00701-5.
- [19] Kaggle, “Cyberbullying Classification.” <https://www.kaggle.com/datasets/andrewmvd/cyberbullying-classification> (accessed Apr. 17, 2023).
- [20] J. Wang, K. Fu, and C.-T. Lu, “Sosnet: A graph convolutional network approach to fine-grained cyberbullying detection,” in *2020 IEEE International Conference on Big Data (Big Data)*, 2020, pp. 1699–1708.
- [21] S. Bird, “NLTK: the natural language toolkit,” in *Proceedings of the COLING/ACL 2006 Interactive Presentation Sessions*, 2006, pp. 69–72.
- [22] G. Grefenstette, “Tokenization,” in *Syntactic wordclass tagging*, Springer, 1999, pp. 117–133.
- [23] S. Sperandei, “Understanding logistic regression analysis,” *Biochemia medica*, vol. 24, no. 1, pp. 12–18, 2014.
- [24] J. Chen *et al.*, “A comparison of linear regression, regularization, and machine learning algorithms to develop Europe-wide spatial models of fine particles and nitrogen dioxide,” *Environment international*, vol. 130, p. 104934, 2019.
- [25] D. Maulud and A. M. Abdulazeez, “A review on linear regression comprehensive in machine learning,” *Journal of Applied Science and Technology Trends*, vol. 1, no. 4, pp. 140–147, 2020.
- [26] S. R. Safavian and D. Landgrebe, “A survey of decision tree classifier methodology,” *IEEE transactions on systems, man, and cybernetics*, vol. 21, no. 3, pp. 660–674, 1991.
- [27] Y. K. Qawqzeh, M. M. Otoom, and F. Al-Fayez, “A Proposed Decision Tree Classifier for Atherosclerosis Prediction and Classification,” *International Journal of Computer Science and Network Security (IJCSNS)*, vol. 19, no. 12, pp. 197–202, 2019.
- [28] L. Breiman, J. Friedman, C. Stone, and R. Olshen, “Classification and regression trees (crc, boca raton, fl),” 1984.
- [29] L. Breiman, “Random forests; uc berkeley tr567,” *University of California: Berkeley, CA, USA*, 1999.
- [30] L. Breiman, “Random Forests for Scientific Discovery,” *Presentation*, pp. 1–167, 2013, [Online]. Available: <http://www.math.usu.edu/adele/RandomForests/ENAR.pdf>.
- [31] J. R. Quinlan, *C4. 5: programs for machine learning*. Elsevier, 2014.
- [32] I. Rish and others, “An empirical study of the naive Bayes classifier,” in *IJCAI 2001 workshop on empirical methods in artificial intelligence*, 2001, vol. 3, no. 22, pp. 41–46.

- [33] E. Frank and R. R. Bouckaert, "Naive bayes for text classification with unbalanced classes," in *Knowledge Discovery in Databases: PKDD 2006: 10th European Conference on Principles and Practice of Knowledge Discovery in Databases Berlin, Germany, September 18-22, 2006 Proceedings 10*, 2006, pp. 503–510.
- [34] Ö. Şahinaslan, H. Dalyan, and E. Şahinaslan, "Naive bayes sınıflandırıcısı kullanılarak youtube verileri üzerinden çok dilli duygu analizi," *Bilişim Teknolojileri Dergisi*, vol. 15, no. 2, pp. 221–229, 2022.
- [35] Y. Wu, K. Ianakiev, and V. Govindaraju, "Improved k-nearest neighbor classification," *Pattern recognition*, vol. 35, no. 10, pp. 2311–2318, 2002.
- [36] G. Guo, H. Wang, D. Bell, Y. Bi, and K. Greer, "KNN Model-Based Approach in Classification," in *On The Move to Meaningful Internet Systems 2003: CoopIS, DOA, and ODBASE*, 2003, pp. 986–996.
- [37] T. Chen *et al.*, "Xgboost: extreme gradient boosting," *R package version 0.4-2*, vol. 1, no. 4, pp. 1–4, 2015.
- [38] T. Chen, T. He, M. Benesty, and V. Khotilovich, "Package 'xgboost,'" *R version*, vol. 90, pp. 1–66, 2019.
- [39] W. S. Noble, "What is a support vector machine?," *Nature biotechnology*, vol. 24, no. 12, pp. 1565–1567, 2006.
- [40] A. Vezhnevets and V. Vezhnevets, "Modest AdaBoost-teaching AdaBoost to generalize better," in *Graphicon*, 2005, vol. 12, no. 5, pp. 987–997.
- [41] X. Li, L. Wang, and E. Sung, "AdaBoost with SVM-based component classifiers," *Engineering Applications of Artificial Intelligence*, vol. 21, no. 5, pp. 785–795, 2008.
- [42] T.-K. An and M.-H. Kim, "A new diverse AdaBoost classifier," in *2010 International conference on artificial intelligence and computational intelligence*, 2010, vol. 1, pp. 359–363.
- [43] J. Son, I. Jung, K. Park, and B. Han, "Tracking-by-segmentation with online gradient boosting decision tree," in *Proceedings of the IEEE international conference on computer vision*, 2015, pp. 3056–3064.
- [44] S. Peter, F. Diego, F. A. Hamprecht, and B. Nadler, "Cost efficient gradient boosting," *Advances in neural information processing systems*, vol. 30, 2017.
- [45] M. Hossin and M. N. Sulaiman, "A review on evaluation metrics for data classification evaluations," *International journal of data mining & knowledge management process*, vol. 5, no. 2, p. 1, 2015.

All-Solid-State PVC-Membrane Cu(II)-Selective Potentiometric Microsensor Based on a Novel Calix[4]arene Derivative

Cigdem CAY¹, Murat YOLCU^{1*}, Serkan SAYIN²

¹ Department of Chemistry, Faculty of Arts&Science, Giresun University, Giresun, Türkiye

² Department of Environmental Engineering, Faculty of Engineering, Giresun University, Giresun, Türkiye

Received: 04/05/2024, **Revised:** 28/06/2024, **Accepted:** 01/07/2024, **Published:** 31/08/2024

Abstract

In this study, 25,27-dihydroxy-26,28-bis(ethoxycarbonylbutyoxo)-5,11,17,23-p-tert-butylcalix[4]arene was used as an ionophore for the preparation of a novel all-solid-state type microsensor to make a selective potentiometric response towards Cu(II) ions. The optimum membrane composition of the microsensor was determined as 2% (w/w) ionophore, 67% (w/w) bis (2-ethylhexyl) sebacate (DOS), 30% (w/w) polyvinylchloride (PVC), and 1%(w/w) potassium tetrakis 4-chlorophenyl borate (KTPCIPB). All-solid-state PVC-membrane Cu(II)-selective microsensor exhibited a highly selective Nernstian response of 31.3±2.1 mV slope ($R^2= 0.997$) with a short response time (<15 s) over the concentration range of 10^{-5} to 10^{-1} mol L⁻¹ of Cu(II) ions for 8 weeks with no significant difference in potentials. The microsensor was effectively performed in the pH range of 5.0–8.0, with a low detection limit of 7.67×10^{-6} mol L⁻¹, and a temperature range of 15–40 °C. The prepared microsensor was successfully used both as an indicator electrode in the potentiometric titration of Cu(II) ions with EDTA and also in the determination of the Cu(II) content of environmental water samples. When the potentiometric results were compared with ICP-OES, they were found to be in good agreement with ICP-OES results at a 95% confidence level.

Keywords: Calixarene, all-solid-state, ion-selective sensor, copper, PVC membrane

Yeni Tip Kaliks[4]aren Temelli Bütünüyle Katı-Hal PVC-Membran Cu(II)-Seçici Potansiyometrik Mikrosensör

Öz

Bu çalışmada, 25,27-dihidroksi-26,28-bis(etoksikarbonilbutyoksi)-5,11,17,23-p-tertilkaliks[4]aren bileşiği Cu(II) iyonlarına karşı seçici bir potansiyometrik yanıt elde etmek için bütünüyle katı hal kontak yeni tip mikrosensör hazırlanmasında ionofor olarak kullanılmıştır. Mikrosensörün optimum membran bileşimi %2 (a/a) ionofor, %67 (a/a) bis (2-etilheksil) sebakat (DOS), %30 (a/a) polivinilklorür (PVC) ve %67 (a/a) bis (2-etilheksil) sebakat (DOS) olarak belirlenmiştir. Bütünüyle katı-hal PVC-membran Cu(II)-seçici mikrosensör, 8 hafta boyunca potansiyellerde önemli bir fark olmadan Cu(II) iyonlarına 10^{-5} - 10^{-1} mol L⁻¹ konsantrasyon aralığında kısa yanıt süresi (<15 s) ve 31,3±2,1 mV eğim ile ($R^2= 0,997$) oldukça seçici bir Nernst yanıtı sergilemiştir. Mikrosensör, $7,67 \times 10^{-6}$ mol L⁻¹ gibi düşük tayin sınırı, 15–40 °C sıcaklık ve pH 5,0–8,0 aralığında etkili bir performans sergilemiştir. Hazırlanan mikrosensör hem Cu(II) iyonlarının EDTA ile potansiyometrik titrasyonunda indikatör elektrot olarak hem de çevresel su örneklerinin Cu(II) içeriğinin belirlenmesinde başarıyla kullanılmıştır. Elde edilen potansiyometrik sonuçlar ICP-OES ile karşılaştırıldığında %95 güven düzeyinde iyi uyum içerisinde olduğu görülmüştür.

Anahtar Kelimeler: Kaliksaren, katı hal kontak, iyon seçici sensör, bakır, PVC membran

Corresponding Author: tmuratyolcu@yahoo.com

Cigdem CAY, <https://orcid.org/0000-0001-7585-6119>

Murat YOLCU, <https://orcid.org/0000-0003-3477-3792>

Serkan SAYIN, <https://orcid.org/0000-0003-0518-3208>

1. Introduction

Potentiometry based on ion-selective electrodes (ISEs), which are one of the electroanalytical methods that have attracted the increasing attention of researchers for a long time due to their advantages such as rapid response, broad dynamic range, low detection limit, procedure, cost-effectiveness, simple instrumentation, preparation, and reasonable selectivity [1, 2]. Potentiometry-based sensors are preferred in many different fields such as determining the qualitative and quantitative analyses of various inorganic and organic ions, medical drug analyses, industrial analyses, environmental monitoring and routine laboratory analyses [3]. Chemical or ion sensors are widely used in sample analysis because they provide rapid results and are suitable for all minimum concentrations and on-line monitoring without requiring any sample pre-treatment [4-6]. Calixarenes, considered third-generation supramolecules, have been used as receptors to identify various ions due to their remarkable ability to construct host-guest type complexes [7, 8]. Besides, their easy synthesis and tailor made functionalization have attracted an intense interest of chemists. In this sense, so far calixarenes have been successfully used effective ionophores for many kinds of guest such as metal cations, anions and neutral molecules [9-11]. Additionally, calixarenes have electron-rich internal cavities and can form complexes with metal ions of compatible sizes through dipole-dipole interaction. Electrochemical techniques have gained much attention recently established the use of calixarenes for heavy metal identification in the field of electroanalysis in the late 80s, especially for the development of ion-selective electrodes. The use of calixarenes in electrodes was expanded to various electrodes using various electroanalytical techniques in the following years. Calixarene derivatives have unique properties in material chemistry [4, 12].

Copper is an element that is quite common in nature, both in metallic form and in various ores and minerals. It can also be found as both complex and solid particles in various types of water, such as groundwater, surface water, seawater, and drinking water [13]. Foods such as seafood and offal, mushrooms, grains and nuts can be listed to meet the need for copper in the human diet. Besides, in addition to these nutrients, a large portion of copper (about 25%) is provided to the human body from drinking water. Copper is a micronutrient essential for the proper functioning of living organisms, but in excess amounts it is toxic and hazardous to health. At the same time, the copper element takes part in many physiological processes, is involved in the synthesis of neuropeptides, has an immunological function and is a cofactor of many redox enzymes. While copper deficiency causes disorders in the functioning of the circulatory system and central nervous system, its excess can cause dysfunctions in the functioning of the internal organs and digestive system, as well as many side effects such as dizziness, nausea, muscle and abdominal pain [14, 15].

Due to the toxic effects of copper element on human and environmental health, it is very important to determine it in different samples. Different analytical methods can be used to determine Cu(II) ion concentration levels, such as inductively coupled plasma optical emission spectroscopy, inductively coupled plasma mass spectroscopy, high-performance liquid chromatography, atomic absorption spectrometry, and anodic stripping voltammetry [16-18]. Listed analytical methods; It cannot be preferred in routine analyzes due to its high costs,

requiring sample pre-treatment and trained personnel, and high energy and time consumption [19-21].

In the present study, a novel potentiometric Cu(II)-selective microsensor, that is an all-solid-state PVC-membrane type, was designed using calix[4]arene derivative as an ionophore. The performance characteristics such as limit of detection, linearity, slope with standard deviation, response time, selectivity, repeatability, reproducibility, pH, temperature ranges of the microsensor were investigated in detail. The microsensor was successfully used for Cu(II) contents of some environmental water samples. The potentiometric results were compared with ICP-OES and it was seen that the results were in good harmony with the ICP-OES results at a confidence level of 95%.

2. Experimental

2.1. Chemicals

Tetrahydrofuran (THF), high molecular weight polyvinylchloride (PVC), o-nitrophenyl octyl ether (NPOE), bis(2-ethylhexyl) sebacate (DOS), dibutyl sebacate (DBS), potassium tetrakis (4-chlorophenyl) borate (KTpClPB), disodium ethylenediaminetetraacetate dihydrate (EDTA-Na₂), graphite, solvents, and all other salts were purchased from Sigma-Aldrich and used without further purification. Ultrapure SU 2227 as an epoxy resin and Desmodur RFE as a hardener were obtained from Victor and Bayer AG, respectively.

2.2. Apparatus

Potential measurements were made using a computer-programmed and multi-channel potentiometric system. A silver/silver chloride electrode (Basi-MF-2079-RE-5B) was used as a reference electrode for potential measurements. Shimadzu (Model AUX220) analytical scale was used in weighing operations. The pH values of the solutions were adjusted by using a Jenway 3040 model Ion Analyser. Deionized water was obtained from Sartorius Stedim (Arium*611UV) deionized water (18.6 MΩ) deionization system. Shimadzu (Model AUX220) analytical scale was used in weighing operations. Metformin molecules were removed from the polymer using a Memmer (GmbH + Co. KG D.91126 Typ: WNB 14) shaker. Weighing operations were performed using an analytical balance from Shimadzu (model AUX220). A Hitachi SU 1510 model instrument was used for Scanning Electron Microscopy (SEM) analysis. Spectro Blue II model instrument was used for Inductively Coupled Plasma-Optical Emission Spectrometry (ICP-OES) analysis. All solutions were prepared using ultra-pure water from a Milli-Q (Millipore Corp.).

2.3. Synthesis of the Calixarene-based ionophore

The calixarene-based ionophore (25,27-dihydroxy-26,28-bis(ethoxycarbonylbutyloxy)-5,11,17,23-*p-tert*-butylcalix[4]arene (**2**)) shown in Figure 1 was synthesized according to the literature procedures [11].

Yield; 44%, mp: 177-180 °C. ¹H-NMR (400 MHz, CDCl₃): δ(ppm) 7.49 (s, 2H, -OH), 7.04 (s, 4H, ArH), 6.80 (s, 4H, ArH), 4.26 (d, 4H, *J* = 12.8 Hz, Ar-CH₂-Ar), 4.15 (q, 4H, *J* = 7.2 Hz, -OCH₂), 3.99 (t, 4H, *J* = 5.6 Hz, -OCH₂), 3.30 (d, 4H, *J* = 12.8 Hz, Ar-CH₂-Ar), 2.48 (t, 4H, *J* = 6.8 Hz, -CH₂), 2.06-2.0 (m, 8H, -CH₂-), 1.28 (s, 18H, Bu^t), 1.26 (t, 6H, *J* = 6.8 Hz, -CH₃), 0.97 (s, 18H, Bu^t); ¹³C-NMR (100 MHz, CDCl₃): δ(ppm) 173.65 (C=O), 150.94, 150.10, 147.00, 141.58, 132.85, 127.97, 125.69, 125.26, 76.07, 60.49, 34.16, 34.03, 31.93, 31.26, 29.60, 21.75, 14.45.

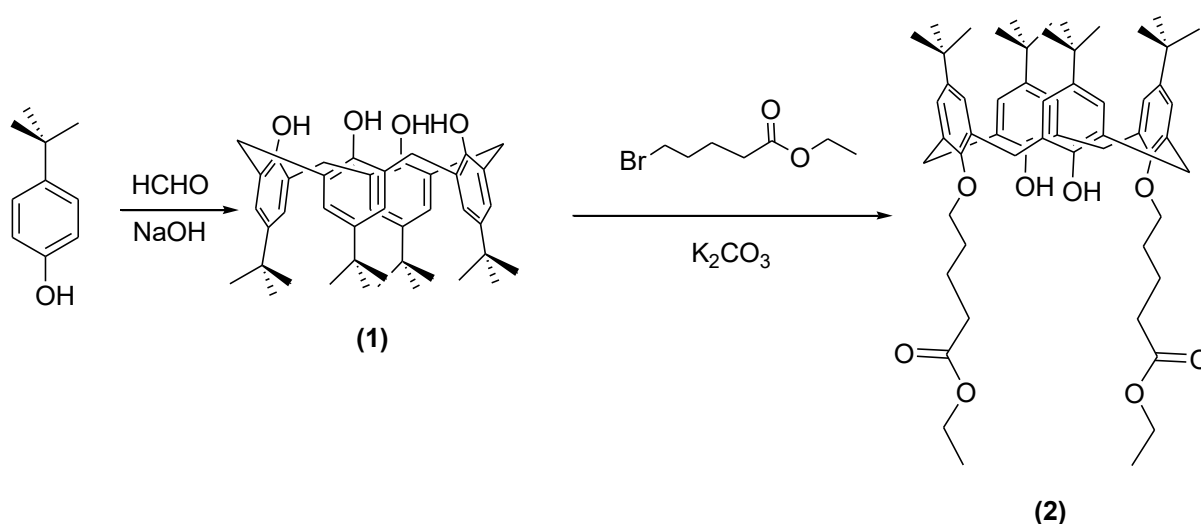


Figure 1. Synthesis scheme of 25,27- dihydroxy -26,28-bis(ethoxycarbonylbutyl-4-yl-oxy)-5,11,17,23-*p-ter*-butylcalix[4]arene

2.4. Fabrication of Cu(II)-Selective Microsensor

The Cu(II)-selective microsensor used in the study was produced according to the procedures described in our previous studies [22]. The microsensor was generally manufactured in two steps. In the first stage, a mixture of solid contacts consisting of 50% (w/w) graphite, 35% (w/w) epoxy and 15% (w/w) hardener in THF was prepared. Then a copper wire with a length of 10 mm and a radius of approximately 0.2 mm was dipped into the prepared solid contact mixture several times until a coating thickness of approximately 0.5 mm was obtained, and then the copper wire was left at room temperature for one day. In the second stage, ion selective membrane cocktail consisting of 2-4% (w/w) ionophore (dispersed in the cocktail), 28-30% (w/w) PVC, 1% (w/w) KTpClPB, and 67-69% (w/w) plasticizer (NPOE, DOS or DBS) was prepared in 2.5 mL THF. The surface of the solid contacts obtained in the first step was coated with this cocktail three or four times and then covered with an ion-selective membrane. The microsensor was left to dry for one day under laboratory conditions. Finally, the dried membrane sensor was soaked in 10⁻² mol.L⁻¹ Cu(NO₃)₂ solution for at least 12 hours for conditioning purposes before use in measurements.

3. Results and Discussions

In order to test the potentiometric properties of the Cu(II)-selective microsensor; parameters such as calibration curve, linear working range, detection limit, repeatability, pH range, response time, selectivity and ratio of membrane components were studied. For this purpose, different PVC-membrane mixtures were prepared and their potentiometric properties were tested according to IUPAC recommendations [23].

3.1. Membrane Composition

Ionophore, plasticizer and polymer types and amounts are important parameters that affect the performance of the potentiometric sensor. Therefore, the effects of the ion-selective membrane composition, which significantly affects the sensitivity and selectivity of the sensor, the nature and amount of the plasticizer, and the amount of the lipophilic additive (KTpCIPB), on the potential performances of Cu(II)-selective microsensor were investigated in detail. The results are shown in Table 1. Plasticizers containing NPOE, DOS and DBS, which are common PVC membrane solvents, were also examined. Membrane No-I prepared based on DOS plasticizer exhibited better potentiometric properties in terms of linear range and detection limit compared to other.

Table 1. Potentiometric performance characteristics of Cu(II)-selective microsensor

No	Composition of Membrane (% w/w)						Potentiometric Properties		
	PVC	NPOE	DOS	DBS	KTCIPB	Ionophore	Slope (mV/decade)	Linear range (mol.L ⁻¹)	Detection limit (mol.L ⁻¹)
I	30	67	-	-	1	2	26.9±1.8	10 ⁻⁵ -10 ⁻¹	5.7x10 ⁻⁵
II	30	-	67	-	1	2	31.3±2.1	10 ⁻⁵ -10 ⁻¹	7.6x10 ⁻⁶
III	30	-	-	67	1	2	27.4±1.7	10 ⁻⁵ -10 ⁻¹	6.3x10 ⁻⁵
IV	28	67	-	-	1	4	27.3±1.6	10 ⁻⁵ -10 ⁻¹	8.5x10 ⁻⁵
V	28	-	67	-	1	4	26.5±2.2	10 ⁻⁶ -10 ⁻¹	3.4x10 ⁻⁶
VI	28	-	-	67	1	4	25.9±1.0	10 ⁻⁵ -10 ⁻¹	6.6x10 ⁻⁵
VII	27	69	-	-	-	2	25.7±2.8	10 ⁻⁵ -10 ⁻¹	4.5x10 ⁻⁵
VIII	27	-	69	-	-	2	29.4±2.0	10 ⁻⁵ -10 ⁻¹	2.4x10 ⁻⁶
IX	27	-	-	69	-	2	27.2±1.2	10 ⁻⁵ -10 ⁻¹	3.9x10 ⁻⁵

The potentiometric response of the prepared microsensor was monitored as a function of Cu(II) concentration in the range 10⁻⁸ to 10⁻¹ mol.L⁻¹. The dynamic potentiometric response of the sensor and calibration curve are shown in Figure 2 and 3, respectively. As can be seen from Figures, the microsensor shows a super-Nernstian behavior with a slope of 31.3±2.1 mV mV/decade (R²= 0.997) over a linear concentration range of 10⁻⁵-10⁻¹ mol.L⁻¹, a lower detection limit of 7.67x10⁻⁶ mol.L⁻¹ and a short response time (t₉₅) of <15 s.

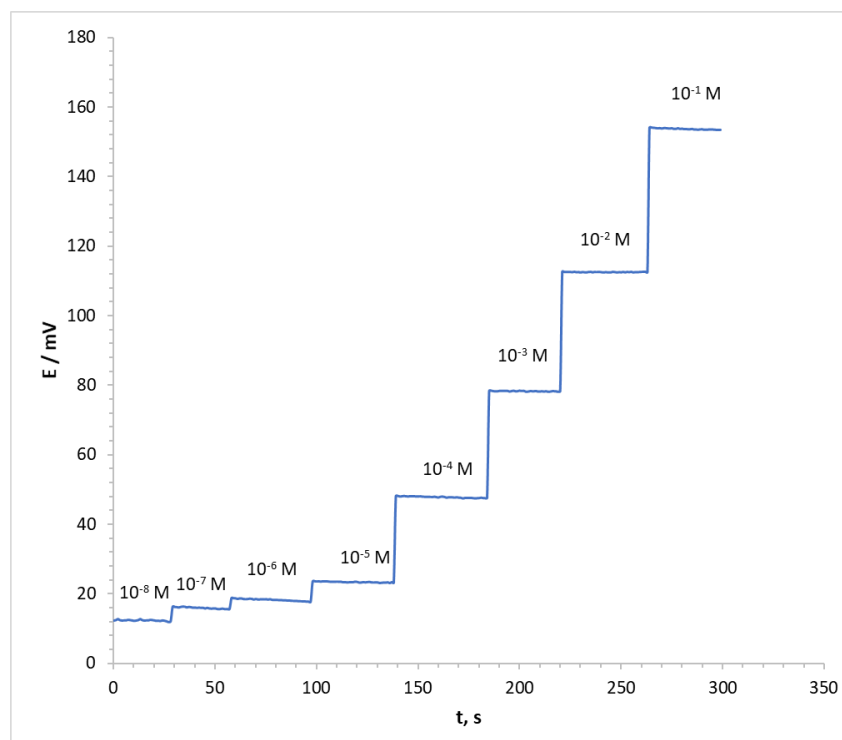


Figure 2. Dynamic potentiometric response of the Cu(II)-selective microsensor

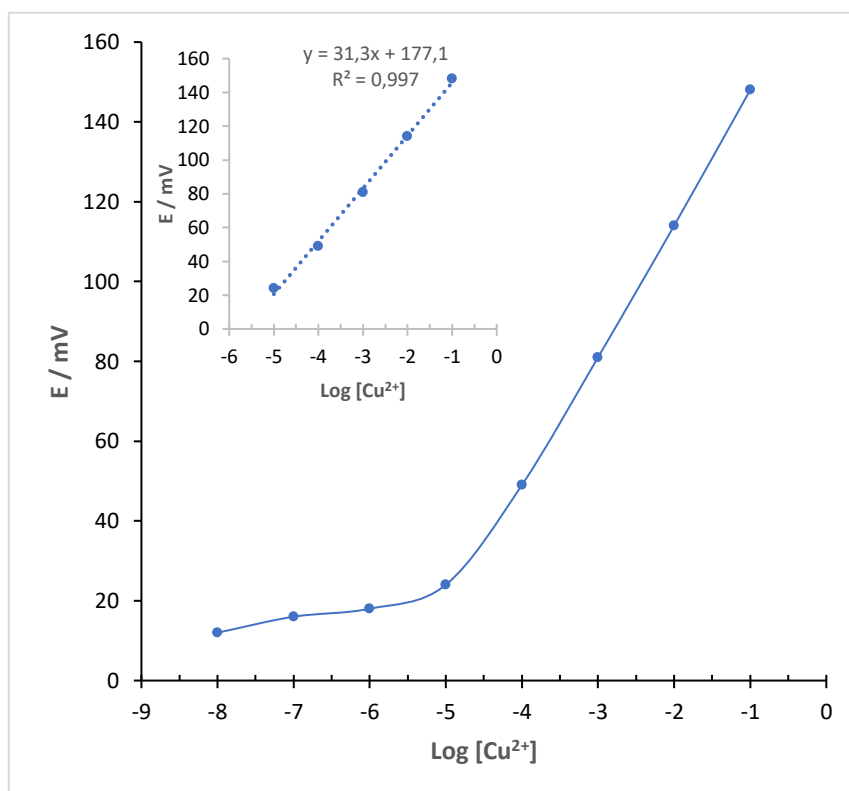


Figure 3. Calibration curves of the Cu(II)-selective microsensor

3.2. The Repeatability and Lifetime

In order to demonstrate the repeatability of the Cu(II)-selective microsensor, potential measurements were conducted in the Cu(II) solutions in the concentration range of 10^{-5} – 10^{-1} mol.L⁻¹. The obtained real-time potential measurements depending on time are shown in Figure 4. As can be seen from Figure 4, the response of the sensor is highly repeatable in the concentration range of 10^{-5} – 10^{-1} mol.L⁻¹ (the average values \pm standard deviations are 21.63 ± 1.69 , 49.53 ± 1.73 , 81.17 ± 1.44 , 112.89 ± 1.25 , 148.61 ± 1.14). The potentiometric measurements in Figure 4 shows that the newly developed microsensor had good potentiometric repeatability and stability. The proposed sensor can also be used for 8 weeks without any significant drift in potential.

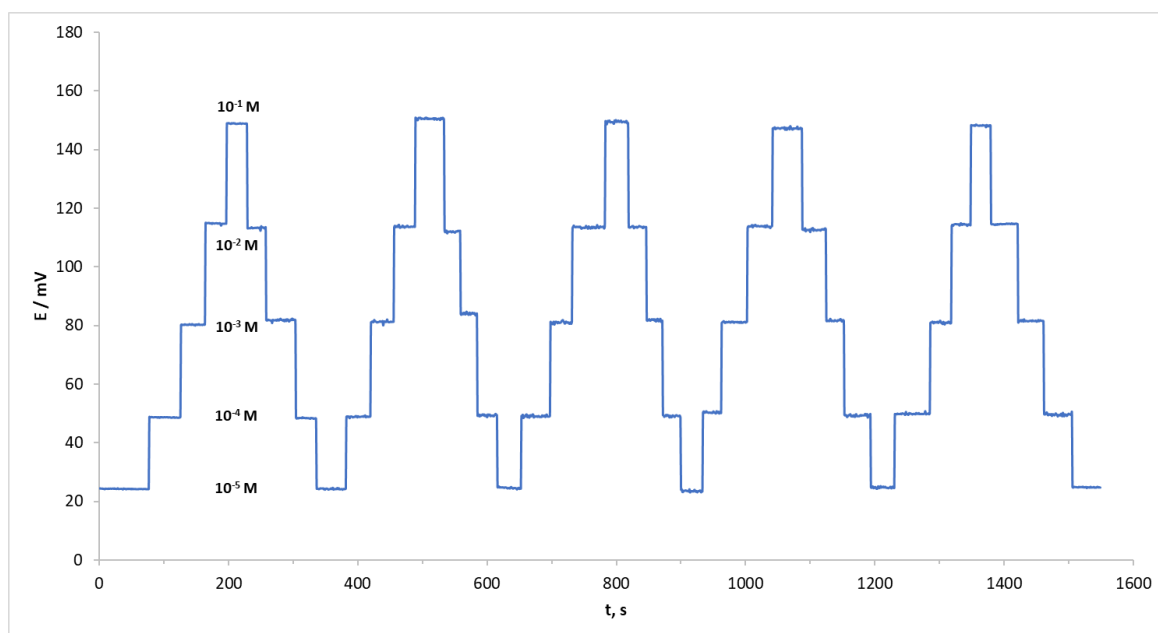


Figure 4. Repeatability measurements of the Cu(II)-selective microsensor

Measurements were performed to determine the lifetime of the Cu(II)-selective microsensor on certain days for 70 days in the range of 10^{-5} to 10^{-1} mol.L⁻¹ Cu²⁺ and the changes in the slope values were examined. The obtained slope values are shown in Figure 5. It is seen that the stability of the microsensor deteriorates significantly after 60 days. The lifetime of the microsensor was calculated to be around 8 weeks as a result.

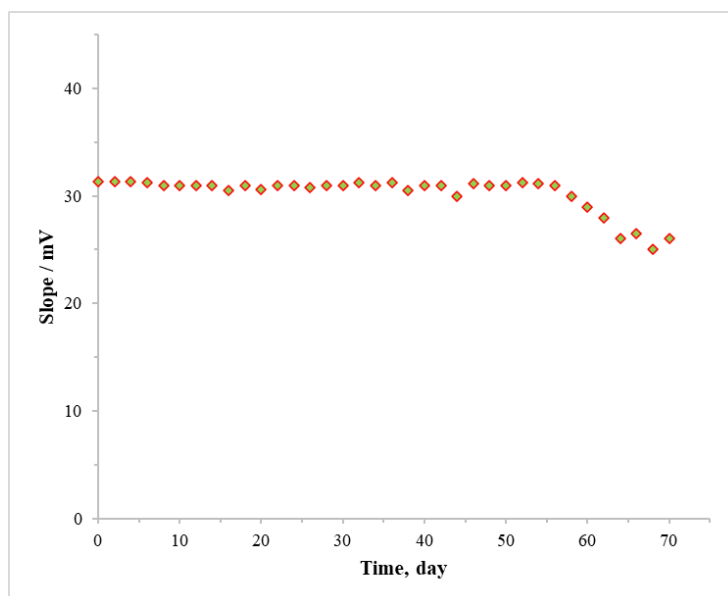


Figure 5. The lifetime graph of the Cu(II)-selective sensor

3.3. Selectivity

The most important property that affects the performance of an ion-selective electrode is selectivity and determines whether the sensor can be used in sample solution containing other ions. The selectivity coefficients of the Cu(II)-selective microsensor were calculated using the separate solution method (SSM) [23]. The logarithmic selectivity coefficients obtained for Cu(II) ions compared to other cations (X^{n+}) are summarized in Table 2. The prepared microsensor was tested against cationic species commonly encountered in samples and exhibited high selectivity for Cu(II) ions.

Table 2. Selectivity coefficients for Cu(II)-selective microsensor

Interferent	$\text{Log } K_{\text{Cu}^{2+}, X^{n+}}^{\text{pot}}$	Interferent	$\text{Log } K_{\text{Cu}^{2+}, X^{n+}}^{\text{pot}}$
Li ⁺	-3.83	Na ⁺	-3.34
K ⁺	-2.38	Ca ²⁺	-3.17
Mg ²⁺	-3.14	Mn ²⁺	-2.70
Zn ²⁺	-2.89	Ni ²⁺	-2.75
Cd ²⁺	-2.62	Co ²⁺	-2.68
Cr ³⁺	-2.80	Pb ²⁺	-2.01

3.4. Effect of pH

One of the parameters that affects the properties of the microsensor is pH. To examine the effect of pH on the sensor response, the sensor potentials were measured over the pH range 2.0–10.0 (adjusted with HNO₃ and NaOH) for 10⁻³ and 10⁻² mol.L⁻¹ Cu(II) solution. The results obtained are given in Figure 6. As can be seen from Figure 6, the potential of the microsensor remained unchanged between pH 5.0–8.0. The potential value varies significantly between pH 2.0 and

5.0. The change of potential in this range can be explained as the response of the sensor to hydronium ions in the membrane phase. When pH was increased above 8, an increase in potential was observed due to the formation of hydroxide complexes of Cu(II) in the basic solution.

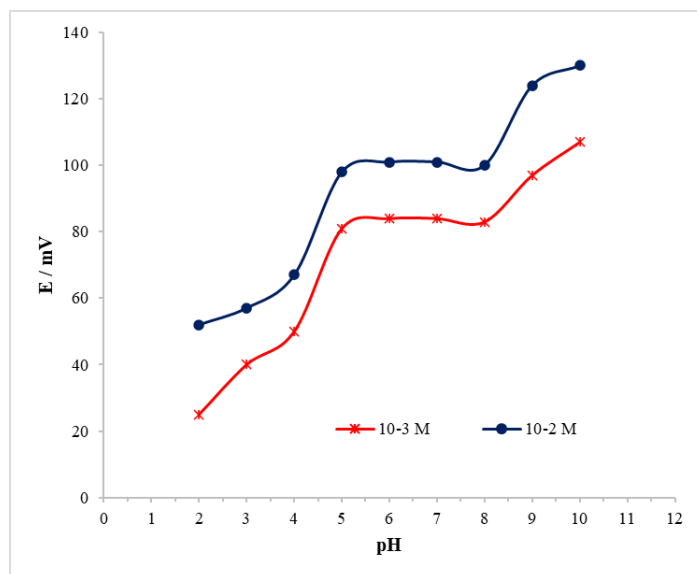


Figure 6. pH-mV graphic of the Cu(II)-selective microsensor

3.5. Temperature Effect

Temperature is among the other important features of ion-selective electrodes. For this purpose, in order to determine the optimum temperature range of the Cu(II)-selective microsensor, it was changed from 5 °C to 70 °C in 10^{-2} mol.L⁻¹ Cu²⁺ solution and the potential values obtained against temperature are shown in Figure 7.

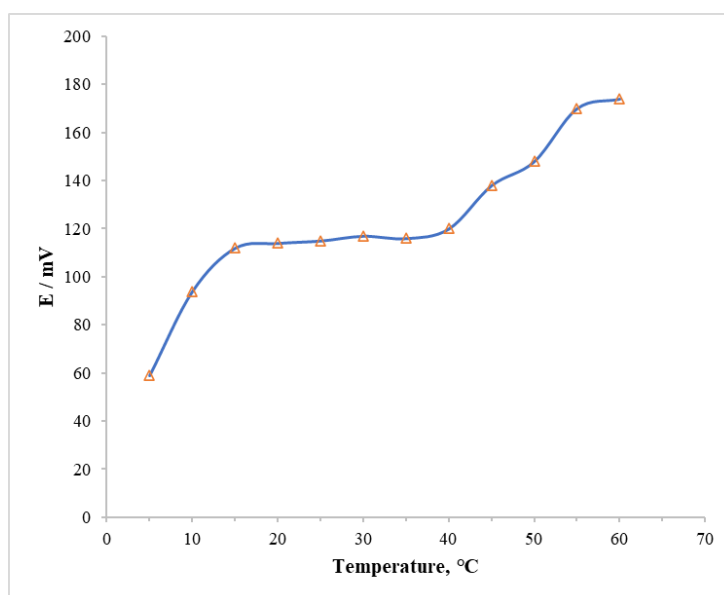


Figure 7. Temperature effect on the Cu(II)-selective microsensor performance

It is seen that there is no significant change in the potential values of the Cu(II)-selective microsensor at approximately 15-40 °C. It has been determined that the sensor is affected by temperatures above 40 °C and is also deformed. As a result, it can be said that the optimum temperature range of the sensor is 15-40 °C.

3.6. Analytical Applications

3.6.1. Potentiometric Titration

It has been observed that Cu(II)-selective microsensor prepared in optimum membrane composition works well under laboratory conditions. To display the applicability of the proposed microsensor in the real samples, the sensor was used as an indicator electrode in the potentiometric titration of 10 mL of 10^{-3} M $\text{Cu}(\text{NO}_3)_2$ with 10^{-3} M EDTA solution (pH=5.5). A typical titration curve is shown in Figure 8. As seen from Figure, the end point of titration (9.5 ± 0.3 mL) can be accurately determined by the sensor.

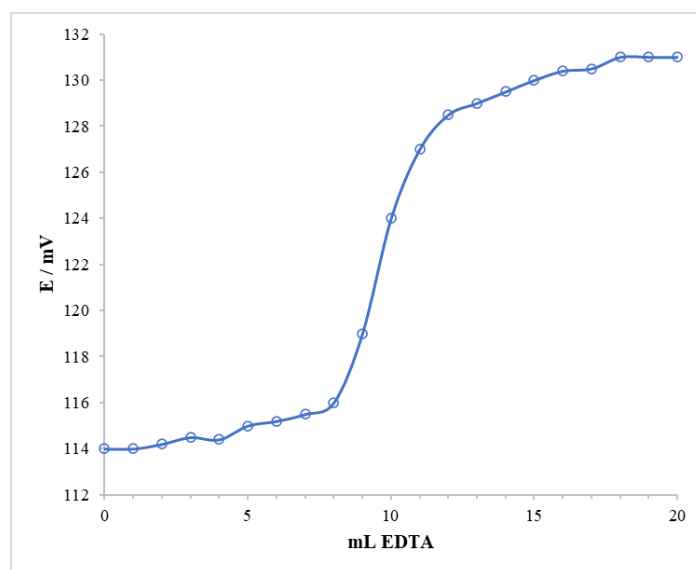


Figure 8. Titration curve of 10 mL 10^{-3} mol.L $^{-1}$ Cu^{2+} with 10^{-3} mol.L $^{-1}$ EDTA

3.6.2. Real Sample Analysis

The prepared Cu(II)-selective microsensor was also applied to some environmental water samples (collected from Giresun Region on the north coast of Turkey) and for potentiometric determination of Cu(II) content in standard reference material (SRM) solution. The ICP-OES method was used as a reference method to evaluate the accuracy, precision and reliability of the results obtained in the accuracy of the potentiometric method. Before potential measurements, water samples were saturated (1:100) and the SRM solution was diluted (100:1). In order to analyze Cu(II) in these different real samples, the standard addition method was used and added Cu^{2+} solutions at the different amounts as indicated in Table 3. Student's *t*-test and the relative error (E_{ra}) values were used for statistical processing of data. The calculated *t* and E_{ra} values are summarized in Table 3. As seen in Table 3, the developed Cu(II)-ISE

displayed very high recovery rates in the analysis of Cu(II) in different real samples. The calculated t value (0.935) was less than the critical t value (3.182) at a 95% confidence level. Moreover, the E_{ra} values were less than 15%. Thus, it can be concluded that the method applying the proposed microsensor is a satisfactory agreement compared with the ICP-MS method. As a result, it can be stated that the developed Cu(II)-selective sensor can be successfully used to determine Cu(II) ions in different real samples.

Table 3. Determination of Cu²⁺ contents in water samples

Sample	Concentration of Cu ²⁺ (ppm) *		E_{ra} (%)	t^c
	Potentiometry	ICP-OES		
Spring water	0.018±0.005	0.016±0.001	12.5	
River water	0.146±0.034	0.132±0.005	10.6	
Top water	0.045±0.007	0.042±0.002	7.1	0.935
Waste water	0.623±0.092	0.594±0.012	4.9	
SRM solution	0.255±0.054	0.240±0.008	6.2	

^a The average values of three determinations ± standard deviation.

^b E_{ra} is the relative error for the potentiometry versus ICP-OES.

^c Calculated t value is 0.935 by a paired t test, the theoretical values of t is 3.182 ($p=0.05$).

3.6.3. Comparison of the Proposed Sensor with the other Cu(II)-selective Sensors

The comparison of the newly developed Cu(II)-selective microsensor with previously proposed Cu(II)-selective sensors or electrodes in the literature in terms of concentration range, detection limit, slope, pH operating range and response time parameters is summarized in Table 4.

Table 4. Comparison of the proposed sensor to the various reported Cu(II)-selective electrodes

Referans	Linear Range, mol.L ⁻¹	Slope, mV/decade	Response Time, s	Detection Limit, mol.L ⁻¹	pH Range
[24]	1.0x10 ⁻⁶ -1.0x10 ⁻¹	29.60	8	8.75x10 ⁻⁷	5.0-9.0
[25]	1.0x10 ⁻⁵ -5.0x10 ⁻¹	30.45	-	1.99x10 ⁻⁶	3.0-6.0
[26]	1.0x10 ⁻⁶ -1.0x10 ⁻¹	28.50	20	4.0x10 ⁻⁷	4.0-7.0
[27]	1.0x10 ⁻⁵ -2.0x10 ⁻¹	28.10	22	2.0x10 ⁻⁶	3.0-8.0
[28]	1.0x10 ⁻⁸ -1.0x10 ⁻¹	29.50	15	5.0x10 ⁻⁶	3.5-6.5
This work	1.0x10 ⁻⁵ -1.0x10 ⁻¹	31.30	<15	7.6x10 ⁻⁶	5.0-8.0

As can be seen from the results in Table 4, it is concluded that the potentiometric properties of the fabricated sensor are comparable to previously reported electrodes in terms of the compared criteria. The concentration range and slope value are similar for all proposed sensors. The proposed Cu(II)-selective microsensor has a lower detection limit, a wider pH operating range,

and relatively shorter response time compared to existing sensors in the literature. Thus, it can be clearly seen that the proposed Cu(II)-selective microsensor has some advantages over other previously developed Cu(II)-selective sensors or electrodes. The resulting Cu(II)-selective microsensor can be considered a good contribution to the list of Cu(II)-selective sensors available in the literature.

4. Conclusion

Calixarene derivatives have unique properties in material chemistry. For real application analysis, those with different functional moiety groups displayed excellent sensing behaviour towards heavy metal ions with good sensitivity, reproducibility, and repeatability. In addition, calixarene derivatives can be used directly as an ionophore in the construction of different chemical sensors, especially in that potentiometry-based ones. In the present work, a novel all-solid-state type PVC-membrane Cu(II)-selective microsensor has been developed a potentiometric sensor selective for Cu(II) ions using a calixarene derivative molecule as an ionophore. The produced Cu(II)-selective microsensor was successfully used as an indicator electrode for potentiometric titrations. The Cu(II)-selective microsensor was also successfully used for accurate, rapid, selective and reproducible determination of Cu(II) ions in environmental samples.

Ethics in Publishing

There are no ethical issues regarding the publication of this study.

Author Contributions

All authors contributed to the study's conception and design. All authors read and approved the final manuscript. Cigdem Cay executed the experiments; Murat Yolcu carried out the manuscript writing, model validation and interpretation and corrections; Serkan Sayin synthesized the compound calixarene and interpretation and corrections.

5. References

- [1] N. Dere, Z. Yolcu, M. Yolcu, A Novel Solid-State PVC-Membrane Potentiometric Dopamine-Selective Sensor Based on Molecular Imprinted Polymer, *Acta Chim Slov*, 69 (2022) 108-115.
- [2] O. Özbek, Ö. Isildak, Potentiometric determination of copper(II) ions based on a porphyrin derivative, *J Chin Chem Soc-Taip*, 69 (2022) 1060-1069.
- [3] M. Yolcu, N. Dere, A novel copper selective sensor based on ion imprinted 2-vinylpyridine polymer, *Can J Chem*, 96 (2018) 1027-1036.
- [4] C.J. Mei, S.A.A. Ahmad, A review on the determination heavy metals ions using calixarene-based electrochemical sensors, *Arab J Chem*, 14 (2021).

- [5] M.S. Engin, S. Sayin, S. Cay, E. Kir, T. Sardohan-Koseoglu, Preparation and characterisation of thiol functionalised-butylcalix[4]arene-embedded polymer inclusion membranes: performance and selectivity, *Int J Environ an Ch*, 99 (2019) 1103-1111.
- [6] V.K. Gupta, S. Kumar, R. Singh, L.P. Singh, S.K. Shoor, B. Sethi, Cadmium (II) ion sensing through p-butyl calix[6]arene based potentiometric sensor, *J Mol Liq*, 195 (2014) 65-68.
- [7] L.X. Chen, H.F. Ju, X.S. Zeng, X.W. He, Z.Z. Zhang, Silver ion-selective electrodes based on novel containing benzothiazolyl calix[4]arene, *Anal Chim Acta*, 437 (2001) 191-197.
- [8] B. Sonmez, S. Sayin, E. E. Yalcinkaya, D. A. Selec, H. B. Yildiz, D. O. Demirkol, S. Timur, Calixarene modified montmorillonite: a novel design for biosensing applications. *RSC Adv.*, 2014, 4, 62895–62902
- [9] H. E. K. Ertürün, A.D. Özel, S. Sayın, M. Yılmaz, E. Kılıç, Development of a pH sensing membrane electrode based on a new calix[4]arene derivative. *Talanta* 132(2015)669–675.;
- [10] S. Kucukkolbasi, S. Sayin, M. Yılmaz, Fabrication and Application of a New Modified Electrochemical Sensor Using Newly Synthesized Calixarene-Grafted Mwcnts for Simultaneous Determination of Cu(II) and Pb(II). *Acta Chim. Slov.* 2019, 66, 839–849.;
- [11] S. Sayin, S. Cay, Novel An Efficient Fluorescent Probe Based on Calix[4]triazacrown-5 With Naphthalimide Group for Co²⁺, Cd²⁺ and Dopamine Detection. *Journal of Fluorescence* (2024) 34:729–741
- [12] P. Kumar, All Solid State Nickel(II)-Selective Potentiometric Sensor Based on an Upper Rim Substituted Calixarene, *Electroanal*, 24 (2012) 2005-2012.
- [13] C. Wardak, M. Grabarczyk, Analytical application of solid contact ion-selective electrodes for determination of copper and nitrate in various food products and drinking water, *J Environ Sci Heal B*, 51 (2016) 519-524.
- [14] K. Pietrzak, C. Wardak, B. Cristóvão, Copper ion-selective electrodes based on newly synthesized salen-type Schiff bases and their complexes, *Ionics*, 28 (2022) 2423-2435.
- [15] M. Bost, S. Houdart, M. Oberli, E. Kalonji, J.F. Huneau, I. Margaritis, Dietary copper and human health: Current evidence and unresolved issues, *J Trace Elem Med Bio*, 35 (2016) 107-115.
- [16] C. Wardak, J. Lenik, Application of ionic liquid to the construction of Cu(II) ion-selective electrode with solid contact, *Sensor Actuat B-Chem*, 189 (2013) 52-59.
- [17] V.K. Gupta, R. Prasad, A. Kumar, Preparation of ethambutol-copper(II) complex and fabrication of PVC based membrane potentiometric sensor for copper, *Talanta*, 60 (2003) 149-160.
- [18] L.P. Singh, J.M. Bhatnagar, Copper(II) selective electrochemical sensor based on Schiff Base complexes, *Talanta*, 64 (2004) 313-319.

- [19] C.D. Gutsche, K.C. Nam, Calixarenes .22. Synthesis, Properties, and Metal Complexation of Aminocalixarenes, *J Am Chem Soc*, 110 (1988) 6153-6162.
- [20] K. Kurzatowska, S. Sayin, M. Yilmaz, H. Radecka, J. Radecki, Calix[4]arene derivatives as dopamine hosts in electrochemical sensors, *Sensor Actuat B-Chem*, 218 (2015) 111-121.
- [21] I. Bitter, A. Grün, G. Toth, B. Balazs, G. Horvath, L. Töke, Studies on Calix(aza)crowus, II. I Synthesis of Novel Proximal Doubly Bridged Calix[4]arenes by Intramolecular Ring Closure of syn 1,3- and 1,2- ω - Chloroalkylamides. *Tetrahedron* 54 (1998) 3857-3870.
- [22] I. Isildak, M. Yolcu, O. Isildak, N. Demirel, G. Topal, H. Hosgoren, All-solid-state PVC membrane Ag-selective electrodes based on diaza-18-crown-6 compounds, *Microchim Acta*, 144 (2004) 177-181.
- [23] P. R. Buck and E. Lindner, "Recommendations for Nomenclature of Ionselective Electrodes," *Pure and Applied Chemistry*, 66-12 (1994) 2527-2536.
- [24] O. Özbek, M.B. Gürdere, C. Berkel, Ö. Isildak, Electroanalytical Determination of Copper(II) Ions Using a Polymer Membrane Sensor, *J Electrochem Sci Te*, 14 (2023) 66-74.
- [25] K. Udomphan, I. Sontawee, I. Dangsanga, 8-Hydroxyquinoline intercalated montmorillonite composite: characterization and application for copper ion determination as potentiometric electrode, *J Solid State Electr*, 27 (2023) 977-989.
- [26] S. Kaur, J. Kaur, M. Rana, J. Sharma, I. Kaur, Salicylaldehyde based Schiff base: synthesis, characterisation and application for selective electrochemical detection of Cu in real samples, *Int J Environ an Ch*, (2023).
- [27] M.A. Abu-Dalo, A.A. Salam, N.S. Nassory, Ion Imprinted Polymer Based Electrochemical Sensor for Environmental Monitoring of Copper(II), *Int J Electrochem Sc*, 10 (2015) 6780-6793.
- [28] V.K. Gupta, L.P. Singh, R. Singh, N. Upadhyay, S.P. Kaur, B. Sethi, A novel copper (II) selective sensor based on Dimethyl 4, 4' (o-phenylene) bis(3-thioallophanate) in PVC matrix, *J Mol Liq*, 174 (2012) 11-16.

Synthesis and antitubercular activities of acetamide-substituted benzazole derivatives

Sule Gursoy^{1,*}, Elif Sevval Ozturk², Bayan Zoatier³, Mahmut Ulger⁴ and Oztekin Algul^{2,3}

¹Department of Biochemistry, Faculty of Pharmacy, Erzincan Binali Yıldırım University, Erzincan, Turkey

²Department of Pharmaceutical Chemistry, Faculty of Pharmacy, Erzincan Binali Yıldırım University, Erzincan, Turkey

³Department of Pharmaceutical Chemistry, Faculty of Pharmacy, Mersin University, Mersin, Turkey

⁴Department of Pharmaceutical Microbiology, Faculty of Pharmacy, Mersin University, Mersin, Turkey

Abstract

Multidrug-resistant *Mycobacterium tuberculosis* strains' increasing emergence and rapid spread necessitate the urgent development of innovative antimycobacterial agents. In pursuit of novel agents, a series of N-(benzazole-2-ylmethyl)-2-substituted phenylacetamide or N-(benzazole-2-ylmethyl)-2-(thiophen-2-yl)acetamide compounds (6-11) were synthesized. Their efficacy against multidrug-resistant *Mycobacterium tuberculosis* was assessed. Compounds exhibited potent antimycobacterial activity with minimum inhibitory concentrations (MIC) ranging from 1.05 to 4.10 µM and demonstrated low cytotoxicity towards fibroblast cell line (L929), as indicated by IC₅₀ values ranging from 196.23 to 487.34 µM and selectivity indices (SI) ranging from 57.23 to 186.11. ADMET predictions suggested that these synthesized compounds possess drug-like properties. Our findings offer a promising starting point for designing more selective and potent antimycobacterial agents.

Keywords: Benzazole, synthesis, *Mycobacterium tuberculosis*, MIC, antitubercular activity

Asetamit Süstitüte Benzazol Türevlerinin Sentezi ve Antitüberküloz Aktiviteleri

Öz

Çoklu ilaca dirençli mikobakterium tüberkülozis suşlarının artan ortaya çıkışı ve hızlı yayılımı, acil olarak yenilikçi antimikobakteriyel ajanların geliştirilmesini gerektirmektedir. Yeni ajanların geliştirilmesi amacıyla, N-(benzazol-2-ilmetil)-2-süstitüe fenilasetamit veya N-(benzazol-2-ilmetil)-2-(tiyofen-2-il)asetamit bileşik serisi (6-11) sentezlendi. Bu bileşiklerin çoklu ilaca dirençli mikobakterium tüberkülozis 'e karşı etkinliği değerlendirildi. Bileşikler, minimum inhibitör konsantrasyonları (MIC) 1.05 ile 4.10 µM arasında değişen güçlü antimikobakteriyel aktivite sergiledi ve IC₅₀ değerleri 196.23 ile 487.34 µM arasında değişen ve seçicilik indeksleri (SI) 57.23 ile 186.11 arasında olan fibroblast hücre hattına (L929) karşı düşük sitotoksitesite gösterdi. ADMET çalışmaları, sentezlenen bileşiklerin ilaç benzeri özelliklere sahip olduğunu göstermektedir. Bulgularımız, daha seçici ve güçlü antimikobakteriyel ajanlar tasarlamak için umut verici bir başlangıç noktası sunmaktadır.

Anahtar Kelimeler: Benzazol, sentez, mikobakteriyum tüberkülozis, MİK, antitüberküloz aktivite

*Corresponding Author: sule.gursoy@erzincan.edu.tr

Sule Gursoy, <https://orcid.org/0000-0001-5236-5974>

Elif Şevval Öztürk, <https://orcid.org/0009-0005-1245-0206>

Bayan Zoatier, <https://orcid.org/0009-0006-5512-3069>

Mahmut Ulger, <https://orcid.org/0000-0002-2015-5435>

Oztekin Algul, <https://orcid.org/0000-0001-5685-7511>

1. Introduction

Since the early 1990s, tuberculosis (TB) has been recognized globally as a significant public health threat, accounting for the highest number of adult deaths due to infectious diseases worldwide. *Mycobacterium tuberculosis* is the primary species responsible for TB infections [1, 2]. Its resurgence in epidemic proportions indicates that substantial efforts are still needed to safeguard patients and healthcare professionals from its potentially fatal consequences [3]. Molecular evidence suggests that TB ranks second globally in terms of death rates caused by a single infectious agent in 2022, causing approximately twice as many deaths as HIV/AIDS. Tuberculosis remains a significant global health issue. According to the World Health Organization (WHO), there is an estimated annual increase of approximately 1.1% in TB cases worldwide, with over 10 million new TB cases reported each year. [4].

Benzazoles derivatives (benzimidazole, benzothiazole and benzoxazole) display a broad spectrum of activities, including antibacterial, antifungal, antitubercular, antimalarial, anti-inflammatory, analgesic, anti-amoebic, antiulcerative, antioxidant, antihypertensive, antiallergic, antiproliferative, antitumor, and anti-HIV-1 properties [5–7]. Due to their straightforward and rapid synthesis along with other advantageous properties, benzazoles hold promise as potential anti-TB agents. Benzazoles have consistently attracted the attention of researchers, not only from synthetic or biosynthetic perspectives but also due to its intriguing biological characteristics [8–19].

Benzazole rings are recognized by living organisms due to their isosteric nature with DNA bases (purine and pyrimidine cores) and their presence in natural structures like the amino acid tryptophan. Despite numerous studies on the antimicrobial activities of benzazole and bioisostere structures and their substituted derivatives, literature on compounds carrying amid linkages in benzazole derivatives is scarce. Particularly, structure-activity studies conducted on the compounds registered in the literature and those designed in this study suggest that the compounds designed in this study may possess antitubercular activity [20–27].

Previous research revealed that benzothiazole and benzoxazole groups demonstrate superior antimicrobial activities compared to other benzazole groups. This led to prioritizing these groups in our current work, with plans to compare them with other benzazole groups in future studies [8, 28–30].

The amide functional group is crucial in the structure of many biologically active molecules. Amide structures are not only stable but also possess highly positive and negative electric charge densities, making them polar structures. This polarity allows drugs containing amide structures to easily interact with biological receptors and enzymes. In addition to facilitating interactions with biological targets, amide-containing drugs are also resistant to rapid metabolic degradation in the body's complex environment. Consequently, due to its significant bond polarity, stability, and conformational versatility, the amide bond stands out as one of the most effective functional groups. The amide functional group is crucial in the structure of biomolecules, including numerous clinically approved drugs. Consequently, the use of the amide bond was planned in the designed bis structures [31–34].

Recent studies on benzazoles and the above literature survey encouraged us to synthesize some new compounds containing benzazole moiety hoping to obtain new compounds with potential antitubercular activity [27]. The inclusion of the amide functional group in the benzoxazole structure has the potential to contribute to the development of various activities. Current studies

have shown that such modifications can enhance biological activity. In this context, our presented study can inspire the development of more effective antituberculosis agents. In our previous research, we investigated the antitubercular effects of compounds with a benzimidazole structure, an isosteric analog of benzoxazole and benzothiazole. In this study, some benzazole derivatives containing an amide linker were designed and synthesized (Figure 1). The results demonstrated significant antitubercular activity [35, 36, 37].

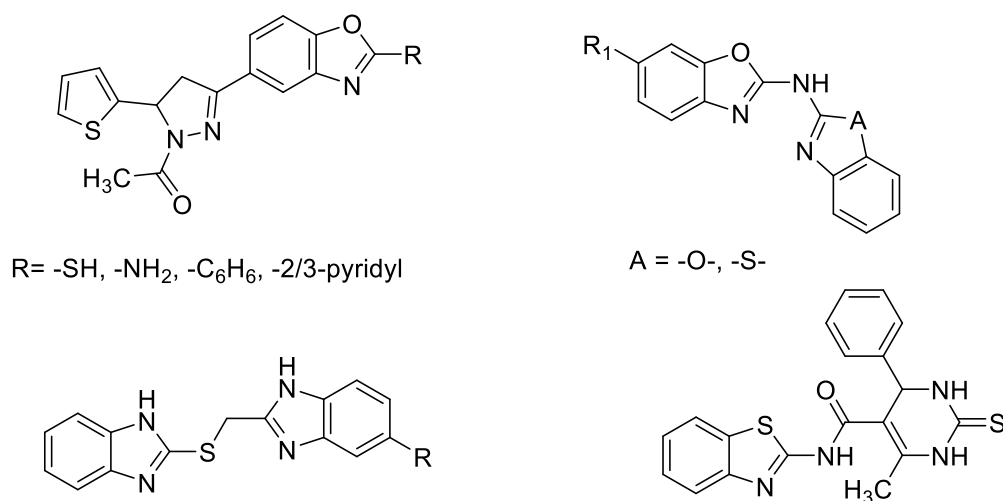


Figure 1. Structures of antitubercular active benzazole compounds

Here, we describe the synthesis of a series of N-(benzazole-2-ylmethyl)-2-substituted phenylacetamide or N-(benzazole-2-ylmethyl)-2-(thiophen-2-yl)acetamide compounds. The structures of the synthesized derivatives were elucidated by the spectroscopic data. Then, we determined antitubercular effects of the synthesized compounds by *in vitro* activity.

2. Material and Methods

2.1. Chemistry

All reagents utilized were of analytical grade, sourced from Sigma-Aldrich, and employed without further purification. Thin-layer chromatography (TLC) was conducted on silica gel-coated F254 Merck plates to monitor reaction progress and product mixtures. Melting points were measured using an Electrothermal-9200 digital apparatus, with recorded values remaining uncorrected. Nuclear magnetic resonance (NMR) spectra, encompassing both ¹H NMR and ¹³C NMR, were acquired employing a Bruker 400 NMR spectrometer for ¹H NMR and a Bruker 100 NMR spectrometer for ¹³C NMR. The NMR spectra were acquired in deuterated solvents such as dimethyl sulfoxide (DMSO-d₆) or chloroform (CDCl₃), with chemical shifts (δH) reported in parts per million (ppm) relative to tetramethylsilane (TMS) as an internal standard. Fourier transform infrared attenuated total reflection (FT-IR ATR) spectra were recorded using a Varian FTS1000 FT-IR spectrometer equipped with a Diamond/ZnSe prism (4000–525 cm⁻¹; number of scans: 250; resolution: 1 cm⁻¹) in the solid state.

2.1.1. General procedure for the synthesis of target compounds (6-11):

Aminomethylbenzazoles (2-aminomethylbenzoxazole/2-aminomethylbenzothiazole) (1.1 mmol) were dissolved in dichloromethane (DCM) (15 mL). 2-Phenylacetyl chloride derivatives or -(thiophen-2-yl)acetyl chloride (1.1 mmol) were added dropwise to the initial solution at 0

°C over a period of 10-30 minutes. The reaction mixture was stirred at 0 °C for two hours. Subsequently, 5 drops of diisopropylethylamine (DIPEA) were added and the reaction mixture was refluxed under a reversing cooler for 24 hours. After confirming the completion of the reaction with TLC, the reaction was terminated, and the solvent was evaporated. DCM (25 mL) was added, and the organic phase was washed with 1N HCl (3 x 20 mL), followed by saturated NaHCO₃ solution (2 x 15 mL) and 15 mL of distilled water. The organic phase was separated, treated with MgSO₄, filtered, and the solvent was evaporated under reduced pressure. The resulting product was purified by column chromatography using an appropriate n-hexane/ethyl acetate mobile phase. The obtained products were recrystallized using an appropriate solvent [38].

2.2. Antitubercular activity

2.2.1. Agar proportion method

Following the guidelines set by the Clinical Laboratory Standards Institute (CLSI), the minimum inhibitory concentration (MIC) values for each synthesized compound were determined using duplicate agar dilution techniques [39]. Each assay included both positive and negative growth controls. Isoniazid (INH; Sigma I3377) and Rifampisin (RIF; Sigma-Aldrich R7382) served as control agents. The MTB H37Rv strain, provided by the National Tuberculosis Reference Laboratory at Refik Saydam National Public Health Agency in Ankara, Turkey, was used as the standard strain.

2.2.2. Cytotoxic activity

Cytotoxic impact of the investigated compounds were assessed using fibroblast L929 and the 3-(4,5-dimethylthiazol-2-yl)-2,5-diphenyl tetrazolium bromide (MTT) colorimetric assay [40, 41].

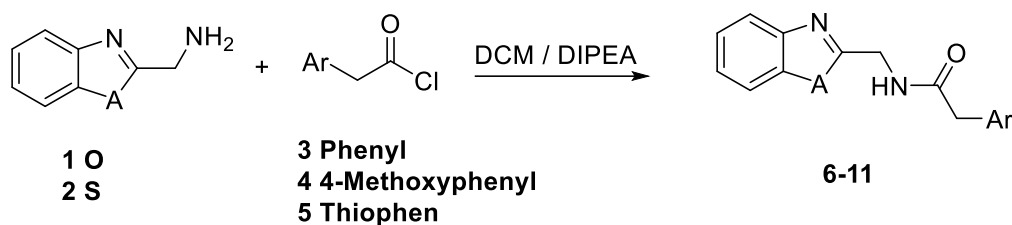
2.3. In silico ADMET prediction

In ADMET studies, the Maestro 11.8 (Schrodinger) program was used. The compounds were minimized after being prepared with LigPrep, and their ADME properties were investigated using the Qikprop module [42]. Predicted toxic properties of compounds were calculated using DataWarrior 5.5.0.

3. Results and Discussion

3.1. Chemistry

The target molecules were synthesized in single steps as depicted in Scheme 1. 2-Aminomethylbenzazoles (**1**, **2**) and non/4-methoy-2-phenylacetyl chloride (**3**, **4**) or 2-(thiophen-2-yl)acetyl chloride (**5**) under reflux, target compounds N-(benzo[d]oxazol or benzo[d]thiazol-2-ylmethyl)-2-phenylacetamide and N-(benzo[d]thiazol or benzo[d]thiazol-2-ylmethyl)-2-(thiophen-2-yl)acetamide (**6-11**) were obtained. Table 1 provides the chemical structures of all compounds.


Scheme 1. General synthetic procedure for compounds **6-11**
Table 1. Structure of all synthesized compounds.

Comp. No	Structure	Comp. No	Structure
6		9	
7		10	
8		11	

N-(benzo[d]oxazol-2-ylmethyl)-2-phenylacetamide (6)

 White solid, m.p. 215-216 °C, R_f 0.53 in chloroform/methanol (9.5:0.5), Yield; 54%.

 $^1\text{H NMR}$ (ppm): δ = 7.49–7.47 (dd, J = 7.0, 2.7 Hz, 2H, aromatic-H), 7.25–7.22 (dd, J = 7.0, 2.7 Hz, 1H, aromatic-H), 7.21 (m, 1H, aromatic-H), 7.20–7.16 (m, 1H, aromatic-H), 7.14–7.12 (m, 1H, aromatic-H), 5.29 (s, 2H, aliphatic- CH_2N -), 3.56 (d, J = 2.1 Hz, 2H, aliphatic- CH_2CO -).

 $^{13}\text{C NMR}$ (ppm): δ = 172.2, 148.5, 138.2, 133.2, 129.3, 128.7, 127.4, 123.1, 115.5, 60.3, 40.8.
 FT-IR (cm^{-1}): 3028, 2969, 2946, 1739, 1444, 1356, 1216.

N-(benzo[d]thiazol-2-ylmethyl)-2-phenylacetamide (7)

 White solid, m.p. 192 °C, R_f 0.55 in chloroform/methanol (9.5:0.5), Yield; 50%.

 $^1\text{H NMR}$ (ppm): δ = 7.85 – 7.81 (m, 2H, aromatic -H), 7.42- 7.40 (ddd, J = 8.2, 7.3, 1.3 Hz, 1H, aromatic -H), 7.38 – 7.29 (m, 1H, aromatic -H), 7.23 – 7.17 (m, 4H, aromatic -H), 7.14 – 7.10 (m, 1H, aromatic -H), 4.69 (s, 2H, aliphatic - CH_2N -), 3.85 ppm (s, 2H, aliphatic - CH_2CO -).

 $^{13}\text{C NMR}$ (ppm) δ = 174.6, 172.2, 172.1, 154.0, 136.6, 136.2, 130.3, 129.6, 127.9, 127.4, 126.4, 123.4, 123.0, 43.75, 42.4.

 FT-IR (cm^{-1}) 3253, 3015, 2969, 2945, 1738, 1365, 1228.

N-(benzo[d]oxazol-2-ylmethyl)-2-(4-methoxyphenyl)acetamide (8)

 White yellow solid, m.p. 220 °C, R_f 0.50 in chloroform/methanol (9.5:0.5), Yield; 65%.

 $^1\text{H NMR}$ (ppm) δ = 7.51 – 7.47 (m, 2H, aromatic -H), 7.21 – 7.17 (m, 2H, aromatic -H), 7.08 – 7.05 (m, 2H, aromatic -H), 6.77 – 6.75 (m, 2H, aromatic -H), 5.30 (s, 2H, aliphatic - CH_2N -), 3.70 (s, 3H, aliphatic - OCH_3), 3.53 ppm (s, 2H, aliphatic - CH_2CO -).

 $^{13}\text{C NMR}$ (ppm) δ = 172.7, 159.0, 148.4, 137.9, 137.9, 130.4, 130.3, 125.2, 123.2, 115.5, 115.4, 114.2, 60.2, 55.2, 40.03 ppm.

 FT-IR (cm^{-1}) 3065, 2969, 1737, 1365, 1228, 1216.

N-(benzo[d]thiazol-2-ylmethyl)-2-(4-methoxyphenyl)acetamide (9)

White solid, m.p. 202 °C, R_f 0.44 in chloroform/methanol (9.5:0.5), Yield; 40%.

^1H NMR ppm δ = 7.85-7.42 (ddd, J = 8.1, 1.2, 0.5 Hz, 2H, aromatic - $\underline{\text{H}}$), 7.40- 7.38 (ddd, J = 8.1, 7.3, 1.2 Hz, 1H, aromatic - $\underline{\text{H}}$), 7.33 – 7.29 (m, 1H, aromatic - $\underline{\text{H}}$), 7.14 – 7.10 (m, 2H, aromatic - $\underline{\text{H}}$), 6.76 – 6.73 (m, 2H, aromatic - $\underline{\text{H}}$), 4.69 (s, 2H, aliphatic - $\underline{\text{CH}_2\text{N}}$ -), 3.84 (s, 2H, aliphatic - $\underline{\text{CH}_2\text{CO}}$ -) 3.64 ppm (s, 3H, aliphatic - OCH_3).

^{13}C NMR ppm δ = 175.0, 172.1, 160.2, 154.0, 136.2, 131.3, 128.5, 127.4, 126.4, 123.4, 123.0, 115.1, 55.7, 43.7, 42.4.

FT-IR (cm^{-1}) 3255, 3001, 2969, 2945, 1739, 1365, 1216.

N-(benzo[d]oxazol-2-ylmethyl)-2-(thiophen-2-yl)acetamide (10)

White yellow solid, m.p. 195 °C, R_f 0.50 in chloroform/methanol (9.5:0.5), Yield; 30%.

^1H NMR (ppm) δ = 7.52- 7.50 (dd, J = 5.5, 2.9 Hz, 2H, aromatic - $\underline{\text{H}}$), 7.22 – 7.16 (m, 2H, aromatic - $\underline{\text{H}}$), 7.15 – 7.14 (dd, J = 5.5, 1.0 Hz, 1H, aromatic - $\underline{\text{H}}$), 6.88 - 6.86 (dt, J = 5.5, 2.9 Hz, 1H, aromatic - $\underline{\text{H}}$), 6.84 – 6.81 (m, 1H, aromatic - $\underline{\text{H}}$), 5.33 (s, 2H, aliphatic - NCH_2 -), 3.81 ppm (d, J = 1.0 Hz, 2H, aliphatic- COCH_2).

^{13}C NMR (ppm) δ = 171.3, 148.2, 134.0, 127.3, 127.0, 125.4, 123.2, 115.5, 115.5, 115.2, 60.7, 35.0.

FT-IR (cm^{-1}) 3015, 2945, 1738, 1579, 1375, 1217, 1078.

N-(benzo[d]thiazol-2-ylmethyl)-2-(thiophen-2-yl)acetamide (11)

White solid, m.p. 240 °C, R_f 0.52 in chloroform/methanol (9.5:0.5), Yield; 30%.

^1H NMR (ppm) δ = 7.82 - 7.81 (dd, J = 2.8, 1.0 Hz, 1H, aromatic - $\underline{\text{H}}$), 7.80 – 7.78 (m, 1H, aromatic - $\underline{\text{H}}$), 7.40 – 7.36 (m, 1H aromatic -H), 7.31 – 7.27 (m, 1H, aromatic -H), 7.19- 7.17 (dd, J = 5.1, 1.0 Hz, 1H, aromatic- $\underline{\text{H}}$), 6.90- 6.87 (d, J = 3.4 Hz, 1H, aromatic -H), 6.87- 6.86 (dd, J = 5.1, 3.4 Hz, 1H, Ar-H), 4.67 (s, 2H, aliphatic - NCH_2 -), 3.74 ppm (s, 2H, aliphatic - COCH_2).

^{13}C NMR (ppm) δ = 173.2, 172.2, 154.0, 137.5, 136.2, 127.9, 127.9, 127.4, 126.4, 126.0, 123.4, 123.0, 42.7, 37.7.

FT-IR (cm^{-1}) 3291, 3015, 2969, 1739, 1655, 1433, 1253, 1229.

3.2. Biological Assay**3.2.1. In Vitro Antitubercular Activity Studies**

The agar proportion method was used to screen all target compounds against MTB H37Rv [35, 43, 44]. Isoniazid (INH) and rifampicin (RIF) served as positive control drugs in the assay. Table 2 displays the in vitro antimycobacterial activity, represented by the MIC values, for both the target compounds and the standard drugs. The three benzothiazole derivatives (7, 9, 11) show significant activities and other compounds exhibit moderate activities. The results of the antimycobacterial activity tests are presented in Table 2.

Table 2. The Anti-TB activity results of all compounds

Compounds	<i>M. tuberculosis</i> H37Rv (μM)	cLogP
6	4.10	1.991
7	2.82	2.656
8	3.30	2.575
9	1.38	1.910
10	2.95	1.637
11	1.05	2.302
INH	0.12	-0.668
RIF	1.00	3.710

3.2.2 Cytotoxicity Assay

In this study, a selectivity index (SI) was also calculated to assess the cytotoxicity of the synthesized compounds (**6-11**) and determine their suitability as therapeutic candidates. The cytotoxicity of compounds **6-11** was evaluated on normal human cells using the MTT cytotoxicity assay performed on fibroblast L929 cells [31,32]. The results indicated that IC_{50} values for the selected compounds ranged from 196.23 to 487.34 μ M, suggesting a low risk of toxicity with favorable selectivity indices (SI) ranging from 57.23 to 186.11 (Table 3).

Table 3. *In vitro* cytotoxic effect for compounds on fibroblast L929 cells with their selectivity indices.

Compound	$IC_{50} \pm SEM$ L929 cells (μ M)	MIC Mtb H37Rv (μ M)	SI ^a
6	234.65 \pm 3.25	4.10	57.23
7	225.62 \pm 2.87	2.82	80.00
8	389.99 \pm 2.74	3.30	118.18
9	196.23 \pm 4.12	1.38	142.20
10	487.34 \pm 5.58	2.95	165.20
11	195.42 \pm 2.38	1.05	186.11

^aSelectivity index (SI) calculated by dividing L929 cells IC_{50} (mean \pm standard error of the mean [SEM]) by MIC against Mtb H37Rv.

3.3. In silico ADMET prediction

In this study, various ADMET properties of the compounds were assessed using in silico methods. The fulfillment of physicochemical parameters is essential for compounds to qualify as potential drugs, as many compounds fail to reach their target sites due to inadequate physicochemical properties.

All compounds adhere to Lipinski's rule of five and Jorgensen's rule of 3%, indicating their potential to possess favorable pharmacokinetic properties critical for drug development. Lipinski's rule of five suggests that compounds with optimal membrane permeability and oral bioavailability typically exhibit no more than five hydrogen bond donors, no more than ten hydrogen bond acceptors, a molecular weight below 500 Da, and a LogP value less than 5. Similarly, Jorgensen's rule of 3% predicts good oral absorption based on additional parameters. The adherence to these rules suggests that the compounds are likely to be well-absorbed and distributed in the body, undergo manageable metabolism, and exhibit low toxicity.

The high human oral absorption (> 95%) of all compounds is indicative of their efficient oral absorption, a crucial factor in drug development. This high oral absorption suggests that the compounds can effectively reach systemic circulation, thereby potentially enhancing their therapeutic efficacy. Moreover, good oral absorption is often associated with improved patient compliance, as oral administration is typically more convenient compared to other routes.

The LogP values of all compounds fall within the recommended range (2.365–3.258), indicating suitable lipophilicity levels. Lipophilicity, reflecting a compound's ability to dissolve in fats, significantly influences its penetration of cell membranes, thereby affecting its pharmacokinetic behavior. Thus, compounds with LogP values within this range may exhibit favorable pharmacokinetic properties related to ADME, suggesting their potential effectiveness and safety as therapeutic agents.

Furthermore, the compounds do not block the predicted HERG K⁺ channels, exhibit high Caco-2 cell permeability, and have no estimated toxic effects. These findings collectively suggest that the compounds possess favorable drug-like properties.

The lack of blockage of the predicted HERG K⁺ channels implies a reduced risk of cardiac side effects, a common concern in drug development. Additionally, the compounds' high Caco-2 cell permeability indicates efficient gastrointestinal absorption, essential for oral drug administration. Moreover, the absence of estimated toxic effects implies a favorable safety profile, enhancing the compounds' potential as promising candidates for further development as therapeutic agents.

Table 4. Some predicted pharmacokinetic properties of compounds 6-11.

Property or Descriptor	6	7	8	9	10	11	Range or recommended values
MW	266,299	282,359	296,325	312,386	272,321	288,382	(130.0 - 725.0)
SASA	530,086	544,13	578,797	601,329	524,522	536,111	(300.0 - 1000.0)
PSA	61,451	49,617	69,912	58,937	61,662	50,831	(7.0 - 200.0)
donorHB	1	1	1	1	1	1	(0.0 – 6.0)
acceptHB	4,5	4	5,25	4,75	4,5	4	(2.0 – 20.0)
QPlogPo/w	2,419	2,838	2,612	3,258	2,365	2,927	(-2.0 / 6.5)
QPlogHERG	-4,289	-4,417	-4,566	-4,689	-4,103	-4,106	(concern below -5)
QPPCaco	1373,382	1331,351	1672,682	1982,716	1200,483	1708,186	(<25 poor, >500 great)
QPPMDCK	1188,467	1539,599	1435,989	2945,398	1813,418	3516,471	(<25 poor, >500 great)
Lipinski Rule of 5 Violations	0	0	0	0	0	0	maximum is 4
Jorgensen Rule of 3 Violations	0	0	0	0	0	0	maximum is 3
% Human Oral Absorption	100	100	100	100	95,906	100	>80% is high <25% is poor
Mutagenic	none	none	none	none	none	none	none
Tumorogenic	none	none	none	none	none	none	none
Reproductive Effective	none	none	none	none	none	none	none
Irritant	none	none	none	none	none	none	none

MW: Molecular weight of the molecule. **SASA:** Total solvent accessible surface area in square angstroms using a probe with a 1.4 Å radius. **PSA:** Van der Waals surface area of polar nitrogen and oxygen atoms and carbonyl carbon atoms. **acceptHB:** Estimated number of hydrogen bonds that would be accepted by the solute from water molecules in an aqueous solution. **donorHB:** Estimated number of hydrogen bonds that would be donated by the solute to water molecules in an aqueous solution. **QPlogPo/w:** Predicted octanol/water partition coefficient. **QPlogHERG:** Predicted IC50 value for blockage of HERG K + channels. **QPPCaco:** Predicted apparent Caco-2 cell permeability in nm/sec. **QPPMDCK:** Predicted apparent MDCK cell permeability in nm/sec. MDCK cells are considered to be a good mimic for the blood-brain barrier.

4. Conclusion

The objective of the current study was to synthesize and examine the antitubercular activities of some new benzazole derivatives with the hope of determining new structures that could be used as potent antitubercular agents.

A novel series of benzazole derivatives (6-11) was synthesized and characterized using various spectroscopic methods. The target compounds (6-11) were assessed for their antitubercular activities against MTB H37Rv. All compounds demonstrated significant activity, with compound 11 exhibiting the most notable efficacy in the series, displaying a MIC value of 1.05 μ M and a selectivity index (SI) of 186.11. This meticulous examination results in the identification of a notably consistent structure-activity relationship, suggesting that the presence of a methoxy group as a substituent enhances both the activity and selectivity of the compounds compared to those without substituents. Moreover, the benzazole structure substituted with a thiophene ring exhibits notably stronger antitubercular activity than the other compounds. Interestingly, the activity of the thiophene group against MTB H37Rv is notable.

To further investigate the effectiveness of linker groups, it is imperative to conduct studies on numerous compounds. These findings from the contribution of antitubercular activity underscore the necessity of comparing benzazole derivatives with linker groups consisting of at least four atoms to those with different atoms. Furthermore, the contributions of aromatic ring substituents to the activity require thorough evaluation.

Future research endeavors aim to enhance the antitubercular efficacy and elucidate the precise mechanism of action.

Acknowledgments

This study is funded by the Research Fund of Erzincan Binali Yıldırım University, Turkey (Project number: TYL-2023-944). We would like to thank Erzincan Binali Yıldırım University for its support.

Conflicts of Interest

The authors declare no conflict of interest.

Ethics in Publishing

There are no ethical issues regarding the publication of this study.

Author Contributions

Gursoy S., Ozturk E. Ş. and Zoatier B. written manuscript; Gursoy S., Ozturk E. Ş., Ulger M. and O. Algul designed the study, prepared protocols, analyzed the data; Gursoy S., Ozturk E. S. and Ulger M. and Zoatier B.; performed the experiments and participated in discussions. All the authors were responsible for the data acquisition, review and editing of the paper.

References

- [1] Nyarko, R.O., Prakash, A., Kumar, N., Saha, P., and Kumar, R. (2021) Tuberculosis a globalized disease: Review. *Asian Journal of Pharmaceutical Research and Development*. 9 (1), 198–201.
- [2] Stubbs, B., Siddiqi, K., Elsey, H., Siddiqi, N., Ma, R., Romano, E., et al. (2021) Tuberculosis and Non-Communicable Disease Multimorbidity: An Analysis of the World Health Survey in 48 Low- and Middle-Income Countries. *International Journal of Environmental Research and Public Health*. 18 (5), 2439.
- [3] Sultana, Z.Z., Hoque, F.U., Beyene, J., Akhlak-Ul-Islam, Md., Khan, M.H.R., Ahmed, S., et al. (2021) HIV infection and multidrug resistant tuberculosis: a systematic review and meta-analysis. *BMC Infectious Diseases*. 21 (1), 51.
- [4] WHO (2023) Global Tuberculosis Report 2023. <https://www.who.int/teams/global-tuberculosis-programme/tb-reports/global-tuberculosis-report-2023>.
- [5] Hernández-López, H., Tejada-Rodríguez, C.J., and Leyva-Ramos, S. (2022) A Panoramic Review of Benzimidazole Derivatives and their Potential Biological Activity. *Mini-Reviews in Medicinal Chemistry*. 22 (9), 1268–1280.
- [6] Yadav, K.P., Rahman, M.A., Nishad, S., Maurya, S.K., Anas, M., and Mujahid, M. (2023) Synthesis and biological activities of benzothiazole derivatives: A review. *Intelligent Pharmacy*. 1 (3), 122–132.
- [7] Sattar, R., Mukhtar, R., Atif, M., Hasnain, M., and Irfan, A. (2020) Synthetic transformations and biological screening of benzoxazole derivatives: A review. *Journal of Heterocyclic Chemistry*. 57 (5), 2079–2107.
- [8] Zoatier, B., Yildirim, M., Alagoz, M.A., Yetkin, D., Turkmenoglu, B., Burmaoglu, S., et al. (2023) N-(benzazol-2-yl)-2-substituted phenylacetamide derivatives: Design, synthesis and biological evaluation against MCF7 breast cancer cell line. *Journal of Molecular Structure*. 1285 135513.
- [9] Yalcin-Ozkat, G., Ersan, R.H., Ulger, M., Ulger, S.T., Burmaoglu, S., Yildiz, I., et al. (2023) Design, synthesis, and computational studies of benzimidazole derivatives as new antitubercular agents. *Journal of Biomolecular Structure and Dynamics*. 41 (7), 2667–2686.
- [10] Veena, K., Raghu, M.S., Yogesh Kumar, K., Pradeep Kumar, C.B., Alharti, F.A., Prashanth, M.K., et al. (2022) Design and synthesis of novel benzimidazole linked thiazole derivatives as promising inhibitors of drug-resistant tuberculosis. *Journal of Molecular Structure*. 1269 133822.

- [11] Panneerselvam, T., Kunjiappan, S., Alagarsamy, V., Saravanan, G., and Parasuraman, P. (2020) Design, Optimization, Synthesis and AntiTB Screening of Benzimidazole Derivatives. *Anti-Infective Agents*. 18 (1), 24–42.
- [12] Yadav, R., Meena, D., Singh, K., Tyagi, R., Yadav, Y., and Sagar, R. (2023) Recent advances in the synthesis of new benzothiazole based anti-tubercular compounds. *RSC Advances*. 13 (32), 21890–21925.
- [13] Bhat, M. and Belagali, S.L. (2020) Structural Activity Relationship and Importance of Benzothiazole Derivatives in Medicinal Chemistry: A Comprehensive Review. *Mini-Reviews in Organic Chemistry*. 17 (3), 323–350.
- [14] Hemeda, L.R., El Hassab, M.A., Abdelgawad, M.A., Khaleel, E.F., Abdel-Aziz, M.M., Binjubair, F.A., et al. (2023) Discovery of pyrimidine-tethered benzothiazole derivatives as novel anti-tubercular agents towards multi- and extensively drug resistant *Mycobacterium tuberculosis*. *Journal of Enzyme Inhibition and Medicinal Chemistry*. 38 (1),.
- [15] Sumit, Kumar, A., and Mishra, A.K. (2021) Advancement in Pharmacological Activities of Benzothiazole and its Derivatives: An Up to Date Review. *Mini-Reviews in Medicinal Chemistry*. 21 (3), 314–335.
- [16] Kamal, U., Javed, N.M., And Arun, K. (2020) Biological Potential Of Benzoxazole Derivatives: An Updated Review. *Asian Journal of Pharmaceutical and Clinical Research*. 28–41.
- [17] Kumar, G., Chauhan, B., Singh, S., and Negi, M. (2022) In-Silico Prediction and Docking Studies Of Novel Synthesized Benzoxazole Derivatives As Anti-Tubercular Activity. *Journal Of Pharmaceutical Negative Results*. 13 (9), 9216–9226.
- [18] Sattar, R., Mukhtar, R., Atif, M., Hasnain, M., and Irfan, A. (2020) Synthetic transformations and biological screening of benzoxazole derivatives: A review. *Journal of Heterocyclic Chemistry*. 57 (5), 2079–2107.
- [19] Ayaz, F., Kheeree, R., Isse, Q.A., Ersan, R.H., and Algul, O. (2018) DNA Base Bioisosteres, Bis-benzoxazoles, Exert Anti-proliferative Effect on Human Prostate and Breast Cancer Cells. *Journal of the Turkish Chemical Society Section A: Chemistry*. 5 (3), 1145–1152.
- [20] Keri, R.S., Rajappa, C.K., Patil, S.A., and Nagaraja, B.M. (2016) Benzimidazole-core as an antimycobacterial agent. *Pharmacological Reports*. 68 (6), 1254–1265.
- [21] Akhtar, W., Khan, M.F., Verma, G., Shaquiquzzaman, M., Rizvi, M.A., Mehdi, S.H., et al. (2017) Therapeutic evolution of benzimidazole derivatives in the last quinquennial period. *European Journal of Medicinal Chemistry*. 126 705–753.

- [22] Bansal, Y. and Silakari, O. (2012) The therapeutic journey of benzimidazoles: A review. *Bioorganic & Medicinal Chemistry*. 20 (21), 6208–6236.
- [23] Park, B., Awasthi, D., Chowdhury, S.R., Melief, E.H., Kumar, K., Knudson, S.E., et al. (2014) Design, synthesis and evaluation of novel 2,5,6-trisubstituted benzimidazoles targeting FtsZ as antitubercular agents. *Bioorganic & Medicinal Chemistry*. 22 (9), 2602–2612.
- [24] Kalalbandi, V.K.A., Seetharamappa, J., Katrahalli, U., and Bhat, K.G. (2014) Synthesis, crystal studies, anti-tuberculosis and cytotoxic studies of 1-[(2E)-3-phenylprop-2-enoyl]-1H-benzimidazole derivatives. *European Journal of Medicinal Chemistry*. 79 194–202.
- [25] Gobis, K., Foks, H., Serocki, M., Augustynowicz-Kopeć, E., and Napiórkowska, A. (2015) Synthesis and evaluation of in vitro antimycobacterial activity of novel 1H-benzo[d]imidazole derivatives and analogues. *European Journal of Medicinal Chemistry*. 89 13–20.
- [26] Awasthi, D., Kumar, K., Knudson, S.E., Slayden, R.A., and Ojima, I. (2013) SAR Studies on Trisubstituted Benzimidazoles as Inhibitors of *Mtb* FtsZ for the Development of Novel Antitubercular Agents. *Journal of Medicinal Chemistry*. 56 (23), 9756–9770.
- [27] Antoci, V., Cucu, D., Zbancioc, G., Moldoveanu, C., Mangalagiu, V., Amariucaimantu, D., et al. (2020) Bis-(imidazole/benzimidazole)-pyridine derivatives: synthesis, structure and antimycobacterial activity. *Future Medicinal Chemistry*. 12 (3), 207–222.
- [28] Barcin, T., Yucel, M.A., Ersan, R.H., Alagoz, M.A., Dogen, A., Burmaoglu, S., et al. (2024) Deep learning approach to the discovery of novel bisbenzazole derivatives for antimicrobial effect. *Journal of Molecular Structure*. 1295 136668.
- [29] Ersan, R.H., Alagoz, M.A., Dogen, A., Duran, N., Burmaoglu, S., and Algul, O. (2022) Bisbenzoxazole Derivatives: Design, Synthesis, *in Vitro* Antimicrobial, Antiproliferative Activity, and Molecular Docking Studies. *Polycyclic Aromatic Compounds*. 42 (6), 3103–3123.
- [30] Ersan, R.H., Bolelli, K., Gonca, S., Dogen, A., Burmaoglu, S., and Algul, O. (2021) Bisbenzimidazole Derivatives as Potential Antimicrobial Agents: Design, Synthesis, Biological Evaluation and Pharmacophore Analysis. *Pharmaceutical Chemistry Journal*. 55 (2), 149–158.
- [31] Wieland, T. and Bodanszky, M. (1991) *The World of Peptides*. Springer Berlin Heidelberg, Berlin, Heidelberg.
- [32] Scattolin, T., Bouayad-Gervais, S., and Schoenebeck, F. (2019) Straightforward access to N-trifluoromethyl amides, carbamates, thiocarbamates and ureas. *Nature*. 573 (7772), 102–107.

- [33] de Figueiredo, R.M., Suppo, J.-S., and Campagne, J.-M. (2016) Nonclassical Routes for Amide Bond Formation. *Chemical Reviews*. 116 (19), 12029–12122.
- [34] Pattabiraman, V.R. and Bode, J.W. (2011) Rethinking amide bond synthesis. *Nature*. 480 (7378), 471–479.
- [35] Veena, K., Raghu, M.S., Yogesh Kumar, K., Pradeep Kumar, C.B., Alharti, F.A., Prashanth, M.K., et al. (2022) Design and synthesis of novel benzimidazole linked thiazole derivatives as promising inhibitors of drug-resistant tuberculosis. *Journal of Molecular Structure*. 1269 133822.
- [36] Šlachtová, V., & Brulíková, L. (2018). Benzoxazole derivatives as promising antitubercular agents. *ChemistrySelect*, 3(17), 4653-4662.
- [37] Yadav, R., Meena, D., Singh, K., Tyagi, R., Yadav, Y., & Sagar, R. (2023). Recent advances in the synthesis of new benzothiazole based anti-tubercular compounds. *RSC Advances*, 13(32), 21890-21925.
- [38] Fu, Y., O'Connor, L.M., Shepherd, T.G., and Nachtigal, M.W. (2003) The p38 MAPK inhibitor, PD169316, inhibits transforming growth factor β -induced Smad signaling in human ovarian cancer cells. *Biochemical and Biophysical Research Communications*. 310 (2), 391–397.
- [39] Susceptibility Testing of Mycobacteria, Nocardiae, and Other Aerobic Actinomycetes. 2nd ed. Wayne, Pennsylvania. (2011)
- [40] Denizot, F. and Lang, R. (1986) Rapid colorimetric assay for cell growth and survival. *Journal of Immunological Methods*. 89 (2), 271–277.
- [41] Mosmann, T. (1983) Rapid colorimetric assay for cellular growth and survival: Application to proliferation and cytotoxicity assays. *Journal of Immunological Methods*. 65 (1–2), 55–63.
- [42] Schrödinger (2024) Schrödinger Release 2024-1: QikProp.
- [43] Burmaoglu, S., Algul, O., Gobek, A., Aktas Anil, D., Ulger, M., Erturk, B.G., et al. (2017) Design of potent fluoro-substituted chalcones as antimicrobial agents. *Journal of Enzyme Inhibition and Medicinal Chemistry*. 32 (1), 490–495.
- [44] S. Maia, M., de Sousa, N.F., Rodrigues, G.C.S., Monteiro, A.F.M., Scotti, M.T., and Scotti, L. (2020) Lignans and Neolignans Anti-tuberculosis Identified by QSAR and Molecular Modeling. *Combinatorial Chemistry & High Throughput Screening*. 23 (6), 504–516.

Effect of deposition parameters on structural and mechanical properties of Novel h-BN doped TiCrNbN coatings

Yaşar Sert^{1*}, Tevfik Küçükömeroğlu¹

¹ Karadeniz Technical University, Engineering Faculty, Mechanical Engineering Department, Trabzon, Turkey

Received: 09/05/2024, Revised: 21/06/2024, Accepted: 11/07/2024, Published: 31/08/2024

Abstract

In this paper, the novel h-BN doped TiCrNbN thin films was deposited on the DIN 1.2714 steel using closed field unbalanced magnetron sputtering (CFUBMS) technique with variable working pressure, bias voltage, and LaB₆ target voltage. The main goal is to determine the contribution of degrees of these parameters on structural and mechanical properties using Analysis of Variance (ANOVA). The deposition parameters were leveled based on L₉ (3³) orthogonal Taguchi design method. Microstructural and thickness of coatings were investigated using SEM. The coatings had granular and flawless surface properties. The thickness of the coatings was determined in the range of 874 nm and 1.69 µm. The deposition parameter that has the highest contribution to coating thickness is working pressure. Hardness and adhesion strength of coatings were determined employing nanohardness and scratch tester, respectively. The highest hardness among the coatings was 24.67 GPa, obtained with the 3x10⁻³ Torr working pressure, 100 V bias voltage and 600 V LaB₆ target voltage parameters. The deposition parameter that has the highest contribution to hardness is working pressure. The coating conditions with the highest hardness exhibited the highest adhesion strength. The superiority of the contribution of working pressure on the adhesion strength was prominent compared to other parameters.

Keywords: CFUBMS, Taguchi, ANOVA, nanohardness, adhesion

Biriktirme Parametrelerinin Yenilikçi h-BN Katkılı TiCrNbN Kaplamaların Yapısal ve Mekanik Özelliklerine Etkisi

Öz

Bu çalışmada, özgün h-BN katkıli TiCrNbN ince filmler, değişken çalışma basıncı, bias gerilimi ve LaB₆ hedef gerilimi ile kapalı alan dengesiz manyetik alanda sıçratma tekniği kullanılarak DIN 1.2714 çelik yüzeyine kaplanmıştır. Çalışmanın motivasyonu, bu değişken parametrelerin, kaplamaların yapısal ve mekanik özelliklerine etki derecelerinin Varyans analizi (ANOVA) kullanılarak belirlenmesidir. Kaplama parametreleri Taguchi L₉ (3³) ortogonal dizin kullanılarak belirlendi. Kaplamaların mikroyapısı ve kesitleri SEM kullanılarak incelendi. Kaplamalar taneli ve kusursuz şekilde üretildi. Kaplamaların kalınlıkları 874 nm ile 1,69 µm aralığında belirlendi. Kaplama kalınlığına en yüksek etki derecesini sağlayan kaplama parametresinin çalışma basıncı olduğu tespit edildi. Kaplamaların sertliği ve taban malzemeye yapışma dayanımları sırasıyla nanosertlik ve çizik test cihazları kullanılarak gözlemlendi. En yüksek sertlik değeri, 3x10⁻³ Torr çalışma basıncı, 100 V bias gerilimi ve 600 V LaB₆ hedef gerilimi parametreleriyle üretilen kaplamada 24,67 GPa olarak elde edildi. Sertliğe en yüksek katkısı olan parametre çalışma basıncı olduğu tespit edildi. En yüksek sertliğe sahip kaplama koşulları aynı zamanda en yüksek adezyon dayanımı performansını da sergiledi. Çalışma basıncının yapışma dayanımına katkısının diğer parametrelere göre üstünlüğü ön plana çıkmıştır.

Anahtar Kelimeler: CFUBMS, Taguchi, ANOVA, nanosertlik, yapışma

*Corresponding Author: yasarsert@ktu.edu.tr

Yaşar Sert, <https://orcid.org/0000-0001-7742-0335>

Tevfik Küçükömeroğlu, <https://orcid.org/0000-0002-4392-9966>

1. Introduction

Increasing the hardness and mechanical performance of tools employed in industry is essential for market competition in today's industrial conditions [1]. In the studies carried out in this context, surface coatings produced under vacuum have come to the fore due to magnificent features such as high hardness and wear performance [2]. Physical vapor deposition (PVD), chemical vapor deposition (CVD), sol-gel, micro-arc oxidation, anodization, thermal spray, etc. have been performed for this goal over the years [3]. Closed field unbalanced magnetron sputtering (CFUBMS) technique is commonly used owing to high homogeneity, adhesion, and usability for variety of substrate materials [4]. Nitride-based thin hard coatings performed with this PVD technique are capable of meeting the needs in the industry [5]. It is known that the mechanical properties of coatings depend on the structural properties that occur during the deposition process. The structural properties of thin films are depending on some deposition parameters such as bias voltage, working pressure, target current or/and voltage, the distance between target and substrate, frequency, and duty time. Since these parameters constantly interact with each other, each combination of them creates a unique structure. In investigating the effects of parameters on the properties of coatings, it is commonly used to keep one variable and the others constant [6]. However, in this technique, long operating time and high costs are encountered to obtain optimum coating properties. In order to overcome this difficulty, the design of experimental (DOE) methods that enable the optimization of complex processes is developed [7]. Among these methods, Taguchi is the most widely used. In the Taguchi method, the findings obtained from the tests of thin films produced by changing multiple parameters simultaneously are analyzed by Signal/Noise (S/N) ratio. Whether any parameter contributes to the coatings is evaluated with the data determined from the S/N graphs. Some studies in the open literature have tried to explain the effects of deposition parameters on coating properties. However, there are rare studies in which the contribution percentages of parameters to properties are examined numerically.

In this study, h-BN doped TiCrNbN coating was deposited to improve the mechanical properties of 1.2714 steel, which is frequently used as a die material in the industry. L9 (3^3) orthogonal design is used for experimental design. The variable parameters are working pressure, bias voltage, and LaB6 target voltage and these variable parameters are leveled at 3 different values. Structural properties and cross-sections of the coatings were examined by scanning electron microscope (SEM). The hardness and adhesion strength of the samples were determined by nanohardness and scratch tests, respectively.

2. Material and Methods

The h-BN doped TiCrNbN coatings were deposited on DIN 1.2714 (C~0.56, Cr~1.1, Mo~0.5, Ni~1.7, V~0.1, and balance Fe) using closed field unbalanced magnetron sputtering in a Teer Coating Ltd. UDP550 system under variable deposition parameters, based on a Taguchi L9 orthogonal design. Deposition parameters are shown in Table 1. Figure 1 shows the magnetron configuration of the targets to deposit the films. Before the deposition, the surfaces of the steel samples were grinded and polished. Afterwards, the ultrasonically cleaned samples are ready for deposition process. In the deposition process, one Ti (%99.95 pure), one Cr (%99.95 pure), one Nb (%99.95 pure), and one LaB6 (%99.95 pure) targets were employed to deposit planned thin films. As seen in Figure 1, the substrates were positioned 70 mm away from the targets within the means of the mechanism. After the samples were placed in the system, ion cleaning was performed on the substrates for 30 minutes in an argon atmosphere to remove any contamination on the surfaces. Afterwards, Cr interlayer was deposited on the steel surface at 10 min. for increasing the adhesion of film. CrN layers for 10 minutes, TiCrN for 20 minutes, TiCrNbN for 20 minutes and TiCrNb-hBN layers for 30 minutes were gradually coated on the samples. The microstructures of the coatings were investigated by scanning electron microscope (SEM), EDS (Energy-dispersive spectroscopy) and XRD (X-Ray diffractometer), respectively. Microscale hardness tests are not suitable for determining hardness values in thin film applications. In order to minimize the effect of the substrate, the hardness of the samples was determined by nano hardness test. The nano-hardness of the coatings was explored by a Bruker Hysitron Ti950 nanohardness tester (using Berkovich indenter, 1 mn load at 5 different points). The bond strength between thin films and substrate were determined using the scratch tester (CSM Revetest RST) having a 200 μm diameter of Rockwell-C diamond pin. A Ducom tribotester (5N load, 150 rpm rotation speed, 6 mm diameter Al_2O_3 abrader) was employed to investigate the wear behavior of samples. The wear volumes of samples were determined by optical profilometer. The wear mechanisms of samples were characterized by SEM.

Table 1. Deposition parameters

Coating No	Working Pressure (Torr) ($\times 10^{-3}$)	Bias Voltage (V)	LaB6 Target Voltage (V)
R1	2	50	600
R2	2	100	700
R3	2	150	800
R4	2.5	50	700
R5	2.5	100	800
R6	2.5	150	600
R7	3	50	800
R8	3	100	700
R9	3	150	600

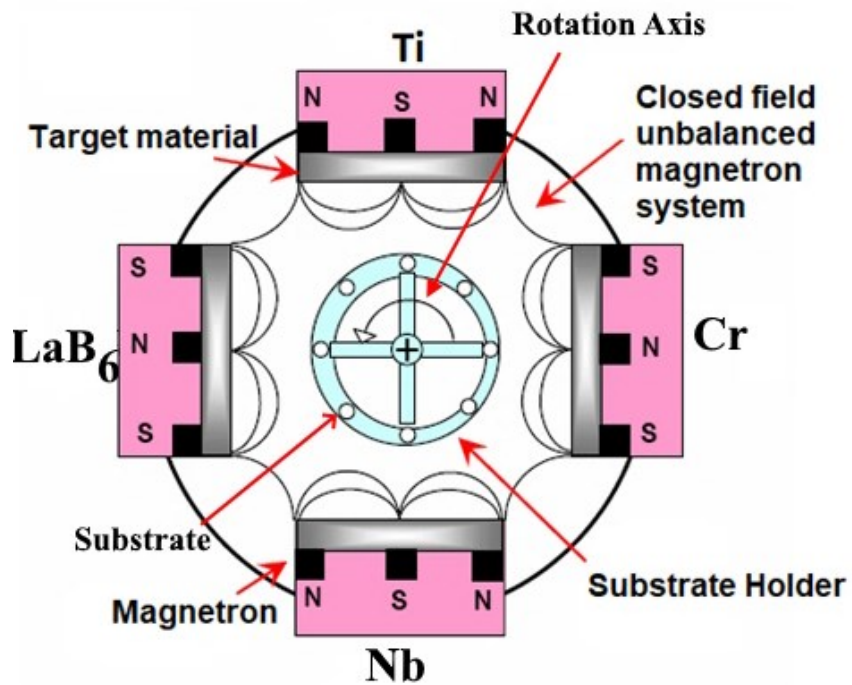
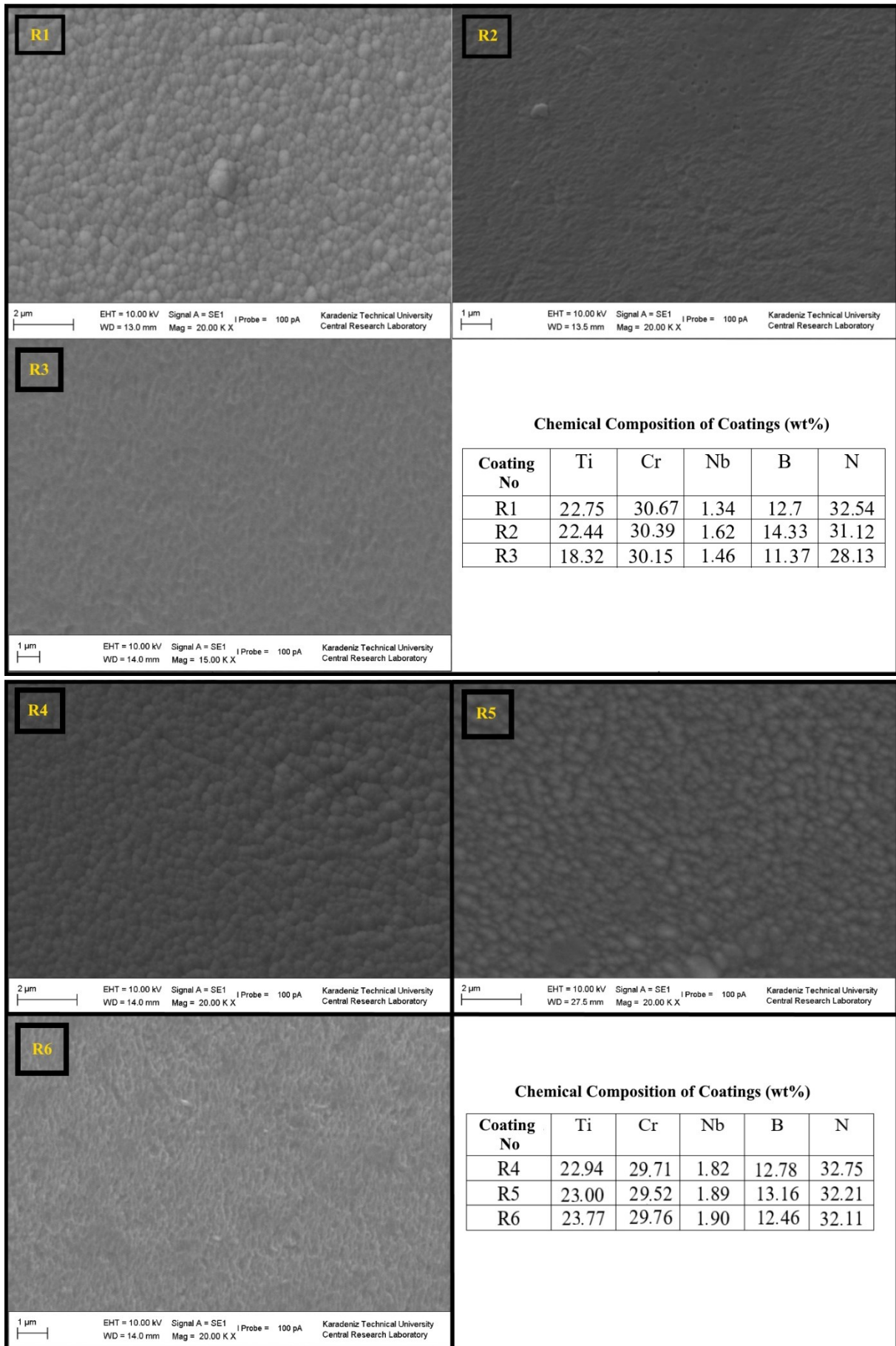


Figure 1. Magnetron sputtering system

3. Results and Discussion

Surface SEM images and chemical compositions of TiCrNb-hBN thin films are given in Figure 2. As can be seen from the Figure 2, the coatings deposited on the DIN 1.2714 surface with the deposition parameters in Table 1 generally have a granular, smooth (without deposition defects) and dense structure. These flawless surface features are achieved by the high power density close field magnetron sputtering method. In this method, a closed magnetic field created by the targets traps the sputtered atoms in the plasma and delivers them directly on the substrates. When the first group (R1, R2 and R3) is examined, it is observed that a denser and fine-grained structure is obtained as the bias voltage increases. The coarse grained structure seen in the R1 coating is due to the low mobility of the sputtered atoms absorbed on the surface [8]. It is evaluated that by increasing the bias voltage value and LaB6 target voltage from 50 V and 600 V to 150 V and 800 V, adatom (adsorbed atom) mobility increases, which enhances the nucleation areas and reduces the grain size. It is obvious that the grain size decreases by increasing the bias voltage during coating processes, which is compatible with various studies in the literature [9]. It is stated that the atoms with increased energy in the plasma diffusely fill the gaps between the grains of the substrate. It is seen that as the LaB6 target voltage is increased (600 V to 800 V), the microstructure changes from a granular to a fibrous. It is determined that the fibrous structure seen in the R3 coating belongs to the “T region” in the coating structure model specified by Thornton [10]. In the elemental analysis of the coatings, it is seen that Cr is dominant in the structure. The reason for this is based on the deposition of Cr and CrN as an interlayer on the substrate. It is also known that one of the most important factors affecting the chemical composition of coatings is sputtering efficiency. This phenomenon is expressed as the amount of atoms sputtered from the target surfaces during the deposition process. In this thin film, the element with the highest sputtering efficiency (1.18) among the target materials is Cr. However, at 150V bias voltage, there is a slight decrease in the boron content due to the re-sputtering effect. Among the elements in the structure, the atomic weight of boron is lighter than other elements. Therefore, by increasing the bias voltage above 100 V, atoms with high kinetic energy cause the lighter boron atoms to re-sputter.

Similar evaluations can be made for R7, R8 and R9 coatings, where the working pressure is kept constant at 3×10^{-3} Torr. It is seen that the R9 coating produced at 150 V bias voltage has cauliflower-like grains. A compact and fine-grained structure is observed in the R8 coating deposited with 100 V bias voltage and 600 V target voltage.



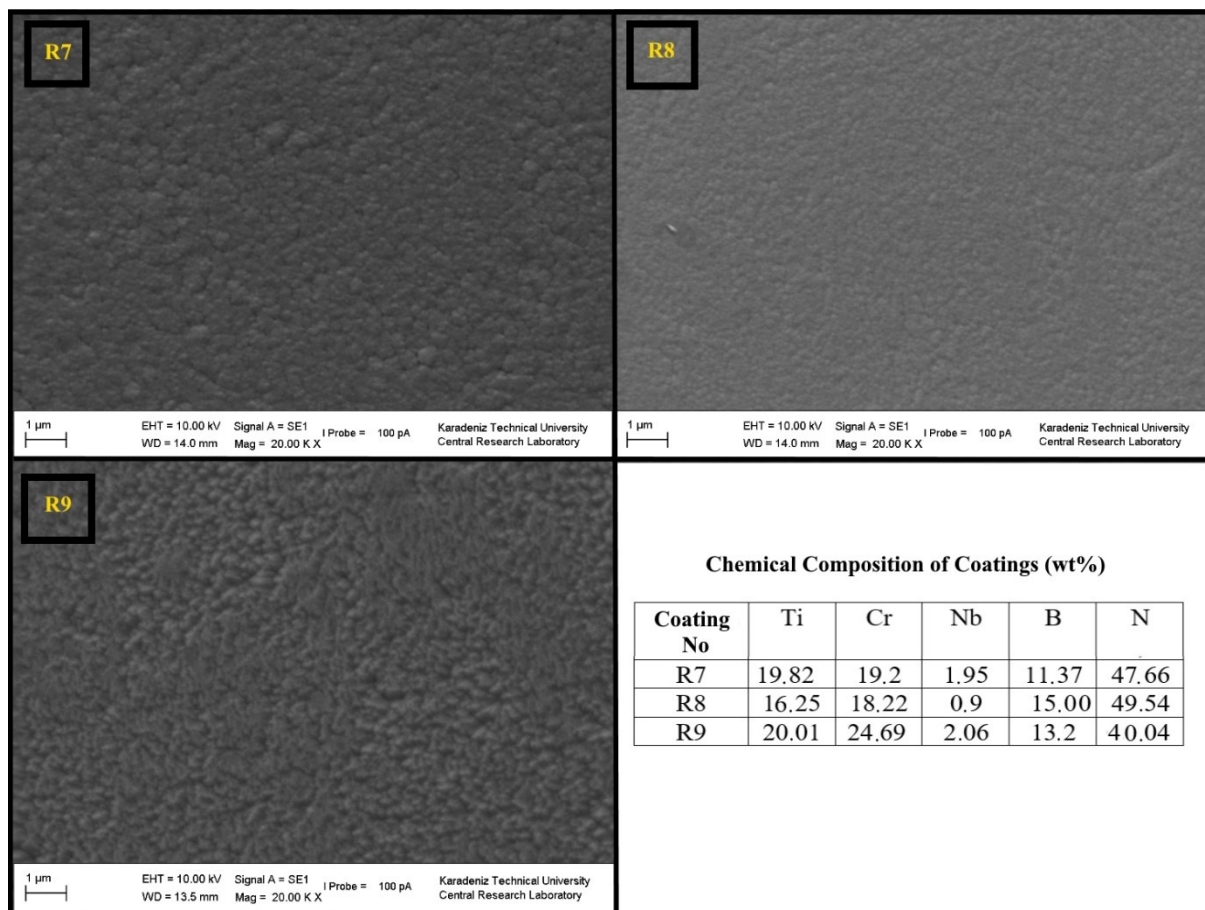


Figure 2. SEM images and chemical compositions of the coatings

Cross-sectional images of R1, R4 and R7 Coatings are given in Figure 3. It is seen that the TiCrNb-hBN layer grows in a columnar structure from the bottom layer to the surface in each of the variable parameters and there are no cracks or gaps between the grains. The thickness values obtained from these images can be seen comparatively in Figure 4. The highest coating thickness is 1.69 at R2 (2×10^{-3} Torr, 100 V bias voltage, and 700 V LaB₆ target voltage). In the statistical study carried out to determine the effects of deposition parameters on the thickness of the coatings, the signal to noise (S/N) ratio is used to determine the degree of contribution of the parameters. S/N ratios of coating thicknesses are determined using Minitab 17 Software, based on the higher-the better criterion. The average S/N chart obtained as a result of the statistical analysis is given in Figure 5. As seen in Figure 5, the parameter that has the greatest contribution (63.65%) on the thickness is the working pressure. The parameter with the lowest contribution is the LaB₆ target voltage (8.36%). Evaluations on coating thicknesses are carried out based on the working pressure which has the dominant contribution percentage. Increasing working pressure enhances the probability of the sputtered atoms colliding with the gas particles in the plasma during their movement to the substrate surface, causing a decrease in the deposition rate [11]. This is also one of the main reasons for the decrease in coating thickness.

There is generally a decrease in coating thickness with increasing bias voltage. This is based on the “re-sputtering” mechanism that occur when the substrate is exposed to higher intensity ion bombardment with increasing bias voltage. Studies in the literature are obtained findings consistent with this situation [12].

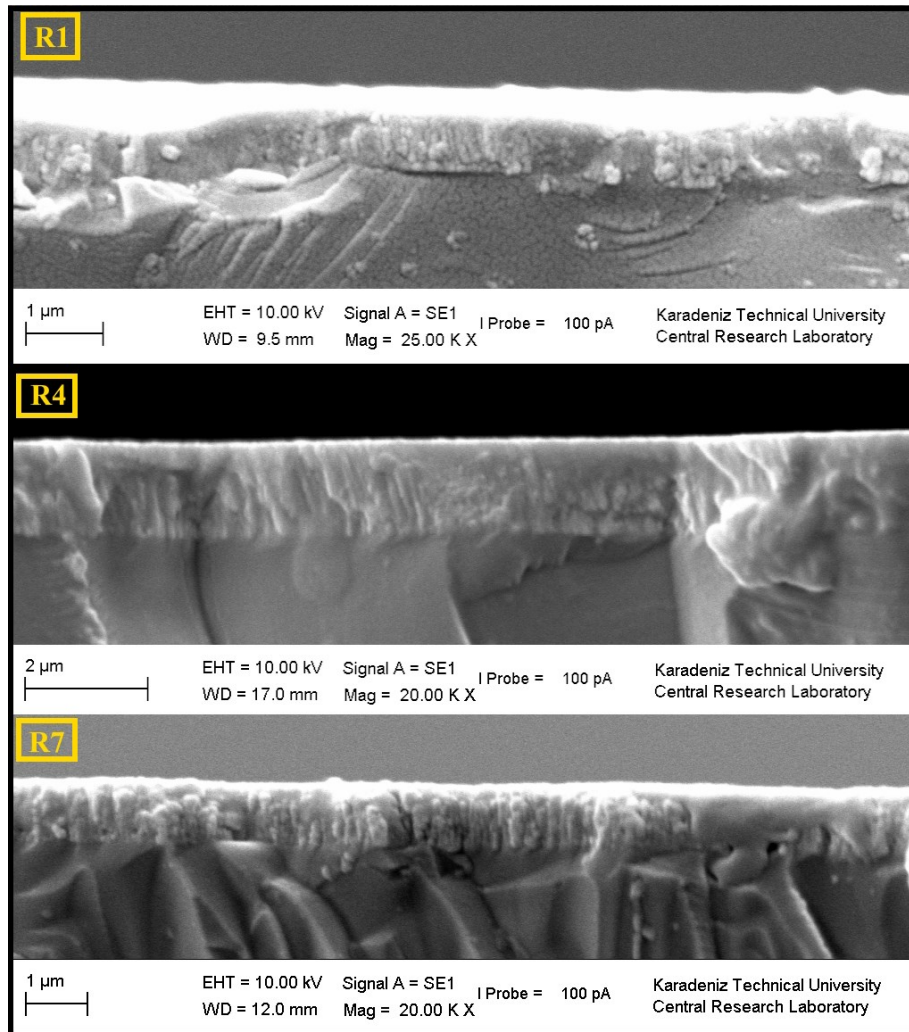


Figure 3. Typical cross-sectional SEM images of R1, R4 and R7 coatings

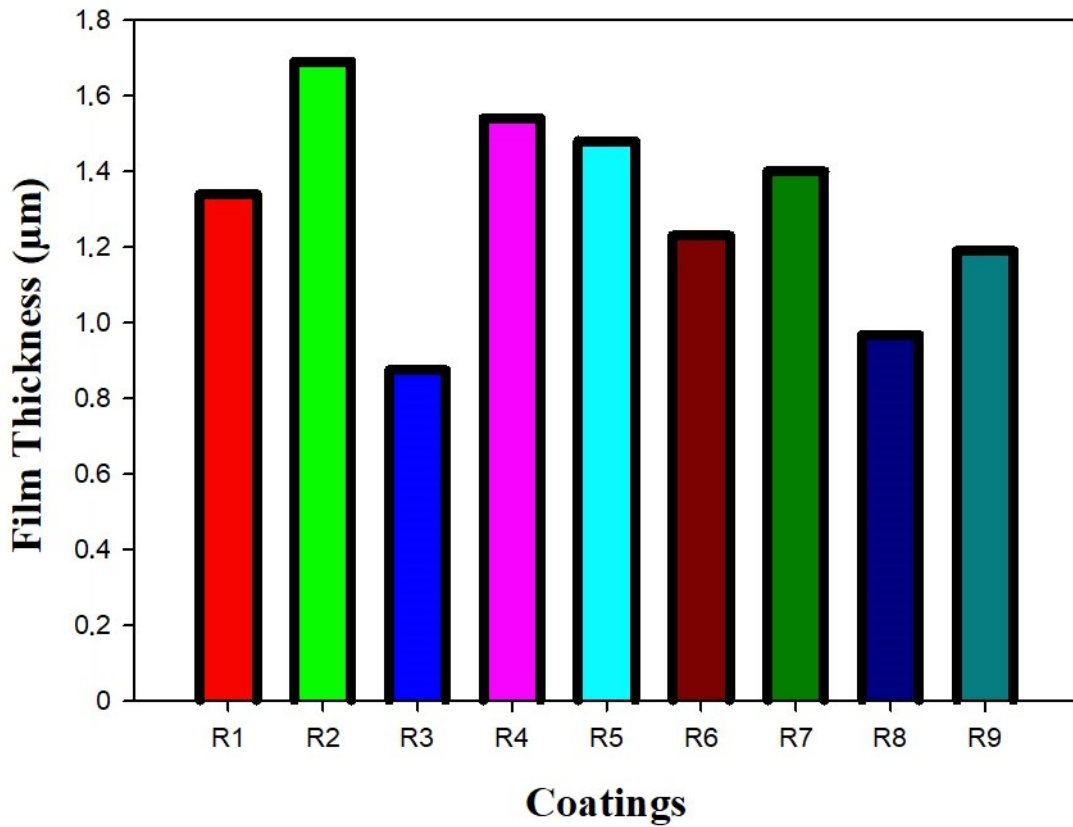


Figure 4. Thickness value of coatings

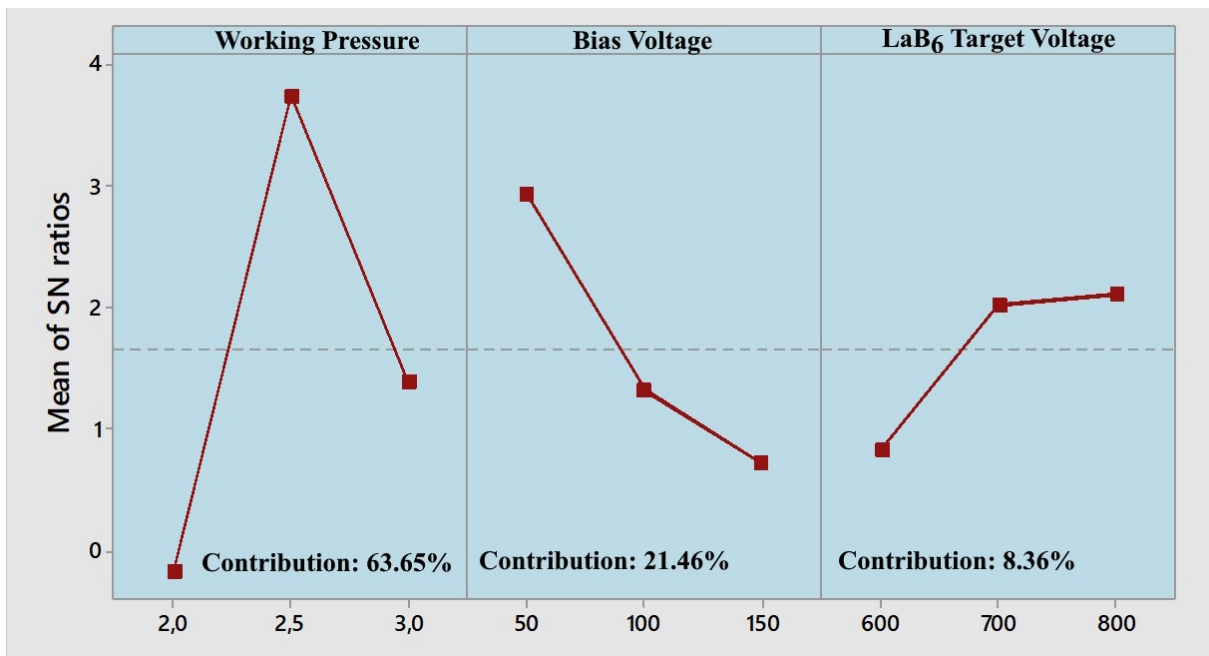


Figure 5. Average S/N Ratios for TiCrNb-hBN thin films in thickness

It is not appropriate to determine the hardness values using the microhardness test in films with coating thickness in the range of 1.00-2.00 µm. In hardness measurement, if the tip penetrates

more than 20-30% of the coating thickness, this indicates that the substrate has an effect on the hardness value of coatings. Therefore, hardness measurements are carried out using nanohardness tests. The average hardness values obtained in the nanohardness test are given comparatively in Figure 6. As can be seen from the figure, the highest nanohardness value is obtained from the coating called R8 (3×10^{-3} Torr working pressure, 100 V bias voltage, 600 V LaB₆ target voltage). It is determined that the hardness value of R8 is approximately 400% superior than the hardness of the 1.2714 tool steel used as the substrate. The average S/N chart obtained as a result of the statistical analysis for nanohardness values is given in Figure 7. As a result of the analysis, the parameter that has the highest contribution to the hardness values of the coatings is the working pressure (65%), while the one that has the least contribution is the LaB₆ target voltage (1%). It is determined that the nanohardness values of the R1, R6 and R8 coatings, where the LaB₆ target voltage is kept constant at 600 V, increases the working pressure increases. The highest hardness in this group is obtained as 24.67 GPa in the R8 coating produces at 3×10^{-3} Torr working pressure and 100 V bias voltage values. When the bias voltage was increases to 150 V, it causes a certain amount of decrease. The increase in hardness that occurs with increasing working pressure value is attributed by the enhancing ion density in the plasma. As the working pressure increases, the ion density level in the plasma increases. Thus, the substrate surface is bombarded with more atoms and a dense and tightly ordered structure is obtained. Many studies in the literature have reported findings that hardness values increase with increasing working pressure [13]. Increasing ion bombardment by increasing the bias voltage value creates preferential regions on the surface of the substrate and enhances the re-nucleation rate. In addition, the kinetic energies of the primary ions sputtered from the target also increase. Ions with high kinetic energy are directed to the substrate more quickly in the plasma, minimizing the formation of dislocations in the deposited coating layer. While these effects are present when the bias voltage is increased from 50 V to 100 V, a negative effect occurs on the hardness value at 150 V. The reason for this is that when the ions, whose velocities increase excessively, hit the surface of the substrate with a force higher than the optimum value at low working pressure levels, they cause the secondary atoms to re-sputtering from the surface.

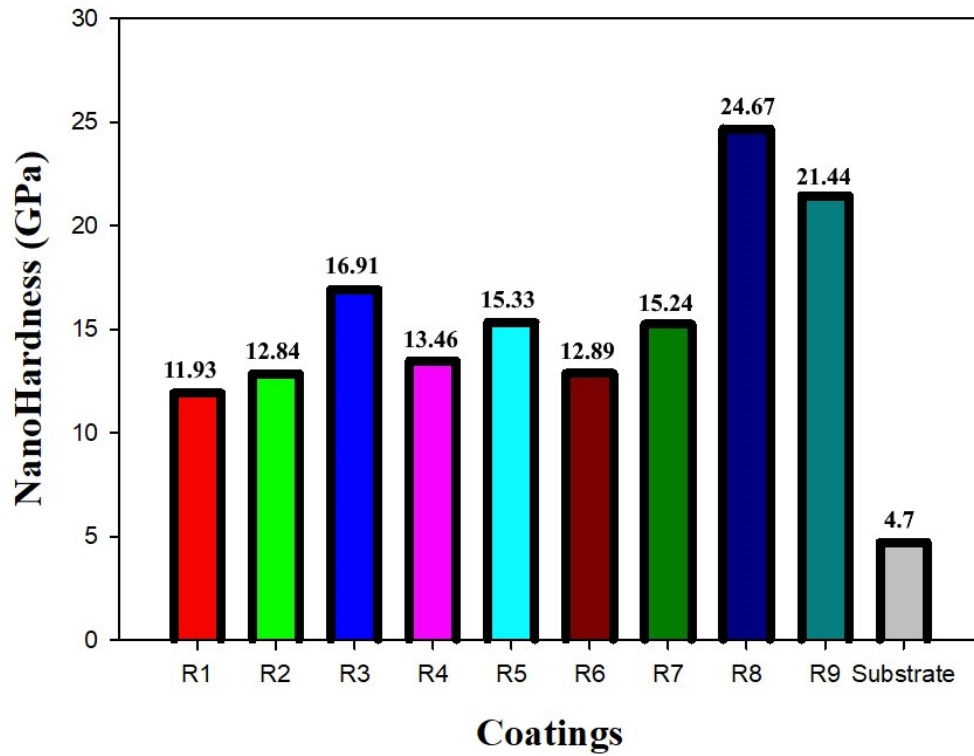


Figure 6. Average nanohardness values of samples

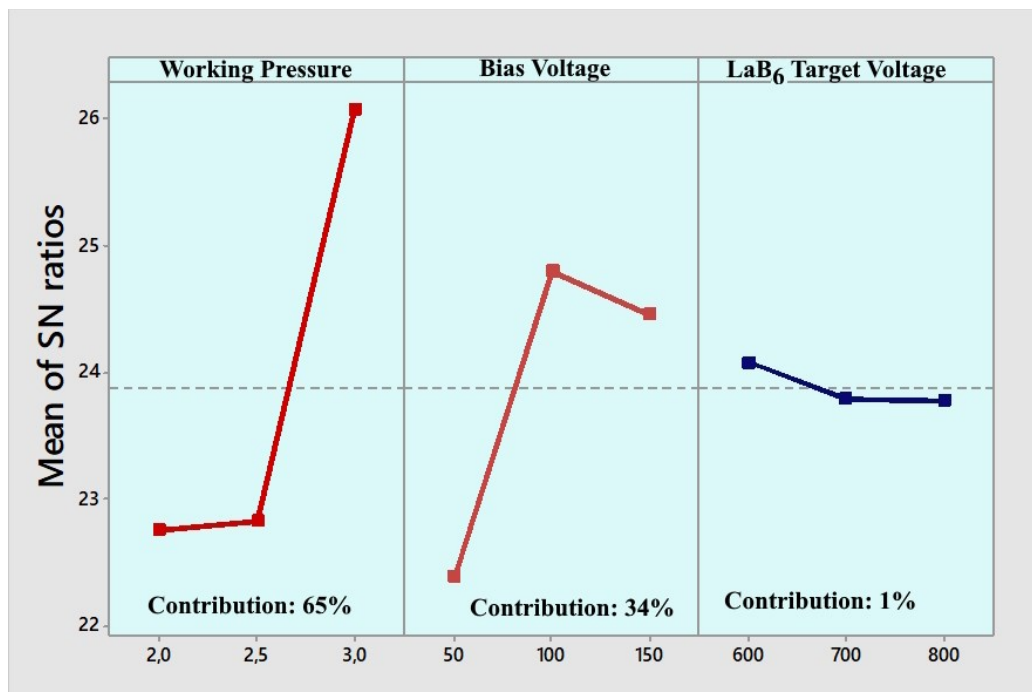


Figure 7. Average S/N Ratios for TiCrNb-hBN thin films in hardness value

The adhesion strength of TiCrNb-hBN coatings is determined by scratch test. Scratch testing is one of the most important techniques used in the characterization and performance

determination of thin and hard coatings. The adhesion strength of coatings is evaluated using critical loads at which failure occurs during the test. L_{c2} critical load value is expressed as the load value at which the coating completely peels off from the substrate and loses its protection. L_{c2} critical load values of the coatings are given in Figure 8. Among the coatings, the highest L_{c2} critical load (adhesion strength) value is obtained from the R8 with 85 N, while the lowest L_{c2} critical load is obtained from the R6 with 13 N. Critical loads are determined by the normal force-friction coefficient graphs given in Figures 9, obtained using an optical microscope and optical profilometer taken from the coatings after the test. Typical scratch results for R1, R4 and R7 coatings are given for each group. S/N ratios of adhesion strength values (Figure 10) are calculated according to the higher the better criterion. It is determined that the most important parameter affecting the adhesion strength values obtained from coatings is the working pressure (89.6%). As in other properties, the lowest contribution is taken from LaB₆ (1.6%). In the R1, R6 and R8 coatings, where the LaB₆ target voltage is kept constant at 600 V, which has the lowest contribution on the adhesion strength values of the coatings at 1.6%, a superior adhesion strength of 85 N is obtained in the R8 coating produced with the highest working pressure (3×10^{-3} Torr). As stated before, as the working pressure increases, the ionization in the plasma increases. This has positive effects on the coating's resistance to plastic deformation and adhesion. By increasing the bias voltage from 50V to 100V in the R8, the adhesion strength of the coating increases as the ions with increases kinetic energy penetrates the surface better and forms a dense structure. In addition, increasing the bias voltage from 50 V to 100 V causes a relief in the lattice structure by reducing the residual stresses. This relief is thought to increase the load-bearing capacity of the coating by increasing its toughness.

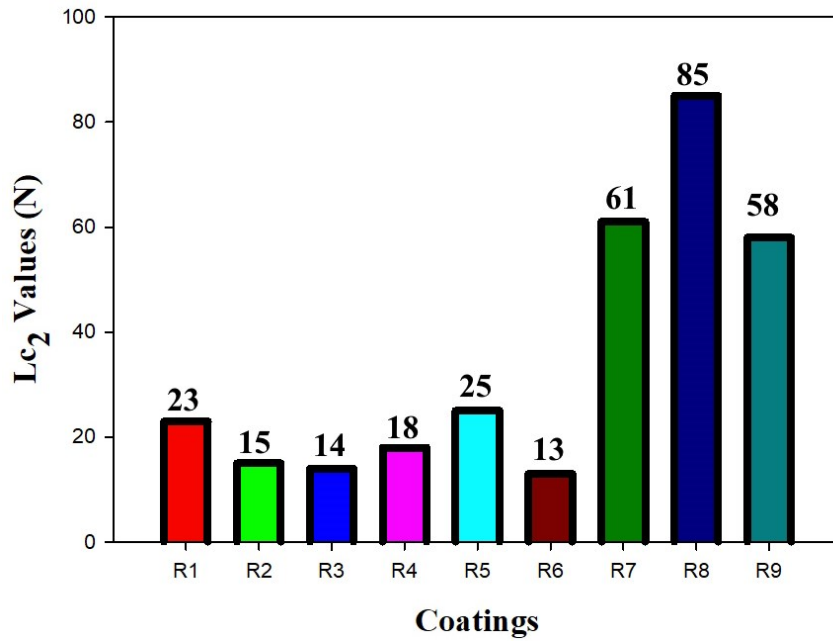


Figure 8. Lc₂ critical load of coatings

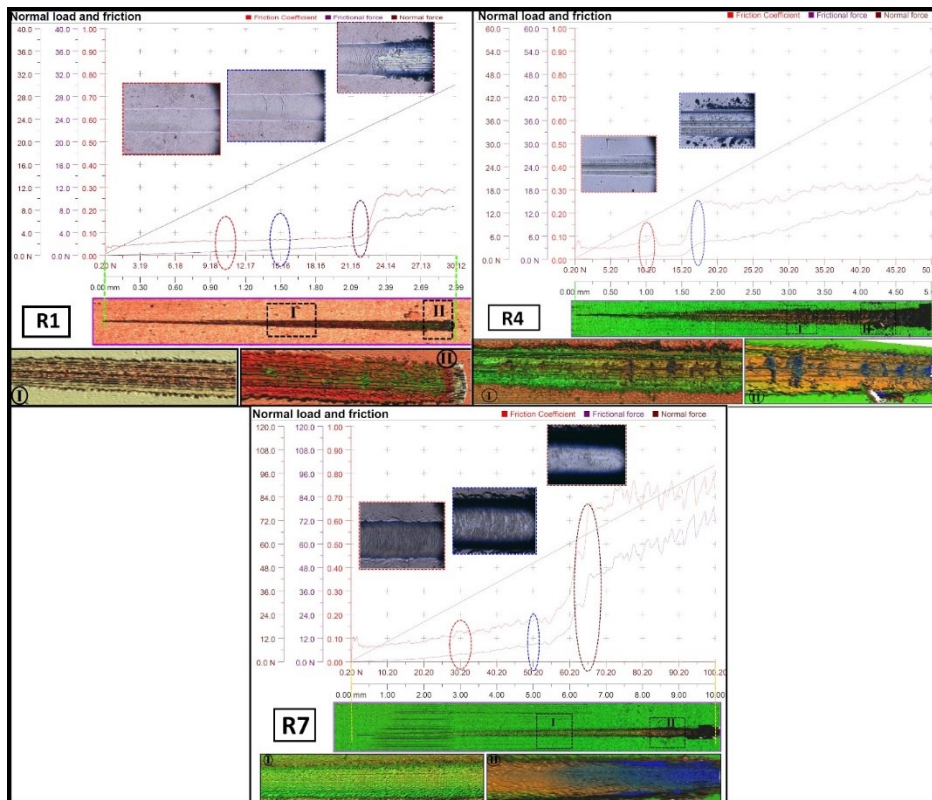


Figure 9. Scratch test results for R1, R4, and R7 coatings

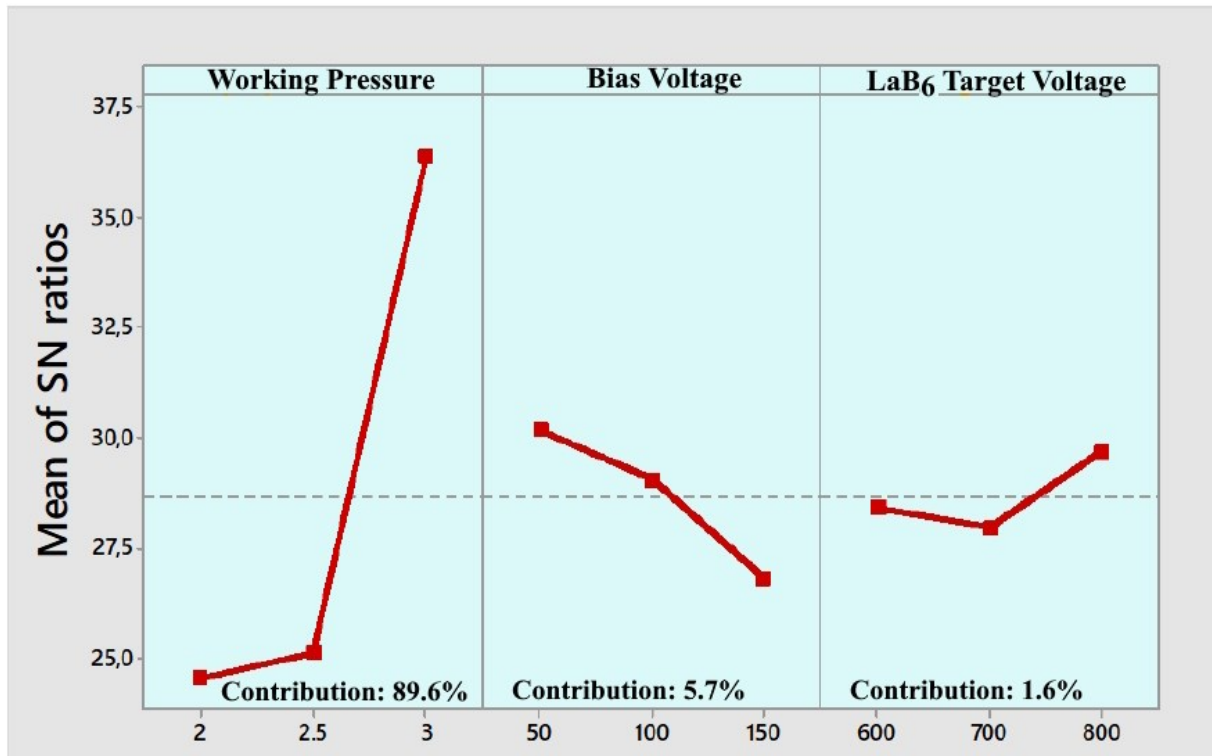


Figure 10. Average S/N Ratios for TiCrNb-hBN thin films in Lc₂ critical load

4. Conclusion

The TiCrNb-hBN thin films were deposited on DIN 1.2714 steel samples using CFUBMS system under the different deposition parameters. The microstructure, nanohardness, adhesion strength properties of coatings were investigated. In addition, the degree of contribution of the variable parameters to these features was revealed by ANOVA analysis.

- 1- TiCrNb-hBN coatings, which have a novel design and recipe, are successfully produced in a granular, smooth and dense structure, free from deposition defects encountered in other coating methods.
- 2- The thickness of the coatings is achieved in the range of 874 nm and 1.69 μm .
- 3- The parameter that has the highest contribution to coating thickness values is working pressure with 63.65%.
- 4- All TiCrNb-hBN coatings increase the nanohardness of the DIN 1.2714 steel sample.
- 5- The highest hardness value is obtained in the R8 coating with a value of 24.67 GPa. This hardness achieved is approximately 400% superior than the hardness value of the substrate.

- 6- The highest adhesion strength is achieved in the R8 coating with a value of 85 N. There is a correlation between hardness and adhesion strength values in coatings.
- 7- Numerical values obtained as a result of ANOVA analysis show the degree of contribution of each parameter to the coating properties. It is a known fact that each coating parameter has different effects on the properties of the coating. This change in numerical data indicates that the effects of each of the parameters designed according to Taguchi on the coating properties are different.

Ethics in Publishing

There are no ethical issues regarding the publication of this study.

Author Contributions

Yaşar Sert: Conceptualization, Methodology, Data, curation, Writing – original draft preparation.

Tevfik Küçükömeroğlu: Supervision, reviewing and editing.

Acknowledgements

The author(s) disclosed receipt of the following financial support for the research, authorship, and/or publication of this article: Scientific and Technological Research Council of Turkey (TUBITAK). Grant No: 5190089.

References

- [1] Haiko, O., Valtonen, K., Kajjalainen, A., Uusikallio, S., Hannula, J., Liimatainen, T., Kömi., (2019) Effect of Tempering on the Impact-Abrasive and Abrasive Wear Resistance of Ultra-High Strength Steels, *Wear*, 440-441, 203098.
- [2] Cheng, W. L., Zhou, Z. F., Shum, P. W., Li, K. Y., (2013) Effect of Ni Addition on The Structure and Properties of Cr-Ni-N Coatings Deposited by Closed-Field Unbalanced Magnetron Sputtering Ion Plating, *Surface and Coatings Technology*, 229 84-89.
- [3] Fotovvati, B., Namdari, N., Dehghanghadikolaei, A. (2019) On Coating Techniques for Surface Protection: A Review, *J. Manuf. Mater. Process*, 3 (1) 28-50.
- [4] Sukuroglu, E. Baran, Ö. Totik Y. Efeoglu, I. (2018) Investigation of high temperature wear resistance of TiCrAlCN/TiAlN multilayer coatings over M2 steel, *Journal of Adhesion and Technology*, 32 1428-1436.
- [5] Schiller, S., Goedicke, K., Reschke, J., Kirchhoff, V., Schneider, S., Milde, F. (1993) Pulsed Magnetron Sputter Technology, *Surface and Coatings Technology*, 61 (1-3) 331-337.
- [6] Rossnagel, S.M., Cuomo, J. J. (1989) Film Modification by Low Energy Ion Bombardment During Deposition, *Thin Solid Films*, 17 (1) 143-156.
- [7] Yu, D., Wang, C., Cheng, X., Zhang, F. (2008) Optimization of Hybrid PVD Process of TiAlN Coatings by Taguchi Method, *Applied Surface Sciences*, 255 (5-1) 1865-1869.
- [8] Gulden, G. Yaylali, B. Efeoglu, I. Totik, Y. Kelly, P. Kulczyk-Malecka, J. (2024) Effect of Nb and V doped elements on the mechanical and tribological properties of CrYN coatings, *Surface and Coatings Technology*, 477 130297.
- [9] Chen, L. Holec, D. Du, Y. Mayrhofer, P.H. (2011) Influence of Zr on Structure, Mechanical and Thermal Properties of Ti-Al-N, *Thin Solid Films*, 59 5503-5510.
- [10] Thornton, J. A. (1986) The microstructure of sputter-deposited coatings, *J Vac Sci Tech A: Vac Surf Films*, 4 3059-3065.
- [11] Wang, X. Wang, L. S. Qi, Z. B. Yue, G. H. Chen, Y. Z. Wang, Z. C. Peng, D. L. (2010) Investigation on the structure and properties of $Al_xCr_{1-x}N$ coatings deposited by reactive magnetron co-sputtering, *Journal of Alloy and Compounds*, 502 243-249.

[12] Skordaris, G. Bouzakis, K. D. Charalampous, P. Kotsanis, T. Bouzakis, E. Bejjani, R. (2018) Bias voltage effect on the mechanical properties, adhesion and milling performance of PVD films on cemented carbide inserts, *Wear*, 404-405 50-61.

[13] Gangopadhyay, S. Acharya, R. Chattopadhyay, A. K. Paul, S. (2010) Effect of substrate bias voltage on structural and mechanical properties of pulsed DC magnetron sputtered TiN–MoS_x composite coatings, *Vacuum*, 84 843-850.

Enhanced Production and Therapeutic Evaluation of TP4 Peptide in *Pichia pastoris* Against Hepatocellular Carcinoma HUH-7 Cells

Seda KILINÇ¹, Mert KARAOĞLAN², Mehmet KUZUCU^{1*}

¹Department of Biology, Graduate School of Natural and Applied Sciences, Erzincan Binali Yıldırım University, Erzincan, Türkiye

²Department of Food Engineering, Graduate School of Natural and Applied Sciences, Erzincan Binali Yıldırım University, Erzincan, Türkiye

Received: 12/08/2024, Revised: 08/08/2024, Accepted: 13/08/2024, Published: 31/08/2024

Abstract

Tilapia piscidin 4 (TP4), a cationic antimicrobial peptide, is recognized for its diverse biological roles, including antibacterial, wound-healing, and anticancer properties. Herein, the codon-optimized sequence of TP4 peptide was expressed using the pPICZαA expression vector containing the AOX1 promoter, a strong and inducible promoter, in the *Pichia pastoris* KM71H expression system. Recombinant TP4 peptide was purified by Ni-NTA affinity chromatography. After purification, the anticancer activity of TP4 was assessed in HUH-7 hepatocellular carcinoma cells, and the underlying mechanisms were determined. In the present study, it was demonstrated for the first time that recombinant TP4 displayed strong anticancer activity in the human HUH-7 cell line. The TP4 antimicrobial peptide can be used as a competitive candidate for the treatment of cancer cells due to its anticancer effects.

Keywords: Tilapia piscidin 4, recombinant peptide, *Pichia pastoris*, HUH-7

Pichia pastoris'te TP4 Peptidinin Artırılmış Üretimi ve Hepatoselüler Karsinom HUH-7 Hücrelerine Karşı Terapötik Değerlendirmesi

Öz

Bir katyonik antimikrobiyal peptidi olan Tilapia piscidin 4 (TP4), anti-bakteriyel, yara iyileştirici ve antikanser özellikleri de dahil olmak üzere çeşitli biyolojik rolüyle tanınmaktadır. Burada, TP4 peptidinin kodon optimizasyonlu dizisi, *Pichia pastoris* KM71H ekspresyon sisteminde güçlü ve indüklenebilir bir promotor olan AOX1 promotörü altında pPICZαA ekspresyon vektörü kullanılarak eksprese edilmiştir. Rekombinant TP4 peptidi, Ni-NTA afinite kromatografisi ile saflaştırılmıştır. TP4'ün saflaştırılmasından sonra TP4'ün antikanser aktivitesi hepatoselüler karsinoma hücrelerinde değerlendirilmiş ve altta yatan mekanizmalar belirlenmiştir. Bu çalışmada ilk kez rekombinant TP4'ün insan HUH-7 hücre hattında güçlü antikanser aktivite gösterdiği belirlenmiştir. TP4 antimikrobiyal peptidi, antikanser etkileri nedeniyle kanser hücrelerinin tedavisinde rekabetçi bir aday olarak kullanılabilir.

Anahtar Kelimeler: Tilapia piscidin 4, rekombinant peptit, *Pichia pastoris*, HUH-7

1. Introduction

Hepatocellular carcinoma (HCC) is the most prevalent type of primary liver cancer. According to World Health Organization statistics in 2022, HCC is the sixth most common type of cancer worldwide. It is also the third most common cause of cancer death after lung and colorectal cancer [1]. Current treatments for cancers in general include radiation, chemotherapy, immunotherapy, and surgical methods. However, limited selectivity in targeting tumor cells and the emergence of resistance in tumor cells are challenges of such treatments. Therefore, new therapeutic methods are necessary [2].

Cancer cells often have negatively charged phosphatidylserine (PS) or anionic structures in their outer membranes, unlike healthy cells that are normally zwitterionic. Among therapeutic peptides, antimicrobial/pore-forming peptides (AMPs) attract attention due to their anticancer effects. AMPs occur naturally in all living organisms and are part of the immune defense mechanism. AMPs have cationic charges and form amphipathic structures in nonpolar solvents. Antimicrobial cationic peptides target cancer cell membranes and induce cell death through necrosis or apoptosis [3-5].

Tilapia piscidin 4 (TP4), a marine antimicrobial peptide and a cationic antimicrobial peptide identified from Nile Tilapia (*Oreochromis niloticus*), is known to exhibit multiple biological functions, including antibacterial, wound-healing, immunomodulatory, and anticancer activities [6-8]. Furthermore, TP4 has attracted attention for its potent anticancer activity in glioblastoma cells, human non-small cell lung cancer cells, and triple-negative breast cancer cells [9,10].

Although AMPs have many features such as scientific research and industrial use, the main factors that limit studies on AMPs are that obtaining AMPs is time-consuming and quite costly. There are three main production methods for obtaining AMPs: direct AMP extraction from natural sources, chemical synthesis, and recombinant techniques. The recombinant method is preferred over chemical synthesis and extraction in many aspects. For example, it is more cost-effective and provides an endless source of peptide production for both research and large-scale production for pharmaceutical use [11-13]. *Pichia pastoris*, a methylotrophic yeast, has recently become the most frequently used expression system for eukaryotic protein production. This is because *P. pastoris* can make post-translational modifications such as correct polypeptide folding, disulfide bond formation, and glycosylation, which are very important for eukaryotic proteins and which bacteria cannot do [14,15].

TP4 peptide, which is the subject of this study, was first produced recombinantly in *P. pastoris* in a study conducted by Neshani et al. (2018). In addition, in studies conducted by Huang et al. (2020) and Tai et al. (2021), TP4 peptide was produced recombinantly in *P. pastoris* and was aimed to be used for different purposes by taking advantage of the high antimicrobial effect of TP4 [16,17].

Recent studies have increasingly focused on the anticancer effects of the TP4 peptide. Su et al. (2019) on glioblastoma cells (U87MG, U251) determined that TP4 increased reactive oxygen

species, decreased ATP, and significantly increased the release of cyclophilin A, a necrotic biomarker [10]. Su et al. (2021) also showed that TP4 can cause necrotic cell death in human synovial sarcoma AsKa-SS and SW982 cell lines [18]. In another study, it was reported that the toxic effect of TP4 on non-small cell lung cancer cells primarily led to necrosis. Additionally, while cell membrane disruption was observed at high concentrations of TP4, it was determined that it resulted in controlled cell death at low concentrations [9]. Furthermore, the cytotoxicity of TP4 was also tested in triple-negative breast cancer (TNBC) cell lines under both in vitro and in vivo conditions. TNBC cells have been shown to activate the FBJ murine osteosarcoma viral oncogene homolog B (*FOSB*), which is counteracted by *TP4* through selective binding to mitochondria and induction of cytosolic Ca^{2+} accumulation. *FOSB* overexpression results in TNBC cell death, whereas inhibition of calcium signaling abrogates *FOSB* induction and blocks TP4-induced TNBC cell death. In conclusion, this study showed that *TP4* strongly induces *FOSB*, especially in TNBC, providing a new therapeutic approach for TNBC through *FOSB* induction [19,20].

Synthetic TP4 peptide was used in studies investigating the anticancer effect of TP4. However, there is no study yet to examine the anticancer effect of recombinant TP4 produced. Additionally, within the scope of this study, TP4 peptide was studied for the first time in HUH-7 hepatocellular carcinoma cells. This study aimed to recombinantly produce the TP4 peptide in the *P. pastoris* expression system. Additionally, the study evaluated the therapeutic potential and anticancer activity of the produced TP4 on HUH-7 hepatocellular carcinoma cells.

2. Material and Methods

Strains and Chemicals

Escherichia coli XL1-Blue strain was used for subcloning and amplification of expression vectors. For the development of *E. coli* cells, LB medium (0.5% yeast extract, 1% peptone and 1% NaCl) was prepared with appropriate antibiotic additions. After cloning, zeocin was added to the LB agar medium to select positive *E. coli* XL1-Blue cell transformants. *P. pastoris* KM71H strain was used as the host system for protein expression. YPD (1% yeast extract, 2% peptone, 2% dextrose) medium was used as preculture to grow transformant *P. pastoris* cells. BMGY (2% glycerol, 1% yeast extract, 2% peptone, 1.34% yeast nitrogen base w/o amino acids, 4×10^{-5} % biotin and 100 mM phosphate buffer, pH 6), BMMY (contained 1% methanol instead of glycerol in BMGY) culture media were used for protein expression studies.

HUH-7 (human hepatocellular carcinoma cell line) was obtained from ATCC (American Type Culture Collection, USA). Phosphate buffer saline (PBS), Heat-inactivated fetal bovine serum, Trypsin–EDTA, Dulbecco’s modified Eagle’s medium (DMEM), L-glutamine, penicillin–streptomycin and MTT (3-(4,5-Dimethylthiazol-2-yl)-2,5-Diphenyltetrazolium Bromide) were purchased from Biological Industries (Biological Industries Co, Beth-Haemek, Israel). Qiagen RNeasy Mini Kit (Qiagen, Hilden, Germany) was used to isolate RNA, and Biorad iScript™ cDNA Synthesis Kit (Bio-Rad Laboratories Inc., Hercules, CA, USA) was used to synthesize cDNA. Human Bax, Bcl-2, Casp3 ELISA kits were from Elabscience Company (Elabscience

Biotechnology, Wuhan, China). All other chemicals were purchased from Sigma Aldrich (Merck KGaA, Darmstadt, Germany).

HUH-7 cell line was cultured in DMEM supplemented with 10 % fetal bovine serum, 1% pen-strep solution, 1% L-Glutamine at 37 °C in a 5% CO₂ incubator and 95% humidity.

2.1. Recombinant Production of TP4

Gene Synthesis and Plasmid Construction

The nucleic acid sequence encoding the TP4 peptide was obtained from NCBI GenBank (accession number XM_002491337). After the DNA sequence encoding the TP4 peptide was determined, restriction enzyme cutting sites, stop codon, G-TEV Protease region and C-terminal 6x His sequence (His-tag, for purification of the peptide) was added to the ends of the sequence. For effective protein production, codon optimization according to the characteristics of host system is very important [21]. Codon optimization of the obtained nucleotide acid sequence was performed according to the *P. pastoris* codon usage frequency table by Genscript (NJ, USA). To obtain the *TP4* gene sequence, 6 primers (Table 1) that were partially complementary to each other were ordered by Sentebiolab Company (Ankara, Türkiye), and these primers were combined by the overlap PCR method, respectively, and a 141 bp length DNA sequence was obtained. PCR products of the 141 bp DNA sequence encoding the TP4 peptide were purified using a commercial purification kit (Hydra, Gel and PCR Purification Kit, Türkiye). TP4 DNA sequence: 5-CTC GAG CAT CAC CAC CAT CAT CAC GAG AAC CTA TAC TTT CAA GGG TTT ATT CAC CAT ATT ATA GGC GGT CTC TTC AGC GCC GGA AAA GCG ATC CAT AGA CTG ATC CGA CGC CGG AGG CGT TGA TCT AGA-3.

Table 1. Overlap primers for synthesis to *TP4* gene.

Primer	Sequence
<i>TP4F1</i>	AAACTCGAGAAAAGACATCACCACCATCATCACG
<i>TP4R1</i>	CCCTTGAAAGTATAGGTTCTCGTGATGATGGTG
<i>TP4F2</i>	ACTTTCAAGGGTTTATTACCATATTATAGGCGG
<i>TP4R2</i>	CGCTTTTCCGGCGCTGAAGAGACCGCCTATAATA
<i>TP4F3</i>	CCGAAAAGCGATCCATAGACTGATCCGACGCCG
<i>TP4R3</i>	TTTTCTAGATCAACGCCTCCGGCGTCGGAT

TP4 gene was cloned into the pPICZ α A vectors from *XhoI-XbaI* restriction sites to construct pPICZ α A-TP4 expression vector. The schematic representation of the vector was given in Fig. 1.

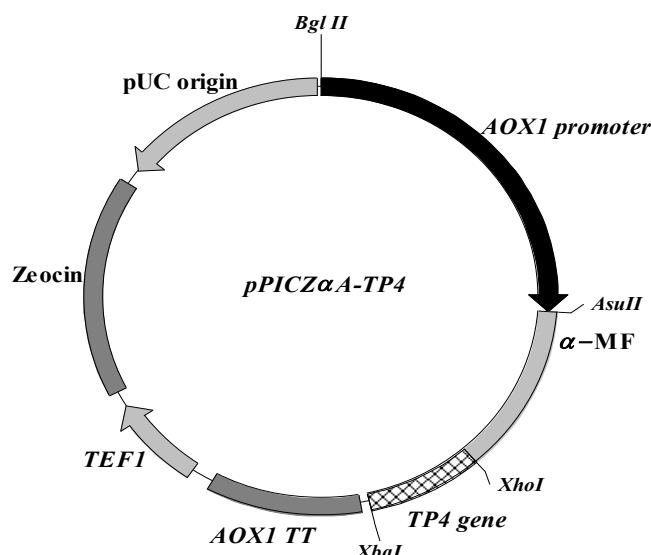


Figure 1. Schematic representation of the constructed expression vector pPICZαA-TP4

Cloning of the *TP4* gene in *P. pastoris*

The expression vector was linearized by digestion with restriction enzymes *SacI* at the *AOX1* promoter site. The expression cassette obtained was transformed into the electrocompetent *P. pastoris* KM71H strain by electroporation using an electroporator (Bio-rad, Gene Pulser Xcell Electroporation System) at 2000 V, 5 ms [22]. The selection of transformant cells was performed on YPD agar plates containing 100 µg/mL zeocin.

Recombinant TP4 Production in Shake-flasks

The recombinant protein production studies were carried out in shake-flask conditions. Selected clone was cultured in 5 mL of YPD medium overnight. The culture was used as inoculum for BMGY medium and incubated for 18 hours for cell accumulation. The cells were harvested by centrifugation at 1200 ×g and transferred to BMMY medium, which is the protein production medium. TP4 production was induced by adding methanol to a final concentration of 1% every 24 hours. The induction phase was continued at 28°C for 216 hours.

Purification of the Recombinant TP4

In this study, the recombinant protein was synthesized with a polyhistidine (6xHis) tag attached to the C-terminus. The use of a histidine tag, particularly the 6×His tag (0.84 kDa), is advantageous due to its small size and lack of charge at physiological pH, which typically does not interfere with the folding, structure, or function of the protein [24]. Moreover, the purification method employed for histidine-tagged proteins relies on immobilized metal affinity chromatography (IMAC), offering efficient purification with high yields. In this technique, the protein of interest selectively binds to transition metal ions (nickel, in this instance) immobilized on a resin matrix via the histidine tag, effectively separating it from other unlabeled proteins in the supernatant. Subsequently, the recombinant protein is eluted from the resin using imidazole, which competes with the histidine tag for binding sites [25].

The produced 6×His labeled TP4 peptide was purified using Ni-NTA resin. The resin was washed with 1×PBS pH 7.4 containing 20 mM imidazole, and then the TP4 peptide attached to the resin was treated 3 times with 1×PBS pH 7.4 elution buffer containing different concentrations of imidazole (50, 100 and 200 mM) [26]. Protein samples in different fractions of the purification process were analyzed by SDS-PAGE. The total protein amount was determined using the Coomassie Bradford Plus Protein Assay Kit according to the kit protocol.

SDS-PAGE Analysis

For the analysis of protein samples taken from the purification steps analyzed by the tricin SDS-PAGE protocol described by Schägger (2006) [23]. The samples were mixed with 4×SDS gel loading buffer in a 20 µL and incubated at 70°C for 10 min. denatured. Then, peptides were separated by electrophoresis in the SDS-PAGE gel, which consisted of two phases: a loading gel containing 4% polyacrylamide and a separation gel containing 16% polyacrylamide.

Electrophoresis was performed in Anode (0.1 M Tris, 0.0225 M HCL pH 8.9) and Cathode Buffer (0.1 M Tris, 0.1 M Tricine, 0.1% SDS, pH 8.25) buffer at 80V for 30 min. and 120V 100 min. was carried out. Then, the gel was stained with Coomassie Brilliant Blue dye and then treated with a decolorizing solution (10% acetic acid, 50% methanol and 40% pure water) to remove the dye, and the resulting SDS-PAGE gel was imaged on ChemiDoc Touch Imaging System (Bio-Rad Laboratories Inc., Hercules, CA, USA).

Antimicrobial Activity

The minimum inhibitory concentration test (MIC) and the minimum bactericidal concentration test (MBC) are important methods to assess the antimicrobial activity levels of the recombinant TP4. MIC and MBC values were determined on *Escherichia coli* (gram-negative) and *Bacillus subtilis*-ATCC 23857 (gram-positive).

The bacteria were activated through batch cultivation in shake-flasks containing sterile Tryptic Soy Broth (TSB) with at 37 °C 200 rpm. Subsequently, 100 µL of the culture was inoculated onto tryptone soy agar (TSA) plates and incubated for 24 hours at 37 °C. Then, a single colony was selected and inoculated into shake-flasks containing sterile TSB, and incubated for 12 hours at 37 °C.

To determine MIC and MBC, Microtitre Broth Dilution Method was used. Seven decreasing serial dilutions of TP4 peptide (50-25-12.5-6.25-3.125-1.56-0.78 µg/mL) applied two bacteria on 96-well plates with 5 replicates. Following incubation at 37 °C for varying durations (6-12-18-24 hours), bacterial growth was assessed by measuring absorbance at 600 nm using a microplate reader. As a negative control, bacterial cultures without TP4 were included, while serial dilutions of 0.01 mg/mL kanamycin used as positive control. Starter culture was prepared in 5 mL TSB and incubated for 18 hours at 37 °C, then the starter culture was inoculated at a ratio of 1/100 into the flask, it was incubated at 37 °C in a shaker at 200 rpm until Optic Density was 0.5. 150 µl of this culture was transferred to each well of the 96-well plate under aseptic

conditions. Following incubation, viable cell counts were calculated based on absorbance values at 600 nm.

2.2. Cell Culture

Cell Viability Assay

The anticancer effects of TP4 against growth of cells was determined using the MTT assay. Firstly, the cancer cells were seeded in 96-well culture plate at 5×10^3 cells per well for 24 hours of incubation. In the literature, TP4 has been applied to various cancer cells at different concentration ranges. Ting et al. (2016) observed that treatment with 15 $\mu\text{g}/\text{mL}$ TP4 was sufficient to kill more than 50% of breast cancer cells within 6 hours. Su et al. (2019) determined that the 50% lethal dose (LD50) of TP4 for glioblastoma cells was 20 $\mu\text{g}/\text{mL}$. In a subsequent study, Su et al. (2021) reported IC50 values of 29.20 and 32.41 $\mu\text{g}/\text{mL}$ for synovial sarcoma cells. The TP4 concentration range for this study was determined by considering the IC50 concentrations reported in previous studies. In this study, TP4 at concentrations of 100, 50, 25, 12.5, 6.25, 3.125, 1.56, and 0.78 $\mu\text{g}/\text{mL}$ was applied to HUH-7 cells for 3, 6, 12, and 24 hours at 37°C, with 5% CO₂ and 95% humidity. At the end of the 3, 6, 12, and 24-hour incubations, 100 μL of MTT reagent was added to each well to determine cell viability. After 3 hours, the absorbance was measured using a microplate reader at 570 nm to calculate the percent cell viability.

RT-PCR Analysis

Total RNA was extracted from HUH-7 cells treated by TP4 (3.5-4.5-5.5 $\mu\text{g}/\text{mL}$) at the end of the 3-h incubation. RT-PCR was performed using specific primers for *BAX*, *BCL-2*, *CASP3* and first strand cDNA synthesis was carried out according to the manufacturer's protocols. *ACTB* was used as the reference gene. Gene expression levels of *BAX*, *BCL-2*, *CASP3*, and *ACTB* were analyzed using primers (Table 2) synthesized by Sentebiolab Company (Ankara, Türkiye).

PCR was performed using a SYBR Green Master Mix (Qiagen, Hilden, Germany) with a reaction mix containing 1 μL cDNA, 2 μL each of primer and 12,5 μL SYBR Green Master Mix (total volume 25 μL). PCR conditions were as follows for one cycle: 95°C for 10 min followed by 45 cycles of 95°C for 15 sec, 64°C for 30 sec and 72°C for 15 sec. Each reaction was run in triplicate. Analysis of relative expression of these genes was performed using the $2^{-\Delta\Delta\text{Ct}}$ method.

Table 2. Primers for detection of genes expression.

Gene	Primer sequence	Reference
<i>BAX</i>	F: 5-AGCAGATCATGAAGACAGGG	[27]
	R: 5-GAAGTTGCCGTCAGAAAACA	
<i>CASP3</i>	F: 5-GCGCTCTGGTTTTTCGTTAAT	[27]
	R: 5-ACCCATCTCAGGATAATCCATTT	

<i>BCL2</i>	F: 5-TATCTGGGCCACAAGTGAAG	[27]
	R: 5-ATTCGACGTTTTGCCTGAAG	
<i>ACTB</i>	F: 5-CACCATGGATGATGATATCGC	[27]
	R: 5-GAATCCTTCTGACCCATGCC	

ELISA Tests

Total protein was extracted from HUH-7 cells treated by TP4 (3.5-4.5-5.5 µg/mL) at the end of the 3-h incubation. To determine protein expression levels of the Bax, Bcl-2, Casp3 on HUH-7 cell treated by TP4 commercial sandwich ELISA kits.

TAS and TOS Analysis

TAS (Total Antioxidant Level) and TOS (Total Oxidant Level) tests measure the total capacity of total antioxidants and oxidants present in a biological sample. Commercially purchased Rel Assay Diagnostic TAS-TOS Assay Kits (Türkiye) were used to determine TAS and TOS status. Proteins purified from TP4-treated cells and stored at -80 °C for use were used as samples. Experiments were carried out in 4 replicates according to the kit protocols.

3. Results and Discussion

Cloning of the *TP4* Gene into Expression Vector

In this study, 141 bp DNA sequence encoding the TP4 peptide was obtained by using the overlap PCR method and sequence was confirmed by agarose gel (Figure 2). After, DNA sequence containing the TP4 *gene* was digested with *XhoI-XbaI* enzymes and ligated to the pPICZαA plasmid digested from the *XhoI-XbaI* enzyme recognition site. The generated expression vector was named pPICZαA-TP4. Ligation mixture was transferred to competent *E. coli* XL1-Blue cells prepared using the CaCl₂ method, and selection was performed on LB Lennox agar medium containing 25 µg/mL zeocin antibiotic. Three colonies grown on antibiotic-containing medium were selected, and the accuracy of the expression vector and the cloned gene was verified *AsuI* ve *SalI* restriction enzymes. The verified expression vector was linearized using the *SacI* restriction endonuclease. Then linearized plasmid was purified by using PCR Purification Kit and it was transferred to competent *P. pastoris* KM71H cells by electroporation technique.

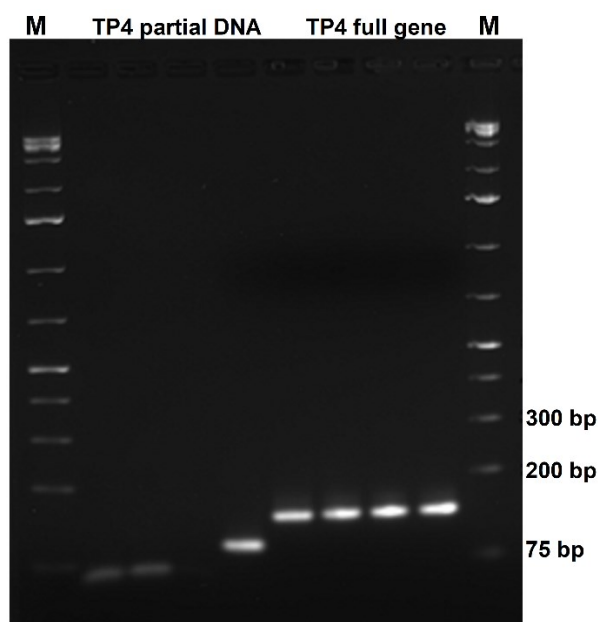


Figure 2. Obtaining the *TP4* gene by overlap PCR. (M: 1kb DNA ladder, Fermentas; Line 1-4: Partial *TP4* DNA fragments; Line 5-8: Full construct of *TP4* gene)

Expression Studies of the *TP4* Gene in *P. pastoris*

After the transformation of the expression vector into the *P. pastoris* KM71H strain made competent by the Lithium-acetate method, the selected clone was first developed in YPD medium at 28°C overnight. The cells grown in YPD medium were inoculated into shake-flask containing 200 mL of BMGY medium and incubated for 18 hours at 28°C and 250 rpm. At the end of the cell accumulation period, the culture was centrifuged and the resulting cell pellet was resuspended in 200 mL of BMMY medium. During the induction phase, methanol, which acts as both a carbon source and inducer, was added to the medium every 24 hours to a final concentration of 1% for 216 h. At the end of the induction phase, cell density of the culture (OD_{600 nm}) was measured and the supernatant sample was collected for purification analysis.

The literature indicates that the recombinant production of TP4 peptide in the *P. pastoris* expression system has been performed using similar methods [11,16,17]. Neshani et al. (2018) cloned the TP4 gene into the pPIC9 vector and expressed it in the *P. pastoris* GS115 strain. Tai et al. (2021) and Huang et al. (2020) both cloned the TP4 gene into the pPICZαA vector and expressed it in the *P. pastoris* X-33 strain. In this study, the TP4 gene was cloned into the pPICZαA vector and expressed in the *P. pastoris* KM71H strain, unlike previous studies. Most *P. pastoris* strains are Mut⁺ (methanol usage positive phenotype) and grow rapidly with methanol induction. However, the KM71H strain is Mut^s, with the AOX1 gene deleted, resulting in slower methanol metabolism due to reliance on the AOX2 gene. Strains with deleted AOX genes can sometimes outperform wild-type strains in recombinant protein production [28]. Additionally, the Mut^s strain offers advantages such as lower costs in large-scale fermentations and reduced contamination risk due to requiring less methanol for induction.

Purification of Recombinant TP4

The supernatant sample collected was used for recombinant TP4 purification. The sample was concentrated and equilibrated with 1×PBS pH 7.4 containing 10 mM imidazole and loaded into the column containing Ni-NTA resin. For elimination of the non-specific binding the column was washed using 1×PBS buffer containing 20 mM imidazole. Then, the column was treated 1×PBS buffer containing different concentrations (50, 100 and 200 mM) of imidazole for elution of the his-tagged TP4 protein. The presence of histidine-tagged TP4 and purified TP4 were determined by the tricine SDS-PAGE gel analysis (Figure 3). Elutions containing recombinant TP4 protein were collected and dialyzed against 1×PBS buffer and the resulting purified protein was used to further analysis.

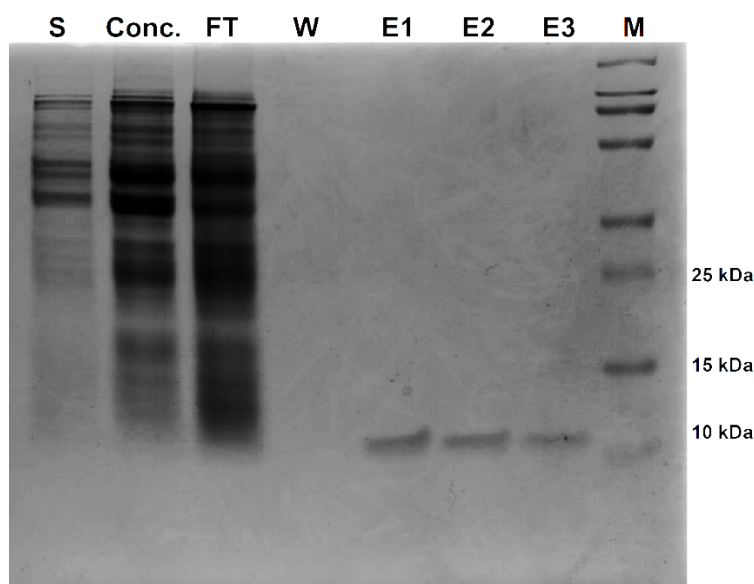


Figure 3. SDS-PAGE analysis of the purification steps of the TP4 protein (M: Protein marker; S: Supernatant sample; Conc.: Concentrated sample; FT: Flow Through; W: Wash (1×PBS containing 20 mM imidazole), E1-3: Elution (1×PBS containing 50, 100, 200 mM imidazole, respectively).

There are three main production methods for obtaining AMPs. These are direct AMP extraction from natural sources, chemical synthesis, and recombinant techniques. The recombinant method is preferred over the chemical method in many respects and has been increasingly considered for peptide production in recent years. Direct extraction of AMPs from natural sources is lengthy and costly, and it also poses a threat to ecosystems by harming many species. The chemical synthesis method involves multiple complex chemical steps, increasing the risk of errors in peptide sequences. Recombinant DNA technology is preferred over chemical and enzymatic synthesis methods in many respects and has been increasingly used for peptide production in recent years [13, 29].

Recombinant TP4 Expression in *P. pastoris* Showed Antimicrobial Activity

First, the antibacterial effect of the recombinant TP4 was determined by MIC and MBC methods. As seen in the results shown in Table 3 and Figure 4, it was determined that TP4 peptide had an antibacterial effect on *E. coli* and *B. subtilis*.

Bacteria have anionic properties, bind to cationic AMP, and disrupt its structure. They bind to negatively charged bacterial cell membranes through electrostatic interactions, disrupting their functions and causing death [30]. In this study, the accuracy of the activity of TP4 produced was examined on gram positive and negative bacteria. As a result, it was determined that even a small amount of TP4 had a very high antibacterial activity.

Table 3. MIC and MBC values of TP4 on strains

Hour	<i>E. coli</i>	<i>B. subtilis</i>	<i>E. coli</i>	<i>B. subtilis</i>
	MIC (µg/mL)	MIC (µg/mL)	MBC (µg/mL)	MBC (µg/mL)
6	3.125	6.25	12.5	12.5
12	3.125	3.125	12.5	12.5
18	6.25	1.56	25	25
24	6.25	1.56	50	25

In the literature, the antibacterial activity of recombinantly produced TP4 was investigated using a similar method [11]. Although the results obtained are partially compatible with the literature, it is thought that the higher MIC and MBC values even in the same bacteria compared to the literature are due to the differences in the parameters during the experiment.

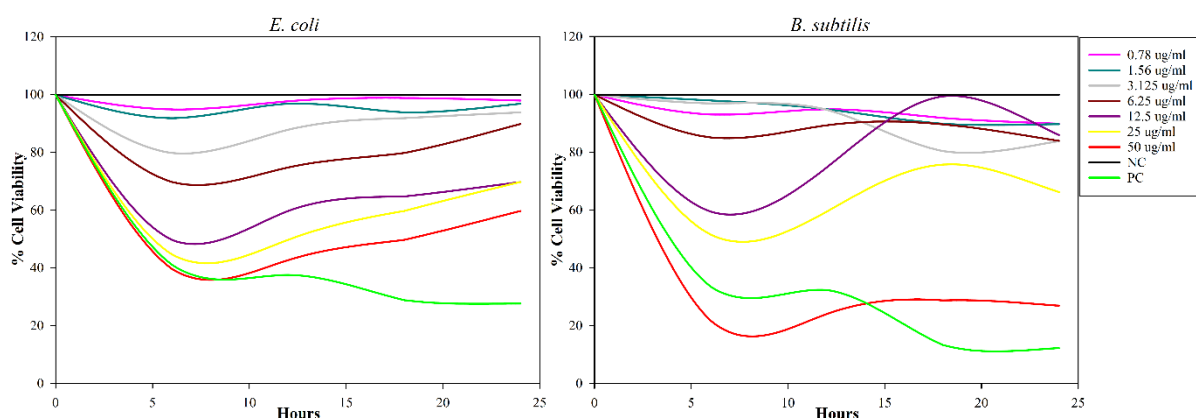


Figure 4. MIC and MBC of TP4 peptide on *E. coli* and *B. subtilis*

TP4 Decreases Cell Viability in HUH-7 Hepatocellular Carcinoma Cells

In this study was investigated anticancer effects of TP4 on HUH-7 hepatocellular carcinoma cells. For this aim, firstly, the cytotoxic effects TP4 on cancerous cells were determined by

MTT cell proliferation assay. Different concentrations of TP4 (100-50-25-12,5-6,25, 3,125, 1,56, 0,78 $\mu\text{g}/\text{mL}$) were applied on HUH-7 cells for 3-, 6-, 12- and 24-hours at 37 °C, 5% CO₂ and 95% humidity. IC₅₀ value was found to be 4.5 $\mu\text{g}/\text{mL}$ for 3-hour incubation by using AA Bioquest IC₅₀ calculator tool. When cell proliferation at different concentrations was examined, it was observed that more than 80% of the cells died with the application of 100 $\mu\text{g}/\text{mL}$ TP4, and 65% of the cells died with 50 $\mu\text{g}/\text{mL}$ TP4. In contrast, the proliferation of cells gradually increased in the control group without treatment. Cytotoxic effects of TP4 are given in Figure 5.

Cancer cells often have negatively charged phosphatidylserine (PS) or anionic structures in their outer membranes, unlike healthy cells that are normally zwitterionic. Antimicrobial cationic peptides target cancer cell membranes and induce cell death through necrosis or apoptosis [4]. In the literature, TP4 has been investigated in various cell lines including SW982 and Aska-SS human synovial sarcoma cells, MDA-MB231, MDA-MB453 and MCF7 breast cancer cells, U87MG and U251 glioblastoma cells [10,18,19]. However, its anticancer effect was investigated for the first time on HUH-7 hepatocellular carcinoma cells. According to the MTT experiment results in HUH-7 cell line, the IC₅₀ value was determined as 4,5 $\mu\text{g}/\text{mL}$. The results obtained were mostly consistent with the literature and the IC₅₀ value was found to be lower than the literature results. This situation is thought to be due to the difference in cell type and protocol.

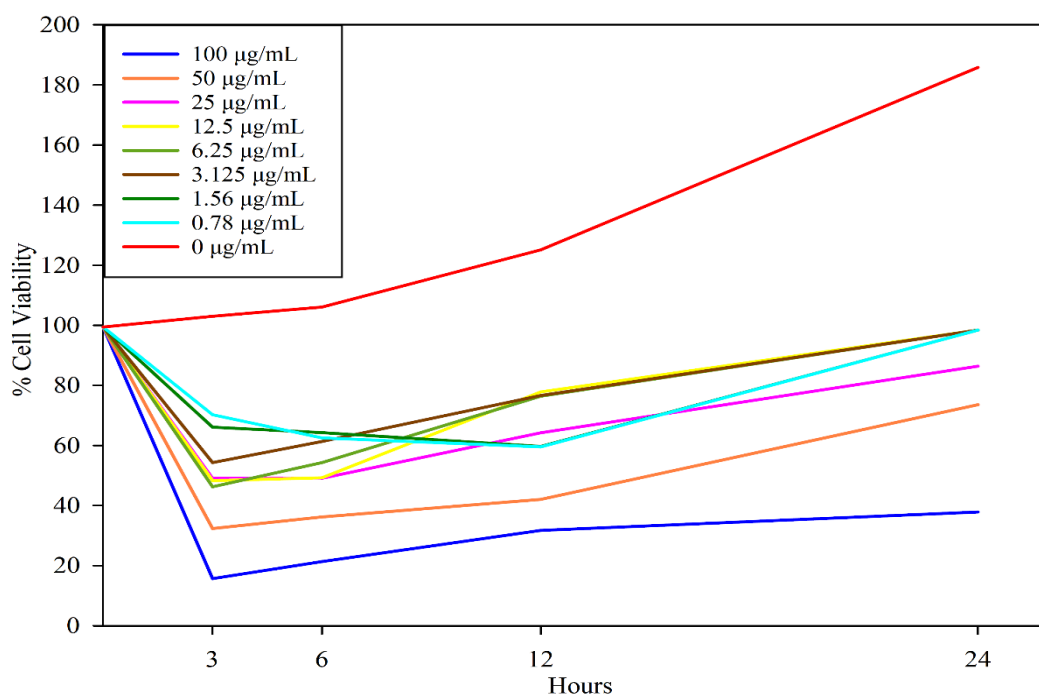


Figure 5. TP4 selectively kills HUH-7 cancer cells. Cell viability in HUH-7 was determined by MTT assay following treatment with varying doses of TP4 (0.78-100 $\mu\text{g}\cdot\text{mL}^{-1}$) at the indicated time-points (3-24h).

TP4 Importantly Effects mRNA and Protein Levels of Cells

Antimicrobial peptides target cancer cells through various mechanisms such as cell membrane disruption, mitochondrial dysfunction, ROS production, and DNA damage, and induce cell death through necrosis or apoptosis [10,31,32]. When the cell is damaged, pro-apoptotic (*BAX* and *CASP3*) or anti-apoptotic (*BCL-2*) genes in the cell are activated, and these genes play an important role in the control of apoptosis [33,34].

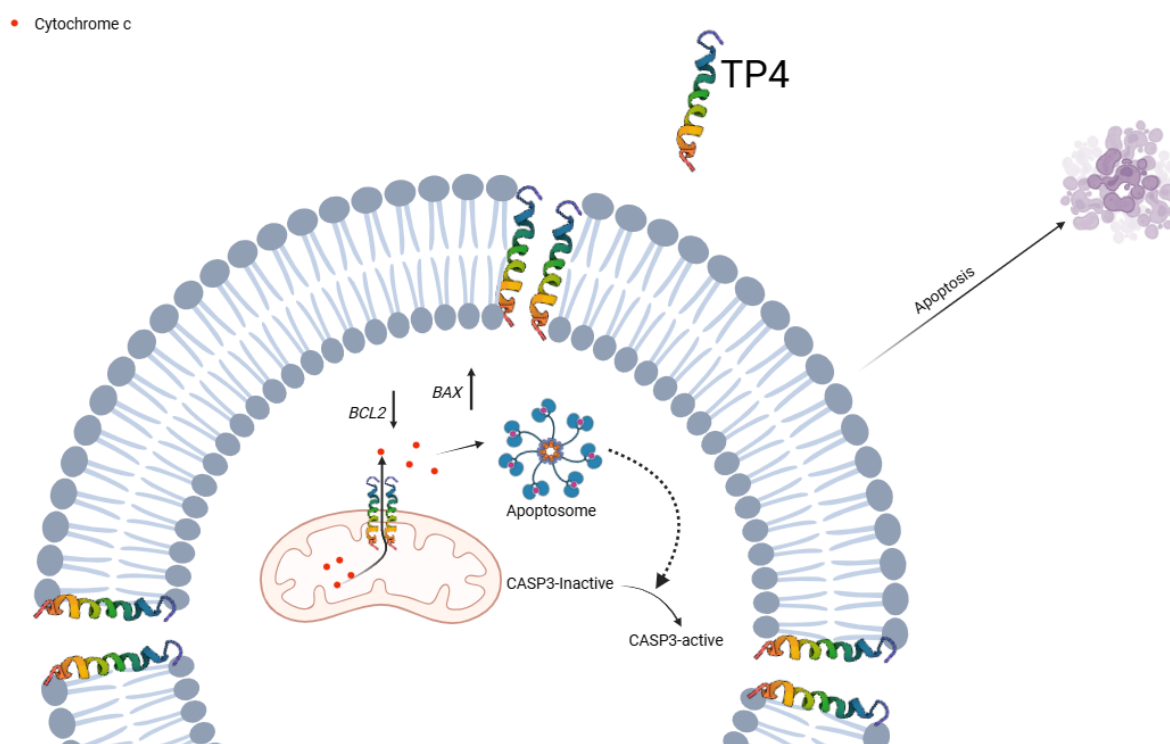


Figure 6. Apoptotic induction of TP4 on HUH-7 cells.

Kuo et al. (2018) applied TP4 stock solution (MSP-4) to MG63 osteosarcoma cells and observed that MSP-4 decreased anti-apoptotic protein BCL-2 levels and increased pro-apoptotic proteins BAX, CASP3 and BID in a dose-dependent manner. The study demonstrated that MSP-4 induced apoptosis via both the intrinsic (mitochondrial) and extrinsic (receptor-mediated) pathways [30, 31]. In this study, gene expression was analyzed using RT-PCR. The results were found to be consistent with the literature. Results showed that treatment with 4.5 $\mu\text{g}/\text{mL}$ TP4 significantly upregulated *BAX* and *CASP3* genes expression on HUH-7 cells. Otherwise, gene expression levels of *BCL-2* downregulated in cells treated with 4.5 $\mu\text{g}/\text{mL}$ TP4 (Figure 7). In cells treated with the same concentration, the ELISA findings of Bax and Casp-3 protein significantly increased compared to control, correlating with increased gene expression levels. The gene expression level of *BCL-2* was decreased in cells treated with 4.5 $\mu\text{g}/\text{mL}$ TP4 (Figure 7). And ELISA result of Bcl-2 protein level was decreased and correlating with gene expression level. These findings provided important information about the pro-apoptotic effects of TP4 on HUH-7 cells. The dual effect of increased pro-apoptotic signals (*BAX* and *CASP3*) and decreased anti-apoptotic signals (*BCL-2*) demonstrated the strong apoptotic effect of TP4.

This study demonstrated that TP4 is particularly important for understanding its therapeutic potential. By promoting apoptosis in cancer cells, TP4 may serve as an effective anti-cancer agent, especially in cases where conventional treatments fail to trigger sufficient apoptotic response. Future research should focus on elucidating the detailed molecular mechanisms by which TP4 modulates these apoptotic pathways and evaluating its effects in various cell types and in vivo models (Figure 6).

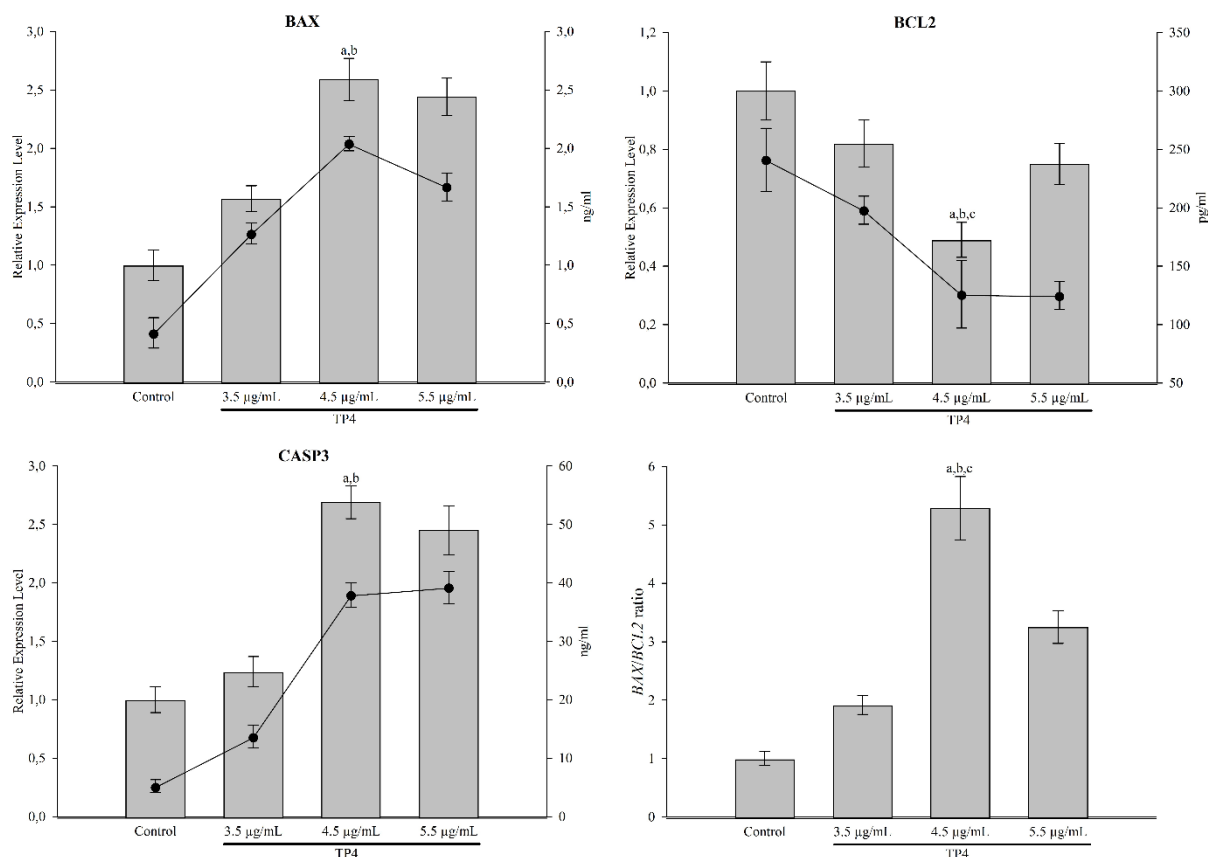


Figure 7. Expression levels of *BAX*, *BCL-2*, *CASP3* and *BAX/BCL-2* ratio in HUH-7 cells. Values are represented as mean \pm standard error of mean. ^a $p < 0.05$ versus control group, ^b $p < 0.05$ versus 3.5 µg/mL TP4-treated group, ^c $p < 0.05$ versus 5.5 µg/mL TP4-treated group.

TAS and TOS Status

Antioxidants play a crucial role in preventing oxidative damage caused by free radicals, whereas oxidants are reactive molecules that can harm cellular structures and contribute to disease. Su et al. (2021) demonstrated that TP4 initiates the production of reactive oxygen species (ROS) and induces necrotic cell death in Aska-SS and SW982 cell lines by reducing levels of antioxidant proteins, such as uncoupling protein-2 and superoxide dismutases SOD-1 and SOD-2. In this study, the total antioxidant status (TAS) and total oxidant status (TOS) in HUH-7 cells were measured using ELISA kits. The results are shown in Figure 8. These findings consistent with the literature, demonstrating that TP4 significantly affects the oxidative balance in HUH-7 cells. The decrease in TAS with increasing TP4 concentration indicates that TP4 induces oxidative stress, raising oxidant levels. The observed decrease in TOS suggests

that TP4 may deplete antioxidants or inhibit cellular antioxidant defenses. This highlights TP4's potential pro-oxidant role, which could cause cellular damage if oxidative stress is not managed. Additionally, the increase in oxidant levels implies that TP4 may stimulate ROS production or impair the cell's ability to neutralize them. Overall, this study shows that long-term oxidative stress can lead to apoptosis in cancer cells, suggesting TP4's potential for anticancer applications.

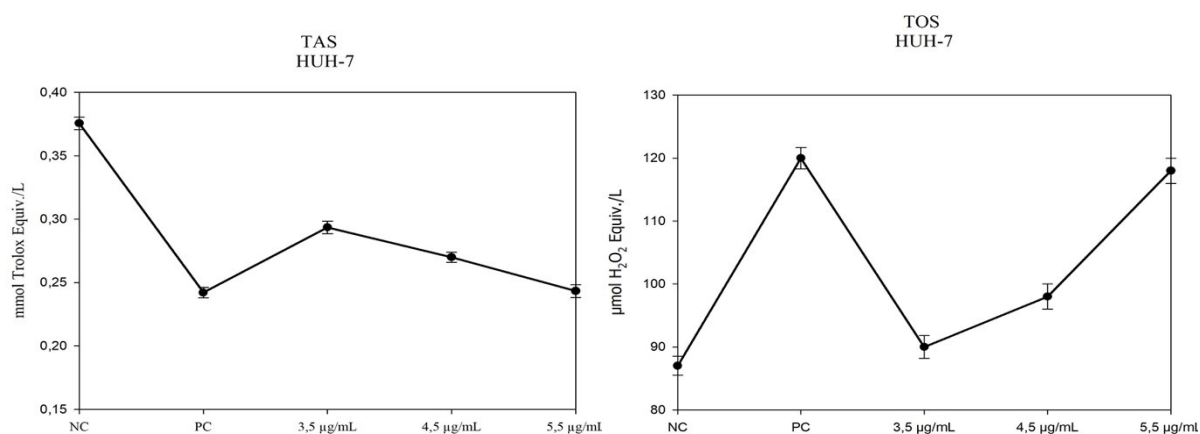


Figure 8. TAS and TOS status on HUH-7 cell line.

4. Conclusion

In this study, the recombinant production of TP4 was carried out in *P. pastoris*, and its effects on HUH-7 hepatocellular carcinoma cells were investigated. The results demonstrated that TP4 exhibits a strong anticancer effect, inducing apoptosis in HUH-7 cells through the induction of oxidative stress and the activation of pro-apoptotic genes. This study is the first to demonstrate that recombinant TP4 exhibits potent anticancer activity in the human HUH-7 cell line. The findings suggest that TP4, an antimicrobial peptide, may serve as a promising candidate for cancer treatment due to its significant anticancer effects. Additionally, investigating the potential synergistic effects of TP4 with other anti-cancer agents may provide valuable information for the development of combination therapies that increase efficacy while minimizing adverse effects.

Ethics in Publishing

There are no ethical issues regarding the publication of this study.

Author Contributions

The authors declare that they have contributed equally to the article.

Acknowledgements

This project was supported by Health Institutes of Türkiye (TUSEB) with project no. 31705.

References

- [1] https://gco.iarc.fr/today/en/dataviz/pie?mode=cancer&group_populations=1&cancers=39&types=1, Ziyaret tarihi: 14.03.2024.
- [2] Chen, Z., Xie, H. et al., (2020) Recent progress in treatment of hepatocellular carcinoma, *Am J Cancer Res.*, 10 (9) 2993-3036.
- [3] Lien, S. and Lowman, H.B. (2003) Therapeutic peptides, *Trends Biotechnol.*, 21(12) 556-62.
- [4] Boohaker, R.J., Lee, M.W., Vishnubhotla, P., Perez, J. M. and Khaled A. R. (2012) The Use of Therapeutic Peptides to Target and to Kill Cancer Cells, *Current Medicinal Chemistry*, 19 3794-3804.
- [5] Chauhan, S., et al., (2021) Antimicrobial peptides against colorectal cancer-a focused review *Pharmacological Research*.
- [6] Peng, K.C. et al., (2012) Five Different Piscidins from Nile Tilapia, *Oreochromis niloticus*: Analysis of Their Expressions and Biological Functions, *plosone*, 7, 11.
- [7] Mahrous, K.F. et al., (2020) Piscidin 4: Genetic expression and comparative immunolocalization in Nile tilapia (*Oreochromis niloticus*) following challenge using different local bacterial strains, *Developmental & Comparative Immunology*.
- [8] Dyshlovoy, S.A. and Honecker, F., (2020) Marine Compounds and Cancer: Updates 2020 *Marine Drugs*, 18, 643.
- [9] Ting, C.H. and Chen, J. Y., (2018) Nile Tilapia Derived TP4 Shows Broad Cytotoxicity toward to Non-Small-Cell Lung Cancer Cells, *Marine Drugs*, 16, 506.
- [10] Su, B.C. et al., (2019) Antimicrobial Peptide TP4 Induces ROS-Mediated Necrosis by Triggering Mitochondrial Dysfunction in Wild-Type and Mutant p53 Glioblastoma Cells, *Cancers*, 11, 171.
- [11] Neshani, A. Et al., (2018) Extended-Spectrum Antimicrobial Activity of the Low Cost Produced Tilapia Piscidin 4 (TP4) Marine Antimicrobial Peptide, *Journal of Research in Medical and Dental Science*, 6 (5) 327-334.
- [12] Zorko, M., Jerala, R. (2010) Production of recombinant antimicrobial peptides in bacteria, *Methods Mol Biol.*, 618,61-6.
- [13] Li, Y. (2011) Recombinant production of antimicrobial peptides in *Escherichia coli*: A review, *Protein Expr Purif.* 80:260-67.
- [14] Hagenson, M.J. (1991) Production of recombinant proteins in the methylotrophic yeast *Pichia pastoris*, *Bioprocess Technol.*, 12, 193-212.

- [15] Cregg, J.M. (2007) *Pichia* Protocols Methods in Molecular Biology Series, Humana Press Inc., 389(2) 1-10.
- [16] Huang, H.N. et al. (2020) Dietary supplementation of recombinant tilapia piscidin 4-expressing yeast enhances growth and immune response in *Lates calcarifer*, *Aquaculture Reports*, 16.
- [17] Tai, H.M. et al. (2021) Scale-up production of and dietary supplementation with the recombinant antimicrobial peptide tilapia piscidin 4 to improve growth performance in *Gallus gallus domesticus*, *PLOS ONE*, 16(6).
- [18] Su, B.C. (2021) Marine Antimicrobial Peptide TP4 Exerts Anticancer Effects on Human Synovial Sarcoma Cells via Calcium Overload, Reactive Oxygen Species Production and Mitochondrial Hyperpolarization, *Mar. Drugs*, 19, 93.
- [19] Ting, C.H. (2016) Targeting FOSB with a cationic antimicrobial peptide, TP4, for treatment of triple-negative breast cancer, *Oncotarget*, 7, 26.
- [20] Hazam, P.K. and Chen, J.Y. (2020) Therapeutic utility of the antimicrobial peptide Tilapia Piscidin 4 (TP4), *Aquaculture Reports*, 17.
- [21] Karaođlan, M., Erden-Karaođlan, F. (2020) Effect of codon optimization and promoter choice on recombinant endo- polygalacturonase production in *Pichia pastoris*. *Enzyme and Microbial Technology*, 139, 109589.
- [22] Wu, S. and Letchworth, G.J. (2004) High efficiency transformation by electroporation of *Pichia pastoris* pretreated with lithium acetate and dithiothreitol, *Biotechniques*, 36,152-154.
- [23] Schagger, H. (2006) Tricine–SDS-PAGE, *Nature Protocols*, 1 (1) 16-22.
- [24] Carson, M. et al. (2007) His-tag impact on structure. *Acta Crystallographica Section D” Structural Biology*, 63(3) 295-301.
- [25] Spriestersbach, A. et al. (2015) “Purification of His-Tagged Proteins” *Methods in Enzymology*, 559, 1-15.
- [26] Karaođlan, M. and Erden-Karaođlan, F. (2021) “Extracellular Production and Purification of the β -glucanase in *Pichia pastoris* Expression System”. *Erzincan University Journal of Science and Technology*, 14 (2) 620-630.
- [27] Gunay, N., & Kuzucu, M. (2023). “Agonistic Effects of Deinoxanthin on Tamoxifen Antiproliferative Activity on HER2 Positive Breast Cancer: An In Vitro Study on MDA-MB-453”. *Erzincan University Journal of Science and Technology*, 16(1), 138-154.
- [28] Karaođlan, M. (2012) “*Pichia pastoris* Alkol Oksidaz (AOX1 ve AOX2) Genlerinin İnaktif Edilmesi ve Elde Edilen Suşun Rekombinant Protein Üretiminde Kullanılması” (Yüksek Lisans), Akdeniz Üniversitesi Fen Bilimleri Enstitüsü, Antalya, 15-19.

- [29] Li, Y. et. al. (2012) “Overview on the recent study of antimicrobial peptides: Origins, functions, relative mechanisms and application” *Peptides*, 37,207–215.
- [30] Zhong, C. et. al. (2020) “A Review for Antimicrobial Peptides with Anticancer Properties: Re- purposing of Potential Anticancer Agents” *BIO Integration*, 1(4), 156-167.
- [31] Deslouches, B. and Peter Di, Y. (2017) “Antimicrobial Peptides with Selective Antitumor Mechanisms: Prospect for Anticancer Applications.” *Oncotarget*, 8(28), 46635-46651.
- [32] Kuo, H.M. et al. (2018) “MSP-4, an Antimicrobial Peptide, Induces Apoptosis via Activation of Extrinsic Fas/FasL- and Intrinsic Mitochondria-Mediated Pathways in One Osteosarcoma Cell Line” *marine drugs*, 16,8.
- [33] Portt, L. et. al. (2011) “Anti-apoptosis and cell survival: A review” *Biochimica et Biophysica Acta* 1813, 238–259.
- [34] Kiraz, Y. ve ark (2016) “Major apoptotic mechanisms and genes involved in apoptosis” *Tumor Biol.*, 37, 8471–8486

Comparison of the Performance of Type-1 and Interval Type-2 Fuzzy PI Controllers for Liquid Level Control in a Coupled Tank System

Hatice NURSOY¹, Abdullah BAŞÇI^{1*}

¹Department of Electrical & Electronics Engineering, Ataturk University, Erzurum, Türkiye

Received: 01/07/2024 Revised: 06/08/2024, Accepted: 09/08/2024, Published: 31/08/2024

Abstract

In this study, liquid level control in a coupled tank system is realized with PI controllers whose parameters are adapted using fuzzy logic approximation methods. Type-1 fuzzy PI control, interval type-2 fuzzy PI control and classical PI+Feedforward control methods are applied to the tank system in real time for different reference liquid levels. The performances of the controllers are compared in terms of system response parameters such as rise time, settling time and overshoot percentage. In addition, the performance evaluation of the controllers over a certain period of time is also compared by calculating integral-based concepts that express error performance metrics such as integral square error (ISE), integral time square error (ITSE), integral absolute error (IAE) and integral time absolute error (ITAE). The obtained results show that the type-2 fuzzy PI controller shows the best performance, followed by type-1 fuzzy PI control and classical PI+FF controller, respectively.

Keywords: PI controller, fuzzy PI controller, couple tank system, liquid level control

İkili Tank Sisteminde Sıvı Seviye Kontrolü için Tip 1 ve Aralık Tip 2 Bulanık PI Kontrolörlerin Performanslarının Karşılaştırılması

Öz

Bu çalışmada, ikili tank sisteminde sıvı seviye kontrolü bulanık mantık yaklaşım yöntemleri kullanılarak parametreleri uyarlanan PI kontrolcüler ile gerçekleştirilmiştir. Tip-1 bulanık PI kontrol, aralık tip-2 bulanık PI kontrol ve klasik PI+ileri besleme kontrol yöntemleri farklı referans sıvı seviyeleri için gerçek zamanlı olarak ikili tank sistemine uygulanmıştır. Kontrolörlerin performansları yükselme zamanı, yerleşme zamanı ve aşım yüzdesi gibi sistem cevabı parametreleri açısından karşılaştırılmıştır. Ayrıca hatanın karelerinin integrali (ISE), zaman ağırlıklı hatanın karelerinin integrali (ITSE), mutlak hatanın integrali (IAE) ve zaman ağırlıklı mutlak hatanın integrali (ITAE) gibi hata performans ölçütlerini ifade eden integral tabanlı kavramların hesaplanmasıyla kontrolcülerin belirli bir süre boyunca gösterdikleri performans değerlendirmesi de sayısal değerlerle ortaya koyularak karşılaştırılmıştır. Elde edilen sonuçlar aralık tip-2 bulanık PI kontrolcünün en iyi performansı gösterdiği ve ardından sırasıyla tip-1 bulanık PI kontrol ve klasik PI+FF kontrolcünün performanslarının iyi olduğu görülmüştür.

Anahtar Kelimeler: PI kontrolör, bulanık PI kontrolör, ikili tank sistemi, sıvı seviye kontrolü

1. Introduction

Efficient control of liquid level systems is a common problem in industrial applications. In liquid level control, it is expected that the liquid level follows the desired level without error, responds quickly and accurately to changes in system dynamics, is resistant to uncertainties and disturbances in the system, and can adapt to changing conditions in the system. Effective and successful control of liquid level systems is important for the reliability and efficiency of industrial processes. Various control methods have been used to control liquid level systems. Some of these studies are as follows [1,5].

PI and PID control techniques are widely used in liquid level control because of their simple structure and ease of parameter setting [6-8]. These controllers have fixed values of the parameters and are not able to adapt themselves to changing conditions. Therefore, they cannot provide the desired results when used to control nonlinear systems. In nonlinear systems, nonlinear control methods can respond quickly to changes in system dynamics and are more effective against parameter uncertainties [9]. In liquid level systems, liquid level control has been carried out using various nonlinear control methods such as adaptive, sliding mode and fractional order controllers with high accuracy against uncertainties [10-12].

Fuzzy logic control method, which is a nonlinear control method and used in liquid level control, has a structure that expresses uncertain situations better than classical logic systems. Fuzzy logic evaluates many situations at the same time and performs system control by making an appropriate inference [13-16]. In order to extend the limit of the fuzzy logic control method to express uncertainties, the boundaries of the membership functions are extended by a kind of spreading operation and the resulting interval type-2 fuzzy logic control method is used in the control of liquid level systems [17,18]. Fuzzy PI control method, which is a combination of classical PI and fuzzy logic control methods, is used as a more robust and adaptive control method in nonlinear systems and in the presence of uncertainty [19-23]. In this control method, the error and error change rate are converted into fuzzy values with the help of membership functions and K_p and K_i values are calculated from these values according to the defined rule tables.

In this study, PI+FF controller and PI controller whose parameters are adapted with type-1 and interval type-2 fuzzy logic control methods are tested in the liquid level control of tank-1 and tank-2 for different reference signals and the controller performances are compared. The results obtained from the real-time studies show that the PI controller whose parameters are adapted using interval type-2 fuzzy logic is better than the PI controller adapted using type-1 fuzzy logic, and the type-1 fuzzy PI is better than the PI+FF controller.

2. Material and Methods

2.1. Material

The coupled tank liquid level system consists of a pump, a water basin, two water tanks and two pressure sensors to measure the liquid level. There are two configurations of this model of tank system. These are the tank 1 and tank 2 configurations. In this system, the pump draws

water from the water basin and pumps the water to tank 1, which is in the upper position. The water from tank 1 flows to tank 2 through the drain hole at the bottom of tank 1 and the water in tank 2 flows to the main water basin through the drain hole at the bottom of tank 2.

2.1.1. Tank 1 Model

In the tank 1 model shown in Figure 1, the level of the liquid in tank 1 is controlled. The system input is the pump voltage and the system output is the water level in tank 1. The volumetric inflow rate (f_{i1}) of water entering the tank and the outflow rate (f_{o1}) of water leaving through the hole in the bottom of the tank are used to determine the mathematical model of the tank 1. Equations (1) and (2) give the volumetric flow rates of water entering and leaving the tank respectively [24].

$$f_{i1} = K_p V_p \quad (1)$$

$$f_{o1} = A_{o1} V_{o1} \quad (2)$$

In the equation, K_p is the pump flow constant ($\frac{cm^2}{s} \frac{1}{V}$), V_p is the actual voltage applied to the pump (volt), A_{o1} is the cross-sectional area of the liquid flow path (cm^2) and V_{o1} is the velocity of the water leaving tank 1 to tank 2 (cm/s).

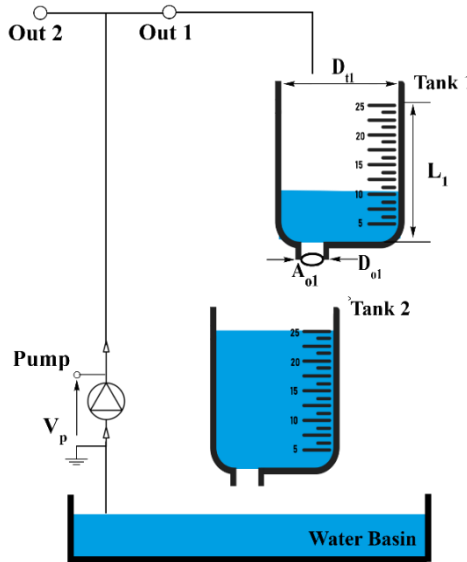


Figure 1. Tank 1 model

The outflow rate is obtained as follows using the Bernoulli equation.

$$V_{o1} = \sqrt{2gL_1} \quad (3)$$

The g in the equation is the gravitational constant. The cross-sectional area of the liquid outlet path for tank 1 can be calculated by using the following equation.

$$A_{o1} = \frac{1}{4} \pi D_{o1}^2 \quad (4)$$

D_{o1} is the diameter of the liquid outlet path of tank 1. Substituting these expressions into equation (2) gives the liquid flow rate as follows.

$$f_{o1} = A_{o1} \sqrt{2gL_1} \quad (5)$$

The first-order differential equation for L_1 is obtained using the mass balance principle for tank 1 as follows.

$$A_{t1} \frac{dL_1}{dt} = f_{i1} - f_{o1} \quad (6)$$

A_{t1} is the cross-sectional area of the tank and by replacing equations (1) and (5) in equation (6) and rearranging equation (6), the tank 1 system model can be expressed as follows.

$$\frac{dL_1}{dt} = \frac{K_p V_p - A_{o1} \sqrt{2gL_1}}{A_{t1}} \quad (7)$$

2.1.2. Tank 2 Model

In the tank 2 model shown in Figure 2, the level control of tank 2 is realized. The system input is the pump voltage and the system output is the water level of tank 2. The water level in tank 2 depends on the water level in tank 1.

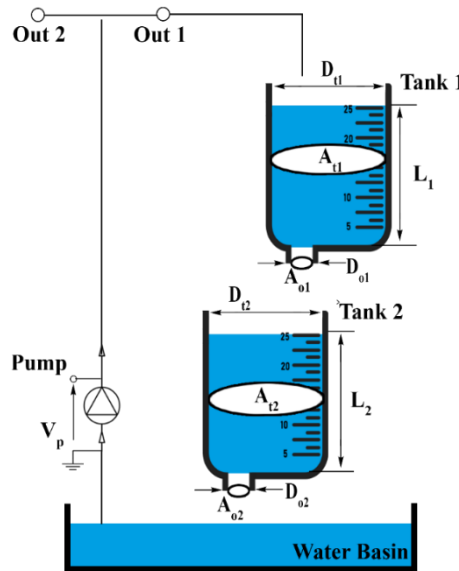


Figure 2. Tank 2 model

The liquid outflow rate for tank 2 is given below.

$$f_{o2} = A_{o2} V_{o2} \quad (8)$$

The liquid outflow rate for tank 2 is obtained using the Bernoulli equation as follows.

$$V_{o2} = \sqrt{2gL_2} \quad (9)$$

The cross-sectional area of the liquid outlet path of tank 2 can be calculated as given in equation (10).

$$A_{o2} = \frac{1}{4} \pi D_{o2}^2 \quad (10)$$

If the cross-sectional area of the liquid outlet path is rewritten in equation (8), the liquid outflow rate of tank 2 is obtained as follows.

$$f_{o2} = A_{o2} \sqrt{2gL_2} \quad (11)$$

The liquid flow rate entering tank 2 is obtained as follows.

$$f_{i2} = A_{o1} \sqrt{2gL_1} \quad (12)$$

If the mass balance principle is written for tank 2, the first order differential equation for L_2 is obtained as follows.

$$A_{t2} \frac{dL_2}{dt} = f_{i2} - f_{o2} \quad (13)$$

If the equations (11) and (12) are replaced in equation (13) and equation (13) is rearranged, the system model for tank 2 is obtained as follows.

$$\frac{dL_2}{dt} = \frac{A_{o1} \sqrt{2gL_1} - A_{o2} \sqrt{2gL_2}}{A_{t2}} \quad (14)$$

2.2. Methods

Liquid level control in the coupled tank system is performed for two different cases. Firstly, the liquid level control of tank 1, whose control block diagram is given in Figure 3, is realized. As can be seen from the figure, the controller determines the pump voltage required for the liquid in tank 1 to follow the reference liquid level.

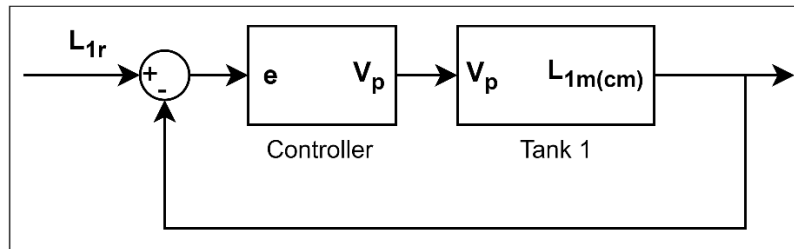


Figure 3. Tank 1 control block diagram

In the second case, the liquid level in tank 2 is controlled. In the control block diagram given in Figure 4, the first controller determines the reference liquid level for tank 1 by using the liquid level error of tank 2. The second controller generates the pump voltage that should be applied to the pump by using the liquid level error of tank 1.

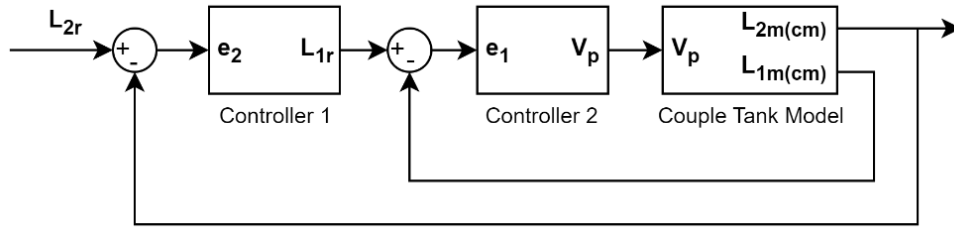


Figure 4. Tank 2 control block diagram

2.2.1. Fuzzy Controller Architecture

The fuzzy controller consists of fuzzification, inference engine and defuzzification, as shown in Figure 5. The crisp values at the fuzzy logic controller input are sent to the inference engine by calculating the fuzzy input sets with the relevant membership functions. The fuzzy input sets received by the inference engine are inferred using the defined rule bases and the fuzzy output sets obtained are sent to the defuzzification interface. The fuzzy output sets received at the fuzzification interface are converted into crisp output values by output membership functions and the selected defuzzification method [25].

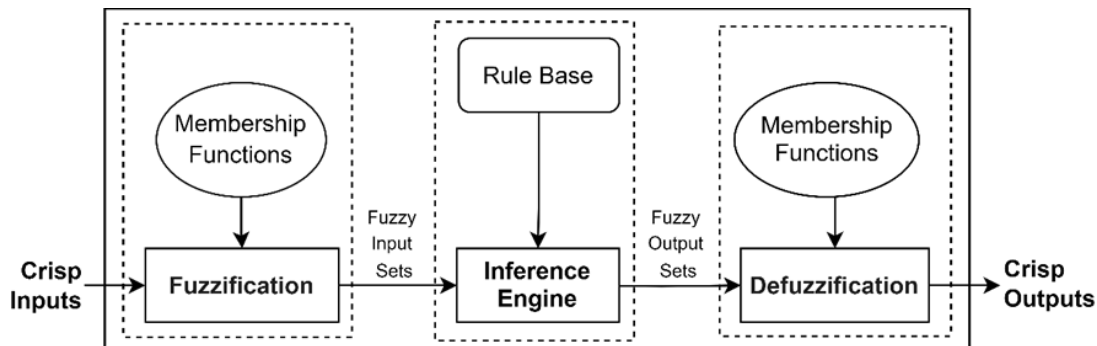


Figure 5. Fuzzy logic model

Different membership functions are used in the fuzzification and defuzzification interfaces. Commonly used membership functions are triangular, trapezoidal, gaussian, generalized bell, π -shaped and s-shaped [26]. In this study, a triangular membership function is used. In the triangular membership function, a defines the start point of the curve, b defines the peak point of the curve and c defines the end point of the curve. The mathematical expression of the triangular membership function is given in equation (15).

$$u(x) = \begin{cases} 0, & x \leq a \\ \frac{x-a}{b-a}, & a \leq x \leq b \\ \frac{c-x}{c-b}, & b \leq x \leq c \\ 0, & x \geq c \end{cases} \quad (15)$$

2.2.1.1. Type-1 Fuzzy PI Controller

The parameters of the classical PI controller are fixed values. When there are sudden disturbances or parameter uncertainties in the system, the performance of the PI controller decreases or deteriorates. Therefore, adapting the PI controller parameters depending on the

error value will increase the performance of the controller [27]. In this study, the adaptation of the parameters of the PI controller is performed using fuzzy logic. The PI controller can be expressed mathematically as follows.

$$PI = K_p e(t) + K_i \int_0^t e(t) d(t) \tag{16}$$

In the equation, K_p and K_i are the proportional and integral gains, respectively, and $e(t)$ is the error value. Equation (17) gives the PI controller whose parameters are adapted using fuzzy logic [27].

$$Fuzzy_PI = X_p G_p e(t) + X_i G_i \int_0^t e(t) d(t) \tag{17}$$

In the equation, X_p and X_i are the outputs of the fuzzy logic controller and, G_p and G_i are the learning rate constants for K_p and K_i . Figure 6 shows the block diagram of the type-1 fuzzy PI controller whose parameters are adapted with fuzzy logic for liquid level control of tank 1.

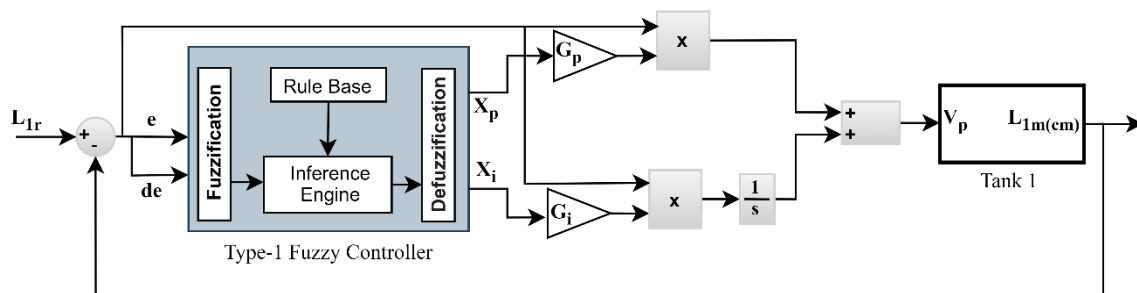


Figure 6. Block diagram of the type-1 fuzzy PI controller for tank 1

The membership functions presented in Table 1 and the fuzzy rules given in Table 2 are used in type-1 fuzzy control for the liquid level control of tank 1. On the other hand, in the liquid level control of the tank 2, there are two different controllers as shown in Figure 4. The structure of each controller is as shown in Figure 6 and the membership functions and rule tables given in Tables 1 and 2 are used in both controllers. However, the learning constants G_p and G_i of the controllers are different values.

Table 1. Input and output membership function.

Input Membership Function		Output Membership Function	
e, de		X_p, X_i	
Linguistic Terms	Range	Linguistic Terms	Range
Negative Big	[-1, -0.4]	Very Small	[0, 0.15]
Negative Small	[-0.7, -0.1]	Medium Small	[0.03, 0.3]
Zero	[-0.4, 0.4]	Small	[0.15, 0.5]
Positive Small	[0.1, 0.7]	Medium	[0.3, 0.7]
Positive Big	[0.4, 1]	Big	[0.5, 0.85]
		Medium Big	[0.7, 0.97]
		Positive Big	[0.85, 1]

Table 2: IF-THEN rule table

e/de	NB	NS	Z	PS	PB
NB	VS	MS	MS	S	M
NS	MS	MS	S	M	B
Z	MS	S	M	B	MB
PS	S	M	B	MB	MB
PB	M	B	MB	MB	VB

2.2.1.2. Interval Type-2 Fuzzy Controller Architecture

The interval type-2 fuzzy controller, whose block diagram is given in Figure 7, basically consists of fuzzification, inference engine, type reduction and defuzzification interfaces. The fuzzy sets of the crisp values at the controller input are calculated using membership functions and sent to the inference engine. The fuzzy input sets to the inference engine are inferred with the defined rule bases and sent to the type reduction interface. In the type reduction interface, the interval type-2 fuzzy output sets are converted into type-1 fuzzy output sets and sent to the defuzzification interface. The type-1 fuzzy output sets are converted into crisp output values by output membership functions and the selected defuzzification method [16,28].

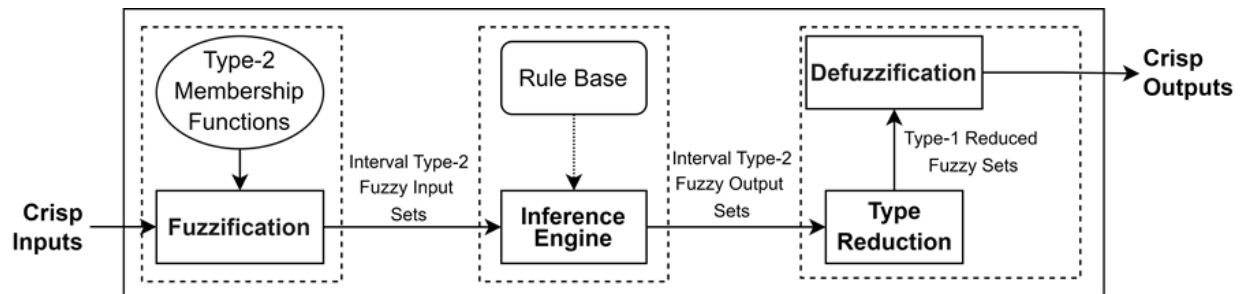


Figure 7. Interval type-2 fuzzy logic model

Interval type-2 fuzzy logic is a generalized form of type-1 fuzzy logic [29]. The set of fuzzy values \tilde{X} in interval type-2, shown in Figure 8, is characterized by the membership function $\mu_{\tilde{X}}(x, u)$ as in equation (19).

$$\tilde{X} = \{((x, u), \mu_{\tilde{X}}(x, u)) \mid \forall x \in X, \forall u \in J_x \subseteq [0, 1]\} \quad (18)$$

$$\tilde{X} = \int_{x \in D_{\tilde{X}}} \int_{u \in J_x \subseteq [0,1]} \frac{\mu_{\tilde{X}}(x,u)}{(x,u)} \quad (19)$$

In the equation, x is the primary variable, $D_{\tilde{X}}$ is the domain, $u \in [0, 1]$ is the secondary variable. J_x denotes the domain and $J_x \subseteq [0, 1]$ for each $x \in D_{\tilde{X}}$. J_x is also called the support of the secondary membership function and the amplitude of $\mu_{\tilde{X}}(x, u)$, called the secondary degree of \tilde{X} , is equal to 1 for $\forall x \in D_{\tilde{X}}$ and $\forall u \in J_x \subseteq [0, 1]$ and is expressed as follows [30,31].

$$\tilde{X} = \int_{x \in D_{\tilde{X}}} \int_{u \in J_x \subseteq [0,1]} \frac{1}{(x,u)} \quad (20)$$

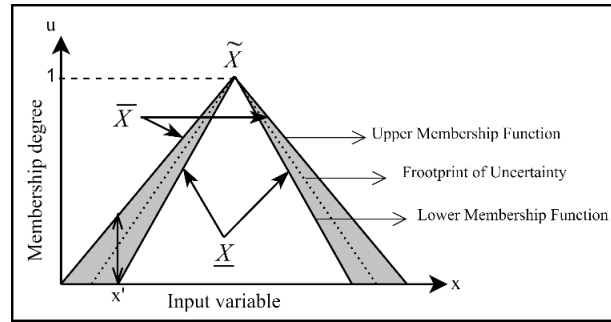


Figure 8. Interval type-2 membership function.

In the interval type-2 membership function given in Figure 8, it is seen that there is an interval in the interval type-2 membership function, unlike type-1 membership functions where the membership degree for each x is a number. The interval type-2 membership function is bounded by two type-1 membership functions, the upper membership function (\bar{X}) and the lower membership function (\underline{X}). The area between \bar{X} and \underline{X} is the footprint of uncertainty [31].

Interval type-2 fuzzy logic IF-THEN rules, inference engine, type reduction, and defuzzification:

The IF-THEN rule for a single-input single-output system is expressed as follows.

$$R^n: \text{IF } x_1 = \tilde{X}_1^n \text{ and } \dots \text{ and } x_l = \tilde{X}_l^n, \text{ THEN } y = Y^n \quad n = 1, 2, \dots, N.$$

Where $\tilde{X}_i^n \quad i = 1, \dots, l$ are interval type-2 fuzzy values, $Y^n = [\underline{y}^n, \bar{y}^n]$ is an interval. For an input vector $x' = (x'_1, x'_2, \dots, x'_l)$ g in Figure 8, the output is calculated as in the following steps [31].

1. For each input vector x'_i , the membership interval X_i^n is calculated in each rule. These membership intervals are expressed as,

$$\left[\mu_{\underline{X}_i^n}(x'_i), \mu_{\bar{X}_i^n}(x'_i) \right], \quad i = 1, 2, \dots, l, \text{ and } n = 1, 2, \dots, N. \tag{21}$$

In the equation, $\mu_{\underline{X}_i^n}(x'_i)$ represents the lower membership function and $\mu_{\bar{X}_i^n}(x'_i)$ represents the upper membership function.

2. The firing interval of n th rule F^n is calculated. This is expressed as the product of the membership degrees of all inputs:

$$F^n(x') = \left[\underline{f}^n, \bar{f}^n \right] \equiv \left[\mu_{\underline{X}_1^n}(x'_1) \times \dots \times \mu_{\underline{X}_l^n}(x'_l), \mu_{\bar{X}_1^n}(x'_1) \times \dots \times \mu_{\bar{X}_l^n}(x'_l) \right],$$

$$n = 1, \dots, N \tag{22}$$

3. Type reduction steps are applied to combine rule trigger intervals $F^n(x')$ and rule results Y^n . There are many types of reduction methods. The most commonly used is the center-of-sets type reduction method [31].

$$Y_{cos} = \frac{\sum_{n=1}^N Y^n F^n}{\sum_{n=1}^N F^n} = \bigcup_{\substack{y^n \in Y^n \\ f^n \in F^n}} \frac{\sum_{n=1}^N y^n f^n}{\sum_{n=1}^N f^n} = [y_l, y_r] \quad (23)$$

$$y_l = \min_{k \in [1, N-1]} \frac{\sum_{n=1}^k \bar{f}^n \underline{y}^n + \sum_{n=k+1}^N \underline{f}^n \underline{y}^n}{\sum_{n=1}^k \bar{f}^n + \sum_{n=k+1}^N \underline{f}^n} \equiv \frac{\sum_{n=1}^L \bar{f}^n \underline{y}^n + \sum_{n=L+1}^N \underline{f}^n \underline{y}^n}{\sum_{n=1}^L \bar{f}^n + \sum_{n=L+1}^N \underline{f}^n} \quad (24)$$

$$y_r = \max_{k \in [1, N-1]} \frac{\sum_{n=1}^k \underline{f}^n \bar{y}^n + \sum_{n=k+1}^N \bar{f}^n \bar{y}^n}{\sum_{n=1}^k \underline{f}^n + \sum_{n=k+1}^N \bar{f}^n} \equiv \frac{\sum_{n=1}^R \underline{f}^n \bar{y}^n + \sum_{n=R+1}^N \bar{f}^n \bar{y}^n}{\sum_{n=1}^R \underline{f}^n + \sum_{n=R+1}^N \bar{f}^n} \quad (25)$$

In the equation, L and R are the switching points. y_l and y_r can be calculated using Karnik-Mendel algorithms as follows [32].

Table 3. Karnic-Mendel type reduction method [32].

Step	For computing y_l	For computing y_r
1.	Initialize $f^n = \frac{f^n + \bar{f}^n}{2}$ and compute $y = \frac{\sum_{n=1}^N y^n f^n}{\sum_{n=1}^N f^n}$	Initialize $f^n = \frac{f^n + \bar{f}^n}{2}$ and compute $y = \frac{\sum_{n=1}^N \bar{y}^n f^n}{\sum_{n=1}^N f^n}$
2.	Find $l \in [1, N - 1]$ s.t. $\underline{y}^l \leq y \leq \dots \underline{y}^{l+1}$	Find $r \in [1, N - 1]$ s.t. $\bar{y}^r \leq y \leq \bar{y}^{r+1}$
3.	Set $f^n = \begin{cases} \bar{f}^n, & n \leq l \\ \underline{f}^n, & n > l \end{cases}$ and compute $y' = \frac{\sum_{n=1}^N y^n f^n}{\sum_{n=1}^N f^n}$	Set $f^n = \begin{cases} \underline{f}^n, & n \leq r \\ \bar{f}^n, & n > r \end{cases}$ and compute $y' = \frac{\sum_{n=1}^N \bar{y}^n f^n}{\sum_{n=1}^N f^n}$
4.	If $y' = y$, stop and set $y_l = y$ and $L = l$; otherwise, set $y = y'$ and go to Step 2.	If $y' = y$, stop and set $y_r = y$ and $R = r$; otherwise, set $y = y'$ and go to Step 2.

The main purpose of the Karnic-Mendel type reduction algorithm is to find the y_l and y_r . When calculating y_l , it uses upper membership degrees for $n \leq l$ and lower membership degrees for $n > l$. When calculating y_r , it uses lower membership degrees for $n \leq r$ and upper membership degrees for $n > r$ [32].

- Finally, a precise output value is calculated using the range of fuzzy results obtained after type reduction. The defuzzied result is calculated as follows.

$$y = \frac{y_l + y_r}{2} \tag{26}$$

2.2.1.3. Interval Type-2 Fuzzy PI Controller

In the interval type-2 fuzzy logic control system with two inputs and two outputs shown in Figure 9, the input values are converted into type-2 fuzzy input sets using the type-2 input membership functions given in Table 4. Interval type-2 output sets are generated using the output membership functions in Table 5 and the rules in Table 2. Type-2 fuzzy values are reduced to type-1 values using the Karnik-Mendel type reduction method given in Table 3. The PI controller parameters K_p and K_i coefficients are adapted using the output values X_p and X_i parameters.

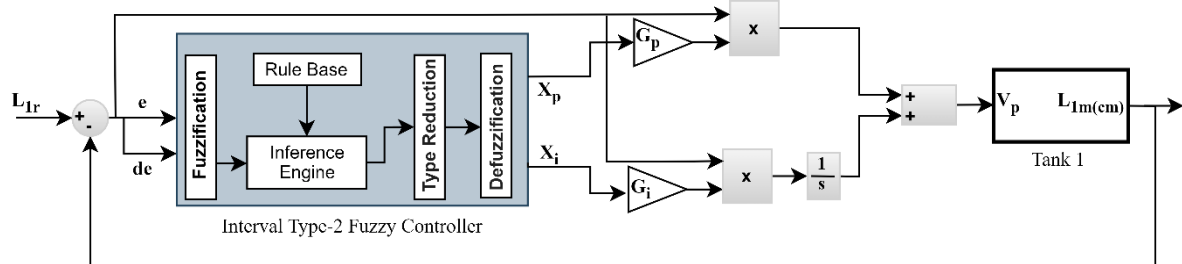


Figure 9. Block diagram of the interval type-2 fuzzy PI controller for tank 1.

Table 4. Input membership function.

Input Membership Function			
e, de			
Linguistic Terms	Upper Parameters	Lower Scale	Low Lag
Negative Big	[-1,-0.4]	0.8	[0.3 0.3]
Negative Small	[-0.7,-0.1]	0.8	[0.3 0.3]
Zero	[-0.4,0.4]	0.8	[0.3 0.3]
Positive Small	[0.1,0.7]	0.8	[0.3 0.3]
Positive Big	[0.4,1]	0.8	[0.3 0.3]

Table 5. Output membership function.

Output Membership Function			
X_p, X_i			
Linguistic Terms	Upper Parameters	Lower Scale	Low Lag
Very Small	[0,0.15]	0.8	[0.3 0.3]
Medium Small	[0.03,0.3]	0.8	[0.3 0.3]
Small	[0.15,0.5]	0.8	[0.3 0.3]
Medium	[0.3,0.7]	0.8	[0.3 0.3]
Big	[0.5,0.85]	0.8	[0.3 0.3]
Medium Big	[0.7,0.97]	0.8	[0.3 0.3]
Very Big	[0.85,1]	0.8	[0.3 0.3]

For tank 2, two different controllers are used as shown in Figure 4. The block structure of each controller is as shown in Figure 9 and the membership functions given in Tables 4 and 5 and the rules given in Table 2 are used in both controllers. However, the learning constants G_p and G_i of the controllers are different values.

3. Results and Discussion

In this study, the liquid level control in a coupled tank system is realised for two different configurations, tank 1 and tank 2 model. The proposed controllers are implemented on both configurations and their performances are tested for different reference liquid levels. The results obtained are compared in terms of system response parameters such as rise time, settling time and maximum overshoot and error performance metrics such as ISE, ITSE, ITAE and IAE. Firstly, the results for the tank 1 model are given in Figures 10-13. Then, the results for the tank 2 model are presented in Figures 14-15.

In order to observe the performance of the controllers in the single tank configuration, a step+sinusoidal reference liquid level was first selected. With the relevant reference, the response of the controllers against constant and slowly changing reference signals was measured. Then, a step+square reference liquid level was applied to observe the performance of the controllers against reference signals that change suddenly with time. The results of PI+FF, type-1 fuzzy PI and interval type-2 fuzzy PI controllers for the related references are given below.

Figure 10 shows that for the step part of the reference signal, the PI+FF controller reaches the reference more quickly than the type-1 fuzzy PI controller, but it overshoots more than the type-1 fuzzy PI controller and settles to the reference signal later. This can also be seen from the values for rise time, overshoot and settling time given in Table 6. It can then be seen that the controller maintains its performance and follows the sinusoidal reference signal with less error. This is also confirmed by the error performance metrics given in Table 7 and Figure 10 (b). On the other hand, Figure 10(c) shows that the type-1 fuzzy PI controller produces a more chattering control signal than PI+FF in order to follow the reference signal. The fact that the amplitude of the chattering component of the generated control signal is not high has prevented a possible negative effect on the system.

Figure 11 shows the results of interval type-2 fuzzy PI controller. Similar to the performance of the type-1 fuzzy PI controller, it is seen that the rise time of PI+FF is lower than the interval type-2 fuzzy PI controller in the tracking of the step part of the reference signal, but in terms of overshoot and settling time, the interval type-2 fuzzy PI controller has lower values. Similarly, it is seen that interval type-2 fuzzy PI controller is better in terms of tracking performance of sinusoidal reference. In addition, compared to the type-1 fuzzy PI controller, the interval type-2 fuzzy PI controller is better in terms of both system response performance and error criterion performance. On the other hand, it is observed that the control signal produced by both fuzzy controllers contains chattering, but the amplitude of the chattering produced by interval type-2 fuzzy PI controller is slightly larger than the type-1 fuzzy PI controller. This small change enables the interval type-2 fuzzy PI controller to follow the reference liquid level better.

Comparison of the Performance of Type-1 and Interval Type-2 Fuzzy PI Controllers for Liquid Level Control in a Coupled Tank System

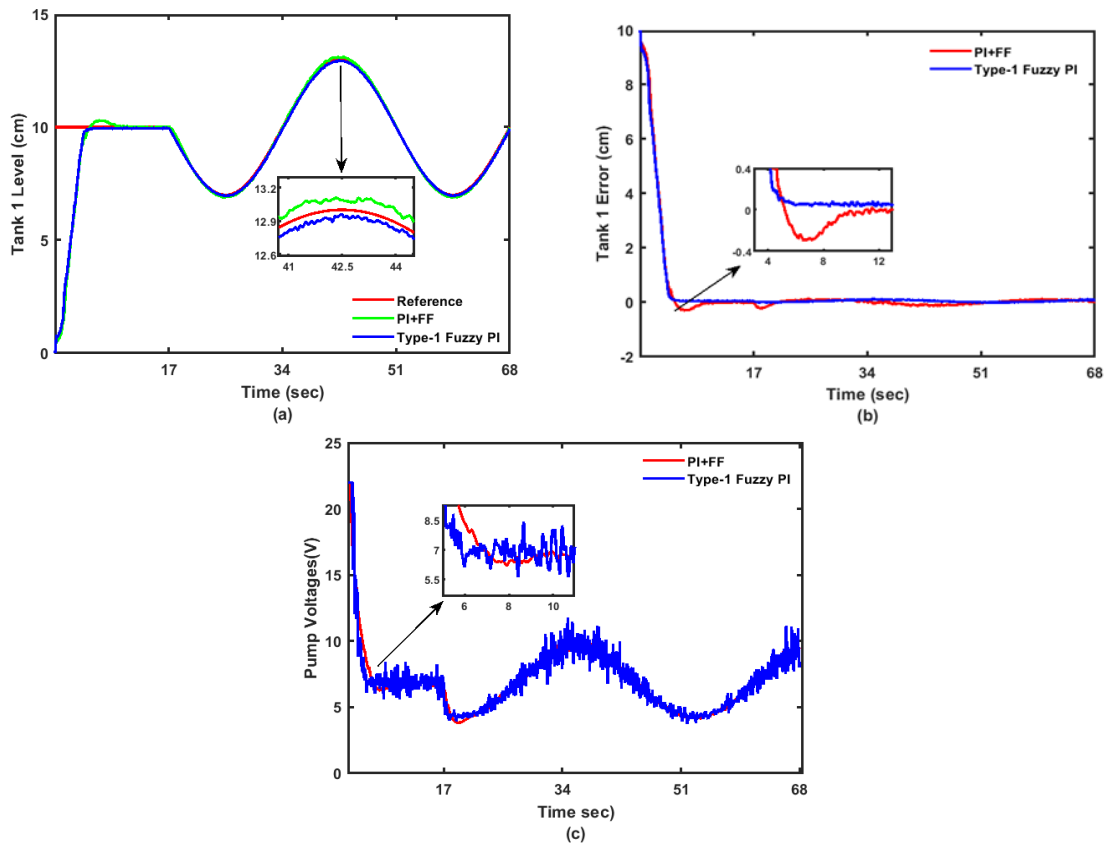


Figure 10. PI+FF and type-1 fuzzy PI controller performances under step + sinusoidal reference for tank 1.

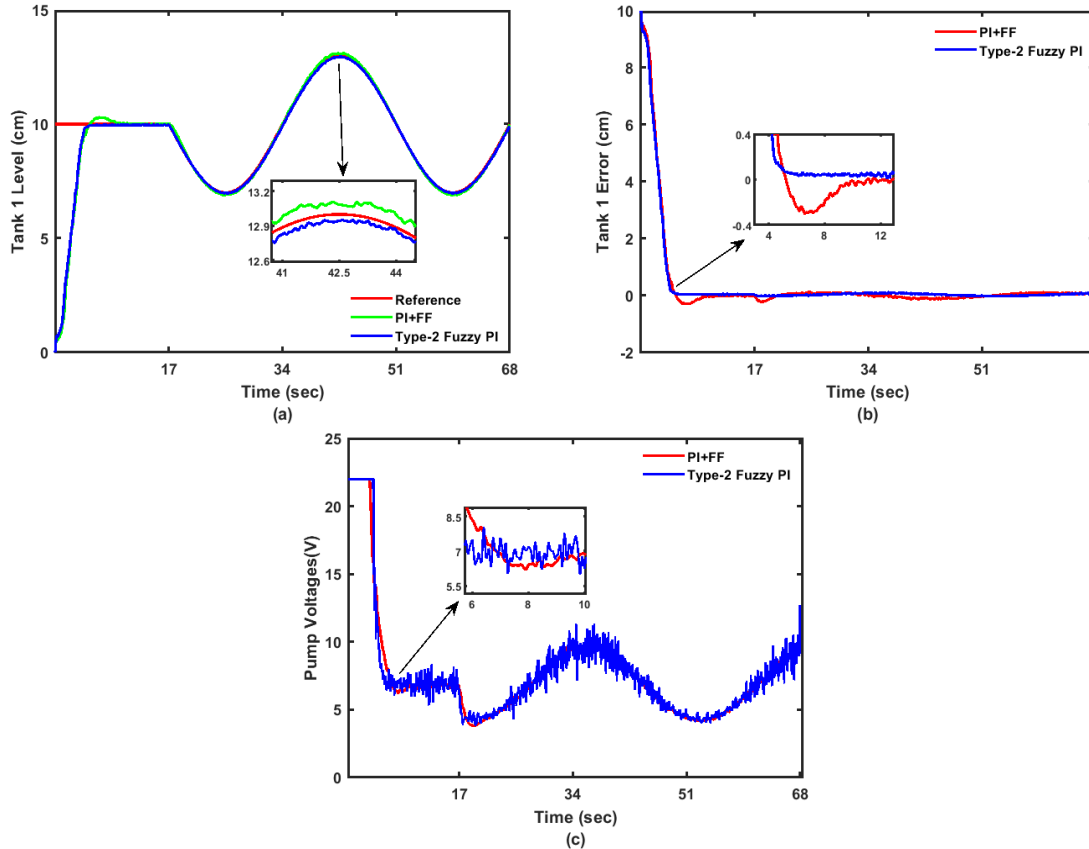


Figure 11. PI+FF and type-2 fuzzy PI controller performances under step + sinusoidal reference for tank 1.

Table 6. System response parameters for step+sinusoidal reference in control of tank 1.

Controllers	Step		
	Rise Time	Overshoots (%)	Settling Time
PI+FF	2.9356	2.7101	7.8981
Tip-1 Fuzzy PI	3.1205	0.22761	4.2772
Interval Tip-2 Fuzzy PI	3.0108	0.14289	4.345

Table 7. Error performance metrics for step+sinusoidal reference in control of tank 1.

Controllers	Step				Sinusoidal			
	ISE	ITSE	ITAE	IAE	ISE	ITSE	ITAE	IAE
PI+FF	174	198.8	43.04	25.02	0.3471	13.47	152.9	3.712
Type-1 Fuzzy PI	163	182.9	40.95	23.79	0.1706	7.248	99.8	2.328
Interval Type-2 Fuzzy PI	162.7	180.6	39.07	23.54	0.1283	5.471	84.1	1.952

Figures 12 and 13 show the results of the controllers for step+square reference liquid level. From figure 12, it is seen that the type-1 fuzzy PI controller follows the reference signal better than the PI+FF controller both in the step part of the reference signal and in the square part of the reference signal. Figure 13 shows that the interval type-2 fuzzy PI controller shows a similar performance with the type-1 fuzzy PI controller. When the system response parameters and error performance metrics given in Tables 8 and 9 are analyzed, it is seen that interval type-2 fuzzy PI controller has the best rise time but type-1 fuzzy PI controller is better in terms of overshoot and settling time. On the other hand, in terms of error performance criteria, PI+FF, type-1 fuzzy PI and type-2 fuzzy PI controllers show the best performance respectively following the step part of the reference signal, but after the addition of the square component in the continuation of the reference signal, the ranking in terms of performance is type-1 fuzzy PI, interval type-2 fuzzy PI and PI+FF. Since the single tank system has a linear model, it is easy to control and therefore the controller performances are close to each other.

Table 8. System response parameters for step+square reference in control of tank 1.

Controllers	Step		
	Rise Time	Overshoots (%)	Settling Time
PI+FF	3.0939	2.982	7.6453
Type-1 Fuzzy PI	3.0171	0.25224	4.2376
Interval Type-2 Fuzzy PI	2.975	0.41267	4.514

Comparison of the Performance of Type-1 and Interval Type-2 Fuzzy PI Controllers for Liquid Level Control in a Coupled Tank System

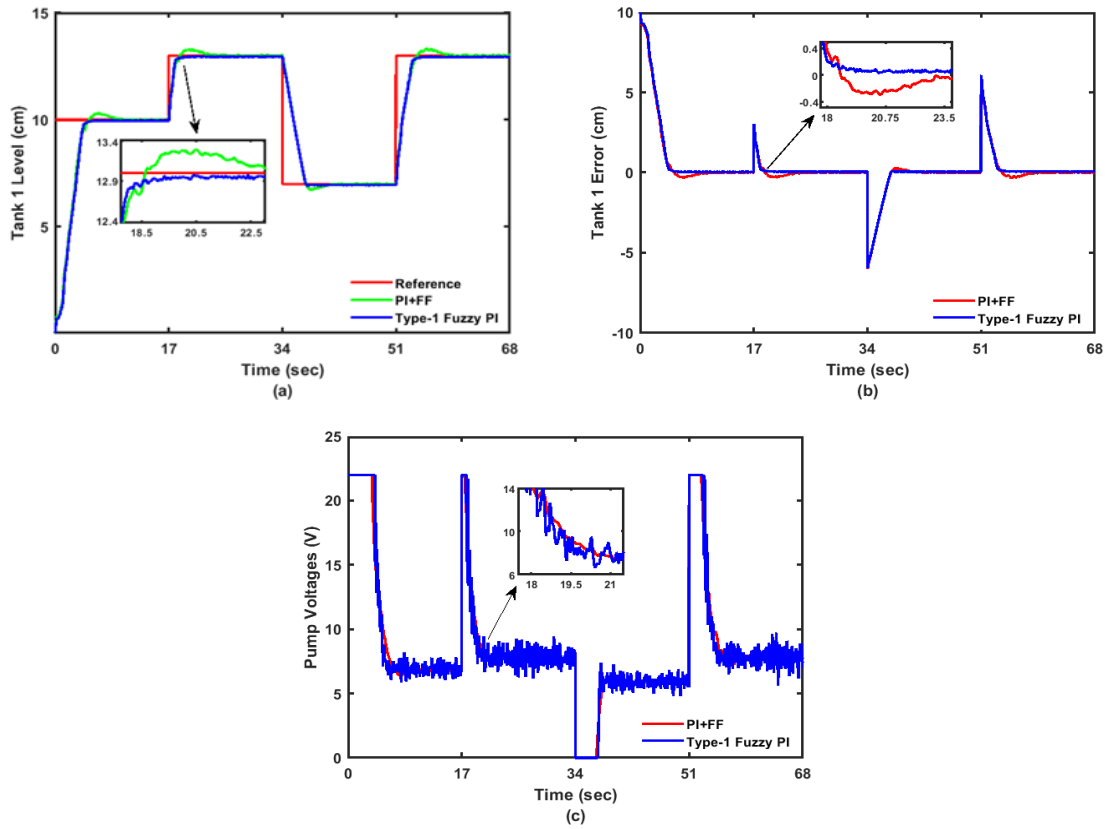


Figure 12. PI+FF and type-1 fuzzy PI controller performances under step + square reference for tank 1.

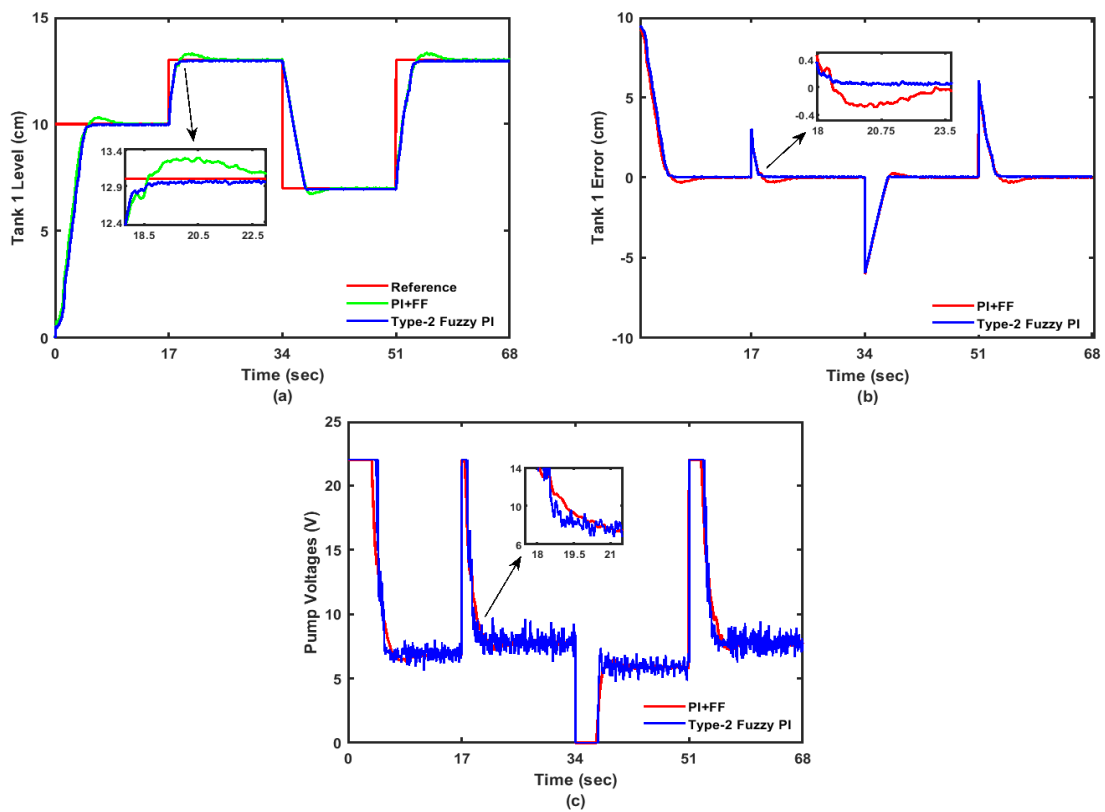


Figure 13. PI+FF and type-2 fuzzy PI controller performances under step + square reference for tank 1.

Table 9. Error performance metrics for step+square reference in control of tank 1.

Controllers	Step				Square			
	ISE	ITSE	ITAE	IAE	ISE	ITSE	ITAE	IAE
PI+FF	157.5	172.1	39.59	23.49	68.35	26.55	832.4	20.97
Type-1 Fuzzy PI	163.4	181.2	38.92	23.57	66.1	2654	828.5	20.59
Interval Type-2 Fuzzy PI	179.1	211	42.4	25.2	66.33	2675	821.5	20.36

In order to observe the performance of the controllers in the tank 2 configuration, a step+sinusoidal reference liquid level is selected and the results of PI+FF, type-1 fuzzy PI and interval type-2 fuzzy PI controllers are given in Figures 14 and 15. When Figure 14 is analyzed, it is seen that the type-1 fuzzy PI controller reaches the reference liquid level faster than the PI+FF controller, but overshoots more and has similar settling times. However, it is seen that the type-1 fuzzy PI controller has a much better performance in tracking the sinusoidal component of the reference signal.

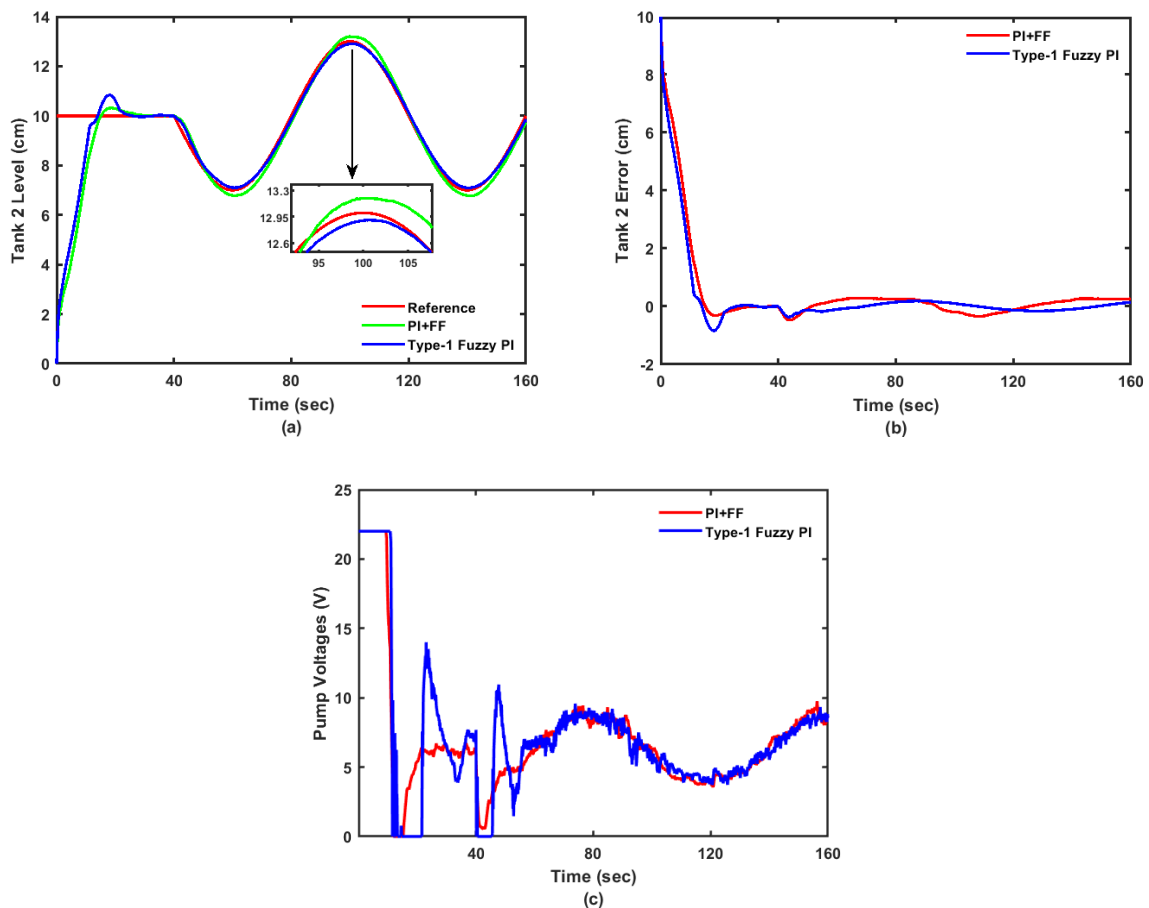


Figure 14. PI+FF and type-1 fuzzy PI controller performances under step + sinusoidal reference for tank 2.

Comparison of the Performance of Type-1 and Interval Type-2 Fuzzy PI Controllers for Liquid Level Control in a Coupled Tank System

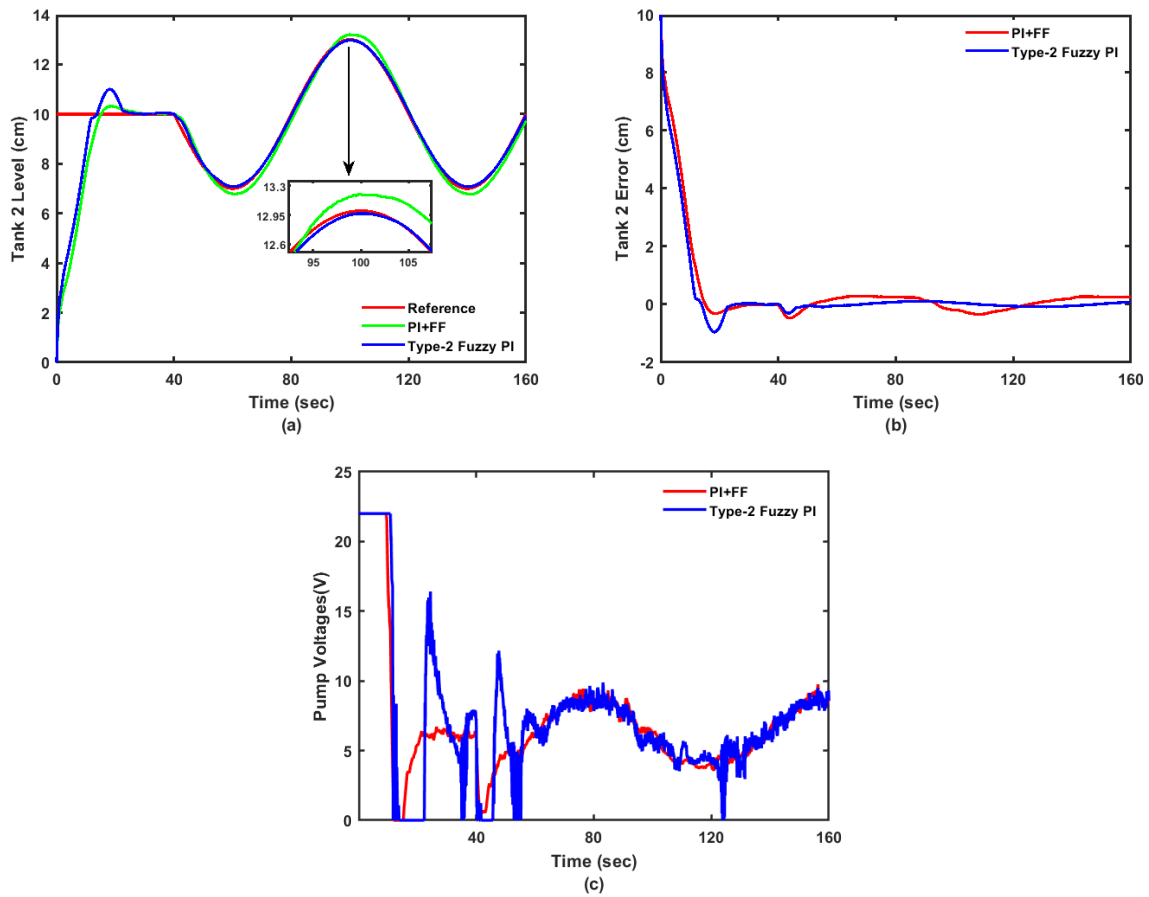


Figure 15. PI+FF and type-2 fuzzy PI controller performances under step + sinusoidal reference for tank 2.

Figure 15 shows that the interval type-2 fuzzy PI controller performs similarly to the type-1 fuzzy PI controller in tracking the step component of the reference signal, but performs much better in tracking the sinusoidal component. This is also seen from the system response parameters given in Table 10 and the error performance metrics given in Table 11. As a result, the interval type-2 fuzzy PI controller performed similar to the type-1 fuzzy PI controller in the control of the single tank configuration, but performed much better than both type-1 fuzzy PI and PI+FF controllers in the tank 2 configuration.

Table 10. System response parameters for step+sinusoidal reference in control of tank 2.

Controllers	Step		
	Rise Time	Overshoots (%)	Settling Time
PI+FF	11.672	5.8034	79.168
Type-1 Fuzzy PI	10.17	10.065	79.124
Interval Type-2 Fuzzy PI	10.228	10.643	79.137

Table 11. Error performance metrics for step+sinusoidal reference in control of tank 2.

Controllers	Step				Sinusoidal			
	ISE	ITSE	ITAE	IAE	ISE	ITSE	ITAE	IAE
PI+FF	365.3	1282	344.1	64.49	6.281	602.1	2469	25.01
Type-1 Fuzzy PI	292.4	928.5	307.8	56,65	2.093	177	1273	13.68
Interval Type-2 Fuzzy PI	292.6	946.2	319.6	57.2	0.7746	57.99	690.6	7.627

4. Conclusion

In this study, PI+FF, type-1 fuzzy PI and interval type-2 fuzzy PI controllers are designed for different reference liquid levels for tank 1 and tank 2 configuration models in a coupled tank system and their performances are compared. The comparison is made in terms of system response parameters such as rise time, settling time and maximum overshoot and error performance metrics such as ISE, ITSE, ITAE and IAE. The obtained results show that the interval type-2 fuzzy PI controller performs the liquid level control in single tank configuration with a similar performance as the type-1 fuzzy PI controller and the performance of both controllers is much better than the PI+FF controller. On the other hand, it is observed that the interval type-2 fuzzy PI controller performs much better than both type-1 fuzzy PI and PI+FF controllers in the tank 2 configuration. As a result, it is observed that the adaptation of the parameters of the PI controller with fuzzy logic improves the control performance of the system.

References

- [1] Sekban, H. T., Can, K., Başçi, A., (2016) The performance analyze and control of a coupled tank liquid-level system via PI & backstepping controllers, National Conference on Electrical, Electronics and Biomedical Engineering (ELECO), Bursa, Turkey.
- [2] Sekban, H. T., Can, K., Basci, A., (2020) Model-based dynamic fractional-order sliding mode controller design for performance analysis and control of a coupled tank liquid-level system, *Advances in Electrical & Computer Engineering*, 20(3), 93-100.
- [3] Esmaili, J. S., Başçi, A., (2021) Design and implementation of LMI-based H2 control for vertical nonlinear coupled-tank system. *International Journal of System Dynamics Applications (IJSDA)*, 10(4), 1-16.
- [4] Yılmaz, M., Can, K., Başçi, A., (2021) PI+ feed forward controller tuning based on genetic algorithm for liquid level control of coupled-tank system, *Journal of the Institute of Science and Technology*, 11(2), 1014-1026.
- [5] Esmaili, J. S., Başçi, A., (2023) Robust output feedback control design for nonlinear coupled-tank system using linear matrix inequalities, *International Journal of Engineering Research and Development*, 15(1), 125-138.

- [6] Jaafar, H.I., Hussien, S. Y. S., Selamat, N.A., Aras, M.S.M., Rashid, M.Z.A., (2014) Development of PID controller for controlling desired level of coupled tank system, *International Journal of Innovative Technology and Exploring Engineering*, 3(9), 32-36.
- [7] Kumar, S., Nagpal, P., (2017) Comparative analysis of P, PI, PID and fuzzy logic controller for tank water level control system, *International Research Journal of Engineering and Technology*, 4(4), 1174-1177.
- [8] Mahapatro, S. A., Subudhi, B., Ghosh S., (2019) Design and experimental realization of a robust decentralized PI controller for a coupled tank system, *ISA Transactions*, 89, 158-168.
- [9] Sekban, H.T., Can, K., Başçi, A., (2016) İkili tank sıvı-seviye sisteminin PI ve geri adımlamalı kontrol yöntemleri ile kontrolü ve performans analizi, In *ELECO International Conference on Electrical and Electronic Engineers*, Bursa.
- [10] Başçi, A. and Derdiyok, A., (2016) Implementation of an adaptive fuzzy compensator for coupled tank liquid level control system, *Measurement*, 91, 12-18.
- [11] Aksu, I. O., Coban, R., (2019) Sliding mode PI control with backstepping approach for MIMO nonlinear cross-coupled tank systems, *International Journal of Robust and nonlinear control*, 29(6), 1854-1871.
- [12] Jegatheesh, A., & Kumar, C. A., (2020) Novel fuzzy fractional order PID controller for nonlinear interacting coupled spherical tank system for level process, *Microprocessors and Microsystems*, 72, 102948-102960.
- [13] Zadeh, L. A., (1965) Fuzzy sets. *Information and control*, 8(3), 338-353.
- [14] Muntaser, A., Suleiman, A. A., Lesewed, A. A., (2015) Synthesis of fuzzy control system for coupled level tanks, In *2015 International Conference on Information Science and Management Engineering (ICISME)*, Tarhona, Libya.
- [15] Yordanova, S., (2016) Fuzzy logic approach to coupled level control, *Systems Science & Control Engineering*, 4(1), 215-222.
- [16] Kumar, R., Kumar, S., (2022) Performance comparison of industrial controller and fuzzy logic controller for water level tank control system, *International Research Journal of Modernization in Engineering Technology and Science*, 4(1), 2582-5208.
- [17] Karnik, N. N., Mendel, J. M., Liang, Q., (1999) Type-2 fuzzy logic systems, *IEEE transactions on Fuzzy Systems*, 7(6), 643-658.
- [18] Loukal, K., Bouguerra, A., Zeglache, S., (2023) Fault tolerant control of two tanks system using gain-scheduled type-2 fuzzy sliding mode controller *IAES International Journal of Artificial Intelligence (IJ-AI)*, 2252(8938), 1158-1168.
- [19] Mahapatro, S. R., Subudhi, B., Ghosh, S., (2014) Adaptive fuzzy PI controller design for

coupled tank system: an experimental validation, Third International Conference on Advances in Control and Optimization of Dynamical System, Kanpur, India.

- [20] Mursyitah, D., Faizal, A., Ismaredah, E., (2018) Level control in coupled tank system using PID-Fuzzy tuner controller, In 2018 Electrical Power, Electronics, Communications, Controls and Informatics Seminar (EECCIS) (pp. 293-298). IEEE.
- [21] Balakrishnaa, A. V., Arun, N. K., (2022) Liquid level control of interacting coupled spherical tank system using PI and fuzzy PI controller, In 2022 3rd International Conference for Emerging Technology (INCET), Batu, Indonesia.
- [22] Saad, M., Alshara M., Mustafa K., (2023) Fuzzy PID controller design for a coupled tank liquid level control system, Wseas Transactions on Systems and Control, 18, 401-408.
- [23] Kumar, R., Kumar, N., Rai, A., Singh, P. P., (2023) Level control of coupled tank system using fuzzy PI feedforward technique, 5th International Conference on Energy, Power and Environment: Towards Flexible Green Energy Technologies (ICEPE), Shillong, India.
- [24] Quanser-Two Tank Manuel, 2005.
- [25] Ödük, M. N., (2019) Bulanık mantık yöntemi ve uygulamaları, Iksad Publications, 160, Ankara.
- [26] Ali, O. A. M., Ali, A. Y., Sumait, B. S., (2015) Comparison between the effects of different types of membership functions on fuzzy logic controller performance, International Journal of Emerging Engineering Research and Technology, 3(3), 76-83.
- [27] Zeb, K., Islam, S. U., Din, W. U., Khan, I., Ishfaq, M., Busarello, T. D. C., Ahmad I., Kim H.J., (2019) Design of fuzzy-PI and fuzzy-sliding mode controllers for single-phase two-stages grid-connected transformerless photovoltaic inverter, Electronics, 8(5), 520.
- [28] Mendel, J. M., John, R. I., Liu, F., (2006) Interval type-2 fuzzy logic systems made simple, IEEE transactions on fuzzy systems, 14(6), 808-821.
- [29] Kumbasar, T., (2016) Aralık değerli tip-2 bulanık PID kontrolörler ve bir çevrimiçi öz-ayarlı mekanizması, Pamukkale Üniversitesi Mühendislik Bilimleri Dergisi, 22(8), 643-649.
- [30] Özek, M. B., & Akpolat, Z. H., (2010) Bulanık mantık için yeni bir yaklaşım: tip 2 bulanık mantık, Engineering Sciences, 5(3), 541-557.
- [31] Wu, D., (2010) A brief tutorial on interval type-2 fuzzy sets and systems, University of Southern California.
- [32] Wu, D., (2013) Approaches for reducing the computational cost of interval type-2 fuzzy logic systems: overview and comparisons, IEEE Transactions on Fuzzy Systems, 21(1), 80-99.

Magnetic Properties of Borided Co-Cr-Mo Alloy

Osman IYI¹, Nazim UCAR^{2*} and Adnan CALIK³

¹Süleyman Demirel University, Institute of Science and Technology, 32260, Isparta, Türkiye

²Süleyman Demirel University, Faculty of Engineering and Natural Sciences, Department of Physics,
32260, Isparta, Türkiye

³Isparta University of Applied Sciences, Faculty of Technology, Mechanical Engineering, 32260, Isparta,
Türkiye

Received: 17/05/2024, **Revised:** 26/08/2024, **Accepted:** 27/08/2024, **Published:** 31/08/2024

Abstract

The magnetic properties of a borided Co-Cr-Mo alloy were studied in this work. The boron process was performed by the powder pack method with Ekabor HM and Ekabor III boron sources at 1123 and 1323 K for 9 h. The magnetic properties were characterized with a vibrating sample magnetometer (VSM). The results show that the non-magnetic Co-Cr-Mo alloy has a low magnetization with the boriding process. In addition, the saturation magnetization (Ms) varies with the boron source and temperature.

Keywords: Co-Cr-Mo alloy, saturation magnetization, magnetic behavior, boriding, boron source

Borlanmış Co-Cr-Mo Alaşımının Manyetik Özellikleri

Öz

Bu çalışmada borlanmış bir Co-Cr-Mo alaşımının manyetik özellikleri incelenmiştir. Bor işlemi, Ekabor HM ve Ekabor III bor kaynakları ile 1123 ve 1323 K'de 9 saat boyunca toz paket yöntemiyle gerçekleştirildi. Manyetik özellikler, titreşimli bir numune manyetometresi (VSM) ile karakterize edildi. Sonuçlar, manyetik olmayan Co-Cr-Mo alaşımının borlama işlemiyle düşük mıknatıslanmaya sahip olduğunu göstermektedir. Ayrıca manyetik doygunluk (Ms) bor kaynağına ve borlama sıcaklığına göre değişir.

Anahtar Kelimeler: Co-Cr-Mo alaşımı, manyetik saturasyon, manyetik davranış, borlama, bor kaynağı

*Corresponding Author: nazimucar@sdu.edu.tr

Osman IYI: <https://orcid.org/0009-0004-4138-7886>

Nazim Ucar: <https://orcid.org/0000-0002-0936-0382>

Adnan Calik: <https://orcid.org/0000-0002-2470-5051>

1. Introduction

Co-Cr-Mo alloy is widely used as orthopedic implant material because it has properties such as high impact and fatigue resistance [1,2]. Meanwhile, when used as an artificial joint implant material, this alloy shows low friction properties and low corrosion resistance due to corrosive body fluid and is subject to wear in a short time [3]. Therefore, a surface coating is applied to the Co-Cr-Mo alloy surface to improve corrosion and wear resistance. Regarding this, Cuao-Moreu et al. [4] showed that the wear resistance of the borided Co-Cr-Mo alloy is higher than that of the untreated Co-Cr-Mo alloy due to the high surface hardness of the boron compounds such as CoB and Co₂B in the boride layer. In addition, it has been shown that the presence of CoB–Co₂B and Co₂B layers on the borided Co-Cr-Mo alloy increases bio-tribocorrosion resistance approximately 2.4 and 1.3 times compared to the unborided Co-Cr-Mo alloy, respectively [5].

An important issue is what kind of changes the increase in the mechanical and tribological properties of materials with the boriding process causes in the magnetic properties of the materials. Generally, studies on the magnetic properties of materials are focused on the effect of thermal properties on magnetic properties [6], the relationship between mechanical and magnetic properties [7], the magneto-structural characteristics of obtained magnetic nanoparticles [8], etc. These studies show that magnetic properties are strongly dependent on microstructure, particularly crystallite size, particle morphology, and structural defects. On the other hand, it has been observed that studies in the literature to investigate the effect of boriding on magnetic properties are limited. In a study conducted by Akkurt et al. [9] on AISI 316L austenitic stainless steel, they observed that boriding not only improved the shielding properties of AISI 316L austenitic stainless steel, but also increased the M_s of this steel. On the contrary, Ekinci [10] found that the boriding process decreased the magnetic saturation in Fe-Ni alloy due to the formation of boride and/or silicide phases with lower magnetic moments. In this study, it will be investigated whether Co-Cr-Mo alloy, which normally has non-magnetic properties, exhibits magnetic properties with the boriding process. Additionally, if it has magnetic behavior, the relationship of this behavior with the boron source and boriding temperature will be examined.

2. Materials and Methods

The chemical composition (wt.%) of the samples of commercially available Co-Cr-Mo alloy used in this study is Co (65%), Cr (30%) and Mo (5%). The solid boriding method was chosen for the boriding process, and Ekabor3 and Ekabor HM commercial powders were used as boron sources. The boriding process was carried out under a controlled atmosphere containing argon gas flow in two different temperature environments, 1123 and 1323 K, and in a furnace environment for 9 hours. Afterwards, the samples whose boriding process was completed were cooled in the oven under a controlled atmosphere. Before microstructural analysis, the polished samples were etched with macroetchant (30 mL HCl, 15 mL HNO₃, 30 mL HF). Boride phases formed on the surfaces of borided samples were determined by SEM and XRD analyses. A vibrating sample magnetometer (VSM) was used to determine the magnetic properties of Co-Cr-MO alloy boronized with different time and boron sources. Measurements were made at room temperature and within a magnetic field range of ± 7 Tesla. From the measured values, M-H graphs were drawn using the masses of the sample.

3. Results and Discussion

Co-Cr-Mo alloy is a non-magnetic material. For this reason, this alloy has a very low mass magnetic susceptibility of $7 \times 4\pi \cdot 10^{-9} \text{ m}^3/\text{kg}$. [11] (The mass susceptibility yields the magnetic moment (or magnetization) per kilogram of material when multiplied by the magnetic field.) In this study, the curves of magnetization (M(H)) measurements due to the magnetic field of Co-Cr-Mo alloy borided with two different boron sources is given in Figure 1. When looking at this graph, the hysteresis loops obtained as a function of boriding source and temperature are clearly visible, as in ferromagnetic materials. However, a low maximum magnetization called saturation magnetization (M_s) was obtained (Fig.1).

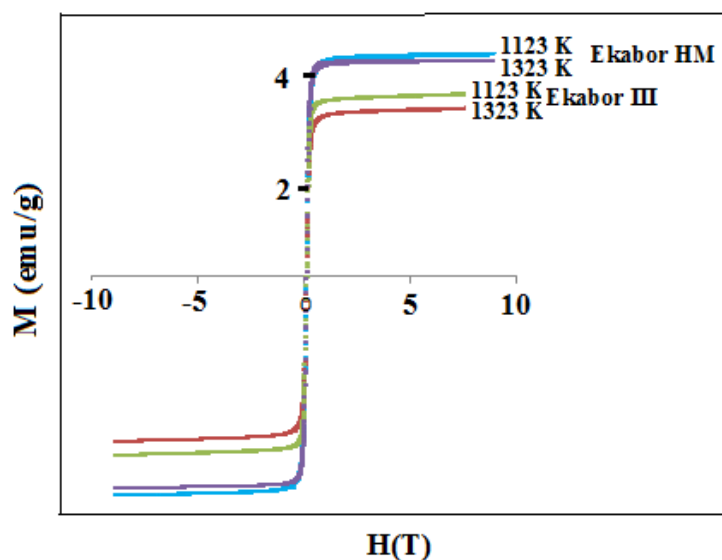


Figure 1. The magnetization of Co-Cr-Mo alloy after boriding process

We think that the $M(H)$ curves seen in Figure 1, which are specific to ferromagnetic materials, are also observed in the non-magnetic Co-Cr-Mo alloy in this study (even if M_s is small), probably due to the boron phases (CoB and Co_2B) formed by the boriding process. Co_2B phase was formed predominantly in the boride layer. (Fig.2). In literature, it has been shown that the Co_2B phase has strong ferromagnetic behavior.

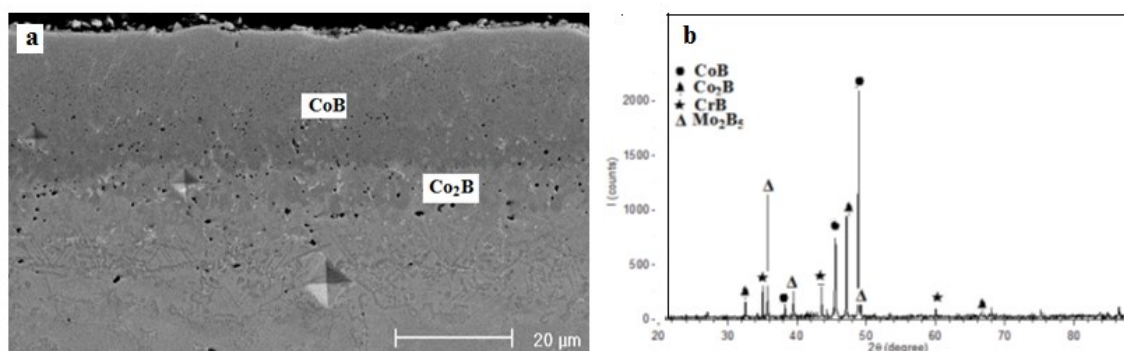


Figure 2. Microstructure of Co-Cr-Mo alloy borided at 1123 K for 9 h (a) and XRD patterns of Co-Cr-Mo alloy borided at 1323 K-9 h (b).

From Fig. 1, we see that the M_s of the Co-Cr-Mo alloy borided with ekabor HM is higher. The M_s attains its maximum value of 4.3 emu/g in Ekabor HM, after which decrease 3.4 emu/g for Ekabor III at 1123 K. The reason for this can be shown by the ferromagnetic Fe atoms in Ekabor

HM (Table 1). In addition, the biggest impact comes from particle size. In many studies, it has been pointed out that M_s values increase with decreasing particle size. In our study, the particle size of Ekabor HM was smaller than that of Ekabor III. These values are $<100 \mu\text{m}$ and $<1400 \mu\text{m}$ for Ekabor HM and Ekabor III, respectively [12].

Table 1. Chemical composition of Ekabor HM and Ekabor III (Weight%)

	B	O	N	Fe	Si	K	F	Ca
Ekabor HM	68.19	1.58	12.65	0.32	11.82	1.27	3.87	0.19
Ekabor III	57.49	7.51	--	--	31.70	0.90	2.42	--

Another important point on Figure 1 is that, while the boriding temperature of Co-Cr-Mo alloys borided with both Ekabor III and Ekabor HM increases, the M_s values decrease slightly. In the literature [10,13-15], it has been pointed out that M_s depends on composition as well as structural changes and the resulting phase. In the first stages of the boriding process (at low boriding temperatures), as mentioned in Ref. [16], the first product formed by B diffusion during boriding of the Co-Cr-Mo alloy is Co_2B , which thermodynamically always has the lowest mole fraction. With increasing B diffusion on the Co_2B surface, Co_2B turns into CoB (Fig. 2.a). With increasing boriding temperature, the phases (CrB and Mo_2B_5) other than CoB and Co_2B are formed, as seen in Fig. 2.b. We think that the movement of the magnetic domains is obstructed by these phases in the boride layer. Thus, M_s decreases with increasing boriding temperature. Another reason for the decrease in M_s is probably the strong interaction of internal forces and defects with the magnetic domain walls. It is well known that the most important microstructural changes are atomic displacements that cause defects and internal stresses in the later stages of the boriding process [17-19]. Corresponding to this, the relationship between B concentration and M_s is stated in a study by Luo et al. [20] on the $\text{Ni}_{50}\text{Mn}_{36.5}\text{Sb}_{13.5}\text{xBx}$ alloy. He showed in his detailed study that since the atomic radius of B is smaller, the increasing amount of B shortens the distance between Mn atoms in the structure. This strengthens the antiferromagnetic coupling between Mn atoms. Consequently, increasing B concentration reduces M_s .

4. Conclusion

In conclusion, while Co–Cr–Mo alloys have been used as superalloys in a broad spectrum of applications that require high strength, oxidation resistance, and wear resistance, this alloy exhibits a small amount of magnetization behavior with the boriding process. At the same time, this behavior seems to depend on the boron source and boriding temperature.

Ethics in Publishing

There are no ethical issues regarding the publication of this study.

Author Contributions

Osman İyi: Designing the study, performing the calculations, evaluating the results

Adnan Çalık: Designing the study, performing the calculations, evaluating the results,

Nazım Uçar: Evaluating the results, writing the article.

References

- [1] Ozturk, O., Turkan, U and Eroglu, A., (2006) Metal ion release from nitrogen ion implanted CoCrMo orthopedic implant material, *Surface and Coatings Technology*, 200, 5687–5697.
- [2] Duan, J., Yang, Y., Zhang, E and Wang, H., (2020) Co-Cr-Mo-Cu alloys for clinical implants with osteogenic effect by increasing bone induction, formation and development in a rabbit model, *Burns Trauma*, 8, tkaa036.
- [3] Bahçe, E., Aslan A. K., Çakır, N and Güler, M. S., (2019)., Investigation of the Surface Properties TaN Based Thin Film Coatings on the CoCrMo Alloy, *The Black Sea Journal of Sciences*, 9, 223-237.
- [4] Cuao-Moreu, C. A., Hernández-Sánchez, E., Alvarez-Vera, M., Garcia-Sanchez, E. O., Perez-Unzueta, A and Hernandez-Rodriguez, M. A. L., (2019) Tribological behavior of borided surface on CoCrMo cast alloy, *Wear*, 426–427, 204–211.
- [5] Delgado-Brito, A. M., Mejía-Caballero, I., AContla-Pacheco, A. D., Pérez Pasten-Borja, R., Castrejón-Sánchez, V. H., Hernández-Ramírez, E. J and Campos-Silva, I., (2024) Bio-tribocorrosion resistance of CoB–Co₂B and Co₂B layers on CoCrMo alloy, *Journal of Vacuum Science and Technology A* 42, 023106.

- [6] Tsai, C.-Y., Tseng, L.-W., Tzeng, Y.-C and Lee, P.-Y., (2022) Magnetic Properties of FeNiCoAlTiNb Shape Memory Alloys, *Crystals*, 12,121.
- [7] Kazantseva, N. V., Davydov, D. I., Terent'ev, P. B., Shishkin, D. A., Demakov, S. L., Yurovskikh, A. S and Romanov, E. P., (2017) Mechanical and Magnetic Properties of Alloys near the Concentration Range of the Existence of Co₃(Al,W) *Intermetallic Compound*, *Physics of Metals and Metallography*, 118, 432–438.
- [8] Mustapić, M., Pajić, D., Novosel, N., Babić, E., Zadro, K., Cindrić, M., Horvat, J., Skoko, Z., Bijelić, M and Shcherbakov, A., (2010) Synthesis, Structural Characterization and Magnetic Properties of Iron Boride Nanoparticles with or without Silicon Dioxide Coating, *Croatica Chemica Acta*, 83, 275–282.
- [9] Akkurt, I., Calik, A and Akyildirim, H., (2011) The boronizing effect on the radiation shielding and magnetization properties of AISI 316L austenitic stainless steel, *Nuclear Engineering and Design*, 241, 55-58.
- [10] Ekinci, C., (2021) Investigation of magnetic and some mechanical properties of borided Fe-Ni alloys, PhD thesis, Süleyman Demirel University, Turkey.
- [11] Ono, Y., (2010) Co-Cr-Mo alloy fine wire, manufacturing method therefor, and planar body, tubular body, stranded wire and cable formed of wire, NHK Spring Co., Ltd. United States Patent.
- [12] Ucar, N., Gülüstan, C and Calik, A., (2021) Microstructural Characterization of Borided Co-Cr-Mo Alloy, *Advances in materials Science*, 21, 90-98.
- [13] Khitouni, N., Hammami, B., Llorca-Isern, N., Mbarek, W. B., Suñol, J. J and Khitouni, M., (2022) Microstructure and Magnetic Properties of Nanocrystalline Fe_{60-x}Co₂₅Ni₁₅Si_x Alloy Elaborated by High-Energy Mechanical Milling, *Materials*, 15, 6483.
- [14] Matthew, A and Willard, M. D., (2013) Nanocrystalline Soft Magnetic Alloys Two Decades of Progress, *Handbook of Magnetic Materials*, 21, 173-342.
- [15] Kulkarni, R., Murty, B.S and Srinivas, V., (2018) Study of microstructure and magnetic properties of AlNiCo(CuFe) high entropy alloy. *Journal of Alloys and Compounds*, 746, 194–199.
- [16] Kartal, L., (2023) Cobalt Boride (Co₂ B) Particle Synthesis by One-step Carbothermic Reduction, *Hittite Journal of Science and Engineering*, 10, 229–235.
- [17] Ortiz-Domínguez, M., Flores-Rentería, M. A., Keddani, M., Elias-Espinosa, M., Damián-Mejía, O., Aldana-González, J. I., Zuno-Silva, J., Medina-Moreno, S. A and González-Reyes, J. G., (2014) Simulation of growth kinetics of Fe₂B layers formed on gray cast iron

during the powder-pack boriding, *Materiali in tehnologije/Materials and technology* 48, 905–916.

- [18] Dzyadykevich, Y. V and Zablotskaya, N. I., (1992) Influence of Copper on the Phase Formation Process in Borosilicide Layers on Niobium and Tantalum, *Soviet Powder metallurgy and metal Ceramics*, 31, 129-133.
- [19] Fojtikova, Z. P. J., Koubsky, T., Musalek, R., Strasky, J., Capek, J., Kyncl, J., Beranek, L and Kolarik, K., (2015) Study of residual stresses, microstructure, and hardness in FeB and Fe₂B ultra-hard layers, *Powder Diffraction*, 30, 83-89.
- [20] Luo, H., Meng, F., Jiang, Q., Liu, H., Liu, E., Wu, G and Wang, Y., (2010) Effect of boron on the martensitic transformation and magnetic properties of Ni₅₀Mn_{36.5}Sb_{13.5}_xBx alloys, *Scripta Materialia*, 63, 569–572.

Lepton Flavor Violation of Tau Decays into Lepton-Gamma in the Minimal Supersymmetric Type-I Seesaw Model

Vael Hajahmad ¹*Rawad Alawadi ²*

^{1,2}Erzincan Binali Yildirim University, Faculty of Arts and Sciences, Physics Department, Erzincan, Turkey

Received: 22/12/2023, **Revised:** 28/06/2024, **Accepted:** 23/08/2024, **Published:** 31/08/2024

Abstract

Experiments have shown that the violation of the lepton flavor so far is only in the neutrino sector (neutrino oscillation). Therefore, we predict it to happen in the charged lepton sector. We present a study of the lepton flavor violation (LFV) of tau lepton decays in two different channels. Tau into muon-gamma and Tau into electron-gamma. The prediction is performed in the Minimal Supersymmetric Standard Model (MSSM) extended by Seesaw Type-I Model (MSSM-Seesaw Type-I Model). The predicted calculations of the upper limit of branching ratio of the two channels are in the order of $\sim 10^{-8} - 10^{-9}$, which is in coincidence with the sensitivity of the future colliders (FCC-ee/CEPC).

Keywords: MSSM, Beyond Standard Model (BSM), Lepton Flavor Violation (LFV), Seesaw Model.

Kısıtlı Minimal Süpersimetri Tip-I Seesaw Modelinde Tau'nun Lepton-Gamma Bozunma Lepton Lezzeti İhlali

Özet

Deneyle, şu ana kadar lepton aromasının ihlalinin yalnızca nötrino sektöründe (nötrino salınımı) olduğunu göstermiştir. Bu nedenle bunun yüklü lepton sektöründe gerçekleşeceğini tahmin ediyoruz. Tau bozunmalarının lepton lezzet ihlaline (LFV) ilişkin iki farklı kanalda bir çalışma sunuyoruz. Tau müon-gamaya ve Tau elektron-gamaya dönüşür. Tahmin, Tahterevalli Tip-I Modeli (MSSM- Tahterevalli Modeli) ile genişletilen Minimal Süpersimetrik Standart Modelde (MSSM) gerçekleştirilir. İki kanalın dallanma oranına ilişkin tahmin edilen hesaplamalar $\sim 10^{-8} - 10^{-9}$ mertebesinde ve bu, gelecekteki çarpıştırıcıların (FCC-ee/CEPC) hassasiyetiyle örtüşmektedir.

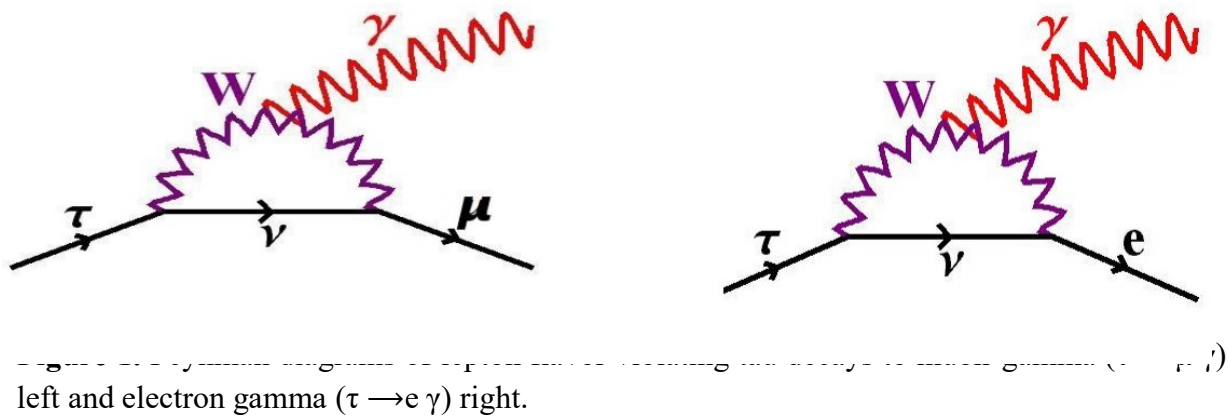
Anahtar Kelimeler: MSSM, Standart Modelin Ötesi (BSM), Lepton Lezzet İhlali (LFV), Seesaw Modeli.

1. Introduction

Collisions of electrons and nuclei in the cosmic rays and in particle accelerators are done at the beginning of the Thirties(1930s), causing the discovery of many particles. Some of them are predicted, others are completely unexpected but discovered by chance. At the beginning it was thought that all of these particles are fundamentals [1]. Later physicists have found hundreds of new particles, which we know nowadays that most of them are not fundamental. Several theories are developed to explain quite well the physical phenomena in nature; the most successful theory is called the Standard Model of particle physics (SM). The SM defines the block of matter as elementary particles called fermions and the force carrier as elementary particles called bosons. Fermions contains two classes six quarks and six leptons where there are four bosons which are exchanged by three of fundamental forces (the strong force, the weak force and the electromagnetic force) [2]. Unfortunately, the SM could not explain all the physical phenomena in nature like Gravity, Dark matter, Dark energy, the origin of neutrino mass, Hierarchy problem, Flavor problem, Unification of forces and other phenomena. Which in turn led to the emergence of the Beyond Standard Model theories (BSM). The Flavor problem is one of the phenomena which SM could not explain it, so the lepton number is conserved in SM but the lepton flavor is not conserved in nature, which is proved by confirming neutrino oscillation experimentally, besides neutrino mass differences and mixing angles [3]. However, the neutrino sector is the only place where the lepton flavor violation (LFV) has been seen so far. Consequently, determining whether or not LFV also exists in the charged lepton sector will be a difficult task for the current and future tests [4]. Based on the discovery of neutrino oscillations, the standard model (SM) with massless neutrinos must be expanded because lepton flavors are not conserved [3]. However, recent advancements in supersymmetric (SUSY) theories, particularly SUSY Grand Unified Theories (GUTs) & variants of Minimal Supersymmetric (MSSM), have made these theories more viable. Lepton flavor violation (LFV) processes have attracted more attention, including: $\tau \rightarrow e \gamma$, $\tau \rightarrow \mu \gamma$, $\mu \rightarrow e \gamma$, $Z \rightarrow l^+ l^-$, $H \rightarrow l^+ l^-$..etc. [5]. LFV processes in tau lepton decays (Z boson and Higgs boson decays) are predicted by several models: Models with heavy neutrinos, Supersymmetry and Extended gauge models [23]. Supersymmetry (SUSY) is considered as the most compelling theory from other theories [24]. Although, the Large Hadron Collider (LHC) has not detected any signs of supersymmetry up to now [25]. SUSY solves the hierarchy problem, provides signs to a dark matter and interprets neutrino masses when it is extended with right-handed Majorana neutrinos [26]. We will focus in our study on tau lepton decays into different lepton flavor ($\tau \rightarrow l \gamma$) where l either electron or muon. The observation of the LFV processes demand theories which interpret large mixing and tiny masses of left-handed neutrinos (Standard Model neutrinos) by the existence of heavy neutrinos [27]. The Seesaw mechanism is a useful SUSY extension for investigation of the tiny masses of neutrinos [28], this means that the new physics scale is about 10^{14} GeV [29]. Which is the best extension being to impose SUSY on the seesaw mechanism [28]. The study considers the Universal Gaugino Masses model which is extended by type-I seesaw model (three right-handed Majorana neutrinos and their supersymmetric partners).

2. Beyond Standard Model (BSM)

The term beyond standard model (BSM) describes theoretical physics frameworks that make an effort to explain phenomena that are not currently covered by the Standard Model (SM) of particle physics [6]. The Standard Model, which defines the fundamental particles and their interactions, is a very successful theory, yet it has some restrictions as mentioned in the introduction and unanswered issues (Gravity, Dark Matter, Hierarchy Problem, Neutrino Masses and) [7]. Several BSM ideas have been put forward to overcome these issues and broaden the standard model. Several prominent extensions consist of (Supersymmetry (SUSY), Grand Unified Theories (GUTs), String Theory and Extra Dimensions and variants of Minimal Supersymmetric (MSSM) [8]. There are many different methods and theories that have been investigated. It's vital to remember that while these theories might provide workarounds for the problems with the Standard Model, experimental proof is necessary to confirm their predictions [9].



2. LFV in MSSM-Seesaw Type-I Model

The study is performed in the scope of the minimal supersymmetric standard model (MSSM) extended by Seesaw Type-I model by adding three right-handed neutrinos, along with their SUSY partners [10]. We focus on two decay channels ($\tau \rightarrow e + \gamma$ and $\tau \rightarrow \mu + \gamma$), where it is anticipated that LFV effects in the charge lepton sector may be detectable as shown in Figure 1. The seesaw mechanism is a straightforward and alluring addition to introduce the neutrino masses [3]. The charged lepton sector encounters lepton flavor violations (LFVs) due to a new additional Yukawa matrix for right-handed neutrinos, just like the quark sector in the Standard Model (SM) [11]. The LFV processes, however, only take place via a loop containing neutrino, and they are suppressed by small neutrino masses. Thus, just the neutrino oscillations can be used to observe the LFV [4]. Due to considerable experimental advancements in recent years, the permitted ranges of the model parameters have altered significantly. The most significant development is that a Higgs boson, whose mass is now determined to be approximately 126 GeV, was discovered at the Large Hadron Collider (LHC) in July 2012 [12].

The super-potential in this case is written as following:

$$W = -y_u \hat{u}_R \hat{H}_u \hat{Q} + y_d \hat{d}_R \hat{H}_d \hat{Q} + y_l \hat{l}_R \hat{H}_d \hat{L} + \mu \hat{H}_u \hat{H}_d + \frac{1}{2} M_R \hat{\nu} \hat{\nu} + y_\nu \hat{\nu} \hat{L} \hat{H}_u \quad (1)$$

- y_u : Yukawa coupling constant for up quarks.
- y_d : Yukawa coupling constant for down quarks.
- y_ν : Yukawa neutrino coupling.
- \hat{Q} : left quark superfield.
- y_l : Yukawa coupling constant for leptons.
- μ : Higgsino mass.
- \hat{u}_R : Right up quark superfield.
- \hat{d}_R : right down quark superfield.
- \hat{l}_R : Right leptons superfield.
- M_R : Heavy Majorana neutrinos masses (right-handed neutrinos mass).
- M_R : Heavy Majorana neutrinos masses (right-handed neutrinos mass).

The soft super-symmetry breaking results in the mass terms of the supersymmetric field particles as well as the triplet coupling constants between the supersymmetric fermions and the Higgs field. The mass terms in the supersymmetric leptons sector is written as the following equation [13].

$$-\mathcal{L}_{soft, lepton} = \sum_{i=gen} m_{\tilde{L}_i}^2 \tilde{L}_i^\dagger \tilde{L}_i + m_{\tilde{l}_{Ri}}^2 \tilde{l}_{Ri}^\dagger \tilde{l}_{Ri} + m_{\tilde{\nu}_{Ri}}^2 \tilde{\nu}_{Ri}^\dagger \tilde{\nu}_{Ri} + \sum_{i,j=gen} A_{ij}^l y_{ij}^l \tilde{l}_{Ri} H_d \tilde{L}_j + A_{ij}^\nu y_{ij}^\nu \tilde{\nu}_{Ri} H_u \tilde{L}_j + h.c. \quad (2)$$

- $m_{\tilde{L}_i}^2$, $m_{\tilde{l}_{Ri}}^2$, $m_{\tilde{\nu}_{Ri}}^2$: The square of mass terms of supersymmetric leptons.
- i, j : Indicates to generation number.
- $T_{ij}^l = A_{ij}^l y_{ij}^l$, $T_{ij}^\nu = A_{ij}^\nu y_{ij}^\nu$: A_{ij}^l , A_{ij}^ν : The terms of the trilinear coupling.
- **h.c.**: Hermitian conjugation.

We assume that Majorana mass is greater than M_{SUSY} ; hence, the appropriate neutrinos should be integrated out and should not contribute to M_{SUSY} in any way [14]. This will produce the Weinberg operator, which combines two left-lepton superfields with two up-Higgs superfields [15].

$$\frac{1}{2} W_{op} \hat{L} \hat{L} \hat{H}_u \hat{H}_u \quad (3)$$

The huge M_R suppresses the Weinberg operator, which violates the lepton-number. After soft symmetry-breaking produces a Majorana mass of left-handed light neutrinos [15]:

$$m_\nu = -\frac{v_u^2}{2} (y_\nu)^T (M_R)^{-1} y_\nu \quad (4)$$

The low neutrino masses imply that the M_R scale is very high. After the electroweak symmetry is broken, this term yields the neutrino mass matrix. where $VEV \simeq 174$ GeV[16].

Using the Constrained MSSM, we assume global conditions at the Grand Unified Theory (GUT): $m_0, m_{1/2}, A_0, \tan\beta, \text{sign}(\mu)$

- Soft Gaugino masses combine to a common value: $M_1 = M_2 = M_3 = m_{1/2}$.
- The square of the symmetry-breaking masses of both supersymmetric fermions and Higgs doublets combine to a common value: $m_{\tilde{l}_R}^2 = m_{\tilde{L}}^2 = m_{\tilde{\nu}}^2 = m_0^2 I$ & $m_{\tilde{H}_u}^2 = m_{\tilde{H}_d}^2 = m_0^2$
- Terms of linear triplet couplings to a common value: $A_l = A_d = A_u = A_\nu = A_0$.
- The ratio of the Higgs vacuum expectation values $\tan\beta$ and the sign of the Higgs mixing term (Higgs mass term) $\text{sign}(\mu)$ are at the electroweak scale.
- All the values of the soft super-potential breaking terms at the electroweak scale are obtained through the Renormalization Group Equations (RGEs).

3. Renormalization Group Equations and Lepton Flavor Violation:

The two parameters of supersymmetric Seesaw Type-I model, are Yukawa neutrino coupling Matrix \mathbf{y}_ν and the right-handed neutrino mass matrix M_R [17]. Left-handed sleptons mass matrix receives an additional contribution from RGEs into LFV occurs in the left-handed sleptons sector [11]. Right-handed sleptons mass matrix does not receive any contribution to the logarithmic approximation. Linear triplet coupling terms are suppressed by the charged leptons masses:

$$\Delta m_{\tilde{L}}^2 = -\frac{1}{8\pi^2} m_0^2 \left\{ 3 + \frac{A_0^2}{m_0^2} \right\} Y_\nu^\dagger Y_\nu \log\left(\frac{M_{GUT}}{M_R}\right) \quad (5)$$

$$\Delta T_l^2 = \frac{-3}{8\pi^2} A_0 Y_l Y_\nu^\dagger Y_\nu \log\left(\frac{M_{GUT}}{M_R}\right)$$

$$\Delta m_{\tilde{e}}^2 = 0$$

$$; \frac{A_0}{m_0} = \text{const} = a_0 \Rightarrow A_0 = a_0 m_0$$

Models with large mixing in \mathbf{y}_ν are achieved [18]: $\mathbf{y}_\nu = D_u U_{PMNS}^\dagger$

- \mathbf{y}_ν : Yukawa neutrino coupling Matrix.
- \mathbf{D}_u : Diagonal Yukawa coupling matrix for top quarks.
- U_{PMNS} : leptonic mixing matrix.

The mixing matrix appears in the Dirac couplings in this scenario, with the Majorana matrix being diagonal, analogous to the quark case. The PMNS matrix then controls the mixing in \mathbf{y}_ν [19].

$$(M_{R1}, M_{R2}, M_{R3}) = (4.0 \times 10^9 \text{ GeV}, 4.0 \times 10^9 \text{ GeV}, 5.9 \times 10^{14} \text{ GeV})$$

The soft SUSY breaking terms A_0 , m_0 , and $m_{1/2}$ as well as $\tan\beta$ are free parameters [19].

4. Results and Discussion

The final variables in the research are: y_ν , M_R , $m_{1/2}$, A_0 , m_0 , $\text{sign}(\mu)$ and $\tan\beta$ [20]. In our calculations, the soft symmetry breaking terms are constrained by several theoretical and experimental conditions, such as the lightest supersymmetric particle of the used model is the neutralino [21]. For heavy Majorana neutrinos masses we will consider the degenerate case as follows: $(M_{R1}, M_{R2}, M_{R3}) = (4.0 \times 10^9 \text{ GeV}, 4.0 \times 10^9 \text{ GeV}, 5.9 \times 10^{14} \text{ GeV})$ [19].

The energy scale of Great Unified Theory (GUT) is fixed to be $M_{\text{GUT}} = 2 \times 10^{16} \text{ GeV}$. The supersymmetric breaking scale is fixed to be $M_{\text{SUSY}} = 10^3 \text{ GeV}$.

We calculate the upper limit of the branching ratio for the two channels $\text{BR}(\tau \rightarrow e \gamma)$ and $\text{BR}(\tau \rightarrow \mu \gamma)$.

First, we calculate the upper limit of the branching ratio BR as a function of m_0 , so we tune the other parameters to get the best value of BR. The tuned parameters values are $\tan(\beta)=5$, $A_0=0 \cdot m_0$, $\mp 2 \cdot m_0 \text{ GeV}$, $m_{1/2}=200 \text{ GeV}$, $\text{sign}(\mu)>0$, $M_{\text{SUSY}}=1000 \text{ GeV}$.

We tune the A_0 parameter value. The best calculated values of BR for $\text{BR}(\tau \rightarrow e \gamma)$ are at $A_0 = \mp 2 \cdot m_0 \text{ GeV}$, $m_0 = 200 \text{ GeV}$. While the best calculated values of BR for $\text{BR}(\tau \rightarrow \mu \gamma)$ are also at $A_0 = \mp 2 \cdot m_0 \text{ GeV}$, $m_0 = 200 \text{ GeV}$. By increasing values of m_0 the values of $\text{BR}(\tau \rightarrow e \gamma)$ and $\text{BR}(\tau \rightarrow \mu \gamma)$ are decreasing as shown in Figure 2.

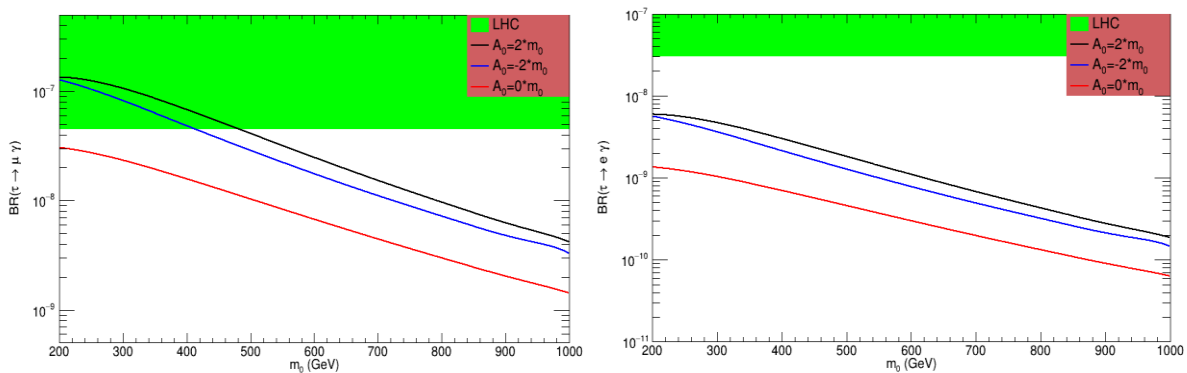


Figure 2. The upper limit of $\text{BR}(\tau \rightarrow e \gamma)$ and $\text{BR}(\tau \rightarrow \mu \gamma)$ as function of m_0 , $\tan(\beta)=5$, $A_0=0 \cdot m_0$, $\mp 2 \cdot m_0 \text{ GeV}$, $m_{1/2}=200 \text{ GeV}$, $\text{sign}(\mu)>0$, $M_{\text{SUSY}}=1000 \text{ GeV}$. $\text{BR}(\tau \rightarrow e \gamma)$ “Left panel”. $\text{BR}(\tau \rightarrow \mu \gamma)$ “Right panel”. Black line for $A_0 = 2 \cdot m_0$, blue line for $A_0 = -2 \cdot m_0$ and red line for $A_0 = 0 \cdot m_0$.

Secondly, we calculate the upper limit of the branching ratio BR as a function of m_0 , so we tune the other parameters to get the best value of BR. The tuned parameters values are $\tan(\beta)=5$, $A_0=2*m_0$ GeV, $m_{1/2}=200, 300, 400, 500$ GeV, $\text{sign}(\mu)>0$, $M_{\text{SUSY}}=1000$ GeV.

We tune the value of the $m_{1/2}$ parameter. The best calculated values of BR for $\text{BR}(\tau \rightarrow e \gamma)$ are at $m_{1/2}=200$ GeV. While the best calculated values of BR for $\text{BR}(\tau \rightarrow \mu \gamma)$ are also at $m_{1/2}=200$ GeV. By increasing values of m_0 the values of $\text{BR}(\tau \rightarrow e \gamma)$ and $\text{BR}(\tau \rightarrow \mu \gamma)$ are decreasing as shown in Figure 3.

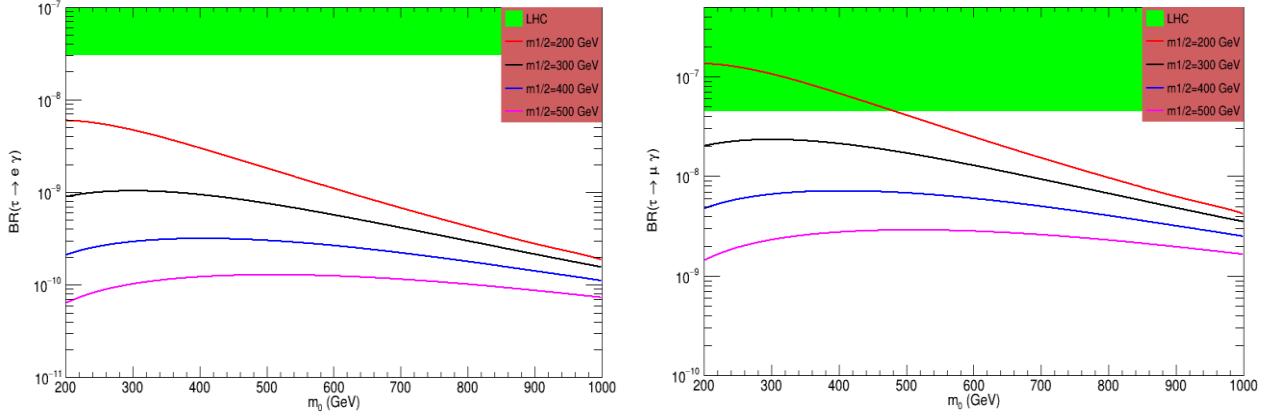


Figure 3. The upper limit of $\text{BR}(\tau \rightarrow e \gamma)$, $(\tau \rightarrow \mu \gamma)$ as function of m_0 , $\tan(\beta)=5$, $A_0=2*m_0$ GeV, $m_{1/2}=200, 300, 400, 500$ GeV, $\text{sign}(\mu)>0$, $M_{\text{SUSY}}=1000$ GeV. The best value of $\text{BR}(\tau \rightarrow e \gamma)$ “Left panel” at $m_{1/2}=200$ GeV (red line). The best value of $\text{BR}(\tau \rightarrow \mu \gamma)$ “Right panel” at $m_{1/2}=200$ GeV (red line).

Thirdly, we calculate the upper limit of the branching ratio BR as a function of $\tan(\beta)$, so we tune the other parameters to get the best value of BR. The tuned parameters values are $m_0=500$, $A_0=2*m_0$ GeV, $m_{1/2}=500$ GeV, $\tan(\beta)=[5 - 55]$, $\text{sign}(\mu)>0/ \text{sign}(\mu)<0$, $M_{\text{SUSY}}=1000$ GeV.

We tune the value of the $\text{sign}(\mu)$ parameter. The best calculated values of BR for $\text{BR}(\tau \rightarrow e \gamma)$ are at $\text{sign}(\mu)>0$ and $\tan(\beta)=55$. While the best calculated values of BR for $\text{BR}(\tau \rightarrow \mu \gamma)$ are also at $\text{sign}(\mu)>0$ and $\tan(\beta)=55$. By increasing values of $\tan(\beta)$ the values of $\text{BR}(\tau \rightarrow e \gamma)$ and $\text{BR}(\tau \rightarrow \mu \gamma)$ are increasing as shown in Figure 4.

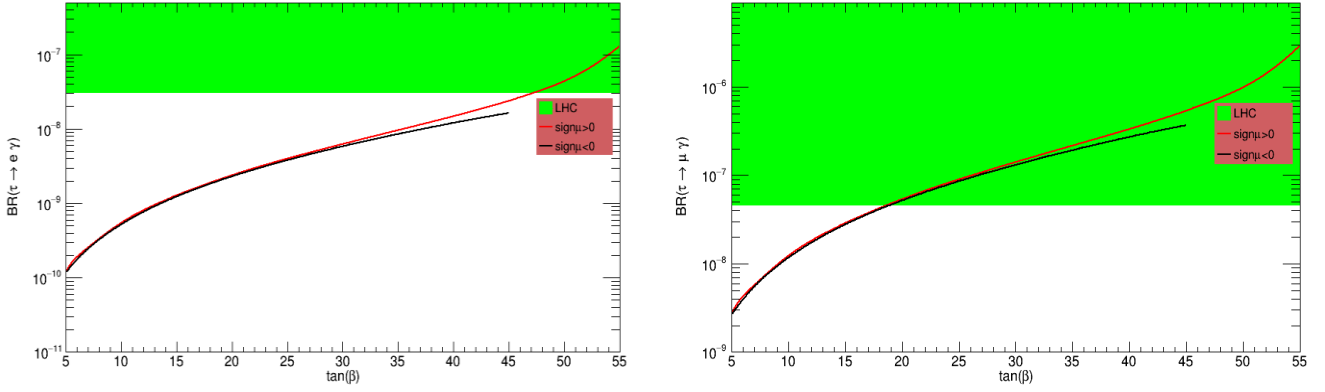


Figure 4. The upper limit of $BR(\tau \rightarrow e \gamma)$ and $BR(\tau \rightarrow \mu \gamma)$ as function of $\tan(\beta)$, $m_0=500$ GeV, $A_0=2*m_0$ GeV, $m_{1/2}=500$ GeV, $\text{sign}(\mu)<0/ \text{sign}(\mu)>0$, $M_{\text{SUSY}}=1000$ GeV. The best value of $BR(\tau \rightarrow e \gamma)$ “Left panel” at $\text{sign}(\mu)>0$ (red line). The best value of $BR(\tau \rightarrow \mu \gamma)$ “Right panel” at $\text{sign}(\mu)>0$ (red line).

Fourthly, we calculate the upper limit of the branching ratio BR as a function of $\cos(\theta)$, so we tune values of other parameters to get the best value of BR . The tuned parameters values are $m_0=m_{1/2}=500$ GeV, $A_0=2*m_0$ GeV, $\tan(\beta)=5$, $\text{sign}(\mu)>0/ \text{sign}(\mu)<0$, $M_{\text{SUSY}}=1000$ GeV.

We tune the value of the $\cos(\theta)$ with respect to $\text{sign}(\mu)$ parameter. The best calculated values of BR for $BR(\tau \rightarrow e \gamma)$ are at $\text{sign}(\mu)>0$ and $\cos(\theta)=1$. While the best calculated values of BR for $BR(\tau \rightarrow \mu \gamma)$ are also at $\text{sign}(\mu)>0$ and $\cos(\theta) = 1$. By increasing values of $\cos(\theta)$ the values of $BR(\tau \rightarrow e \gamma)$ and $BR(\tau \rightarrow \mu \gamma)$ are increasing as shown in Figure 5.

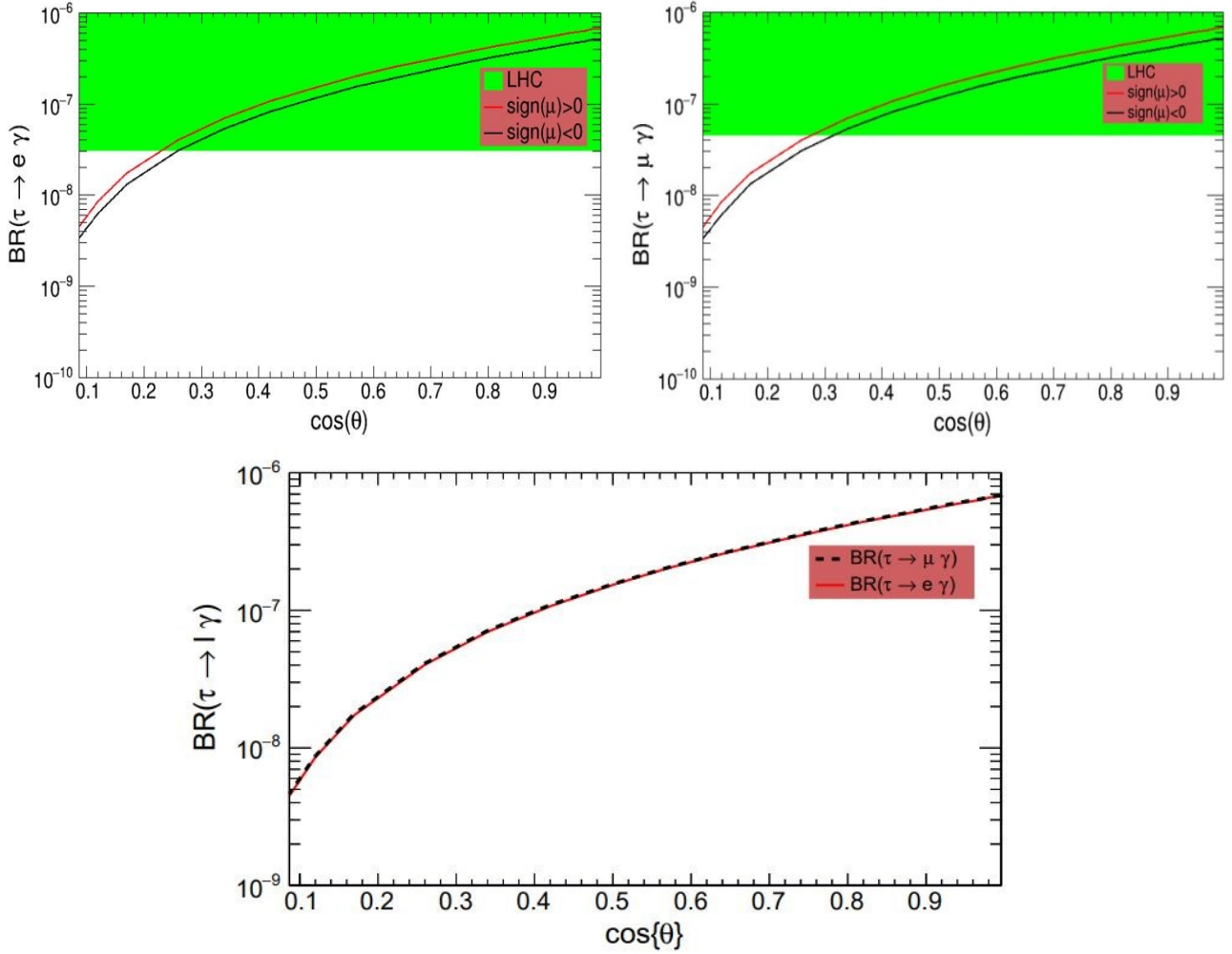


Figure 5. The upper limit of $BR(\tau \rightarrow e \gamma)$ and $BR(\tau \rightarrow \mu \gamma)$ as function of $\cos(\theta)$, $m_0=m_{1/2}=200$ GeV, $A_0=2*m_0$ GeV, $\text{sign}(\mu)>0/ \text{sign}(\mu)>0$, $M_{\text{SUSY}}=1000$ GeV. The best value of $BR(\tau \rightarrow e \gamma)$ “Left panel” at $\text{sign}(\mu)>0$ (red line). The best value of $BR(\tau \rightarrow \mu \gamma)$ “Right panel” at $\text{sign}(\mu)>0$ (red line). Bottom figure shows the upper limit of BR for the two channels only when $\text{sign}(\mu)>0$.

Last and not least, we calculate the upper limit of the branching ratio BR as a function of m_0 , final tuned parameters values are $A_0=2*m_0$ GeV, $m_{1/2}=200$ GeV, $\tan(\beta)=5$, $\text{sign}(\mu)>0$ and $M_{\text{SUSY}}=1000$ GeV. We tune the value of the m_0 parameter .

Best calculated values of $BR(\tau \rightarrow e \gamma)$ are at $m_0=200$ GeV and the best calculated values of $BR(\tau \rightarrow \mu \gamma)$ are also $m_0=200$ GeV. By increasing values of m_0 the values of $BR(\tau \rightarrow e \gamma)$ and $BR(\tau \rightarrow \mu \gamma)$ are decreasing as shown in Figure 6.

By comparing the results of the upper limit of the branching ratio for the two considered channels $BR(\tau \rightarrow e \gamma)$ and $BR(\tau \rightarrow \mu \gamma)$ as shown in the figure below, we conclude here that the upper limit value for the muon-gamma channel is better than that for the electron-gamma channel. Thus, the probability to detect LFV process in muon-gamma channel is most likely.

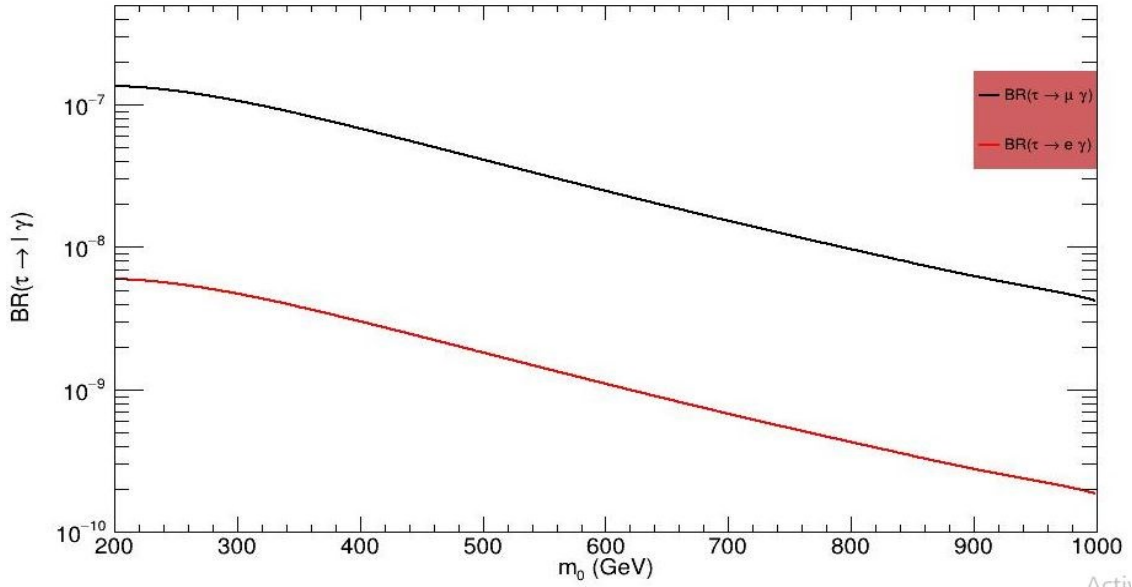


Figure 6. The upper limit of $BR(\tau \rightarrow \ell, \gamma)$ as function of m_0 . Where $\tan(\beta)=5$, $A_0=2*m_0$ GeV, $m_{1/2}=200$ GeV, $\text{sign}(\mu)>0$, $M_{SUSY}=1000$ GeV. The best value the upper limit of branching ratio BR is for $(\tau \rightarrow \mu \gamma)$ channel (black line), where the one for the $(\tau \rightarrow e \gamma)$ channel is less probable (red line).

5. Conclusion

In this article, lepton flavor violation (LFV) of the tau lepton decays $(\tau \rightarrow \ell \gamma)$, where $\ell = \text{muon}$ or electron, in the minimal supersymmetric standard model (MSSM) extended by the Seesaw Type-I model are studied in this article. In supersymmetric models, the Seesaw-I mechanism can be realized by adding three right-handed neutrinos. Universal Gaugino masses with the degenerate case scenario is considered. Because of light neutrino masses, Majorana neutrinos scale is about $(10^{13} - 10^{14})$ GeV and Yukawa coupling of neutrinos Y_ν is ~ 1 . From numerical calculations we found that the branching ratios BRs of tau lepton decays $(\tau \rightarrow \ell \gamma)$ are decreasing when increasing the values of universal scalar mass m_0 and Gaugino masses ($m_{1/2}$). While the values of BRs are increasing when the values of trilinear parameter A_0 , $\tan(\beta)$ and $\cos(\theta)$ are increasing. The best values of $BR(\tau \rightarrow \ell \gamma)$ are at input parameters: $m_0 = 200$ GeV, $m_{1/2} = 200$ GeV, $\tan(\beta)=5$, $\text{sign}(\mu) > 0$, and $\cos(\theta)=0.61$. The obtained results for tau decays $(\tau \rightarrow e \gamma)$, $(\tau \rightarrow \mu \gamma)$ are close to the experimental limits in BABAR and BELL. We observed the best value for $\tau \rightarrow e \gamma$ which is around $\sim 4 \times 10^{-9}$, while the experimental limit in BABAR is around $< 3,3 \times 10^{-8}$. We obtained also the best values for $\tau \rightarrow \mu \gamma$ which is around $\sim 1.3 \times 10^{-8}$, while the experimental limit in BELL is around $< 4,2 \times 10^{-8}$. Furthermore, the obtained values of BR of $BR(\tau \rightarrow \ell \gamma)$ for some parameters are in the range of the expected experimental upper limit for the LHC [22] as shown in figure(2-5). Also, the values of $BR(\tau \rightarrow \ell \gamma)$ are coincidence with the sensitivity of future colliders (FCC-ee/CEPC) [22]. Thus, the lepton flavor violation of the tau lepton decays in the MSSM-Seesaw Type-I model can be realized and can be observed in future colliders.

Ethics in Publishing

There are no ethical issues regarding the publication of this study.

Acknowledgements

I would like to thank Erzincan Binali Yildirim University, Physics Department, and my research group for all the efforts they provided to obtain the results and complete this work.

References

- [1] F. A. Aharonian, A. A. Belyanin, E. V Derishev, V. V Kocharovsky, and V. V Kocharovsky, “Constraints on the extremely high-energy cosmic ray accelerators from classical electrodynamics,” *Phys. Rev. D*, vol. 66, no. 2, p. 23005, 2002.
- [2] P. H. Frampton, P. Q. Hung, and M. Sher, “Quarks and leptons beyond the third generation,” *Phys. Rep.*, vol. 330, no. 5–6, pp. 263–348, 2000.
- [3] E. Arganda and M. J. Herrero, “Lepton flavour violation in constrained MSSM-seesaw models,” *arXiv Prepr. arXiv0810.0160*, 2008.
- [4] T. Goto, Y. Okada, T. Shindou, M. Tanaka, and R. Watanabe, “Lepton flavor violation in the supersymmetric seesaw model after the LHC 8 TeV run,” *Phys. Rev. D*, vol. 91, no. 3, p. 33007, 2015.
- [5] C. Csaki, “The minimal supersymmetric standard model,” *Mod. Phys. Lett. A*, vol. 11, no. 08, pp. 599–613, 1996.
- [6] J. D. Lykken, “Beyond the standard model,” *arXiv Prepr. arXiv1005.1676*, 2010.
- [7] A. Belyaev, D. Ross, A. Belyaev, and D. Ross, “Beyond the Standard Model (BSM),” *Basics Nucl. Part. Phys.*, pp. 347–359, 2021.
- [8] S. Raby, “Supersymmetric grand unified theories,” *Lect. Notes Phys*, vol. 939, no. 1, 2017.
- [9] M. Khlopov, “What comes after the Standard Model?,” *Prog. Part. Nucl. Phys.*, vol. 116, p. 103824, 2021.
- [10] J. Turner, “Leptonic Flavour Symmetries and their Cosmological Dynamics.” Durham University, 2017.
- [11] V. Brdar, A. J. Helmboldt, S. Iwamoto, and K. Schmitz, “Type I seesaw mechanism as the common origin of neutrino mass, baryon asymmetry, and the electroweak scale,” *Phys. Rev. D*, vol. 100, no. 7, p. 75029, 2019.
- [12] M. Spira, A. Djouadi, D. Graudenz, and R. M. Zerwas, “Higgs boson production at the LHC,” *Nucl. Phys. B*, vol. 453, no. 1–2, pp. 17–82, 1995.
- [13] M. Dine, “What is the scale of supersymmetry breaking?,” *Nucl. Phys. B-Proceedings Suppl.*, vol. 52, no. 1–2, pp. 201–205, 1997.

- [14] A. Das, P. S. B. Dev, and R. N. Mohapatra, “Same sign versus opposite sign dileptons as a probe of low scale seesaw mechanisms,” *Phys. Rev. D*, vol. 97, no. 1, p. 15018, 2018.
- [15] F. Staub, “Exploring New Models in All Detail with SARAH,” *Adv. High Energy Phys.*, vol. 2015, pp. 1–126, 2015.
- [16] S. Jana, N. Okada, and D. Raut, “Displaced vertex signature of type-I seesaw model,” *Phys. Rev. D*, vol. 98, no. 3, p. 35023, 2018.
- [17] J. F. Kamenik and M. Nemevšek, “Lepton flavor violation in type I+ III seesaw,” *J. High Energy Phys.*, vol. 2009, no. 11, p. 23, 2009.
- [18] A. Abada, D. Das, A. Vicente, and C. Weiland, “Enhancing lepton flavour violation in the supersymmetric inverse seesaw beyond the dipole contribution,” *J. High Energy Phys.*, vol. 2012, no. 9, pp. 1–34, 2012.
- [19] J. Gierbach, S. Mertens, U. Nierste, and S. Wiesenfeldt, “Lepton flavour violation in the MSSM,” *J. High Energy Phys.*, vol. 2010, no. 5, pp. 1–48, 2010.
- [20] J. Ellis, J. Hisano, M. Raidal, and Y. Shimizu, “New parametrization of the seesaw mechanism and applications in supersymmetric models,” *Phys. Rev. D*, vol. 66, no. 11, p. 115013, 2002.
- [21] M. Hirsch, F. R. Joaquim, and A. Vicente, “Constrained SUSY seesaws with a 125 GeV Higgs,” *J. High Energy Phys.*, vol. 2012, no. 11, pp. 1–33, 2012.
- [22] Vicente. A, “Higgs Lepton Flavor Violating Decays in Two Higgs Doublet Models,” *Frontiers in Physics*, vol. 2019, no. 7, pp. 00174, 2019.
- [23] T. Davidek and L. Fiorini, “Search for lepton-flavor-violating decays of bosons with the atlas detector,” *Frontiers in Physics*, vol. 2020, no. 8, pp.00149, 2020.
- [24] A. Canepa, “Searches for supersymmetry at the large hadron collider,” *Reviews in Physics*, vol. 2019, no. 4, pp.100033, 2019
- [25] K.S. Babu, I. Gogoladze and C.S. Un, “Proton lifetime in minimal susy su(5) in light of lhc results,” *Journal of High Energy Physics*, vol. 2022, no. 2, pp. 00164, 2022.
- [26] H. Baer, V. Barger and H. Serce, “Lepton flavor violation from susy with nonuniversal scalars,” *Phys. Rev. Res.*, vol. 2019, no. 1, pp.033022, 2019.
- [27] ATLAS collaboration, “Search for charged lepton-flavour violation in z-boson decays with the atlas detector,” *Nat. Phys.*, vol. 2021, no. 17, pp. 819-825, 2021.
- [28] T. Goto, Y. Okada, T. Shindou, M. Tanaka and R. Watanabe, “Lepton flavor violation in the supersymmetric seesaw model after the lhc 8 tev run,” *Phys. Rev. D*, vol. 2015, pp. 033007, 2015.
- [29] J. Cao, Z. Xiong and J.M. Yang, “Lepton flavor violating z-decays in supersymmetric seesaw model,” *Eur. Phys. J. C*, vol. 2004, no. 32, pp. 245, 2004.

Synthesis of Tungsten Disulfide on B-N-Doped Carbon Nanotubes to Enhance the Electrochemical Performance of Supercapacitors

Yasar Ozkan YESİLBAG^{1*}, Fatma Nur TUZLUCA YESİLBAG¹, Ahmad HUSEYİN² and
Ahmed Jalal Salih SALIH²

¹Department of Physics, Erzincan Binali Yıldırım University, Erzincan 24100, Turkey

²Erzincan Binali Yıldırım University Graduate School of Natural and Applied Sciences,
Department of Physics, Erzincan 24100, Turkey

Received: 16/07/2024, Revised: 04/08/2024, Accepted: 23/08/2024, Published: 31/08/2024

Abstract

In this research, boron and nitrogen-doped carbon nanotubes (B-N-CNTs) were synthesized at 900°C using the FCCVD method. Carbon, nitrogen, and boron as source materials were simultaneously introduced using a batch-mode droplet reactor and ferrocene as a catalyst. B-N-CNTs were obtained with diameters ranging from 10 - 50 nm and lengths around 30 – 80 µm. These B-N-CNTs were thoroughly characterized and structurally analyzed. Subsequently, tungsten disulfide (WS₂) nanosheets on B-N-CNTs were synthesized using the hydrothermal method to design a composite material and were investigated as electrodes for supercapacitors. The morphological properties of B-N-CNT@WS₂ were determined by various analytical techniques such as XRD, FESEM, XPS, and EDS. B-N-CNT@WS₂ was investigated as an electrode for supercapacitors in two- and three-electrode cells. In the three-electrode cell, B-N-CNT@WS₂ exhibited a specific capacitance of 320 F g⁻¹ at a current density of 0.5 A g⁻¹, while the two-electrode cell showed a capacitance of 41 F g⁻¹. The symmetric supercapacitor at a current density of 5 A g⁻¹ exhibited excellent structural stability by preserving 90% of its specific capacitance after 9000 cycles in the 1 V potential range.

Keywords: B-N-CNTs, WS₂, composite electrode, supercapacitor

Süperkapasitörlerin Elektrokimyasal Performansının İyileştirilmesi için B-N-Katkılı Karbon Nanotüpler üzerine Tungsten Disülfürün Sentezi

Öz

Bu çalışmada, FCCVD yöntemi kullanılarak 900°C'de bor ve nitrojen katkılı karbon nanotüpler (B-N-CNT) sentezlenmiştir. Kaynak malzeme olarak karbon, nitrojen ve bor, katalizör olarak ferrosenin olduğu toplu modlu damlacık reaktörü kullanılarak eş zamanlı olarak dahil edilmiştir. Çapları 10 - 50 nm arasında değişen ve uzunlukları 30 - 80 µm civarında olan B-N-CNT'ler elde edilmiştir. Bu B-N-CNT'ler kapsamlı bir şekilde karakterizasyonu yapılmıştır. Daha sonra, B-N-CNT'ler üzerine tungsten disülfür (WS₂) nanotabakaları, kompozit bir malzeme tasarlamak için hidrotermal yöntem kullanılarak sentezlenmiş ve süperkapasitörler için elektrotlar olarak araştırılmıştır. B-N-CNT@WS₂'nin morfolojik özellikleri XRD, FESEM, XPS ve EDS gibi çeşitli analitik tekniklerle belirlenmiştir. B-N-CNT@WS₂, hem iki hem de üç elektrotlu hücrelerde süperkapasitörler için bir elektrot olarak araştırılmıştır. Üç elektrotlu hücrede, B-N-CNT@WS₂, 0.5 A g⁻¹ akım yoğunluğunda 320 F g⁻¹'lik spesifik bir kapasitans sergilerken, iki elektrotlu hücrede 41 F g⁻¹'lik bir kapasitans göstermiştir. Simetrik süperkapasitör ise 5 A g⁻¹ akım yoğunluğunda 1 V potansiyel aralığında 9000 döngüden sonra kapasitesinin %90'ini koruyarak mükemmel yapısal kararlılık sergilemiştir.

Anahtar Kelimeler: B-N-CNTs, WS₂, kompozit elektrot, süperkapasitör

*Corresponding Author: oyesilbag@erzincan.edu.tr

Yasar Ozkan YESİLBAG, <https://orcid.org/0000-0002-2519-3078>

Fatma Nur TUZLUCA YESİLBAG, <https://orcid.org/0000-0003-4383-2432>

Ahmad HUSEYİN, <https://orcid.org/0000-0002-2260-2593>

Ahmad Jalel Salih SALIH, <https://orcid.org/0000-0002-1760-5423>

1. Introduction

Due to the increasing demand for efficient and sustainable energy storage technology, driven by the escalating consumption of fossil fuels and their depletion, there is a growing search for alternative solutions and the development of new and environmentally energy sources (Wang et al., 2015; Tu et al., 2016). Alternative electrical energy emerges as the most popular option to address this issue as it is generated from clean and renewable sources such as wind and solar (Dai et al., 2016). Extensive efforts are being made to store electrical energy safely and environmentally, with batteries and supercapacitors being one solution (Choudhary et al., 2016). Supercapacitors, also known as double-layer capacitors, consist of opposing electrodes separated by an insulator (Tomko et al., 2011; Wu et al., 2012). Energy is stored in supercapacitors in the form of electric charges on the surface of the electrodes, allowing for rapid discharge when needed (Yesilbag et al., 2022). Supercapacitors are characterized by fast charge and discharge rates, long-term cycle life, and the ability to withstand many charge-discharge cycles compared to conventional batteries. However, they still suffer from lower energy storage capacity compared to batteries. Thus, efforts are focused on improving their performance for applications requiring large amounts of energy. Supercapacitors excel in their ability to store and release energy quickly and efficiently, making them ideal for various applications in renewable energy and energy storage systems (Tuzluca Yesilbag & Huseyin, 2024).

In recent years, researchers have focused on using nanomaterials as electrodes for supercapacitors (Kinoshita et al., 2019; Béguin et al., 2014). Nanomaterials emerge as an excellent option for manufacturing supercapacitor electrodes due to their excellent conductivity and large surface area (Li et al., 2018). Recently, hybrid nanomaterials with one-dimensional, two-dimensional, and three-dimensional structures have been synthesized to enhance the electrochemical performance of supercapacitors. Among the one-dimensional materials, carbon nanotubes (CNTs) and boron and nitrogen-doped carbon nanotubes (BCN) have shown promise as electrode materials for supercapacitors and batteries (Yesilbag et al., 2021). Also, WS₂ nanosheets were synthesized on reduced graphene oxide (RGO) using a molten salt process, exhibiting a high specific capacitance of 2508.07 F g⁻¹ at a scan rate of 1 mV s⁻¹ due to the synergistic effect of WS₂ and RGO (Kim et al., 2011; Zhang et al., 2014; Chen et al., 2011). CNTs were introduced to improve the conductivity of WS₂. WS₂@CNT exhibited good specific capacitance of up to 752.53 mF cm⁻² at a scan rate of 20 mV s⁻¹ (Yang et al., 2020).

In this study, boron- and nitrogen-doped carbon nanotubes were synthesized using the Floating Catalyst Chemical Vapor Deposition (FCCVD) system. The doping process enhances the nanotube electron and ion transport during charge and discharge, increasing mechanical flexibility and contributing to pseudocapacitance. Transition metal dichalcogenide (WS₂) was synthesized on B-N-CNT without additional treatment. B-N-CNT@WS₂ was examined as electrode materials for supercapacitors and exhibited good capacitive properties.

2. Materials and Methods

2.1. Synthesis of B-N Doping CNTs by Chemical Vapor Deposition:

B-N-CNTs were synthesized using the FCCVD method, which is a modified version of the chemical vapor deposition method. In batch-mode droplet reactor, methanol, boric acid, and acetonitrile were used as sources for B, N, and C, respectively. Ferrocene ($C_{10}H_{10}Fe$) was used as a catalyst. Initially, methanol (CH_3OH) and boric acid (H_3BO_3) were mixed in a weight ratio of 1%, and then acetonitrile (C_2H_3N) was added. 0.15 g of ferrocene powder was placed in a quartz tube at the front of the furnace. The mixed carrier gas ($H_2=30$ sccm, $Ar=60$ sccm) was initially sent upon reaching the desired temperature of $900^\circ C$. Then, the gas flow rate was changed to $Ar=500$ sccm and $H_2=300$ sccm, and ferrocene was vaporized to initiate the growth process of B-N-CNTs. The solution injection rate was 10 ml/hour. The growth process continued for half an hour, and then the process was stopped while the flow of gases continued $Ar=60$ sccm and $H_2=30$ sccm until it reached room temperature. B-N-CNTs were collected from the walls of the quartz tube.

2.2. Synthesis of Tungsten Disulfide (WS_2):

Tungsten disulfide nanosheets were synthesized using the hydrothermal method. In this method, 1 g of oxalic acid ($C_2H_2O_4$), 0.3 g of sodium tungstate dihydrate, and 0.4 g of thioacetamide were taken in 50 ml of deionized water and mixed for an hour at room temperature. Then, the solution was transferred to a Teflon-lined autoclave with a capacity of 100 ml and heated to $200^\circ C$ for 12 h. After the process, the powder was washed with water several times and dried in an oven at $60^\circ C$ for 24 h.

2.3. Electrochemical Measurements:

The electrode was coated on carbon cloth consisting of active material, carbon black, and binder (PDVF) with a weight ratio of 8:1:1. Sample areas of 1×1 cm² were immersed in the electrolyte and tested as working electrodes. Electrochemical measurements of cyclic voltammetry (CV) and galvanostatic charge-discharge (GCD) were performed using a three-electrode system with a platinum (Pt) counter electrode and Ag/AgCl reference electrode. A 6 M KOH solution was used as the electrolyte. Electrochemical impedance spectroscopy (EIS) was performed over a frequency range from 10 kHz to 10 mHz. The specific capacitance (C_s) was calculated from GCD curves using the following equations:

$$C = I \times t / m \times V$$

where I is the constant discharge current, t is the discharge time, V is the potential window, and m is the mass of the active material. Additionally, measurements were carried out in a symmetrically design two-electrode cell in a 6 M KOH electrolyte using B-N-CNT@ WS_2 electrodes.

3. Results and Discussion

Figure 1 depicts the synthesis steps for the B-N-CNT@WS₂ electrode. Briefly, B-N-CNTs were synthesized via the FCCVD process, followed by powder collection, HCl washing, and sonication. After then, B-N-CNTs and WS₂ precursor materials was put into the autoclave for a hydrothermal growth.

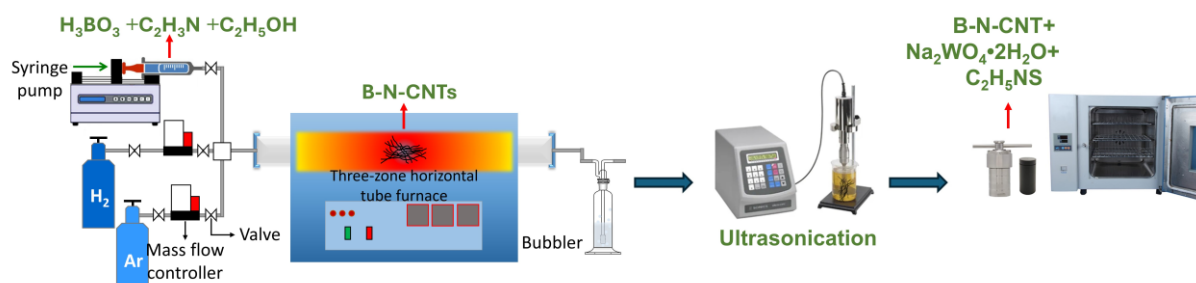


Figure 1. Schematic diagram of B-N-CNT@WS₂ synthesis.

In our previous study, B-N-CNTs were grown at 900°C and appeared as intertwined threads adhering to each other; hence, ultrasonic treatment was employed to separate them (Yesilbag et al., 2022). This process facilitates electron transfer on the one hand and provides a high surface area on the other hand. The FESEM images demonstrate the successful synthesis of B-N-CNT@WS₂, as shown in Figure 2 (a-c). The full area EDS analysis of B-N-CNT@WS₂ shown in Figure 3 showed that the atomic concentrations of W, S, B, C, N, and O were observed without any impurities.

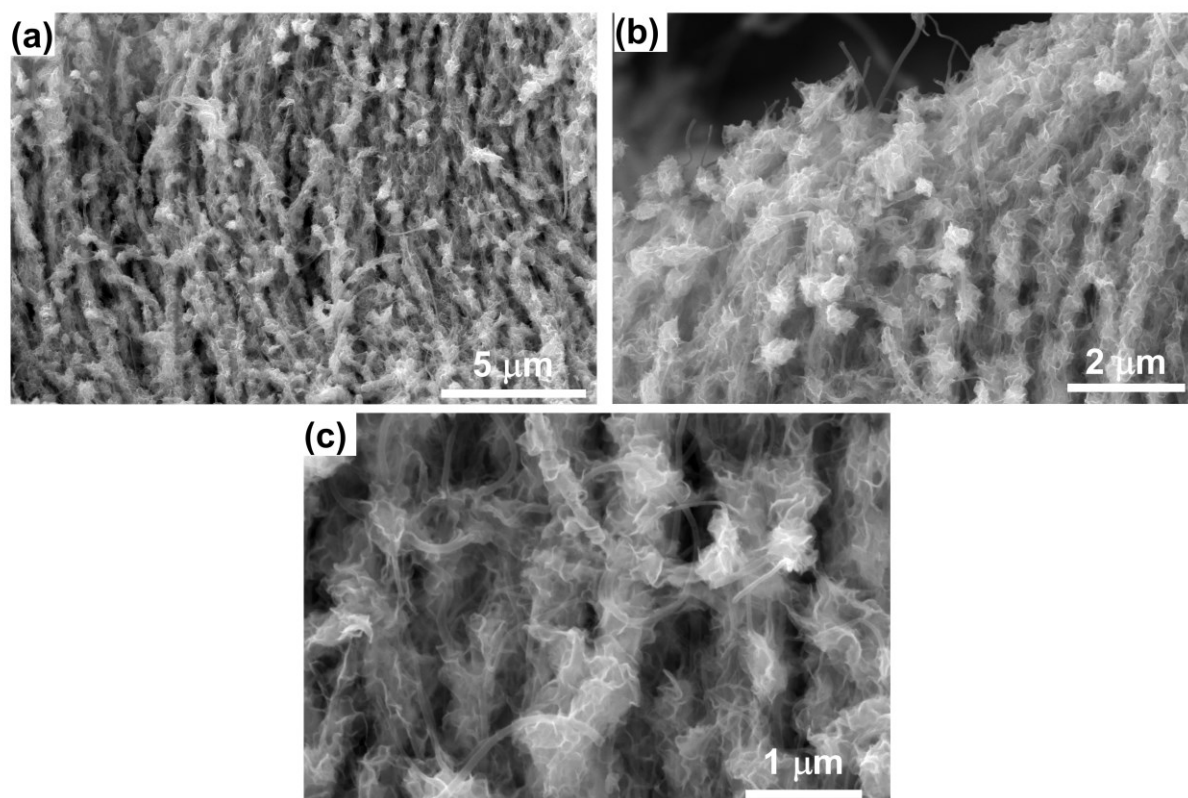


Figure 2. FESEM images for B-N-CNT@WS₂.

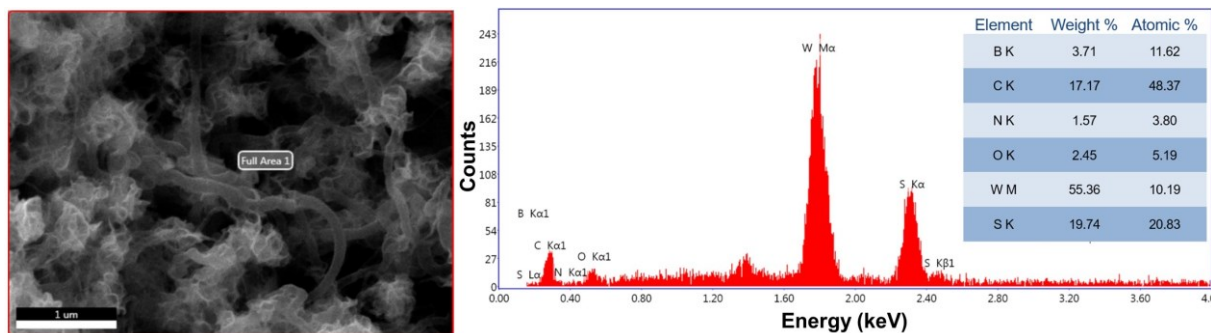


Figure 3. Full area EDS analysis for B-N-CNT@WS₂.

XRD analysis was conducted to analyze further and confirm B-N doping into the CNTs. Figure 4 shows an XRD pattern attributed to JCPDS card no: 41-1487 of graphitic structure B-N-doped carbon and JCPDS Card No: 84-1398 of WS₂, confirming the successful synthesis of B-N-CNT@WS₂.

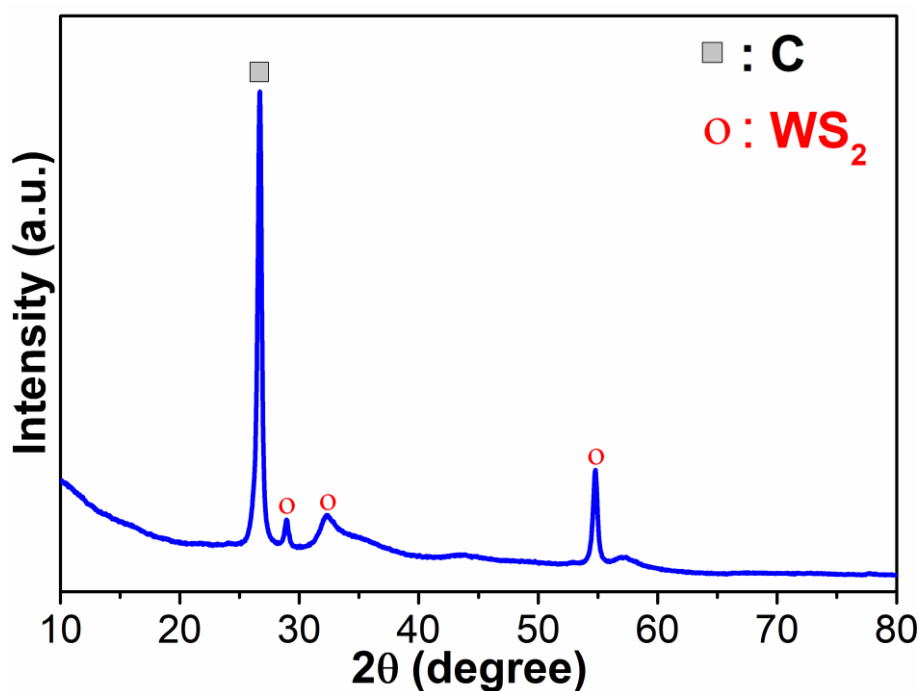


Figure 4. XRD analysis for B-N-CNT@WS₂ composite electrode material.

Through XPS analysis of B-N-CNT@WS₂, all elements B, C, N, W, S, and O appeared in the full spectrum, indicating the presence of peaks corresponding to B 1s, C 1s, N 1s, W 4f, S 2p, and O 1s (Figure 5 (a)). In the high-resolution XPS spectrum, the binding energies of C 1s, B 1s, and N 1s found at 285 eV, 185.5 eV, and 402 eV was shown in Figure 5 (b), (c), and (d), respectively. This indicates that boron and nitrogen bond to carbon. Additionally, peaks for W appeared at 36.4 eV and 34.5 eV, corresponding to W 4f_{7/2} W 4f_{5/2}, respectively (Figure 5 (e)). Moreover, in Figure 5 (f), the peaks for S appeared at 168.1 eV and 161.9 eV, corresponding to S 2p_{3/2} and S 2p_{1/2}, respectively, confirming the successful synthesis of WS₂.

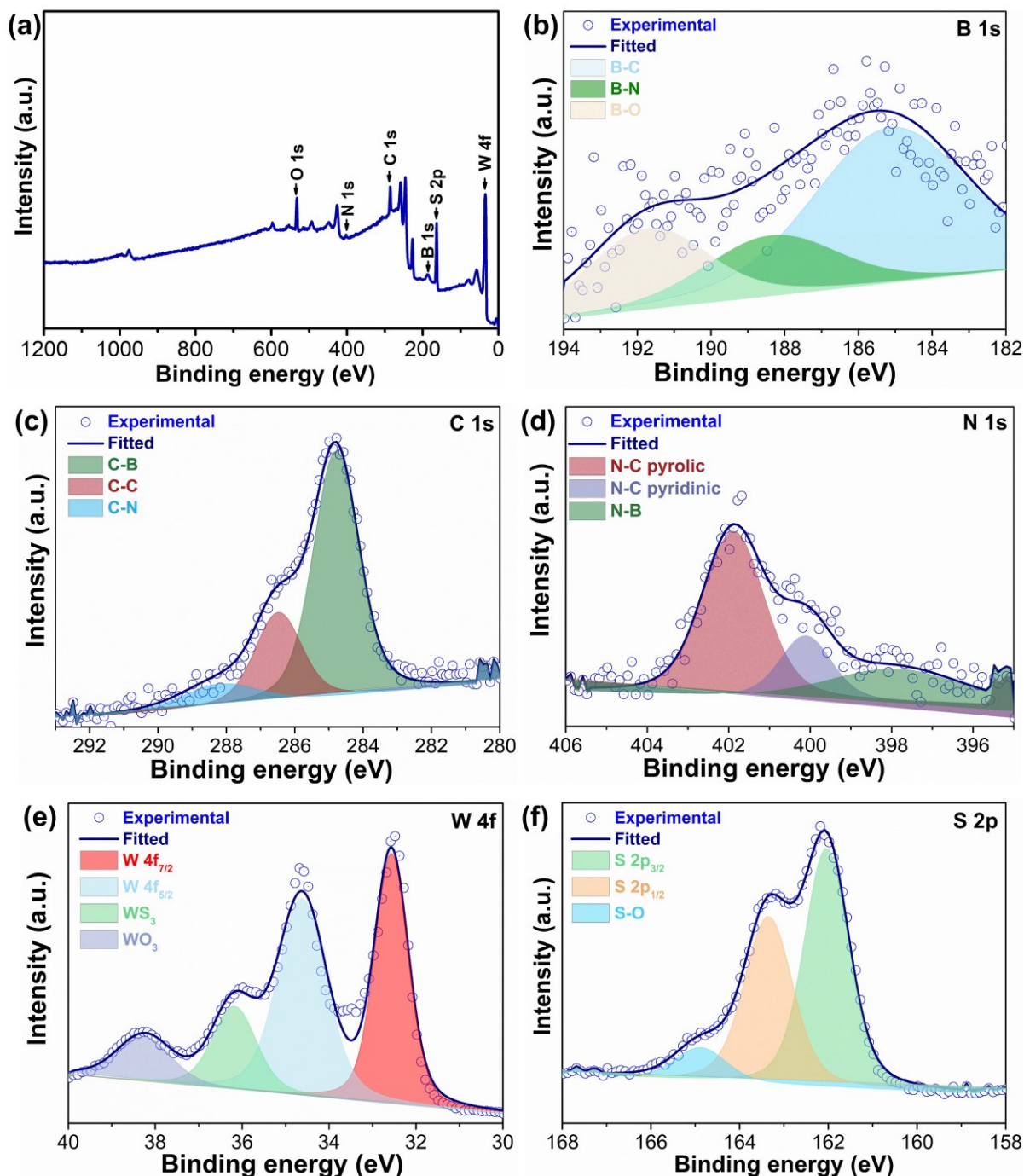


Figure 5. (a) XPS full spectrum of B-N-CNT@WS₂, the high-resolution spectrum of peaks (b) B 1s, (c) C 1s, (d) N 1s, (e) W 4f, and (f) S 2p.

Electrochemical measurements for the B-N-CNT@WS₂ electrode were conducted in a 6 M KOH electrolyte in a three-electrode system. In Figure 6 (a), the CV curves show broad shapes within the voltage range of -1.1 V to -0.2 V, indicating a mixture of EDLC and surface Faradaic processes occurring on the electrode surface. Small peaks are observed at -0.8 V and -0.5 V, corresponding to the surface oxidation and reduction processes of WS₂. Various scan rates 5-100 mV s⁻¹ were applied, showing minimal changes in shapes, indicating capacitive properties and excellent performance. In Figure 6 (b), charge/discharge curves exhibit nearly symmetric triangular shapes, confirming the good capacitive behavior of the B-N-CNT@WS₂ electrode.

Figure 6 (c) illustrates the specific capacitance values at 0.5, 1, 2, 5, and 10 A g⁻¹ current densities 320, 286, 210, 195, and 186 F g⁻¹ respectively. Electrochemical behavior is further confirmed by EIS measurement shown in Figure 6 (d). The B-N-CNT@WS₂ electrode displays a parallel curve to the y-axis in the low-frequency range, indicating good capacitive behavior.

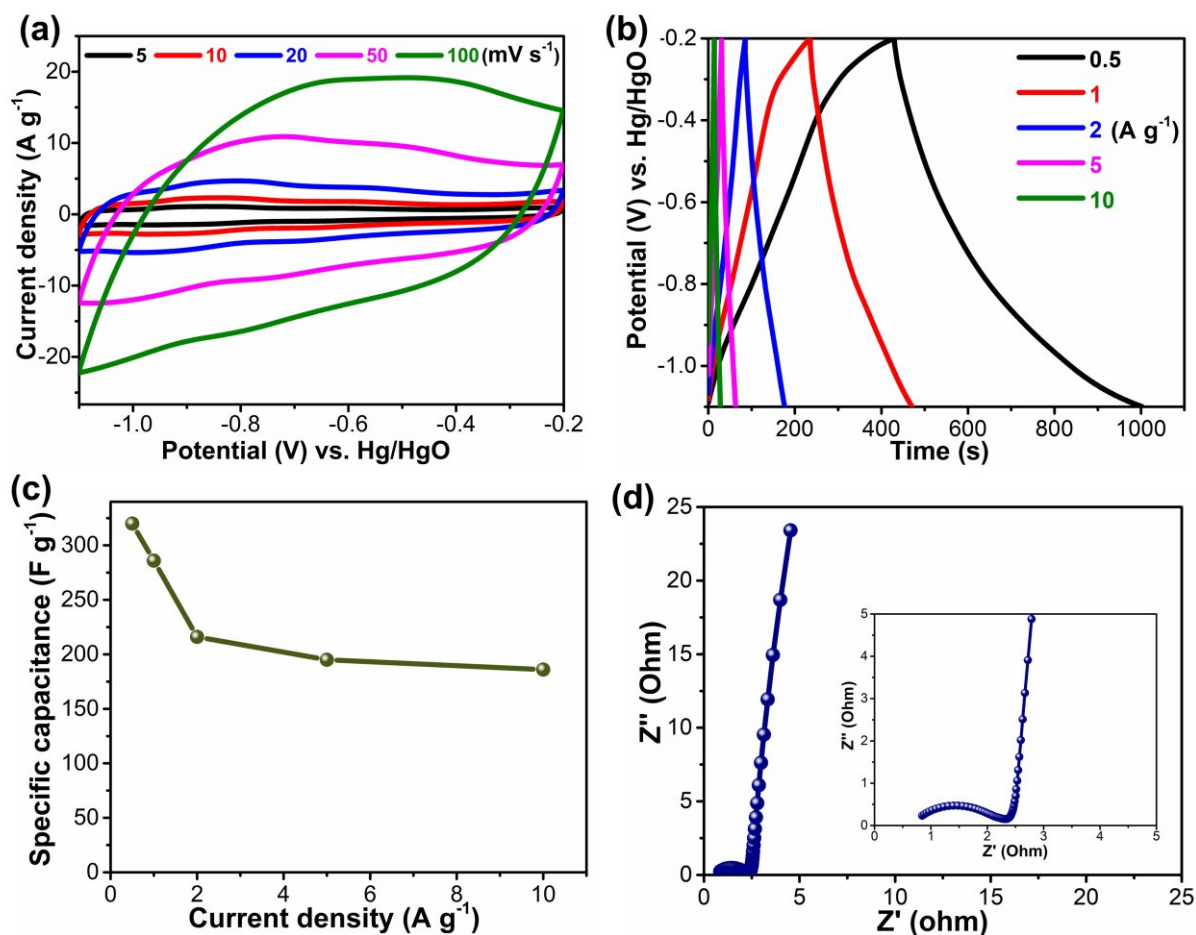


Figure 6. (a) CV curves at scan rates of 5-100 mVs⁻¹, (b) GCD curve at current densities of 0.5-10 A g⁻¹, (c) specific capacitance values, (e) Nyquist curves for EIS measurement (inset is enlarged high-frequency region).

A symmetrical supercapacitor (SSC) B-N-CNT@WS₂//B-N-CNT@WS₂ was assembled in two-electrode cell. CV and GCD measurements of the SSC were conducted within the voltage range 0-1 V, as shown in Figure 7 (a) and (b). The CV curves appeared rectangular, and the CV area increased with the scan rate, indicating capacitive behavior and reversibility. Figure 7 (c) shows the specific capacitance values of the SSC at current densities 0.5, 1, 2, and 5 A g⁻¹ to be 41, 25, 20, and 18.4 F g⁻¹, respectively. Moreover, to evaluate the cycling stability of the SSC, a test was conducted at a current density of 5 A g⁻¹, demonstrating a high stability of 90% after 9000 cycles, as shown in Figure 7 (d). In the EIS spectrum in Figure 7 (e), the intersection of the semicircle with the x-axis is ESR, and its value is 0.46 ohms, while the diameter of the semicircle is R_{ct}, and its value is 0.51 ohms.

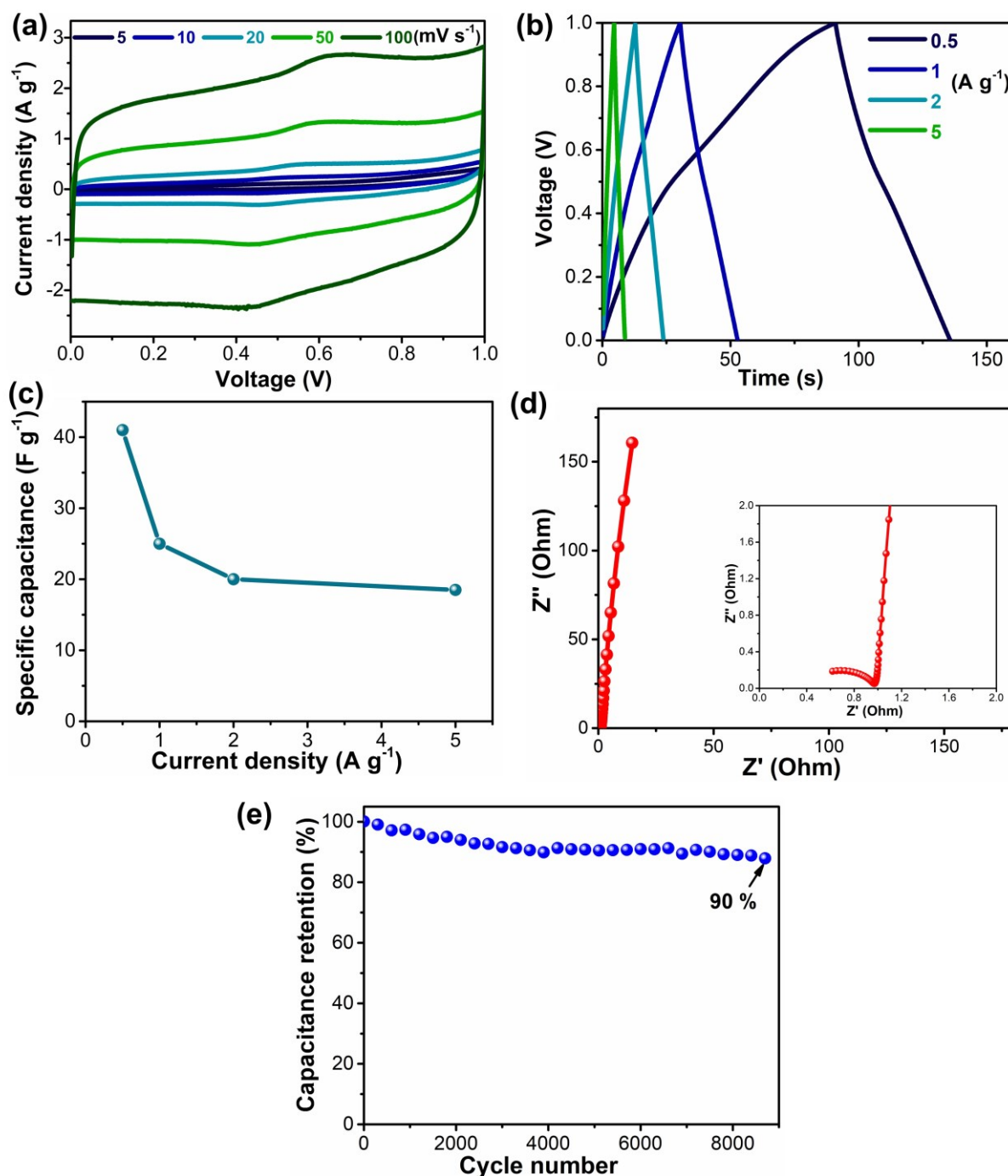


Figure 7. (a) CV curves at scan rates 5-100 mV s^{-1} for the SSC, (b) GCD curves at different current densities in the 0-1 V potential range, (c) specific capacitance values, (d) Nyquist plot, (e) Long-term cycling stability at 5 A g^{-1} current density.

4. Conclusion

In conclusion, the B-N-CNT@WS₂ electrode was synthesized in two stages. Initially, B-N-CNT was synthesized at a temperature of 900°C using the FCCVD method, followed by the WS₂ synthesis on the B-N-CNT surface via hydrothermal treatment. The B-N-CNT@WS₂ electrode was studied through structural and morphological analyses using characterization techniques such as XRD, FESEM, and XPS. WS₂ nanosheets were grown homogeneously on

BCN nanotubes, creating a synergistic effect. The B-N-CNT@WS₂ composite electrode shows a higher specific capacitance of 320 F g⁻¹ at a current density of 0.5 A g⁻¹. Moreover, the SSC demonstrated the specific capacitance 41 F g⁻¹ at a current density of 0.5 A g⁻¹, with a capacitance retention rate of 90% after 9000 cycles.

Acknowledgments

This work was supported by the Scientific and Technical Research Council of Turkey, TUBITAK, under Grant Number 217M323.

Ethics in Publishing

There are no ethical issues regarding the publication of this study.

Author Contributions

Yasar Ozkan Yesilbag: Ideas; formulation or evolution of overarching research goals and aims; Acquisition of the financial support for the project leading to this publication.

Fatma Nur Tuzluca Yesilbag: Preparation, creation, and presentation of the published work, specifically visualization/ data presentation.

Ahmad Huseyin: Performing the experiments and data collection.

Ahmed Jalal Salih SALIH: Performing the experiments and data collection.

5. References

- Béguin, F., Presser, V., Balducci, A., & Frackowiak, E. (2014). Carbons and electrolytes for advanced supercapacitors. *Advanced materials*, 26(14), 2219-2251.
- Chen, Z., Hou, L., Cao, Y., Tang, Y., & Li, Y. (2018). Gram-scale production of B, N co-doped graphene-like carbon for high performance supercapacitor electrodes. *Applied Surface Science*, 435, 937-944.
- Choudhary, N., Li, C., Chung, H. S., Moore, J., Thomas, J., & Jung, Y. (2016). High-performance one-body core/shell nanowire supercapacitor enabled by conformal growth of capacitive 2D WS₂ layers. *ACS nano*, 10(12), 10726-10735.
- Dai, Y., Wu, X., Sha, D., Chen, M., Zou, H., Ren, J., ... & Yan, X. (2016). Facile self-assembly of Fe₃O₄ nanoparticles@WS₂ nanosheets: a promising candidate for supercapacitor electrode. *Electronic Materials Letters*, 12, 789-794.
- Kim, Y. S., Kumar, K., Fisher, F. T., & Yang, E. H. (2011). Out-of-plane growth of CNTs on graphene 2- for supercapacitor applications. *Nanotechnology*, 23(1), 015301.
- Kinoshita, T., Karita, M., Nakano, T., & Inoue, Y. 2019. "Two step floating catalyst chemical vapor deposition including in situ fabrication of catalyst nanoparticles and carbon nanotube forest growth with low impurity level". *Carbon*, 144, 152-160.

- Li, S., Zhang, N., Zhou, H., Li, J., Gao, N., Huang, Z., ... & Kuang, Y. (2018). An all-in-one material with excellent electrical double-layer capacitance and pseudocapacitance performances for supercapacitor. *Applied Surface Science*, 453, 63-72.
- Tomko, T., Rajagopalan, R., Aksoy, P., & Foley, H. C. (2011). Synthesis of boron/nitrogen substituted carbons for aqueous asymmetric capacitors. *Electrochimica acta*, 56(15), 5369-5375.
- Tu, C. C., Lin, L. Y., Xiao, B. C., & Chen, Y. S. (2016). Highly efficient supercapacitor electrode with two-dimensional tungsten disulfide and reduced graphene oxide hybrid nanosheets. *Journal of Power Sources*, 320, 78-85.
- Tuzluca Yesilbag, F. N., & Huseyin, A. (2024). Designing CuO@MnCo₂O₄ nanowire arrays electrode on copper foam and foil substrates via chemical synthesis methods for asymmetric supercapacitor. *Journal of Energy Storage*, 80, 110148.
- Wang, J., Li, X., Zi, Y., Wang, S., Li, Z., Zheng, L., ... & Wang, Z. L. (2015). A flexible fiber-based supercapacitor-triboelectric-nanogenerator power system for wearable electronics. *Advanced Materials*, 27(33), 4830-4836.
- Wu, Z. S., Zhou, G., Yin, L. C., Ren, W., Li, F., & Cheng, H. M. (2012). Graphene/metal oxide composite electrode materials for energy storage. *Nano Energy*, 1(1), 107-131.
- Yang, X., Li, J., Hou, C., Zhang, Q., Li, Y., & Wang, H. (2020). Skeleton-structure WS₂@CNT thin-film hybrid electrodes for high-performance quasi-solid-state flexible supercapacitors. *Frontiers in chemistry*, 8, 442.
- Yesilbag, Y. O., Yesilbag, F. N. T., Huseyin, A., & Ertugrul, M. (2022). The hierarchical synthesis of tungsten disulfide coated vertically aligned boron carbon nitride nanotubes composite electrodes for supercapacitors. *Journal of Energy Storage*, 52, 104964.
- Yesilbag, Y. O., Yesilbag, F. N. T., Huseyin, A., Salih, A. J. S., & Ertugrul, M. (2022). MnO₂ nanosheets synthesized on nitrogen-doped vertically aligned carbon nanotubes as a supercapacitor electrode material. *Journal of Alloys and Compounds*, 925, 166570.
- Zhang, X., Zhang, H., Li, C., Wang, K., Sun, X., & Ma, Y. (2014). Recent advances in porous graphene materials for supercapacitor applications. *Rsc Advances*, 4(86), 45862-45884.

Assessment of Alternative International Organizations for Turkey Using Machine Learning Algorithms

Ömer Çağrı Yavuz ^{1*}

¹Trabzon Üniversitesi, Türkiye

Received: 16/08/2024, **Revised:** 21/08/2024, **Accepted:** 27/08/2024, **Published:** 31/08/2024

Abstract

The distribution of power balances among countries has driven states to become part of an international system within the context of the principles of territorial integrity, sovereignty, and independence. Turkey's process of joining the European Union (EU), which dates back to 1959, has been supported by various reforms and harmonization packages. However, the prolonged negotiations have led Turkey to explore other organizations. In recent times, Turkey, while not completely abandoning its bid for EU membership, has been considering membership in alternative organizations, particularly the Shanghai Cooperation Organization (SCO). In this study, the proximity of Turkey to EU and SCO member countries is evaluated by creating a dataset that includes various indicators for 34 countries. Subsequently, the dataset was grouped based on various indicators. The Naive Bayes and K-Nearest Neighbors algorithms were applied to the five different datasets obtained. In these applications, Turkey was positioned in relation to two different classes based on the EU and SCO member countries, depending on various indicators. The results of the applications, along with the performance metrics obtained for the two different algorithms, are presented.

Keywords: European Union, Shanghai Cooperation Organization, machine learning, classification

Türkiye için Alternatif Uluslararası Örgütlerin Makine Öğrenmesi Algoritmalarıyla Değerlendirilmesi

Öz

Ülkelerin güç dengesindeki dağılımlar devletleri toprak bütünlüğü, egemenlik ve bağımsızlık ilkeleri bağlamında uluslararası bir sistemin parçası olmaya itmiştir. Türkiye'nin 1959 yılına kadar uzanan Avrupa Birliği (AB)'ne katılma süreci çeşitli reformlar ve uyum paketleriyle desteklenmektedir. Ancak uzun süren müzakerelerin neticelenmemesi Türkiye'yi farklı örgütlere yönelmeye itmiştir. Son dönemde Avrupa Birliği üyeliğinden tam olarak vazgeçmeyen Türkiye'nin başta Şangay İşbirliği Örgütü (ŞİÖ) olmak üzere alternatif örgütlere üyeliği değerlendirilmektedir. Bu çalışma kapsamında Türkiye'nin AB ve ŞİÖ üyesi ülkelere yakınlığının değerlendirilmesi amaçlanarak 34 ülkenin çeşitli göstergelerini içeren bir veri seti oluşturulmuştur. Sonrasında oluşturulan veri seti çeşitli göstergelere bağlı olarak gruplandırılmıştır. Elde edilen beş farklı veri setine Naive Bayes ve K En Yakın Komşu algoritması uygulanmıştır. Bu uygulamalarda çeşitli göstergelere bağlı olarak Türkiye, AB ve ŞİÖ üyesi ülkelerin yer aldığı iki farklı sınıfa göre konumlandırılmıştır. Yapılan uygulamalarda iki farklı algoritma için elde edilen performans metrikleriyle birlikte tahmin edilen değerlere yer verilmiştir.

Anahtar Kelimeler: Avrupa Birliği, Şangay İşbirliği Örgütü, makine öğrenmesi, sınıflandırma

1. Introduction

In today's world politics, the uncertainties that emerged in the aftermath of the Cold War have led to a search for a new order. The distribution in the balance of power has pushed states to become part of an international system in the context of the principles of territorial integrity, sovereignty and independence. At the beginning of a new order, the power of states over world politics is associated with their share in the world economy. Along with economic power, military power is also seen as an important element for states to maintain and strengthen their current situation [1]. Along with military and economic power, social indicators including consumption, education and health parameters are considered in determining the socioeconomic status of states [2]. Finally, environmental and infrastructural indicators are also considered important in assessing the welfare and holistic development of states [3]. In the light of all these indicators, various states come together to form international institutions and organizations. In this respect, Turkey's possible cooperation with international organizations and institutions is also evaluated. In particular, it is emphasized that the negotiations between Turkey and the European Union (EU), which started in 2005, are important for Turkey in terms of keeping up with the globalizing economy and politics [4]. With the start of the negotiations, Turkey has been inspired by the EU in its foreign policy and has developed a more active line [5]. However, there are ups and downs in the relationship between Turkey and the EU due to problems such as judicial independence, human rights, freedom of expression and the Cyprus problem [6]. In addition, elements such as the rule of law, democratic freedoms and respect for minorities are also taken as issues that have a negative impact on Turkey and the EU negotiations [7]. In addition to these negativities, the EU's migration policies have led to various partnerships and agreements with Turkey [8].

With the dissolution of the Union of Soviet Socialist Republics, the United States of America (USA) has become a unipolar power center by gaining power in world politics. On the other hand, Russia's desire to prevent the US from approaching the Eurasian region and the border problems between China and Central Asian countries brought Russia and China together. In addition to Russia and China, Kazakhstan, Tajikistan, and Kyrgyzstan also joined the talks. As a result of the negotiations of these 5 countries, the agreement, which is referred to as the foundation of Shanghai 5, was signed in 1996 and the Shanghai Cooperation Organization (SCO) was officially established in 2001 with the participation of Uzbekistan [9].

Turkey's full membership to the SCO started to be discussed due to the EU's attitude towards Turkey, uncertainties in the relations, and the negotiations that have not been concluded for a long time during the process in which financial markets were transferred to the east. Accordingly, Turkey applied for full membership to the SCO in 2011. Afterwards, it was accepted as a dialogue country [10]. In recent years, Turkey has been engaged in joint economic, social and cultural activities with the SCO member Turkic Republics [11]. Along with these activities, the trade relations developed with China increase the cooperation between Turkey and the SCO [12].

Turkey's process of joining the EU, which dates back to 1959, has been supported by various reforms and harmonization packages. However, the protracted negotiations have led Turkey to

turn to different organizations. Recently, Turkey, which has not completely given up on EU membership, has been considering membership in the SCO and the Eurasian Economic Union [13]. Especially the SCO is considered as an organization that Turkey can join commercially as an alternative to the EU [14].

The problems encountered in Turkey's accession process to the European Union bring along uncertainties. Along with these uncertainties, Turkey's SCO membership is being discussed. Turkey's membership to the European Union and other alternative international organizations is becoming complex. Various artificial intelligence techniques are used to solve such complex problems. With these techniques, data can be processed, interpreted, analyzed and classified. These techniques are frequently used in the field of International Relations to solve complex problems based on data analysis. For example, Katagiri and Min (2015) applied machine learning techniques to US diplomatic documents. These documents were obtained from the digitization of the US Foreign Relations 1945-1980 collection. The aim of the applications is to predict the perceived threat from the documents. As a result of the study, it was emphasized that the methods used will contribute to the testing of International Relations theories [15]. In another study, machine learning algorithms were used to detect patterns in North Korea's military provocations. For this purpose, news articles of the Korean Central News Agency between 1997 and 2013 were analyzed. As a result of the analysis, 82% success was achieved. As a result of the study, it was stated that the use of machine learning techniques in similar studies will be beneficial [16]. Another study using machine learning algorithms aims to predict country risk. For this purpose, four different algorithms were applied to a dataset consisting of macroeconomic indicators of 75 countries between 2015-2019. As a result of the study, it was stated that the highest success was obtained with the K Nearest Neighbor (KNN) algorithm and it was emphasized that high success was achieved in the applications [17]. In another study, the performance of two different algorithms was compared. In this direction, data from EU candidate and member countries were analyzed. In the light of these data, it was aimed to evaluate the effect of the factor of increasing the level of economic development on the EU membership of the countries. As a result of the study, the most effective variables in the EU membership process were revealed [18]. In another study, two different algorithms were used to detect terrorist attacks and their economic damage, which is one of the most difficult problems for governments to deal with. As a result of the study, performance metrics obtained from the algorithms were given and various suggestions were presented [19]. Within the scope of this study, a dataset was created to evaluate Turkey's relationship with the SCO and the EU. For the dataset consisting of 34 records, Naive Bayes and KNN algorithms were applied and performance metrics were compared.

The objective of this study is to illustrate the applicability of machine learning algorithms in addressing similar classification problems within the field through the applications conducted in the context of this research. Furthermore, the study offers a distinct perspective on the international organizations to which Turkey is aligned, based on various indicators and quantitative data.

The aim of this study is to demonstrate the applicability of machine learning algorithms in solving similar classification problems in the field with the applications made within the scope of this study. In addition, international organizations that Turkey is close to depending on different indicators are presented from a different perspective depending on quantitative values.

2. 2. Material and Methods

2.1. Data Collection

The dataset used in this study consists of general indicators, economic indicators, social indicators, environmental and infrastructural indicators of 35 countries, including 26 EU member states, 8 SCO member states and Turkey. The dataset, consisting of records from 2021, consists of eight different attributes. The records in the dataset were obtained from the data.un.org website developed by the United Nations (UN) Statistics Department. In the dataset, the class representing the SCO is assigned a value of 0 and the class containing EU member states is assigned a value of 1. Thirty percent of the records in the dataset were used for testing and 70 percent for training. Naive Bayes and KNN algorithms were applied to the obtained dataset. The applications were realized using Python sklearn library.

The dataset examined in this study consists of records related to various indicators of 35 different countries. It is anticipated that in future studies, more effective and efficient results can be achieved through applications conducted with more comprehensive datasets, which are supported by document-based research and expert opinions on these indicators and their related records.

2.2. Naive Bayes

Naive Bayes, a probabilistic algorithm, is a popular algorithm based on Bayes' theorem. The algorithm is based on the assumption of independence between attributes, hence the name "naive". This independence assumption implies conditional independence between attributes. Although this is not suitable for concrete problems, it shows high performance in solving different problems in various fields [20].

In the Naive Bayes algorithm, where learning is performed on the training dataset, the learning process is performed on the training dataset. After the probabilistic calculation, the record with the highest value is assigned to the relevant class [21]. The formula used for this calculation is given below. In the formula below

- $P(A/B)$, the probability of A in situation B,
- $P(B/A)$, the probability of B in situation A,
- $P(A)$, the probability of state A,
- $P(B)$ denotes the probability of state B.

$$P(A/B) = \frac{P(B/A) * P(A)}{P(B)}$$

2.3. K-Nearest Neighbor (KNN)

The KNN algorithm developed by Cover and Hart is frequently used to solve nonlinear classification problems. The K value in the calculations refers to the number of nearest neighbors. The distances of the value to be classified to K number of neighbors are calculated. This calculation process is based on Euclidean distance measurement [22]. For example, for K=7, the distances of the 7 points closest to the value to be classified are calculated. Then, the classes in which the 7 points are included are examined and assignment to the closest class is made.

2.4. Performance Metrics

In applications with machine learning algorithms, various metrics are used to evaluate the performance of the models. In this study, accuracy, precision, sensitivity and f1 score are among the most commonly used performance metrics. These performance metrics are calculated with the values in the confusion matrix. There are four basic variables in the confusion matrix: True Positive (TP), True Negative (TN), False Positive (FP) and False Negative (FN). TP refers to the number of correctly predicted positive (1) values, while TN refers to the number of correctly predicted negative (0) values. Similarly, FN refers to the number of incorrectly predicted negative values and FP refers to the number of incorrectly predicted positive values.

The formulas used to calculate the accuracy, precision, sensitivity and f1 score based on these values are given in Table 1.

Table 1. Performance metrics

Accuracy	Precision	Recall	F1 Skoru
$\frac{(TP + TF)}{(TP + TF + FP + FN)}$	$\frac{TP}{(TP + FP)}$	$\frac{TP}{(TP + FN)}$	$2 * \frac{Precision * Recall}{Precision + Recall}$

3. Results and Discussion

Within the scope of the study, Naive Bayes and KNN algorithms were applied to the dataset consisting of indicators from Turkey, EU member countries and SCO member countries. The dataset used in the first application consists of 8 attributes. The dataset was then grouped into general indicators, social indicators, economic indicators, environmental and substructural indicators. The training dataset used in the study consists of records of EU and SCO countries. After the learning has taken place, Turkey's data is considered and it is aimed to predict the classes to which Turkey belongs depending on the indicators.

The attributes and the indicators used in the applications are given in Table 2.

Table 2. Attribute and groups

Attribute	Group
Population Density	General Indicators
Surface Area	
GDP	Economic Indicators
CPI	
Health Expenditures	Social Indicators
Education Expenditures	
Internet Usage	Environmental and Infrastructural Indicators
Energy Supply Per Capita	

The attributes considered in the study are given above. From these attributes, the classes in which Turkey is included are estimated. The class with EU member countries is labeled as 1 and the class with SCO member countries is labeled as 0.

The accuracy values obtained with Naive Bayes and KNN algorithms in the first application with the dataset including all indicators and the final results obtained from the algorithms are given in Table 3. In the table below, 1 represents the EU and 0 represents the SCO.

Table 3. Accuracy values and predicted values

	Naive Bayes	KNN
Accuracy	0.81	0.94
Predicted Class	1	1

As seen in Table 3, in the application with the dataset including all indicators, an accuracy value of 0.81 was obtained with the Naive Bayes algorithm and 0.94 with the KNN algorithm. In addition, a value of 1 was obtained for both algorithms in the predictions made for the class that Turkey will be in. This shows that Turkey is in the class of EU member states for all indicators in the predictions made with Naive Bayes and KNN algorithms.

In the applications, high accuracy values were obtained for both algorithms. However, the use of more than one performance metric in classification problems contributes to the reliability of the results. In this direction, the precision, sensitivity values and F1 scores obtained with the Naive Bayes algorithm applied to the dataset including all indicators are given in Table 4.

Table 4. Performance metrics (Naive Bayes)

	Precision	Recall	F1 Score
0	1,00	0,50	0,67
1	0,78	1,00	0.88

The performance metrics obtained with KNN in the application with the dataset including all indicators are also given in Table 5.

Table 5. Performance metrics (KNN)

	Precision	Recall	F1 Score
0	1,00	0,75	0,86
1	0,88	0,75	0,93

The performance metrics obtained in the applications with the dataset consisting of 8 different attributes are given above. In order to evaluate Turkey's proximity to EU and SCO member countries in terms of different parameters, four different datasets were created by grouping these attributes as general indicators, social indicators, economic indicators, environmental and infrastructural indicators. Each dataset consists of two attributes. The accuracy values and predicted values obtained with Naive Bayes and KNN algorithms in the applications with general indicators including population density and surface area records of the countries are given in Table 6.

Table 6. Accuracy values and predicted values (General Indicators)

	Naive Bayes	KNN
Accuracy	0.90	0.94
Predicted Class	0	1

As can be seen in Table 6, for general indicators, Turkey is in the class of SCO member countries in the application with the Naive Bayes algorithm, while it is in the class of EU member countries in the application with the KNN algorithm.

In the application with 34 different countries' economic indicators consisting of GDP and CPI records, the accuracy values and predicted values obtained with Naive Bayes and KNN algorithms are given in Table 7.

Table 7. Accuracy values and predicted values (Economic Indicators)

	Naive Bayes	KNN
Accuracy	0.90	0.97
Predicted Class	0	0

In the applications where high performance was obtained from both algorithms, it was observed that Turkey was in the class of SCO member countries in terms of economic indicators.

The accuracy values and predicted values obtained with Naive Bayes and KNN algorithms in the application with social indicators consisting of health and education expenditures, which are considered to evaluate the socioeconomic status of states, are given in Table 8.

Table 8. Accuracy values and predicted values (Social Indicators)

	Naive Bayes	KNN
Accuracy	0.62	0.79
Predicted Class	1	0

As can be seen in Table 8, lower accuracy values were obtained in the applications made with the dataset containing social indicators compared to the applications made with the datasets containing general indicators and economic indicators. In the application with the Naive Bayes algorithm, Turkey was positioned in the class of EU member countries, while in the application with the KNN algorithm, Turkey was positioned in the class of SCO member countries.

Finally, the accuracy and predicted values obtained in the applications with environmental and infrastructural indicators, including records on internet usage and per capita energy supply, are given in Table 9.

Table 9. Accuracy values and predicted values (Environmental and Infrastructural Indicators)

	Naive Bayes	KNN
Accuracy	0.54	0.85

Predicted Class	1	1
-----------------	---	---

With 5 different datasets, the performance metrics and predicted values obtained in the applications vary. In order to convey this situation as a whole, the accuracy values and predicted values obtained with Naive Bayes and KNN algorithms for 5 different datasets are given in Table 10.

Table 10. Accuracy values and predicted values

Group	Algorithm	Accuracy	Turkey's class
Indicators	Naive Bayes	0.81	EU
	KNN	0.94	EU
General Indicators	Naive Bayes	0.90	SCO
	KNN	0.94	EU
Economic Indicators	Naive Bayes	0.90	SCO
	KNN	0.97	SCO
Social Indicators	Naive Bayes	0.62	EU
	KNN	0.79	SCO
Environmental and Infrastructural Indicators	Naive Bayes	0.54	EU
	KNN	0.85	EU

4. Conclusion

Despite long negotiations, reforms and harmonization packages, Turkey's EU accession process, which has not been finalized, has brought about various debates. Turkey's membership status in other international organizations is being evaluated since the membership process has not yielded a final result. In 2011, the SCO, which was applied for full membership and was accepted as a dialogue country, is one of these organizations.

In this study, a dataset consisting of various indicators of EU and SCO member countries was created with the aim of estimating Turkey's proximity to EU and SCO member countries. Naive

Bayes and KNN algorithms were applied to the dataset. In addition, four different groups were created for the evaluation of various indicators and different applications were made with a total of five different datasets.

In the applications made with the dataset consisting of records on surface area, population density, CPI, GDP, education expenditures, health expenditures, internet usage and energy supply per capita, Turkey is positioned in the class of EU member states. In line with the high performance metrics obtained from the applications with the dataset including all indicators, it can be said that Turkey is close to the EU in terms of general indicators.

In two different applications made with the dataset consisting of the population density and surface area records of the countries, it was observed that Turkey was positioned in different classes. While the population density of countries such as Finland, Latvia and Sweden in the class of EU member countries is low, the population density of Malta, the Netherlands and Belgium in the same class is high. Similarly, in the class of SCO member countries, India and Pakistan have high population densities while Kazakhstan and Kyrgyzstan have low population densities. It can be said that the difference in the result values obtained from the algorithms is due to this situation.

In the application with the dataset including education and health expenditures, the Naive Bayes algorithm achieved lower performance than the KNN algorithm. In the application with the KNN algorithm, it was observed that Turkey was positioned in the class of SCO member countries in terms of social indicators. While the average annual health expenditure of EU member countries is 8.21%, the average annual health expenditure of SCO member countries is 5.1%. Similarly, while the average education expenditure for EU member countries is 4.96%, the average for SCO member countries is 3.7%. The fact that Turkey's health expenditures are 4% and education expenditures are approximately 3% is similar to the result obtained in the application with the KNN algorithm. In addition, Iran and Kyrgyzstan allocate more to health expenditures than other SCO member countries.

High performance was obtained for both algorithms in the applications with the dataset including CPI and GDP records. In the applications with economic indicators, Turkey is positioned in the class of SCO member countries. In terms of economic indicators, Turkey is in the class of SCO member countries, while in terms of environmental and infrastructural indicators, Turkey is in the class of EU member countries. The same result was obtained for two different algorithms in the applications with environmental and infrastructural indicators.

It is important to process and transform raw data obtained from various sources in different disciplines into meaningful data. Processing and transforming data into information contributes to decision-making processes. In this study, machine learning algorithms were applied to the dataset created in line with the data obtained from the search engine provided by the United Nations System. In this direction, it is aimed to demonstrate the applicability of machine learning algorithms in forecasting applications involving different datasets. In addition, this study is expected to contribute to interdisciplinary studies using machine learning algorithms.

Ethics in Publishing

There are no ethical issues regarding the publication of this study.

References

- [1] Kut, G., (2019) Uluslararası sistem ve kurallara dayalı dünya düzeni: çok taraflı denge arayışları, Boğaziçi Üniversitesi-TÜSİAD Dış Politika Forumu Araştırma Raporu.
- [2] Danzer, A. M., Dietz, B., Gatskova, K., Schmillen, A., (2014) Showing off to the new neighbors? Income, socioeconomic status and consumption patterns of internal migrants, *Journal of Comparative Economics*, 42(1), 230-245.
- [3] Frischmann, B. M., (2012) *Infrastructure: The social value of shared resources*, Oxford University Press.
- [4] Zucconi, M., (2009) The impact of the EU connection on Turkey's domestic and foreign policy, *Turkish Studies*, 10(1), 25-36.
- [5] Müftüler-Baç, M., (2020) Turkish foreign policy, its domestic determinants and the role of the European Union, In *Turkey and the EU: Accession and Reform* (pp. 71-82), Routledge.
- [6] Özer, M. A., (2009) Avrupa Birliği'ne tam üyeliğin eşliğinde Türkiye, *Yönetim ve Ekonomi Dergisi*, 16(1), 89-105.
- [7] Uysal, C., (2001) Türkiye-Avrupa Birliği ilişkilerinin tarihsel süreci ve son gelişmeler, *Akdeniz İ.İ.B.F. Dergisi*, 1(1), 140-153.
- [8] Martin, N., (2019) From containment to realpolitik and back again: A realist constructivist analysis of Turkey–EU relations and the migration issue, *JCMS: Journal of Common Market Studies*, 57(6), 1349-1365.
- [9] Khaleqi, Z. A., Oghli, J. S., (2021) Şangay İşbirliği Örgütü ve Türkiye'nin olası ilişkileri, *Pearson Journal*, 6(12), 107-116.
- [10] Yener, M. C., (2013) Küresel düzende yeni arayışlar: Şangay İşbirliği Örgütü ve Türkiye, *Uluslararası Ekonomik Sorunlar*, 13 (46), 71-91.
- [11] Özalp, M., (2019) Türkiye'nin Şanghay İşbirliği Örgütü'ne olası üyeliğinin Avrasya politikasına etkileri, *Manas Sosyal Araştırmalar Dergisi*, 8(4), 3439-3469.
- [12] Günay, E., Çetiner, S., Sevinç, S., Kütükçü, E., (2019) Tarihi İpek Yolundan Modern İpek Yolu Projesine: Türkiye-Çin Ekonomik İşbirliği Çerçevesinde Orta Koridor ile Kuşak ve Yol Girişimi, *Kahramanmaraş Sütçü İmam Üniversitesi İktisadi ve İdari Bilimler Fakültesi Dergisi*, 9(2), 157-175.

- [13] Saygın, D, Erdem, A. D., (2021) Avrupa Birliği'ne katılım sürecinin Türkiye siyasetine yansımaları: alternatif örgütler, *Uluslararası İlişkiler ve Diplomasi*, 4(1), 80-107.
- [14] Ongan, E., (2021) Avrupa Birliği ve Şangay İşbirliği Örgütü Türkiye ilişkilerinin değerlendirilmesi, *The Journal of Academic Social Science*, (112), 259-266.
- [15] Katagiri, A., Min, E., (2015) Identifying threats: Using machine learning in international relations, In annual meeting of the American Political Science Association.
- [16] Whang, T., Lammbrau, M., & Joo, H. M., (2018) Detecting patterns in North Korean military provocations: what machine-learning tells us, *International Relations of the Asia-Pacific*, 18(2), 193-220.
- [17] Doğan, S., Türe, H., (2022) Makine öğrenmesi teknikleri ile ülke riski tahmini, *Fiscaoeconomia*, 6(3), 1126-1151.
- [18] Altaş, D., Gülpınar, V., (2012) Karar ağaçları ve yapay sinir ağlarının sınıflandırma performanslarının karşılaştırılması: Avrupa Birliği örneği, *Trakya University Journal of Social Science*, 14(1).
- [19] Vaibhav, S., (2020) Predicting success of terrorist attack and extent of its economic impact using data mining, *International Journal for Research in Applied Science and Engineering Technology*, 8(5), 1965-1972.
- [20] Zhang, H., (2004) The optimality of Naive Bayes. *AA*, 1(2), 3.
- [21] Chandra, B., Gupta, M., (2011) An efficient statistical feature selection approach for classification of gene expression data. *Journal of biomedical informatics*, 44(4), 529-535.
- [22] Cover, T., Hart, P., (1967) Nearest neighbor pattern classification. *IEEE Transactions on Information Theory*, 13(1), 21-27.